Transactions of the ASME

Journal of Engineering for Power (ISSN 0022-0825) is edited and published quarterly at the offices of The American Society of Mechanical Engineers, United Engineering Center, 345 E. 47th St., New York, N. Y. 10017. ASME-TWX No. 710-581-5267, New York. Second Class postage paid at New York, N.Y., and at additional mailing offices.

CHANGES OF ADDRESS must be received at Society headquarters seven weeks before they are to be effective. Please send old label and new address.

PRICES: To members, $30.00, annually; to nonmembers, $60.00. Single copies, $20.00 each. Add $5.00 for postage to countries outside the United States and Canada.

INDEXED by the Engineering Index, Inc.

Journal of Engineering for Power

Published Quarterly by The American Society of Mechanical Engineers
VOLUME 103 • NUMBER 2 • APRIL 1981

257 Influence of Mach Number and End Wall Cooling on Secondary Flows in a Straight Nozzle Cascade (80-GT-52)
C. H. Sieverding and Ph. Wilputte

265 A New Approach for Erosion Prediction Due to Fly Ash (80-GT-96)
R. Kotwal and W. Tabakoff

271 On the Pressure Losses Due to the Tip Clearance of Centrifugal Blowers (80-GT-139)
M. Ishida and Y. Senoo

279 Vorticity Modeling of Blade Wakes behind Isolated Annular Blade-Rows: Induced Disturbances in Swirling Flows (80-GT-140)
C. S. Tan

288 Rotordynamic Instability in Centrifugal Compressors—Are All the Excitations Understood? (80-GT-149)
J. M. Vance and F. J. Laudadio

294 Effect of Sodium, Potassium, Magnesium, Calcium, and Chlorine on the High Temperature Corrosion of In-100, U-700, IN-792, and MAR M-509
C. E. Lowell, S. M. Sidik, and D. L. Deadmore

308 Advances in Labyrinth Seal Aeroelastic Instability Prediction and Prevention (80-GT-151)
D. R. Abbott

313 The Effect of Aerodynamic Phase Lag on the Twin Vibration Mode Model of Aeroengine Fan Flutter (80-GT-166)
R. A. J. Ford

319 Redesign of Structural Vibration Modes by Finite-Element Inverse Perturbation (80-GT-167)
K. A. Stetson and I. R. Harrison

326 Blade Excitation by Elliptical Whirling in Viscous-Damped Jet Engines (80-GT-168)
N. Klompas

331 Creep Rupture Behavior of Selected Turbine Materials in Air, Ultra-High Purity Helium, and Simulated Closed Brayton Helium Working Fluids (80-GT-173)
R. L. Ammon, L. R. Eisenstatt, and G. O. Yatsko

338 Preliminary Design Analysis of a Catalytic Ceramic Structure in a Turbine Combustor (78-WA/GT-10)
W. S. Y. Hung, W. H. Dickson, and S. M. DeCorso

345 Averaging Methods for Determining the Performance of Large Fans from Field Measurements (80-JPGC/Pwr-1)
P. M. Gerhart

348 Utility Operations: An Effective and Economic Approach to Operator Training (80-JPGC/Pwr-2)
B. C. Studley

358 Vibration in Nuclear Heat Exchangers Due to Liquid and Two-Phase Flow (80-C2/NE-4)
W. J. Heilker and R. Q. Vincent

367 Calculations of Three-Dimensional, Viscous Flow and Wake Development in a Centrifugal Impeller
J. Moore and J. G. Moore

SYMPOSIUM PAPERS: *MEASUREMENT METHODS IN ROTATING COMPONENTS OF TURBOMACHINERY*

373 Preface
B. Lakshminarayana and P. Runstadler, Jr.

374 Techniques for Aerodynamic and Turbulence Measurements in Turbomachinery Rotors
B. Lakshminarayana

393 Measurements of the Mean Flow Velocity and Velocity Fluctuations at the Exit of an FC Centrifugal Fan Rotor
D. Raj and W. B. Swim

400 Measurement of Turbine Rotor Blade Flows
R. P. Dring and H. D. Joslyn

406 Conventional Probes for the Relative Flow Measurement in a Turbomachinery Rotor Blade Passage
N. Sitaram, B. Lakshminarayana, and A. Ravindranath

415 Experimental Analysis Methods for Unsteady Flow in Turbomachines
R. Larguier

424 Efficient Laser Anemometer for Intra-Rotor Flow Mapping in Turbomachinery
J. A. Powell, A. J. Strazisar, and R. G. Seasholtz

(*continued on page 264*)

430 Laser Anemometer Measurements in a Transonic Axial Flow Compressor Rotor
A. J. Stazisar and J. A. Powell

438 Optical Advances in Laser Transit Anemetry
A. E. Smart, D. C. Wisler, and W. T. Mayo, Jr.

445 Mean Flow Measurements Near the Plane of an Open Rotor Operating with an Inlet Velocity Gradient
M. L. Billet

451 Flow Instability at the Inlet of a Centrifugal Compressor
G. Flueckiger and A. Melling

457 Laser-Optical Blade Tip Clearance Measurement System
J. P. Barranger and M. J. Ford

461 Flutter Spectral Measurements Using Stationary Pressure Transducers
A. P. Kurkov

468 Temperature and Pressure Measurement Techniques for an Advanced Turbine Test Facility
F. G. Pollack and R. P. Cochran

473 The Design, Development and Operation of Gas Turbine Radio Telemetry Systems
J. G. B. Worthy

ANNOUNCEMENTS

307 Change of address form for subscribers

480 Information for Authors

C. H. Sieverding
Associate Professor.

Ph. Wilputte
Postgraduate Student

von Karman-Institute
Genese, Belgium

Influence of Mach Number and End Wall Cooling on Secondary Flows in a Straight Nozzle Cascade

This paper describes the results of an experimental study of the effect of Mach number and end wall cooling on the secondary flow in a straight nozzle cascade with an aspect ratio of $h/c = 0.83$. The tests were performed for the outlet Mach numbers $M_2 = 0.1$, 0.6 and 0.8. The cooling tests are done for one specific cooling configuration consisting of three double rows of injection holes positioned at the leading edge, inside the blade passage and in the throat. The flow was injected into the direction of the free stream direction. The tests are carried out for two cooling mass flow ratios: $\dot{m}/\dot{m}_{tot} = 0.02$ and 0.045. The corresponding injection to main flow pressure ratios are: 1.0, 1.16 for $M_2 = 0.6$ and 1.0, 1.26 for $M_2 = 0.8$. The flow surveys are made with three-directional pressure probes.

Introduction

A few years ago a comprehensive experimental program was started at VKI with the aim of understanding secondary flows in turbine bladings more clearly. The combination of flow visualizations (oil flow and laser light sheet techniques) and extensive five hole pressure probe measurements resulted in a much improved idea of the three-dimensional flow development through straight cascades [1]. This fundamental low speed test program on straight cascades was continued in order to further investigate the effect of blade loading and blade loading distribution, the results of which will be reported in the near future.

The present paper deals with two other aspects of secondary flows:

1 the extension of low speed test data to high speed flow conditions with comparison of results

2 the effect of a specific side wall film cooling system on secondary flows

The problems of high speed tests are in general twofold: (1) restriction of the size of the test program because of limitations of the available high pressure air supply, (2) increased probe blockage effect at high Mach numbers amplified by the fact that the limitations in air supply imposed a scaling down of the blade dimensions with respect to those used at low speed. This limitation with regard to downstream measurements is not a real handicap in the sense that we expect that the essential features of the three-dimensional flow development throughout the cascade are preserved when passing from incompressible to compressible flow cases.

The influence of the side wall cooling on the secondary flows depends of course on the amount of coolant flow, its distribution across the blade passage and the injection flow geometry. The tests described in this paper refer only to one particular cooling configuration and can therefore not give a general solution to the problem. However, the results of this particular configuration can be used to give an idea of the order of magnitude of the injection effect on both the losses and outlet flow angles and give some guidance for future research work in this area.

Experimental Apparatus

Test Facility. The test facility used for this investigation is a high speed blowdown tunnel with exhaust to atmospheric pressure via a diffuser (Fig. 1(*a*)). The test section is formed by two rotatable steel or perspex side walls, between which the blades are mounted, and wooden cascade section end walls. A sudden area enlargement in pitchwise direction is located at the cascade outlet. The maximum test section dimensions are: 50 mm ($\perp$ blade height) × 200 mm.

Ideally, the end wall cooling tests should be done with coolant injection through both side walls. Such an arrangement was not feasible in the present case due to an interference of the probe traversing mechanism with the side wall coolant injection systems.

Hence, the coolant flow was injected only through the wall opposite to the one through which the probe is introduced into the test section. Figure 1(*b*) shows a photograph of the test section with the probe traversing mechanism in its place. The side wall with the probe carriage is made out of perspex which allows an easy control of the probe position in the test section. The opposite side wall with the coolant injection system is made out of steel.

Blade and Cascade Geometry. All tests reported herein are carried out on the same nozzle blade section which was already investigated in [1] at low speed flow conditions. The blade is in fact the root section of a NACA annular nozzle cascade [2].

The cascade geometry is as follows:

chord length $c = 60$ mm
space to chord ratio $s/c = 0.725$
stagger angle $\gamma = 42.5$ deg
inlet blade angle $\beta_1' = 10$ deg
arc cos $o/s = 67.7$ deg
blade height $h = 50$ mm
aspect ratio $h/c = 0.83$

Note: the chord length of the nozzle section tested previously at low

Contributed by the Gas Turbine Division and presented at the Gas Turbine Conference and Products Show, New Orleans, La., March 10–13, 1980, of THE AMERICAN SOCIETY OF MECHANICAL ENGINEERS. Manuscript received at ASME headquarters December 11, 1979. Paper No. 80-GT-52.

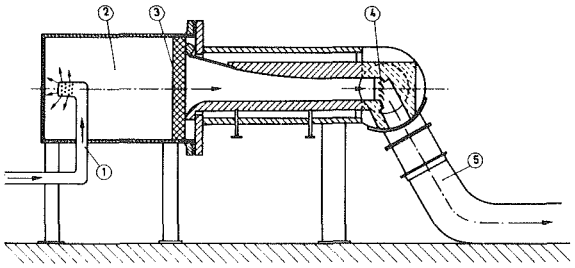

Fig. 1(*a*) High speed cascade tunnel

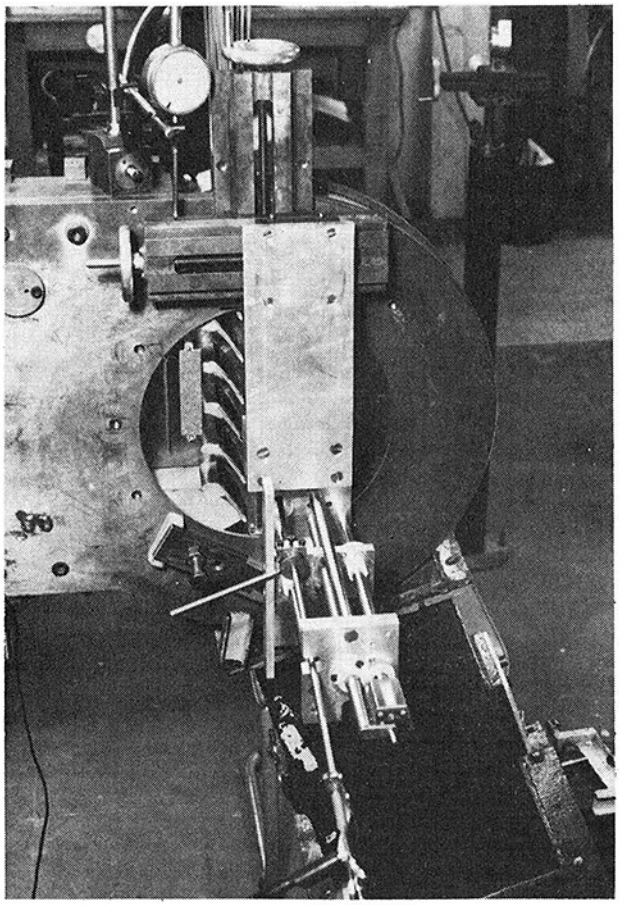

Fig. 1(*b*) View on test section

speed was $c = 120$ mm. With a corresponding blade height of $h = 100$ mm, the aspect ratio h/c was the same for the low and the high speed tests.

Measuring Technique. Due to the reduced chord length it was decided to use a four-hole probe (Fig. 2) rather than a five-hole probe to make possible measurements closer to the side wall. With tubes of 0.4 mm outer diameter the first measurement was taken at approximately 0.3 mm from the wall. However, because of slight vibrations of the probe head combined with a slight bending of the probe stem, the general error in the positioning of the probe is estimated to be of the order of ±0.1 mm.

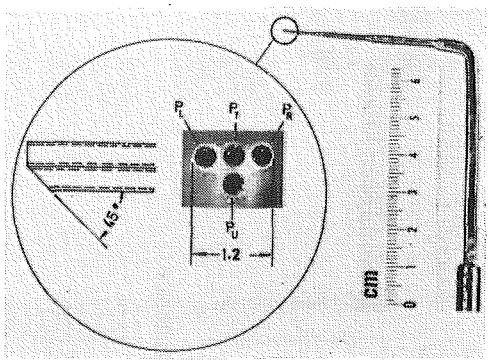

Fig. 2 Four-hole probe

The static pressure is measured by means of side wall pressure tappings. The estimated experimental uncertainties associated with the four-hole probe are as follows:
linear position: ±0.1 mm
flow angles: ±0.5 deg (except near the wall)
losses: ±10 percent of absolute loss value.
The test data are recorded on magnetic tape and processed on a MITRA 15 computer. The measurements near the wall are corrected for the influence of the velocity gradient.

Test Program and Test Conditions. The measuring planes are indicated in Fig. 3 for both the present high speed tests and the previous low speed tests. In each plane 15 equidistant spanwise traverses were made, each traverse containing 17 measuring points from 0.3 mm wall distance to mid-span.

Tests were made at outlet Mach numbers of $M_2 = 0.6$ and 0.8. The traverses at $M_2 = 0.8$ were limited to the last measuring plane because of expected probe blockage effects. The traverses within the blade passage were made only for the tests with a solid side wall; i.e., without cooling ejection.

The tests with side wall cooling were done for two cooling mass flow rates. Details about the cooling system are given later. All tests are done with a natural inlet end wall boundary developing over an inlet duct length of approximately 1 m. The test conditions are summarized in Table 1.

The inlet end wall boundary layer profiles are very similar for all three test conditions (Fig. 4). In all cases, the end wall boundary layer profile is fully turbulent.

Contrary to the low speed tests in reference [1] which were performed with a tripping wire on the blade suction side slightly downstream of the suction side velocity peak ($x/c \cong 0.34$), no tripping wire was used for the high speed tests.

Tests without Cooling

The test results are presented in the form of the kinetic energy loss coefficient:

$$\zeta = \frac{V^2_{2,IS} - V_2^2}{V^2_{2,IS}}$$

Nomenclature

c = chord length
h = blade height
M = Mach number
o = throat
P = pressure
s = space
V = velocity
X,Y,Z = coordinates
β = flow angle
β' = blade angle
$\Delta\beta$ = angle difference with respect to angle at mid span
δ = boundary layer thickness
δ^* = displacement thickness
ζ = losses
κ = specific heat ratio
ν = dynamic viscosity

Subscripts

0 = total
1 = upstream
2 = downstream
ax = axial
c = coolant air
ℓ = local
p = profile
s = static, secondary
MS = mid span
IS = isentropic

Superscripts

$\bar{}$ = pitchwise averaged
$\bar{\bar{}}$ = pitch- and spanwise averaged

and the over- or underturning angle

$$\Delta\beta = \beta - \beta_{MS}$$

where β_{MS} is the flow angle at mid-blade height.

The spanwise and pitchwise averaged losses over a whole measuring plane can be computed as

$$\bar{\bar{\zeta}} = \frac{1 - (\overline{\overline{P_{0,\ell}}}/\overline{\overline{P_{01,MS}}})^{(\kappa-1)/\kappa}}{1 - (\overline{P_{s_2}}/\overline{\overline{P_{01,MS}}})^{(\kappa-1)/\kappa}}$$

Note: one bar $\underline{\wedge}$ pitchwise averaged values and two bars $\underline{\underline{\wedge}}$ pitch- and spanwise averaged values.

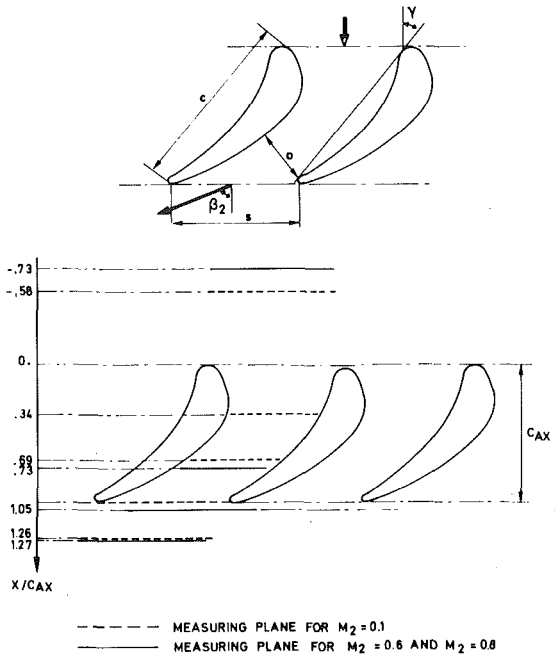

Fig. 3 Cascade and location of measurement planes

Table 1

Outlet Mach number M_2	0.6	0.8	0.1 (ref. [1])
-relative inlet end wall displacement thickness δ^*_1/h	0.0398	0.0393	0.0375
-upstream total pressure P_{01} [bar]	1.2	1.35	1.0
-upstream total temperature T_{01} [K]	280	280	291
-Reynolds number $(c.\ V_2)/\nu_2$	1.1×10^6	1.76×10^6	2.6×10^5
-turbulence intensity Tu [percent]	1	1	0.5

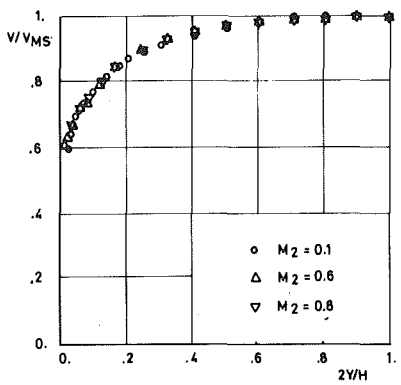

Fig. 4 Inlet end wall boundary layer profiles

The above expression includes the losses due to the inlet boundary layer. If we are only interested in the growth of the losses through the cascade, the following expression is more suitable:

$$\bar{\bar{\zeta}}' = \frac{1 - (\overline{\overline{P_{0,\ell}}}/\overline{\overline{P_{01}}})^{(\kappa-1)/\kappa}}{1 - (\overline{P_{s_2}}/\overline{\overline{P_{01,MS}}})^{(\kappa-1)/\kappa}}$$

The growth of the secondary losses is then

$$\overline{\overline{\zeta'}}_s = \bar{\bar{\zeta}}' - \bar{\zeta}_{MS}$$

All losses are mass averaged values.

The static pressure P_{s_2} used for the evaluation of the above loss terms is taken from side wall pressure tappings. The assumption is made that the spanwise variation of the static pressure is negligible.

Losses. The growth of the secondary losses through the cascade is presented in Fig. 5 for the outlet Mach numbers M = 0.1, 0.6 and 0.8. The figure shows that the increase of secondary losses starts for both low speed and high speed flows at around $x/c_{ax} = 0.6$.

Basically, one might ascribe three possible contributions to an increase in secondary losses: (1) boundary layer growth on the side wall; (2) corner losses, and (3) losses due to the interference of the end wall boundary layer with the suction side boundary layer. In reference [1] it was already shown that there is nothing like a continuously growing end wall boundary layer. In fact, within the blade passage a considerable amount of the incoming end wall boundary layer is removed from the end wall under the influence of the transverse pressure gradient and pushed on to the blade suction surface, leaving behind a very thin end wall boundary layer. However, at the cascade exit the end wall boundary layer increases again very rapidly and within a short distance behind the trailing edge plane the end wall boundary layer losses reach approximately the same level as at the cascade inlet. An attempt to illustrate this is made in Figure 6 which presents the spanwise loss distribution upstream and downstream of the cascade for the outlet Mach number $M_2 = 0.6$. For comparison reasons the

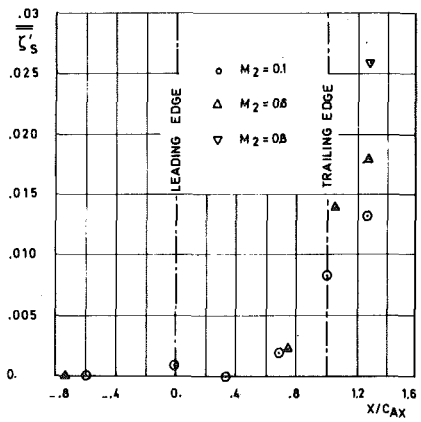

Fig. 5 Growth of secondary losses through cascade

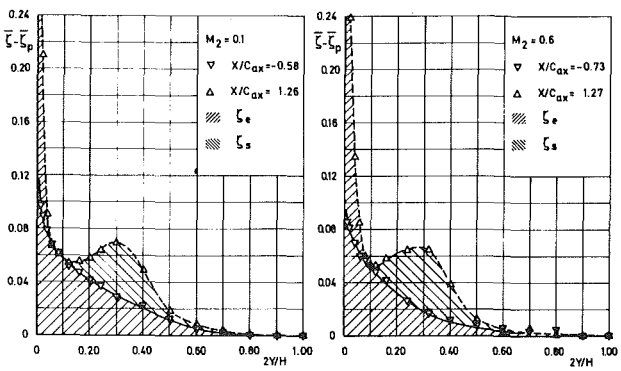

Fig. 6 Spanwise distribution of upstream and downstream end wall losses

measured downstream loss distributions were corrected by subtracting everywhere along the span the profile losses measured at mid span. The downstream losses can be decomposed into two parts as indicated in the figure: an end wall boundary layer part ζ_e (including the corner losses) presented by the area //// and superimposed on it a loss fraction ζ_s (area \\\\) which represents the sum of the low energy boundary layer material carried over from the end wall to the blade suction side and the interference losses due to the interaction of this end wall boundary layer material with the suction side flow. Due to the fact that the downstream end wall losses ζ_e are nearly equal to the losses of the upstream end wall boundary layer, except very close to the wall, the term ζ_s can be looked at as representing the amount of secondary losses generated by the cascade. These losses ζ_s will be redistributed with increasing downstream distance over the whole blade height while at the same time the end wall boundary layer and the associated end wall losses continue to increase. (The term "annulus loss" in a turbine stage should be limited strictly to this increase of the end wall boundary layer loss above the level existing at the blade inlet).

The downstream measurements in Fig. 5 show a considerable varaiation of the losses with the outlet Mach number. However, due to the fact that the Mach number variation involves important Reynolds number variation the question arises whether the loss variation is a Mach number or a Reynolds number effect. The strong increase of Re with M_2 would suggest a decrease of losses rather than an increase which is in fact shown by the data, although one might argue that what applies to the two-dimensional cascade flow does not necessarily apply to secondary flows where the end wall boundary layer undergoes very drastic changes.

As far as the Mach number effect is concerned, one can think of at least three different contributions to the losses:

1 The increase of the outlet Mach number results in a change of the pressure gradient across the blade passage causing both a higher transport of end wall boundary layer material to the blade suction side and increased interference losses due to the interaction between this cross flow and the main flow.

2 The reorganization of the end wall boundary layer right behind the trailing edge should depend on changes of the pitchwise and spanwise pressure gradients, which in turn are Mach number dependent.

3 In spite of the almost identical inlet end wall boundary layer displacement thickness δ^*/h for all three cases, the inlet losses differ considerably for the three outlet Mach numbers, when referring the inlet end wall energy deficit to the outlet flow conditions. In the present case one obtains for the inlet losses defined in the above way:

M_2	0.1	0.6	0.8
$\bar{\zeta}$	0.019	0.015	0.011

Hence the loss increase through the cascade is calculated using different inlet end wall losses which leads to an over-estimation of the Mach number effect. The last statement indicates that there is no easy way to determine in a correct way the secondary losses generated in a cascade.

Figure 7 shows the downstream spanwise secondary loss distribution for all three Mach numbers (these curves include of course the losses due to the inlet end wall boundary layer). Keeping in mind that the inlet boundary layer profiles are very similar for all outlet flow conditions, one can conclude that there is in fact a small Mach number effect, which shows up in the immediate proximity of the wall and in the interference region between the cross flow and the main flow which is characterized by the loss maximum at around $2y/h \approx 0.25$ to 0.30.

The full details of the downstream losses (measuring plane x/c_{ax} = 1.26–1.27) are shown in the loss contour plots in Fig. 8.

The numbers on the iso-loss lines are percentages of losses. The losses are defined as

$$\zeta = \frac{1 - (P_{0(y,z)}/\overline{P_{01,MS}})^{(\kappa-1)/\kappa}}{1 - (\overline{P_{s_2}}/\overline{P_{01,MS}})^{(\kappa-1)/\kappa}}$$

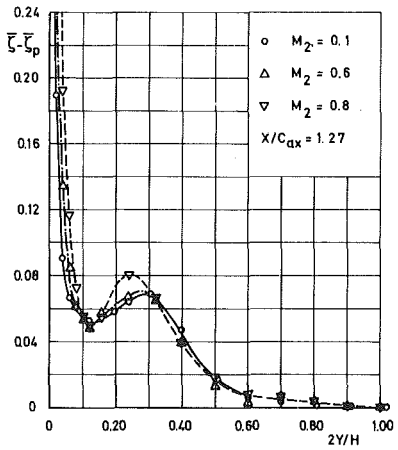

Fig. 7 Comparison of spanwise secondary loss distribution for three outlet Mach numbers

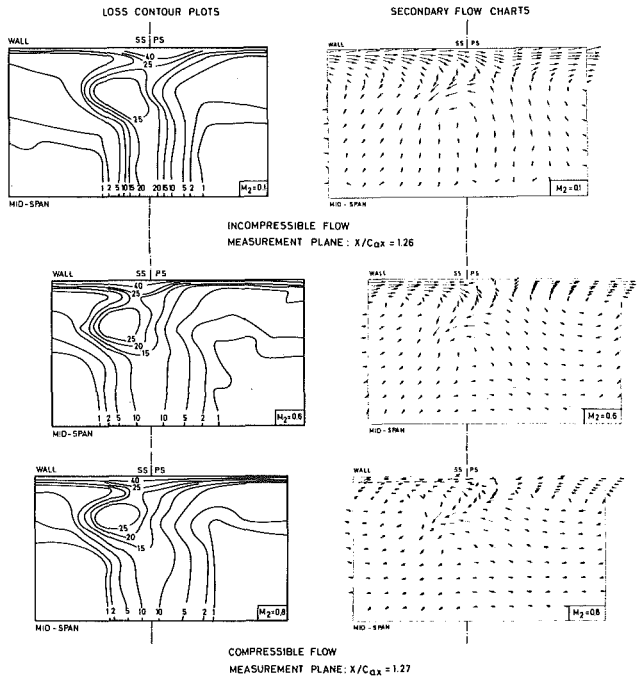

Fig. 8 Loss contour plots and secondary flow charts

The most striking aspect of the loss contour plots is of course the low energy region situated on the suction side of the wake center-line at a wall distance of about 25 → 30 percent of the half blade height. As indicated before, this loss core is the result of the combined effect of low energy material transfer from the end wall to the blade suction side and the interaction of this flow with the main flow over the blade. The loss core is apparently strongest for $M_2 = 0.1$. The reason for this is found in the higher level of the underlying profile losses.

The shape of the 40 percent iso-loss line for $M_2 = 0.1$ indicates the presence of corner losses in the downstream measuring plane. With increasing Mach number, this phenomenon tends to disappear.

Secondary Flow Charts and Spanwise Outlet Flow Angle Distribution. For the definition of the secondary velocity component let us refer to Fig. 9. Use is made of a coordinate system in which in a given point P the x-axis is aligned with the mid span velocity at the same pitchwise position, y points into the spanwise direction and the coordinate z is normal to the x-y plane such that the x,y,z coordinates form a right handed system. Then the secondary velocity vector $\vec{V}_s$ at point P will be defined as the projection of the velocity vector $\vec{V}$ at point P onto the plane y-z. For the presentation in Fig. 8, the secondary flow vector $\vec{V}_{s,z}$ is turned around the y-axis until it

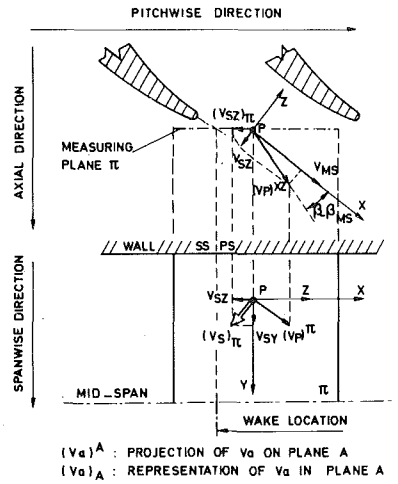

Fig. 9 Definition of secondary velocity components

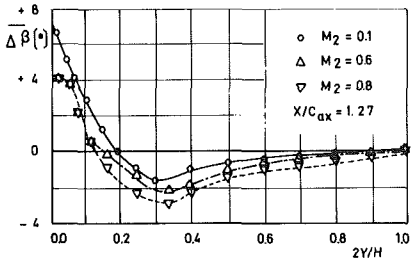

Fig. 10 Spanwise angle distribution

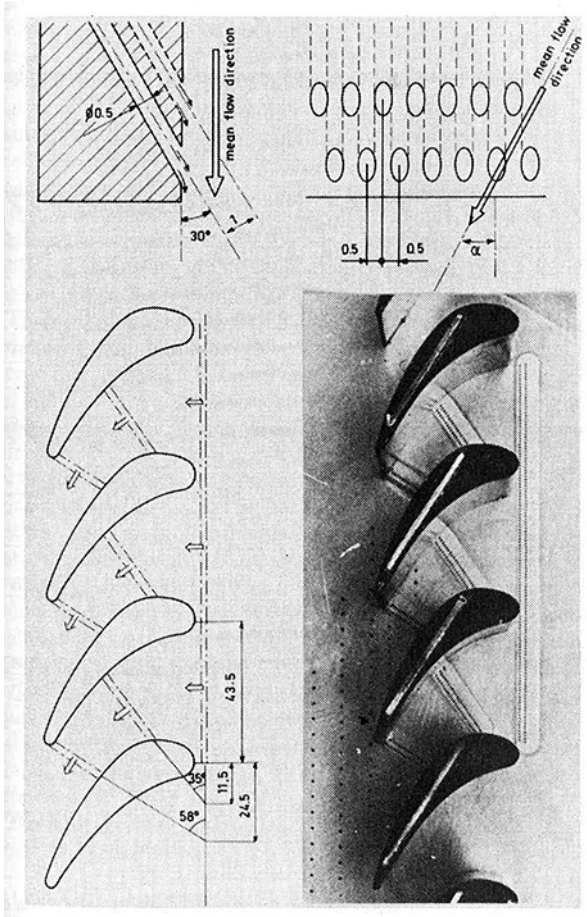

Fig. 11 End wall cooling configuration

lies in the measuring plane such that the secondary velocity charts show the real secondary velocities and not a projection of the secondary velocity from the y-z plane onto the measuring plane.

It has to be noticed that the scale of the velocity vectors in Fig. 8 is not the same for the incompressible and the compressible flow cases.

The passage vortex is of course the predominant flow aspect. The center of the passage vortex moves slightly towards the wall with increasing Mach number, which explains the displacement of the low energy core in the same direction as shown in Fig. 7. The incompressible flow case indicates the existence of a second vortex in the wake region which turns opposite to the passage vortex. In reference [1], the hypothesis was put forward that this vortex motion could be associated with the trailing edge vortex and the remaining vorticity of the suction side leg of the leading edge vortex. The traces of this vortex disappear, however, with increasing Mach number.

Some significant differences between the incompressible and compressible flow cases seem to exist with respect to the secondary velocity vector near the end wall on the pressure side of the wake. For both $M_2 = 0.6$ and 0.8 a singular point is noticed which interrupts the continuity of the velocity vectors along the wall observed for $M_2 = 0.1$. The overall effect is apparently a decrease of the overturning (i.e., positive value of $\Delta\beta$) as shown in the spanwise angle distribution in Fig. 10.

A decrease of the overturning near the wall should for continuity reasons entail a decrease of the underturning towards mid span. The test data show, however, on the contrary a further increase of the underturning for the compressible flow cases. This situation is not well understood.

Tests with End Wall Cooling

Cooling Configuration. The cooling configuration consists of three inserts in the wall with double rows of holes positioned at: (a) just ahead of the leading edge; (b) inside the blade passage and (c) in the throat (Fig. 11). All holes are inclined at an angle of 30 deg with respect to the wall. The holes for each injection insert are parallel to each other. The axis of the holes form a right angle with the insert and point into the mean direction of the potential flow stream lines. Both the lateral spacing between two holes and the distance between the two rows of holes for each insert is 1 mm. Each insert covers the full passage width. Three out of five blade passages are equipped with these inserts. The schematic of the injection apparatus is shown in Fig. 12. The cooling air supply pressure and temperature is the same for all injection holes.

Figure 13 shows schematically the interference of the coolant flow with the end wall flow. The end wall streamlines were drawn on the basis of oil flow visualizations in reference [1]. The angle difference between the direction of the injected coolant flow and the end wall streamlines could be beneficial for two reasons: (1) a rapid spreading out of the coolant flow and (2) a possible reduction of the cross flow which ultimately might lead to a reduction of the secondary losses.

As mentioned earlier, the blade profile used in these experiments is the root section of a NASA annular nozzle cascade [2]. It is worth noting that the NASA used the mid span section of this vane for side wall coolant studies in an annular cascade configuration. For comparison the coolant configuration used by NASA is shown in Fig. 14 [3].

Test Conditions and Test Program. The test conditions were in general the same as for the solid wall case. Table 2 only gives additional information with respect to the specific character of the tests with side wall cooling.

The numbers for the coolant mass flows refer to an injection through both side walls. In reality, coolant flow was injected only through one side wall. The coolant mass flow is measured with a rota-meter with an accuracy of ±5 percent.

The downstream flow was surveyed for $M_2 = 0.6$ in the measurement planes $x/c_{ax} = 1.05$ and 1.27 and for $M_2 = 0.8$ at $x/c_{ax} = 1.27$ (trailing edge plane: $x/c_{ax} = 1.0$).

Test Results. The influence of the side wall cooling on the span-

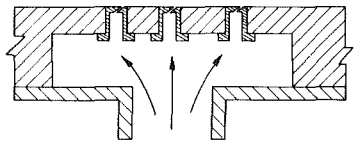

Fig. 12 Schematic of injection apparatus

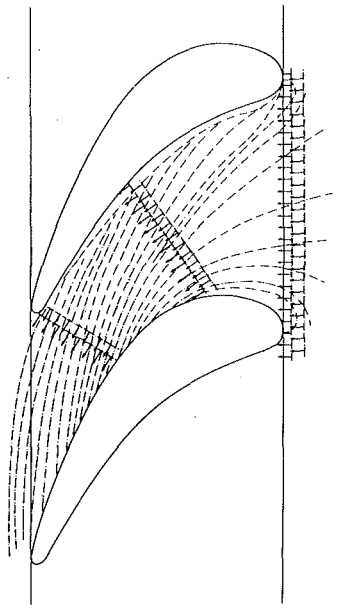

Fig. 13 Coolant flow and end wall streamlines

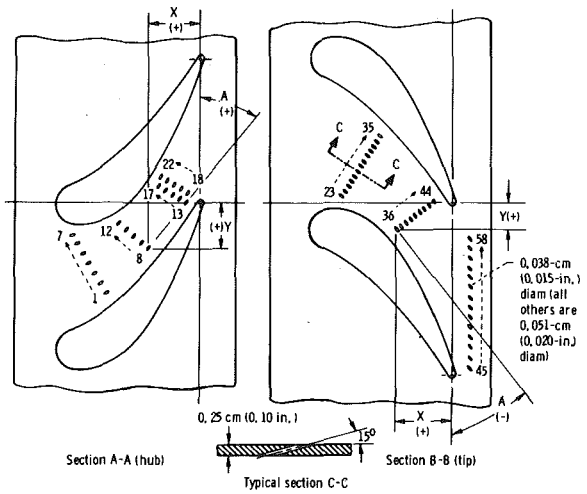

Fig. 14 Cooling configuration of NASA for annular cascade

Table 2

Outlet Mach number M_2	0.6	0.8
-total pressure of main flow, P_{01} [bar]	1.2	1.35
-total pressure of coolant flow, P_{0c} [bar]	1.2; 1.4	1.35; 1.7
-total temperature of main flow, T_{01} [K]	280	280
-total temperature of coolant flow, T_{0c} [K]	280	280
-percentage of coolant mass flow [percent]	2.0; 4.5	2.0; 4.5

wise flow angle and loss distribution at M = 0.6 and 0.8 is presented in Fig. 15. The losses are based on the primary flow conditions and do not take into account the effect of differences between the cooling air supply conditions and the primary flow conditions. Such differences can in fact not be considered for the spanwise loss distribution because it would require a detailed knowledge of the mixing between the coolant and the primary flow. On the contrary, the evaluation of an overall pitch- and spanwise mass averaged loss coefficient allows to take the coolant flow into account. An absolute correct evaluation of the cascade performance would, however, require the knowledge of the coolant conditions at the exit of the injection holes. It should of course be noted that care has to be taken in applying the following results directly to turbine flow. The condition $T_{0c} = T_{01}$ in the present experiment means that the momentum flux ratio between main and coolant flow is not properly simulated.

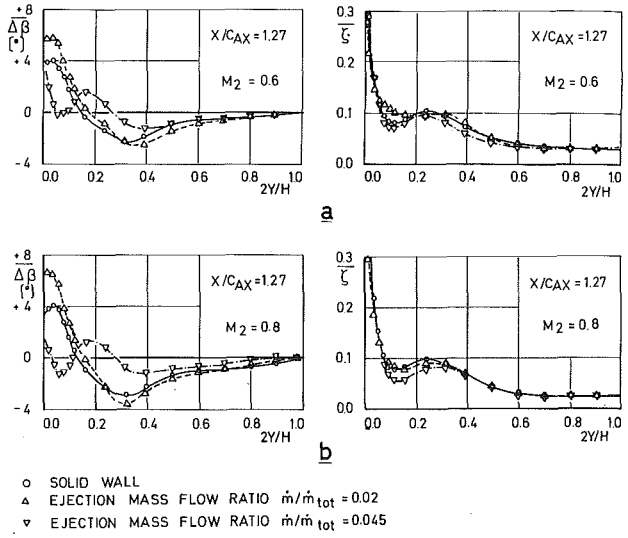

Fig. 15 Influence of end wall cooling on spanwise loss and angle distribution

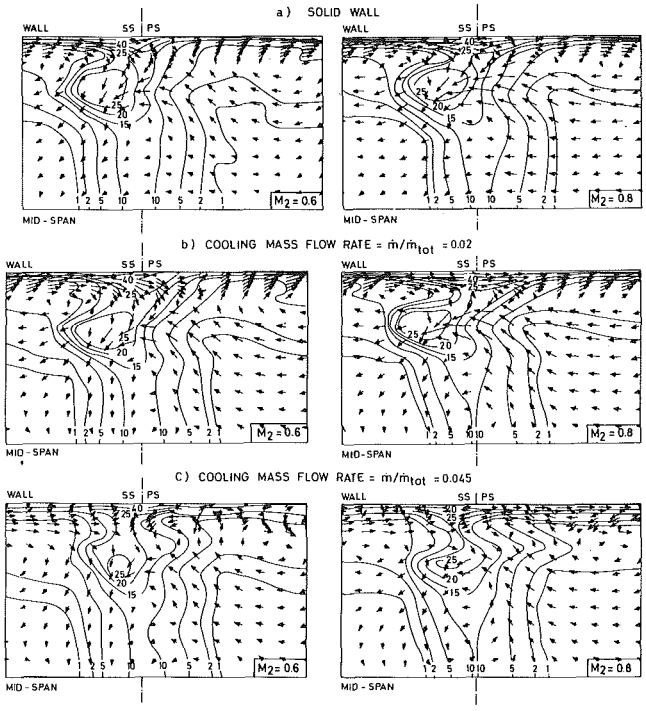

Fig. 16 Secondary flow charts and loss contour plots showing influence of side wall coolant

The most remarkable changes occur for the spanwise flow angle distribution. For the low coolant mass flow rate the influence is limited to the near wall region, where a slight increase of the overturning is observed. This is interesting because in the solid wall case a decrease of the overturning was noticed from $M_2 = 0.1$ to 0.6 and 0.8. Important changes occur for the high injection rate. Both the underturning and overturning are greatly reduced such that the spanwise angle variation deviates very little from the mid span value. This is particularly striking for $M_2 = 0.8$ ($\Delta\beta_{max} \approx \pm 1.3$ deg). The secondary flow chart (Fig. 16) indicates indeed drastic changes with the secondary velocity vectors for $M_2 = 0.8$. These changes affect in turn considerably the iso-loss lines. Compared to the solid wall case, the high loss core on the wake suction side is considerably reduced. The reason is probably that due to the reduced secondary velocities, the transport of low energy material from the end wall to the suction surface has significantly decreased and hence also the interference losses between this cross flow and the main flow over the blade suction side. In addition to this effect there is of course the direct effect of the injected high energy coolant flow.

Contrary to the high coolant mass flow rate ($\dot{m}/\dot{m}_{tot} = 0.045$), the iso-loss lines are little modified by the small coolant mass flow rate ($\dot{m}/\dot{m}_{tot} \approx 0.02$). In the spanwise loss distribution, the losses remain practically unchanged for $M_2 = 0.8$ while at $M_2 = 0.6$ there is even a local increase of losses around the wall distance $2y/h = 0.1$.

Conclusion

The secondary flow losses are a form of mixing and skin friction losses which predictably increase with Mach number. The difficulty with secondary flow losses is that the phenomenon increasing the skin friction losses and enhances the mixing losses is Mach number dependent and is at present not predictable.

The test data also clearly indicate a significant influence of end wall cooling air injection upon the losses and exit air angle distribution. The data suggest that the influence of cooling air should be considered in the selection of the optimum blading angle as well as in the prediction of turbine efficiency. Three cooling air parameters should be considered as significant: the coolant to main stream total pressure ratio, the coolant mass flow ratio and the angle between coolant flow, main flow and end wall boundary layer.

The nonlinear effect of the coolant on both the losses and the outlet of flow angle suggests that we are in presence of an injection pressure ratio effect rather than a mass flow effect. Similar observations have been made for trailing edge coolant ejection.

Acknowledgments

This work was partially sponsored by the European Research Office of the US Army under Grant Number DA ER0-75-G-074. The authors are also grateful to Dr P. McDonald for his interest and his valuable suggestions.

References

1 Marchal, Ph. and Sieverding, C. H., "Secondary Flows within Turbomachinery Bladings," AGARD CP 214, 1977.

2 Whitney, J., et al., "Cold-Air Investigation of a Turbine for High Temperature Engine Application," NASA TN D 3751.

3 Goldman, L. J. and McLallin, K. L., "Effect of End Wall Cooling on Secondary Flows in Turbine Stator Vanes," AGARD CP 214, 1977.

The most remarkable changes occur for the spanwise flow angle distribution. For the low coolant mass flow rate the influence is limited to the near wall region, where a slight increase of the overturning is observed. This is interesting because in the solid wall case a decrease of the overturning was noticed from $M_2 = 0.1$ to 0.6 and 0.8. Important changes occur for the high injection rate. Both the underturning and overturning are greatly reduced such that the spanwise angle variation deviates very little from the mid span value. This is particularly striking for $M_2 = 0.8$ ($\Delta\beta_{max} \approx \pm 1.3$ deg). The secondary flow chart (Fig. 16) indicates indeed drastic changes with the secondary velocity vectors for $M_2 = 0.8$. These changes affect in turn considerably the iso-loss lines. Compared to the solid wall case, the high loss core on the wake suction side is considerably reduced. The reason is probably that due to the reduced secondary velocities, the transport of low energy material from the end wall to the suction surface has significantly decreased and hence also the interference losses between this cross flow and the main flow over the blade suction side. In addition to this effect there is of course the direct effect of the injected high energy coolant flow.

Contrary to the high coolant mass flow rate ($\dot{m}/\dot{m}_{tot} = 0.045$), the iso-loss lines are little modified by the small coolant mass flow rate ($\dot{m}/\dot{m}_{tot} \approx 0.02$). In the spanwise loss distribution, the losses remain practically unchanged for $M_2 = 0.8$ while at $M_2 = 0.6$ there is even a local increase of losses around the wall distance $2y/h = 0.1$.

Conclusion

The secondary flow losses are a form of mixing and skin friction losses which predictably increase with Mach number. The difficulty with secondary flow losses is that the phenomenon increasing the skin friction losses and enhances the mixing losses is Mach number dependent and is at present not predictable.

The test data also clearly indicate a significant influence of end wall cooling air injection upon the losses and exit air angle distribution. The data suggest that the influence of cooling air should be considered in the selection of the optimum blading angle as well as in the prediction of turbine efficiency. Three cooling air parameters should be considered as significant: the coolant to main stream total pressure ratio, the coolant mass flow ratio and the angle between coolant flow, main flow and end wall boundary layer.

The nonlinear effect of the coolant on both the losses and the outlet of flow angle suggests that we are in presence of an injection pressure ratio effect rather than a mass flow effect. Similar observations have been made for trailing edge coolant ejection.

Acknowledgments

This work was partially sponsored by the European Research Office of the US Army under Grant Number DA ER0-75-G-074. The authors are also grateful to Dr P. McDonald for his interest and his valuable suggestions.

References

1 Marchal, Ph. and Sieverding, C. H., "Secondary Flows within Turbomachinery Bladings," AGARD CP 214, 1977.

2 Whitney, J., et al., "Cold-Air Investigation of a Turbine for High Temperature Engine Application," NASA TN D 3751.

3 Goldman, L. J. and McLallin, K. L., "Effect of End Wall Cooling on Secondary Flows in Turbine Stator Vanes," AGARD CP 214, 1977.

DISCUSSION

G. J. Hanus[1]

The authors suggest that a possible benefit of end-wall cooling, in addition to thermal protection, is the dynamic interaction effect of the coolant jets and the end-wall core flow. This effect is manifest through a shifting of the streamlines of the core flow near the end-wall due to a coolant-jet, core-flow streamline deflection phenomenon. Results are shown for both spanwise loss as well as trailing edge flow angle distribution for two end-wall cooling fractional flow rates. These results tend to support the possible hydrodynamic benefit of strategically placed end-wall cooling configurations. A note of caution, however, must be included on how the coolant test condition relates to the reported physics of the primary flow. Results of discharge flow angle and loss distribution for the test cases, in which $T_{01} = T_{0c}$, may not be representative of the distributions one would find in an actual engine application in which $T_{01} \cong 2T_{0c}$.

Thermodynamic and hydrodynamic modeling of high-temperature turbomachinery component flow at reduced flow conditions has been successfully applied for many years [1, 2]. By carefully choosing P_{01}, T_{01} and T_{0c}, proper geometric scaling can produce thermodynamic and hydrodynamic similarity between actual engine conditions and reduced-scale laboratory tests. Although the authors have maintained the proper conditions for local Reynolds number simulation over the blade surfaces (assuming the local Mach number distributions were matched with the modeled NASA cascade), they have failed to simulate realistic end-wall coolant jet/end-wall boundary layer interaction by allowing the total temperature of the coolant and mainstream to be identical. The reported over and underturning of the discharge angle as well as the loss distribution for the two fractional coolant flows would not be representative of what would occur in an actual engine environment at these coolant flow ratios. For the same fractional coolant flow conditions under high-temperature turbine operation, the physics of the coolant jet/end-wall boundary layer flow, though qualitatively similar may be quantitatively dramatically different.

To simulate the proper coolant-jet/end-wall boundary layer interaction, the following constraints must be met.

$$1 \quad \left(\frac{\rho_c V_c}{\rho_\infty V_\infty}\right)^{\text{engine}(E)} = \left(\frac{\rho_c V_c}{\rho_\infty V_\infty}\right)^{\text{simulation}\ (S)}$$

$$2 \quad \left(\frac{\rho_c V_c^2}{\rho_\infty V_\infty^2}\right)^{E} = \left(\frac{\rho_c V_c^2}{\rho_\infty V_\infty^2}\right)^{S}$$

$$3 \quad \left(\frac{\theta}{d}\right)^{E}_{\text{inj}} = \left(\frac{\theta}{d}\right)^{S}_{\text{inj}}$$

Where θ = momentum thickness, d = coolant hole diameter, ∞ = free stream, inj = at injection site, and c = coolant conditions.

The authors have chosen item 3 as the proper ratio as might be expected in an engine environment. However, combining 1 and 2, and assuming the same medium is used to simulate the engine environment, the following condition must be met to provide the proper dynamic simulation of the end-wall cooling phenomenon,

$$(T_{0c})^S = \frac{(T_{0\infty})^S}{(T_{0\infty})^E}(T_{0c})^E$$

The authors have chosen $(T_{0c})^S = (T_{0\infty})^S$ which clearly implies that $(T_{0c})^E = (T_{0\infty})^E$, a condition which is unrealistic.

Assuming that the ratio of total coolant hole area to core flow area is representative of an engine configuration and that the injection momentum flux ratio is the dominate parameter in jet/core flow interaction, the results of Fig. 15 for the ejection mass flow ratios of 0.02 and 0.045 are actually more representative of what one might expect for an engine environment under a cooling condition of $(\dot{m}/\dot{m}_{TOT})^S/\sqrt{\alpha}$, where $\alpha \equiv \rho_c/\rho_\infty$. Since the jet trajectories (and hence jet/end-wall core flow streamline interaction) are greatly influenced by the momentum flux ratio, caution should be exercised in trying to incorporate the results of Fig. 15 into any design process.

References

1 Colladay, R. S., and Stepka, F. S., "Similarity Constraints in Testing of Cooled Engine Parts," "NASA TN D-7707, June 1974.

2 Hanus, G. J., "Gas Film Cooling of a Modeled High-Pressure, High-Temperature Turbine Vane with Injection in the Leading Edge Region from a Single Row of Spanwise-Angled Coolant Holes," Ph.D. Dissertation, Mechanical Engineering Department, Purdue University, West Lafayette, Ind., May 1976.

[1] Principal Research Engineer, The Trane Co., La Crosse, Wisc. 54601. Assoc. Mem ASME.

Authors' Closure

We agree with Dr. Hanus that it would be desirable to properly simulate the momentum flux ratio. However, it is difficult to perform as detailed measurements as described in this paper, with main stream temperatures which might be three times as high as the cooling flow temperatures. This difficulty might eventually be overcome by using mixtures of gases of different densities. Such tests are at present under way at VKI. The results will be published in due time.

R. Kotwal
Graduate Research Assistant.
Mem. ASME

W. Tabakoff
Professor
Mem. ASME

Department of Aerospace Engineering
and Applied Mechanics,
University of Cincinnati,
Cincinnati, Ohio

A New Approach for Erosion Prediction Due To Fly Ash

With increasing interest in the burning of coal in industrial gas turbines, there is also concern for the precise determination of the erosive effects on the turbine components. Series of experiments were conducted to determine the effects of fly ash constituents, particle size, particle velocity, angle of attack and target temperature on the erosion of iron and nickel base alloys. Based on the experimental results, a semi-empirical equation has been obtained for the prediction of the erosion losses. This equation provides a new technique for predicting the metal erosion due to the fly ash produced by the conventional burning of coal.

Introduction

The major problem confronting earlier developers of coal-burning turbines is the serious erosion of turbine blades and other components caused by the fly ash contained in the combustion gases. It is possible to remove approximately 85 percent by weight of the ash in these gases using cyclones. However, small particles ranging in size between 1 and 20 μm still pass through the cyclones and enter the turbine. The severity of this problem can be judged from the fact that a gas turbine operating on pulverized coal combustion is considered to have a short life. Typical ash concentrations for such a turbine are about 7.8 mgm/ft^3 [1]. The damage is caused principally by erosion of the blade trailing and leading edges. Several changes in the blade design to reduce the erosion problem have been made. These include changing the blade configurations to direct the ash towards the turbine casing instead to the rotor hub, and providing large annular space between the first stage stator and rotor blades through which the ash can centrifuge to the casing. Some designs have introduced wear strips at the base of the rotor and stator blades to minimize the erosion at these points. Nabors, et al. [1] estimated that the maximum life of the stator blades would be 5000 hr and that of the rotor blades 10,000 hr. This is far below the minimum life expectancy of a commercial power plant. A thorough knowledge of the various parameters which influence the extent of erosion damage is required to improve the life and the aerodynamic performance of turbomachinery operating in an ambient with fly ash particles. The future of advanced turbomachinery for use in the coal industry, gasification, mining, pipelines' gas transport, powder coal burning, coal-oil gas refinery, and many others is dependent upon this understanding.

Previous mathematical models [2–4] used to predict erosion rates consider only the influence of parameters such as particle velocity and angle of attack. The effects of composition and particle size should also be considered in order to predict the erosion rates of heterogeneous abrasives such as fly ash. This paper takes into consideration these additional parameters in the development of a semiempirical equation which can be used to predict metal erosion due to fly ash produced during the conventional burning of coal.

Preliminary studies were carried out with the following purposes. First, to find out the variation in the amount of erosion caused by fly ash particles acquired from different sources; and second, to understand the nature of the constituents in the fly ash.

Experimental Erosion Study of 304 Stainless Steel. Experiments were conducted on erosion test rigs developed by Grant, et al. [5] and Tabakoff, et al. [6]. Four types of fly ash acquired from different sources with different compositions and particle sizes were used. The four types of fly ash were: (1) Cincinnati Gas and Electric Company (CG&E), (2) Kingston I, (3) Kingston II, and (4) Exxon. Kingston II fly ash was obtained by the removal of large coarse particles, by using sieves, from Kingston I ash. A series of erosion tests were carried out using these fly ashes. The chemical analyses of three types of fly ash are given in Table 1, and the particle size distributions

Table 1 Chemical analysis of fly-ash

Substance	Amount Present (%)		
	Kingston Fly-Ash	CG&E Fly-Ash	Exxon Fly-Ash
Si	54.39	48.08	15.40
Al	28.58	21.16	25.40
Fe	10.08	20.05	5.53
Ca	1.28	--	7.20
Ti	0.47	--	--
Mg	1.04	0.93	3.84
Na	0.20	0.64	0.59
K	2.09	--	1.16
S	1.03	1.20	0.05
P_2O_5	0.06	--	--
SO_4	--	--	22.4
Cl	--	--	0.14
PO_4	--	--	0.25
C	--	--	1.2
F	--	--	0.02
Undetermined	0.78	7.94	16.82
Total	100.00	100.00	100.00

Contributed by the Gas Turbine Division of The American Society of Mechanical Engineers and presented at the Gas Turbine Conference and Products Show, New Orleans, La., March 10–13, 1980. Manuscript received at ASME Headquarters December 19, 1979. Paper No. 80-GT-96.

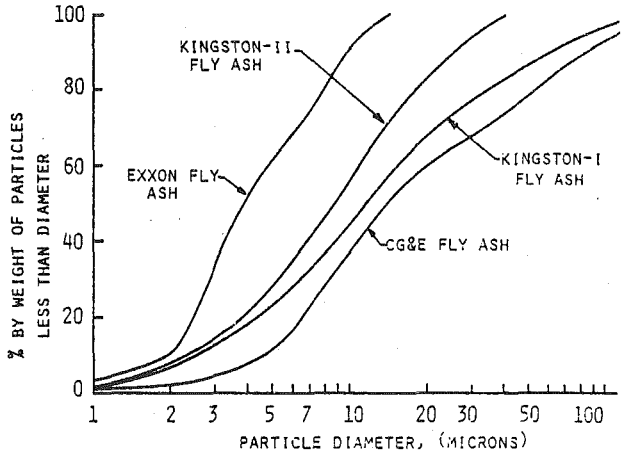

Fig. 1 Fly ash particle size distributions

are shown in Fig. 1. The mean particle sizes of CG&E, Kingston I, Kingston II and Exxon fly ash were 38.4μ, 28μ, 15μ and 3.9μ respectively.

Figure 2 shows the measured erosion on 304 stainless steel subject to various angles of attack by the fly ash particles. The tests were carried out at room temperature and for a particle velocity of 450 ft/s. It can be seen in this figure that the erosion loss reduces significantly when the coarse particles from the Kingston I fly ash were removed. The erosiveness of CG&E fly ash is observed to be smaller than that of Kingston I fly ash. The results presented in this figure also show that Exxon fly ash is least erosive among the four samples of fly ash tested.

Kingston and CG&E fly ash were produced during the conventional combustion of coal. From Table 1, it can be seen that the compounds of aluminum, silicon and iron are the major constituents of these samples of fly ash. The composition of Exxon fly ash is quite different and contains $CaSO_4$ as one of the major constituents. This is because Exxon fly ash was generated during the fluidized-bed combustion of coal using dolomite as the sorbent for capturing sulfur dioxide.

Fly Ash Composition. The constituents of fly ash from a given furnace are related to many factors, such as coal composition and size, initial state of raw coal, fuel burning rate, combustion efficiency and methods of fly ash collection. The principal ash-forming minerals in coal are as follows: aluminosilicates [Kaolinite $Al_4Si_4O_{10}(OH)_8$, illite $KAL_2(AlSi_3O_{10})(OH)_2$, and mixed layer clay minerals]; sulfides (primarily pyrite FeS_2); carbonates (calcite $CaCO_3$), siderite $FeCO_3$ and ankerite $CaCO_3$-$FECO_3$-$MgCO_3$); and quartz (SiO_2).

The character of the fly ash is related to the thermal changes which the mineral matter undergoes during the combustion of coal. Ash composition is generally reported in terms of percent weight of metal oxides in their highest oxidation state. Chemical analyses of a large number of U.S. fly ash [7] produced during the conventional combustion of coal show ranges in composition given in Fig. 3. These representative data show that there is a large variation in the amounts of various substances that are present in fly ash. For example, the percent by weight of aluminum compound in a fly ash may be as low as 10 and as high as 60. The fly ash contains compounds of silicon, aluminum and iron and smaller amounts of compounds containing titanium, calcium, magnesium, sodium, potassium and sulfur. These compounds occur in fly ash primarily as silicates, oxides and sulfates, along with lesser amounts of phosphates and carbonates.

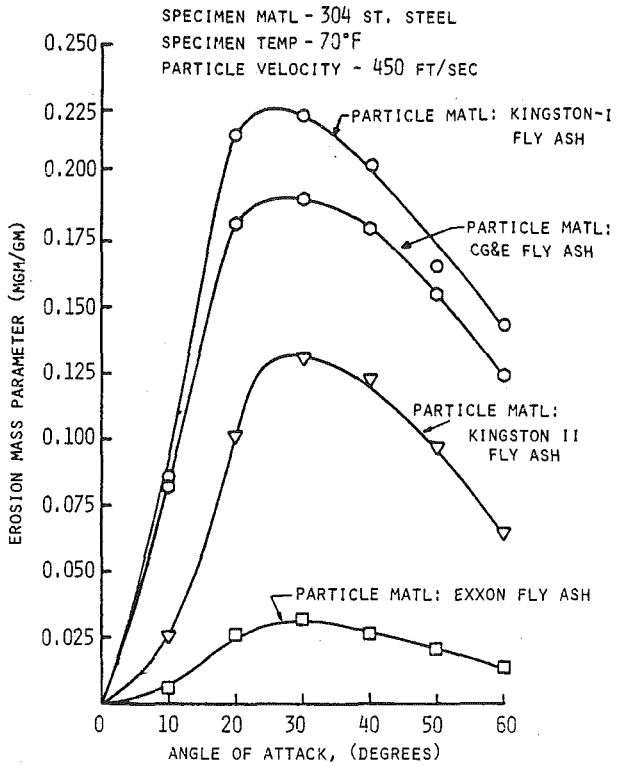

Fig. 2 Erosion caused by various types of fly ash particles (experimental results)

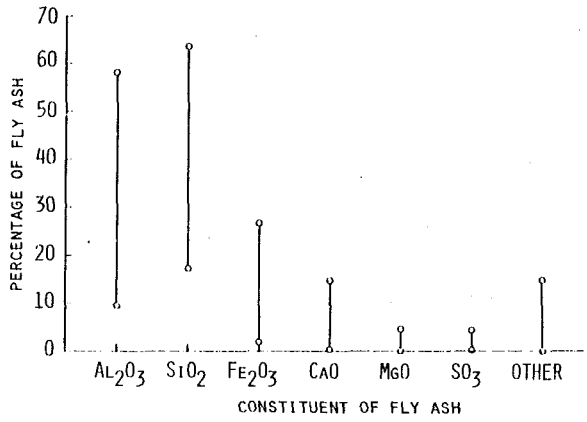

Fig. 3 Ranges in analysis of fly ash (reference [7])

Erosion Prediction Equation. It is evident that the prediction of erosion caused by fly ash particles is complicated because of the varying properties of fly ash. It is desirable to determine which constituents in fly ash affect metal erosion. The usual method of doing this is to control all other constituents and change only the constituent being considered. This approach cannot be taken in the case of fly ash because its constituents are inseparable. Hence, it was decided to develop a semi-empirical equation which relates the erosive characteristics of a fly ash to that of the commercial abrasives. The effects of chemical composition and particle size distribution in the fly ash

Nomenclature

D = particle diameter
m = total number of different substances in the fly ash
n = a number to account for the particle size effect in the erosion prediction equation
V = particle velocity
W_i = percent by weight of commercial abrasive particles corresponding to ith substance in the fly ash
ω_j = percent by weight of commercial abrasive particles having diameter D_j
ϵ = erosion mass parameter, expressed as milligrams of material eroded per gram of abrasive impacted on the specimen surface
ψ = erosion constant
μ = microns
α = impingement angle

will be included in this equation. It will be shown that the equation is general in nature and can be extended to erosion wear situations involving different materials, particle velocities, impingement angles and target temperatures. The amount of material removed by a unit mass of fly ash particles ϵ, can be expressed as follows:

$$\epsilon = \psi \sum_{i=1}^{m} \sum_{j=1}^{n} W_i\{\epsilon_{ij}\omega_j\} \tag{1}$$

where ψ = erosion constant, the value of this constant depends on the properties of the fractional components of the fly ash and the properties of the abrasives available commercially. W_i = percent by weight of commercial abrasive particles corresponding to ith substance in the fly ash, e.g., the commercial abrasives silica (SiO_2), alumina (Al_2O_3) and iron oxide (Fe_2O_3) correspond to silicon, aluminum and iron compounds respectively in the fly ash. ϵ_{ij} = erosion due to unit mass of commercial abrasive particles having diameter D_j and corresponding to ith substance in the fly ash. ω_j = percent by weight of commercial abrasive particles having diameter D_j, and corresponding to particle size distribution in the fly ash. m = total number of different substances in the fly ash. n = a number which can be selected depending on the erosion versus particle size relationship (for higher values of n, the accuracy of the present analysis improves).

Equation (1) can be simplified by the following considerations. From the results presented in Fig. 3, the percent by weights of all the substances (constituents) in the fly ash except those of aluminum, silicon and iron compounds are negligible, i.e.,

$$W_i \ll W_1, W_2, W_3 \quad \text{for} \quad i > 3. \tag{2}$$

Equation (2) suggests a value of 3 for the variable m in equation (1). Therefore equation (1) can be written in the following form.

$$\underset{\text{erosion due to fly ash}}{\epsilon} = \psi \Big[\underbrace{\sum_{j=1}^{n} W_1\epsilon_{1j}\omega_j}_{\text{erosion due to alumina}} + \underbrace{\sum_{j=1}^{n} W_2\epsilon_{2j}\omega_j}_{\text{erosion due to silica}} + \underbrace{\sum_{j=1}^{n} W_3\epsilon_{3j}\omega_j}_{\text{erosion due to iron oxide}} \Big] \tag{3}$$

The equation above can be further simplified by examining the experimental results presented in Fig. 4. This figure shows the results of the tests in which 304 stainless steel alloy was eroded by 25 microns alumina, silica and iron oxide particles. The tests were conducted at room temperature with particle velocities of 450 ft/s. It can be seen that the magnitudes of erosion due to alumina and silica particles are comparable but the magnitudes of erosion due to alumina and iron oxide differ markedly. For example, at an impingement angle of 30 deg (keeping in mind that the average particle size is the same), the erosiveness of the silica and iron oxide are, respectively, about 65 and 1 percent based on 100 percent for alumina. Tests at elevated temperature (900°F) also revealed similar results. Terefore it can be assumed that the erosion due to iron oxide may be neglected and equation (3) can be rewritten as follows.

$$\epsilon = \psi \Big[\sum_{j=1}^{n} W_1\epsilon_{1j}\omega_j + \sum_{j=1}^{n} W_2\epsilon_{2j}\omega_j \Big] \tag{4}$$

The values of W_1 and W_2 can be obtained from the chemical analysis of the fly ash. The particle size analysis of the fly ash provides the values for ω_j. For a given target material, the values of ϵ_{1j} and ϵ_{2j} can be obtained from erosion versus particle size characteristics of alumina and silica particles respectively (as will be shown later). The appropriate value of ψ is not easily estimated, because the shape, hardness and strength of the particles in the fly ash are so different from those in conventional form. In view of the present uncertain nature of the particles in fly ash, it is preferable to establish this quantity by erosion experiments involving the abrasives and target material of interest. The effects of angle of attack, particle velocity and target temperature can be included by substituting the appropriate values for the variables ϵ_{1j} and ϵ_{2j} on the right hand side of equation (4).

Application of Erosion Prediction Equation. In the following discussion, equation (4) will be used to predict the erosion caused by

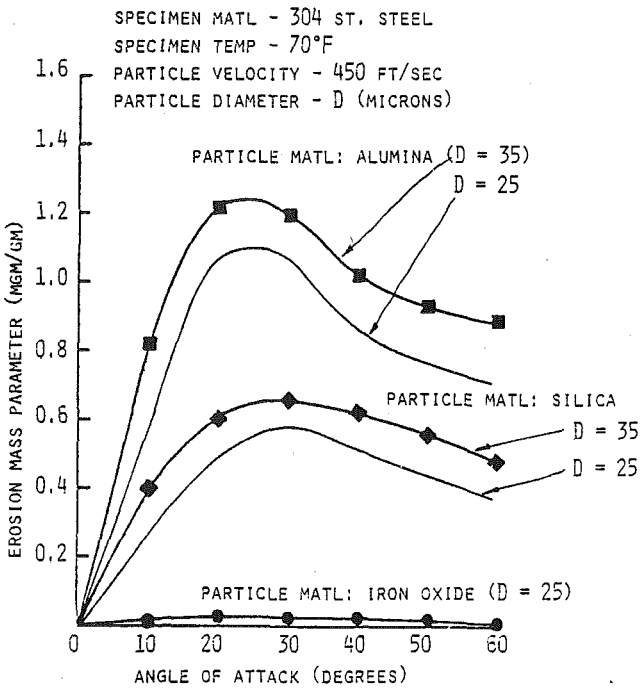

Fig. 4 Erosion versus angle of attack for different commercial abrasives (experimental results)

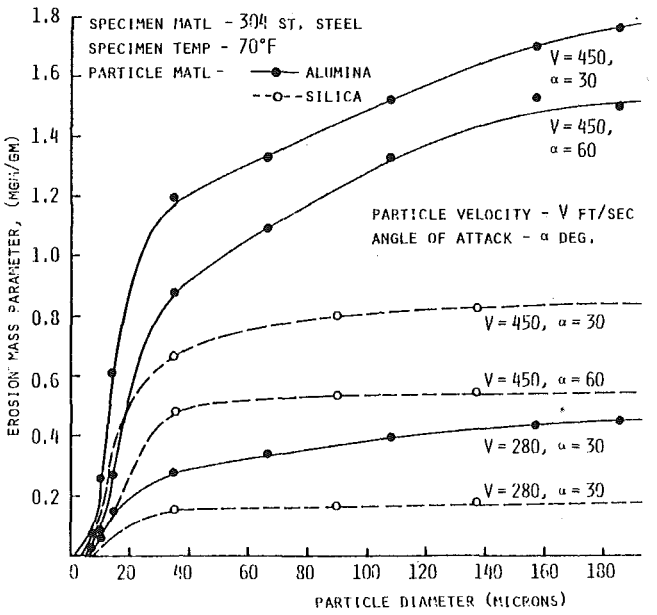

Fig. 5 Erosion versus particle size at room temperature (experimental results)

different types of fly ash particles on three target materials, namely 304 stainless steel, Rene 41 and INCO 718. These alloys are widely used in turbomachinery applications. Data on fly ash erosion for such materials is not available in the literature. Therefore before using this equation, it is necessary to obtain data on the amount of erosion caused by alumina and silica particles of various sizes and the value of the erosion constant ψ.

Figure 5 shows the test data for the variation in erosion wear of 304 stainless steel as a function of particle size. The tests were carried out at room temperature. The results are presented for two angles of attack (30 and 60 deg) and two particle velocities (280 and 450 ft/s).

Figure 6 shows the erosion versus particle size plots for three target materials; namely, 304 stainless steel, Rene 41 and INCO 718. The

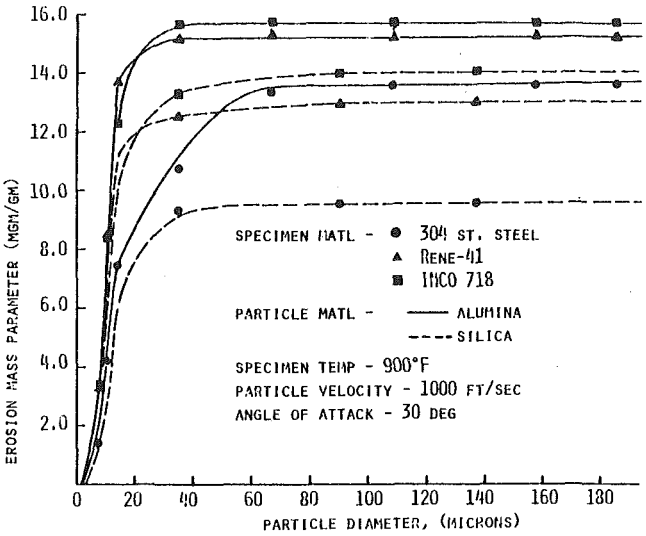

Fig. 6 Erosion versus particle size at 900°F (experimental results)

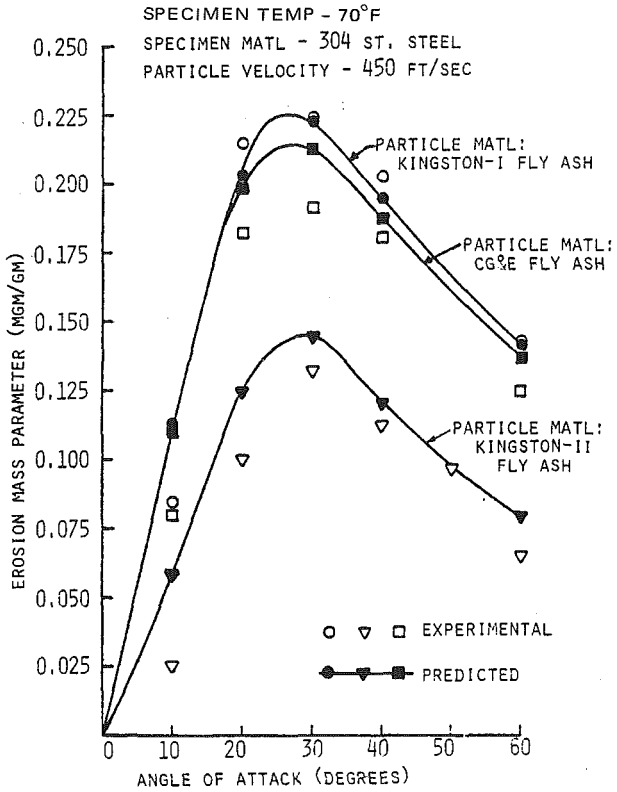

Fig. 7 Erosion versus angle of attack (experimental and predicted results)

Table 2 Value of erosion constant in equation (4)

Target Material	Target Temperature (°F)	Particle Velocity (ft/sec)	Angle of Attack (degree)	Erosion Constant ψ
304 St. Steel	70	200–500	0–90	0.65
304 St. Steel	900	500–1000	30	0.425
Rene 41	900	500–1000	30	0.480
INCO 718	900	500–1000	30	0.525

test results are shown for a target temperature of 900°F and a particle velocity of 1000 ft/s. Only one impingement angle was employed (30 deg) which was close to the angle of maximum erosion for all three target materials.

For a given target temperature, one erosion test was conducted for each target material using CG&E fly ash particles. The results of these tests and the results presented in Figs. 5 and 6 were used in equation (4) to evaluate the value of the erosion constant ψ. Table 2 lists the values of the erosion constant ψ for the three target materials. The value of ψ was found to be between 0.425 and 0.65. The variation in the value of this constant tends to confirm the complexity of the material property parameters and abrasive property parameters which are controlling the erosion.

Using the appropriate values for ψ and other quantities in equation (4), the erosion mass parameter values for other fly ash particles were obtained. Figure 7 shows the experimental and predicted erosion mass parameter values for 304 stainless steel and three different fly ash particle types. The predicted and experimental erosion values of 304 stainless steel, Rene 41 and INCO 718 by using CG&E fly ash for specimen temperature of 900°F and angle of attack of 30 deg, are shown in Fig. 8. There is good agreement between the predicted and experimental erosion results, thus verifying the usefulness of equation (4) to predict the erosion resistance of a material under attack by fly ash particles. Additional experimental data using fly ash may be found in reference [8].

To facilitate the use of equation (4), a simple computer program was developed. This program was used to study the effects of fly ash composition and particle size distribution on the erosion of a material. For a given target material of interest, the appropriate value of the erosion constant ψ and the erosion values for different sizes of alumina and silica particles (such as shown in Figs. 5 and 6), were provided as input to this program.

The procedure outlined above was used to estimate the erosion on the three target materials (304 stainless steel, Rene 41 and INCO 718) caused by various types of fly ash having assumed compositions and particle size distributions. Table 3 shows 12 different fly ash compositions which were investigated in this study. These compositions were chosen on the basis of ranges in fly ash composition that occurs in

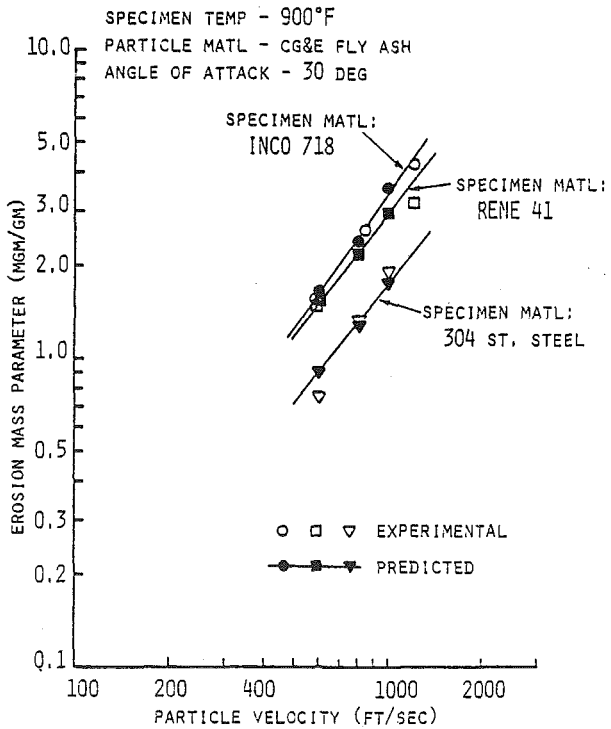

Fig. 8 Erosion versus particle velocity (experimental and predicted results)

practice. Figure 9 shows the 15 different particle size distribution numbers, N, considered (from $N = 1$ to $N = 15$) plotted versus the particle diameters (1 to 200 μm). The fly ash compositions are identified by capital letters (A, B, C, . . . L) as shown in Table 3. A particular fly ash is therefore identified by a combination of a letter and a number. Among the fly ash compositions studied, composition A (with 30 percent Al compound and 60 percent Si compound) and composition L (with 30 percent Al compound and 40 percent Si compound) gave maximum and minimum erosion values, respectively, and composition G (with 30 percent Al compound and 50 percent Si compound) gave an intermediate erosion value, for a given particle size distribution. Therefore, computed erosion results will be presented for these three fly ash compositions only.

Figure 10 shows the estimated relative erosion caused by different types of fly ash particles on 304 stainless steel specimens at room temperature. The results are presented for two angles of attack (30 and 60 deg) and two particle velocities (280 and 450 ft/s). The spread in the erosion data shown by the three symbols for a given particle size distribution indicates the effect of fly ash composition. The effect of fly ash content is significant when the larger particles (greater than 30μ) are present in the fly ash. For a given fly ash composition, particle size distributions $N = 5$ (with particles 1–10μ) and particle size distribution $N = 6$ (with particles 80–100μ) were found to be the least and most erosive, respectively.

The predicted dependence of the erosion mass parameter on the fly ash compositions and particle size distributions is shown in Figs. 11–13. The results are presented for the three target materials (304 stainless steel, Rene 41 and INCO 718). These results were obtained from the computer program for a target temperature of 900°F, a particle velocity of 1000 ft/s and an angle of attack of 30 deg. At these conditions the computed results show that 304 stainless steel has a higher erosion resistance compared to Rene 41 and INCO 718. It is seen that the earlier observations (Fig. 10) regarding the effects of composition and particle distribution in the fly ash on the room temperature erosion are true for the elevated temperature erosion also. The computed results also show that the effect of fly ash composition on erosion is more significant in the case of high velocity particles impinging a target material at elevated temperatures.

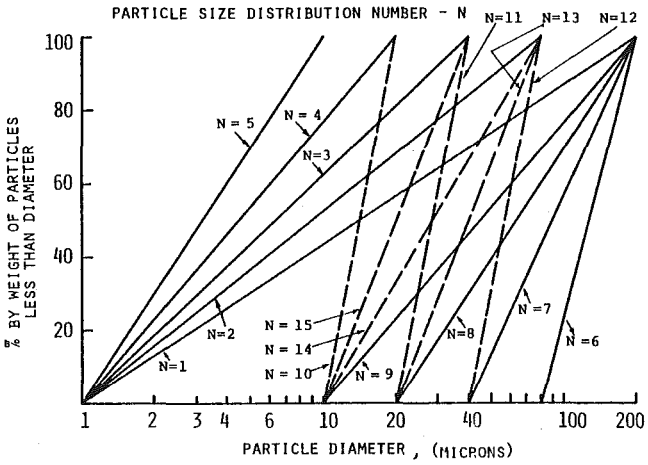

Fig. 9 Assumed particle size distributions

Table 3 Assumed fly ash compositions

Composition Name	Fly Ash Composition			
	Si Compound	Al Compound	Fe Compound	Other
A	60.00	30.00	5.00	5.00
B	60.00	25.00	10.00	5.00
C	60.00	20.00	15.00	5.00
D	55.00	30.00	10.00	5.00
E	55.00	25.00	15.00	5.00
F	55.00	20.00	20.00	5.00
G	50.00	30.00	15.00	5.00
H	50.00	25.00	20.00	5.00
I	50.00	20.00	25.00	5.00
J	45.00	30.00	20.00	5.00
K	45.00	25.00	25.00	5.00
L	40.00	30.00	25.00	5.00

Summary and Conclusions

The most important findings of the present study were concerned with the amount and the nature of the erosion caused by different types of fly ash on three different materials (304 stainless steel, Rene 41 and INCO 718). A model to predict erosion (in the form of a semi-empirical equation), was developed which takes into account the effects of composition, particle size and complicated structure of the fly ash particles. It was shown that the technique is general in nature and can be extended to erosion wear situations involving different materials, particle velocities, impingement angles and target temperatures. This equation relates the erosive characteristics of a fly ash to that of the commercial abrasives. The equation was simplified by assuming that, for the fly ash, the percent by weight of all the substances (constituents) excluding that of aluminum, silicon and iron compounds are negligible. This assumption is true only for fly ash produced during the conventional combustion of coal. There was good agreement between the predicted erosion values and the test results, as shown in Figs. 7 and 8.

The study of a variety of fly ashes shows that their erosiveness is

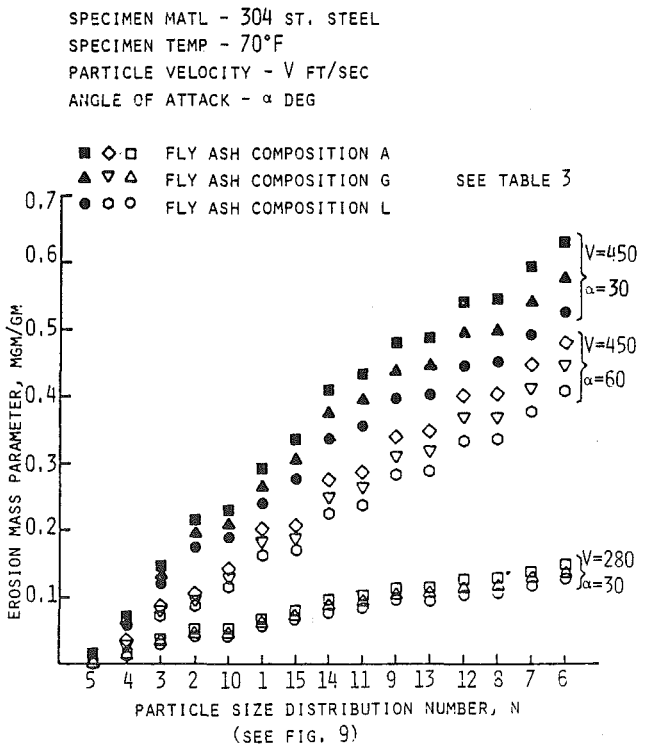

Fig. 10 Relative erosion loss caused by different types of fly ash on 304 stainless steel specimens (predicted results)

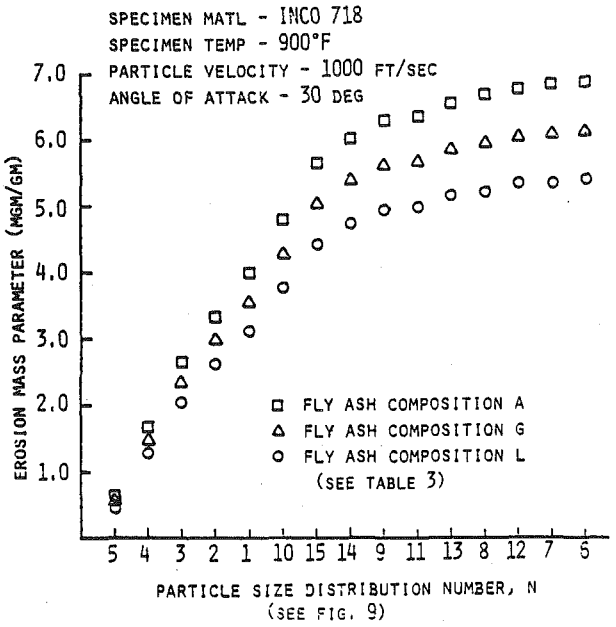

Fig. 11 Relative erosion loss caused by different types of fly ash particles on INCO-718 specimens (predicted results)

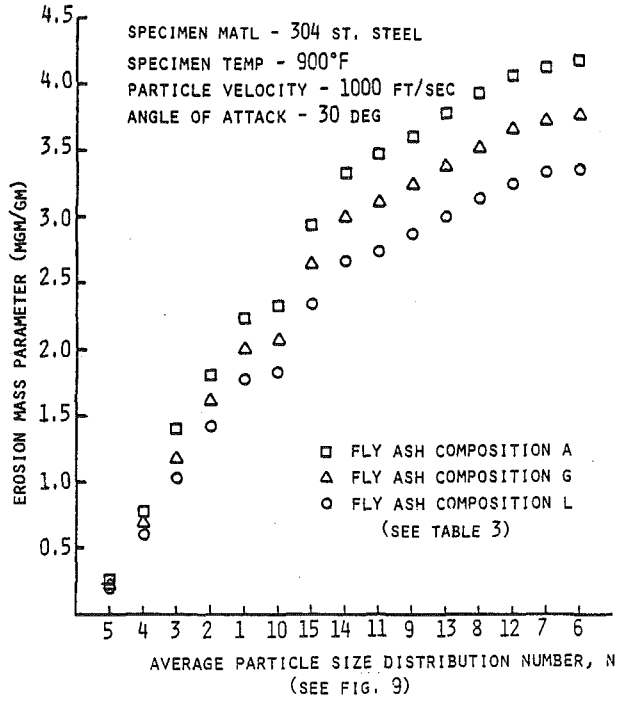

Fig. 12 Relative erosion loss caused by different types of fly ash particles on 304 stainless steel specimens (predicted results)

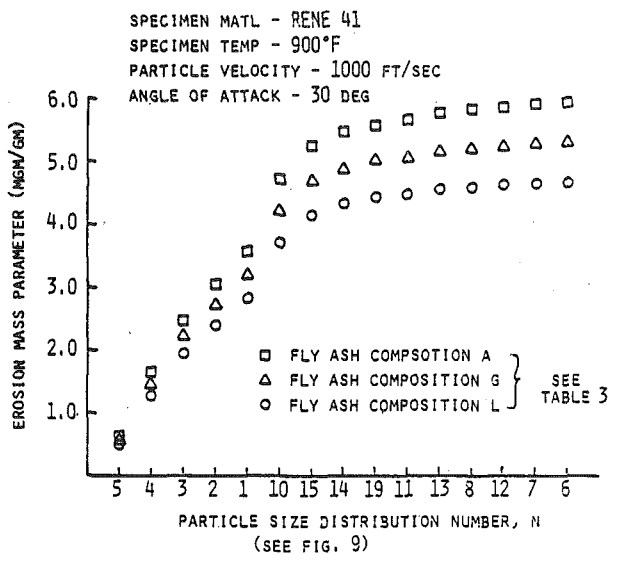

Fig. 13 Relative erosion loss caused by different types of fly ash particles on Rene 41 specimens (predicted results)

directly proportional to the percentage of the aluminum and the silicon compounds. The effect of fly ash content on erosion is significant when larger particles (greater than 30μ) are present. The computed results also show that the effect of fly ash composition on erosion is more significant in the case of high velocity particles impinging a target material at elevated temperatures. The predicted and test results show that the erosion mass parameter increases at a rapid rate with increasing particles diameter up to about 40 μm and at a slower rate with further increase in particles diameter.

Acknowledgments

This research was sponsored by ERDA Contract No. E(49-18)-2465. The authors wish to express their appreciation for the useful discussions provided by Dr. J. Moteff.

References

1 Nabors, W. M., Strimbeck, D. C., Cargill, R. W. and Smith, J., "Bureau of Mines Progress in Developing the Coal Burning Gas Turbine Power Plant," ASME *Journal of Engineering for Power*, April 1965, pp. 215–222.

2 Finnie, I., "The Mechanism of Erosion of Ductile Metals," *Proceedings of 3rd National Congress of Applied Mechanics, Trans ASME*, 1958, pp. 527–532.

3 Bitter, J. G. A., "A Study of Erosion Phenomena, Part I and Part II," *Wear*, Vol. 6, 1963, pp. 5–21 and pp. 169–190.

4 Neilson, J. H., and Gilchrist, A., "Erosion by a Stream of Solid Particles," *Wear*, Vol. 2, 1968, pp. 111–122.

5 Grant, G. and Tabakoff, W., "Erosion Prediction in Turbomachinery Resulting from Environmental Solid Particles," *Journal of Aircraft*, Vol. 12, No. 5, May 1975, pp. 471–478.

6 Tabakoff, W. and Wakeman, T., "Test Facility for Material Erosion at High Temperature," ASTM Special Technical Publication, No. 664, 1979.

7 White, H. J., "Effect of Fly Ash Characteristics on Collector Performance," *JAPCA*, Vol. 15, May 1955, pp. 37–50, 62.

8 Tabakoff, W., Kotwal, R. and Hamed, A., "Erosion Study of Different Materials Affected by Coal Ash Particles," *Wear*, Vol. 52, 1979, pp. 161–173.

M. Ishida
Associate Professor,
Faculty of Engineering,
Nagasaki University,
Nagasaki, Japan

Y. Senoo
Professor,
Research Institute of Industrial Science,
Kyushu University,
Fukuoka, Japan
Mem. ASME

On the Pressure Losses Due to the Tip Clearance of Centrifugal Blowers

The pressure distribution along the shroud is measured for three types of centrifugal impeller at seven different values of tip clearance each. The change of input power due to a change of tip clearance is related to the effective blockage at the impeller tip. Since the change of input power is little for the test cases, the variation of local pressure gradient along the shroud is mostly attributed to the change of local pressure loss. The local pressure loss is related to the local tip clearance ratio and to the local pressure gradient based on the deceleration of relative velocity in the impeller. Since the local pressure gradient is largest near the throat of the impeller, for many impellers the clearance ratio at the throat is used as the representative value. The tip clearance loss is related to the clearance ratio and the pressure rise based on the deceleration of relative velocity in the impeller. A good correlation is observed in all cases at various flow rate.

Introduction

For high pressure ratio centrifugal compressors, open shroud impellers are common. It is well known that impeller performance is eroded by the leakage flow through the clearance between the impeller blade-tip and the stationary shroud surface.

According to references [1–6], in cases of centrifugal pumps, the rate of decrease in efficiency is one point for each percent of the tip clearance ratio at the impeller exit. In cases of centrifugal compressors, Pampreen [7] shows that the efficiency loss is only one-third of a point for each percent of tip clearance ratio. It is not clear why the decrement of efficiency due to tip clearance ratio is different for centrifugal compressors from that for centrifugal pumps.

The tip clearance effect on axial pumps and compressors is studied by many investigators. According to Pfleiderer [1], in cases of axial pumps the decrement of efficiency is proportional to the tip clearance ratio, and the rate of decrease in efficiency is twice as much as that for centrifugal pumps. Recently, considering the mechanism of tip clearance losses such as the induced velocities in a inviscid flow and the spanwise flow inside the boundary layer near the tip, Lakshminarayana [8] proposed a semi-empirical expression for the tip clearance loss.

In the present paper, using two entirely different types of centrifugal blowers, one with a radial blade impeller and the other with a backward leaning blade impeller, the pressure distribution along the shroud is measured at different values of tip clearance. The local pressure loss along the shroud is related to the local tip clearance ratio and to the local pressure rise based on the deceleration of relative velocity in the impeller, and finally a good correlation is found between the tip clearance loss and the deceleration in the impeller.

Experimental Apparatus

The meridional profiles of two test blowers are shown in Figs. 1(*a*) and (*b*), respectively. The impeller of R-blower has 20 radial blades and inducers, and the specific speed is about 0.584. The impeller of B-blower has 16 blades which incline backward; the exit angle of the blades is 45 deg, and the specific speed is about 0.433. Later the B-impeller was modified so that the deceleration of relative velocity in the impeller was low at the flow rate $\varphi = 0.357$. For the modification, the blades were thickened by adding epoxy resin on the pressure side of each blade; as a result the mean blade exit angle became 41 deg.

The tip clearance of these blowers was changed by inserting a shim at the position marked A or B in Fig. 1(*a*) and A in Fig. 1(*b*) so that the shroud moves axially relative to the impeller. For each blower the axial clearance at the exit of impeller c_2 was varied seven times as listed in Table 1. In the case of R-blower, even when the shroud was axially moved relative to the rotor, the blade tip clearance at the inlet of inducer did not change because the clearance was radial. The blade tip clearance along the shroud varied from the inlet to the exit of impeller as shown in Fig. 2. In the case of B-blower the tip clearance was constant along the shroud because of the straight shroud profile. In Table 1, the clearance ratio at the exit of impeller λ_2 and that at the throat λ_t are shown in addition to the tip clearance, where the clearance ratio is the ratio of the tip clearance to the local blade height.

In the present experiment, the R-blower was operated at 4000 rpm and the B-blower at 2000 rpm. The flow rate was controlled with a conical damper at the entrance of a plenum chamber upstream of the suction pipe of the blower. Between the plenum and the suction pipe, there was a entrance nozzle with which the flow rate was measured. Static pressure was measured at 12 positions along the shroud for each blower. These positions are numbered from 0 to 11 and are indicated in Figs. 1(*a*) and (*b*). At each position the static pressure was measured at four circumferentially located pressure taps and the mean value was used. The air was axisymmetrically discharged from the blower to the atmosphere through a parallel wall vaneless diffuser. The input shaft torque, and the bearing torque without the impeller were measured with a strain gauge torque meter.

Contributed by the Gas Turbine Division of The American Society of Mechanical Engineers and presented at the Gas Turbine Conference and Products Show, New Orleans, La., March 10–13, 1980. Manuscript received at ASME Headquarters January 2, 1980. Paper No. 80-GT-139.

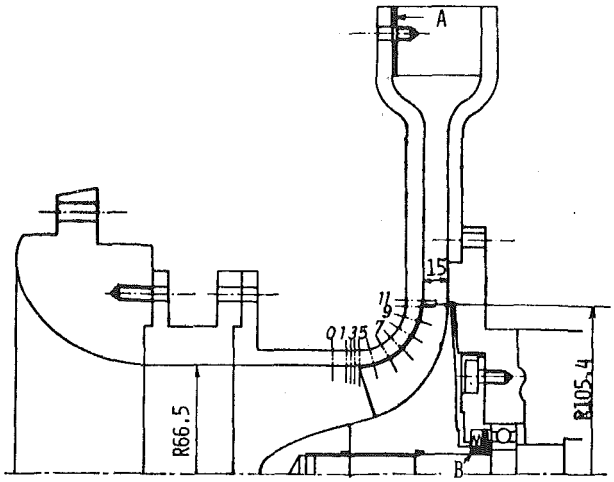

Fig. 1(*a*) R-blower

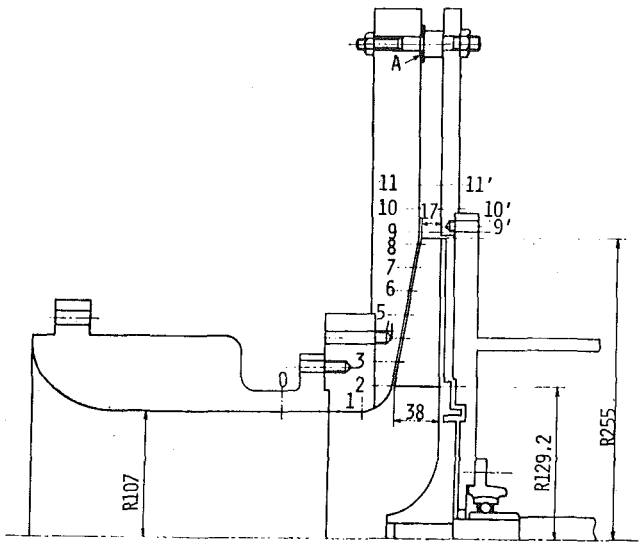

Fig. 1(*b*) B-blower

Fig. 1 Meridional profile of test impeller

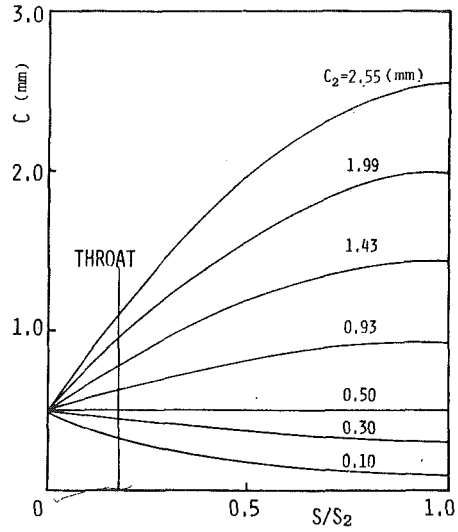

Fig. 2 Tip clearance distributions along shroud; R-blower

Table 1 Tip clearance and tip clearance ratios at exit and throat of impellers

R.BLOWER			B.BLOWER		
C_2 (mm)	λ_2	λ_t	C_2 (mm)	λ_2	λ_t
0.10	.007	.011	0.25	.015	.007
0.30	.020	.015	1.00	.059	.029
0.50	.033	.016	1.54	.091	.045
0.93	.062	.021	2.02	.119	.059
1.43	.095	.026	2.56	.151	.074
1.99	.130	.031	3.04	.179	.088
2.55	.170	.036	3.58	.211	.104

Experimental Results and Discussions

Impeller Characteristics. The characteristic curves of R-blower and B-blower are presented in Figs. 3(*a*) and (*b*) respectively, where η is the efficiency, ψ_{2T} is the total pressure coefficient and ψ_2 is the static pressure coefficient at the exit of impeller. The total pressure is the sum of the measured wall static pressure at the exit of the impeller and the dynamic pressure which is estimated using the measured flow rate and the input shaft torque. The mechanical loss is not included in the efficiency in Fig. 3(*a*), while it is included in Fig. 3 (*b*). The left ends of the characteristic curves represent the critical conditions to surge. In both Figs. 3(*a*) and (*b*), the total pressure, the static pressure and the efficiency become lower as the tip clearance ratio becomes larger for the entire operating flow range.

Figure 4 shows the decrement of efficiency from the efficiency at the tested minimum clearance condition. The abscissa is the tip clearance ratio at the impeller exit, and the parameter is the flow coefficient. In this figure, the broken line indicates the experimental mean value of centrifugal compressors presented in [7], and the chain line indicates the value based on Pfleiderer's empirical equation for centrifugal pumps. In the case of R-blower, when the flow rate is not far from the best efficiency flow rate the decrement of efficiency is about 3 points for 10 percent tip clearance ratio and the data are near the broken line. In the case of B-blower, the data near the best efficiency flow rate are a little lower than the chain line, that is, the decrement of efficiency is about 8 points for 10 percent tip clearance ratio. The rate of decrement in efficiency for the the B-blower is more than double the rate for the R-blower.

Input Shaft Torque. The circumferential component of absolute velocity at the exit of impeller V_{u2} is estimated from the measured input shaft torque and the flow rate considering the bearing torque and the disk friction torque. Figure 5 shows the circumferential component of velocity at the impeller exit for given flow coefficients. In the cases of R-blower and B-blower the circumferential component of velocity or the input shaft torque is hardly influenced by the change of tip clearance, but the cases of B2-blower it is decreased by in-

Nomenclature

b = blade height
c = tip clearance
D = impeller diameter
p = static pressure
P = total pressure
Q = volume flow rate
r = radius
S = length along shroud
U = peripheral velocity
V_u = circumferential velocity
W = relative velocity
β = blade angle
Δ = change due to tip clearance
η = total to total efficiency
$\lambda = c/b$, tip clearance ratio
ρ = density
$\varphi = Q/2\pi r_2 b_2 U_2$, flow coefficient
$\psi = (p - p_0)/(\rho U_2^2/2)$, static pressure coefficient
$\Delta\psi_\ell$ = pressure loss due tip clearance
$\psi_2 = \psi$ at impeller exit
ψ_{2T} = total pressure coefficient at impeller exit
ψ_D = static pressure rise due to deceleration of relative velocity, defined in equation (4)
$\psi_{min} = \psi$ for the case with the minimum value of λ_2
$\Delta\psi_{2input}$ = isentropic change of ψ_2 due to tip clearance

Subscripts

0 = upstream of impeller
2 = exit of impeller
t = throat

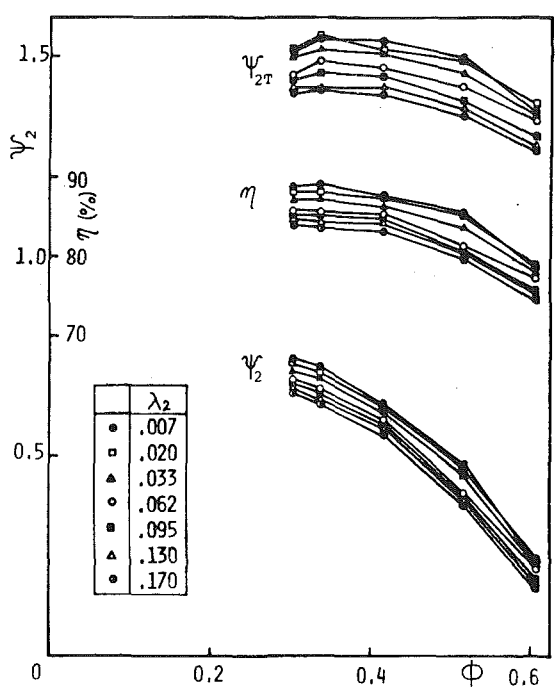

Fig. 3(*a*) R-blower

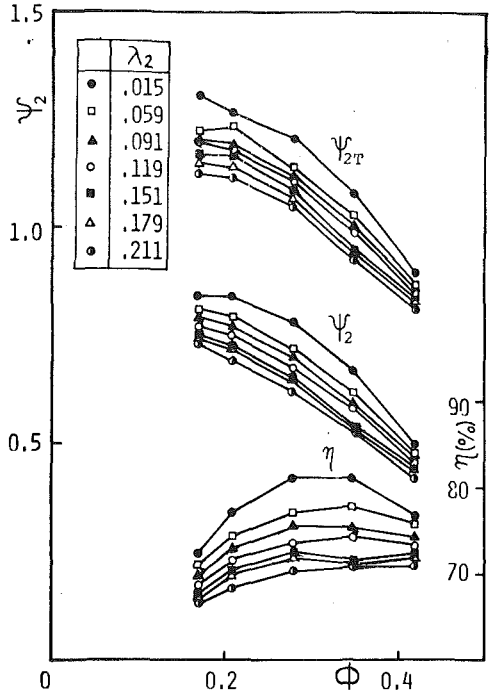

Fig. 3(*b*) B-blower

Fig. 3 Change of characteristic curves due to tip clearance (Uncertainty of $\psi_2 = \pm 0.008$, of $\eta = \pm 1.9$ percent, and of $\varphi = \pm 0.003$)

creasing the tip clearance. Similar trend is reported in the literature [2, 6], the data of which are also included in Fig. 5. It is noticed that the inclinations of these lines are different from one blower to another blower or to another pump, but the lines at different flow rates for each blower or each pump are roughly parallel each other.

These lines are represented by straight lines and the inclination is plotted in Fig. 6 against the cotangent of blade angle. Although the points for the R-blower and the B-blower are a little scattered, these points are roughly on a straight line. In one-dimensional flow analysis, the circumferential component of velocity at the impeller exit is expressed as

$$V_{u2}/U_2 = 1 - s - \varphi \cdot \cot \beta_2 \tag{1}$$

where s is the slip factor. If the decrement of V_{u2} is assumed to be entirely caused by the increment of φ or the decrease of effective area at the impeller exit, differentiating equation (1)

$$\Delta(V_{u2}/U_2) = -\Delta\varphi \cdot \cot \beta_2$$

$$\frac{\Delta(U_{u2}/U_2)}{\Delta\lambda_2} = -(\Delta\varphi/\Delta\lambda_2) \cdot \cot \beta_2 \tag{2}$$

The inclination in Fig. 6 is 0.3 for many pumps and blowers. According to equation (2), the inclination is equal to $\Delta\varphi/\Delta\lambda_2$. It is presumed that the larger the tip clearance is the narrower the effective flow area would be in the impeller, as a result for a given flow rate the effective flow coefficient increases in proportion to the increment of tip clearance ratio. Since the number of data is not many and some of them are scattered, this relation is tentative and it is expected that the blade loading and some other factors may influence the relation.

Loss Distribution along the Shroud. In the present experiment, the pressure along the shroud was measured for each impeller at five flow rates for seven different values of tip clearance. In Figs. 7(*a*) and (*b*), the pressure distribution along the shroud are presented at three representative flow rates. The ordinate is the static pressure coefficient ψ, the abscissa is the location along the shroud, $S/S_2 = 0$ corresponds to the leading edge of inducer and $S/S_2 = 1.0$ corresponds to the exit of the impeller. The numbers in Figs. 7(*a*) and (*b*) indicate the static pressure taps which are shown in Figs. 1(*a*) and (*b*). In the case of R-blower, as the shroud is moved away from the rotor to increase the tip clearance, the locations of static pressure taps relative

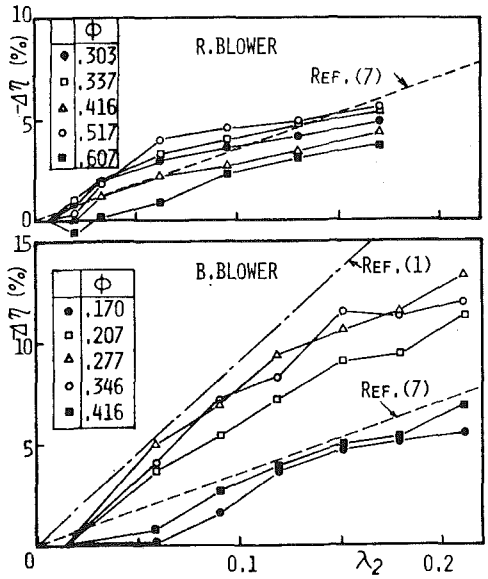

Fig. 4 Decrement of efficiency due to tip clearance (Uncertainty of $-\Delta\eta = \pm 1.9$ percent)

to the leading edge of inducer are different for each tip clearance ratio λ_2. In Fig. 7(*a*), position No. 4 is located just behind the leading edge of inducer, position No. 5 corresponds to the throat section of the inducer and the inducer portion ends at position No. 7.

The pressure distribution between No. 0 and No. 3, demonstrates that the tip clearance effect hardly appears upstream of the impeller. The dotted lines are evaluated from the measured pressure distribution for $\lambda_2 = 0.007$ by subtracting the pressure rise due to the centrifugal force, and they indicate the pressure distributions based on the deceleration of relative velocity in the impeller. It becomes clear that the pressure rise in the inducer portion is primarily due to the deceleration of relative velocity and the pressure rise between No. 7 and No. 10 is dominated by the centrifugal force. It is noticed that in the radial blade portion the pressure distribution for each tip clearance is almost parallel to each other or the tip clearance has little effect on the pressure gradient while in the inducer portion and especially

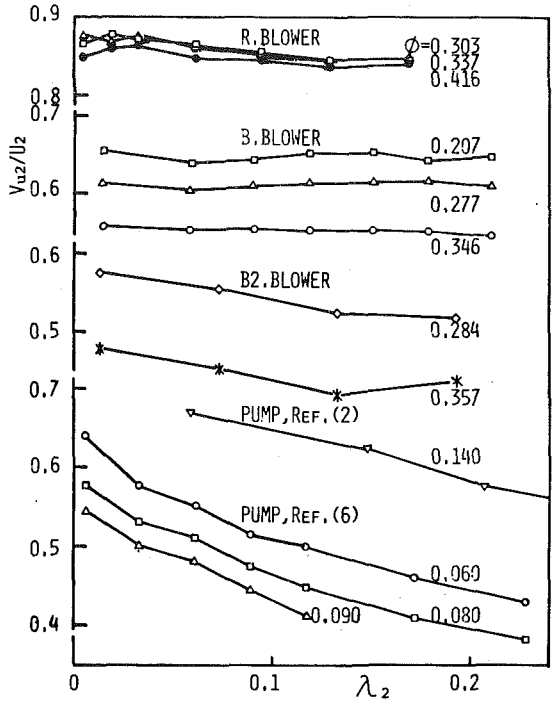

Fig. 5 Variation of circumferential component of velocity due to tip clearance (Uncertainty of $V_{u2}/U_2 = \pm 0.011$)

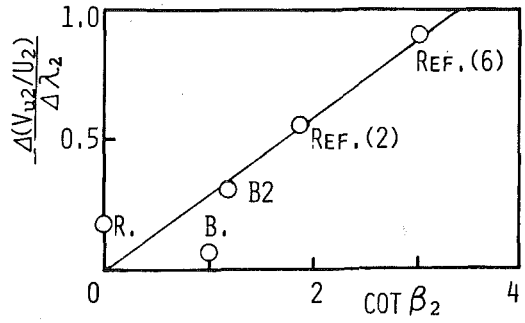

Fig. 6 Correlation of input torque and tip clearance for centrifugal blowers and pumps (Uncertainty of ordinate variable = ±0.20)

near the throat the pressure gradient is significantly influenced by the tip clearance.

The pressure-lines for different values of λ_2 cross each other between positions No. 4 and No. 5 and/or between No. 5 and No. 6, and a brief explanation may be in order. The first of all the location of pressure taps No. 4 relative to the leading edge of inducer is different for different values of λ_2, and the difference of the measured pressure at position No. 4 does not indicate the change of pressure distribution near the leading edge due to the tip clearance. At the design flow rate the flow near the leading edge of inducer is accelerated by the blockage of inducer blades, and at the larger flow rate the flow is further accelerated due to the turning by the inducer blades and the pressure falls along the shroud near the leading edge. Position No. 4 is just before the leading edge of inducer at large λ_2, and it moves into the inducer as λ_2 decreases. Therefore the pressure at No. 4 falls with decreasing λ_2 and the pressure drop becomes significant as the flow rate increases.

If the data at position No. 4 are connected with the data at position No. 5 by straight lines, they will cross each other if the pressure at No. 5 is higher in the order of smaller λ_2. For a flow rate which is not too much more than the design flow rate, this is the case. However if the flow rate is very large $\varphi = 0.517$, position No. 5 is near the throat of the inducer and the pressure is lowest. The inducer blades accelerate the flow while the tip clearance somewhat reduces the acceleration of flow. Therefore the pressure at No. 5 is lower in the order of smaller

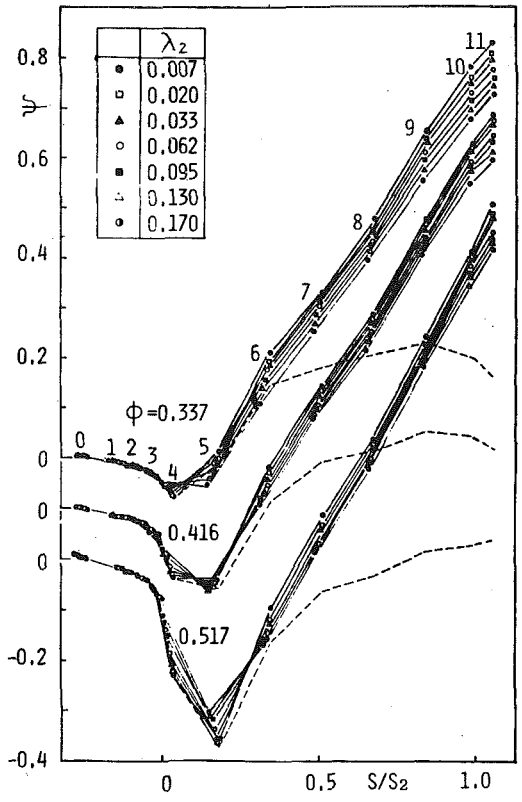

Fig. 7(*a*) R-blower

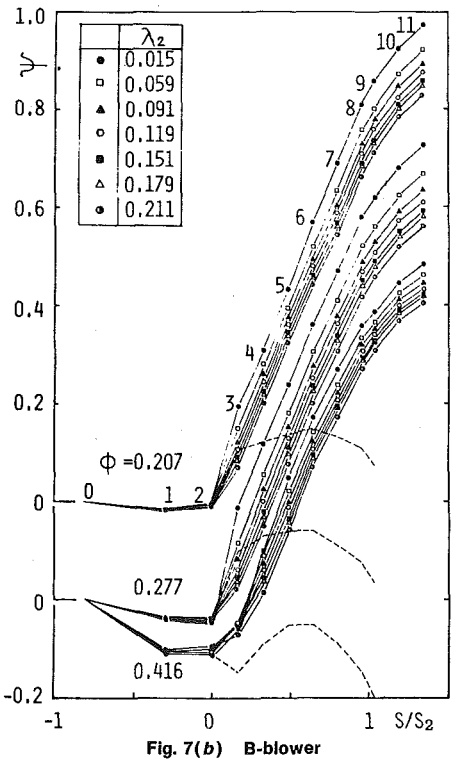

Fig. 7(*b*) B-blower

Fig. 7 Static pressure distribution along shroud (Uncertainty of $\psi = \pm 0.008$)

λ_2. Between positions No. 5 and No. 6 there is a steep deceleration regardless of the flow rate, and the pressure gradient is obviously steeper as the tip clearance is smaller. Consequently the pressure at position No. 6 is higher in the order of smaller λ_2. Therefore, for the large flow rate where the order of pressure at No. 5 is inverse, the lines connecting the pressure points at No. 5 and No. 6 cross each other.

In Fig. 7(*b*), position No. 2 corresponds to the inlet of impeller and

position No. 3 corresponds to the throat. The pressure distribution between No. 0 and No. 2 is hardly influenced by the tip clearance. The pressure distributions between No. 3 and No. 11 for various tip clearance ratios are parallel to each other at flow rates $\varphi = 0.207$ and 0.277. That is, the influence of tip clearance is concentrated at the throat section where the pressure rise due to the deceleration of relative velocity is large. In the case of large flow rate $\varphi = 0.416$, the effect of tip clearance hardly appears in the throat section where the flow is accelerated, and the tip clearance effect is concentrated between No. 3 and No. 5 where the deceleration is large.

Figures 8(a) and (b) indicate the decrement of static pressure $-\Delta\psi$, which is calculated from the data shown in Figs. 7(a) and (b) in accordance with the following expression, where $\psi_{\min}$ is the ψ for the minimum value of λ_2 in the present series of experiment.

$$-\Delta\psi = (\psi_{\min} - \psi) - (\psi_{\min} - \psi)_{s=0} \tag{3}$$

The term in the second parenthesis is the value at $S/S_2 = 0$. The abscissa is the position along the shroud S/S_2, and the parameter is the tip clearance ratio at the exit λ_2. The pressure drop evaluated by equation (3) presents the decrement of pressure which is accumulated along the shroud, and it approximately represents the accumulated pressure loss. According to these figures the local pressure loss due to the tip clearance appears mostly near the throat region. However, in cases where the flow rate is larger, $\varphi = 0.517$ for the R-blower and 0.416 for the B-blower, the pressure loss does not occur between the inlet and the throat. Correlating the local pressure loss to the local deceleration rate indicated as dotted lines in Figs. 7(a) and (b), it is anticipated that the significant pressure loss due to the tip clearance is closely related to the large local deceleration of relative velocity.

Correlation between Pressure Loss and Deceleration of Relative Velocity. Assuming that a potential core exists in each channel of the impeller, the relative velocity in the impeller is calculated from the measured pressure distribution along the shroud for the minimum tip clearance condition, and the relative velocity distributions are shown as solid lines in Figs. 9(a) and (b) for the R-blower and the B-blower, respectively. The chain lines in Fig. 9(a) are the values which are predicted by the quasi-three-dimensional potential flow analysis [9]. The experimental values in the inducer portion agree well with the prediction in all flow rates, but the difference between experiment and theory becomes larger downstream because of the growth of boundary layer. In the case of R-blower, except for the entrance region for high flow rate, the flow is decelerated monotonously to the exit of impeller, although the inclination is larger in the first half. In the case of B-blower the flow is decelerated in the front half of the impeller, but it is accelerated in the last half, and the over-all deceleration ratio from the inlet to the exit of impeller W_1/W_2 is almost unity.

The correlation between the pressure loss and the deceleration of relative velocity is examined. At first the maximum and the minimum relative velocities $W_{\max}$ and $W_{\min}$ in the impeller are measured in Figs. 9(a) and (b) for each flow rate, and the pressure rise based on the deceleration is calculated as follows.

$$\psi_D = (W_{\max}/U_2)^2 - (W_{\min}/U_2)^2 \tag{4}$$

The apparent pressure loss in Figs. 8(a) and (b), is partly based on the decrement of power, or the decrement of circumferential component of absolute velocity $-\Delta V_{u2}$, as shown in Fig. 5. The isentropic change of static pressure at the impeller exit due to the change of input power is calculated by the following equation.

$$\Delta\psi_{2\text{input}} = 2(\Delta V_{u2}/U_2) \cdot (1 - V_{u2}/U_2) \tag{5}$$

Therefore, the net pressure loss $\Delta\psi_\ell$ due to the tip clearance is evaluated as follows.

$$\Delta\psi_\ell = -(\Delta\psi_2 - \Delta\psi_{2\text{input}}) \tag{6}$$

According to reference [10], the tip clearance loss in axial flow turbine cascades is proportional to the tip clearance to the 0.78 power and to the blade loading. In the present experiment, it is assumed that the blade loading may be replaced by the pressure rise due to the decel-

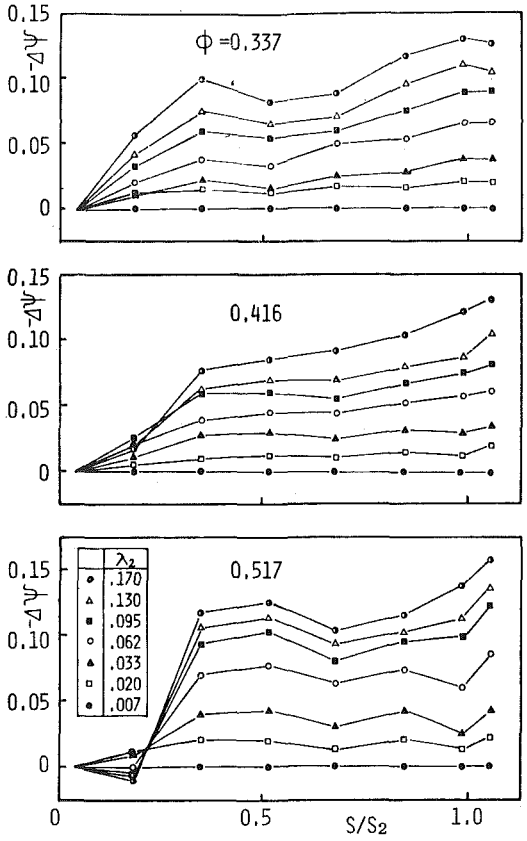

Fig. 8(a) R-blower

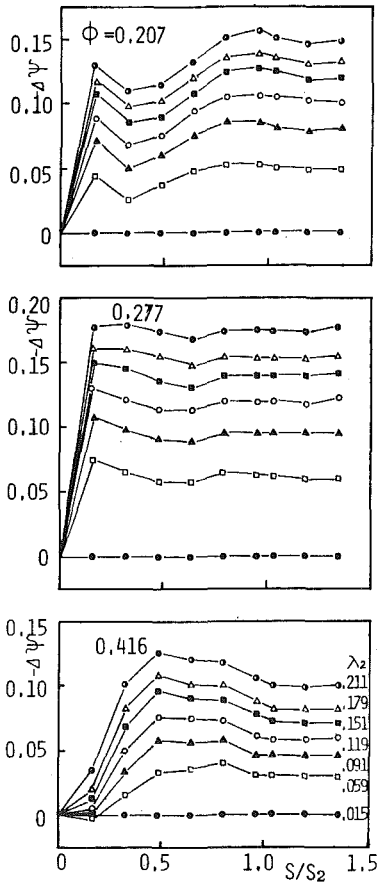

Fig. 8(b) B-blower

Fig. 8 Distribution of pressure-decrement along shroud due to tip clearance (Uncertainty of $-\Delta\psi = \pm 0.008$)

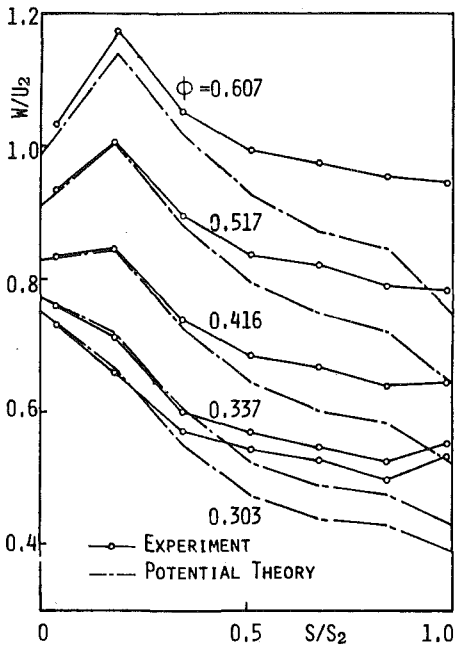

Fig. 9(*a*) R-blower

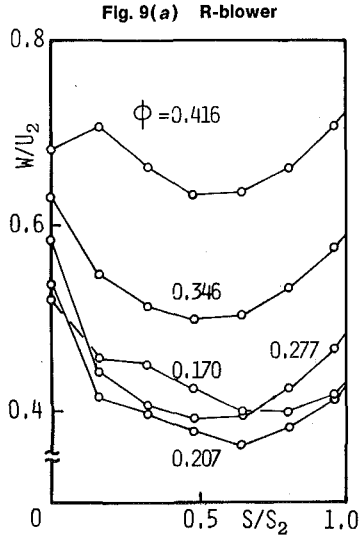

Fig. 9(*b*) B-blower

Fig. 9 Relative velocity distribution along shroud (Uncertainty of $W/U_2 = \pm 0.004$)

eration of relative velocity in the impeller, and the tip clearance ratio at throat λ_t is adopted rather than the tip clearance ratio at the exit λ_2 as the representative tip clearance ratio, because the deceleration of relative velocity is largest at the throat.

The increment of pressure loss due to tip clearance $\Delta\psi_\ell$ obtained above was evaluated relative to the minimum tip clearance condition in the series of test. As a rule it should be evaluated to the zero tip clearance condition. Therefore, after plotting the ratio $\Delta\psi_\ell/\psi_D$ against λ_t, the difference of pressure loss between $\lambda_{t\min}$ and $\lambda_t = 0$ is assumed. Considering the additional pressure rise in the impeller for the case of $\lambda_t = 0$, the value of ψ_D for $\lambda_t = 0$ is evaluated and all the data of $\Delta\psi_\ell$ and ψ_D which were referred to the minimum value of λ_t are corrected so that they are referred to $\lambda_t = 0$. These values are expressed as $\Delta_0\psi_\ell$ and ψ_{DO} and the ratio is plotted against λ_t in Fig. 10. The experimental data for both blowers are plotted, where each symbol mark represents a specific flow rate. The letters R and B on the line represent the values at the minimum clearance conditions of R and B-blowers respectively. These experimental data are approximated by the following empirical equation, in the same fashion as Dunham's empirical equation [10].

$$\Delta_0\psi_\ell = K \cdot \lambda_t{}^n \cdot \psi_{DO} \tag{7}$$

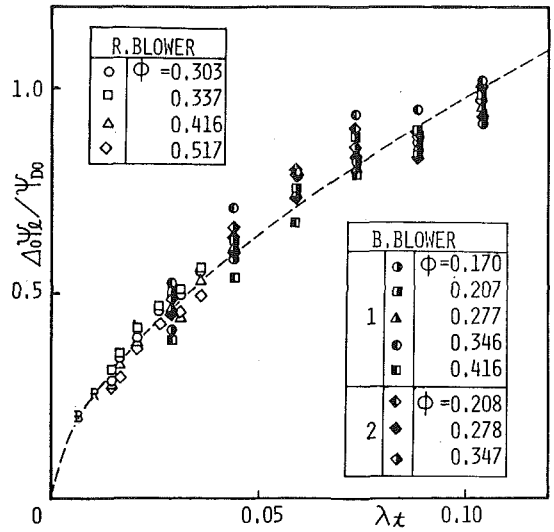

Fig. 10 Correlation between the new pressure loss parameter and the tip clearance at the throat (Uncertainty of ordinate variable is ±0.02 for R-blower and ±0.07 for B-blower)

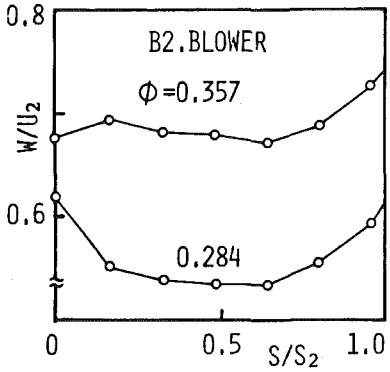

Fig. 11 Relative velocity distribution along shroud; B2-blower (Uncertainty of $W/U_2 = \pm 0.004$)

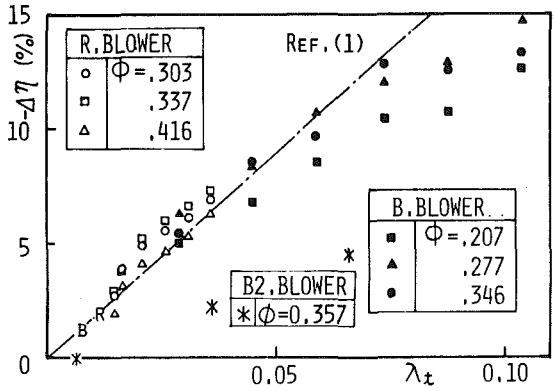

Fig. 12 Decrement of efficiency versus tip clearance ratio at the throat at flow coefficients not far from the optimum flow rate (Uncertainty of $-\Delta\eta = \pm 1.9$ percent)

The dotted line in Fig. 10 represents equation (7) with $K = 3.9$ and $n = 0.6$.

B2-impeller was designed so that the deceleration of relative velocity was low at the flow rate $\varphi = 0.357$. The velocity distribution was calculated with the static pressure along the shroud at two flow rates and the results are presented in Fig. 11.

In Fig. 12, the decrement of efficiency due to the tip clearance is plotted against the tip clearance ratio at the throat for the three test blowers. Only the data near the best efficiency flow rate are included. The experimental data of R-blower and B-blower are scattered along a single curve, but two data points of B2-blower are considerably below the rest of data. Comparing Fig. 12 with Fig. 4 it is clear that

the tip clearance ratio at the throat is the representative clearance ratio of the impeller. The chain line in Fig. 12 indicates Pfleiderer's empirical equation for axial pumps [1]. The experimental data are near the chain line for $\lambda_t < 0.06$, and the efficiency drop is about 9 points when the tip clearance ratio at the throat is 5 percent. The rate of efficiency drop is nearly equal to that of axial flow pumps. It is presumed that the deceleration of relative velocity in many blowers and that of axial pumps is approximately equal to each other, because it is limited by separation of flow. Consequently for many centrifugal blowers and axial pumps the relationship between the efficiency drop and the tip clearance ratio at the throat is represented by Fig. 12. However, it is possible to design impellers so that they are not sensitive to the tip clearance like B2-blower, providing that the deceleration in the impeller is properly controlled.

In the case of B-blower as shown in Fig. 9(*b*), the deceleration of relative velocity is significant only near the entrance region of the impeller. According to the present theory the reduction of pressure loss may be possible if the tip clearance near the entrance region is made narrower.

A ring is attached to the shroud of B-blower as shown on the left hand side of Fig. 13, and the experimental pressure distribution along the shroud for this shroud condition is indicated with open circles. Without the ring and when the tip clearance at the exit λ_2 is the same as the above case, the pressure distribution is indicated with closed circles. Without the ring and when the tip clearance λ_2 is made much smaller so that the tip clearance at the throat λ_t is nearly equal to the above case, the pressure distribution is indicated with triangles. Comparing the open circles with the triangles, it is apparent that the ring is not long enough to completely remove the pressure loss due to the large tip clearance. The ring should be extended to position No. 4 at least. The performances of these blowers are compared in Fig. 14. Although the ring is not long enough, the ring has improved the performance of the blower considerably in comparison with the ordinary blower which has the identical tip clearance at the exit λ_2. This experiment clearly demonstrates the significance of the clearance near the throat for the performance of blowers, although the local value of the clearance at the throat alone does not thoroughly represent the effects of the entire tip clearance along the shroud.

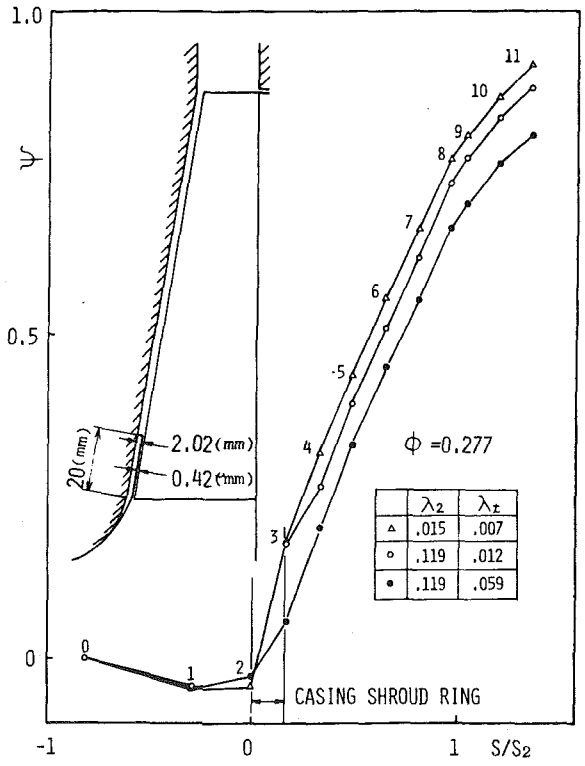

Fig. 13 Pressure distribution along shroud with a shroud ring (Uncertainty of $\psi = \pm 0.008$)

Prediction of Efficiency Drop Based on Tip Clearance. The decrement of impeller efficiency due to tip clearance consists of two parts, the increment of pressure loss in the impeller and the reduction of input power providing that the loss in the impeller remains constant. They are expressed as follows.

$$\Delta\eta = (1 - \eta) \cdot \Delta V_{u2}/V_{u2} - \Delta\psi_\ell/(2V_{u2}/U_2) \tag{8}$$

The first term may be estimated using equation (2) and the second term using equation (7). The decrement of impeller efficiency for the three test impellers was predicted using these equations, and the results are compared with the experimental values in Fig. 15, where the data at flow rates far from the best efficiency condition are excluded. Most of the predicted values are within the ±1 percent band. It should be noted that for the present calculation the experimental pressure distribution was used for ψ_D in equation (7). In cases of R and B-blowers the first term in equation (8) is small compared with the second term. In the cases of B2-blower at $\varphi = 0.357$, which are indicated as stars, the deceleration of relative velocity is little, and the first and the second terms are about equal magnitude. It is presumed that for pumps and blowers with a small blade angle at the impeller exit the efficiency drop due to the first term is significant even if the deceleration in the impeller is little.

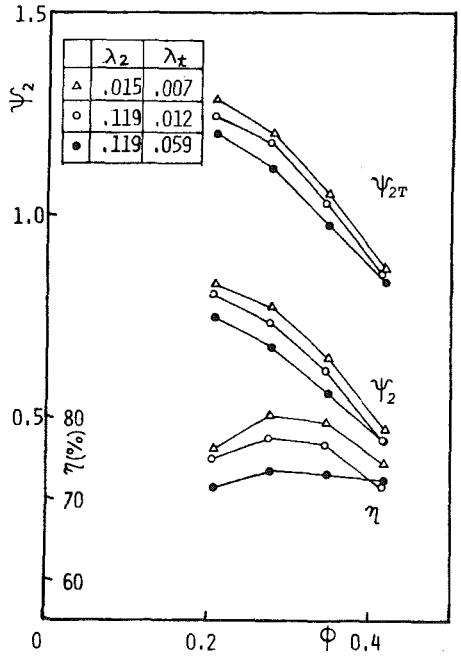

Fig. 14 Improvement of blower characteristics by means of a shroud ring (Uncertainty of $\psi_2 = \pm 0.008$, of $\eta = \pm 1.9$ percent and of $\varphi = \pm 0.003$)

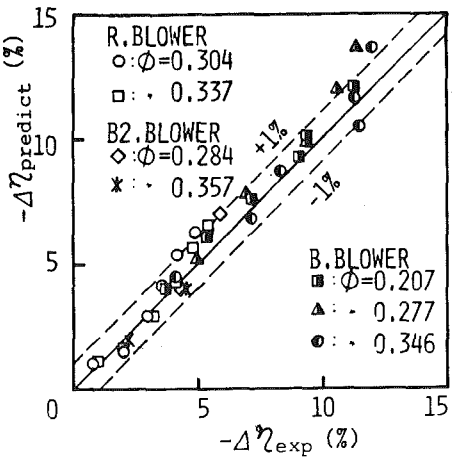

Fig. 15 Comparison of predicted and experimental efficiency-changes due to tip clearance (Uncertainty of $\Delta\eta_{exp} = \pm 1.9$ percent)

Conclusions

The effect of tip clearance on the pressure distribution along the shroud is examined experimentally using two entirely different test blowers, and the following conclusions are derived.

1 The pressure loss due to tip clearance is relatively small in the region where the relative velocity is nearly constant or accelerated in the impeller.

2 The pressure loss due to tip clearance is proportional to the pressure rise based on deceleration of the relative velocity.

3 Since the deceleration rate is maximum near the throat for most impellers, the clearance ratio at the throat should be used as the representative clearance ratio. The pressure loss due to tip clearance is proportional to the tip clearance ratio to the six-tenths power.

4 If the tip clearance near the entrance region of impeller is locally made narrower, where the deceleration of relative velocity is significant, a considerable improvement in performance is expected.

5 The decrement of input torque due to the clearance is related to the blockage of effective area at the impeller exit.

Acknowledgment

The authors are grateful to Messers. H. Haraguchi, K. Kotoura and M. Yokoyama for construction of the experimental apparatus and for securing the experimental data.

References

1 Pfleiderer, C., *Die Kreisel Pumpen,* 5-Auflage, Springer-Verlag, 1961, pp. 99.

2 Kurian, T., and Krishna, H. C. R., "An Experimental Investigation on the Clearance Effects of Semi Open Radial Flow Impellers," 5th Australasian Conference on Hydraulics and Fluid Mechanics, 1974, pp. 44–51.

3 Plutecki, J., and Wajda, A., "The Influence of an Axial Clearance between a Semi-Open Impeller and a Casing on Pump Parameters, By Example of H1-150 Pump," *Proceedings of 5th Conference on Fluid Machinery,* at Budapest, Vol. 2, 1975, pp. 833–845.

4 Wood, G. M., Welna, H., and Lamers, R. P., "Tip-Clearance Effects in Centrifugal Pumps," Trans ASME, Vol. 85, 1965, pp. 932–940.

5 Nanjo, T., Murakami, M., and Heya, N., "Study of High Speed Rotation Pump with Open Impeller," *Trans JSME,* Vol. 24, No. 141, 1958, pp. 319–324, in Japanese.

6 Murakami, M., and Minemura, Y., "Effects of Side Clearance of Semi-Open Impeller Pumps under Air Admitting Conditions," *Trans. JSME,* Vol. 42, No. 354, 1976, pp. 489–496, in Japanese.

7 Pampreen, R. C., "Small Turbomachinery Compressor and Fan Aerodynamics", *Trans ASME,* Vol. 95, 1973, pp. 251–256.

8 Lakshminarayana, B., "Method of Predicting the Tip Clearance Effects in Axial Flow Turbomachinery," *Trans ASME,* Vol. 92, 1970, pp. 467–480.

9 Senoo, Y., and Nakase, Y., "An Analysis of Flow Through a Mixed Flow Impeller," *Trans ASME,* Vol. 94, 1972 pp. 43–72.

10 Dunham, J., and Came, P. M., "Improvements to Anley-Mathieson Method of Turbine Performance Prediction," *Trans ASME,* Vol. 92, 1970, pp. 252–256.

C. S. Tan

Postdoctoral Associate,
Gas Turbine and Plasma Dynamics Laboratory,
Department of Aeronautics and Astronautics,
Massachusetts Institute of Technology,
Cambridge, Mass 02139

Vorticity Modeling of Blade Wakes behind Isolated Annular Blade-Rows: Induced Disturbances in Swirling Flows

A general analysis is proposed for studying the fluid-mechanical behavior of blade wakes from an annular blade-row in highly swirling flow. The coupling between the centrifugal force and the vorticity, which is inherent to highly swirling flows, can significantly modify the wake behavior from that in a two-dimensional situation. In steady flow, theoretical considerations show that a blade wake consists primarily of two distinct types of vorticity: (1) trailing vorticity shed from the blade due to a spanwise variation in blade circulation; and (2) vorticity associated with defects in stagnation pressure (or rotary stagnation in relative coordinate system). Three types of disturbances can be identified in the resulting three-dimensional disturbance field: (1) the exponentially decaying type (potential, irrotational), (2) the purely convected type (rotational), and (3) the nonconvected type (both rotational and irrotational parts). Type (3) arises because of the interaction of centrifugal and Coriolis forces with (1) and (2). It is found that near the blade row the nonconvected disturbances grow linearly in magnitude with the axial distance. However, although those nonconvected disturbances associated with the trailing vorticity (also called Beltrami vorticity) persist for moderate distances downstream, they eventually decay inversely with the axial distance, irrespective of the types of swirl distribution. In contrast, those parts of nonconvected disturbances which are induced by the vorticity caused by (rotary) stagnation pressure defects persist indefinitely downstream for any type of swirl other than free-vortex. In the limit of free-vortex swirl, all disturbances decay at least inversely with the axial distance downstream.

I Introduction

Many analyses have been carried out in recent studies of three-dimensional fluid flow in axial turbomachinery [1–9]. Early theoretical attempts to treat the three-dimensional (inviscid) flow in axial compressors or ducted fans were restricted to lightly loaded blade rows. Consequently, the effects of strong swirl downstream of a blade row were neglected. Nevertheless, the resulting theories have yielded useful information regarding the three-dimensional effects. Other analyses (the secondary flow and the shear flow theories) represent attempts to analyze exclusively some particular aspect of three-dimensional effects; some of these studies have been quite successful in describing and predicting certain three-dimensional flow phenomena due to spanwise variation of loading [10] and finite blade spacing [11]. But many of these theories are based on a rectilinear cascade model, thus precluding the study of those three-dimensional effects due to the swirl which is inherent downstream of a blade row.

Recent advances in analytic theory have made possible consideration of three-dimensional effects resulting from blade wakes in highly swirling flow downstream of a blade-row. In the calculation of velocities induced by the trailing vorticity of a nonuniformly loaded rectilinear cascade for incompressible flow, McCune and Hawthorne [12], using Beltrami flow and lifting line concepts, proposed a theory whereby the downstream three-dimensional disturbances (induced by the trailing vorticity) are linearized about the exit mean flow. That work essentially removed the need for restriction to lightly loaded blade-rows for purposes such as described in this study. Cheng extended the analysis of reference [12] to the case of annular blade rows inducing a nearly free vortex flow [13, 14]. The above analyses show that the three-dimensional induced velocities at each lifting line (representing a blade) increase with the blade loading. However, the latter analyses [13, 14] also assumed that these induced disturbances are purely convected; consequently, they were unable to predict certain significant effects due to the swirl. Adebayo [15] proposed an analysis whereby the restriction of "nearly free-vortex exit flow" could be removed, thus permitting the consideration of three-dimensional induced disturbances in a strongly sheared and/or skewed Beltrami flow.

Kerrebrock [16] has examined the general problem of the behavior of small disturbances in a swirling compressible flow. He showed that shear disturbances can propagate in an environment of swirling throughflow (i.e., they are not purely convective), and, as a result, pressure disturbances are coupled to vorticity and entropy disturbances. Greitzer [17] and Strand [17] also showed clearly this coupling

Contributed by the Gas Turbine Division of The American Society of Mechanical Engineers and presented at the Gas Turbine Conference & Products Show, New Orleans, La., March 10–13, 1980. Manuscript received at ASME Headquarters January 2, 1980. Paper No. 80-GT-140.

between the pressure and vorticity disturbances in swirling flow. Tan [18, 19], in analyzing the induced effects of the blade-wakes formed from the boundary layers on the blades and the trailing vorticity [19], found that the disturbances in a swirling throughflow grow in magnitude within a certain distance downstream of the blade-row before beginning to decay inversely with such axial distance. A similar behavior has also been noted for a circumferential inlet distortion through a blade-row (represented by an actuator disk) inducing a free vortex swirl [18, 20].

The analysis proposed here constitutes a generalization of the analyses proposed in references [18] and [19]. The Clebsch transformation method [21, 22] for describing a flow field is used. In the analysis, a blade wake in steady flow is shown to consist of two distinct types of vorticity: (1) trailing vorticity shed from the blade due to a spanwise variation in blade circulation; and (2) the vorticity associated with stagnation (or rotary stagnation) pressure defect due to viscous or other loss mechanism occurring as the fluid passes over each blade. The former is the direct analogue of the trailing vorticity of classical wing theory, while the latter represents the viscous wake originating from the blade boundary layers. Such separate consideration of vorticity types will help in the physical understanding of the phenomena involved, as the behavior of the induced disturbances can readily be explained in terms of the downstream development of the vorticity field. The analysis is focussed mainly on the induced-flow effects of blade wakes. Hence, viscous effects, i.e., the diffusion of vorticity in the blade wakes, are not of primary interest and are not considered. No restriction is imposed as to the types of swirl distribution except that the stagnation (or the rotary stagnation in rotor coordinates) pressure non-uniformities are taken to be of small magnitude. It is hoped that an understanding of the induced-flow effects of blade wakes in the swirling flow in turbomachines can lead to a better comprehension of the internal aerodynamics of such machines.

II Theoretical Considerations

With uniform (irrotational) incoming flow to an isolated rotor (or blade-row), we can write Euler's equations of motion for the steady flow (in rotor coordinates) of an inviscid, incompressible fluid in the form

$$\mathbf{W} \times \boldsymbol{\Omega} = \nabla \left(\frac{P_t^*}{\rho} \right) \tag{1}$$

where $\mathbf{W}$ is the relative velocity, $\mathbf{W} \equiv \mathbf{V} - \omega r \hat{e}_\theta$, P_t^* the rotary stagnation pressure, ρ the density, and $\boldsymbol{\Omega}$ the absolute vorticity ($\boldsymbol{\Omega} \equiv \nabla \times \mathbf{V}$). A general solution [18, 20] to equation (1) is given by

$$\boldsymbol{\Omega} = \boldsymbol{\Omega}_\tau + \boldsymbol{\Omega}_B = \nabla \left(\frac{P_t^*}{\rho} \right) \times \nabla \tau + \lambda \mathbf{W} \tag{2}$$

where λ is any scalar and $\nabla\tau$ satisfies equation (4) below. The part $\lambda\mathbf{W} = \boldsymbol{\Omega}_B$ satisfies the homogeneous (Beltrami) equation

$$\mathbf{W} \times \boldsymbol{\Omega}_B = 0 \tag{3}$$

Thus, sheets of this type of vorticity (i.e., the trailing vorticity mentioned in (1)) cannot support static pressure changes across them. The other part, $\boldsymbol{\Omega}_\tau = \nabla(P_t^*/\rho) \times \nabla\tau$, is the vorticity associated with variations in the rotary stagnation pressure. The quantity τ is the Darwin-Lighthill-Hawthorne fluid particle "drift time" [22, 23] satisfying the relation

$$\mathbf{W} \cdot \nabla \tau = 1 \tag{4}$$

The variation of τ from streamline to streamline can often be interpreted in terms of the resulting stretching of vortex filaments accounting for the development of streamwise vorticity other than the Beltrami part [20, 24]. As written in equation (2), both $\boldsymbol{\Omega}_\tau$ and $\boldsymbol{\Omega}_B$ are divergence-free.

The analysis can be linearized by expanding the wake-induced nonaxisymmetric disturbance flow ($\tilde{\mathbf{w}}$) about the axisymmetric throughflow ($\overline{\mathbf{W}}$). This is possible whenever the variation in P_t^* caused by the blade solid surfaces (e.g., high Reynolds Number flow) is small. There is no restriction on the extent of spanwise variation in blade circulation [15] as long as the inverse of the parameter (2 × solidity × (aspect ratio of blade)) is small [19]; this parameter is approximately $2\pi/B$ [24, 25], where B is the blade number.

The application of the continuity equation

$$\nabla \cdot \mathbf{W} = 0 \tag{5}$$

allows us to write

$$\mathbf{W} = \overline{\mathbf{W}} + \tilde{\mathbf{w}} = \nabla\alpha \times \nabla\beta \tag{6}$$

and

$$\overline{\mathbf{W}} = \nabla\alpha \times \nabla\psi \tag{7}$$

We note that P_t^* is constant along a streamline of the mean flow because $\overline{\mathbf{W}} \cdot \nabla \tilde{P}_t^* = 0$ (also, $\overline{\mathbf{W}} \cdot \nabla \bar{\tau} = 1$) in the linearized analysis. Thus, we have

$$P_t^* = P_t^*(\alpha, \psi) = \tilde{P}_t^*(\alpha, \psi) + \text{constant} \tag{8}$$

Without restriction, we can choose $\alpha = \theta - f(r, z)$ [12, 24, 25], so that ψ is the Stokes streamfunction for $\overline{\mathbf{W}}$: $f(r, z)$ for the present case is given by

$$f(r, z) = \int_0^z \frac{\overline{W}_\theta}{r \overline{W}_z} dz \approx \frac{\overline{W}_0}{\overline{W}_z} \frac{z}{r}; \quad \text{along constant } \psi \tag{9}$$

We have used (r, θ, z) as the cylindrical coordinate system (Fig. 1). The subscripts r, θ, z denote components in each respective direction.

Because the trailing vorticity is highly concentrated in wake sheets [12, 24] and because of the linearization introduced above, we can write the mean vorticity as

$$\overline{\boldsymbol{\Omega}} = -\frac{B}{2\pi} \frac{d\Gamma}{d\psi} \overline{\mathbf{W}} \tag{10}$$

and the nonaxisymmetric vorticity as

$$\tilde{\boldsymbol{\Omega}} = -\nabla S(\alpha) \times \nabla \Gamma(\psi) + \nabla \left(\frac{\tilde{P}_t^*}{\rho} \right) \times \nabla \bar{\tau} \tag{11}$$

where

Γ is the blade circulation,

$S(\alpha) = -\sum_{n=1}^{\infty} \frac{i e^{inB\alpha}}{n\pi}$ is the sawtooth function [26], and

$\bar{\tau} = \int_0^z \frac{dz}{W_z}$ is the *mean* drift time [22, 23].

In general, we can write the perturbation velocity $\tilde{\mathbf{w}}$ as a sum of an irrotational part $\nabla\phi$, where ϕ is the velocity potential, and a solenoidal part $\mathbf{A}$ so that

$$\tilde{\mathbf{w}} = \nabla\phi + \mathbf{A} \tag{12}$$

It follows from equation (11) that the vector $\mathbf{A}$ can be written as

$$\mathbf{A} = \frac{\tilde{P}_t^*}{\rho} \nabla \bar{\tau} + S(\alpha) \nabla \Gamma(\psi) \tag{13}$$

The first part of $\mathbf{A}$ results from the vorticity associated with a variation in P_t^* while the second results from the trailing vorticity.

Using continuity, $\nabla \cdot \tilde{\mathbf{w}} = 0$, we readily obtain an equation for the perturbation potential ϕ (the upstream flow is simply irrotational and decays exponentially away from the blade-row). For analytical convenience, we can write ϕ as

$$\phi - z \int_h^r \sum_{n=1}^{\infty} \frac{P_n}{\overline{W}_z^2} \frac{d\overline{W}_z}{dr'} e^{inB\alpha} dr'$$

so that the equation for ϕ becomes

$$\nabla^2\phi = -\nabla \cdot \left\{ \sum_{n=1}^{\infty} \frac{P_n}{\overline{W}_z} e^{inB\alpha} \hat{e}_z + \sum_{n=1}^{\infty} \frac{i e^{inB\alpha}}{n\pi} \frac{d\Gamma}{d\psi} \frac{\partial\psi}{\partial r} \hat{e}_r \right\} + \frac{z}{r^2} \sum_{n=1}^{\infty} n^2 B^2 \int_h^r \frac{P_n}{\overline{W}_z^2} \frac{d\overline{W}_z}{dr'} e^{inB\alpha} dr'$$

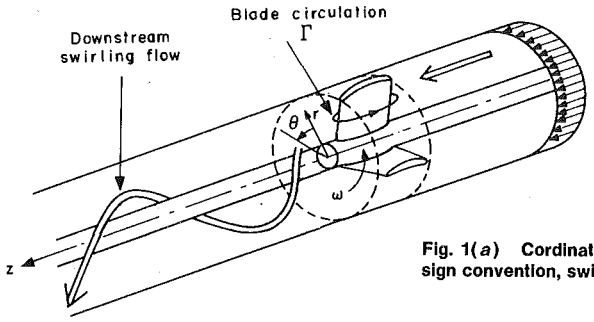

Fig. 1(*a*) Cordinate system, circulation sign convention, swirling flow

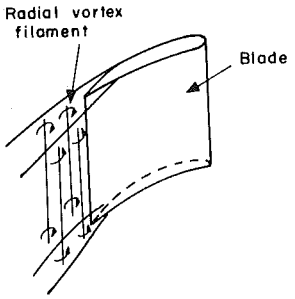

Fig. 1(*b*) Boundary-layer wake from a blade

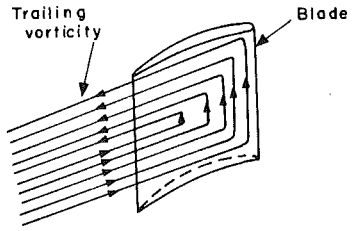

Fig. 1(*c*) Trailing vorticity from a blade

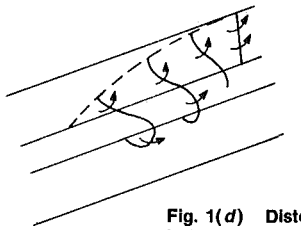

Fig. 1(*d*) Distortion of vortex filament in free vortex swirl

Fig. 1

$$+ z \sum_{n=1}^{\infty} n^2 B^2 \int_h^r \frac{1}{r'^2} \frac{\overline{W}_\theta}{\overline{W}_z} \frac{P_n}{\overline{W}_z^2} \frac{d\overline{W}_z}{dr'} e^{inB\alpha} dr' \quad (14)$$

where we have used $(\tilde{P}_t^*/\rho) = \Sigma_{n=1}^{\infty} P_n e^{inB\alpha}$ and $(\hat{e}_r, \hat{e}_\theta, \hat{e}_z)$ as the unit vectors in the cylindrical coordinate system. All lengths have been nondimensionalized with respect to the tip radius, e.g., h is the hub-to-tip radius. Equation (14) is to be solved under the boundary conditions at hub and tip that the radial velocities vanish there.

Solution of equation (14) yields the downstream three-dimensional perturbation in the form

$$\tilde{\mathbf{w}} = \nabla\phi$$

$$\left.\begin{aligned} &+ \sum_{n=1}^{\infty} \frac{d\Gamma}{d\psi} \frac{\partial\psi}{\partial r} \frac{i}{n\pi} e^{inB\alpha}\hat{e}_r + \sum_{n=1}^{\infty} \frac{P_n}{\overline{W}_z} e^{inB\alpha}\hat{e}_z \quad [(\mathrm{I})] \\ &\quad + i\frac{z}{r} \sum_{n=1}^{\infty} nB \int_h^r \frac{P_n}{\overline{W}_z^2} \frac{d\overline{W}_z}{dr'} e^{inB\alpha} dr' \hat{e}_\theta \\ &- iz \sum_{n=1}^{\infty} nB \int_h^r \frac{\overline{W}_\theta}{r'\overline{W}_z} \frac{P_n}{\overline{W}_z^2} \frac{d\overline{W}_z}{dr'} e^{inB\alpha} dr' \hat{e}_z \quad [(\mathrm{II})] \\ &\quad + \sum_{n=1}^{\infty} \int_h^r \frac{P_n}{\overline{W}_z^2} \frac{d\overline{W}_z}{dr'} e^{inB\alpha} dr' \hat{e}_z \quad [(\mathrm{III})] \end{aligned}\right\} \quad (15)$$

The velocity potential ϕ is given by

$$\phi = \underbrace{\left[\sum_{n=1}^{\infty} \sum_{p=1}^{\infty} A_{np}^d R_{np}(r) e^{inB\theta} e^{-\lambda_{np} z} \right.}_{[(\mathrm{IV})]}$$

$$\left. \underbrace{+ \sum_{n=1}^{\infty} \sum_{p=1}^{\infty} R_{np}(r) e^{inB\theta} Z_{np}(z)}_{[(\mathrm{V})]} \right] \quad (16)$$

where $R_{np}(r)$ are the (by now familiar) orthogonal and normalized cylinder functions [1–9] and the λ_{np} are the corresponding radial eigenvalues determined by satisfaction of the boundary conditions at the hub and tip. The first double sum is the exponentially decaying homogeneous solution typical of annular flows. By substituting (16) in (14), the $Z_{np}(z)$ (see Appendix I) are determined through the use of the orthogonality of the $R_{np}(r)$ and $e^{inB\theta}$ and the application of the hub and tip boundary conditions. Their form is given in Appendix I.

We note that the Fourier Bessel coefficients A_{np}^d (and a similar set A_{np}^u for the upstream flow disturbance) in equation (16) can be determined through the application of matching conditions at the blade-row. Because $\overline{V}_\theta = (B\Gamma/2\pi r)$, the mean flow and the perturbation flow are related through the boundary conditions at the blade-row.

III Behavior of Wake-Induced Disturbances and Analytical Behavior of the Solution

The theoretical considerations in (II) show that in steady flow, a blade wake consists of two distinct types of vorticity: (1) the trailing vorticity, and (2) the vorticity associated with the rotary stagnation pressure defect. The resulting solution indicates that the three-dimensional disturbances may be classified into the following types

1 the exponentially decaying (irrotational); (IV)
2 the purely convected (rotational); (I)
3 the nonconvected (containing both rotational and irrotational

parts); (II) and (III) are rotational while (V) is irrotational.

The Roman numerals above refer to the various terms as marked in equations (15) and (16). It can be noted that the nonconvected disturbances can have different phases among themselves and from the other types of distrubances.

For small z, Taylor expansion in z shows that the magnitude of these nonconvected disturbances grows linearly with z. This trend agrees with the prediction as well as experimental results in reference [17]. For large z, the method of stationary phase shows that the various integrals appearing in $Z_{np}(z)$ have an asymptotic behavior such that they decay at least inversely with z. However, the nonconvected disturbances represented by the integrals in (II) have an asymptotic behavior which indicates that they do not decay at all, but persist indefinitely downstream. Since a pressure field is needed to drive these nonconvected disturbance fields, a nonaxisymmetric persistent pressure field is therefore associated with the persistence of the wake-induced nonconvected disturbances downstream. Thus, there is a strong interaction between the pressure and the vorticity disturbances as was noted in reference [16] (and reference [17] as well). The purely convected disturbances are simply carried along by the mean flow and therefore do not induce a pressure field.

It is worth noting that the trailing vorticity does not contribute directly to the oscillating nonconvected disturbances far downstream; rather, it is the nonconvected disturbances induced by the vorticity associated with a variation in P_t^* which are persisting downstream (compare with reference [16]).

In the limit of free vortex flow, $(d\overline{W}_z/dr) = 0$, only terms in (IV) and the first integral of $Z_{np}(z)$ (in Appendix I) remain; thus, the nonconvected disturbances in this case are seen to grow in strength within a certain distance downstream of the blade-row before beginning to decay inversely with the axial distance. Such behavior agrees with the results in references [18–20].

Mathematically, the above results are also in correspondence with the often-used Riemann-Lebesque Theorem, which states that integrals, e.g., such as those occurring in $Z_{np}(z)$, approach zero as z approaches infinity, provided that the integrand without the exponential factor (which here is to some extent related to the radial distribution of P_t^* or the blade circulation) is Riemann-integrable and provided also that the integral converges absolutely. In other words, the requirement of the Riemann-integrability condition requires simply that the radial distribution of P_t^* and the blade circulation be sufficiently smooth at the exit of the blade row.

Finally, we note that if P_t^* or $d\Gamma/dr$ has a spike at some point $r = r_0$ along the blade span such that it assumes roughly the character

$$\tilde{P}_t^* \text{ or } \frac{d\Gamma}{dr} \sim C_0\delta(r - r_0) \tag{17}$$

where C_0 is some constant, and δ is the Dirac delta function [26]. Then the perturbation in fluid properties could effectively persist "forever" downstream of the blade-row, irrespective of the type of swirl distribution.

The behavior of the blade-wakes as described above will be further studied in terms of the downstream development of the vorticity field in Section (IV).

IV Development of Downstream Vorticity Field

The downstream perturbation vorticity is given by

$$\tilde{\Omega}^d = \frac{1}{r}\sum_{n=1}^{\infty} inB\frac{P_n}{\overline{W}_z}e^{inB\alpha}\hat{e}_r + \left\{\frac{1}{r}\frac{\overline{W}_\theta}{\overline{W}_z}\sum_{n=1}^{\infty}\frac{B}{\pi}\frac{d\Gamma}{d\psi}\frac{\partial\psi}{\partial r}e^{inB\alpha} - \sum_{n=1}^{\infty}\frac{1}{\overline{W}_z}\frac{dP_n}{dr}e^{inB\alpha} + \frac{z}{\overline{W}_z^2}\frac{d}{dr}\left(\frac{\overline{V}_\theta}{r}\right)\sum_{n=1}^{\infty}inBP_ne^{inB\alpha}\right\}\hat{e}_\theta + \left\{\frac{1}{r}\sum_{n=1}^{\infty}\frac{B}{\pi}\frac{d\Gamma}{d\psi}\frac{\partial\psi}{\partial r}e^{inB\alpha} + i\frac{z}{r}\sum_{n=1}^{\infty}nB\frac{P_n}{\overline{W}_z^2}\frac{d\overline{W}_z}{dr}e^{inB\alpha}\right\}\hat{e}_z \tag{18}$$

At the exit plane of the blade row, other than the Beltrami vorticity, the vortex filaments lie on the axial plane only (assuming $dP_n/dr = 0$). Equation (17) illustrates the development of (θ, z) components of vorticity with z (note the secularity in z) accounting for the growth in the streamwise vorticity. This growth in secondary vorticity is associated with a radial variation of angular velocity and axial velocity of the fluid particles (since vortex filaments are frozen onto fluid particles). For free-vortex flow, $\overline{W}_z$ is uniform, but $(\overline{V}_\theta/r)$ varies radially; thus the radial vortex filaments associated with $p_t{}^*$ are turned and distorted into a spiral form around the axis. The resulting tangential component of vorticity contributes to secondary vorticity. At very large distances downstream, the distance between adjacent spiral becomes infinitesimally small that one could hardly single out such distinct wakes even though they are as originally structured as the arrangement of the blade-row itself. Such distortion of vortex filaments could have accounted for the ultimate vanishing of the nonconvected disturbances.

At the other extreme of solid body rotation flow, $(\overline{V}_\theta/r)$ is uniform, but $\overline{W}_z$ varies radially, the resulting radial differential convection of the radial vortex filaments by the mean flow produces axial vorticity which contributes to the growth in streamwise vorticity. In this case, the fluid particles have the same angular velocity throughout, thus no distortion of radial vortex filaments in the way described above occurred. Therefore the blade-wakes are expected to retain their original structure but not their vorticity composition. This may have helped to explain the persistence of nonconvected disturbances far downstream.

V An Example

An example for an isolated rotor in which the blade-wakes have trailing vorticity only is presented here. It corresponds to a nearly free-vortex downstream swirl with

hub-to-tip ratio h of 0.64,

blade number B of 23,

rotor tip speed/axial velocity of 2.4,

(stagnation pressure increase)/[1/2ρ × (rotor speed)^2] of 0.5 and a blade-circulation of

$$\Gamma = 0.172\left\{1 + 0.2\left[\cos\frac{(r-h)}{(1-h)}\pi\right]\right\}$$

The chosen spanwise variation in blade circulation is such that $d\Gamma/dr|_h = d\Gamma/dr|_1 = 0$, which are necessary for satisfying the hub and tip boundary conditions (see Appendix II).

The upstream and the downstream flow are matched in the actuator disc limit at the blade row. Because the blade-wakes have trailing vorticity only, no exit flow angle condition is imposed and used as a matching boundry condition at the blade-row. The computed results (Figs. 2–5) show that the three-dimensional perturbed velocity components increase steadily before beginning to decrease at about $z/r_t = 0.5$ to a negligible value at $z/r_t = 1.5$ (r_t is the tip radius), in agreement with the above results. Such substantial blade-to-blade variations can be attributed to the interaction of the trailing vorticity with the swirling downstream flow. Had we assumed the non-axisymmetric disturbances to be convected by the mean flow, we would have obtained entirely different results as shown in Figs. 6–9. There it is seen that the perturbed static pressure, tangential, and axial velocities decrease to a negligible level at about $z/r_t = 0.05$. Figure 2 also indicates that other harmonics of the static pressure disturbance may have become stronger from about $z/r_t = 0.3$ to $z/r_t = 0.75$.

In an attempt to illustrate another effect due to the induced effects of blade-wakes, we have also computed the induced upwash angle at the lifting line (Fig. 10) to compare with that computed from the axisymmetric actuator disc theory. It is important to point out that such an indication of the induced effects on the upwash angle can only be taken on a qualitative, and not on a quantitative basis since a lifting line model cannot represent a blade-row in all its detail (e.g., location of the leading and trailing edges).

VI Summary and Conclusions

1 A general theory has been developed to analyze the behavior of blade wakes in steady-swirling flow. It shows that a blade-wake consists of two distinct types of vorticity: (i) trailing vorticity shed from the blade due to a spanwise variation in blade circulation; and (ii) the vorticity associated with a rotary stagnation pressure defect due to viscous or other loss mechanisms occurring as the fluid passes over each blade.

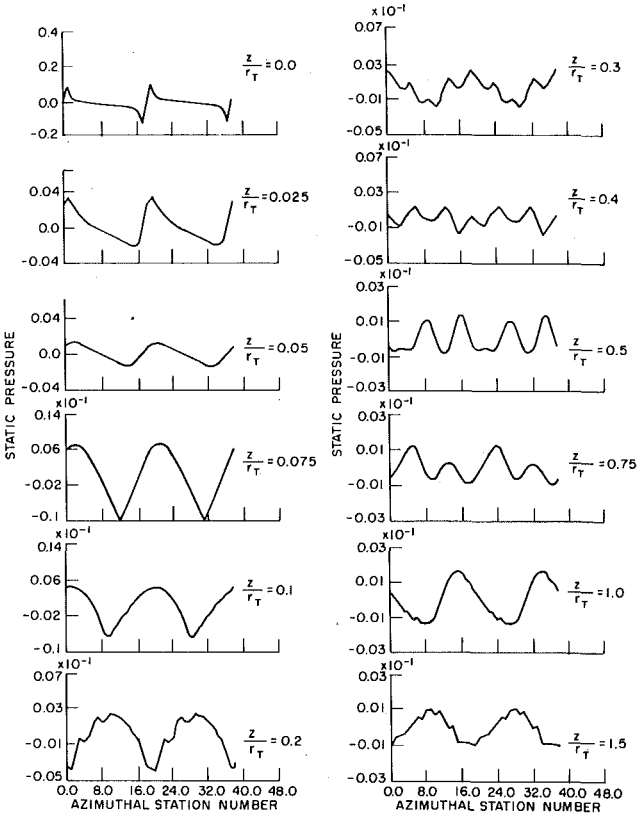

Fig. 2 Circumferential variation of static pressure perturbation (normalized by ρW_z^2) over two blade passages downstream of the rotor at $r/r_T = 0.8$ (n.b.: In Figs. 2–9, the direction of rotation is to the right and the positive θ-direction corresponds to traversing from the pressure side to the suction side of the blade across the blade passage.)

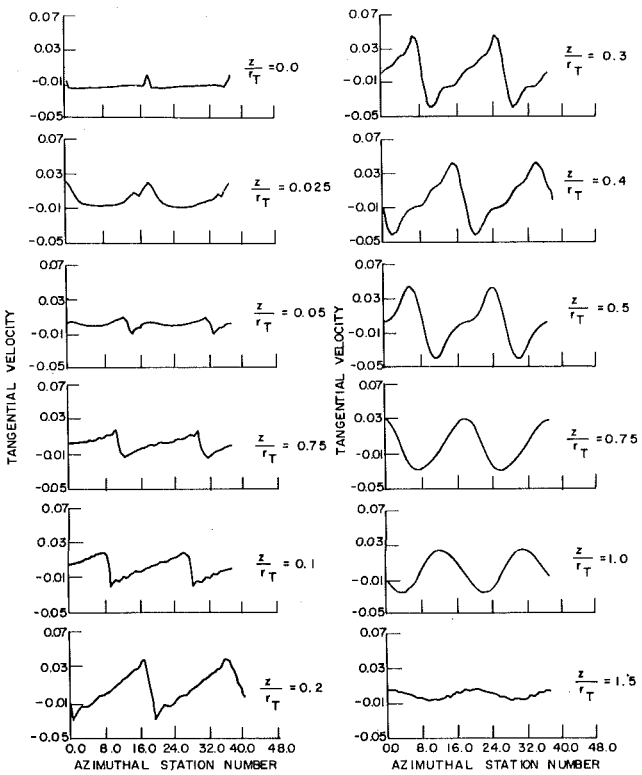

Fig. 4 Circumferential variation of tangential velocity perturbation (normalized by W_z) over two blade passages downstream of the rotor at $r/r_T = 0.8$

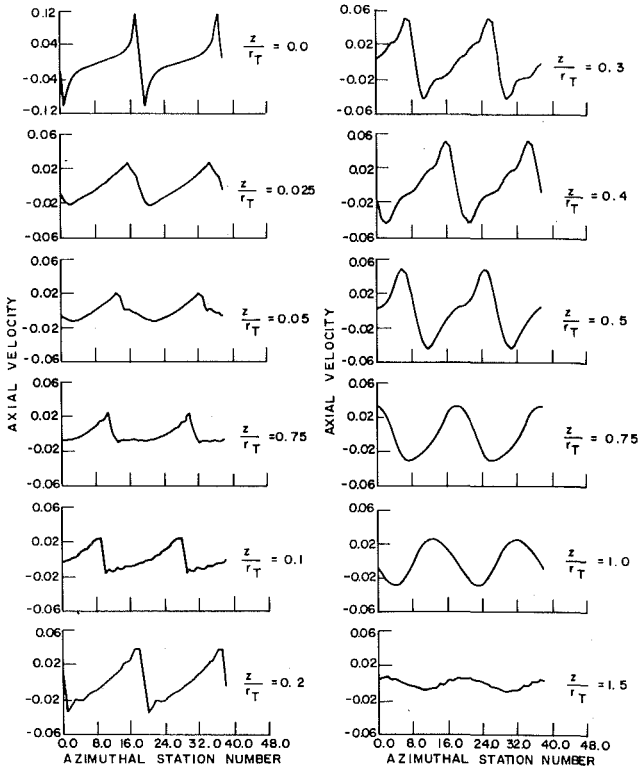

Fig. 3 Circumferential variation of axial velocity perturbation (normalized by W_z) over two blade passages downstream of the rotor at $r/r_T = 0.8$

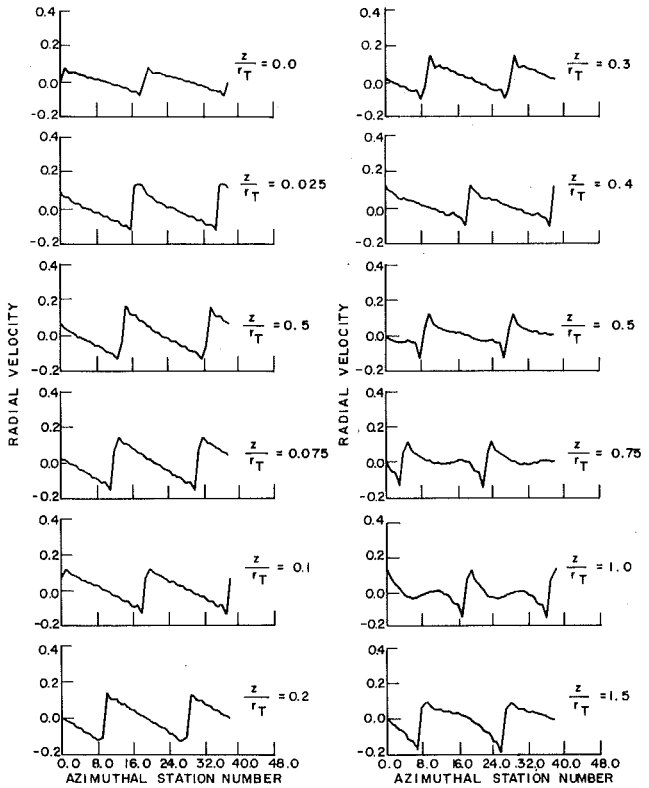

Fig. 5 Circumferential variation of radial velocity perturbation (normalized by W_z) over two blade passages downstream of the rotor at $r/r_T = 0.8$

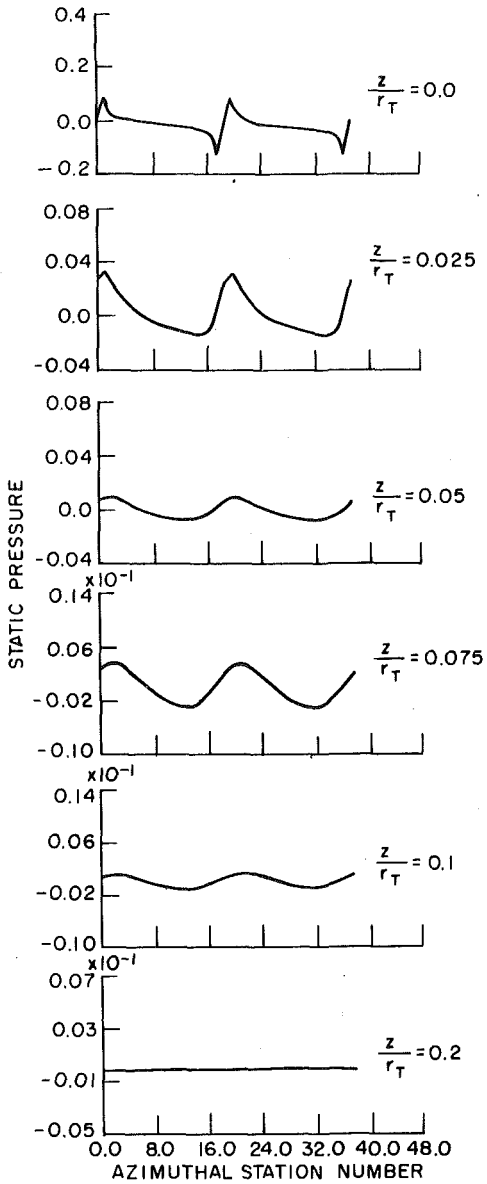

Fig. 6 Static pressure perturbation (normalized by $\rho \overline{W}_z^2$) over two blade passages downstream of rotor at $r/r_T = 0.8$ as given by analysis based on the assumption that wake-induced disturbances are purely convected

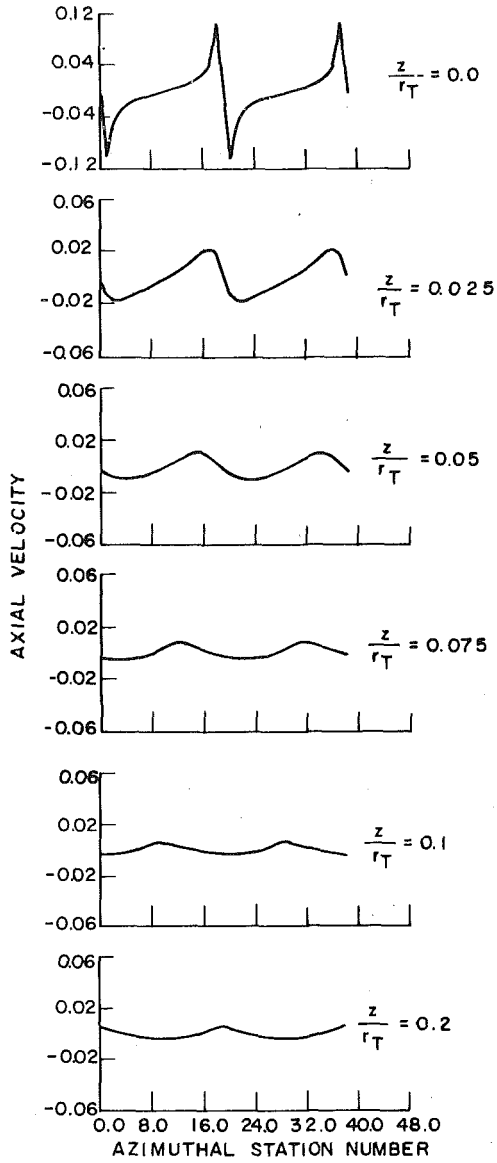

Fig. 7 Axial velocity perturbation (normalized by $\overline{W}_z$) over two blade passages downstream of rotor at $r/r_T = 0.8$ as given by analysis based on the assumption that wake-induced disturbances are purely convected

2 The behavior of the induced disturbances in swirling throughflow is modified significantly from that of the two-dimensional description. The nonconvected disturbances associated with the trailing vorticity persist for a moderate distance downstream of the blade-row, but always decay inversely with the axial distance eventually, irrespective of the type of swirl. However, for non-free vortex swirl, the disturbances induced by the vorticity associated with a variation in rotary stagnation pressure persist indefinitely downstream. In addition a static pressure field is associated with these nonconvected disturbances. Thus pressure and vorticity disturbances are coupled.

3 The behavior of the disturbances induced by the blade wakes is closely related to (and therefore can be explained in terms of) the downstream development of vorticity in an environment of swirling throughflow.

4 In the limit of free-vortex flow, the disturbances increase in magnitude for a moderate distance before decaying inversely with the axial distance. However, if the radial distribution of the rotary stagnation pressure or the radial gradient in blade-circulation has a spike at some radial location, the resulting induced disturbances can persist indefinitely downstream.

5 It is an error to assume that the wake-induced disturbances in a swirling throughflow are purely convected by the mean flow. An analysis based on such an assumption would be erroneous.

Acknowledgment

Even though the author should be considered responsible for the results and ideas presented in this paper, he would like to think of this work as a direct outgrowth of the joint effort with Professor J. E. McCune of the Gas Turbine and Plasma Dynamics Laboratory, MIT, and Professor Sir William R. Hawthorne, Master of Churchill College, Cambridge, England. In the absence of their effort, this work would not have been possible. He is also indebted to Professor E. M. Greitzer of the Gas Turbine and Plasma Dynamics Laboratory, MIT, for his critical ear and comments at various stages of the analytical work, and the discussion leading to the results in Appendix II.

The research is supported by the Air Force Office of Scientific Research, AFSC, U.S. Air Force, under contract No. F49620-78-C-0084.

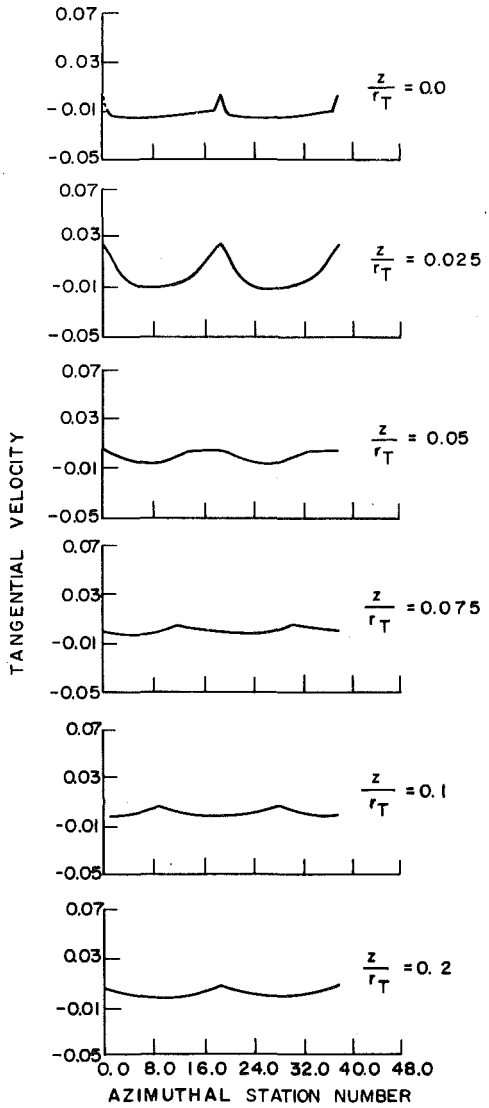

Fig. 8 Tangential velocity perturbation (normalized by $\overline{W}_z$) over two blade passages downstream of rotor at $r/r_T = 0.8$ as given by analysis based on the assumption that wake-induced disturbances are purely convected

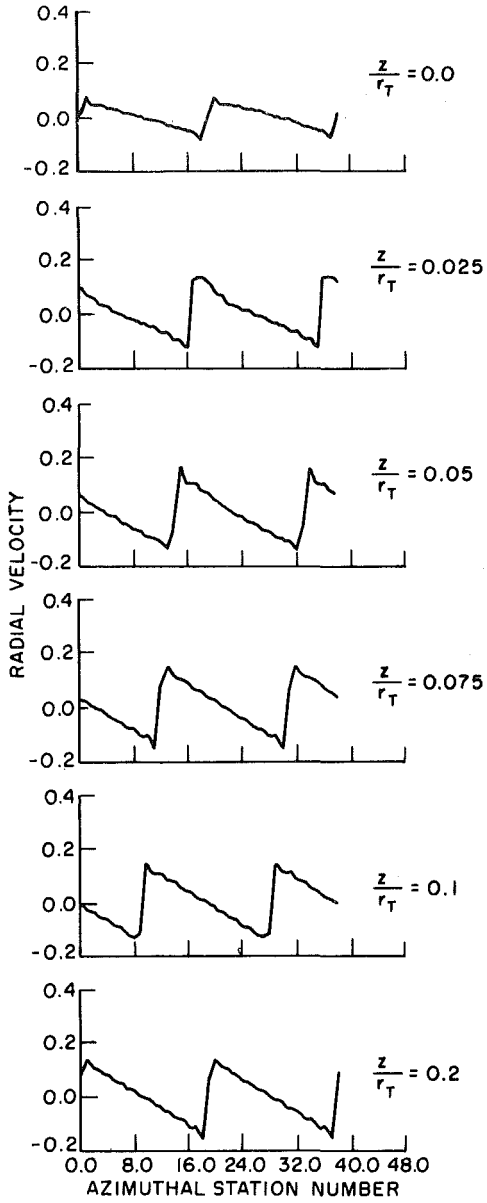

Fig. 9 Radial velocity perturbation (normalized by $\overline{W}_z$) over two blade passages downstream of rotor at $r/r_T = 0.8$ as given by analysis based on the assumption that wake-induced disturbances are purely convected

References

1 Namba, M., "Lifting Surface Theory for a Rotating Subsonic or Transonic Blade Row," Aeronautic Research Council, R&M No. 3740.

2 Falcao, A. F., deO., "Three-Dimensional Flow Analysis in Axial Turbomachines," PhD thesis, Eng. Dept., Cambridge University, 1970.

3 McCune, J. E., "A Three-Dimensional Theory of Axial Compressor Blade Rows—Subsonic, Supersonic and Transonic," PhD thesis, Cornell Univ. 1958. (See also, USAFOSR TN-58-72, *Journal of Aeronautical Space Science,* Vol. 25, 1958, pp. 544, 616.)

4 Okurounmu, O., and McCune, J. E., "Transonic Lifting Surface Theory for Axial Flow Compressors," United Aircraft Res. Labs., E. Hartford, CT, Report No. K 213580-1, 1971.

5 Okurounmu, O., and McCune, J. E., "Lifting Surface Theory of Axial Compressor Blade Rows: Part I—Supersonic Compressor," *AIAA Journal,* Vol. 12, 1974, p. 1363.

6 Okurounmu, O., and McCune, J. E., "Lifting Surface Theory of Axial Compressor Blade Rows: Part II—Transonic Compressor," *AIAA Journal,* Vol. 12, 1974, p. 1372.

7 McCune, J. E., and Okurounmu, O., "Three-Dimensional Flow in Transonic Axial Compressor Blade Rows," *Proceedings for Institute Symposium of Fluid Mechanics,* Acoustics and Design of Turbomachinery, Penn State Univ., Ed. B. Lakshminarayana, W. R. Britisch and W. S. Gearhart, 1970. (See also, NASA Sp. Publ. SP-304, Pt 1 (N75-11174), p. 155.)

8 McCune, J. E., and Dharwadkar, S. P., "Lifting-Line Theory for Subsonic Axial Compressor Rotors," MIT Gas Turbine Lab. Report No. 110, July 1972.

9 Homicz, G. F. and Lordi, S. A., "Three-Dimensional Lifting-Surface Theory for an Annular Blade Row," presented at ASME Gas Turbine Conference, Mar. 11–15, 1979.

10 Hawthorne, W. R., "Rotational Flow through Cascades," Part I, *Quarterly Journal of Mechanics and Applied Mathematics,* Vol. 8, 1955, pp. 266–280.

11 Hawthorne, W. R., and Armstrong, W. D., "Rotational Flow through Cascades," Part II, *Quarterly Journal of Mechanics and Applied Mathematics,* Vol. 8, 1955, pp. 280–292.

12 McCune, J. E., and Hawthorne, W. R., "The Effects of Trailing Vorticity on the Flow through Highly-Loaded Cascades," *Journal of Fluid Mechanics,* 1976.

13 Cheng, W. K., "A Three-Dimensional Theory for the Velocity Induced by a Heavily Loaded Annular Cascade of Blades," SM thesis, Aero & Astro, MIT, June 1975.

14 Cheng, W. K., "Uniform Inlet Three-Dimensional Transonic Beltrami Flow through a Ducted Fan," MIT GTL Report 130, 1977.

15 Adebayo, A. O., "Three-Dimensional Beltrami Flow in Turbomachinery with Strong Arbitrary Swirl," PhD thesis, MIT, June 1978.

16 Kerrebrock, J. L., "Small Disturbances in Turbomachine Annuli with Swirl," GTL Report No. 125, MIT, 1975. Also *AIAA Journal 15,* 6, June 1977.

17 Gretizer, E. M., and Strand, T., "Asymmetric Swirling Flow in Turbomachine Annuli," ASME JOURNAL OF ENGINEERING FOR POWER, 100, 1978, p. 618.

18 Tan, C. S., "Three-Dimensional Vorticity-Induced Flow Effects in Highly-Loaded Axial Compressors," PhD thesis, MIT, June 1978.

19 Tan, C. S., "Three-Dimensional Incompressible and Compressible Beltrami Flow through a Highly-Loaded Isolated Rotor," to be published as GTL report.

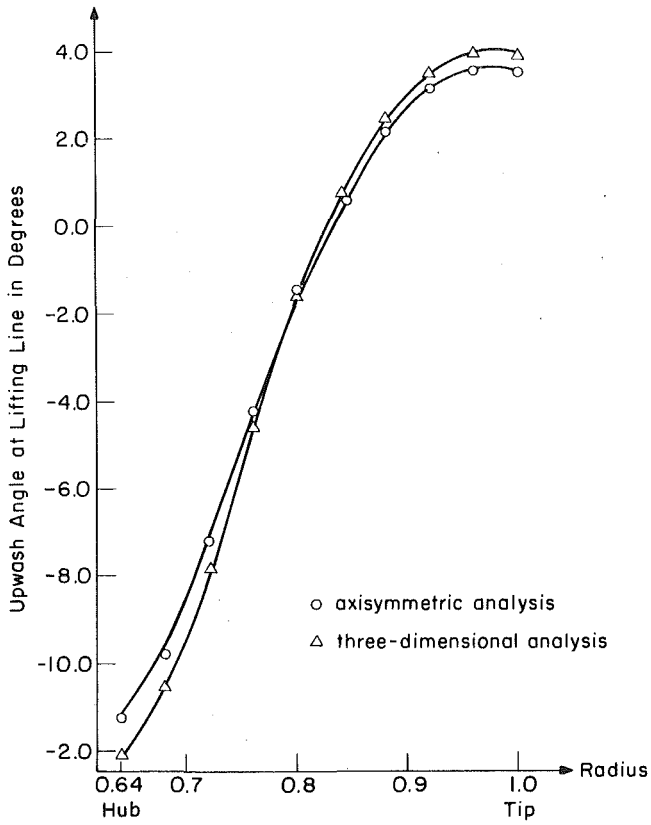

Fig. 10 Radial variation of upwash angle at lifting lines (blade No. 23)

20 Hawthorne, W. R., McCune, J. E., Mitchell, N. A., and Tan, C. S., "Non-Axisymmetric Flow through an Annular Actuator Disc; Inlet Distortion Problem," prep. for ASME mtg, London, Apr. 1978. Published in *Journal of Engineering for Power*, Vol. 100, 1978, p. 664.

21 Lamb, H., *Hydrodynamics*, 6th Ed., Cambridge University Press, Cambridge, 1932.

22 Hawthorne, W. R., "On the Theory of Shear Flow," MIT GTL Report No. 88, 1966.

23 Lighthill, M. J., "*Drift*," *Journal of Fluid Mechanics*, Vol. 1, pp. 31–53, 1956, note also "Corregenda to Drift," *Journal of Fluid Mechanics*, 1957, Vol. 2, pp. 311–2.

24 McCune, J. E., "Three-Dimensional Inviscid Flow through a Highly-Loaded Transonic Compressor Rotor," *Proceedings Workshop of Transonic Flow through Turbomachinery*, T. C. Adamson, Ed., 1977.

25 McCune, J. E., "Three-Dimensional Flow in Highly-Loaded Axial Turbomachines," MS. No. 56180(22S2), *Zeitschrift fuer Angewandte, Mathematik und Physik*, Nov. 1977.

26 Lighthill, M. J., *An Introduction to Fourier Analysis and Generalized Functions*, Cambridge University Press, Cambridge, 1959.

APPENDIX I

Definitions and Derivations

On substituting (16) in (14) we obtained

$$\sum_{n=1}^{\infty}\sum_{p=1}^{\infty} e^{inB\theta} \times \left\{Z_{np}\left(\frac{d^2R_{np}}{dr^2}+\frac{1}{r}\frac{dR_{np}}{dr}-\frac{n^2B^2}{r^2}R_{np}\right)+\frac{d^2Z_{np}}{dz^2}R_{np}\right\}$$
$$= -\frac{1}{r}\frac{\partial}{\partial r}\left(r\sum_{n=1}^{\infty}\frac{ie^{inB\alpha}}{n\pi}\frac{d\Gamma}{d\psi}\frac{\partial\psi}{\partial r}\right)-\frac{\partial}{\partial z}\left(\sum_{n=1}^{\infty}\frac{P_n}{\overline{W}_z}e^{inB\alpha}\right)$$
$$+\frac{z}{r^2}\sum_{n=1}^{\infty}n^2B^2\int_h^r\frac{P_n}{\overline{W}_z^2}\frac{d\overline{W}_z}{dr'}e^{inB\alpha}dr'$$
$$+z\sum_{n=1}^{\infty}n^2B^2\int_h^r\frac{1}{r'^2}\frac{\overline{W}_\theta^2}{\overline{W}_z^2}\frac{P_n}{\overline{W}_z^2}\frac{d\overline{W}_z}{dr'}e^{inB\alpha}dr' \quad (A\text{-}1)$$

The $R_{np}(r)$ must satisfy

$$\frac{d^2R_{np}}{dr^2}+\frac{1}{r}\frac{dR_{np}}{dr}+\left(\lambda_{np}^2-\frac{n^2B^2}{r^2}\right)R_{np}=0 \quad (A\text{-}2)$$

Hence for each n,

$$\sum_{p=1}^{\infty}\left(\frac{d^2Z_{np}}{dz^2}-\lambda_{np}^2Z_{np}\right)R_{np}$$
$$= -\frac{1}{r}\frac{\partial}{\partial r}\left(r\frac{i}{n\pi}\frac{d\Gamma}{d\psi}\frac{\partial\psi}{\partial r}e^{-inB\frac{z}{r}\frac{\overline{W}_\theta}{\overline{W}_z}}\right)$$
$$-\frac{\partial}{\partial z}\left(\frac{P_n}{\overline{W}_z}e^{-inB\frac{Z}{r}\frac{\overline{W}_\theta}{\overline{W}_z}}\right)$$
$$+\frac{z}{r^2}n^2B^2\int_h^r\frac{P_n}{\overline{W}_z^2}\frac{d\overline{W}_z}{dr'}e^{-inB\frac{z}{r}\frac{\overline{W}_\theta}{\overline{W}_z}}dr'$$
$$+zn^2B^2\int_h^r\frac{1}{r'^2}\frac{\overline{W}_\theta^2}{\overline{W}_z^2}\frac{P_n}{\overline{W}_z^2}\frac{d\overline{W}_z}{dr'}e^{-inB\frac{z}{r}\frac{\overline{W}_\theta}{\overline{W}_z}} \quad (A\text{-}3)$$

Upon multiplying this equation by $rRnq$ and integrating from $r = h$ to 1 we obtain, by virtue of the orthogonality of $\{Rnq\}$

$$\frac{d^2Z_{np}}{dz^2}-\lambda_{np}^2Z_{np}(z)$$
$$=\left\{-\int_h^1 R_{np}\frac{\partial}{\partial r}\left[r\frac{i}{n\pi}\frac{\partial\Gamma}{\partial\psi}\frac{\partial\psi}{\partial r}e^{-inB\frac{z}{r}\frac{\overline{W}_\theta}{\overline{W}_z}}\right]dr\right.$$
$$+inB\int_h^1 R_{np}\frac{\overline{W}_\theta}{\overline{W}_z}\frac{P_n}{W_z}e^{-inB\frac{z}{r}\frac{\overline{W}_\theta}{\overline{W}_z}}dr$$
$$+zn^2B^2\int_h^1\frac{R_{np}}{r}\left[\int_h^r\frac{P_n}{\overline{W}_z^2}\frac{d\overline{W}_z}{dr'}e^{-inB\frac{z}{r'}\frac{\overline{W}_\theta}{\overline{W}_z}}dr'\right]dr$$
$$+zn^2B^2\int_h^1 rR_{np}\left[\int_h^r\frac{1}{r'^2}\left(\frac{\overline{W}_\theta}{\overline{W}_z}\right)^2\frac{P_n}{\overline{W}_z^2}\frac{d\overline{W}_z}{dr'}e\right.$$
$$\left.\left.-inB\frac{z}{r'}\frac{\overline{W}_\theta}{\overline{W}_z}dr'\right]dr\right\} \quad (A\text{-}4)$$

The solution of (A-4) by the method of variation of parameters yields the particular solution as

$$Z_{np}(z)=-\int_h^1 F_{np}(r,z)\left[\frac{i}{n\pi}r\frac{d\Gamma}{d\psi}\frac{\partial\psi}{\partial r}\frac{dR_{np}}{dr}+inB\frac{\overline{W}_\theta}{\overline{W}_z}R_{np}\frac{P_n}{\overline{W}_z}\right]dr$$
$$-zn^2B^2\int_h^1\frac{R_{np}}{r}\left[\int_h^r F_{np}(r',z)\frac{P_n}{\overline{W}_z^2}\frac{d\overline{W}_z}{dr'}dr'\right]dr$$
$$-zn^2B^2\int_h^1 rR_{np}\left[\int_h^r F_{np}(r',z)\frac{1}{r'^2}\left(\frac{\overline{W}_\theta}{\overline{W}_z}\right)^2\frac{d\overline{W}_z}{dr'}\frac{P_n}{\overline{W}_z^2}dr'\right]dr$$
$$+i2n^3B^3\int_h^1\frac{R_{np}}{r}\left[\int_h^r F_{np}(r',z)\frac{P_n}{r'\overline{W}_z^2}\left(\frac{\overline{W}_\theta}{\overline{W}_z}\right)\frac{d\overline{W}_z}{dr'}dr'\right]dr$$
$$+i2n^3B^3\int_h^1 rR_{np}\left[\int_n^r F_{np}(r',z)\frac{P_n}{r'^3\overline{W}_z^2}\left(\frac{\overline{W}_\theta}{\overline{W}_z}\right)^3\right.$$
$$\left.\times\frac{d\overline{W}_z}{dr'}dr'\right]dr\Bigg\} \quad (A\text{-}5)$$

where

$$F_{np}(r,z)=\frac{e^{-inB\frac{z}{r}\frac{\overline{W}_\theta}{\overline{W}_z}}}{\left[\lambda_{np}^2+\frac{n^2B^2}{r^2}\left(\frac{\overline{W}_\theta}{\overline{W}_z}\right)^2\right]}.$$

The normalized cylinder functions used here and in the text are given by

$$R_{np}(r)=\frac{J_{nB}(\lambda_{np}r)-\frac{J'_{nB}(\lambda_{np})}{Y'_{nB}(\lambda_{np})}Y_{nB}(\lambda_{np}r)}{\left\{\int_h^1 r\left[J_{nB}(\lambda_{np}r)-\frac{J'_{nB}(\lambda_{np})}{Y'_{nB}(\lambda_{np})}Y_{nB}(\lambda_{np}r)\right]^2dr\right\}^{1/2}} \quad (A\text{-}6)$$

where the J_{nB} and Y_{nB} are the Bessel Functions of the first and second kind, and the primes on J_{nB} and Y_{nB} indicate differentiation with respect to argument.

APPENDIX II

A Note on the Necessity of the Vanishing of Spanwise Gradient of Blade Circulation at the Hub and Tip of an Axial Turbomachine for Irrotational Inlet Flow[1]

Since the flow upstream is irrotational, the circulation around circuit C is zero (see Fig. 11), i.e.,

$$\oint_C V ds = 0 \tag{B-1}$$

By Kelvin's theorem, the circulation around C must remain zero when it deforms and wraps around a particular blade as shown in Fig. 11. Thus,

$$\Gamma_2 - \Gamma_1 = (r_2 - r_1)\overline{\Delta v_r} = \delta r \overline{\Delta v_r} \tag{B-2}$$

where $\overline{\Delta v_r}$ is the average radial velocity jump across the trailing vortex sheet in the region δr (this implies that $\Gamma_2 \neq \Gamma_1$).

Let Γ_w be the blade circulation at the wall, then

$$\Gamma_w - \Gamma_1 = \frac{d\Gamma}{dr}(r_w - r_1) + 0(r_w - r_1)^2 \tag{B-3}$$

For r_1 sufficiently close to the wall

$$\Gamma_w - \Gamma_1 = \frac{\overline{d\Gamma}}{dr}(r_w - r_1) = \overline{\Delta v_r}(r_w - r_1) \tag{B-4}$$

where $\overline{\ }$ denotes the average value.

But,

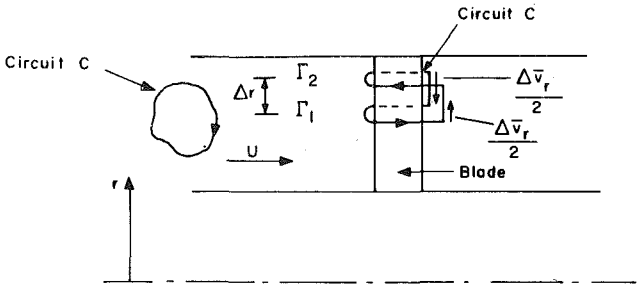

Fig. 11

$$\overline{\Delta v_r} = (\overline{\Delta v_r})_w + \left(\frac{d\overline{\Delta v_r}}{dr}\right)_{\text{wall}}(r_w - r_1)h \tag{B-5}$$

where $0 \leq h < 1$.

As $(\overline{\Delta v_r})_w = 0$ (no normal velocity at the wall)

$$\frac{d\Gamma}{dr} < \left(\frac{d\overline{\Delta v_r}}{dr}\right)_{\text{wall}}(r_w - r_1) \tag{B-6}$$

so that

$$\frac{\overline{d\Gamma}}{dr} \to \left(\frac{d\Gamma}{dr}\right)_{\text{wall}} \to 0 \tag{B-7}$$

for $r_1 \to r_w$ as long as $(\overline{d\Delta v_r}/dr)$ is a good function in the sense of Lighthill [26].

Hence, the blade-circulation has no spanwise gradient at the hub and tip for irrotational inlet flow.

[1] Dr. L. H. Smith has brought to my attention the fact that he has explained this condition more generally in his paper on "Secondary Flow in Axial-Flow Turbomachinery," *Trans ASME,* 1977, pp. 1065–1955. For this, the author is grateful.

Rotordynamic Instability in Centrifugal Compressors—Are All the Excitations Understood?

J. M. Vance
Dresser Industries Associate Professor.

F. J. Laudadio
Research Associate.

Department of Mechanical Engineering,
Texas A&M University,
College Station, Tex

A published history of rotordynamic instability problems with centrifugal compressors is documented from the literature. Established theory for computerized stability analysis is reviewed, and the use of cross-coupled stiffness and damping coefficients to represent destabilizing forces is explained. A derivation of cross-coupled stiffness coefficients for torquewhirl is presented. Experimental measurements made on a simple test rig with a radial-vaned impeller are described, which show that a working fluid can exert destabilizing forces on such an impeller. These forces must be considered, in addition to journal bearing and internal hysteresis excitations, if accurate predictions of rotordynamic instability thresholds are to be made. Several classifications of these forces are hypothesized.

Introduction

As the pressure and delivery flow ratings of modern centrifugal compressors have increased, serious nonsynchronous whirling problems have appeared in some machines which were designed to operate above the first shaft bending critical speed. Nonsynchronous whirling is usually indicative of incipient rotordynamic instability, with the motion growing destructively large if either a speed threshold or load threshold (or both) is exceeded. Such instabilities cannot be detected by no-load shop tests, and in some cases the design pressures and power requirements are so high as to make full-load testing very expensive.

The purpose of this paper is to review the current state of knowledge about the destabilizing excitations which produce nonsynchronous whirling in centrifugal compressors, and to suggest the possibility of additional excitations which have not been heretofore identified or studied. A better understanding of the destabilizing forces acting in these machines would improve the efficiency of trouble-shooting rotordynamic problems, and could also lead to improved compressor impeller/rotor designs with better inherent stability.

Background

Rotor dynamics is one of the areas in applied mechanics which has a long and productive history of intensive investigation. Rankine [1] made an investigation of shaft whirling over one hundred years ago. Since that time, many basic questions of rotor dynamics have been resolved, but advances in rotating machinery performance have raised new ones.

The most predominant type of motion which has been observed and predicted in rotor-bearing systems is *synchronous whirl,* in which the rotor center whirls at the speed of shaft rotation. In this case, the phase angle between the unbalance vector and the rotor whirl vector can change only if the speed changes. The driving force in synchronous whirl is mass unbalance (either static or dynamic) and the whirl amplitude can be controlled by a combination of refined balancing and adjustment of rotation speed away from critical speeds. This paper is not concerned with synchronous whirl or rotor balancing methods.

Motions in which the deflected rotor center whirls at a speed different from the shaft speed have been called *nonsynchronous whirl.* They are usually potentially more destructive. Some troublesome types which have been studied are:

1 *Oil whip,* which is excited by fluid film bearing forces when the shaft speed reaches twice the first critical speed [2],
2 *Parametrically excited whirl,* associated with the critical speed separation due to asymmetric rotor inertia or stiffness properties [3] or pulsating torque [4] and
3 *Friction-induced whirl,* which is excited by internal hysteresis in rotating parts at speeds above the first flexural critical speed [5].

All three of these self-induced motions can be unstable with increasing speed.

As the power and torque ratings of modern rotating machines have increased, serious nonsynchronous shaft whirling problems have appeared in some machines which are sensitive to the work load. In 1965, Alford [6] published a paper which describes the phenomenon thusly: "Whirling occurs in the direction of rotation. . . Large power inputs to the compressor rotor appear to increase the hazard of whirl. The vibration problem was encountered only at the full 100 percent power rating of the engine." Alford goes on to describe a theory of aerodynamic exciting forces due to variable blade tip clearance in axial flow machines. According to Ehrich [7] the tip clearance theory was first hypothesized by Fiske, McClurkin and Fehr of the General Electric Company in 1947. It has never been experimentally verified.

Alford's work was a landmark paper, since it was the first published explanation of a torque-load-dependent destabilizing mechanism, and is the basis for cross-coupled stiffness input to computerized stability analyses in current use by rotor dynamicists. However, it should be remembered that Alford developed the theory for axial flow machines, and it does not seem reasonable to apply it to centrifugal machines.

Contributed by the Gas Turbine Division of THE AMERICAN SOCIETY OF MECHANICAL ENGINEERS and presented at the Gas Turbine Conference and Products Show, New Orleans, La., March 10–13, 1980. Manuscript received at ASME Headquarters January 3, 1980. Paper No. 80-GT-149.

After listing eight different mechanisms known to excite vibration instability in rotating machinery, Ehrich [8] states: "While this tabulation accounts for many observed incidents of instability in turbomachinery, there are occasions reported where other excitation mechanisms must be sought, particularly when the instability is induced by increases in mass flow rate."

In a paper published in 1975 [9], Wachel describes in detail the case histories of three different centrifugal compressors which exhibited load-dependent nonsynchronous vibration. In his case No. 2, "the unit was running at 11,000 rpm with a small amplitude of instability at 4500 cpm. When the suction pressure was increased, the vibration tripout occurred. . . At a constant speed, the subsynchronous frequency was a function of the pressure ratio across the compressor. The design discharge pressure could not be reached."

In another paper presented at the same conference with the above, Fowlie and Miles [10] describe similar problems with high pressure centrifugal compressors: "Destructive vibration of the reinjection centrifugal compressors delayed startup of Chevron's Kaybob Gas Plant. The main vibration was an unstable type whose frequency was substantially below the running speed. . . Not even the leading rotor dynamics consultants could simulate these rotors. . . We believe full-pressure, full-speed mechanical testing in the factory is essential for new machines near or beyond the boundaries of verified field experience. Research and development in this area is required by the manufacturers and the consultants to develop reliable prediction methods of the instability phenomena."

In 1975 and 1976 the first author was involved in an engineering consulting job to identify and correct sources of nonsynchronous instability in a centrifugal compressor used for natural gas reinjection in an oilfield. Attempts to bring this machine up to the design pressure and load produced nonsynchronous whirling of an amplitude proportional to the load, so that vibration trip-outs were actuated long before full load was reached. This machine was fully stabilized by redesigning the shaft to a larger diameter (raising the critical eigenvalue), which necessarily reduced the rated design discharge pressure, due to the axial flow restriction by the larger shaft.

Most of the machines discussed above passed full speed, no load, shop tests before being installed for service with no evidence of a vibration problem.

Field observations of some of the machines described above indicated that the nonsynchronous vibration was often acceleration-dependent as well as load-dependent. That is, a higher load and speed could be reached without vibration trip-out if it was approached slowly. Since the vibration in these cases was not synchronous, it must be a different phenomenon than the effect of acceleration on the critical speed response analyzed by several investigators in the past.

Established Theory

Lund [11] has extended the Myklestad-Prohl transfer matrix method to rotor-bearing systems which include damping and destabilizing cross-coupled stiffness and damping coefficients. Whereas the Myklestad-Prohl method yields only the imaginary part of the eigenvalues (i.e., the natural frequencies), the Lund method yields complex eigenvalues (i.e., both the natural frequencies and the logarithmic decrement, which is a stability predictor).

The coordinates used in Lund's analysis are shown in Fig. 1. In general, the stiffness and damping coefficients form the matrices which define the forces and moments on each disk in the x and y directions.

For example, the force on a disk in the x direction, due to disk displacement and velocity, is

$$F_x = -K_{xX}x - K_{xy}Y - C_{xx}\dot{X} - C_{xy}\dot{Y} - K_{x\alpha}\dot{\alpha} - K_{x\beta}\dot{\beta} - C_{x\alpha}\dot{\alpha} - C_{x\beta}\dot{\beta}$$

and the matrix equation for the forces in all directions (on a single disk) is

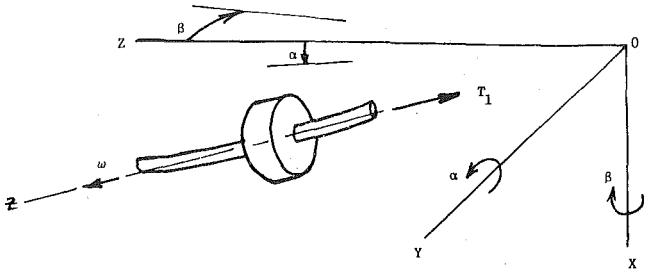

Fig. 1 Coordinates for linearized stability analysis

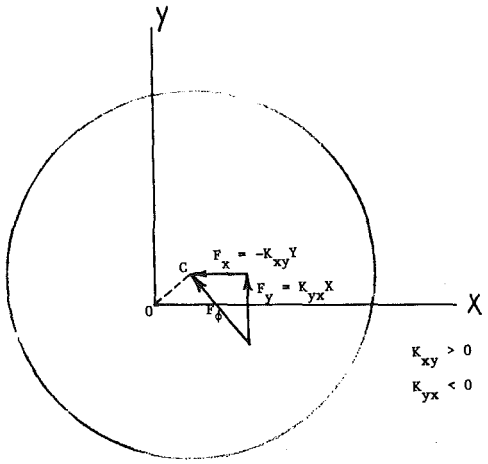

Fig. 2 Cross-coupled stiffness representation of destabilizing force in a deflected rotor disk

$$\begin{Bmatrix} F_x \\ F_y \\ F_\alpha \\ F_\beta \end{Bmatrix} = - \begin{bmatrix} K_{xx}K_{xy}K_{x\alpha}K_{x\beta} \\ K_{yx}K_{yy}K_{y\alpha}K_{y\beta} \\ K_{\alpha x}K_{\alpha y}K_{\alpha\alpha}K_{\alpha\beta} \\ K_{\beta x}K_{\beta y}K_{\beta\alpha}K_{\beta\beta} \end{bmatrix} \begin{Bmatrix} x \\ y \\ \alpha \\ \beta \end{Bmatrix} - \begin{bmatrix} C_{xx}C_{xy}C_{x\alpha}C_{x\beta} \\ C_{yx}C_{yy}C_{y\alpha}C_{y\beta} \\ C_{\alpha x}C_{\alpha y}C_{\alpha\alpha}C_{\alpha\beta} \\ C_{\beta x}C_{\beta y}C_{\beta\alpha}C_{\beta\beta} \end{bmatrix} \begin{Bmatrix} \dot{X} \\ \dot{Y} \\ \dot{\alpha} \\ \dot{\beta} \end{Bmatrix},$$

where F_α and F_β are actually *moments* on the disk.

It can be seen that there are a total of 32 stiffness and damping coefficients defining the forces and moments on each disk. The off-diagonal elements are called the cross-coupled coefficients, and are often associated with the destabilizing mechanisms. For example, Fig. 2 shows how a positive K_{xy} and negative $K_{yx} = -K_{xy}$ produces a tangential force driving forward whirl. It has been shown that oil film (journal) bearings, internal rotor hysteresis, and Alford's force all produce cross-coupled stiffness coefficients [2, 5, 6]. The magnitude of these coefficients is not accurately known. In fact, the greatest limitation of Lund's method (as with all other stability analyses) is the lack of accurate information about the types and magnitudes of destabilizing excitations which exist in real machines and which are to be used as input to the computer program.

The only two exciting forces theorized to date which are work-load dependent are: (1) The blade tip-clearance theory described by Alford [6] for axial flow machines, (2) The torquewhirl theory described in reference [12]. Neither of these theories have been experimentally verified by a controlled test in a real machine or by a test apparatus, although both of them are now in use by rotor dynamics engineers as input to linearized stability analysis computer programs (such as Lund's analysis described above).

The linearized equations of motion have realistic meaning only for small motions about the equilibrium, since the forces are all described by constants which do not remain constant for large motions. The (unstable) solution which grows indefinitely with time soon grows into a new regime in which the *nonlinear* equations govern. This is the regime which may have bounded solutions even though the linearized analysis predicts instability. Reference [12] gives such a bounded solution for a simple model where load torque drives the whirling motion (torquewhirl), while reference [13] shows that the zero whirl solution to the *linearized* equations of reference [12] is *unstable* in

the sense of Lyapunov. Thus we see that the field engineer's definition of instability in rotating machines (i.e., any nonsynchronous vibration) may actually be compatible with mathematical predictions, once the nonlinear regime is considered with its bounded solutions. These ideas are expanded further in reference [14].

The basic idea underlying the torquewhirl theory is that the load torque vector on an impeller disk will tend to remain aligned with the disk (due to axisymmetry), and thus will have a component which acts on the whirl coordinate whenever the disk becomes misaligned by the mode shape of the flexible rotor. It can be shown that the torquewhirl generalized forces produce cross-coupled stiffness coefficients, as follows:

For the rigid shaft, flexible joint, torquewhirl model in reference [12] the disk rotation and translation coordinates are not independent (i.e., they are related by a kinematic constraint). The constraint equations are $R = \ell\theta$ in polar coordinates or $X^2 + y^2 = (\ell \sin\theta)^2$ in inertial coordinates, (see Fig. 3).

Since the equations and generalized forces in reference [12] are written in terms of Euler angles ϕ, and θ, a coordinate transformation is required to derive the stiffness and damping coefficients.

First, the generalized torque Q_ϕ of reference [12] can be expressed as a tangential force

$$F_\phi = Q_\phi/R,$$

and the generalized moment Q_ϕ can be expressed as a radial force

$$F_R = Q_\theta/\ell \cos\theta$$

It is Q_ϕ (or F_ϕ) which contains the destabilizing torquewhirl forces. The transformation to x and y is

$$F_x = F_R \cos\phi - F_\phi \sin\phi$$
$$F_y = F_R \sin\phi + F_\phi \cos\phi$$

where

$$\sin\phi = y/(x^2 + y^2)^{1/2}$$
$$\cos\phi = x/(x^2 + y^2)^{1/2}$$

For the aerodynamic case (see [12]), the generalized torque Q_ϕ is

$$Q_\phi = T_s - \overline{C}_L(\dot\psi + \dot\phi \cos\theta)^2 \cos\theta - C_d(\ell^3 \sin^3\theta)\dot\phi^2,$$

where T_s = shaft torque; C_L = disk load coefficient; $\overline{C}_d$ = nonlinear damping coefficient; the shaft speed ω_s is $\omega_s = \dot\psi + \dot\phi$.

The shaft torque equals the disk load torque so that

$$T_s = \overline{C}_L(\dot\psi + \dot\phi \cos\theta)^2$$

Therefore the generalized torque Q_ϕ can be expressed as

$$Q_\phi = T_s[1 - \cos\theta] - \overline{C}_d(\ell^3 \sin^3\theta)\phi^2.$$

The destablizing part of Q_ϕ is the first term from the expression just above. The equivalent tangential force F_ϕ is

$$F_\phi = Q_\phi/R = T_s(1 - \cos\theta)/R$$

The required relationships between R, θ, and α, and x, y are

$$R = (x^2 + y^2)^{1/2}$$
$$x = \alpha\ell$$
$$y = -\beta\ell$$
$$\text{and } \theta = (\alpha^2 + \beta^2)^{1/2}$$

Therefore, in terms of x and y, we can write

$$F_\phi = \frac{T_s\left[1 - \cos\dfrac{(x^2 + y^2)^{1/2}}{l}\right]}{(x^2 + y^2)^{1/2}}$$

Keeping only the first two terms of the cosine series yields

$$F_\phi = (T_s/2\ell^2)(x^2 + y^2)^{1/2} \text{ or}$$
$$F_x = -F_\phi \sin\phi = -(T_s/2\ell^2)y$$

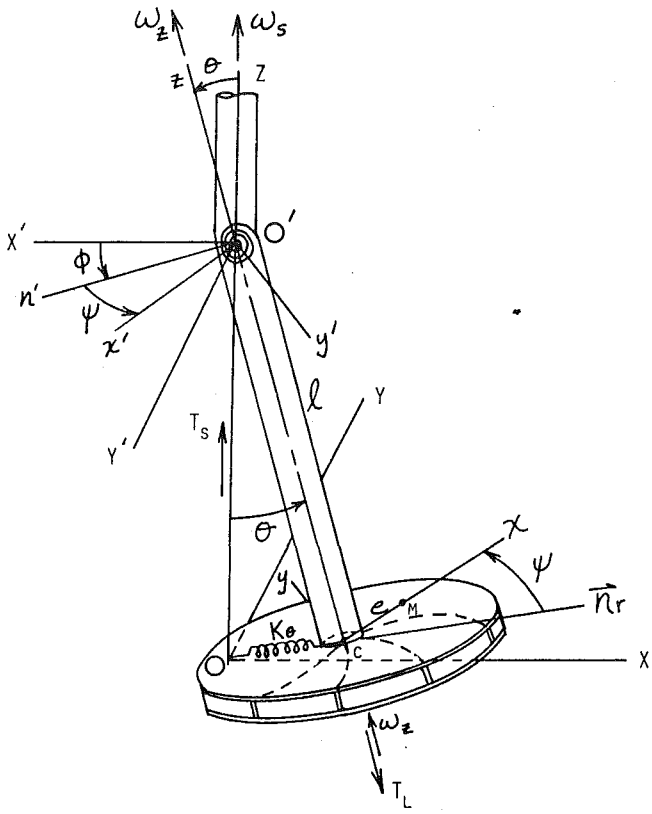

Fig. 3 Rigid rotor model from reference [12]

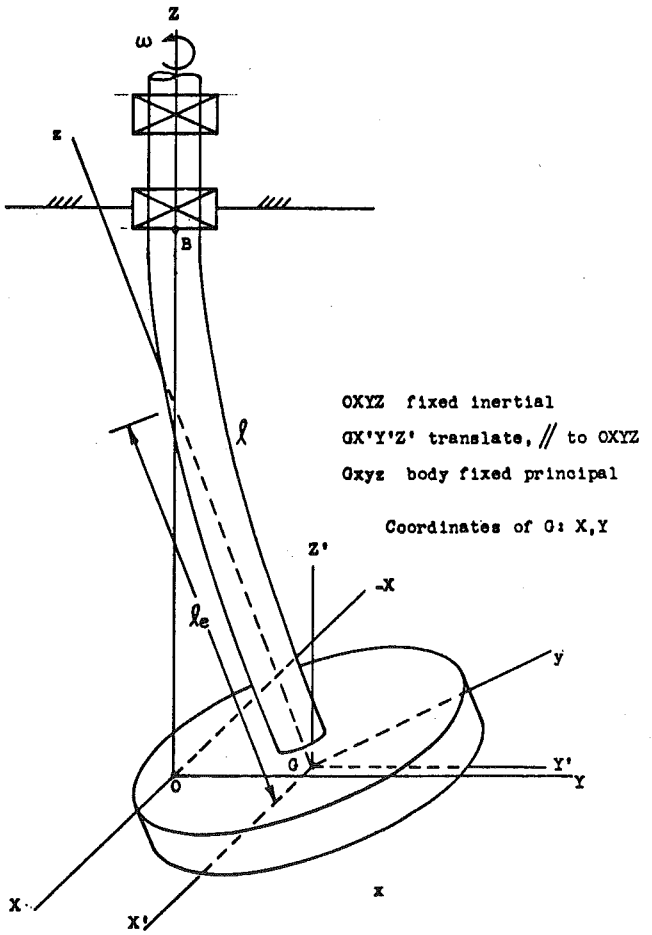

Fig. 4 Flexible rotor coordinates

Table 1 Classification of shaft whirling instabilities in rotating machinery

Diagnostic Information	Self-Excited Nonsynchronous Whirl	Parametrically Excited Whirl
Sources of Excitation	Oil film bearings ("oil whip"), internal friction in rotating parts, trapped fluid in rotor, tip clearance effects in axial flow bladed disks ("Alford's force"), labyrinth seals, ring seals, high gas pressure in centrifugal stages, rotor/stator rubbing friction (induces backward whirl), high torque loading on disks misaligned by the mode shape ("torque-whirl"), variable angle of attack on blades of axial stages ("propeller whirl flutter", can be forward or backward), dense or viscous fluid in impeller housings	Asymmetric shaft stiffness, asymmetric rotor inertia, pulsating torque
Whirl Frequency Ratio f/fs	Almost always subsynchronous, typically 0.3 - 0.8	Usually supersynchronous, f/fs > 1.0
Shaft Speeds Where Encountered	Supercritical speeds, especially at $2w_{CR}$ and above	Subcritical speeds
Effective Solutions	Stiffen shafts or shorten bearing spans to raise bending critical speeds, Asymmetric bearing supports, Squeeze-film bearing dampers, Soften bearing supports to allow dampers to operate effectively	Squeeze-film bearing dampers, remove asymmetries, isolate pulsating torque with torsionally soft coupling

$$F_y = F_\phi \cos \phi \approx (T_s/2\ell^2)x$$

By inspection, it can be seen that the cross-coupled stiffnesses are

$$K_{xy} = T_s/2\ell^2$$
$$K_{yx} = -T_x/2\ell^2$$

It is interesting to note that K_{xy} and K_{yx} have the same form as Alford's coefficients for the effect of tip clearance asymmetry in axial flow turbomachinery [6].

As a crude approximation, the above torquewhirl coefficients (K_{xy},K_{yx}) could be used for a flexible-shaft model by taking ℓ as the axial distance from the disk plane to a virtual pivot point, as determined by the mode shape (see ℓ_e in Fig. 4). Notice that, as ℓ_e becomes short, the cross-coupled coefficients from torquewhirl can become larger than the Alford coefficients.[1] More importantly, the torquewhirl coefficients apply to centrifugal machines as well as to axial-flow machines.

Last year, the torquewhirl theory was applied to the NASA Space Shuttle Main Engine Turbopumps [13] in an attempt to analyze the nonsynchronous whirl instabilities which have been encountered in developmental testing. Under certain simplifying assumptions about the mode shape, it was shown that torquewhirl could be the destabilizing force in the oxygen pumps, if less than five percent of critical damping is present in the machine.

Thus, although these load-dependent excitation theories (Alford and torquewhirl) still have not been experimentally verified, they are being used by analysts as the best information available to explain the rotordynamic instabilities occurring in highly loaded turbomachinery.

Theoretical Predictions versus Field Measurements

It is extremely difficult at the present time to predict rotordynamic instability problems, especially the threshold of stability, accurately *a priori*. This is due to the lack of an accurate quantification of the destabilizing coefficients, as discussed above. It is also the author's opinion that destabilizing forces exist in centrifugal machines which have not yet been identified. This opinion is based on observations of field measurements and their lack of correlation with computer simulations using the currently known excitations as input.

A summary of the known excitations, with diagnostic information and the known effective "cures," are given in Table 1.

One area in which there is very good agreement of field data with theoretical predictions is the effect of rotor shaft stiffness. All of the cases of rotordynamic instability in compressors known to the authors occurred in machines operating above the first shaft bending critical speed. Computer simulations will always predict that stiffening the shaft will raise the threshold speed of instability, and this has been verified by actual retrofit modifications to several different machines. It is interesting to note that a high ratio of shaft stiffness to bearing support stiffness also has a favorable effect on synchronous response problems (i.e., unbalance response) [15].

Experimental Observations from a Simple Test Rig

A simple test rig has been set up in the Rotor Dynamics and Machinery Vibrations Laboratory at Texas A&M University to observe the effect of a working fluid, swirling in a housing, on the dynamics of an impeller with radial vanes. Figure 5 shows the impeller, which is supported vertically from a very flexible quill shaft. The shaft stiffness was kept low to produce a low critical speed and to allow the fluid dynamic effects on the impeller to predominate. The shaft is supported from ball bearings, so that there is no possibility of "oil whip" from fluid film bearings as a destabilizing influence.

The impeller has been run both in the atmosphere, with no housing, and submerged in a working fluid (kerosene) contained in a cylindrical housing, open at the top. Figures 6 and 7 are photographs of the test rig, with and without the fluid container. Variable speed is obtained with a d-c gearmotor drive unit. The speed is measured with a proximity probe pulse tachometer and electronic digital counter. Figure 8 shows a time trace and frequency spectrum of the pendular vibrations (nonrotating) of the impeller suspended in the atmosphere. The frequency spectrum shows the natural frequency in air to be 45 cpm, and the time trace shows the logarithmic decrement to be 0.0198, which corresponds to 0.315 percent of critical damping, a very lightly damped system. Gyroscopic effects from rotation cause the actual

[1] Although the rigid-shaft model of reference [12] becomes less reasonable as $\ell_e \to 0$.

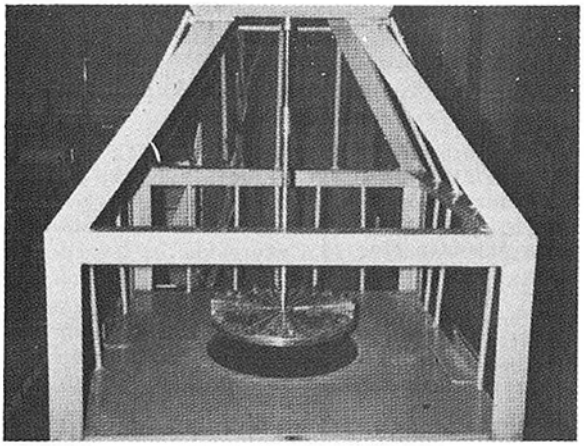

Fig. 5 Test rig impeller

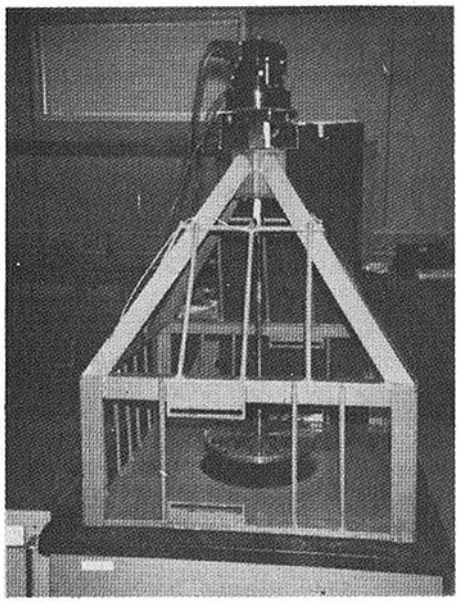

Fig. 6 Test rig without fluid container

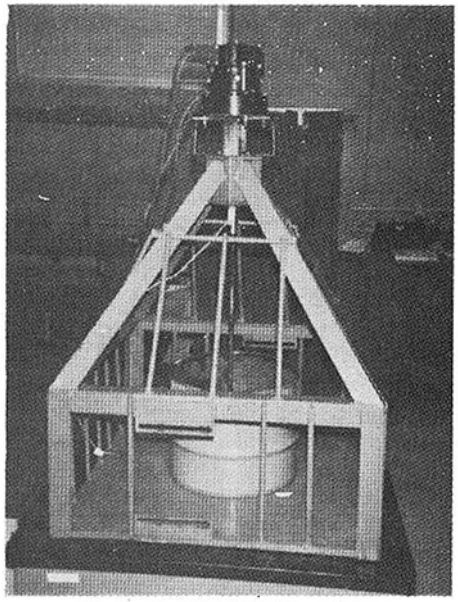

Fig. 7 Test rig with fluid container

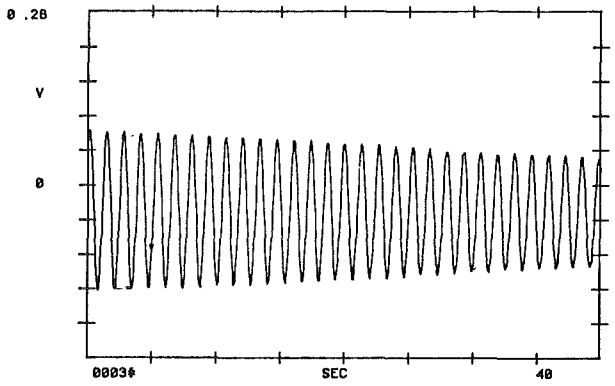

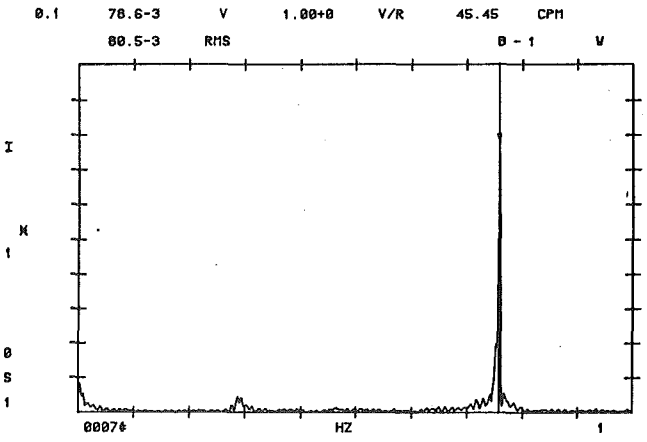

Fig. 8 Time trace and frequency spectrum of test rig impeller vibrations

critical speed to be slightly higher than 45 cpm. The damping comes from atmospheric drag, and from internal hysteresis in the shaft assembly. The latter is known to be destabilizing on forward whirl, as described previously, if the internal damping is large enough relative to the external damping.

Rotating tests showed the impeller to be stable in the atmosphere up to a speed of 112 rpm, or 2.5 times the critical speed. Above 112 rpm, the impeller executes backward whirl with a small triangular orbit which neither grows larger nor dies out (log. dec. = 0). At no speed below 5000 rpm is the impeller unstable in forward whirl in the atmosphere, thus showing internal hysteresis to be a relatively insignificant destabilizing influence in this test rotor.

Rotating tests with the impeller submerged in kerosene produced a critical speed of 40 rpm. The reduction in critical speed is caused by the virtual mass of the working fluid [16]. At supercritical speeds, the impeller is stable from 45 rpm to 150 rpm, (up to 3.75 times the critical speed). Above 150 rpm the impeller becomes unstable in forward subsynchronous whirl, with an orbit which grows with time. At speeds between 314 rpm and 360 rpm the impeller executes either forward or backward nonsynchronous whirl, depending on whether a perturbation is supplied. In this speed range the orbits reach a constant amplitude and do not grow further. Above 500 rpm the impeller becomes unstable in backward whirl with an orbit that grows with time.

Thus it is seen that the working fluid has a profound influence on the dynamics of a radial-vaned impeller, but it would be incorrect to imply much more than this statement from such a simple apparatus. It must be recognized that a centrifugal compressor develops much higher pressures around the impeller, and produces radial, as well as circumferential, fluid velocities.

Some Hypothesized Destabilizing Excitations

The tests described above point inescapably to the probability that the working fluid in a centrifugal compressor exerts destabilizing forces on its impellers. These forces must be considered, in addition to journal bearing effects and internal hysteresis, if accurate predictions of instability thresholds are to be made. An indirect effect from the fluid is torquewhirl, already discussed.

It is interesting to attempt a classification of the types of fluid forces which can act on impellers. For example, consider a shrouded impeller with a small axial clearance to the nonrotating diaphragm. This amounts to a very large thrust bearing, which can generate unbalanced viscous shears on the impeller disk, or even circumferential pressure variations from Reynold's effect.

Similarly, a small radial clearance space around the radius of a thick rotating shroud could act as a large journal bearing, and produce cross-coupled coefficients acting on the impeller.

Interestingly, it is neither the thrust bearing nor the journal bearing effect which produced the nonsynchronous whirling observed in the simple test rig of the previous section. The clearances were too large to produce significant film pressures[2] (1.27 cm, or 0.5 in.) The phenomena in the test rig must be produced by more complex interactions between the fluid and the vaned impeller.

Conclusions

The intent of this paper has been to stimulate thought in new directions on the problem of centrifugal compressor instabilities. At present, the following statements can be made:

1 Rotordynamic instability of centrifugal compressors has occurred in a number of machines, with a high cost to both the user and the manufacturer.

2 Although computer simulations can predict the general effect of design variables, accurate predictions of stability thresholds cannot presently be made *a priori*, due to a lack of quantified data on the destabilizing forces.

3 Both computer predictions and field data have shown that a high ratio of shaft stiffness to bearing support stiffness is stabilizing.

4 The instability excitation mechanisms in centrifugal compressors are not fully understood. Research is needed to identify the significant destabilizing forces which act on radial impellers, and quantify them.

References

1 Rankine, W. A., "On the Centrifugal Force of Rotating Shafts," *Engineer*, London, Vol. 27, 1869, p. 249.

2 Hori, Y., "A Theory of Oil Whip," ASME *Journal of Applied Mechanics*, June 1959, pp. 189–198.

3 Crandall, S. H., and Brosens, P. J., "On the Stability of Rotation of a Rotor With Rotationally Unsymmetric Inertia and Stiffness Properties," ASME *Journal of Applied Mechanics*, Dec. 1961, pp. 567–570.

4 Eshleman, R. L., and Eubanks, R. A., "Effects of Axial Torque on Rotor Response: An Experimental Investigation," ASME Paper No. 70-WA/DE-14, ASME Winter Annual Meeting, Nov. 29–Dec. 3, 1970, New York.

5 Gunter, E. J., Jr., *Dynamic Stability of Rotor-Bearing Systems*, NASA-SP-113, 1966.

6 Alford, J. S., "Protecting Turbomachinery From Self-Excited Rotor Whirl," ASME JOURNAL OF ENGINEERING FOR POWER, Oct. 1965, pp. 333–334.

7 Ehrich, F. F., "Identification and Avoidance of Instabilities and Self-Excited Vibrations in Rotating Machinery," ASME Paper No. 72-DE-21, Design Engineering Conference, Chicago, May 8–11, 1972.

8 Ehrich, F. F., "An Aeroelastic Whirl Phenomenon in Turbomachinery Rotors," ASME Paper No. 73-DET-97, Design Engineering Technical Conference, Cincinnati, Sept. 9–12, 1973.

9 Wachel, J. C., "Nonsynchronous Instability of Centrifugal Compressors," ASME Paper Co. 75-PET-22, Petroleum Mechanical Engineering Conference, Tulsa, Sept. 21–25, 1975.

10 Fowlie, D. W., and Miles, D. D., "Vibration Problems with High Pressure Centrifugal Compressors," ASME Paper No. 75-PET-28, Petroleum Mechanical Engineering Conference, Tulsa, Sept. 21–25, 1975.

11 Lund, J. W., "Stability and Damped Critical Speeds of a Flexible Rotor in Fluid Film Bearings," ASME *Journal of Engineering for Industry*, May 1974, pp. 509–517.

12 Vance, J. M., "Torquewhirl—A Theory to Explain Nonsynchronous Whirling Failures of Rotors with High Load Torque," ASME JOURNAL OF ENGINEERING FOR POWER, April 1978, pp. 235–240, Paper No. 76-DE-29.

13 Tison, J. D., *Dynamic Stability Analysis of Overhung Rotors With High Load Torque*, Master of Engineering Thesis, Mechanical Engineering, University of Florida, 1977.

14 Vance, J. M., and Tison, J. D., "Analysis and Interpretation of Nonsynchronous Whirling in Turbomachinery," ASME Paper No. 78-DET-76, 7th Vibrations Conference, St. Louis, Sept. 9–12, 1979.

15 Barrett, L. E., Gunter, E. J., and Allaire, P. E., "Optimum Bearing and Support Damping for Unbalance Response and Stability of Rotating Machinery," ASME Paper No. 77-GT-27, Gas Turbine Conference, Philadelphia, March 27–31, 1977.

16 Walston, W. H., Ames, W. F., and Clark, L. G., "Dynamic Stability of Rotating Shafts in Viscous Fluids," ASME *Journal of Applied Mechanics*, June, 1964, pp. 291–299.

[2] Although the unbalanced viscous shear forces are probably significant.

C. E. Lowell
S. M. Sidik
D. L. Deadmore

National Aeronautics and Space Administration,
Lewis Research Center,
Cleveland, Ohio

Effect of Sodium, Potassium, Magnesium, Calcium, and Chlorine on the High Temperature Corrosion of In-100, U-700, IN-792, and MAR M-509

The effects of potential impurities, such as Na, K, Mg, Ca, and Cl, in coal-derived liquid fuels on accelerated corrosion of IN-100, U-700, IN-792, and Mar M-509 were investigated using a Mach 0.3 burner rig for times to 200 hr in 1 hr cycles. These impurities were injected in combination as aqueous solutions into the combustor. Other variables were time, temperature, and fuel-to-air ratio. The experimental matrix was a central composite fractional factorial design divided into blocks to allow modification of the design as data was gathered. The extent of corrosion was determined by metal consumption, τ.

Introduction

If coal-derived liquids are to become important sources of fuel for power turbines, the effects of trace element impurities on the accelerated corrosion of the turbine must be evaluated. The effects of some of these impurities are known to be adverse. For example, sodium, potassium and vanadium have been identified [1–3] by many investigators as being sources of accelerated corrosion when petroleum fuels are burned. On the other hand, some impurities are known to reduce corrosion, e.g., calcium, magnesium [4, 5]. However, there are many impurities whose effects are not known and certainly the effects of the interaction of various impurities are largely unknown. There are two potential approaches to determining the effects of the impurities. The first one is to test many real fuels; by testing a broad spectrum of such fuels the effects of the various impurities from the analyses of the fuels combusted can be inferred. The advantages to this approach are that one uses real fuels and the data that one obtains are under conditions closely approaching those found in a real gas turbine. The disadvantages of such tests are that the data obtained are relevant only to the fuels actually tested. Also, currently there are very few liquid coal-derived fuels that are available in quantities sufficient for such tests. The second approach would be to start with the clean fuel and dope it with the impurities of interest in a parametric fashion. The advantage of this approach is that such impurity combinations can be carefully controlled and varied in a systematic fashion allowing the prediction of attack due to any composition. The disadvantages of such tests are that they do not burn real fuel under real turbine operating conditions and that the large number of impurities of interest require many, many tests to be made.

The work described in this report is confined exclusively to the doping approach. The object of this effort is to evaluate the effects of time, temperature, and impurity content on corrosion. The approach used was to burn clean fuels in a burner rig and add aqueous solutions of the impurity combinations required to the combustion gases. The impurities chosen for these tests were sodium, potassium, calcium, magnesium and chlorine. The parametric additions of the impurities were statistically designed to minimize the number of tests. While weight change measurements were made, these data cannot be used to satisfactorily evaluate the extent of hot corrosion attack. The types of deposits were evaluated by X-ray diffraction, while the extent of attack was determined by measuring metal consumption.

Contributed by the Gas Turbine Division of THE AMERICAN SOCIETY OF MECHANICAL ENGINEERS and presented at the Gas Turbine Conference and Products Show, New Orleans, La., March 10–13, 1980. Manuscript received at ASME Headquarters January 3, 1980. Paper No. 80-GT-150.

Materials

The compositions of the alloys used in this program are listed in Table 1. The cobalt-base alloy Mar M-509 is a typical vane material which is generally considered to have good hot corrosion resistance due to its high chromium content. The three nickel-base alloys turbine blade cover a range of hot corrosion resistance: IN-792 has moderately good hot corrosion resistance, while U-700 has somewhat poorer hot corrosion resistance, and IN-100 has the least resistance to such attack. All of the alloys were cast by a commercial vendor into the shape shown in Fig. 1(a). All samples were grit blasted and cleaned with alcohol. Prior to test each sample was measured along a diameter in the center of the expected hot zone (Fig. 1(a)) with a bench micrometer to precision of ± 2 μm and weighed to ± 0.2 mg.

Procedure

A burner rig typical of the four used for these tests is shown in Fig. 1 (b) and has been described in reference [6]. Briefly, each rig is a nominal Mach 0.3 type fired with A-1 jet fuel whose sulfur content was determined to be 0.035 ± 0.014 wt/percent over over the duration of the tests. The fuel-to-air ratio was varied from about 0.035 to 0.055. The dopants were injected into the combustion chamber as an aqueous solution. Eight samples were rotated rapidly in front of the exhaust nozzle and reached the desired temperature in a few minutes. After each one hour exposure the burner pivoted away and a forced-air

Table 1 Composition of alloys (all values are weight percent)

ELEMENT	IN-100	U-700	IN-792	MarM-509
Cr	10	14.2	12.7	23
Ni	Bal.	Bal.	Bal.	10
Co	15	15.5	9.0	Bal.
Al	5.5	4.2	3.2	-
Ti	4.7	3.3	4.2	0.2
Mo	3.0	4.4	2.0	-
W	-	-	3.9	7
Ta	-	-	3.9	3.5
Nb	-	-	0.9	-
V	1.0	-	-	-
Mn	-	< .01	-	-
Fe	-	0.1	-	-
Si	-	< 0.1	-	-
Zr	0.6	< .01	0.10	0.5
B	0.014	0.02	0.02	-
C	0.18	0.06	0.2	0.6

cooling nozzle was directed on the specimens for three min. Then this cycle was repeated. After 40 cycles one sample of each alloy was removed and a new sample put in its place. After 100 cycles the samples were removed, weighed, washed, and reweighed. This gave, for each alloy, a sample at 40, 60 or 100 hr. Washing consisted of immersion of each sample blade in 300 cc's of water at 80°C followed by a soft brushing in running water, an alcohol rinse, and air drying. The samples were then sectioned along the plane shown in Fig. 1(*a*), which is the center of the hot zone, and where all temperature measurements were made during the run. The cut sections were mounted metallographically, polished and etched. Thickness measurements were made to determine the final thickness at maximum penetration and to calculate maximum metal loss (τ). While both the initial and final thicknesses were measured to precision of 2 ± μm, experience has shown [7] that resultant change in thickness is only accurate to about ±20 μm due to the irregularity of attack and other factors outlined in reference [7].

The surface of each of the 100 hr samples were scraped for X-ray diffraction analysis. A few milligrams from each sample were obtained and analyzed using a Guinier-deWolff camera. This type of focusing camera was necessary because the complexity of the patterns of the deposits resulted in overlapping diffraction lines.

Statistical Design and Analysis

Experimental Variables and Plans. The experimental design used in this program is a modification of a class of experimental designs [8, 9]. These are all generalizations of plans as illustrated in Fig. 2. Figure 2 shows an experiment consisting of two parts, a square (or cube) with a star radiating from the center point. In the cube part, presence of a letter denotes that variable to be at its high level, while absence of a letter indicates the variable is at its low level. The symbol (1) denotes all the variables are at their low level. The extremes of the star are denoted by capital letters with plus or minus.

In the current experiment we consider the seven variables listed in Table 2. The original plan consisted of 92 treatment combinations to be run in five groups (blocks). Each block of samples is designed to isolate the effects of certain variables and their interactions. A number of changes were made during the progress of the experiment and the complete list of the observed data is given in Table 3. The first four columns of Table 3 give the observed metal recession for IN-100, U-700, IN-792 and Mar M-509, respectively. The next five columns

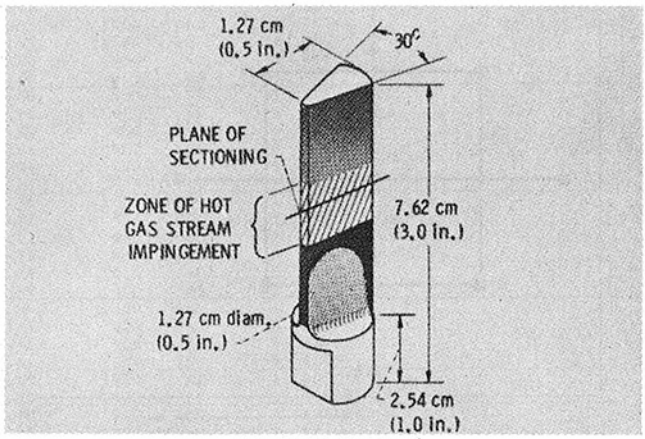

Fig. 1(*a*) Test bar

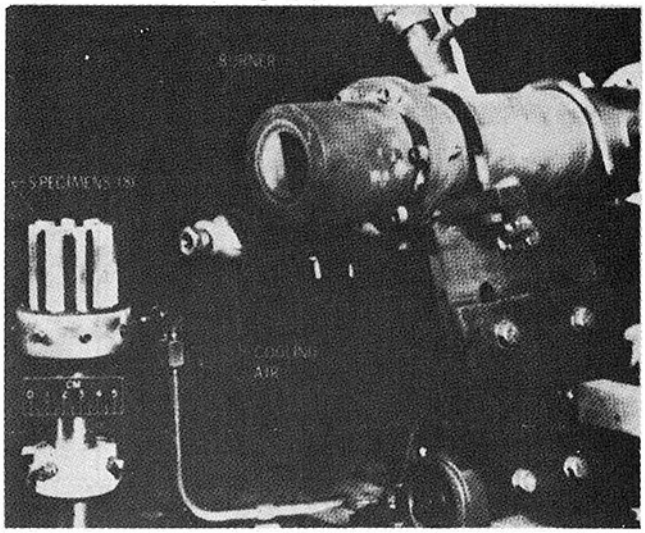

Fig. 1(*b*) Burner rig

Fig. 1 Hot corrosion apparatus and test specimen

give the parts per million by weight of combustion gases of Na, K, Mg, Ca and Cl. Column ten gives the test temperatures, and column 11 gives the time of exposure. The last two columns identify the rig on which the test was run and the letter code for the treatment combination as defined above. A number of changes in the test plan were made in the progress of the runs. The first of these resulted from a data review toward the end of block two. Because of the good correlations obtained at that point, blocks three and four were condensed. Block five, consisting of the star points was run in its entirety.

A second condensation came about towards the end of the completion of block two and before the start of block five. At this point a reevaluation of the aims of the program made it clear that the dopants should be considered in terms of elements rather than compounds. This is primarily because it would be difficult, if not impossible, to analytically identify the compound(s) in which the various impurities were present because of the low levels of concentrations found in these fuels.

We therefore redefined the independent impurity variables of interest as parts per million of the elements Na, K, Mg, Ca and Cl. This change had the effect of reducing considerably the orthogonality of the original design. The effect was primarily that Cl was rather highly correlated with Mg and Ca, less highly correlated with Na and K, and had no effect on a correlation of Cl with temperature and with time. However, it did mean that the Cl concentrations tended to be on average considerably higher than the other variables. This approach had little effect on the fit of the data.

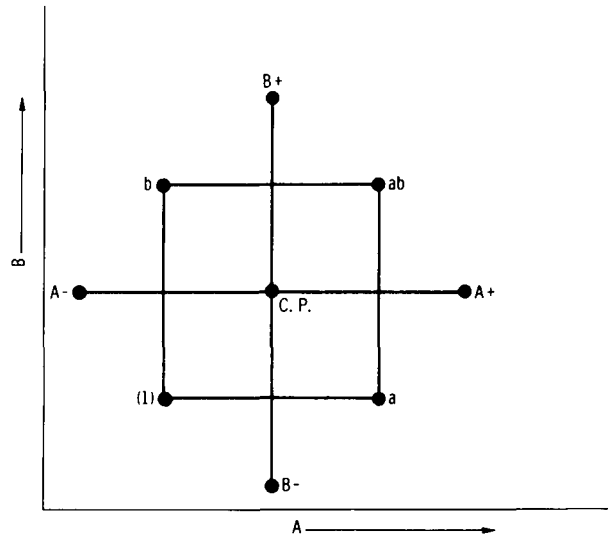

Fig. 2 A central composite factorial design for two variables, *A* and *B* • *A* ± and *B* ± denote axial or star points; *C* • *P.* denotes a center point; and *a*, *b*, *ab*, and (1) denote cube points

In order to alleviate this correlation problem and to verify that only the presence of the individual elements matter, several additional runs were made which expanded the scope of the experiment somewhat. These runs are identified by the code EXPAND in column 13 of Table 3. In addition, one set of runs was made with no dopants, that is, oxidation only tests. These lare labeled OXIDAT in column 13 of Table 3.

To illustrate the scope of the program, a series of parametric plots of the levels of the independent variables have been provided. Not all pairs are plotted, as several such plots are very similar. In particular Fig. 3(*a*) plots ppm Na versus ppm Mg. Na versus Cl, K versus Mg, and K versus Ca are very similar and hence not separately plotted. Likewise, Fig. 3(*b*) shows Na versus temperature with *K* versus temperature being almost identical. Figure 3(*c*) plots Mg versus temperature with Ca versus temperature being almost identical.

Inclusion of Other Variables. Besides the primary design variables it was necessary to include the possibility that fuel-to-air ratios had an effect on τ [10], and that there could be systematic biases from one burner rig to another. The comparison of rig effects can be included by the use of dummy variables. That is, a pair of independent variables r_1 and r_2 equals $(-1, -1)$ for rig one, equals $(-1, +1)$ for rig two, equals $(+1, -1)$ for rig three and equals $(+1, +1)$ for rig four. Then the three variables r_1, r_2 and $r_1 r_2$ will reflect the following differences:

r_1 measures (rig 3 + rig 4) − (rig 1 + rig 2)

r_2 measures (rig 2 + rig 4) − (rig 3 + rig 4)

$r_1 r_2$ measures (rig 1 + rig 4) − (rig 2 + rig 3)

Fuel-to-air ratio was considered as a variable only for the center point runs since it was not recorded in detail for all of the runs.

Uses of the Center Points. The center point of a central composite design is typically repeated a number of times (in this case there were 14 repetitions) during the execution of the overall experiment. The primary reason for this is that, since the center point has all the controllable variables held at nominally identical levels, these replicates provide (1) an independent measure of the inherent variability or reproducibility of the results; (2) this error estimate may then be compared to the error estimate obtained from fitting more complicated equations to all of the data to determine if the more general equation is adequate; (3) if the center points are interspersed in time then they can often be used to check for drift or trends that might be occurring due to changing conditions over the course of the runs. The model used for this analysis is $\log \tau = \beta_0 + \beta_1 \times \log \text{time} + \beta_2 f/a + \beta_3 r_1 + \beta_4 r_2 + \beta_5 r_1 r_2 + \epsilon$.

Full Data Analysis. The fundamental form of the model chosen is a power law in time, that is, $\tau = \alpha_1 t^{\alpha_2}$ where the rate constant α_1 is a function of the remaining variables, that is, Na, K, Mg, Ca, Cl, time, temperature, and the rigs. More specifically, we use τ =

Table 2 The seven initial variables and their levels

		Star (-)	Cube (-)	Center Point	Cube (+)	Star (+)
A	NaCl	.04 PPM	.20	.45	1.0	4.95
B	Na_2SO_4					
C	KCl					
D	K_2SO_4					
E	$MgCl_2$					
F	$CaCl_2$					
G	TEMP	800°C	900	950	1000	1100

Table 3 Summary of test variables and results

τ(μm)				ppm					(°C)	(hr)		
IN100	U700	IN792	WP509	NA	K	MG	CA	CL	TEMP	TIME	RIG	ID
317	294	142	154	0.90	0.90	0.45	0.45	3.21	950	40	1	CPD
554	444	148	73	0.90	0.90	0.45	0.45	3.21	950	60	1	CPD
639	708	254	227	0.90	0.90	0.45	0.45	3.21	950	100	1	CPD
258	359	163	103	0.90	0.90	0.45	0.45	3.21	950	40	2	CPD
328	641	202	125	0.90	0.90	0.45	0.45	3.21	950	60	2	CPD
433	757	257	113	0.90	0.90	0.45	0.45	3.21	950	100	2	CPD
105	113	109	87	0.90	0.90	0.45	0.45	3.21	950	40	3	CPD
224	116	199	76	0.90	0.90	0.45	0.45	3.21	950	60	3	CPD
222	132	169	161	0.90	0.90	0.45	0.45	3.21	950	100	3	CPD
2858(1)	4338	1569	1798	0.90	0.90	0.45	0.45	3.21	950	40	4	CPD
3598	6698	1703	988	0.90	0.90	0.45	0.45	3.21	950	60	4	CPD
363	594	209	213	0.90	0.90	0.45	0.45	3.21	950	100	4	CPD
94	85	83	138	1.20	1.20	1.00	1.00	5.90	1000	40	1	ACEFG
126	174	99	205	1.20	1.20	1.00	1.00	5.90	1000	60	1	ACEFG
258	201	133	166	1.20	1.20	1.00	1.00	5.90	1000	100	1	ACEFG
77	54	27	44	0.40	2.00	1.00	1.00	5.90	900	40	2	CDEF
74	88	48	77	0.40	2.00	1.00	1.00	5.90	900	60	2	CDEF
678	698	628	1308	0.40	2.00	1.00	1.00	5.90	900	100	2	CDEF
328	938	1048	888	1.20	1.20	0.20	0.20	3.39	1000	40	3	ACG
1218	1358	638	848	1.20	1.20	0.20	0.20	3.39	1000	60	3	ACG
1408	1508	1248	2068	1.20	1.20	0.20	0.20	3.39	1000	100	3	ACG
97	98	85	126	0.40	2.00	1.00	0.20	4.49	1000	40	4	CDEG
128	99	91	94	0.40	2.00	1.00	0.20	4.49	1000	60	4	CDEG
136	121	108	251	0.40	2.00	1.00	0.20	4.49	1000	100	4	CDEG
171	95	61	58	1.20	1.20	1.00	0.20	4.99	900	40	1	ADE
313	162	189	209	1.20	1.20	1.00	0.20	4.99	900	60	1	ADE
1310	230	201	225	1.20	1.20	1.00	0.20	4.99	900	100	1	ADE
764	284	180	205	2.00	2.00	0.20	0.20	3.39	900	40	2	ABCD
1299	723	230	242	2.00	2.00	0.20	0.20	3.39	900	60	2	ABCD
2490	1305	491	317	2.00	2.00	0.20	0.20	3.39	900	100	2	ABCD
339	98	103	124	1.20	1.20	1.00	0.20	4.49	900	40	3	ACE
696	107	151	135	1.20	1.20	1.00	0.20	4.49	900	60	3	ACE
1417	404	312	217	1.20	1.20	1.00	0.20	4.49	900	100	3	ACE
240	130	93	83	0.90	0.90	0.45	0.45	3.21	950	40	4	CP1
270	138	93	95	0.90	0.90	0.45	0.45	3.21	950	60	4	CP1
548	491	173	154	0.90	0.90	0.45	0.45	3.21	950	100	4	CP1
3768	2788	929	398	0.90	0.90	0.45	0.45	3.21	950	40	1	CP2
287	354	134	135	0.90	0.90	0.45	0.45	3.21	950	60	1	CP2
838B	1108B	1848	1128	0.90	0.90	0.45	0.45	3.21	950	100	1	CP2
527	661	380	189	1.20	1.20	0.20	0.20	1.43	1000	40	2	BDG
540	923	450	154	1.20	1.20	0.20	0.20	1.43	1000	60	2	BDG
1102	1527	739	402	1.20	1.20	0.20	0.20	1.43	1000	100	2	BDG
356	68	75	36	1.20	1.20	0.20	1.00	4.80	900	40	3	ACF
733B	1158	428	588	1.20	1.20	0.20	1.00	4.80	900	60	3	ACF
1312B	1568	2478	838	1.20	1.20	0.20	1.00	4.80	900	100	3	ACF
486	110	62	64	1.20	1.20	0.20	1.00	2.84	900	40	4	BDF
731B	898	398	728	1.20	1.20	0.20	1.00	2.84	900	60	4	BDF
1384	148	210	162	1.20	1.20	0.20	1.00	2.84	900	100	4	BDF
98	120	93	126	0.40	0.40	0.20	1.00	2.84	1000	40	1	FG
151	143	83	87	0.40	0.40	0.20	1.00	2.84	1000	60	1	FG
203	236	157	93	0.40	0.40	0.20	1.00	2.84	1000	100	1	FG
226	242	123	98	0.90	0.90	0.45	0.45	3.21	950	40	2	CP3
244	403	116	116	0.90	0.90	0.45	0.45	3.21	950	60	2	CP3
373	749	254	143	0.90	0.90	0.45	0.45	3.21	950	100	2	CP3
133	129	128	121	2.00	0.40	1.00	0.20	4.99	1000	40	3	ABFG
121	227	93	150	2.00	0.40	1.00	0.20	4.99	1000	60	3	ABFG
132	217	199	169	2.00	0.40	1.00	0.20	4.99	1000	100	3	ABFG
948	738	668	528	2.00	0.40	1.00	1.00	6.41	900	40	4	ABEF
437	58	58	44	2.00	0.40	1.00	1.00	6.41	900	60	4	ABEF
839	79	70	96	2.00	0.40	1.00	1.00	6.41	900	100	4	ABEF
591	632	345	127	2.00	2.00	0.20	1.00	4.80	1000	40	1	ABCDFG
1324	994	490	262	2.00	2.00	0.20	1.00	4.80	1000	60	1	ABCDFG
1355	1495	1005	328	2.00	2.00	0.20	1.00	4.80	1000	100	1	ABCDFG
298	67	49	74	0.40	0.40	0.20	0.20	1.43	900	40	2	(1)
461	638	69	99	0.40	0.40	0.20	0.20	1.43	900	60	2	(1)
2338	1068	2078	1348	0.40	0.40	0.20	0.20	1.43	900	100	2	(1)
1358	1918	428	858	0.90	0.90	0.45	0.45	3.21	950	40	3	CP4
156	878	96	117	0.90	0.90	0.45	0.45	3.21	950	60	3	CP4
346	303	215	190	0.90	0.90	0.45	0.45	3.21	950	100	3	CP4
144	146	108	94	1.20	1.20	1.00	1.00	6.41	1000	40	4	ADEFG
164	229	134	149	1.20	1.20	1.00	1.00	6.41	1000	60	4	ADEFG
230	292	181	163	1.20	1.20	1.00	1.00	6.41	1000	100	4	ADEFG
412	136	66	98	1.20	1.20	0.20	1.00	3.57	900	40	1	ACF
569	133	89	74	1.20	1.20	0.20	1.00	3.57	900	60	1	ACF
1192	156	90	150	1.20	1.20	0.20	1.00	3.57	900	100	1	ACF
990	551	307	113	1.20	1.20	0.20	0.20	2.15	1000	40	2	BCG
1738	944	382	184	1.20	1.20	0.20	0.20	2.15	1000	60	2	BCG
2040	1464	547	309	1.20	1.20	0.20	0.20	2.15	1000	100	2	BCG
357	468	215	133	2.00	2.00	1.00	0.20	5.72	1000	40	3	ABCDEG
641	606	277	127	2.00	2.00	1.00	0.20	5.72	1000	60	3	ABCDEG
912	785	626	186	2.00	2.00	1.00	0.20	5.72	1000	100	3	ABCDEG
1678	1948	978	368	1.20	1.20	1.00	1.00	5.17	1000	40	4	BDEFG
2308	1498	1548	678	1.20	1.20	1.00	1.00	5.17	1000	60	4	BDEFG
439	498	193	282	1.20	1.20	1.00	1.00	5.17	1000	100	4	BDEFG
687	130	300	139	0.40	2.00	0.20	0.20	2.15	900	40	1	CD
983	217	336	215	0.40	2.00	0.20	0.20	2.15	900	60	1	CD
1661	431	541	365	0.40	2.00	0.20	0.20	2.15	900	100	1	CD
328	265	112	146	2.00	0.40	0.20	1.00	4.08	1000	40	2	ABFG
344	692	309	1338	2.00	0.40	0.20	1.00	4.08	1000	60	2	ABFG
538	709	494	184	2.00	0.40	0.20	1.00	4.08	1000	100	2	ABFG
124	132	104	150	0.40	2.00	0.20	1.00	3.57	1000	40	3	CDFG
118	162	115	207	0.40	2.00	0.20	1.00	3.57	1000	60	3	CDFG
174	207	136	245	0.40	2.00	0.20	1.00	3.57	1000	100	3	CDFG
768	658	1168	888	1.20	1.20	1.00	0.20	5.72	900	40	4	ACE
236	137	144	125	1.20	1.20	1.00	0.20	5.72	900	60	4	ACE
1134	227	220	188	1.20	1.20	1.00	0.20	5.72	900	100	4	ACE

(1) Omitted, Second Pass.

Table 3 continued

τ(μm)				ppm					(°C)	(hr)		
IN100	U700	IN792	MM509	NA	K	MG	CA	CL	TEMP	TIME	RIG	ID
457B	58B	164B	119B	1.20	1.20	1.00	0.20	3.76	900	40	1	BDF
875	190	172	167	1.20	1.20	1.00	0.20	3.76	900	60	1	BDF
1634	576	197	242	1.20	1.20	1.00	0.20	3.76	900	100	1	BDF
368	54	64	63	1.20	1.20	0.20	1.00	4.08	900	40	2	ADF
671	109	73	67	1.20	1.20	0.20	1.00	4.08	900	60	2	ADF
1393	170	137	108	1.20	1.20	0.20	1.00	4.08	900	100	2	ADF
74A(2)	76A	81A	35A	0.40	0.40	1.00	0.20	3.76	1000	40	3	EG
38A	93A	96A	9A	0.40	0.40	1.00	0.20	3.76	1000	60	3	EG
113A	142A	129A	121A	0.40	0.40	1.00	0.20	3.76	1000	100	3	EG
96B	73B	92B	98B	1.20	1.20	0.20	0.20	2.66	1000	40	4	ADG
130B	145B	143B	52B	1.20	1.20	0.20	0.20	2.66	1000	60	4	ADG
208B	203B	252B	234B	1.20	1.20	0.20	0.20	2.66	1000	100	4	ADG
655	237	341	66	2.00	0.40	0.20	0.20	2.66	900	40	1	AB
1011B	149B	239B	57B	2.00	0.40	0.20	0.20	2.66	900	60	1	AB
1791B	437B	482B	55B	2.00	0.40	0.20	0.20	2.66	900	100	1	AB
295B	72B	41B	46B	2.00	2.00	1.00	1.00	7.13	900	40	2	ABCDEF
397B	62B	74B	50B	2.00	2.00	1.00	1.00	7.13	900	60	2	ABCDEF
1034B	149B	95B	72B	2.00	2.00	1.00	1.00	7.13	900	100	2	ABCDEF
47A	57A	29A	34A	0.40	0.40	1.00	1.00	5.17	900	40	3	EF
57A	131A	24A	75A	0.40	0.40	1.00	1.00	5.17	900	60	3	EF
59A	91A	15A	39A	0.40	0.40	1.00	1.00	5.17	900	100	3	EF
120	128	65	94	1.20	1.20	1.00	1.00	7.13	1000	40	4	ACEFG
109	160	111	117	1.20	1.20	1.00	1.00	7.13	1000	60	4	ACEFG
214	213	132	139	1.20	1.20	1.00	1.00	7.13	1000	100	4	ACEFG
397B	150B	86B	90B	0.90	0.90	0.45	0.45	3.21	950	40	1	CPEND
424B	192B	88B	80B	0.90	0.90	0.45	0.45	3.21	950	60	1	CPEND
653B	909B	227B	89B	0.90	0.90	0.45	0.45	3.21	950	100	1	CPEND
175	97	80	109	0.90	0.90	0.45	0.45	3.21	950	40	2	CPEND
298	246	172	77	0.90	0.90	0.45	0.45	3.21	950	60	2	CPEND
745	751	224	139	0.90	0.90	0.45	0.45	3.21	950	100	2	CPEND
93	95	73	46	0.90	0.90	0.45	0.45	3.21	950	40	3	CPEND
172	95	92	79	0.90	0.90	0.45	0.45	3.21	950	60	3	CPEND
363	362	143	130	0.90	0.90	0.45	0.45	3.21	950	100	3	CPEND
204	84	83	42	0.90	0.90	0.45	0.45	3.21	950	40	4	CPEND
204B	480B	99B	56B	0.90	0.90	0.45	0.45	3.21	950	60	4	CPEND
321B	777B	153B	130B	0.90	0.90	0.45	0.45	3.21	950	100	4	CPEND
1194	592	296	73	5.40	0.90	0.45	0.45	10.15	950	40	4	A+
1635	956	369	100	5.40	0.90	0.45	0.45	10.15	950	60	4	A+
2861	1474	709	129	5.40	0.90	0.45	0.45	10.15	950	100	4	A+
132A	99A	26A	118A	0.90	0.90	0.45	4.95	11.17	950	40	4	F+
85A	113A	95A	95A	0.90	0.90	0.45	4.95	11.17	950	60	4	F+
276A	142A	131A	32A	0.90	0.90	0.45	4.95	11.17	950	100	4	F+
78	103	69	39	0.90	0.90	4.95	0.45	16.33	950	40	3	E+
127	107	90	76	0.90	0.90	4.95	0.45	16.33	950	60	3	E+
133	124	111	41	0.90	0.90	4.95	0.45	16.33	950	100	3	E+
96B	68B	83B	31B	0.90	0.90	0.45	0.45	3.21	950	40	3	CPSTAR1
93B	110B	106B	63B	0.90	0.90	0.45	0.45	3.21	950	60	3	CPSTAR1
230B	105B	128B	140B	0.90	0.90	0.45	0.45	3.21	950	100	3	CPSTAR1
38	50	62	100	0.49	0.90	0.45	0.45	3.21	950	40	3	B-
96	108	50	120	0.49	0.90	0.45	0.45	3.21	950	60	3	B-
121	138	79	154	0.49	0.90	0.45	0.45	3.21	950	100	3	B-
272	361	138	76	0.90	5.40	0.45	0.45	7.29	950	40	4	C+
355	539	309	130	0.90	5.40	0.45	0.45	7.29	950	60	4	C+
636	652	448	234	0.90	5.40	0.45	0.45	7.29	950	100	4	C+
177B	95B	47B	125B	0.90	0.90	0.45	0.04	2.48	950	40	3	F-
336B	338B	121B	115B	0.90	0.90	0.45	0.04	2.48	950	60	3	F-
478B	551B	130B	233B	0.90	0.90	0.45	0.04	2.48	950	100	3	F-
168B	17B	21B	27B	0.90	0.90	0.45	0.45	3.21	800	40	3	G-
272B	23B	32B	46B	0.90	0.90	0.45	0.45	3.21	800	60	3	G-
859B	29B	27B	106B	0.90	0.90	0.45	0.45	3.21	800	100	3	G-
206	243	162	189	0.90	0.90	0.45	0.45	3.21	1100	40	4	G+
270	257	183	172	0.90	0.90	0.45	0.45	3.21	1100	60	4	G+
344	453	255	336	0.90	0.90	0.45	0.45	3.21	1100	100	4	G+
99	95	65	116	0.90	0.90	0.45	0.45	3.21	950	40	4	CPSTAR2
215	198	95	95	0.90	0.90	0.45	0.45	3.21	950	60	4	CPSTAR2
578	565	215	125	0.90	0.90	0.45	0.45	3.21	950	100	4	CPSTAR2
1379	846	279	352	0.90	5.40	0.45	0.45	3.21	950	40	3	D+
1105	1105	383	351	0.90	5.40	0.45	0.45	3.21	950	60	3	D+
3522	2149	1010	682	0.90	5.40	0.45	0.45	3.21	950	100	3	D+
123	131	79	97	0.90	0.90	0.04	0.45	2.01	950	40	4	E-
543	583	213	99	0.90	0.90	0.04	0.45	2.01	950	60	4	E-
335B	472B	305	123	0.90	0.90	0.04	0.45	2.01	950	100	4	E-
116	85	66	66	0.49	0.90	0.45	0.45	2.58	950	40	3	A-
114	68	75	125	0.49	0.90	0.45	0.45	2.58	950	60	3	A-
164	73	110	162	0.49	0.90	0.45	0.45	2.58	950	100	3	A-
255	130	78	97	0.90	0.49	0.45	0.45	2.84	950	40	4	C-
227	140	92	109	0.90	0.49	0.45	0.45	2.84	950	60	4	C-
383	312	145	82	0.90	0.49	0.45	0.45	2.84	950	100	4	C-
1239	1529	304	103	5.40	0.90	0.45	0.45	3.21	950	40	4	B+
2309	2399	564	202	5.40	0.90	0.45	0.45	3.21	950	60	4	B+
3290	3950	981	420	5.40	0.90	0.45	0.45	3.21	950	100	4	B+
143	72	58	87	0.90	0.49	0.45	0.45	3.21	950	40	3	D-
146	74	99	113	0.90	0.49	0.45	0.45	3.21	950	60	3	D-
207	122	124	101	0.90	0.49	0.45	0.45	3.21	950	100	3	D-
298	54	63	129	1.20	1.20	1.00	0.20	4.99	900	40	3	ADE-2
641	105	167	171	1.20	1.20	1.00	0.20	4.99	900	60	3	ADE-2
1397	329	200	227	1.20	1.20	1.00	0.20	4.99	900	100	3	ADE-2
105	125	135	120	1.20	1.20	1.00	0.20	5.72	900	40	4	ACE-2
630	155	235	134	1.20	1.20	1.00	0.20	5.72	900	60	4	ACE-2
1125	248	272	236	1.20	1.20	1.00	0.20	5.72	900	100	4	ACE-2
546	80	121	139	0.40	1.20	0.20	0.20	1.43	900	40	3	D
916	101	164	142	0.40	1.20	0.20	0.20	1.43	900	60	3	D
1577	299	410	263	0.40	1.20	0.20	0.20	1.43	900	100	3	D
252	132	73	45	1.20	2.00	0.20	1.00	4.80	900	40	4	ACDF
596	121	77	62	1.20	2.00	0.20	1.00	4.80	900	60	4	ACDF
1105	142	221	88	1.20	2.00	0.20	1.00	4.80	900	100	4	ACDF

(2) Omitted, First Pass.

Table 3 continued

τ(μm)				ppm					(°C)	(hr)		
IN100	U700	IN792	MM509	NA	K	MG	CA	CL	TEMP	TIME	PIG	ID
449	80	105	A1	0.40	1.20	0.20	0.20	2.15	900	40	3	C
840	93	235	166	0.40	1.20	0.20	0.20	2.15	900	60	3	C
1414	291	293	257	0.40	1.20	0.20	0.20	2.15	900	100	3	C
129	70	58	43	1.20	0.40	0.20	1.00	4.08	900	40	4	AE
393	78	468	218	1.20	0.40	0.20	1.00	4.08	900	60	4	AE
1223	105	30	91	1.20	0.40	0.20	1.00	4.08	900	100	4	AE
292A	89A	729	185A	1.20	0.40	1.00	0.20	3.76	900	40	3	BE
530B	50B	135A	168A	1.20	0.40	1.00	0.20	3.76	900	60	3	BE
1545A	1098	2419	219A	1.20	0.40	1.00	0.20	3.76	900	100	3	BE
88	53	54	66	2.00	1.20	1.00	1.00	7.13	900	40	4	ABCEF
349	92	52	58	2.00	1.20	1.00	1.00	7.13	900	60	4	ABCEF
950	84	87	99	2.00	1.20	1.00	1.00	7.13	900	100	4	ABCEF
594	636	285	100	2.00	1.20	0.20	1.00	4.08	1000	40	3	ABDFG
920	942	334	132	2.00	1.20	0.20	1.00	4.08	1000	60	3	ABDFG
1177	1541	681	210	2.00	1.20	0.20	1.00	4.08	1000	100	3	ABDFG
681	412	331	119	1.20	2.00	0.20	0.20	2.15	1000	40	4	BCDG
803	562	344	185	1.20	2.00	0.20	0.20	2.15	1000	60	4	BCDG
1291	963	926	201	1.20	2.00	0.20	0.20	2.15	1000	100	4	BCDG
96	82	65	97	0.90	0.90	0.45	0.45	3.21	950	40	4	CPEFLS)1
248	144	52	120	0.90	0.90	0.45	0.45	3.21	950	60	4	CPEFLS)1
539	362	134	115	0.90	0.90	0.45	0.45	3.21	950	100	4	CPEFLS)1
141	101	77	91	0.90	0.90	0.45	0.45	3.21	950	40	3	CPEFLS)2
217	205	93	85	0.90	0.90	0.45	0.45	3.21	950	60	3	CPEFLS)2
304	230	114	191	0.90	0.90	0.45	0.45	3.21	950	100	3	CPEFLS)2
496	82	54	79	0.58	1.23	1.26	0.95	0.46	900	40	3	EXPAND 1
809	136	88	108	0.58	1.23	1.26	0.95	0.46	900	60	3	EXPAND 1
1446A	814B	1478	1488	0.58	1.23	1.26	0.95	0.46	900	100	3	EXPAND 1
872	442	244	271	1.50	3.50	1.00	0.75	0.60	900	40	4	EXPAND 3
1413	620	345	329	1.50	3.50	1.00	0.75	0.60	900	60	4	EXPAND 3
2677	1831	817	476	1.50	3.50	1.00	0.75	0.60	900	100	4	EXPAND 3
541	116	42	142	1.60	0.50	1.05	0.79	0.48	900	40	3	EXPAND 5
962	203	66	133	1.60	0.50	1.05	0.79	0.48	900	60	3	EXPAND 5
1819	482	181	232	1.60	0.50	1.05	0.79	0.48	900	100	3	EXPAND 5
6678	228A	145A	145A	4.70	1.50	0.93	0.63	0.60	900	40	4	EXPAND 7
1366	1077	337	218	4.70	1.50	0.93	0.63	0.60	900	60	4	EXPAND 7
1948	1652	759	209	4.70	1.50	0.93	0.63	0.60	900	100	4	EXPAND 7
120	94	96	77	0.58	1.23	1.26	0.95	0.46	1000	40	3	EXPAND 2
174	308	175	81	0.58	1.23	1.26	0.95	0.46	1000	60	3	EXPAND 2
246	670	202	140	0.58	1.23	1.26	0.95	0.46	1000	100	3	EXPAND 2
1523	721	415	309	1.50	3.50	1.00	0.75	0.60	1000	40	4	EXPAND 4
2123	1002	451	393	1.50	3.50	1.00	0.75	0.60	1000	60	4	EXPAND 4
3716	1655	924	600	1.50	3.50	1.00	0.75	0.60	1000	100	4	EXPAND 4
435	432	149	99	1.60	0.50	1.05	0.79	0.48	1000	40	3	EXPAND 6
822	585	317	201	1.60	0.50	1.05	0.79	0.48	1000	60	3	EXPAND 6
1022	999	525	200	1.60	0.50	1.05	0.79	0.48	1000	100	3	EXPAND 6
1738	1417	766	304	4.70	1.50	0.93	0.63	0.60	1000	40	4	EXPAND 8
2434	1743	780	426	4.70	1.50	0.93	0.63	0.60	1000	60	4	EXPAND 8
4184	3343	1386	693	4.70	1.50	0.93	0.63	0.60	1000	100	4	EXPAND 8
28	26	36	20	0.00	0.00	0.00	0.00	0.00	900	40	4	OXIDAT
29	19	28	38	0.00	0.00	0.00	0.00	0.00	900	60	4	OXIDAT
-999(3)	25	29	70	0.00	0.00	0.00	0.00	0.00	900	100	4	OXIDAT
62	47	155	154	0.00	0.00	0.00	0.00	0.00	1100	40	1	OXIDAT
53	88	175	201	0.00	0.00	0.00	0.00	0.00	1100	60	1	OXIDAT
75	78	259	294	0.00	0.00	0.00	0.00	0.00	1100	100	1	OXIDAT
42	57	72	72	0.00	0.00	0.00	0.00	0.00	1000	40	2	OXIDAT
-999	26	72	-999	0.00	0.00	0.00	0.00	0.00	1000	60	2	OXIDAT
36	39	101	112	0.00	0.00	0.00	0.00	0.00	1000	100	2	OXIDAT
21	-999	66	42	0.00	0.00	0.00	0.00	0.00	950	40	3	OXIDAT
81	-999	55	47	0.00	0.00	0.00	0.00	0.00	950	60	3	OXIDAT
32	-999	44	137	0.00	0.00	0.00	0.00	0.00	950	100	3	OXIDAT
420	737	161	103	0.90	0.90	0.45	0.45	3.21	950	80	1	CPD
362	637	172	117	0.90	0.90	0.45	0.45	3.21	950	80	2	CPD
413	571	141	91	0.90	0.90	0.45	0.45	3.21	950	80	3	CPD
319	583	118	78	0.90	0.90	0.45	0.45	3.21	950	80	4	CPD
1009	2066	531	233	0.90	0.90	0.45	0.45	3.21	950	200	1	CPEND
1023	1150	403	177	0.90	0.90	0.45	0.45	3.21	950	200	2	CPEND
544	779	275	124	0.90	0.90	0.45	0.45	3.21	950	200	3	CPEND
702	928	366	166	0.90	0.90	0.45	0.45	3.21	950	200	4	CPEND

(3) Omitted, Negative τ

$C_1(\mathrm{Na})\cdot C_2(\mathrm{K})\cdot C_3(\mathrm{Mg})\cdot C_4(\mathrm{Ca})\cdot C_5(\mathrm{Cl})\ t^{\beta 1}\exp\cdot 10\ (\beta_2 + \beta_3\ T + \beta_4\ T^2 + \beta_5 r_1 + \beta_6 r_2 + \beta_7 r_1 r_2 + \epsilon)$ where τ = metal recession, Na, K, Mg, Ca, Cl = respective dopant levels in ppm, t = time in hours, T = temperature −950 °C divided 50 °C. r_1 and r_2 = dummy variables indicating test rig, ϵ = the unobservable random error and each of the C_i are of the form:

$$C_i = \phi_{i1} + (1 - \phi_{i1}) \exp(-x\phi_{i2})$$

This functional form has the following properties: (1) It is essentially a power law in time so that at time zero there is no attack; (2) the impurity functions have the value of unity at 0 concentration and are asymptotic to ϕ_{i1} as concentrations go to infinity; (3) the second order polynomial in the temperature of the exponential term will allow for maximal rate of attack for some temperature if β_4 is less than zero and (4) indicates a belief that the experimental error is proportional in nature rather than additive. It should be pointed out that this type of curve fit requires the use of non-linear regression.

The behavior of this family of impurity functions is indicated in Fig. 4. The value of ϕ_1 is an asymptote such that ϕ_1 is greater than 1, and the function is monotonically increasing. The parameter ϕ_2 must be greater than zero and indicates the rapidity of approach to the asymptote. Large values indicate rapid approach and small values indicate slow approach. If ϕ_1 is less than 1 the function is monotonically decreasing to ϕ_1. Small values of ϕ_2 indicate a slow approach and large values a rapid approach.

Results and Discussion

X-Ray Diffraction of Deposits. As a result of the many different test conditions on four alloys, there is plethora of X-ray diffraction data. These data are presented and discussed in detail in the Appendix. In general, the dopants tended to form the same types of deposits regardless of the concentration or the combinations with other elements. Mg in the combustion products tended to deposit as MgO. Ca, on the other hand reacted with sulfur in the fuel to form primarily Ca sulfate. As expected from other work [11] Na and K also deposited as sulfates. In the case of Na, Na_2SO_4 was the primary phase, however, it was found in three separate crystallographic modifications. K, when present in appreciable quantities, was found as K_2SO_4 and it also combined with the Na_2SO_4 to form a mixed sulfate $K_xNa_{2-x}SO_4$. Throughout the analyses a set of unknown lines consistently occurred for which no match could be made with the powder diffraction file. By correlating the presence of these lines with the concentrations of the dopants, we were able to determine that this was probably a phase primarily composed of Na with some K and Ca as a sulfate. This phase

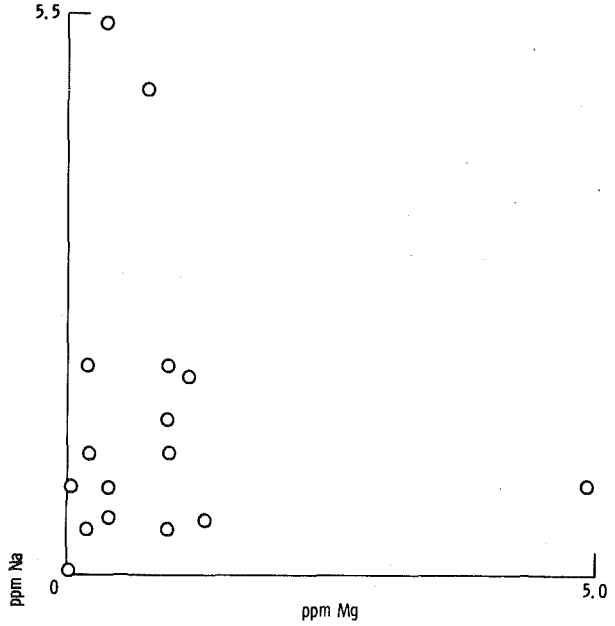

Fig. 3(*a*) Na and Mg. The plots of Na versus Ca, K versus Mg, and K versus Ca are similar.

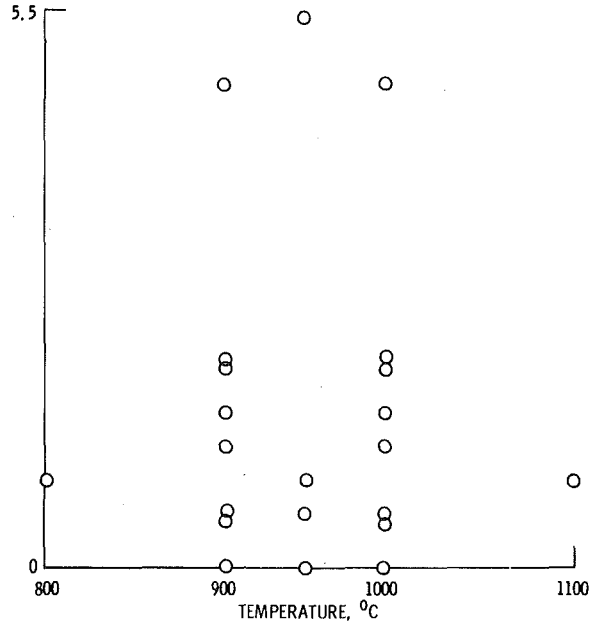

Fig. 3(*b*) Temperature and Na. The plot of K versus *T* is similar.

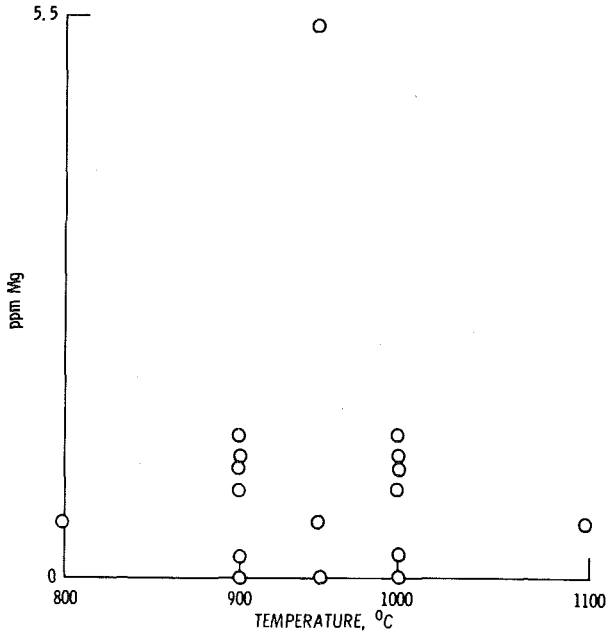

Fig. 3(*c*) Temperature and Mg. The plot of Ca versus *T* is similar.

Fig. 3 The scope of the program

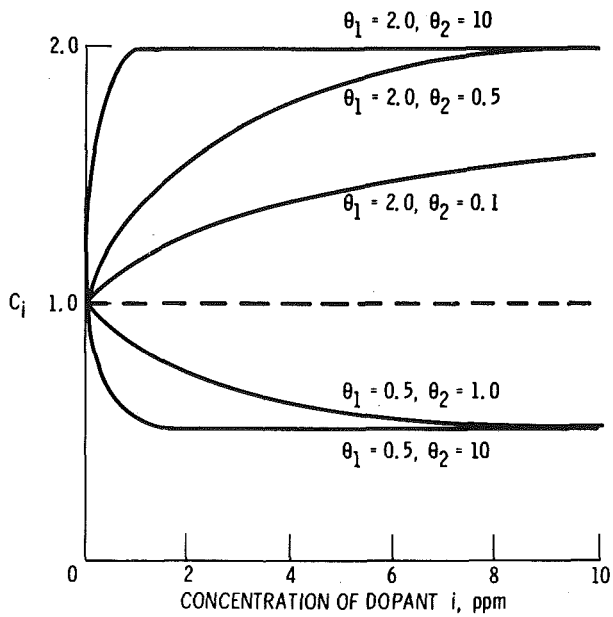

Fig. 4 The response of C_i to concentration of dopant "*i*" as affected by variations θ_1 and θ_2

was then synthesized as shown in the Appendix and determined to be approximately $Na_8K_2Ca(SO_4)_6$. The above phases accounted for the vast majority of those found in the deposits. Twice a $Na_2Ca_2(SO_4)_3$, glauberite, was found and a few weak lines which were never identified were seen in a few of the patterns.

The presence of these phases presented few surprises, as such sulfate forming reactions have generally been found in these types of tests and have usually led to accelerated corrosion. This is especially true in the cases of Na and K sulfates and their mixtures. The complications introduced by the Na, K sulfates and the Na, K, Ca sulfates is that these compounds form liquid deposits over temperature ranges which are largely unknown. As will be seen from the discussion of the metal recession data, high metal recessions are associated, as would be expected, with large concentrations of Na and K sulfates.

Metal Recession Data—Center Point Analysis. Plots of the raw data for the center points are given on log-log scale in Fig. 5. The plots are done separately for each rig. Table 4 presents the results of the regression analysis for each alloy.

The analysis of the IN-100 center point data indicates that the exponent of time is (within sampling error). = 1. This would indicate the corrosion is proceeding via a surface reaction. Such reactions would indicate that no protective layer is being formed during the corrosion process and would probably result in highly accelerated corrosion, and indeed IN-100 is known to be a very corrosion-prone material [11].

The coefficient of the fuel-to-air ratio is negative by a significant amount indicating that as fuel-to-air increases at this temperature the corrosion rate decreases. These results are not in agreement with the fuel-to-air ratio effects observed on Mar M-509 as shown in reference [10], and indicate that, quite probably, fuel-to-air as a variable, like so many other variables as found in reference [11], affect different alloys differently.

The coefficients of the rig effects imply that rigs one and two are similar as are rigs three and four, but the two sets differ significantly. This difference is apparent from the raw data plots of Fig. 5. It is interesting to note that rigs 1 and 2 are combined on one table in the

laboratory and rigs 3 and 4 are on another table. While nominally all four rigs are built to the same specifications and presumably identical, it is quite obvious from the data that rig to rig variations do exist at a level significant enough to be detected in this type of experiment.

The variance and the standard deviation estimates are 0.0142 and 0.119, respectively. The approximate 95 percent confidence limits derived from chi-square distributions are 0.0099. This is less than or equal to the variance which is less than or equal to 0.0219. These limits are given in Table 4. When fitting the log of metal recession, the estimate of standard deviation can be used to provide approximate proportional error limits on τ. For example, the distribution of log τ values for a fixed time, fuel-to-air ratio, and rig has a standard deviation, σ, so that log $(\tau) \pm 2\sigma$ is estimated by the log $(\tau) \pm 2s$. Upon taking the antilog we find that $\tau \times 10^{\pm 2s}$, so that $10^{\pm 2s}$ represents proportional error limits. For the IN-100 we obtained -0.58 and $+1.73$ indicating that two σ limits are from about 42 percent low to 73 percent high.

The U-700 center point data indicate that the coefficient of the log time is significantly larger than 1. This indicates a reaction faster than surface controlled, possibly due to alloy depletion effects. The-fuel-to-air coefficient is significantly negative and hence indicates decreasing attack with increasing fuel-to-air as was found with the IN-100. There are two significant rig effects with the larger being rigs 1 and 2 versus rigs 3 and 4, again as was found with the IN-100. Proportional 2σ limits there are estimated to be 50 percent low to 142 percent high.

The coefficient on time for the center point data of IN-792 is 0.87, only slightly smaller than 1. This could possibly indicate a corrosion process that is partially surface controlled and partly diffusion controlled. The fuel-to-air coefficient is not significantly different from zero and hence, appears to be not involved in the corrosion of this alloy. There is one significant rig effect, being the difference between rigs 1 and 2 and rigs 3 and 4 as found on the preceeding two alloys. Proportional 2σ limits are estimated as 42 percent low and 73 percent high.

The Mar M-509 center point results indicated a coefficient in time of about 0.6 which is not significantly different from 0.5. This may indicate a primarily diffusion controlled reaction. The microstructure of the attack zone found on the Mar M-509 alloys both in this study (Fig. 6) and in previous work [11], indicate that the attack is largely down grain boundaries, presumably requiring the transport over a rather long distance and may be the cause of the low exponent in time.

There is a significant fuel-to-air effect but no significant rig effects were observed. However, as was the case in the other three alloys, the fuel-to-air coefficient was negative in direct contrast to the results found in reference [10]. This may be related to the differences between the two types of experiments in which the referenced work was obtained on stationary samples and the current data are obtained on samples rotated in the manner described above. However, in the absence of further work the anomaly cannot be fully explained. The proportional two σ limits are estimated as 49 percent low to 95 percent high.

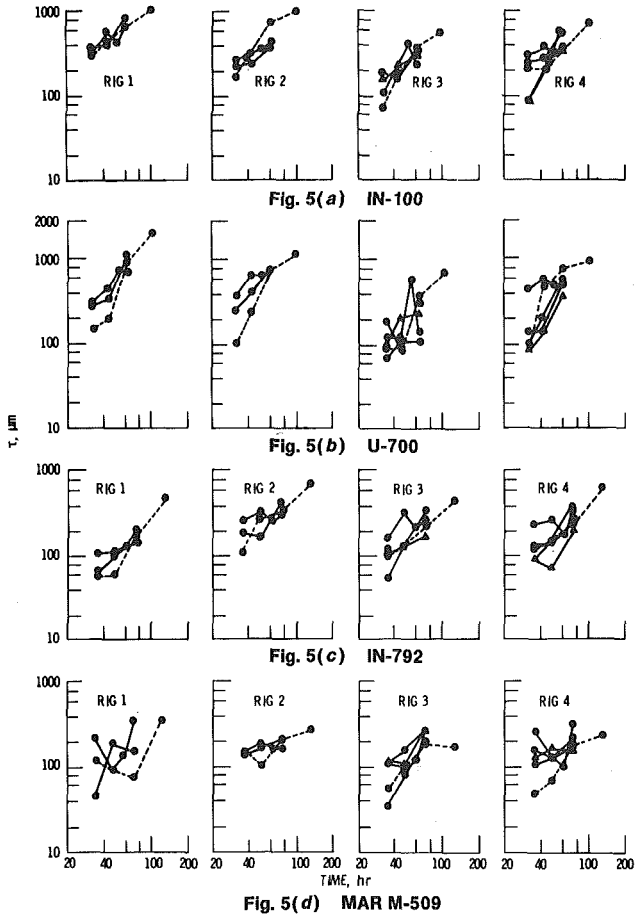

Fig. 5(a) IN-100

Fig. 5(b) U-700

Fig. 5(c) IN-792

Fig. 5(d) MAR M-509

Fig. 5 Effects of rig and time on the center point metal recession

Table 4 Center point regression analyses (56 data points per alloy)

	IN-100			U-700			IN-792			MM 509		
	EST COEF	STD DEV COEF	t	EST COEF	STD DEV COEF	t	EST COEF	STD DEV COEF	t	EST COEF	STD DEV COEF	t
β_0	1.032			.631			.715			1.420		
log (time)	.98	.082	12.04	1.36	.132	10.36	.87	.082	10.61	.60	.099	6.02
F/A	$-.67\times10^{-3}$	$.25\times10^{-3}$	-2.69	-1.22×10^{-3}	$.40\times10^{-3}$	-3.02	$-.30\times10^{-3}$	$.25\times10^{-3}$	-1.21	$-.96\times10^{-3}$	$.3\times10^{-3}$	-3.15
r_1	-.11	.016	-6.97	-.14	.026	-5.39	-.068	.016	-4.16	-.006	.020	-.29
r_2	$.26\times10^{-2}$	.016	.16	6.1×10^{-2}	.026	2.31	1.99×10^{-2}	.016	1.22	2.9×10^{-2}	.020	1.45
r_1r_2	$.56\times10^{-1}$	.018	3.17	$.41\times10^{-1}$	.028	1.44	$-.16\times10^{-1}$	.018	-.89	$-.26\times10^{-1}$	.021	-1.24
R^2		82.1			76.5			73.6			45.7	
$\hat{\sigma}^2$	.0099	.0142	.0219	.0257	.0367	.0568	.0099	.0141	.0219	.0146	.0209	.0323
$\hat{\sigma}$		.119			.192			.119			.145	
$10^{\pm 2\hat{\sigma}}$	.58		1.73	.41		2.42	.58		1.73	.57		1.95

Table 5 Results of model fitted by dropping points labeled (*a*) and (*b*) in Table 3

	IN-100		U-700		IN-792		MarM-509	
	ϕ_1	ϕ_2	ϕ_1	ϕ_2	ϕ_1	ϕ_2	ϕ_1	ϕ_2
Na	336.4	.07666	105.2	.06592	259.4	.007793	2.667	.2838
K	90.66	.01373	13.10	.1801	15.77	.1606	8.384	.1166
Mg	.4661	2.039	.7399	1.009	.5489	2.598	2.773	.02431
Cl	.2312	.5443	.2430	.3541	.4104	.5023	.1856	.1334
Ca	.4345	6.000	.6070	.7410	.1953	.9624	.4914	.2500
β log t	.9950		1.062		.8218		.6515	
β	-.08192		-.4103		.3137		.6720	
βT	-.1234		.1870		.1227		.05806	
βT^2	.04424		-.05006		-.004882		.02438	
βr_1	-.05016		-.09450		-.05501		-.02612	
βr_2	-.02319		.01082		-.03358		-.02606	
$\beta r_1 r_2$	.01930		.007929		.005913		.001433	
SSQ TOT	44.54		44.06		25.01		13.23	
SSQ RES	7.19		7.53		4.23		3.86	
R^2	.839		.829		.831		.708	
n	203		200		205		203	
$\hat{\sigma}^2$	.0387		.0411		.0225		.0208	
$\hat{\sigma}$	.197		.203		.150		.144	
$10^{\pm 2\hat{\sigma}}$	(.404 , 2.47)		(.393 , 2.55)		(.501 , 1.99)		(.515 , 1.94)	

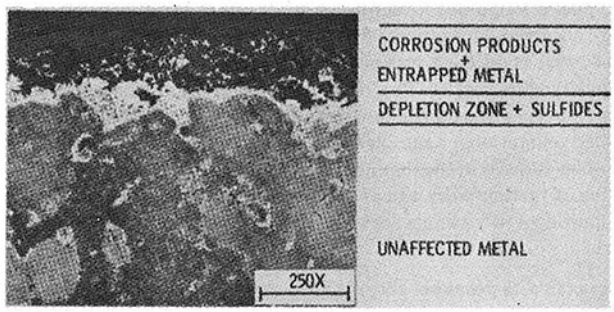

Fig. 6(*a*) IN-100

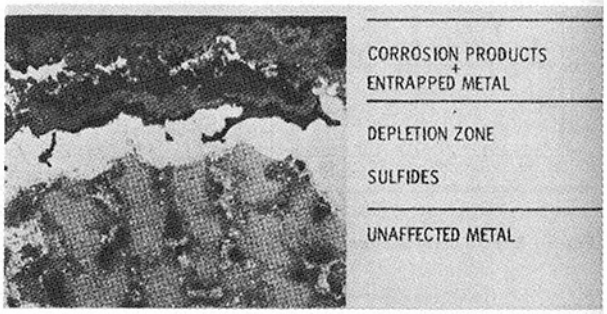

Fig. 6(*c*) IN-792

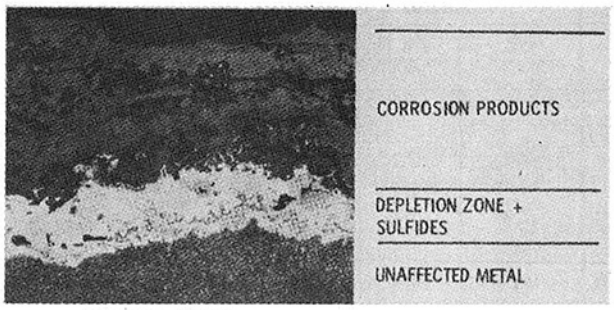

Fig. 6(*b*) U-700

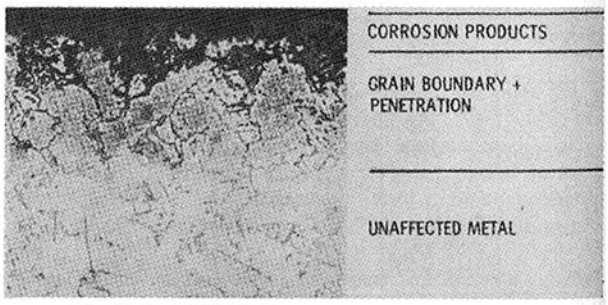

Fig. 6(*d*) MAR M-509

Fig. 6 Microstructural attack after 200 one-hour cycles under center point conditions (950°C, 0.9Na, 0.9K, 0.45Ca, 0.45Mg, 3.21Cl)

Analysis of the Full Data Set. The model of the equation was fitted to all the available data for each alloy by a least squares method. The self-consistency of the data was examined by computing the residuals for each available observation. This consists of computing the predicted values of $\log \hat{\tau}$ for each data point and subtracting that from the observed $\log \tau$. These residuals were examined in sets of 12. Because of the experimental procedure consisting of three pins of each alloy at 40, 60 and 100 hr it is quite possible that there is some correlation structure underlying these 12 observations due to some common uncontrolled unknown variables. Scaled squared distances from the origin of these vectors of dimension 12 were computed, ordered from the smallest to the largest, and plotted on a chi-squared probability scale (see Section 6.4 of Gnanadesikan [12] for details). If the residuals

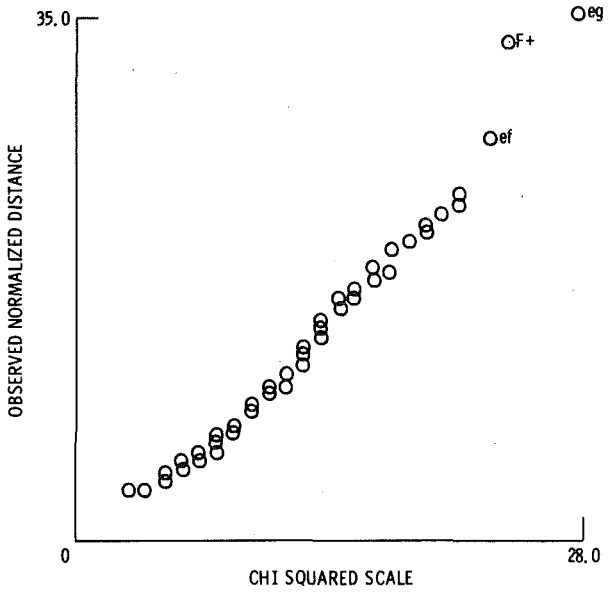

Fig. 7 Probability plot of pass residuals

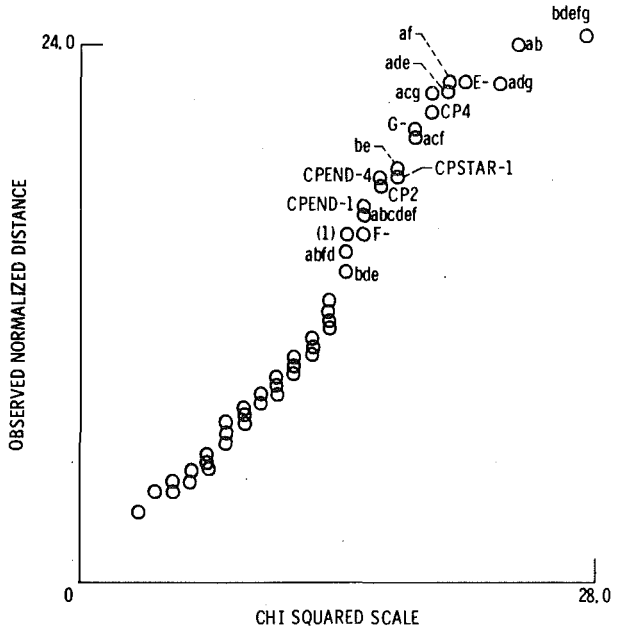

Fig. 8 Probability plot of pass two residuals

$(\log \hat{\tau} - \log \tau)$ are normally distributed with no significant inability observed of the calculated model to fit the data, the plot should be a straight line. Figure 7 shows the resulting plot which looks somewhat like a straight line except for possibly points *ef*, *F+* and *eg*. These points were deleted (indicated by *A* in Table 3) and the models refit. The estimated coefficients were not much different. The residuals for this fit were calculated and plotted with the result presented in Fig. 8. This plot seems to indicate two different straight lines with points 35, 36, 28 as possible bad points. The two straight lines may be interpreted as indicating two error processes. Upon examining the data points on the steeper of the two lines it appears that almost all of them involve a situation where τ of 60 hr is less than τ of 40 hr for one or more of the alloys. No other pattern was seen to emerge. After a detailed, two step analysis of the remaining data examination, all the data points labeled *B* in Table 4 were also dropped as being suspect and the models again refitted. These are the results given in Table 5. On comparison it was noted that the largest difference was in the estimated s value. For the models fit to the edited data set, Table 5, we obtained s values much more in accord with the center point fit. This fact along with the fitted equations being quite similar for all three fits, leads us to conclude the results of the use of the edited data yielded the best results.

Errors. Before discussing the relative effects of the variables on each alloy, the estimates of the residual experimental error and the impact of this error on the results to follow will be discussed. The model is of the form $\tau = \alpha_1 t^{\alpha 2} 10^{\epsilon}$ where ϵ is a random error. The estimates of Table 5 which are labeled $\hat{\sigma}^2$ are estimates of the variance of ϵ. Plus and minus two standard errors about the model equation is thus given by: $\alpha_1 t^{\alpha 2} \times 10^{\pm 2\sigma}$. Table 5 represents the factors $10^{-2\sigma}$, $10^{+2\sigma}$. It is thus seen that approximately 95 percent of the observations should fall within a factor of two for IN-792 and Mar M-509. The 95 percent tolerance limit is slightly larger, about 2.5, for IN-100 and U-700. It must be noted that this is strictly true only if the ϵ are independent and normally distributed, the model as stated is correct, and we know what the true values of α_1, α_2 are. The probability plots of Figs. 7 and 8 indicate approximate normality. We are not sure of the choice of the model. It has several features that are desirable but clearly cannot be assumed to be exactly correct. We must allow for the possibility of a future different model being more chemically precise. Due to the rather large experimental error it will be difficult to distinguish among competing models unless: (1) They are grossly different, or (2) we perform very extensive experimentation. All discussion is in terms of the chosen model. We then come to the point that we have only estimated the coefficients. There are errors and uncertainty in each of these, and hence, uncertainty in the fitted equation. There are no exact methods available for quantifying this uncertainty in the case of nonlinear least squares. The existing approximate techniques are cumbersome and of uncertain validity.

What we are most interested in are those variables which cause changes in the depth of attack that are greater than the changes due to random sampling.

Sodium. Increasing sodium levels increase the rate of attack for all four alloys. The increase is especially dramatic for IN-100 and U-700. From Table 5, the asymptotic values are for IN-100, 336.4; for U-700, 105.2; for IN-792, 259.4; and for Mar M-509, 2.667. These values are slightly misleading since they are not approached within the sodium levels observed in the experiment, except for Mar M-509. Figure 9(*a*) shows a rate factor for sodium over the interval 0-5 ppm. Although not plotted, the factor for sodium is 107.8 at 5 ppm; for IN-100, U-700 and IN-792 it is evident that the change in attack over the 0-5 ppm range is considerably larger than the experimental error, while for Mar M-509 the change is close to the error limits. There are evidently real differences between the rate of each alloy also. As an approximation consider that at 2 ppm the predicted factors and the error limits are

	$\tau 10^{-2\hat{\sigma}}$	τ	$10^{+2\hat{\sigma}}$
IN 100	19.7	48.7	120.3
U-700	5.5	13.9	35.4
IN-792	2.5	5.0	10.0
MM-509	.88	1.7	3.3

These results are consistent with published data [11] inasmuch as they indicate that increases in sodium are a cause of increasing attack, and that the alloys corrode in approximately the order one would expect, mainly the most corrosion resistant, Mar M-509 through the least corrosion resistant, IN-100.

Potassium. Increasing values of potassium cause increasing rates of attack. The numerical values defining the rate function are given in Table 5, and the functions plotted over 0–5 ppm in Fig. 9(*b*). The change in C_k over that range is clearly larger than the random error effects, but appears to be about the same for each alloy.

Magnesium. Increasing magnesium concentrations decreases attack for all but the Mar M-509 alloy. The Mar M-509 alloy indicates essentially no effect over the range plotted, 0-5 ppm, while for the other alloys the change in attack is about the same. Thus, this study would indicate that magnesium is a favorable element as would be concluded from reference [13], but not especially so. The behavior of IN-100 and IN-792 are very much alike. These results are plotted in Fig. 9(*c*).

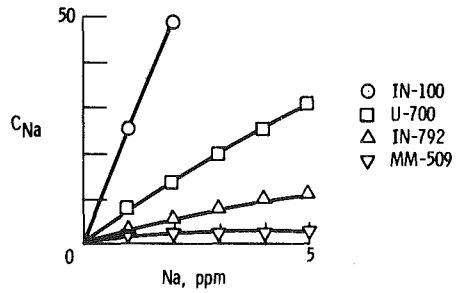

Fig. 9(*a*) Sodium

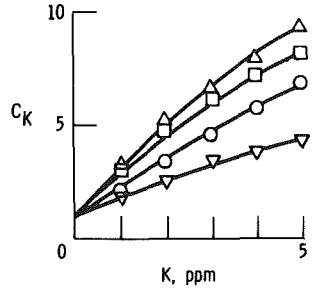

Fig. 9(*b*) Potassium

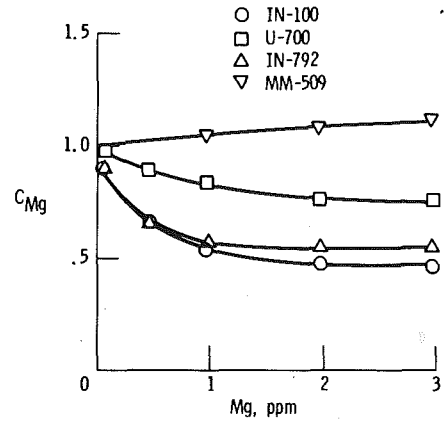

Fig. 9(*c*) Magnesium

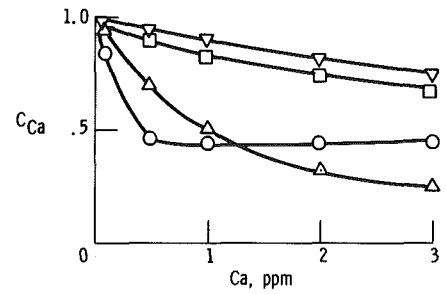

Fig. 9(*d*) Calcium

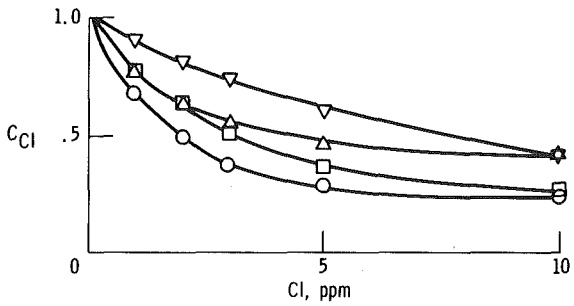

Fig. 9(*e*) Chlorine

Fig. 9 Effect of concentration on C_i

Calcium. Calcium appears to be a favorable additive as increasing calcium concentration leads to decreasing attack for all alloys. The numerical values in Table 5 indicate rate reductions of from 0.195 to 0.607. These limits are nearly achieved within the levels of calcium examined and the factors are plotted from 0-3 ppm in Fig. 9(*d*). For IN-100 and IN-792 there is a very rapid reduction in rate, while for U-700 and for Mar M-509 reduction is not so rapid. Over the range of 0-5 ppm the change in the function is larger than the error limits. These data are certainly consistent with the inhibitor data published in reference [13], which found that calcium decreased corrosion to some degree.

Chlorine. Chlorine also appears to be a beneficial dopant. The numerical values of Table 5 indicate asymptotic reduction of rate of attack from 0.1856 to 0.4104 depending upon the alloy. Chlorine concentrations range from 0-16 ppm, the rate ractors are plotted from 0–10 ppm for each alloy in Fig. 10. This indicates the response to be rather similar for each alloy. The reduction in attack due to the chlorine is greater than the error limits. These results are somewhat surprising as earlier work in burner rigs [11] indicated that chlorine was probably a cause of accelerated hot corrosion, although the data were certainly not unambiguous. In this case all of the data seem to strongly indicate that chlorine, when present, can be a cause of reduction of hot corrosion and not of acceleration. This is consistent with the results of Smeggil [14].

Rigs. One important and disturbing variable to consider is rig effects. The rigs are nominally identical; whatever variability there is from one rig to another is a lower bound on the differences that could result between two different labs. This is because many things change from lab to lab, least among them the rigs. In our model the rig effect is included through the inclusion of the two dummy variables, r_1 and r_2. Table 6 presents the deviation of each rig from a nominal or mean rig by indicating the value of $10^{**}(r_1 + r_2 + r_1 r_2)$. It is thus seen that rig 1 tends to yield attack results about 13–24 percent higher than nominal, while rig 4 yields results about 11–16 percent lower than nominal. Rigs 2 and 3 are about average in their effect on corrosion attack.

Temperature. The model chosen for the temperature rate factor has the obvious drawback that there are no temperature—dopant interaction terms. It would be expected that Mg would not have an interaction effect over the range of interest. It forms MgO which probably acts only as either an inert solid or as a slight inhibitor [13]. However, MgO is a solid at all test temperatures. Cl has been shown to remain largely in the gas [15] and whether there should be a Cl—temperature interaction is questionable. One would expect Na-, K-, and Ca-temperature interactions as these form sulfates whose dew points and melting points may be in the test temperature range. Since it is generally assumed that accelerated corrosion occurs primarily at temperatures between the melting point and the dew point of the deposits, the composition of the deposit should strongly influence the shape of the temperature—corrosion curve.

At this stage of the development these types of interactions have not been included in the model. Nevertheless, the temperature profiles predicted by the model are in reasonable agreement with the observed data which would indicate that the potential interaction terms are not necessarily first order effects over the temperature range of interest here. Further refinements in the model may include the temperature-dopant interaction terms provided that their effects are greater than the uncertainty in the data.

Concluding Remarks

An attempt has been made to study the corrosion attack of turbine airfoil alloys as a function of Na, K, Ca, Mg, Cl, temperature, and time utilizing a statistically designed burner rig program. An attack model was developed from these results which, while obviously incomplete, seems to account for most of the important first order effects. As more data become available, modification and refinement of the model should allow greater predictive ability.

Table 6 Estimated rig variation from nominal ($r_i = 0, 4_2 = 0$)

Dummy Variables		Rig No.	$10^{\beta r_1 + \beta r_2 + \beta r_1 r_2}$			
r_1	r_2		IN-100	U-700	IN-792	MM 509
-1	-1	1	1.24	1.23	1.24	1.13
-1	+1	2	1.02	1.25	1.04	1.00
+1	-1	3	.90	.77	.94	1.00
+1	+1	4	.88	.84	.83	.89

Table 7 Phases present in deposits

R.O. _____

DATE _____

RUN CODE	RIG	Dopant Composition (ppm) Na	K	Mg	Ca	Cl	Temp. (°C)	Phases Present (Relative Strength of X-Ray Diffraction Patterns) s = strong, m = medium, w = weak MgO	$NaSO_4$	$CaSO_4$	$xNa_{(2-x)}SO_4$	(1) $Na_8Ca_2K_1SO_4$	(2) Substrate Oxides	Other Known Phases	Unknown Pattern
Center Points	All	0.90	0.90	0.45	0.45	3.21	950	S	W	M		M	W		
A^+	4	5.40	0.90	0.45	0.45	10.15	950	M	S						
AB	1	2.00	0.40	0.20	0.20	2.66	900	M	S				W		
A^-	3	0.49	0.90	0.45	0.45	2.58	950	M		S					
B^+	4	5.40	0.90	0.45	0.45	3.21	950	M	S						
B^-	3	0.49	0.90	0.45	0.45	3.21	950	M		S					
C^+	4	0.90	5.40	0.45	0.45	7.29	950	S			S				
C	3	0.40	1.20	0.20	0.20	2.15	900	S			S	M	W		
CD	1	0.40	2.00	0.20	0.20	2.15	900	S			S				
C^-	4	0.90	0.49	0.45	0.45	2.84	950	S		M		S			W
D^+	3	0.90	5.40	0.45	0.45	3.12	950	S			S				
D	3	0.40	1.20	0.20	0.20	1.43	900	S			S	M	M		
D^-	3	0.90	0.49	0.45	0.45	3.21	950	S		S		S			
E^+	3	0.90	0.90	4.95	0.45	16.33	950	S		M			W		
EG	3	0.40	0.40	1.00	0.20	3.76	1000	S		S					
E^-	4	0.90	0.90	0.04	0.45	2.01	950					S	S		
F^+	4	0.90	0.90	0.45	4.95	11.17	950	W		S					
FG	1	0.40	0.40	0.20	1.00	2.84	1000	S		S					
F^-	3	0.90	0.90	0.45	0.04	2.48	950		S				S		
EF	3	0.40	0.40	1.00	1.00	5.17	900	S		S			W		
G^+	4	0.90	0.90	0.45	0.45	3.21	1100	S				S			
G^-	3	0.90	0.90	0.45	0.45	3.21	800	S				S			
ACG	3	1.20	1.20	0.20	0.20	3.39	1000		M		W		S		
ADG	4	1.20	1.20	0.20	0.20	2.66	1000	W	M		M		S		
BCG	2	1.20	1.20	0.20	0.20	2.15	1000		M		W		S		W
BDG	2	1.20	1.20	0.20	0.20	1.43	1000		S	W	W		S		W
ABCD	2	2.00	2.00	0.20	0.20	3.39	900	W	S		S	W	S		W
BCDG	4	1.20	2.00	0.20	0.20	2.15	1000	W			S		S		
BE	3	1.20	0.40	1.00	0.20	3.76	900	S	S			S			
ABEG	3	2.00	0.40	1.00	0.20	4.99	1000	S	M						W
ADE-I	1	1.20	1.20	1.00	0.20	4.99	900	S	M	W	M				W
ADE-II	3	1.20	1.20	1.00	0.20	4.99	900	S	S					(W) Na_2CaSO_4	
ACE-I	4	1.20	1.20	1.00	0.20	5.72	900	S	M		W				
ACE-II	4	1.20	1.20	1.00	0.20	5.72	900	S			M	M			
BCE	3	1.20	1.20	1.00	0.20	4.49	900	S	M		W				
BDE	1	1.20	1.20	1.00	0.20	3.76	900	S	W		M				
ABCDEG	3	2.00	2.00	1.00	0.20	5.72	1000	S	M		M		M		
CDEG	4	0.40	2.00	1.00	0.20	4.49	1000	M		M	M				
ABFG	2	2.00	0.40	0.20	1.00	4.08	1000					S	M		
AF	4	1.20	0.40	0.20	1.00	4.08	900	M		M		S			
ACF	3	1.20	1.20	0.20	1.00	4.80	900	M	S	M					W
ADF	2	1.20	1.20	0.20	1.00	4.08	900	S		S		S			W
BCF	1	1.20	1.20	0.20	1.00	3.57	900	S		S	W	S			W
BDF	4	1.20	1.20	0.20	1.00	2.84	900	S	S	S					W
ACDF	4	1.20	2.00	0.20	1.00	4.80	900	S				S		$K_2Ca_2(SO_4)_3$	
ABDFG	3	2.00	1.20	0.20	1.00	4.08	1000		M			S			W
ABCDFG	1	2.00	2.00	0.20	1.00	4.80	1000		S				M		
CDFG	3	0.40	2.00	0.20	1.00	3.57	1000			S			M		
ABEF	4	2.00	0.40	1.00	1.00	6.41	900	S		M					M
ABCEF	4	2.00	1.20	1.00	1.00	7.13	900	S		W		S			W
ABCDEF	2	2.00	2.00	1.00	1.00	7.13	900	S		S		S	W		W
ACEFG	4	1.20	1.20	1.00	1.00	7.13	1000	S	M	S					

NASA-C-8010 (10-24-51)

(1) See text of Appendix for discussion of this phase.

(2) Substrate oxides usually strongest on IN-100 samples.

Table 7 continued

RUN CODE	RIG	Dopant Composition (ppm) Na	K	Mg	Ca	Cl	Temp. (°C)	Phases Present (Relative Strength of X-Ray Diffraction Patterns) S = strong, m = medium, w = weak MgO	$NaSO_4$	$CaSO_4$	$KxNa_{(2-x)}SO_4$	$Na_8Ca_2K_1SO_4$	Substrate Oxides	Other Known Phases	Unknown Pattern
ADEFG	4	1.20	1.20	1.00	1.00	6.41	1000	S		S					
BDEFG	4	1.20	1.20	1.00	1.00	5.17	1000	S		S					
BCEFG	1	1.20	1.20	1.00	1.00	5.90	1000	S		S			W		
CDEF	2	0.40	2.00	1.00	1.00	5.90	900	S		S					
(L)	2	0.40	0.40	0.20	0.20	1.43	900	S			M		S		M
1	3	0.58	1.23	1.26	0.95	0.46	900	M			W		S	$K_2Ca_2(SO_4)_3$	
2	3	0.58	1.23	1.26	0.95	0.46	1000			W			S		
3	4	1.50	3.90	1.00	0.75	0.60	900	M			S				W
4	4	1.50	3.90	1.00	0.75	0.60	1000				M		S		
5	3	1.90	0.50	1.05	0.79	0.48	900	S					S		M
6	3	1.90	0.50	1.05	0.79	0.48	1000	S					S		M
7	4	4.70	1.50	0.83	0.63	0.60	900	M	S		W				
8	4	4.70	1.50	0.83	0.63	0.60	1000	M	S		W				

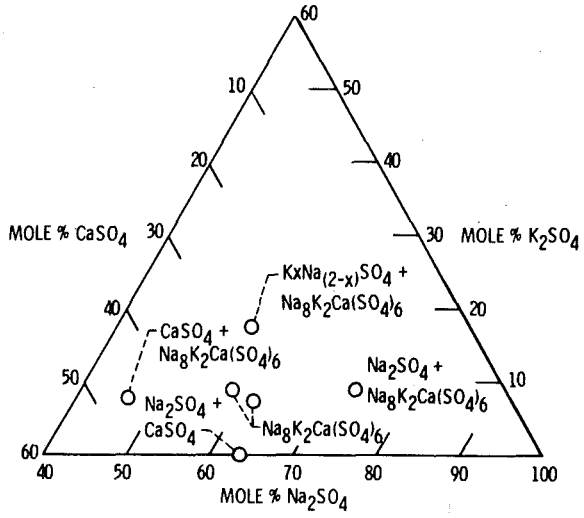

Fig. 10 Sulfate phase map

References

1 Stringer, J. F., "Hot Corrosion in Gas Turbines," MCIC-72-08, Battelle Columbus Labs., Columbus, Ohio, June 1972.

2 Stringer, J. F., "High Temperature Corrosion of Aerospace Alloys," AGARD-AG-200, Advisory Group for Aerospace Research and Development, Paris, 1975.

3 Lunt, H. E., "Hot Corrosion in Gas Turbines," ASME Paper No. 77-WU/Fu-3, Nov. 1977.

4 Lee, S. Y., Young, W. E., and Vermes, G., "Evaluation of Additives for Prevention of High Temperature Corrosion of Superalloys in Gas Turbines," ASME Paper No. 73-GT-1, Apr. 1973.

5 Zetlmeisl, M. H., May, W. R., and Annond, R. R., "Corrosion Inhibitor for Vanadium-Containing Fuels," U. S. Patent 3,926,577, Dec. 1975.

6 Lowell, C. E. and Deadmore, D. L., "Effect of a Chromium-Containing Fuel Additive on Hot Corrosion," *Corrosion Science*, Vol. 18, 1978, pp. 747–763.

7 Lowell, C. E. and Probst, H. B., "Effects of Composition and Testing Conditions on Oxidation Behavior of Four Cast Commercial Nickel-Base Superalloys," NASA TN D-7705, 1974.

8 Davies, O. L., ed., *The Design and Analysis of Industrial Experiments*, 2nd ed., rev., Hafner, New York, 1956.

9 Box, G. E. P., Hunter, W. G., and Hunter, J. S., *Statistics for Experimenters, An Introduction to Design, Data Analysis, and Model Building*, John Wiley and Sons, New York, 1978.

10 Deadmore, D. L., Lowell, C. E., and Kohl, F. J., "The Effect of Fuel-to-Air Ratio on Burner-Rig Hot Corrosion," *Corrosion Science*, Vol. 19, 1979, pp. 371–378.

11 Deadmore, D. L., and Lowell, C. E., "Burner Rig Alkalai Salt Corrosion of Several High Temperature Alloys," NASA TM X-73659, 1977.

12 Gnanadesikan, R., *Methods for Statistical Data Analysis for Multivariate Observations*, Wiley and Sons, New York, 1977.

13 Deadmore, D. L., and Lowell, C. E., "Inhibition of Hot Salt Corrosion by Metal Additives," DOE/NASA/2953-78/2, NASA TM-78966, 1978.

14 Kohl, F. J., Stearns, C. A., and Fryburg, G. C., "Sodium Sulfate: Vaporization Thermodynamics and Role in Corrosion Flames," *Metal-Slag-Gas Reactions and Processes*, Z. A. Foroulis and W. W. Smeltzer, eds., The Electrochemical Society, Inc., Princeton, N.J., 1975, pp. 649–664.

15 Smeggil, J. G. and Bornstein, N. S., "Study of the Effects of Gaseous Environments on Sulfidation Attack of Superalloys," R77-912613-5, United Technologies Research Center, East Hartford, Conn., 1977 (NASA-CR-135348).

APPENDIX

X-Ray Diffraction Results for Deposits by Ralph G. Garlick

The Guinier-deWolff focusing camera method was used for analysis of the powder samples. This method was used chiefly because it offers better separation of peaks than the other available methods in the range of lattice spacings where peak overlap often leads to problems in phase identification. This method also offers the advantage of the ability to run 4 samples under the same diffraction conditions at the same time and having the resulting four patterns on 1 film for comparison. This is ideal for comparison of deposits on the four alloys for the same deposit conditions.

The results of the diffraction analyses are summarized in Table 7. Under each phase the letters indicate the relative intensity of the pattern for that phase compared to other phases present, *S* indicating strong, *M* medium, and *W* weak. The center points are summarized as if they were 1 run and, although there was some variability in results, the major phases present were substantially the same for all runs. Sampling to get powder for X-Ray analysis was done primarily for analysis of the deposited material and attempts were made to avoid including the substrate oxides formed on the sample. In many cases this was not possible, as indicated in the table. The absense of substrate in the X-Ray sample, therefore does not indicate that none was present on the sample. As expected, substrate oxide was most often present in the IN-100 samples. Na_2SO_4, presented in the Table as one phase, was actually various combinations of three separate phases—types I, III, and V Na_2SO_4, with types I and V more commonly present. In most cases only one type of Na_2SO_4 was present in a sample. The $K_xNA_{(2-x)}SO_4$ formed in many of the samples is a hexagonal phase with a range of composition of at least from $K_{0.67}Na_{1.33}SO_4$ to $K_{1.5}Na_{0.5}SO_4$ with the unit cell increasing in size as the K/Na ratio increases [16].

The column designated $Na_8K_2Ca(SO_4)_6$ is an estimate of the formula for a phase (or phases) present in many of the samples. As previously indicated, a set of unknown lines occurred frequently in certain samples. By correlating the presence and relative strength of this pattern with concentrations of dopants it was determined that the phase was probably a sulfate with Na the principle cation, and small amounts of Ca and K also necessary. To synthesize this material, several samples in this composition range were mixed from the components Na_2SO_4, $CaSO_4$, and K_2SO_4. These mixtures were heated at 900 °C for 4 hr, cooled and X-Ray diffraction patterns run for the resulting materials. The results are summarized in the three component phase map, Fig. 10. The sample with no potassium (Na/Ca/K

= 7/2/0) consisted of $Na_2SO_4 + CaSO_4$. All other samples contained the unknown phase, with 2 samples containing only these unknown lines. These samples were those of Na/Ca/K ratios of 8/2/1 and 7/2/1, indicating a range of composition for the unknown phase. We have designated this phase as $Na_8K_2Ca(SO_4)_6$ which certainly represents the approximate composition. The other samples in the synthesis attempt consisted of this phase plus the sulfate one would expect from the composition (e.g., Na_2SO_4 for Na/Ca/K = 8/1/1).

Advances in Labyrinth Seal Aeroelastic Instability Prediction and Prevention

D. R. Abbott

Manager,
Advanced Mechanical Design,
Aircraft Engine Group,
General Electric Company,
Lynn, Mass. 01910

Fatigue cracking of an aircraft engine labyrinth seal occurred during pre-flight factory testing. Testing in a static rig revealed that the seal could be aeroelastically excited by the labyrinth leakage air flow. An earlier analytical model used for stability analysis was extended to account for the effect of acoustic natural frequency on the aeroelastic stability. The new model predicted that the ratio of acoustic and mechanical natural frequencies was of vital importance in determining if the nature of the pressure fluctuations within the labyrinth seal teeth provided either positive or negative aerodynamic damping to the seal. The analytical results were verified by further rig testing and also by correlation with test results for several other seals tested as part of a labyrinth seal technology program. A mechanical friction damper sleeve was designed to suppress the aeroelastic instability. The damper sleeve was tested in a rotating rig to evaluate its damping characteristics. The aircraft engine was qualified with the newly designed damper which has demonstrated its effectiveness for eight years of service and half a million hours of operation without incident.

Introduction

Labyrinth air seals are widely used in turbomachinery. Their purpose is to provide air seals between adjacent annular spaces where these spaces are enclosed partially by static structure and partially by rotating structure. A labyrinth seal therefore comprises a rotating part and a static part. The rotating part of the seal has several fin-shaped seal teeth typically supported by cylindrical structure. The static part of the seal usually has a structure supporting a surface which is tolerant of rubbing by the tips of the rotating seal teeth. This rub surface is sometimes made of abradable material, but, for high temperature seals, is usually made of very thin metal honeycomb.

Labyrinth air seals are not perfect seals. The clearance between each seal tooth and the static rub surface acts as an annular orifice and the seal as a whole acts as a series of orifices. The seal leakage flow depends on the number of seal teeth, the seal diameter, clearance and the pressures in the annular spaces being sealed. A small diameter aircraft engine seal with characteristics which allow operation at tight clearances may have a leakage flow as little as 0.1 percent of the main engine flow. A larger diameter seal where the final operating clearances are set by rubs during transient operation will typically have a leakage flow of 0.5 percent of the main engine flow. The available energy in the leakage flow is considerable and has often caused aeroelastically excited seal vibration with subsequent fatigue failure.

The purpose of this paper is to describe a particular aeroelastically excited vibration problem and how it was solved, and to contribute a new understanding of the aeroelastic vibration phenomenon and how it may be prevented.

Contributed by the Gas Turbine Division of THE AMERICAN SOCIETY OF MECHANICAL ENGINEERS and presented at the Gas Turbine Conference and Products Show, New Orleans, La., March 10–13, 1980. Manuscript received at ASME Headquarters January 8, 1980. Paper No. 80-GT-151.

Vibration Problems in Labyrinth Seals

Labyrinth seals have often been susceptible to vibration. Several different mechanisms have been identified as the cause of vibration. Some of these mechanisms have been described in references [1–5]. Each of these references describes at least one case where the vibration was caused by aeroelastic instability excited by the seal leakage flow.

References [2] and [5] describe how aeroelastic instability may be prevented by adjusting the seal clearances. Although this does result in some increase in seal leakage flow, the effect of this increased leakage in reducing engine performance was not considered to be significant.

References [1, 3], and [4] describe how the aeroelastic instability of rotating seals may be prevented by mechanical damping devices and also records the fact that there are no known cases of vibration where a rotating seal has been supported on the low pressure side.

References [1–4] also define design parameters which can be used to determine if aeroelastic instability would occur and, hence, if clearance adjustments or mechanical dampers are needed for its prevention.

The vibration problem which will be described led to a new analytical model which predicts some of the empirically observed phenomena noted in the above references.

The Success of Mechanical Dampers

Mechanical damping devices which provide friction damping have generally been very successful. Reference [3] describes the solution to a stationary seal vibration problem and also describes the use of damper rings to protect rotating seals from vibration. Reference [4] describes further applications of damper rings to rotating seals and also describes the use of a damper sleeve to protect a rotating tube from vibration.

A typical application of a damper ring on a rotating seal is shown in Fig. 1. Two seals are shown in this figure. The outer (upper) seal

is supported on its low pressure side and is not provided with a damper ring. As previously noted in references [1, 3], and [4], there are no known cases of vibration problems with rotating seals supported in this way. The inner (lower) seal is supported on its high pressure side and is provided with a damper ring.

The criterion used in determining damper ring effectiveness is to select a location on the seal where the flexural circumferential strain of the seal is a maximum. An analysis of several low frequency vibration modes was carried out and a damper ring position selected which would be effective in all of these vibration modes.

Based on all of the design experience available at the time, both seals were considered to be completely protected from aeroelastic instability. This proved to be the case for the outer seal which has always operated without problems. The inner seal, however, did not operate as successfully as all the earlier designs which were provided with damper rings.

Some Unexpected Problems

Although the inner seal was considered to be completely protected from aeroelastic instability, during factory testing of engines a total of four seals suffered from fatigue cracks. Two cases occurred on an earlier version of the inner seal shown in Fig. 1. This earlier seal had its damper ring located at the extreme left-hand end of the seal. Since the damper ring was obviously not providing enough damping, a careful analysis of the possible vibration modes was carried out and it was determined that the damper ring position shown in Fig. 1 would be considerably more effective. The seal was redesigned as shown but again two seals cracked. A typical fatigue crack is shown in Fig. 2. The fatigue cracks never progressed beyond the extent shown, and were not detrimental to engine operation. In fact, none of the cracks were discovered until routine teardown inspections were carried out.

As a result of these problems, a program was set up to design and evaluate an effective damper and also to understand the vibratory mechanism which was causing the cracks. The part of the program which led to the understanding of the vibratory mechanism will be described first.

Stability Testing

A static rig was designed to test the seal at the leakage flow conditions which would occur in an engine. A photograph of the rig is shown in Fig. 3. The space between the inner and outer seals was pressurized over a range of pressures which would simulate engine operation. Three displacement probes were positioned as shown in Fig. 3. These displacement probes measured vibratory displacements of the inner seal. Three dynamic pressure probes were placed in the honeycomb cells of the static seal (Fig. 1) to measure any pressure oscillations between the seal teeth.

The results of this test were that the inner seal would commence to vibrate over a wide range of leakage flows. Typical displacement and pressure traces are shown in Fig. 4. The vibration mode was identified as a three nodal diameter mode which is the lowest frequency vibration mode for this seal. It may be noted from Fig. 4 that the pressure oscillations lead the displacement in phase. This is a classic case of aeroelastic instability where the pressure forces lead the motion and provide enough work input to overcome any natural damping in the system.

Another objective of this test was to determine the effect of the natural frequency of circumferential acoustic waves of the seal stability. Since the unstable mode had been identified as a three nodal diameter mode, it was decided to add six weights to the inner seal as shown in Fig. 3. By successively adding increasingly heavy weights, it was possible to decrease the natural frequency of the inner seal until it was equal to or less than the natural frequency of a three nodal diameter acoustic wave. The result of this phase of testing was that with the mechanical frequency equal to or less than the acoustic frequency, the seal vibration could no longer be excited by the leakage flow. This was a new result which could not be predicted by existing analytical models. Based on this newly observed phenomenon, the existing analytical models were extended to include the effect of acoustic natural frequency on seal stability.

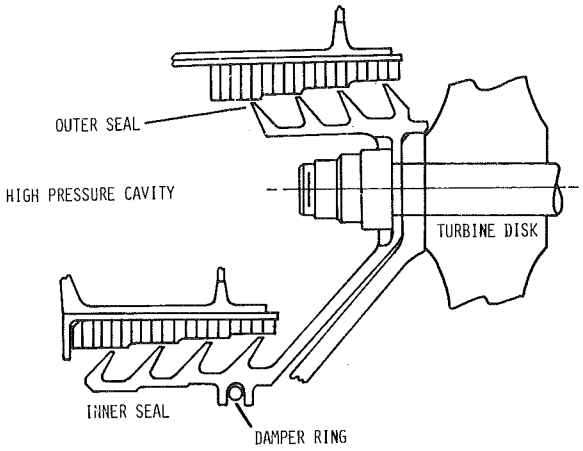

Fig. 1 Inner and outer labyrinth air seals

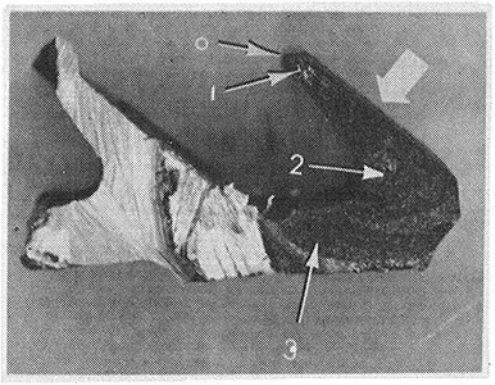

Fig. 2 Inner seal fatigue crack. Dark, oxidized area is the fatigue crack. O denotes fatigue origin; 1, 2, 3 = progression of the crack

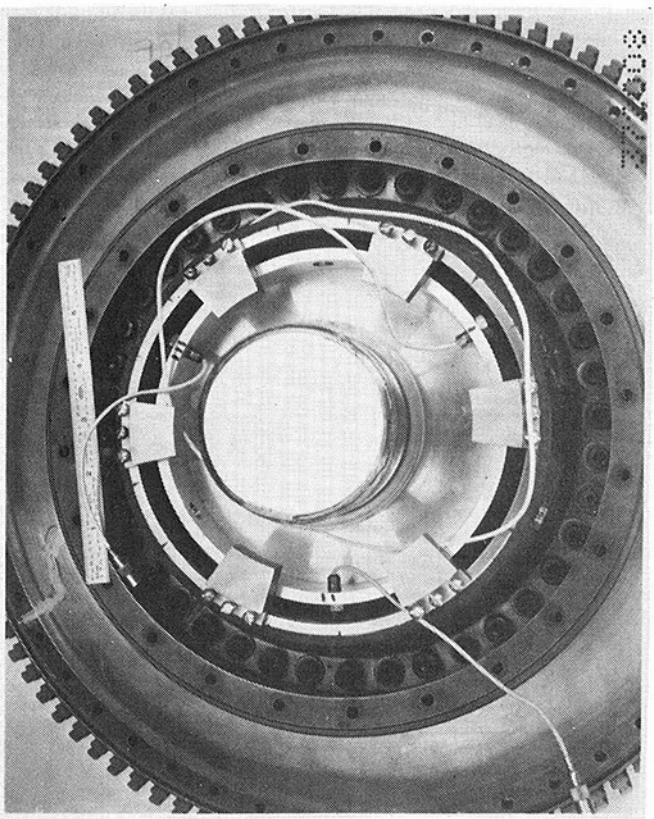

Fig. 3 Aeroelastic test rig. Rotating seal, displacement probes, and weights for adjusting frequency may be seen

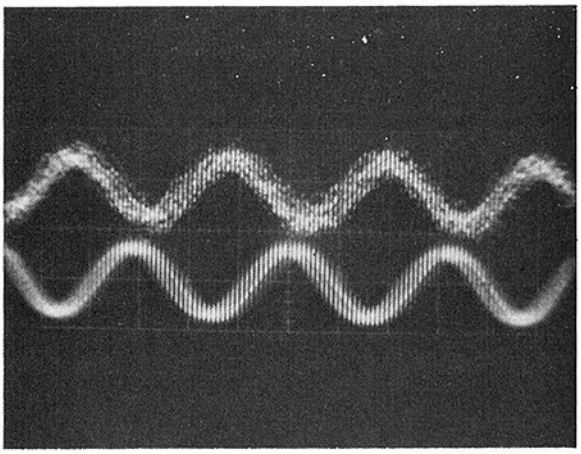

Fig. 4 Flow excited vibration. Upper trace of pressure oscillations leads lower trace of displacement by 140 deg. Time axis from left to right

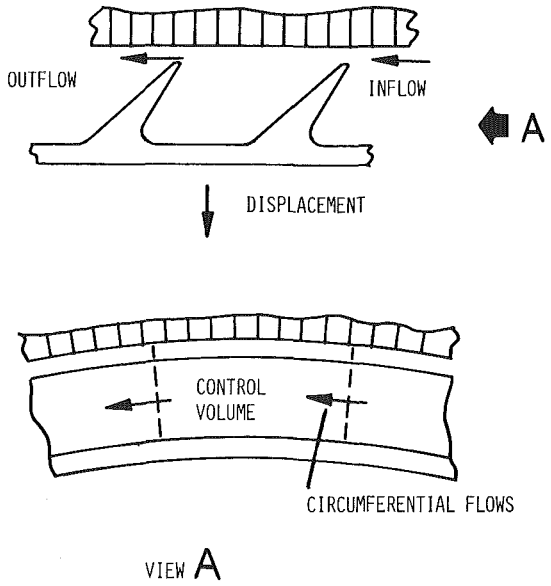

Fig. 5 Analytical model of flow in the seal

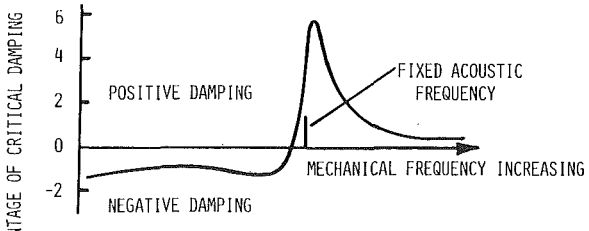

Fig. 6(*a*) Low pressure side support

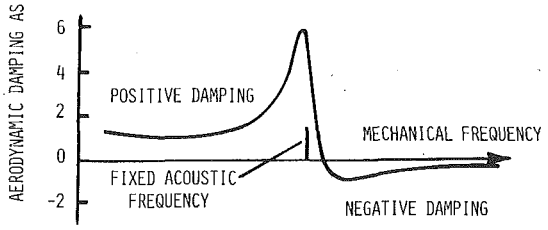

Fig. 6(*b*) High pressure side support

Fig. 6 Aerodynamic damping characteristics

A New Analytical Model

The model which had previously been used for the study of seal aeroelastic instability is described in reference [2]. This model was extended to account for circumferential air flow and pressure variations within the seal teeth. The new model is shown in Fig. 5. The equations which govern the pressure and flow in the control volume shown in the figure are as follows:

1 A continuity equation relating the net mass rate of flow into the control volume with the rate of increase of mass within the volume.

2 A circumferential momentum equation relating the time rate of change of momentum within the control volume with the net pressure force acting on the control volume.

3 A pressure-density relationship which was taken to be isentropic. This relationship introduces the velocity of sound in the circumferential direction.

Thus, for each seal cavity, there are three equations with four independent variables. These variables are the air density, pressure, circumferential velocity and the seal displacement which changes the magnitude of the control volume. These three equations can be reduced to a single differential equation relating pressure and displacement.

The method of solution employed was to assume a mechanical vibration of given amplitude, number of nodal diameters and frequency. This allows calculation of the corresponding amplitude and phase of the pressure fluctuations within the cavity. For a seal with N teeth and, hence, $(N\text{-}1)$ cavities, the pressure amplitude and phase are unknown for each cavity, so that there are two $(N\text{-}1)$ simultaneous equations to be solved. A computer program was written to allow input of any seal geometry and solve these simultaneous equations. The program then calculates the damping coefficient C_P and stiffness coefficient K_P in the following simplified differential equation for the seal motion.

$$\frac{Md^2X}{dt^2} + (C_M + C_P)\frac{dX}{dt} + (K_M + K_P)\,X = 0 \qquad (1)$$

Where: M = seal effective mass, X = seal displacement, C_M = mechanical damping coefficient, C_P = aerodyamic damping coefficient, K_M = mechanical stiffness coefficient, and K_P = aerodynamic stiffness coefficient.

The final output of the program is the aerodynamic damping expressed as a fraction of the critical damping.

In the cavities between the seal teeth, the natural frequency of circumferential acoustic waves is given by

$$\text{acoustic frequency} = \frac{nc}{2\pi R} \qquad (2)$$

Where: n = number of circumferential waves, c = velocity of sound, and R = seal tooth cavity mean radius.

For a given seal diameter, the acoustic frequency does not depend on the other mechanical details of the seal.

Typical outputs from the program are shown in Fig. 6. The characteristic for a seal with low pressure side support is shown in Fig. 6(a). With a low mechanical frequency, the aerodynamic damping is negative. As the seal is stiffened and its frequency increased, there occurs a change to positive damping just below the acoustic natural frequency. A further increase in mechanical frequency produces a peak in positive damping which then decreases in magnitude but always remains positive even at very high mechanical frequencies. The characteristic for a seal supported on the high pressure side is shown in Fig. 6(b). For this type of support, the damping characteristic is reversed. The damping is positive for low mechanical frequencies and has a peak positive value just below the acoustic natural frequency. There occurs a change to negative damping just above the acoustic natural frequency and the damping remains negative even at very high mechanical frequencies.

The figures show clearly that a low pressure side supported seal can only be unstable if its mechanical natural frequency is less than the acoustic natural frequency and that a high pressure side supported seal can only be unstable if its mechanical natural frequency is greater than the acoustic natural frequency. This analytical prediction was

certainly in accord with the stability testing which has been described for the engine seal. The engine seal had a high pressure side support and was unstable when tested. However, as was previously described, it became stable and could no longer be excited by its leakage flow when weights were added to reduce its natural frequency below the acoustic natural frequency.

As a result of this clear analytical prediction on stability, the test results for other seals were obtained for correlation with the prediction.

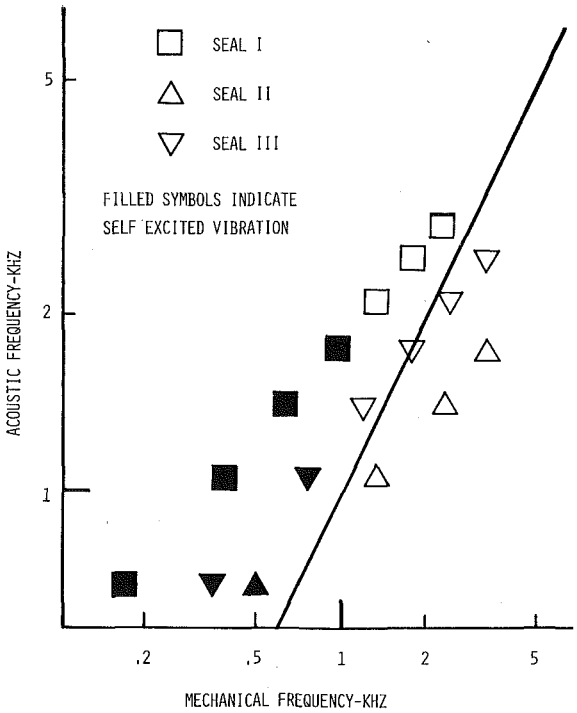

Fig. 7(*a*) Low pressure side support

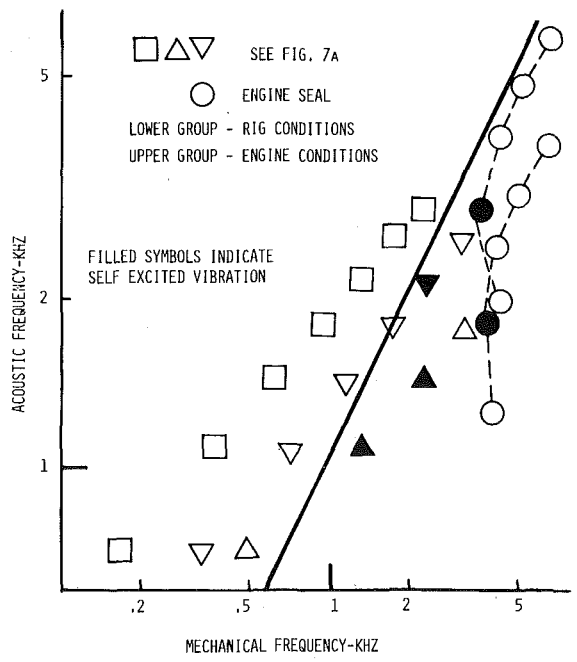

Fig. 7(*b*) High pressure side support

Fig. 7 Correlation of test results

The Analysis Confirmed

Prior to the vibration problems encountered with the engine seal, there had been a series of tests on the stability of labyrinth seals in a rig similar to that used for the engine seal shown in Fig. 3. Three seals had been specially made as part of a labyrinth seal technology program to investigate the stability of labyrinth seal technology program to investigate the stability of labyrinth seals. These three seals could be supported either on their high pressure or low pressure sides and had been tested in the same way that the engine seal was tested. The results of these stability tests were available for correlation with the *new analytical predictions about stability.*

The correlation of the results for these three seals together with the results for the engine seal are shown in Fig. 7. In these figures, the acoustic frequency is plotted against the mechanical frequency for each vibration mode of each seal. For each seal, the lowest frequency mode on the acoustic frequency scale is a two nodal diameter mode. The higher frequencies shown for each seal are successively the three nodal diameter mode, four nodal diameter mode, etc. The filled symobls in each figure indicate the vibration modes in which self-excited vibration due to the leakage flow occurred. A line of equal mechanical and acoustic frequency has been plotted in each figure. The results for seals with low pressure side support are shown in Fig. 7(*a*). The only vibration modes excited were those where the mechanical frequency was less than the acoustic frequency. The lowest frequency modes were most susceptible to vibration. The results for seals with high pressure side support are shown in Fig. 7(*b*). In this case, the only vibration modes excited were those where the mechanical frequency modes which exceeded the acoustic frequency were most susceptible to vibration.

The excellent correlation of all of these test results with the analytical prediction clearly confirms the validity of the analytical model.

The Prevention of Further Failures

It may be seen from Fig. 7(*b*) that the engine seal mechanical natural frequencies become close to the acoustic natural frequencies at engine operating conditions. Referring to Fig. 6(*b*), this condition corresponds to the peak of negative damping for seals with high pressure side support.

The close proximity of the acoustic and mechanical natural frequencies during engine operation now indicated that the aerodynamic destabilizing forces were greater than had been experienced with the many seals which had previously successfully operated with damper rings. More damping than could be provided with a damper ring was required for this particular seal. A damper sleeve was designed to fit the inner labyrinth seal. This design is shown in Fig. 8.

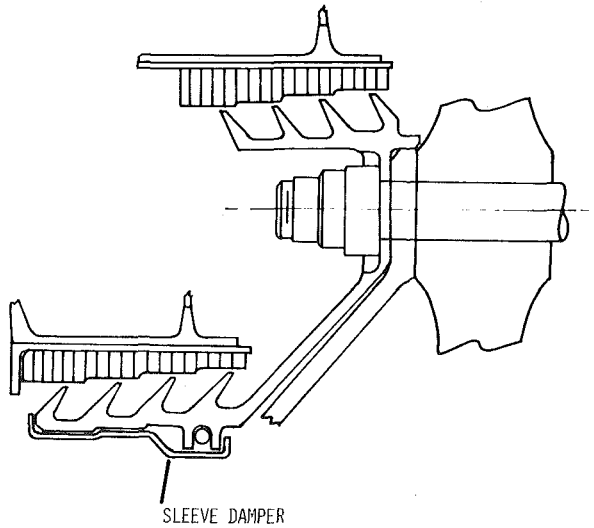

Fig. 8 Inner labyrinth seal with damper sleeve

To confirm that this design would provide more damping, a forced vibration test was carried out in a rig. It was considered essential to fully simulate centrifugal effects so the rig was operated to a speed of 18,000 rpm to cover the full operating range of the engine. The seal was excited by a pulsed air jet through a range of frequencies which included the three nodal diameter mode. The seal was tested with the damper ring in place and then again with the damper sleeve in place. The seal was strain gaged to measure the stresses during each test. The results of the tests showed that the damper sleeve reduced the vibratory stress level to 40 percent of that obtained with the damper ring. This was considered to be completely acceptable.

The engine was qualified with the damper sleeve which has now demonstrated its effectiveness for eight years of service and half a million hours of operation without incident.

Conclusions

1 Mechanical damping devices have proven to be completely effective in preventing labyrinth seal vibration.

2 The largest aerodynamic destabilizing forces occur when the acoustic and mechanical natural frequencies are almost equal. These conditions require more effective mechanical dampers such as sleeve dampers.

3 Base on the test results shown in Fig. 7, some conclusions can be made on the type of seal support which gives inherent stability. However, it should be noted that the test results were obtained for stationary seals which were specifically designed to have either high or low pressure side support. For a rotating seal, the mechanical frequency is the frequency which would be measured by an observer moving at the same tangential velocity as the air in the seal tooth cavities. Thus for each vibration mode, both the forward and backward mechanical wave frequencies must be considered. Some seals do not clearly have either type of support. An example of such a seal is shown in reference [5], where support is provided at both ends. The conclusions which apply to a well-defined high or low pressure support as illustrated in Fig. 1 do not apply to seals supported at both ends. Despite these complications, it should be clear from Figs. 6 and 7 that it is possible to design seals with inherent stability. A seal supported on the high pressure side can be made stable if at all operating conditions and in all vibration modes its mechanical frequency is less than the acoustic frequency. Unfortunately there are other criteria—e.g., Campbell criteria—which make it undesirable for a seal to be designed with a low natural frequency. This approach is not recommended so that seals with high pressure support should be provided with mechanical dampers or other means to provide stability. However, a seal with low pressure side support can be made inherently stable if it is stiff enough to ensure that its mechanical frequency always exceeds the acoustic frequency. The outer seal shown in Fig. 1 is an example of the successful application of this principle.

Acknowledgments

The author gratefully acknowledges the encouragement and assistance of J. A. Alford and F. F. Ehrich in the preparation of this paper.

References

1 Alford, J. S., "Protection of Labyrinth Seals from Flexural Vibration," ASME JOURNAL OF ENGINEERING FOR POWER, Apr 1964, pp. 141–148.

2 Ehrich, F. F., "Aeroelastic Instability in Labyrinth Seals," ASME Paper No. 68-GT-32.

3 Alford, J. S., "Labyrinth Seal Designs Have Benefitted from Development and Service Experience," SAE Paper No. 710435, National Air Transportation Meeting, Atlanta, Ga., May 1971.

4 Alford, J. S., "Nature, Causes and Prevention of Labyrinth Air Seal Failures," *Journal of Aircraft*, Vol. 12, No. 4, Apr 1975, pp. 313–318.

5 Lewis, D. A., Platt, C. E., Smith, E. B., "Aeroelastic Instability in F100 Labyrinth Air Seals," AIAA Paper No. 78–1087, AIAA/SAE 14th Joint Propulsion Conference, July 1978.

The Effect of Aerodynamic Phase Lag on the Twin Vibration Mode Model of Aeroengine Fan Flutter

R. A. J. Ford

School of Mechanical and Industrial Engineering,
University of New South Wales,
Kensington, New South Wales,
Australia

An earlier paper analyzed aeroengine fan flutter in terms of twin orthogonal vibration modes in the fan. This paper extends the analysis by incorporating variable aerodynamic phase lags between a blade motion and the resulting aerodynamic forces. The extended analysis predicts two independent kinds of flutter. If the total damping within each mode is negative, each mode develops a self-sustaining vibration at its own natural frequency. This was not predicted by the earlier twin mode analysis. Even when the damping in each mode is positive an interaction between the modes can cause flutter under some conditions. This behavior is basically of the form described in the earlier paper, but there are significant detailed changes when variable aerodynamic phase lags are introduced.

Introduction

Supersonic unstalled flutter in aeroengine fans is a self excited unstable vibration which imposes a limit to the maximum speed of the fan. Prediction methods are needed for assessing whether flutter will occur within the operating speed range of a particular fan design. It is also necessary to know how to modify a fan which is susceptible to flutter so that the problem can be eliminated in the most effective manner.

Flutter occurs when a mechanical vibration of the fan gives rise to unsteady aerodynamic forces which feed energy into the fan and sustain (or increase) the vibration amplitude [1–3]. There are two aspects to the phenomenon:

1 The mechanical behavior of the fan. Flutter is very sensitive to the deflected shapes of the individual blades of the fan, and the relative motion between them.

2 The unsteady aerodynamic behavior of the fan. This determines the unsteady aerodynamic forces generated in response to unsteady motion of the blades.

Any flutter analysis must model both aspects.

Experimental studies of real fans reveal pairs of spatially orthogonal vibration modes which have similar shapes but slightly different natural frequencies. These independent vibrations can occur simultaneously so that each blade in the fan responds to both modes (but differently in each) and the total response of the blade is the sum of two components. The resultant motion depends upon the relative phase and amplitude of these two components.

In an earlier analysis flutter was seen as an interaction between the modes of an orthogonal pair, in which the response of each blade in one of the twin modes produces aerodynamic forces on the blades which drive the second mode, and vice versa [4]. This is shown in the feed-back loop of Fig. 1. Flutter occurs if the aerodynamic forces due to Mode I provide suitable and sufficient excitation for driving Mode II while at the same time the aerodynamic forces due to Mode II provide suitable and sufficient excitation for Mode I. This requires (1) correct phasing between the two modes, and (2) forces which are large enough to sustain the motion.

Previous work [4] showed that phasing determines the frequency at which flutter will occur, if it occurs at all whereas whether flutter actually does occur depends upon the relationship between the aerodynamic forces and the mechanical response of the fan. The earlier paper developed the analysis in terms of a two component aerodynamic model with a fixed temporal phase between each blade deflection and the aerodynamic unsteady force which it causes. This paper extends the analysis by allowing the temporal phase between deflection and force to be varied.

Twin Mode Model Assuming Zero Aerodynamic Phase Lag

Aerodynamic Forces. For the purposes of this paper the unsteady aerodynamic forces due to a vibrating blade will be simplified to two components (see reference [4]).

1 Bending forces due to bending deflections. For this component zero aerodynamic phase lag would correspond to forces in temporal phase with velocities (i.e., in temporal quadrature with deflections).

2 Bending forces due to twisting deflections. For this component zero aerodynamic phase lag would correspond to forces in temporal phase with deflections.

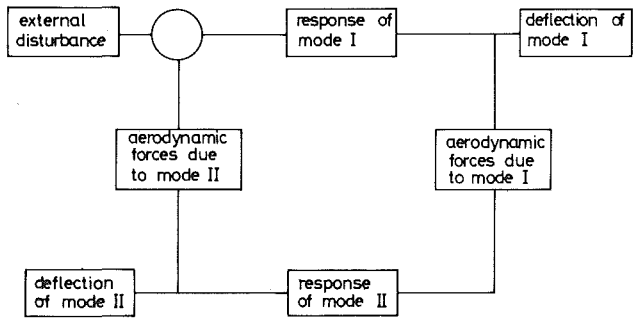

Fig. 1 The interaction of orthogonal modes to give flutter

Contributed by the Gas Turbine Division of THE AMERICAN SOCIETY OF MECHANICAL ENGINEERS for presentation at the Gas Turbine Conference and Products Show, New Orleans, La., March 10–13, 1980. Manuscript received at ASME Headquarters January 8, 1980. Paper No. 80-GT-166.

These are generally the major contributions, however extra terms can be added if required, at the expense of some additional complexity.

It is further assumed that the aerodynamic forces for each mode are independent of motion in the other mode.

A net energy input (or output) for the vibration modes can be provided only by those force components in phase spatially with similar deflections. For example, bending forces in phase spatially with bending deflections can excite or damp the motion, whereas bending forces in spatial quadrature with bending deflections have no net effect.

General Behavior. The interaction between twin vibration modes can most readily be seen for the simplified case of zero aerodynamic phase lag. Fig. 2 shows conditions at the clapper ring of a fan (the ring formed by the locked part span shrouds or snubbers) under this assumption. Within each mode, the spatial phase between twist and flap waves is 90 deg (¼ wave). It can be seen from the figure that in each mode bending forces due to twist are spatially in phase with bending deflections in the twin, thus deflections in one mode produce forces phased to interact with the other mode. Bending forces due to bending deflections are in spatial phase with their own deflections, i.e., in spatial quadrature with the twin mode, and cannot couple the modes, but provide "damping" (+ or −) within each mode (force proportional to velocity). Negative damping corresponds to excitation within a mode and only occurs when aerodynamic phase lags are present, as described below.

If we now consider the tip, Fig. 3, the spatial phase between the twist and flap waves is not generally 90 deg [5]. In this case, the aerodynamic bending force due to twist must be resolved into two components. One component is ¼ wave displaced from the flap wave and couples the two modes as before; the other component is in spatial phase with the flap wave, and in temporal phase too, and its effect is to alter the effective stiffness of the mode.

Thus for an elemental annulus at any radius the integrated (circumferential) effects of the two classes of forces are (i) force due to bending: a velocity damping term within each mode, (ii) force due to twist: (*a*) an additional stiffness term within each mode due to spatial in phase component, (*b*) an excitation of the other mode (cross coupling) due to the spatial quadrature component. The overall behavior of the fan is the result of the integrated effect of conditions at all radial stations.

Mode Description. The interaction of the two modes can be examined by considering them to be two independent single-degree-of-freedom systems as below.

Effective mass m_1;m_2

Damping term $\left(\frac{2c}{c_0}\right)_1$; $\left(\frac{2c}{c_0}\right)_2$: mechanical damping plus (i) above

Stiffness term k_1; k_2: mechanical stiffness plus (ii) above

Effect of Aerodynamic Phase Lags

The previous section showed how considerations of spatial phase determine whether the effects of a given force are contained within a mode or cross couple the two modes of an orthogonal pair. These two situations are now examined separately.

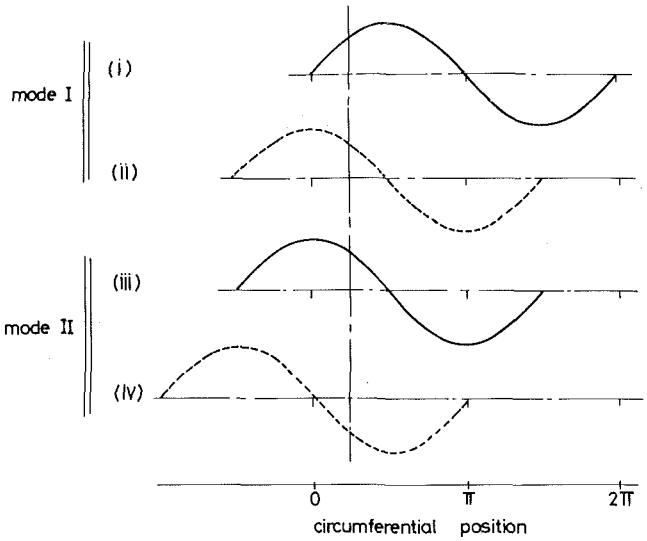

Fig. 2 Displacements and forces at the clapper ring for zero aerodynamic phase lag: (i) Mode I: flap and (in temporal quadrature) force due to flap. (ii) Mode I: twist and force due to twist. (iii) Mode II: flap and (in temporal quadrature) force due to flap. (iv) Mode II: twist and force due to twist

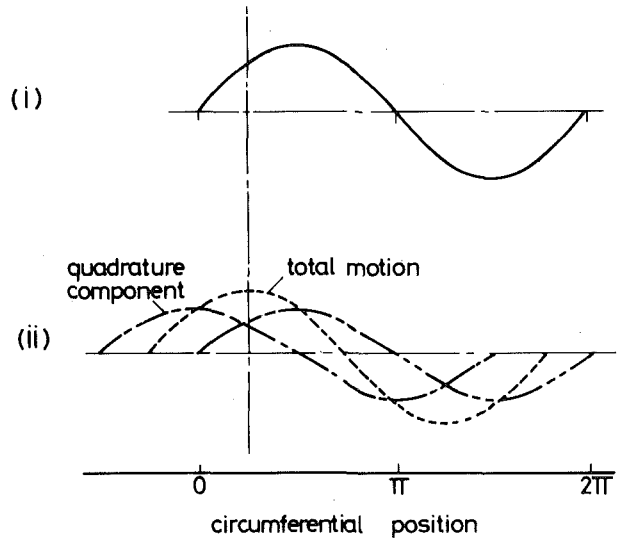

Fig. 3 Displacements and forces at the tip of fan for zero aerodynamic phase lag: (i) flap and (in temporal quadrature) force due to flap. (ii) twist and force due to twist showing in phase and quadrature components

Forces Contained within a Mode. The equation of motion for a single degree of freedom vibrating system is:

$$m\ddot{x} + c\dot{x} + kx = F\cos(pt) \tag{1}$$

This is shown in the form of a phasor diagram in Fig. 4(*a*).

In Fig. 4(*b*) the force system corresponding to the two component aerodynamic model is superimposed upon the basic mechanical response. Fig. 4(*b*) can be recast in the form of Fig. 4(*a*) if we define an

Nomenclature

A, A' = angles on phasor diagram, Fig. 5
A_1, A_2 = aerodynamic response coefficients for each mode
B' = angle on phasor diagram, Fig. 5
c = damping coefficient
c_e = effective damping coefficient
c_m = coefficient of mechanical damping
c_0 = critical damping coefficient
C = aerodynamic coupling term (equation (9))
E = phase angle on phasor diagram, Fig. 5
F = amplitude of driving force
F_F = amplitude of aerodynamic force on a blade due to flapping motion
F_T = amplitude of aerodynamic force on a blade due to twisting deflection
k_1, k_2 = stiffness within each mode
k_e = effective stiffness
k_m = mechanical stiffness
m_1, m_2 = effective mass in each mode
M = combined mechanical response (equation (9))
p = forcing frequency
x = instantaneous deflection
X_1, X_2 = amplitude of motion for each mode
α = aerodynamic phase lag for F_F
θ = aerodynamic phase lag for F_T
ϕ = temporal phase angle between flap responses
ω_1, ω_2 = natural frequencies of each vibration mode

Subscripts

1 = lower frequency mode
2 = higher frequency mode

effective damping coefficient and an effective stiffness as below.

$$c_e = c_m + \frac{F_F \cos\alpha - F_T \sin\theta}{px} \tag{2}$$

$$k_e = k_m + \frac{F_F \sin\alpha + F_T \cos\theta}{x} \tag{3}$$

Thus if the dependence of F_F, α, F_T and θ upon frequency and amplitude is known and the mechanical properties are also known, then the resultant effective stiffness and damping can be calculated. The aerodynamic forces are generally much less than the mechanical stiffness and often have a negligible effect on the equivalent stiffness. However, aerodynamic forces often outweigh the mechanical damping term and can provide the major damping component in the vibration response. Equation (2) also shows that if θ and α are non-zero c_e can become zero or negative.

Forces which Cross Couple the Mode. These are provided by the spatial quadrature components of the forces due to twist. The effect of aerodynamic phase lag on this component is shown on the phasor diagrams in Fig. 5.

Types of Flutter Behavior

With this model there are two categories of flutter behavior: Case 1, instability arising from within a vibration mode. Case 2, instability caused by interaction between modes.

Case 1 Instability of a Single Mode. A single mode becomes unstable if the damping is negative. Under these conditions the vibration occurs at the natural frequency of the mode and the amplitude steadily increases.

Under these conditions no interaction between modes is necessary for flutter to occur. However, the components of the forces due to twist in Mode I which are in spatial quadrature with Mode I still drive Mode II and vice versa. If the conditions are such that both modes approach negative damping at the same time then the total motion is composed of:

(i) Mode I at ω_1 self excited
(ii) Mode II at ω_1 driven by Mode I
(iii) Mode II at ω_2 self excited
(iv) Mode I at ω_2 driven by Mode II

The motion which would then be observed is:

At ω_1: A standing wave (i.e. fixed in relation to the fan) displaced from Mode I towards Mode II

At ω_2: A standing wave displaced from Mode II towards Mode I. A frequency analysis of the flutter vibration would reveal two discrete frequencies under these conditions.

Case 2 Instability Caused by Interacting Modes. Instability of this kind can occur whether or not aerodynamic phase lags are present.

For this analysis assume that the stiffness and damping in each mode have been determined in the form of effective coefficients of stiffness and damping. Phasor diagrams for each of the modes are given in Figs. 5(*a*) and 5(*b*) and show how the forces and displacements must be arranged in order for the interaction to be possible. Note that in one mode twist is in phase with flap whereas in the other mode it is 180° out of phase with flap. This results from the two modes being ¼ wave displaced [4]. Interactive flutter is possibly only if the excitation for Mode I can be provided by the force due to twist from Mode II while at the same time the excitation for Mode II is provided by the force due to twist from Mode I.

It can be seen from Fig. 5 that instability requires angles A' and B' to be equal. However, the lag angles mean that in order to achieve this the two modes are different amounts from resonance (shown as 90-A and E-90), and therefore one mode is more strongly excited than the other.

Values of A, B and E and the corresponding flutter frequency, p, can be obtained from the relationships below (which can be obtained from Fig. 5)

$$A + \theta = B - \theta \tag{4}$$

$$B = 180 - E \tag{5}$$

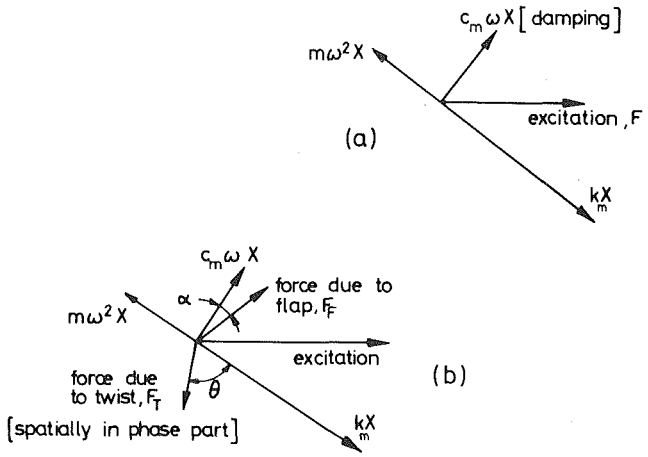

Fig. 4 Phasor diagrams showing forces acting within a single degree of freedom vibrating system (*a*) mechanical system only. (*b*) aerodynamic forces added

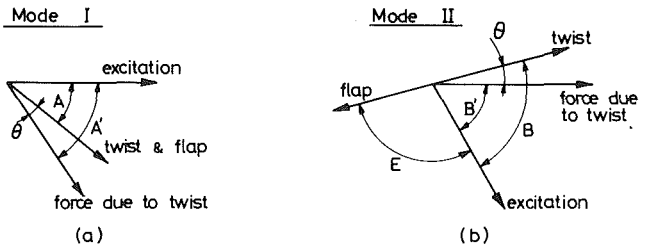

Fig. 5 Phasing of twin modes for flutter to occur

and the standard results for a single degree of freedom system

$$\tan A = \frac{\frac{2c\,p}{c_0\omega_1}}{1 - \left(\frac{p}{\omega_1}\right)^2} \tag{6}$$

$$\tan E = \frac{\frac{2c\,p}{c_0\omega_2}}{1 - \left(\frac{p}{\omega_2}\right)^2} \tag{7}$$

The flutter pattern is given by the vector sum of the two flap responses [5] and this requires values for the relative amplitudes of the two modes and the relative phase between them. The phase between the two flap responses is given by:

$$\phi = 90 + \tfrac{1}{2}(E - A)$$

The ratio of amplitudes is given by:

$$\left(\frac{X_1}{X_2}\right)^2 = \frac{A_1 k_2}{A_2 k_1} \frac{\sqrt{\left(1 - \left(\frac{p}{\omega_1}\right)^2\right)^2 + \left(\frac{2c\,p}{c_0\omega_1}\right)^2}}{\sqrt{\left(1 - \left(\frac{p}{\omega_2}\right)^2\right)^2 + \left(\frac{2c\,p}{c_0\omega_2}\right)^2}} \tag{8}$$

where A_1, A_2 are constants describing the aerodynamic response to unsteady blade motion.

Fig. 6 shows the aerodynamic phase lag which corresponds to a given flutter frequency and also shown the resulting phase between flap responses. Fig. 7 shows the relative mode strengths for the same conditions. Note that the phase between flap responses is 90 deg only at one particular value of p/ω_1, and in this case the two modes are not of equal strength.

Figure 8 shows the total deflected shape at various stages of the vibration cycle for one set of conditions. It is clear from the figure that the pattern is not a simple traveling wave and that the amplitude of each blade is different under these conditions.

Predicting the Onset of Interactive Flutter. The criterion for

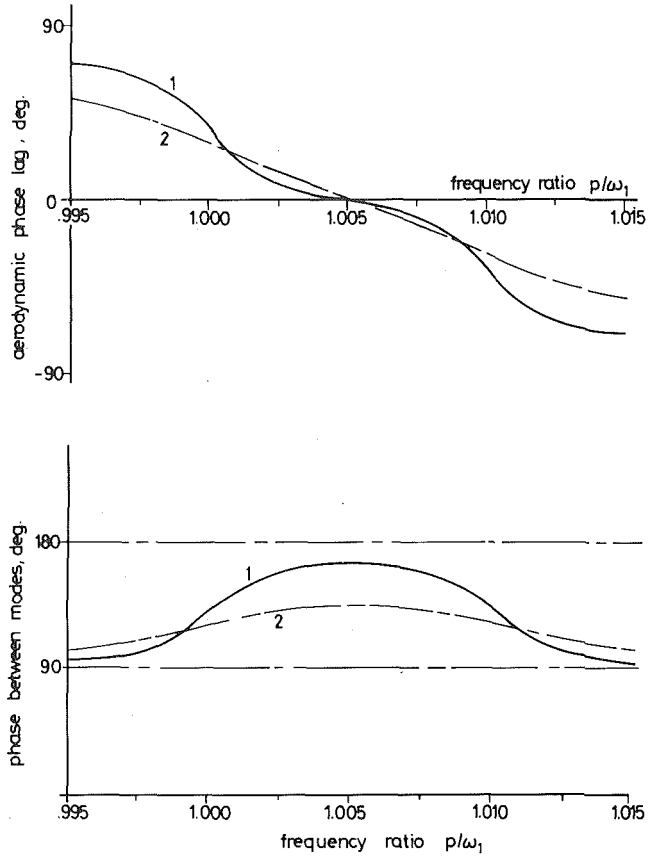

Fig. 6 Phase between modes and corresponding aerodynamic phase lag versus frequency ratio for $\omega_1/\omega_2 = 0.99$: (i) $2c/c_0 = 0.003$; (ii) $2c/c_0 = 0.01$

the onset of interactive flutter is developed elsewhere [4] and is:

$$\frac{k_1 k_2}{A_1 A_2} \leqslant \frac{1}{\sqrt{\left(1-\left(\frac{p}{\omega_1}\right)^2\right)^2+\left(\frac{2c}{c_0}\frac{p}{\omega_1}\right)^2}} \times \frac{1}{\sqrt{\left(1-\left(\frac{p}{\omega_2}\right)^2\right)^2+\left(\frac{2c}{c_0}\frac{p}{\omega_2}\right)^2}} \tag{9}$$

or $C \leqslant M$.

C is a dimensionless measure of the aerodynamic coupling between modes which is present in the vibration; strong coupling is represented by low values. M prescribes the degree of cross coupling that must be present before flutter occurs, and is the reciprocal of the product of the mechanical impedances of the twin modes. Low values of M represent a lower liklihood of flutter.

In order to determine the flutter boundary the value of M is calculated using the value of p derived from the previous section, and this value of M is then compared with the coupling term. Flutter is predicted if C is less than M.

Figure 9 plots M as a function of frequency for two values of damping. The zero phase lag case corresponds to $p/\omega_1 = 1.005$. The low damping curve has two peaks centered about the two natural frequencies ω_1 and ω_2. If the phase lag on the twist response is such as to bring the flutter frequency near these peaks then flutter will occur more easily than for the zero phase lag condition, and some of the benefit obtained from the split natural frequencies is lost. This can be seen in Fig. 10 which plots M against damping for zero phase lag and also for a variable phase lag which maintains the flutter frequency on one of the peaks.

The effect of phase lag (twist response) on the flutter boundary is shown again in Fig. 11 which replots Fig. 9 in terms of phase lag θ instead of frequency.

Which Type of Flutter Occurs?

In general a flutter speed can be computed for single mode flutter and for interactive flutter, and the behavior corresponding to the lower

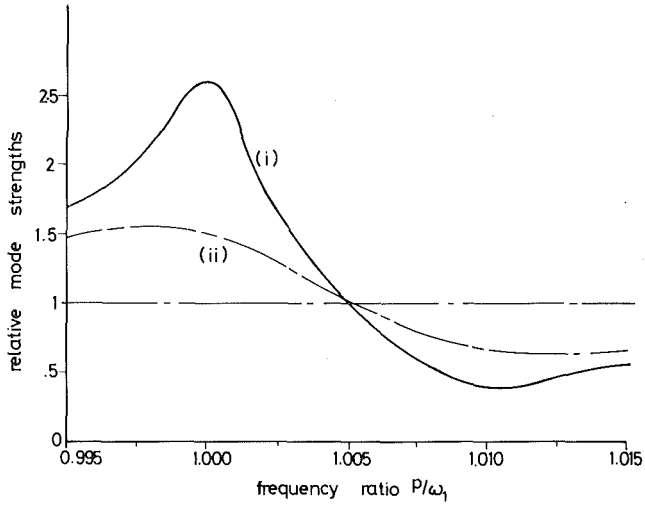

Fig. 7 Relative mode strengths versus frequency ratio for $\omega_1/\omega_2 = 0.99$: (i) $2c/c_0 = 0.003$; (ii) $2c/c_0 = 0.01$

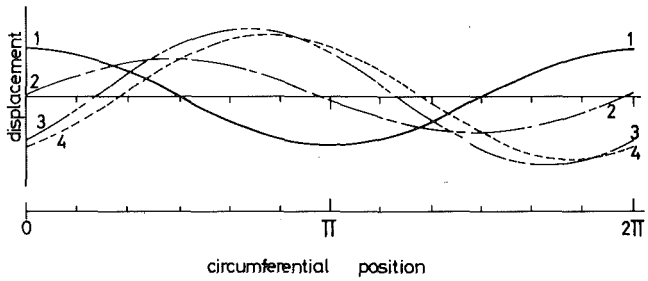

Fig. 8 Deflected shape for unequal mode strengths. Time interval between curves $\pi/4\omega$, figures denote time sequence. Phase between modes 132°, relative mode strength 1.3:1

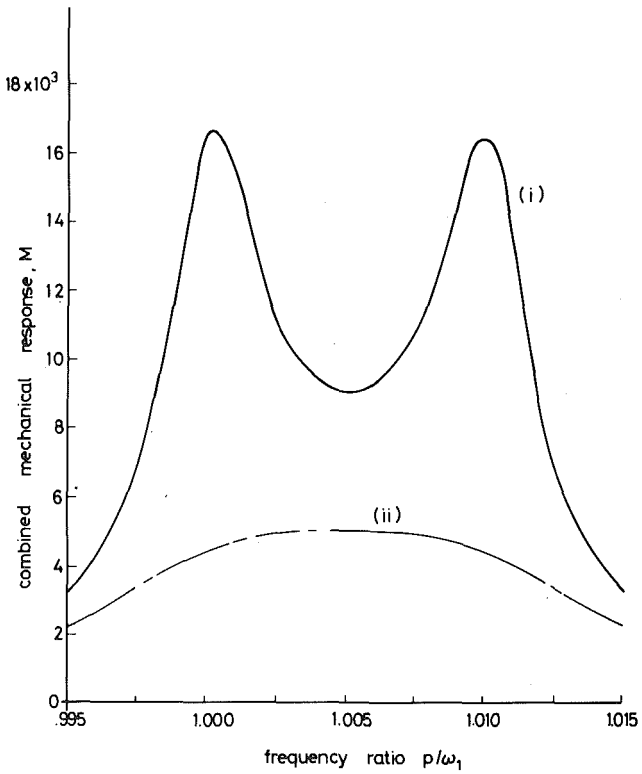

Fig. 9 M versus frequency for $\omega_1/\omega_2 = 0.99$: (i) $2c/c_0 = 0.003$; (ii) $2c/c_0 = 0.01$

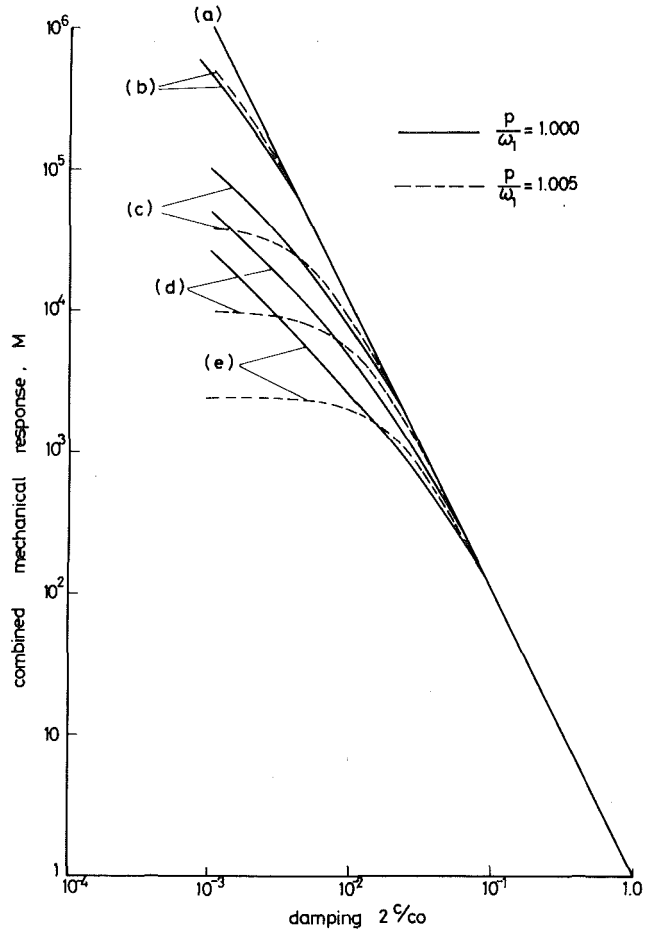

Fig. 10 *M* versus damping ratio: (*a*) $\omega_1/\omega_2 = 1.000$, (*b*) $\omega_1/\omega_2 = 0.999$, (*c*) $\omega_1/\omega_2 = 0.995$, (*d*) $\omega_1/\omega_2 = 0.990$, (*e*) $\omega_1/\omega_2 = 0.980$

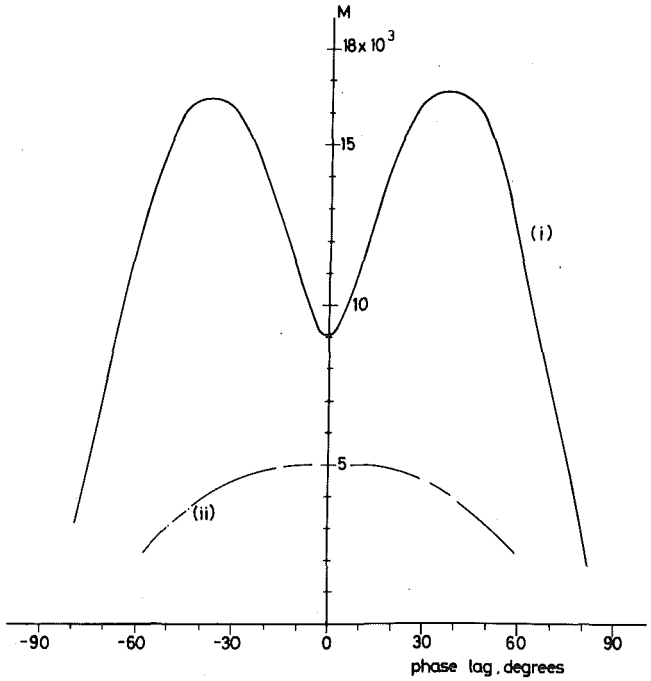

Fig. 11 *M* versus aerodynamic phase lag for $\omega_1/\omega_2 = 0.99$

fan speed will determine the flutter boundary. At speeds beyond this boundary it is possible for both types of flutter to occur simultaneously and, as they are independent, the effects can be superimposed. At any specified speed the behavior of an aeroengine fan will therefore fall into one of the following categories:

Category	Damping	Cross-coupling	Resultant Behavior
1	Positive damping	$C > M$	No flutter
2	Positive damping	$C < M$	Interactive flutter
3	Negative damping	$C > M$	Single mode flutter
4	Negative damping	$C < M$	Interactive flutter (reverse wave) + single mode flutter

Discussion

Controlling Flutter. One method of control is to add mechanical or aerodynamic damping. If single mode flutter is present damping within each mode must be negative and flutter can only be eliminated by incorporating additional damping equal in magnitude to the negative damping. If interactive flutter is also present, at least twice this amount of damping must be added in order to eliminate flutter by this means.

The reasons for the more persistent nature of interactive damping can be seen from Fig. 12 which plots *M* for both positive and negative damping. The curve is symmetrical about zero damping. As damping is added the interactive flutter becomes more prominent (assuming the cross coupling term *C* is constant) until it reaches a maximum at zero damping and finally disappears when the *M* curve is recrossed (i.e. $C > M$).

Interactive flutter can also be controlled by modifying the cross coupling term *C*. This can be achieved by altering the mode shape so that the ratio (twist)/(flap) is reduced and the lift due to torsion term is also reduced for a given linear displacement. Increasing the mechanical stiffness of the fan also has a favorable effect. The tendency

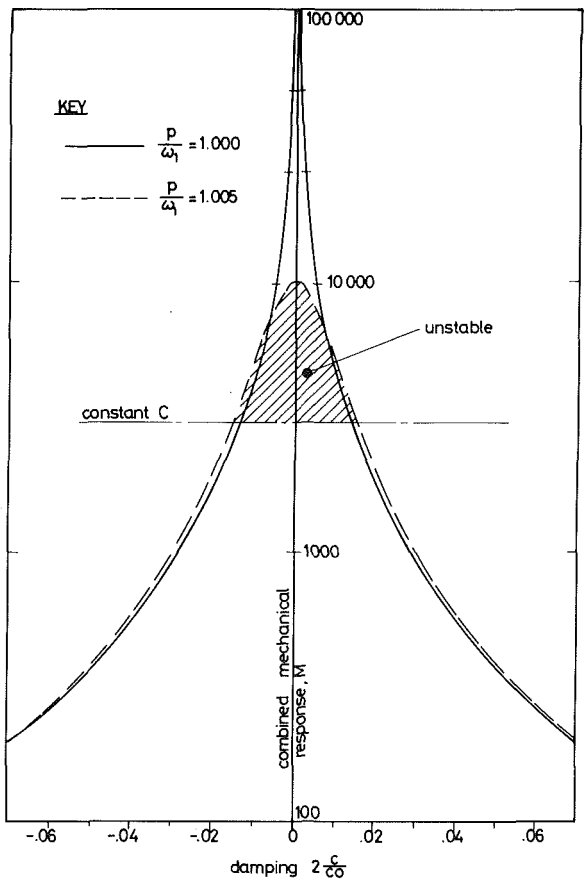

Fig. 12 *M* versus damping, including negative damping

towards this kind of flutter is also reduced if the value of M is reduced by increasing the modal frequency split. None of these approaches directly affect single mode flutter.

Experimental Considerations. The above analysis can be directly applied to existing test procedures.

As the flutter speed for either flutter mechanism is approached, the damping in that flutter mode tends to zero and even low levels of excitation from elsewhere in the structure will produce significant deflections at the relevant flutter frequency. This condition of incipient flutter would enable the flutter behavior to be studied without entering the true aerodynamically excited flutter regime and it is then not necessary to operate at the large (infinite) vibration amplitudes which occur with zero or negative damping.

Single mode flutter would appear as vibration at two discrete frequencies (for an orthogonal pair), with both vibration modes stationary with respect to the fan. If, however, the analyst is looking for a traveling wave he might find one, as the combined vibration can also be described in terms of a traveling wave of varying amplitude and a stationary wave of varying amplitude.

Interactive flutter would appear as a vibration at a single frequency (per mode shape) and would be composed of a stationary component and a rotating component of constant amplitude.

If conditions are such that the flutter speeds for both types of flutter are coincident than three vibration frequencies might be detectable as the common flutter speed is approached. However, phase lags might cause two of these to be almost coincident.

Thus analysis of test data could indicate the applicability of the two types of flutter behavior described in this paper. It may also be possible to deduce the aerodynamic phase lags within an operating fan by working the analysis backwards.

Conclusions

The twin orthogonal mode analysis of fan flutter has been extended to incorporate the effects of aerodynamic phase lag. The extended analysis predicts two independent kinds of flutter.

If the damping within each mode is negative each mode develops a self sustaining vibration at its own natural frequency. This was not predicted by the earlier twin mode analysis [4].

If the aerodynamic coupling between modes is sufficient (as determined by the modal frequency split and damping) an interaction between the modes can cause flutter. This can occur whether the damping is positive, negative or zero. This behavior is of the form described earlier [4] and the conclusions are unchanged. However, there are some additional factors introduced by the inclusion of aerodynamic phase lags. Two of these are: (i) The two modes of an orthogonal twin have different amplitudes. (ii) Aerodynamic phase lags can reduce the benefit to be obtained from increasing the modal frequency split.

If both types of flutter are present and control is effected by increasing the damping, then single mode flutter would be eliminated first. Interactive flutter is more persistent and would require at least twice the damping necessary to eliminate the single mode kind.

This analysis can be investigated by making simple measurements on fluttering fans, and these investigations would provide additional insight into flutter phenomena.

Acknowledgment

This work was begun in 1977 at the Advanced Research Laboratory of Rolls Royce Ltd. The author wishes to acknowledge the contributions of Dr. C. A. Foord and Dr. C. J. Moore, of that Laboratory, and also to thank those in other groups at Rolls Royce Ltd. who contributed to the study through their discussions.

References

1 Carta, F. O., "Coupled Blade-Disk-Shroud Flutter Instabilities in Turbojet Engine Rotors," ASME JOURNAL OF ENGINEERING FOR POWER, Vol. 89, July 1967, pp. 419–426.

2 Mikolajcak, A. A., et al, "Advances in Fan and Compressor Blade Flutter Analysis and Prediction," *Journal of Aircraft,* Vol. 12, Apr. 1975, pp. 325–333.

3 Halliwell, D. G., "The Characteristics Prediction and Test Analysis of Supersonic Flutter in Turbofan Engines," *I. Mech. E.,* Paper C187/76, Conference on Vibrations in Rotating Machinery, Sept. 1976.

4 Ford, R. A. J., and Foord, C. A., "An Analysis of Aeroengine Fan Flutter Using Twin Orthogonal Vibration Modes," ASME Paper No. 79-GT-126, Presented at the Gas Turbine Conference, San Diego, Ca., Mar. 12–15, 1979.

5 Hockley, B. S., Ford, R. A. J., and Foord, C. A., "Measurement of Fan Vibration Using Double Pulse Holography," ASME Paper No. 78-GT-111, Presented at the Gas Turbine Conference, London, England, Apr. 9–13, 1978.

K. A. Stetson
Senior Research Engineer.

I. R. Harrison
Assistant Research Engineer.

Instrumentation Lab. (81),
United Technologies
Research Center,
East Hartford, Conn.

Redesign of Structural Vibration Modes by Finite-Element Inverse Perturbation

A previously developed technique for redesigning the vibrational properties of structures, by inverting the first-order perturbation analysis of the equations of motion, has been applied to a NASTRAN finite element analysis for plates and shells. The program finds the minimal changes to the thicknesses of the plate elements necessary to effect a given set of changes in the modal frequencies and shapes. Results have been obtained for a flat cantilever plate, a cantilever segment of a cylinder, and for a compressor blade for a jet engine.

Introduction

In a previous paper [1], we described a computer program for redesigning structures to effect desired changes in the shapes and frequencies of their vibration modes, by making the smallest possible change in the structure. This was the outgrowth of a general perturbation analysis of the equations of motion of a structure [2] and the development of an inversion of that analysis [3]. The program described in reference [1] accepted holographically obtained data on the vibration modes of a physical model. As a consequence, it was limited to plate-like structures with no in-plane vibrations. It was further limited as a design tool by the need to build a new physical structure after each application of the program. This was required to determine the degree to which the redesign was successful and to obtain a new starting point should an iterative continuation of the procedure be desired [1].

Many of these limitations have been eliminated by reformulating our inverse perturbation design program to accept vibration mode data provided by a NASTRAN finite element analysis. This paper presents a discussion of this new program and the results that have been obtained for three test structures, the last of which is an actual compressor blade designed for a jet engine. In its present form, the program accepts mesh point displacements and rotations in global coordinates from the NASTRAN output, accepts physical constants and a set of desired changes from the designer, and processes these data to obtain an ensemble of new element thicknesses so as to effect the desired changes with the minimum change to the structure. Because the solution is based on first-order perturbation theory, it is approximate, and a new NASTRAN analysis of the redesign can be used as a starting point for a second application of the procedure, etc. This program is limited only to structures that can be analyzed with triangular plate elements and for which changes in element thicknesses alone are desired.

We will begin with a discussion of the equations involved in this new program; this will be followed by a discussion of its component programs; and, finally, the numerical results will be presented and discussed.

Contributed by the Gas Turbine Division of THE AMERICAN SOCIETY OF MECHANICAL ENGINEERS found presented at the Gas Turbine Conference and Products Show, New Orleans, La., March 10–13, 1980. Manuscript received at ASME Headquarters January 8, 1980. Paper No. 80-GT-167.

Mathematical Formulation

Let us present here the specific equations that relate to this program. First, let the design variable be the percentage change in thickness of the plate or shell, $\Delta h(x, y)/h(x, y)$, where $h(x, y)$ is the thickness of the structure, and x and y are spatial coordinates in its surface. This design variable is expanded as a series of functions, $\theta(x, y)$, called perturbation functions, which are functions of the coordinates, x and y. The coefficients of the series are determined, in part, by the set of changes that are desired, (Δ), which can be written as a row matrix. The Δ's are related to percentage changes in frequency, and to coefficients of admixture between mode shapes. (Admixture between mode shapes implies that the mode shapes of an altered structure may be expressed as linear combinations of the mode shapes of an unaltered structure). The final set of factors in the equation that determines the percentage changes in thickness is the inverse of what we may call a perturbation matrix, $[B]$. Thus, the primary equation of inverse perturbation is

$$\Delta h(x,y)/h(x,y) = (\Delta)[B]^{-1}(\theta(x,y))^T. \quad (1)$$

In equation (1), the necessary set of perturbation functions have been arranged as a row matrix, $(\theta(x, y))$ and the superscript T denotes the transposed matrix; i.e., a column matrix. In order to define the matrix $[B]$, it is necessary to specify the set of changes (Δ) and the set of perturbation functions (θ). (Note: the functional dependence of θ on x and y is implied throughout.) The perturbation functions are formed from products of parameters obtained from pairs of vibration modes, or from squares and products of parameters obtained from a single mode. Thus, we may identify perturbation functions by a double subscript θ_{nk}, or θ_{nn}, depending on whether the perturbation function is formed from two vibration mode shapes $\Phi_n(x, y)$ and $\Phi_k(x, y)$, or from $\Phi_n(x, y)$ alone. Similarly, the change parameters (Δ) may be characterized by double subscripts, Δ_{nk} being related to the amount of mode shape Φ_k that is found added to Φ_n as a result of the structural change, and Δ_{nn} being related to the change in frequency of the nth mode. The specification of any change parameter requires the inclusion of the corresponding perturbation function in equation (1). In this way, the number of degrees of freedom in changing the structure (i.e., the perturbation functions) matches the number of constraints (i.e., the change parameters).

With this in mind, let us define the elements of the perturbation matrix, b_{pq}. The double subscripts of the change variables, and the

perturbation functions, may be ordered in some arbitrary, but mutually consistent way. Let the double subscript nk correspond to the single index p, and some other subscript pair lm correspond to 'q'. Then, the element b_{pq} is defined by

$$b_{pq} = \int\int \theta_p(x, y)\theta_q(x, y)dxdy, \tag{2}$$

where the integration is carried out over the surface of the structure. In this particular program, however, the structure has been divided into discrete elements so that the integrations will extend only over the elements, and the contributions of the elements summed to obtain the coefficient b_{pq}.

In order to define the perturbation functions, we must first define the mode functions according to the form they take in the NASTRAN program. Each element of the shell-like structures considered in this program is a triangular platelet of uniform thickness which may bend out of its plane to any shape describable by a cubic polynomial (minus the x^2y term), and may deform and rotate homogeneously within its plane. In terms of a coordinate system local to each element, we may define the mode function, vectorially, as

$$\underline{\underline{\Phi}}_n = \hat{i}\Phi_{nx} + \hat{j}\Phi_{ny} + \hat{k}\Phi_{nz}, \tag{3}$$

where $\hat{i}$, $\hat{j}$ and $\hat{k}$ are unit vectors in the x, y and z direction, with z being out of the plane of the element, and the origin located at one of the corners of the element. The components of $\underline{\underline{\Phi}}_n$ are, in their polynomial forms:

$$\Phi_{nx} = a_{n1} + a_{n2}x + a_{n3}y, \tag{4}$$

$$\Phi_{ny} = b_{n1} + b_{n2}x + b_{n3}y, \text{ and} \tag{5}$$

$$\Phi_{nz} = c_{n1} + c_{n2}x + c_{n3}y + c_{n4}x^2 + c_{n5}xy + c_{n6}y^2 + c_{n7}x^3 + c_{n8}xy^2 + c_{n9}y^3. \tag{6}$$

The perturbation functions, which may now be defined, are most easily expressed as the sum of four terms: (1) an inertial term, θ_m, (2) a term related to bending strain, θ_{sb}; (3) a term related to membrane strain, θ_{sm}, and (4) a term relating to transverse sheer strain, θ_{ss}. Thus,

$$\theta_p = \theta_{mp} + \theta_{sbp} + \theta_{smp} + \theta_{ssp} \tag{7}$$

where the subscript p denotes the mode pair nk. The perturbation function, it should be noted, is a scalar. The first term of equation (7) is

$$\theta_{mp} = -(\omega_n \rho h/\omega_k M_k)\underline{\underline{\Phi}}_n \cdot \underline{\underline{\Phi}}_k, \tag{8}$$

where ω_n and ω_k are the natural frequencies, in radians, of modes n and k, ρ is volume density, and M_k is the model mass of the kth mode, defined by

$$M_k = \int\int \rho h \underline{\underline{\Phi}}_k \cdot \underline{\underline{\Phi}}_k \, dx \, dy. \tag{9}$$

To define the second and third terms, let us first define the matrix $\mathbf{G}_s$ as

$$\mathbf{G}_s = [Eh/\omega_n\omega_k M_k(1-\nu^2)]\begin{bmatrix} 1 & \nu & 0 \\ \nu & 1 & 0 \\ 0 & 0 & (1-\nu)/2 \end{bmatrix}, \tag{10}$$

where E is Young's modulus and ν is Poisson's ratio. We may now define $\mathbf{G}_b$ as

$$\mathbf{G}_b = \mathbf{G}_s h^2/4. \tag{11}$$

Now,

$$\theta_{sbp} = (\Phi''_{nz})\mathbf{G}_b(\Phi''_{kz})^T, \tag{12}$$

where

$$(\Phi''_{kz}) = (\Phi^{xx}_{kz}, \Phi^{yy}_{kz}, 2\Phi^{xy}_{kz}), \text{ and}$$
$$(\Phi''_{nz}) = (\Phi^{xx}_{nz}, \Phi^{yy}_{nz}, 2\Phi^{xy}_{nz}), \tag{13}$$

with the superscripts denoting partial differentiation with respect to the superscript variables. Next,

$$\theta_{smp} = (\Phi'_{nxy})\,\mathbf{G}_s(\Phi'_{kxy}), \tag{14}$$

where

$$(\Phi'_{nxy}) = (\Phi^x_{nx}, \Phi^y_{ny}, \Phi^x_{ny} + \Phi^y_{nx}), \text{ and}$$
$$(\Phi'_{kxy}) = (\Phi^x_{kx}, \Phi^y_{ky}, \Phi^x_{ky} + \Phi^y_{kx}). \tag{15}$$

Finally,

$$\theta_{ssp} = (\Phi'''_{nz})\,\mathbf{G}_{ss}(\Phi'''_{kz})^T \tag{16}$$

where

$$\mathbf{G}_{ss} = [Eh^5/\omega_n\omega_k M_k\, 12(1-\nu^2)(1-\nu)]\begin{bmatrix} 1 & 0 \\ 0 & 1 \end{bmatrix}, \text{ and} \tag{17}$$

$$(\Phi'''_{nz}) = [(\Phi^{xxx}_{nz} + \Phi^{yyx}_{nz}), (\Phi^{yyy}_{nz} + \Phi^{xxy}_{nz})], \text{ and}$$
$$(\Phi'''_{kz}) = [(\Phi^{xxx}_{kz} + \Phi^{yyx}_{kz}), (\Phi^{yyy}_{kz} + \Phi^{xxy}_{kz})].$$

Define the change parameters, (Δ), in terms of the percentage changes in frequency and coefficients of admixture:

$$\Delta_{nn} = [(1 + \Delta\omega_n/\omega_n)^2 - 1], \text{ and} \tag{19}$$

$$\Delta_{nk} = C_{nk}(\omega_n^2 - \omega_k^2)/\omega_n\omega_k, \tag{20}$$

where C_{nk} is the admixture coefficient. The new mode shape, $\underline{\underline{\Phi}}'_n$, is expressable in terms of the old mode shapes by the series

$$\underline{\underline{\Phi}}'_n = \underline{\underline{\Phi}}_n + \sum C_{nk}\underline{\underline{\Phi}}_k, \tag{21}$$

where the term for $n = k$ is omitted from the summation.

The format of the NASTRAN analysis requires some degree of approximation in implementing equation (1). First of all, whatever new design is generated, it should have plate elements of constant thickness, or else the analysis of the new structure becomes very difficult. This means that the values of the perturbation functions in equation (1) should be made constant for each element by taking the average value over the element. Another difficulty arises in the computation of the matrix coefficients, b_{pq}, via equation (2). If the integrations over each element are carried out as indicated, with products of the polynomials of equations (4–6), then the resulting integrands may be as high as twelfth order polynomials. To avoid the awkwardness of having to deal with such large polynomials, we decided to approximate the perturbation functions within elements by their average values therein. This made evaluation of the matrix coefficients, via equation (2), simpler and, simultaneously, provided constant changes in thickness for the plate elements.

Computer Program Descriptions

A number of component programs were required in order to implement the design procedure. As described in the following paragraphs, they included the primary routines for: (1) accepting the NASTRAN data, processing them and forming coefficient data files (POSTPR); (2) accepting the data files and computing the associated perturbation functions (NASTY); and (3) accepting the perturbation functions and performing the redesign (CHANGNAST), as well as various ancillary routines for performing checks (TESTNASTY, C2 and DISP2V), and subroutines for simplifying some of the programming.

POSTPR Program. This program accepts, as input, the displacements and rotations of the grid points of the finite elements in a NASTRAN vibration-mode analysis, in what is referred to as the global coordinate system. These displacements and rotations are converted to sets of coordinates that are local to each element. The displacements and rotations are then used, together with equations (4–6), to solve for the coefficients that determine the internal deformations of the elements; i.e., the a's, b's, and c's of equations (4–6). This is done for each NASTRAN vibration mode, and the resulting arrays of coefficients are stored in data files for use in subsequent programs.

NASTY Program. This program forms perturbation functions from equations (7–15), and takes their average value over each triangle. Two subroutines (POLVOL and TRIANG) were written to facilitate this computation. POLVOL finds the value of the integral

of the product of two polynomials over a triangular region in the x, y plane, while TRIANG, a subroutine to POLVOL, integrates any term of the two-dimensional polynomial over the triangular region. NASTY itself is a subroutine to the main inverse perturbation program (CHANGNAST).

CHANGNAST Program. This is the primary inverse perturbation design program, and it has been written so that it may use perturbation functions generated either by NASTY (and, therefore, NASTRAN) or by PERTNAST; an updated version of the original program that generates perturbation functions from experimental holographic data. CHANGNAST accepts the various material parameters (Young's modulus, Poisson's ratio, density, and the vibration mode frequencies), as well as the desired change parameters, i.e., the Δ_{nk} values. It thereupon computes the necessary perturbation functions, forms the perturbation matrix, and generates the new design via equation (1), which it can make available on punched cards. It also prints the modal masses, the perturbation matrix, the determinant of the perturbation functions that comprise the new design, and the root-mean-square change in the element thicknesses. Finally, via a subroutine called NASTDL, it computes the various perturbations that may be expected, even for the parameters that are unconstrained, by a formula that is more accurate than the perturbation formula used for the inversion process [1].

TESTNASTY Program. This program will print the values of the perturbation functions formed by NASTY, and compute the Rayleigh quotients (the ratio of maximum potential energy to maximum kinetic energy in the vibration cycle) and the check for orthogonality of the stiffness functions [1]. It will also compare NASTRAN computations of the variation modes with holographic data when the vibration mode is a scalar function. It does this by computing the mode-function value of the NASTRAN solution at the center of each section of the structure for which the holographic data have been digitized.

C2 Program. This program takes NASTRAN solutions for the vibration modes of an original and modified structure, and computes the admixture coefficients that best describe the new modes as a series of the old modes.

DISP2V Program. This program computes vectorial displacements, in one plane, of a plate or shell from data provided by two holographic interferograms of a vibration mode. (The third component is assumed to be zero). By selecting the centers of the sections of the interferograms to be digitized so that they correspond to the NASTRAN grid points, direct comparison can be made to the NASTRAN analysis.

Analytical and Experimental Investigations

NASTRAN Modeling of the Vibration Modes. The first computations performed were the NASTRAN analyses of both a uniform plate and a uniform shell segment. The plate was 15.24 cm long by 12.7 cm wide by 0.317 cm thick, and the shell segment was a 45 degrees arc of a cylindrical shell, 7.62 cm long, with an outer radius of 7.62 cm and a thickness of 0.317 cm. Schematic illustrations of the structures, as divided into triangular elements for the NASTRAN analyses, are presented in Fig. 1. Material parameters were taken to be: Young's modulus, E, 6.1×10^{11} dynes/cm^2; density, ρ, 2.7 grams/cm^3; and Poisson's ratio, ν, 0.31. (These were experimentally determined for an aluminum alloy available in stock). The boundary conditions for the clamped edges were imposed by requiring that the displacements and rotations of the grid points along the clamped edges by zero.

Real structures were built to check these models. The comparison of the mode frequencies of the structures, as obtained via NASTRAN and experimentally, are presented in Table 1 for the first three vibration modes.

The NASTRAN computations of the frequencies for the vibration modes of the plate are all lower than the experimental values by approximately 14 percent. Four percent of the difference is due to the thickness of the experimental plate (0.33 cm not 0.317), while the remaining 10 percent is quite probably due to a premature cutoff of

Table 1

Vibration Mode	Plate	
	NASTRAN	Experimental
f_1	105.6 Hz	120.6 Hz
f_2	293.3 Hz	333.8 Hz
f_3	642.2 Hz	730.6 Hz
Vibration Mode	Shell	
	NASTRAN	Experimental
f_1	898.7 Hz	806.0 Hz
f_2	1280.0 Hz	1380.0 Hz
f_3	4118.0 Hz	4080.0 Hz

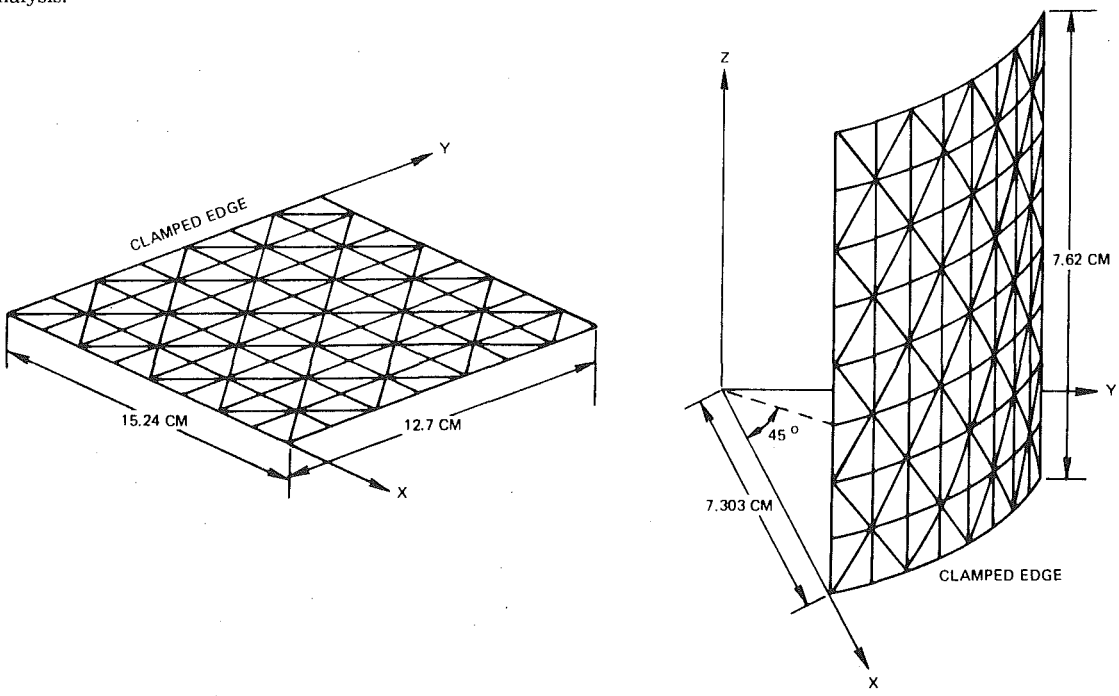

Fig. 1 Element break-up of a cantilevered plate and a cantilevered segment of a cylinder

the iterative solution for the eigenvector in the NASTRAN computations. The consistency suggests a systematic error, and this is supported by the Rayleigh quotient checks presented later.

The NASTRAN computations for the modal frequencies of the shell give results that lie both above and below the experimental values. It is suspected that the first mode frequency, which is in error by over 10 percent, may be the victim of a difficulty in adequately modeling the boundary condition where the shell is attached to the base.

System Checks. The mode shapes for both the plate and the shell were compared to holographic results. The errors found were quite small and within the accuracy of holographic measurement. In the case of the shell, the holograms were recorded with two illuminations so as to provide vectorial mode shapes.

The next computations involved the orthogonality checks and Rayleigh quotient checks. The former measure the degree to which the stiffness functions between modes are orthogonal, and the latter measure the ratio of maximum potential to maximum kinetic energy during the vibration cycle of a mode [1]. The orthogonality parameters should be zero and the Rayleigh quotients should be unity. These results are presented in Table 2.

Table 2

Mode Index (nk)	Orthogonality Parameter	
	Plate	Shell
1, 2	-.01141	-.000004
1, 3	-.00019	+.085832
2, 3	+.00309	.000000
Mode Index (nk)	Rayleigh Quotient	
	Plate	Shell
1, 1	1.0735	1.0282
2, 2	1.1047	1.0245
3, 3	1.1082	1.0852

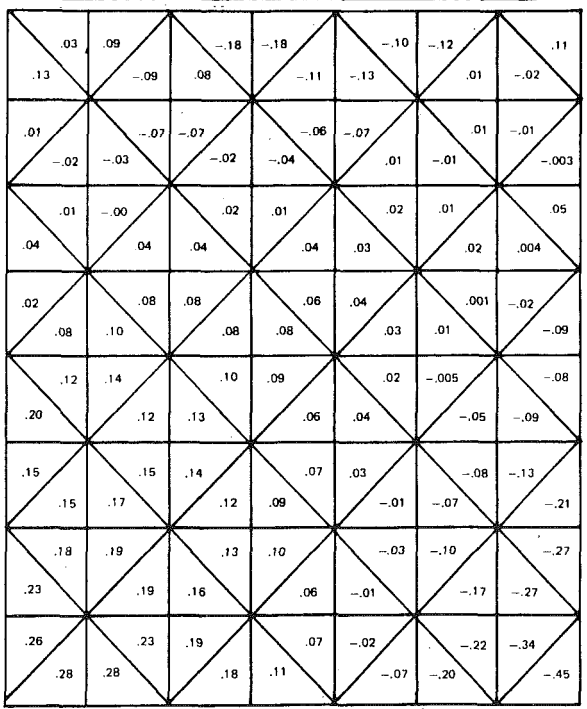

Fig. 2(*a*) New design for the flat plate. The numbers represent the fractional change in thickness of each element ($\Delta h/h$) and the clamped edge is at the top

Structural Redesign and Correlation. The next two tasks were to redesign the structures and evaluate the results via a second NASTRAN analysis. Both the cantilever plate and the cylindrical shell segment were redesigned subject to four constraints: (1) lowering of the first mode frequency by 5 percent ($\Delta\omega_1/\omega_1 = -.049$) (2) raising of the second mode frequency by 5 percent ($\Delta\omega_2/\omega_2 = +.051$), (3) an admixture coefficient of the first to the second mode of magnitude 0.125 ($C_{21} = \pm.125$), and (4) an admixture coefficient of the third to the second mode of magnitude 0.025 ($C_{23} = -.025$). (For the plate, the C_{21} parameter was positive, and for the shell it was negative. These sign conventions were necessary to generate the same shift in the node line of the second mode on both the plate and the shell, and they resulted only from a change in the sign conventions between the NASTRAN analyses of the plate and the shell.) The results provided structures which could be fabricated, and which had root-mean-square thickness changes of 12.7 percent for the plate and 14.5 percent for the shell.

The new designs, as arrays of the fractional changes in thickness of the triangular elements of the plate and shell, respectively, are presented in Figs. 2(*a*) and 2(*b*).

The designs of Figs. 2(*a*) and 2(*b*) were analyzed by NASTRAN to determine the new frequencies and mode shapes of these structures. The modes of the original structures were then used to form a series to approximate (to least-square-error) the shape of the new second mode, and, therefore, to give the resulting admixture coefficients C_{21} and C_{23}.

The final results are presented in Table 3 together with the results predicted by the more accurate perturbation calculation mentioned earlier in the description of the CHANGNAST program, and considered further in reference [1].

Pratt and Whitney Aircraft provided us with an opportunity to evaluate the inverse perturbation technique on a compressor blade, which they had analyzed using NASTRAN. A diagram of the mesh of blade elements used in the analysis is shown in Fig. 3, and a resonance diagram of the compressor, made up of a disk and a set of these blades, is presented in Fig. 4. The mode frequencies are plotted as a function of speed, along with the engine-order excitation curves. It was felt that the vibratory performance of the rig could be improved by increasing the frequency of the seventh mode, which, at the maximum rig speed, had the same value as the eighteenth engine order excitation. Thus, the design requirements were to increase the fre-

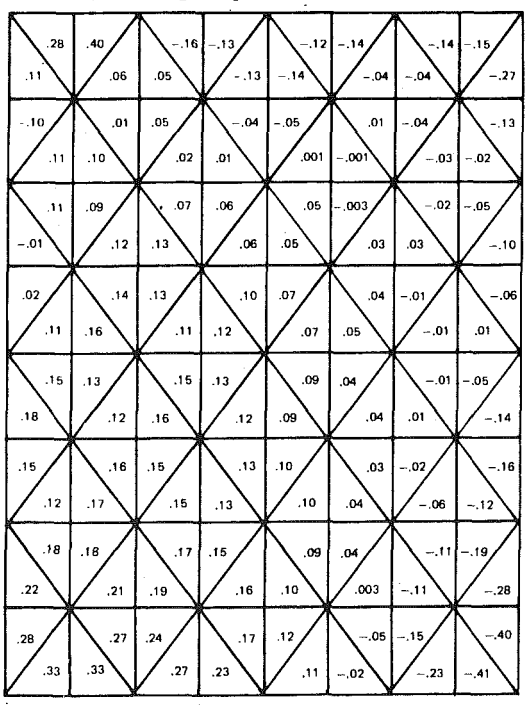

Fig. 2(*b*) New design for the 45 deg arc of a cylindrical shell

Table 3

Constraint	Design	Plate Results		Shell Results	
		NASTRAN	Perturbation	NASTRAN	Perturbation
Change in 1st Mode Frequency, $\Delta\omega_1/\omega_1$	-.049	-.027	-.037	-.042	-.041
Change in 2nd Mode Frequency, $\Delta\omega_2/\omega_2$	+.051	+.076	+.067	+.084	+.079
Admixture Coefficient 1st Mode to 2nd Mode C_{21}	Plate +.125	+.102	+.124		
	Shell -.125			-.112	-.118
Admixture Coefficient 3rd Mode to 2nd Mode C_{23}	-.025	-.021	-.026	-.027	-.028

quency of the seventh mode by 10 percent while containing the frequencies of the first six modes to be unchanged.

The first seven mode shapes for the blade, as provided by the Pratt and Whitney NASTRAN analysis, are presented in Fig. 5. The lines represents contours of constaint magnitude of vibration, and the resonant frequencies were: first mode-321 Hz, second mode-1,196 Hz, third mode-1259 Hz, fourth mode-2515 Hz, fifth mode-2639 Hz, sixth mode-3240 Hz, and seventh mode-3,813 Hz. No constraints were placed on the shape of the vibration modes, nor on the frequencies of the modes higher than the seventh.

Two passes were run on the compressor blade. That is, we used the original NASTRAN analysis of the blade and the CHANGES program to design a new blade (new thicknesses), and the NASTRAN analysis of the new blade, using the new thicknesses, was again run through the CHANGES program. On the first pass, as shown in Fig. 6, our design goal was a zero frequency change for the first six modes and a 10 percent increase in the seventh mode. The results of the NASTRAN analysis of this first redesign indicated that the greatest frequency change among the first six modes was 1.6 percent (first mode) while the seventh mode frequency was increased by 6.1 percent.

On the second pass, our design goals were to return the first six frequencies to their original values, and to increase the frequency of the seventh mode by the remaining 3.9 percent. The results of this design change provided a total frequency change of plus 8.7 percent of the seventh mode and no change, from the original frequencies, greater than 2 percent (shown in the third mode) for the first six modes.

The vibration mode shape of the seventh mode was not constrained and did change with each redesign, as can be noted by observing line number 3 in each of the three diagrams illustrated in Fig. 7. Figure 8 shows the polarity of the thickness changes for the blade elements; the blackened elements are those that were thinned by the design process, and the white elements are those that were thickened. Thus, it can be seen that there will be a change in the airfoil shape. To examine this effect, we looked at the airfoil shape at the tip and at 70 percent span which were chosen not because they are typical, but because they are the spans with the largest changes in thickness. To get a rough plot of how the airfoil changed, we straightened out the cord and made the elements of equal size. Thickness changes were symmetrically distributed between the two surfaces, and are plotted in Figs. 9 (tip) and 10 (70 percent span) using an exaggerated scale of 0.1 in. of thickness (vertical), to several in. in length (horizontal). The distribution of the centers of the elements (black dots) lie along two lines. Therefore, we have drawn a profile for each line. The upper row of centers corresponds to the upper airfoil shape, and the lower row of centers corresponds to the lower shape. At the tip, the airfoil has been thinned at the leading edge, and then thickened, by approximately 25 mils, farther to the left. At the 70 percent span point, the new shape is also irregular, but here the new blade is thicker where

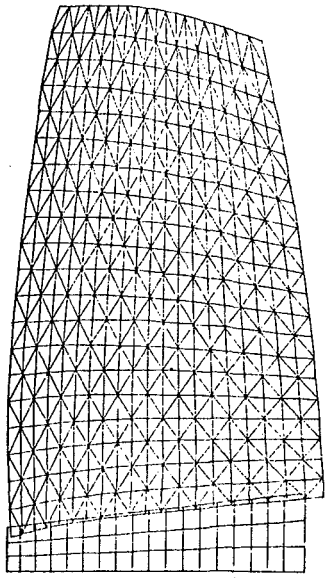

Fig. 3 Element break-up for a compressor blade

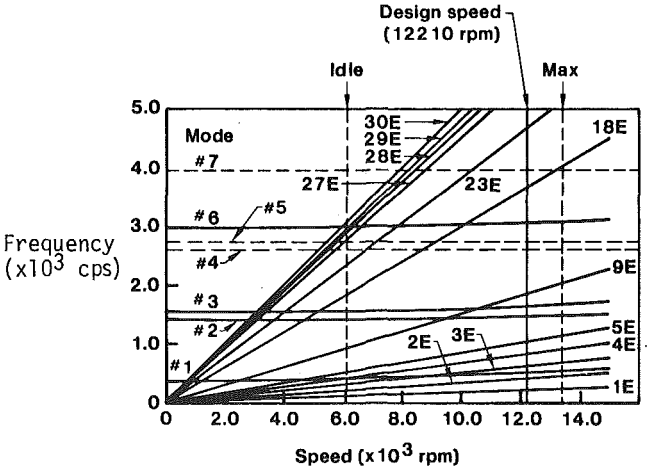

Fig. 4 Resonance diagram for a disk with a set of blades

the tip airfoil was thinned. It is our feeling that the individual variation in thickness is not as important as the overall envelope of thickness, and we are quite confident that these element thicknesses could be smoothed without changing the new mode properties.

Discussion

The technique of inverse perturbation has been shown to work with finite element vibration analyses as inputs. The results obtained with

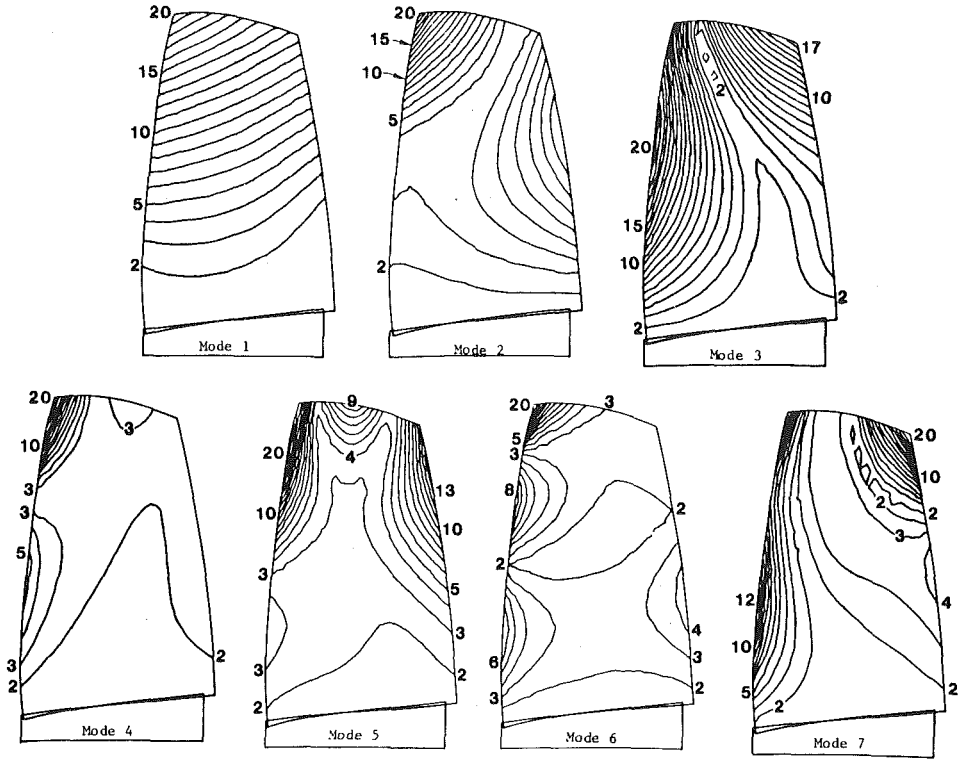

Fig. 5 The first seven modes of the blade modeled in Fig. 3. Lines are contours of constant vibration magnitude

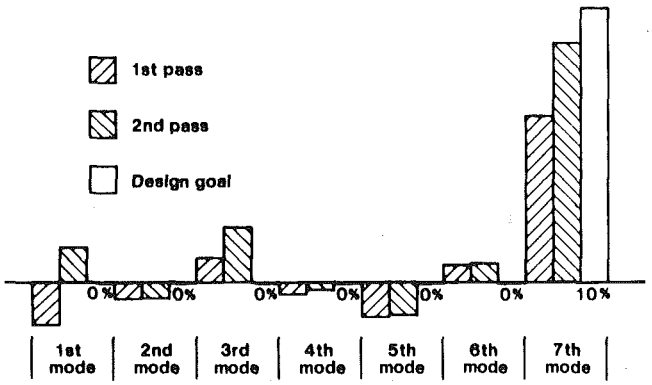

Fig. 6 Graph of the result of inverse perturbation design. The third bar in each section is the design goal, the first bar is the result of the first redesign, and the middle bar is the result of second redesign starting from the results of the first.

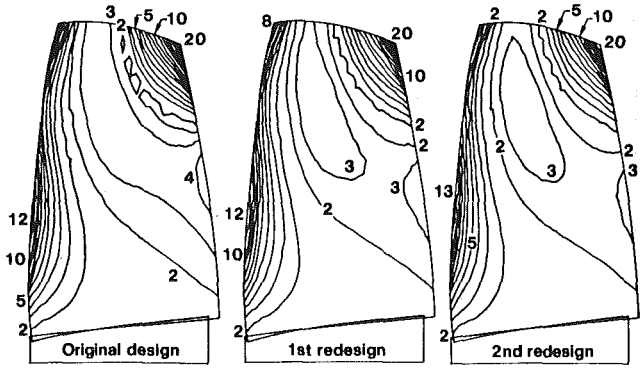

Fig. 7 Changes in the seventh vibration mode shape

the compressor blade illustrate a number of important features of the program. First, the program was executed only with the 800 elements that model the blade and not with the 54 elements that model the root. Consequently, the root was not changed in the redesigning of the blade, and it seems resonable that other critical regions of the blade could also be withheld from the process in the same way. It is also interesting to note that, as shown in Figs. 9 and 10, this program generates smaller changes in thickness where the blade is already thin. These areas make smaller contributions to the perturbation functions and, therefore, receive smaller changes. This fact makes it desirable to use the program iteratively when a large change in the modal frequencies or shapes is attempted. A large change, applied in one step, can generate negative thicknesses, whereas its application in several small changes would avoid this. If an area became thin as the result of the first step in the design, it would not be thinned so much in the successive steps because of the reformulation of the perturbation functions.

With regard to Fig. 6, the question may be asked as to whether a third iteration could be expected to achieve a design closer to the goal. This seems doubtful for the following reason. The resulting changes in the first six modal frequencies indicate an error level in the computations. This error level appears constant between the two itera-

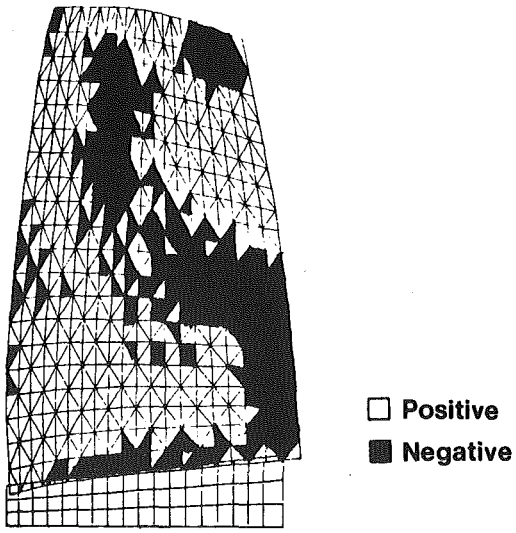

Fig. 8 Polarity of design changes of element thicknesses

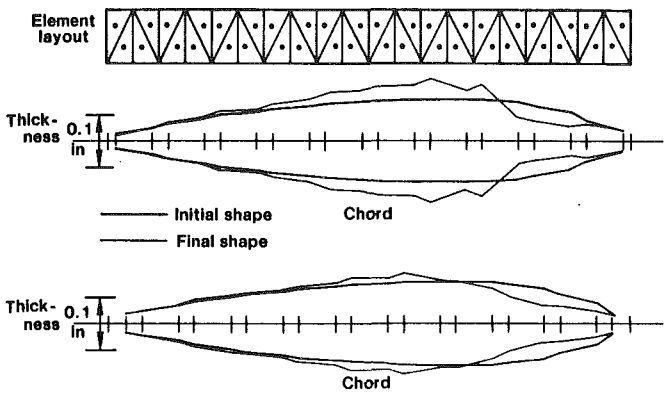

Fig. 9 Simplified representation of change in airfoil at tip

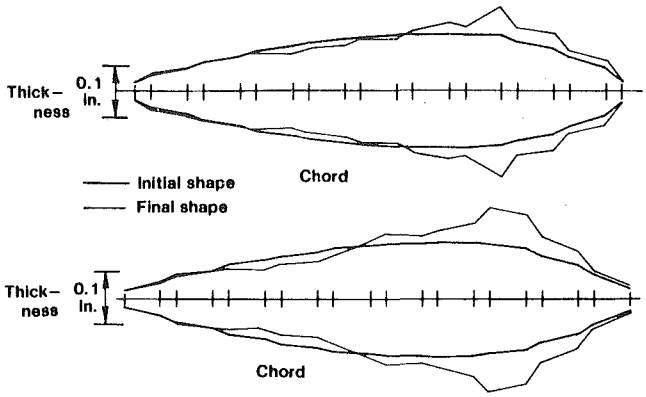

Fig. 10 Simplified representation of change in airfoil at 70 percent of span

tions, and the remaining increase desired for the seventh mode after the second iteration is of the same magnitude as the error level. Thus, a third iteration may have only a random chance of moving toward the design goal. The source of this error level has not been established, but there is good likelihood that it is inherent in the NASTRAN analyses, which are approximate.

Finally, it is of interest to know how this redesign affected the entire weight of the blade. This may be computed by summing the change in masses of all the elements and dividing by the total mass. The result is that the blade increased in weight by 4.25 percent. The product of element mass times radius from the center of the disk, when summed, gives a parameter, which multipled by the square of rotation speed, gives the centrifugal loading of the blade. Similarly, the sum of the product of element radius times change in element mass normalized by the total mass-radius product gives the change in centrifugal loading. This is an increase of 4.48 percent.

In conclusion, it must be kept in mind that this program does not, as yet, allow for design of such usual parameters as cord length, aspect ratio, twist, camber, etc. It is hoped that further work will permit modification of this design routine to make it more general.

References

1 Stetson, K. A., Harrison, I. R., and Palma, G. E., "Redesigning Structural Vibration Modes by Inverse Perturbation, Subject to Minimal Change Theory," *Computer Methods in Applied Mechanics and Engineering,* Vol. 16, 1978, pp. 151.

2 Stetson, K. A., "Perturbation Method of Structural Design Relevant to Holographic Vibration Analysis," *AIAA Journal,* Vol. 13, 1975, pp. 457.

3 Stetson, K. A., Palma, G. E., "Inversion of First-Order Perturbation Theory and its Application to Structural Design," *AIAA Journal,* Vol. 14, 1976, pp. 454.

Blade Excitation by Elliptical Whirling in Viscous-Damped Jet Engines

N. Klompas

Design Engineer,
Gas Turbine Division,
General Electric Company,
1 River Rd.,
Schenectady, N. Y. 12345

An extension of the author's earlier method of analyzing multi-shaft jet engine dynamics accounting for flexibility of bladed disks is outlined to calculate the first whirl harmonic for given nonlinear characteristics of squeeze-film dampers. A second whirl harmonic, of which experimental verification is found in Campbell's paper of 1924, is shown induced by orbit ellipticity. The possibility that this harmonic, especially due to backward whirling, may be a source of blade excitation at higher frequencies than currently recognized from linear analysis is discussed by relating some engine experience.

Introduction

Current practice in design of turbomachines accounts for bladed disk excitation by standing waves due to wakes in the working fluid. However, it is known that experimental jet engines have sustained blade failures which could not be explained by this phenomenon and might reasonably be suspected of having been caused by shaft whirling. My earlier papers [1] and [2] have shown that elliptical whirling drives traveling waves in bladed disks at speeds equal to the sum and the difference of the rotating speed and the whirling speed. However, the resulting frequencies of excitation have been too low to explain some of the suspicious failures. Therefore, this paper discusses some possible secondary effects of elliptical whirling which might produce significant excitation at higher frequencies.

The author's observation during the early 1970s of two different types of turbine blade failures in an experimental engine illustrate the need for considering secondary sources of blade excitation. Although the failures were corrected by appropriate design changes, some question of their sources remained. This paper presents some data relating to these failures and describes their probable causes as secondary effects of elliptical whirling. The author hopes that the paper will forewarn designers of possible higher excitation frequencies due to the second whirl harmonic and will encourage study into the response of squeeze-film dampers in elliptical operation.

Engine Experience

A two-shaft experimental engine was found prone to shaft vibration during its early running in a test cell and sustained failures in blades of both rotors. The first few tests did not reach full speed because of shaft vibration and failure of LP turbine blades occurred during these tests. These failures initiated as simple fatigue cracks at the root section of the airfoil. The cause was concluded as excitation in the first bending mode, despite the original design having carefully avoided interference of blade natural frequencies with possible frequencies of excitation due to standing waves. Stiffening of these blades proved effective in eliminating further failures.

Each of the next series of tests came within five percent of reaching full speed. However, each attempt was interrupted near its goal by sudden increase in vibration level and failure of HP turbine blades. The failures were confined to blade tips which appeared shattered. A photograph of both a failed and an original blade tip is shown in Fig. 1. Although not visible in the photograph, the failed blades usually displayed cracks in walls near the tip. Stiffening of the HP shaft eliminated the vibration and the blade failures. Moreover, the blades were ultimately redesigned to be less susceptible to the observed failures.

Recent examination of clearancometer traces taken near the peak speed attained during the second series of tests reveals highly elliptical orbit of rotor motion relative to the stator. That two clearancometer traces of a compressor stage showed a wide variation in phase angle between the oscillating clearance and a reference blade is evidence that the motion of the rotor with respect to the casing was not circular. The conclusion that the orbit was highly elliptical is derived next.

Interpretation of Clearancometer Traces

Figure 2 shows the orientation of the two clearancometers at 45 deg from vertical on each side. They were located on a compressor stage near the middle of the HP spool which was supported by bearings at each end. Clearancometer traces taken simultaneously at a speed near the highest speed reached are shown in Fig. 3. A coordinate system for derivation of the orbit is also shown in Fig. 2.

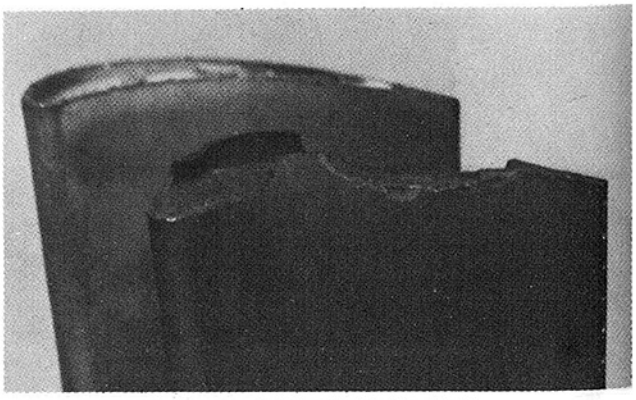

Fig. 1 Cracked tip of HP turbine blade

Contributed by the Gas Turbine Division of THE AMERICAN SOCIETY OF MECHANICAL ENGINEERS for presentation at the Gas Turbine Conference and Products Show, New Orleans, La., March 10–13, 1980. Manuscript received at ASME Headquarters January 8, 1980. Paper No. 80-GT-168.

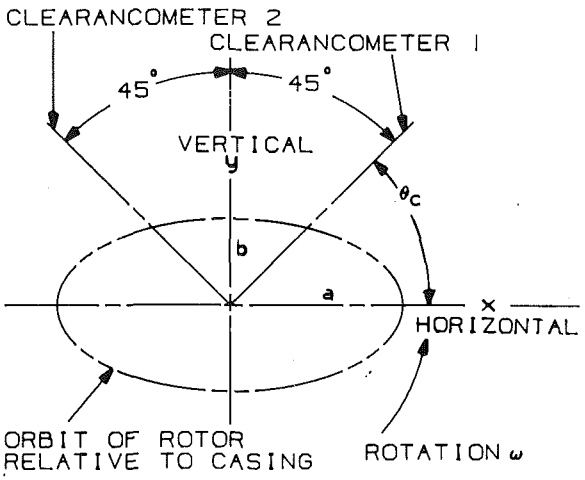

Fig. 2 Coordinate system for interpretation of clearancometer traces

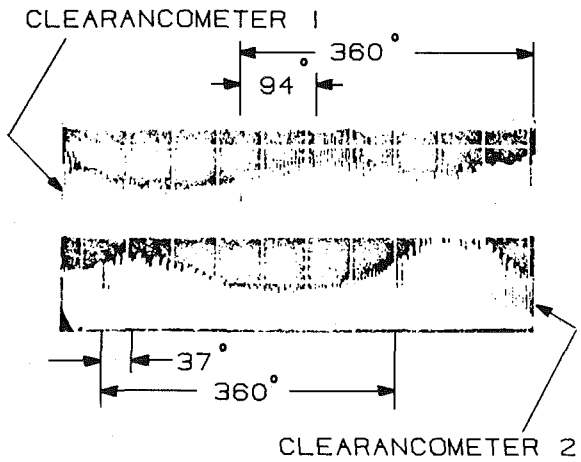

Fig. 3 Clearancometer traces: $\beta = 90$ deg + 37 deg − 94 deg = 33 deg (0.58 rad)

The assumption of an ellipse with vertical and horizontal axes is the first step in determining the orbit from the traces. This assumption follows from the author's earlier analysis [1] of unbalance response in a system containing the essential conditions of this engine. The numerical example had shown that the orbits remain symmetrical over the full rotor for a single unbalance location. This symmetry may be predicted by examining the equations of motion which are formulated as equilibrium equations at a damped bearing. It is seen that film stiffness introduces flexibility into the system without changing its symmetry and damping introduces coupling forces in two sets of orthogonal reference frames. These coupling forces may be considered as independent exciting forces for the conditions of frequency near resonance and of light damping. Therefore the unbalance forces and the damping forces excite components of the basic mode shape in each set of frames. Vector addition yields total deflections which are also a component of the mode shape and are contained in a common set of frames. The total unbalance in the engine may be expressed as exciting forces in the two sets of orthogonal reference frames. Again,

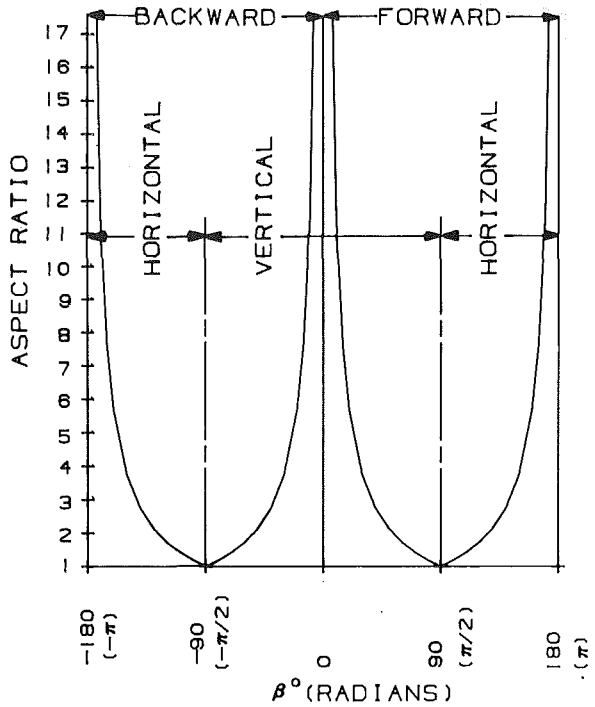

Fig. 4 Relationship of orbit to angle β

with all deflections being components of the basic mode shape, vector addition yields a similar shape.

This conclusion of orbit symmetry may be verified by examination of the clearancometer traces. The spikes in the traces are due to one blade which was shortened to provide a reference scale for amplitude calculation. Measurement relative to this reference shows that the amplitude of clearance variation is equal at the two clearancometers. If a highly elliptical orbit is assumed, as will be shown next, symmetry may be deduced from this equality.

On acceptance of the constraint to a symmetrically oriented ellipse, data measured from the clearancometer traces are sufficient to define the orbit. The variation in clearance read by a clearancometer may be expressed as

$$C = b \cos(\omega t - \theta_c) + (a - b) \cos\theta_c \cos\omega t \qquad (1)$$

where a and b are the amplitudes along the x and y axes, respectively. A peak in this variation occurs when the derivative with respect to t is zero. The angle of shaft rotation between peaks at the two clearancometers is measured from the traces and is designated β. With vertical symmetry of clearancometer locations, the angle of shaft rotation ωt at the instant of peak is $(\pi - \beta)/2$ at clearancometer 1 and $(\pi + \beta)/2$ at clearancometer 2. The derivative of equation (1) at either peak simplifies to the equation of the elliptical orbit

$$(a - b)/b = \sqrt{2} \sin(\beta/2 - \pi/4)/\cos(\beta/2) \qquad (2)$$

Solution of equation (2) showing the aspect ratio of the ellipse, its orientation and direction of motion over the possible range of β is shown in Fig. 4. The angle β measured from the traces of Fig. 3 is 0.58

Nomenclature

C = clearancometer reading
F = force at bearing
F_{aa}, F_{bb} = amplitudes of forces along axes due to fluid film stiffness
F_{ab}, F_{ba} = amplitudes of forces along axes due to fluid film damping
ΔF = amplitude of higher order harmonic force
D = effective stiffness at damped bearing
K_f = fluid film stiffness coefficient
B_f = fluid film damping coefficient
θ = angular coordinate
β = angular rotation of shaft between peak readings on clearancometers
ω = angular velocity of shaft rotation
Ω = angular velocity of whirling
x, y = horizontal and vertical coordinates
Also, y, = deflection in plane of reference
a, b = amplitudes of motion along axes
t = time

Subscripts

c = clearancometer location
r = whirl, or radial
s = whip
t = tangential
u = due to unbalance
x, y = direction of coordinate x, y
i, j = dummy indices
(2) = second harmonic
(1) = first harmonic

radians; from equation (2) the aspect ratio of the ellipse is 3.35, the orientation is vertical and the direction is forward.

Secondary Effects Of Damper

My earlier paper [1] has shown that elliptical whirling drives traveling waves in bladed disks at speeds equal to the sum and the difference of the rotating speed and the whirling speed. The resulting frequencies of excitation for both turbine blades described above were too low to explain the failures. However, it will be shown that secondary waves at higher speeds can be induced by squeeze-film dampers such as were used in the engine.

The primary effects of film nonlinearity may be accounted for by iteration of linear analysis. The linear analysis described in [1] is ideally suited to iteration for fluid flim nonlinearity because solution of forces and orbits of motion across films is an isolated step which can be independently repeated until the orbits match the given film characteristics. Moreover, an accounting for possible dynamic response of flexible bladed disks is included in the solution. Accordingly, a procedure for calculating the first order solution, which may be called the first harmonic, to the unbalance response of a complete engine is outlined in the Appendix.

As explained above, the orbits near a critical speed are symmetrically oriented ellipses. The corresponding variation in fluid film thickness is illustrated in Fig. 5 as an elliptical orbit of motion across the film. The first harmonic of the force transmitted by film stiffness is shown as the two components

$$F_{r(1)} = \{F_{aa} + (F_{aa} - F_{bb}) \cos 2\Omega t\}/2$$
$$F_{t(1)} = F_{aa} \sin 2\Omega t/2 \tag{3}$$

where F_{aa} and F_{bb} are the amplitudes of the oscillating forces at the axes. The symmetrically varying force attributed to film stiffness can match that of the actual fluid film only at the axes because the film response loses symmetry with increasing ellipticity.

The difference between the actual force and that assumed by the linear analysis must be satisfied by deviation from elliptical orbits. Determination of this deviation as higher order harmonics of whirling would reveal speeds of secondary traveling waves which might excite blade vibration. Although methods for calculating these harmonics are not known, the speed and direction of the second harmonic may be derived by considering the inherent film behavior.

The force transmitted by the fluid film may be considered as the sum of a symmetric and a nonsymmetric component. Figure 6 shows a curve which illustrates the nature of the nonsymmetric component. This curve reflects the assumption of force increase due to film convergence and reversible decrease due to divergence, although reversibility is not essential to the conclusion which will follow. Assuming circular whirling for higher order harmonics, the lowest harmonic of the portion of the film force not satisfied by the first order solution is, for forward whirling

$$F_{r(2)} = -\Delta F_{(2)} \sin 2\Omega t \tag{4}$$

This force may be expressed as components in the horizontal and vertical direction

$$F_x = -\Delta F_{(2)} \sin 2\Omega t \cos \Omega t$$
$$F_y = -\Delta F_{(2)} \sin 2\Omega t \sin \Omega t \tag{5}$$

After simplification, these components become

$$F_x = -\Delta F_{(2)} \{\cos (3\Omega t - \pi/2) + \sin \Omega t\}/2$$
$$F_y = -F_{(2)} \{\sin (3\Omega t - \pi) + \cos \Omega t\}/2 \tag{6}$$

The first terms of these two components describe a radial force rotating forward at three times the whirling speed. Backward whirling would reverse its direction of rotation. Therefore, it is clear that elliptical whirling would induce a second harmonic with motion in the same direction and at three times the speed of the first harmonic.

It is our fortune that an experimental demonstration of this harmonic has been recorded in the technical literature; Campbell [3] found evidence of it in the early twenties. He produced clear records revealing a wave traveling forward at twice the rotating speed in the disk of his wheel-testing machine. He hypothesized that both a backward and a forward traveling wave could be excited by unbalance when the hortizontal and vertical stiffnesses of the bearing supports are not equal. His observation of the forward wave is verified by records of motion at three cycles per revolution and at two cyles per revolution registered by a stationary and rotating coil, respectively.

The author's linear analysis [1, 2] shows that only the backward wave is excited by unbalance and would have arisen inevitably in the experiment. Campbell cautioned that evidence of the backward wave would have been difficult to obtain because it would have required the ability to determine whether the necessary one per revolution record of a stationary coil was due to a backward wave or due to the primary effects of unbalance. Therefore, it is now concluded that he had recorded evidence of the second harmonic.

Campbell's observation of a forward wave does not reveal a higher frequency than that obtained from linear analysis for a single rotor. However, the present finding that the second harmonic might appear as a wave traveling backward at four times the rotating speed should be of interest to engine designers. Moreover, the forward wave may be significant in high bypass turbofan engines.

Probable Causes of Blade Failures

The HP blade failure, shown in Fig. 1, was probably caused by intermittent tip rubbing. Interference at the blade tip would cause a blade to be plucked twice per revolution. The failure exhibited signs of impact and perhaps excitation at very high frequency rather than at the low frequency of plucking. However, it is likely that repeated sharp impact and release from constraints, or plucking, would excite

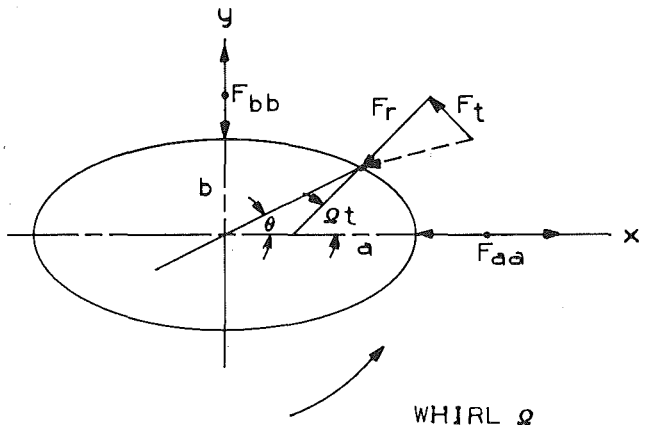

Fig. 5 First order force due to film stiffness

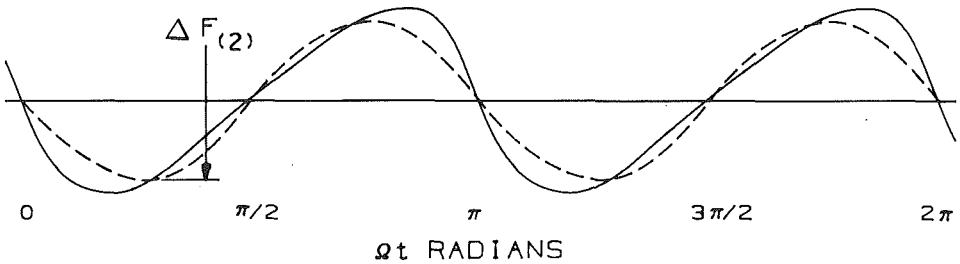

Fig. 6 Nature of nonsymmetric component of force due to film stiffness

periods of free vibration in modes associated with very high frequencies. Although it is not possible to relate this failure to higher harmonics of whirling, its occurrence provides additional evidence of orbit ellipticity in this engine.

Assumption of the second harmonic induced by backward whirling appears to be the only possible link between the LP turbine failures and shaft vibration. This harmonic would have driven a wave of tangential force at a speed which would have excited the first mode of blade vibration. It remains then to determine the likelihood that backward whirling was encountered during the first few tests.

The earlier studies [1, 2] and the study by Pederson [4] show that whirling associated with successive critical speeds alternates in orbit orientation and direction. Therefore, it may be assumed that the engine had encountered a lower critical speed associated with backward whirling in horizontally inclined orbits. Evidence of severe rubbing by compressor blades indeed was observed after one of the earliest tests. The marks on the casing were inclined from horizontal approximately 30 deg in the direction opposite of rotation. This incident may be now considered as evidence of backward whirling because it would be reinforced by rubs and might be driven into an unstable orbit by increasing intensity of rubbing. Moreover, the orbit would deflect from the horizontal as was observed; Fig. 7 illustrates the possible reinforcement and deflection. Forward whirling, on the other hand, would be constrained by rubbing. Therefore, the evidence available supports the possibility that the second harmonic induced by backward whirling caused failure of the LP turbine blades.

Discussion

The prediction of the second order whirling speed and its direction are based on the simple observation that the film force cannot remain symmetric when the motion in an elliptical orbit crosses an axis. At a small distance before the axis is reached this force would be either higher or lower than at the same distance beyond the axis, whereas symmetry of the ideal stiffness assumed in linear analysis would require the force to be equal at these two locations. Since the film responds through hydrodynamic forces which vary with direction of motion as well as location in the orbit, the change between converging and diverging film thickness during shifts across axes must be highly significant.

The effects of orbit ellipticity on operation of squeeze-film dampers have not been treated in the technical literature. The recent paper by Pan and Tonnesen [5] has analytically shown higher harmonic orders of fluid film forces due to eccentric operation. However, the author feels that whirl orbit ellipticity is more significant than eccentricity because severe vibration usually develops forces which are much higher than those due to gravity or initial misalignment of centering springs.

Campbell's pioneering experiment [3] provides an excellent verification of the second harmonic film force derived in the present paper. Since his film was in a journal bearing, the force would be closer to linear than that of a squeeze-film damper. Therefore, a squeeze-film damper would produce a stronger second harmonic and, possibly, a significant third harmonic.

The author hopes that this paper will stimulate further study into the film characteristics and their application to the study of engine dynamics. The Appendix is offered as a guide for further investigation. However, the present study should signal an alert to possible blade excitation at frequency which is either the sum or the difference of the rotating speed and three times the whirling speed.

Summary and Conclusions

Some evidence of high whirl ellipticity in an experimental engine was shown and its link to blade failures of two turbine stages was suggested. The probable cause of HP turbine blade failures was tip plucking, while that of LP turbine blades was a traveling wave of force due to the second whirl harmonic induced by backward elliptical whirling.

By comparing the conditions of symmetry possible for the fluid film force of a squeeze-film damper and those assumed in linear analysis, the speed and direction of the second whirl harmonic were derived.

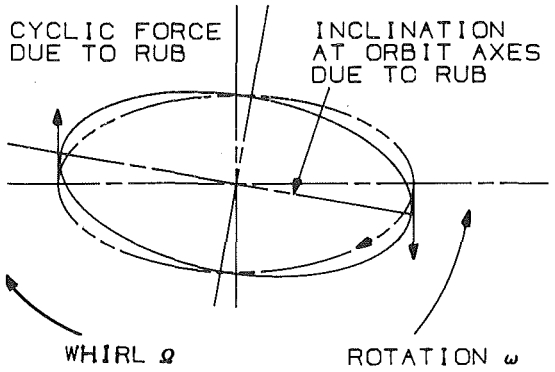

Fig. 7 Influence of tip rubs on backward whirl

The conclusion that a wave traveling at three times the speed in the direction of whirling is induced by ellipticity was found confirmed experimentally by Campbell [3].

The basic film characteristics needed for first order solution of elliptical whirling were defined. Their application to the analysis of engines with flexible disks and anisotropic mounting stiffness was outlined. Although further investigation into characteristics of squeeze-film dampers operating with elliptical orbits is necessary to improve the analysis, the possibility of blade excitation at frequency which is either the sum or the difference of the rotating speed and three times the whirling speed was established.

References

1 Klompas, N., "Significance of Disk Flexing in Viscous-Damped Jet Engine Dynamics," ASME JOURNAL OF ENGINEERING FOR POWER, Oct. 1978, pp. 647–654.

2 Klompas, N., "Theory of Rotor Dynamics with Coupling of Disk and Blade Flexibility and Support Structure Asymmetry," presented at the 1974 ASME Gas Turbine Conference and Products Show, Paper No. 74-GT-159.

3 Campbell, W., "Protection of Steam Turbine Disk Wheels from Axial Vibration," Paper No. 1920, TRANS ASME, Vol. 46, 1924, pp. 31–160.

4 Pedersen, P. T., "On Forward and Backward Precession of Rotors," Report No. 17, Danish Center for Applied Mathematics and Mechanics, Technical University of Denmark, Sept. 1971.

5 Pan, H. T., and Tonnesen, J., "Eccentric Operation of the Squeeze-Film Damper," *Journal of Lubrication Technology*, July 1978, pp. 369–378.

APPENDIX

Reference [1] outlines a procedure for calculating critical speed and unbalance response of a multi-shaft jet engine supported by a structure of anisotropic stiffness. The effects a flexible disks and damped bearings are included in the analysis. However, the behavior of squeeze-film dampers is assumed linear and symmetric despite the introduction of elliptical orbits. The need for improvement in the determination of film characteristics is noted and is illustrated further by the present paper. This appendix extends the outlined procedure to calculate the first order solution if nonlinear film characteristics are known.

Equations (3) of the present paper define two components of the force across the film attributed to film stiffness in the linear solution. This force is the vector sum of two components in phase with two components of motion defining an elliptical orbit and is characterized by the amplitudes of the oscillating forces F_{aa} and F_{bb} transmitted at the stationary axes. Two oscillating damping forces, F_{ab} and F_{ba}, are also needed for complete linear simulation of the film. For a given elliptical orbit with amplitudes a and b on the axes, these forces transmitted across the film are defined as

1 At the instant of displacement a, in direction to resist motion

F_{aa} = Force along the axis

F_{ba} = force normal to the axis

2 At the instant of displacement b, in direction to resist motion

F_{bb} = force along the axis

F_{ab} = force normal to the axis

These four forces which characterize the response of the film are transformed into two stiffness coefficients, K_{fr} and K_{fs}, and two damping coefficients, B_{fr} and B_{fs}, by the following equations where deflection a is assumed on the horizatonal axis which is in the plane of reference for the whip coordinate.

$$K_{fr} = F_{bb}/b$$
$$B_{fr} = F_{ab}/\Omega b \tag{7}$$

are the whirl coefficients.

$$K_{fs} = (F_{aa} - F_{bb})/(a - b)$$
$$B_{fs} = (F_{ab} - F_{ba})/\Omega(a - b) \tag{8}$$

are the whip coefficients if whirling is forward, and

$$K_{fs} = (F_{aa} + F_{bb})/(a + b)$$
$$B_{fs} = (F_{ab} + F_{ba})/\Omega(a + b) \tag{9}$$

if whirling is backward. These equations may be checked by multiplying the coefficients by the appropriate whip and whirl deflections, and the whirling speed Ω for the damping coefficients, and adding the results to obtain the forces assumed for the film.

Reference [1] characterizes the elastic system as a stiffness matrix and an array of disturbing forces associated with the four free deflections at each damped bearing. Integers assigned to these free deflections are used to define the matrix of stiffness coefficients D where the element D_{ji} is the force synchronous with deflection i which is required constrain the free deflections to zero execpt deflection j which is 1. Also, an array of forces F_u is calculated to account for unbalance in the exciting shaft. The force f_{uj} is the force synchronous with free deflection j which is necessary to constrain all free deflections to zero when the unbalance is applied.

The stiffness matrix, the array of unbalance forces and the film coefficients associated with the damped bearings characterize the full system. To formulate the final set of equations, a second set of coordinates is added in a plane of reference 90 deg ahead of the whirl plane containing the unbalance and in the corresponding whip plane. These additional coordinates contain the deflections due to damping. Response of the elastic system remains the same for both sets of coordinates. Eight equilibrium equations of each damped bearing provide for solution of the full system.

These equations are solved simultaneously to obtain values for the free deflections. Back-substitution accounting for the deflections and forces in the full elastic system associated with each of these values and with the unbalance force yields all deflections and forces. Elliptical orbits and phase relationships relative to the plane of unbalance are obtained over the full damped system. Repeated solution of these equations can be carried out until the orbit of motion across the film and the coefficients correspond to the film data. Thus, a stable first order solution to the nonlinear problem would be obtained by iteration.

A critical speed is signified by zero for the value of the determinant associated with the simultaneous equilibrium equations when film damping is neglected. Back-substitution with one of the free deflections arbitrarily prescribed yields the corresponding mode shape.

For simplicity, only one damped bearing is assumed in the following derivation of the final equations. Integers are assigned to the free deflections, 1 to shaft whirl, 2 to shaft whip, 3 to bearing housing whirl, and 4 to bearing housing whip. Integers 5–8 are assigned in the same order to the deflections in the coordinates added to account for damping. Then, the eight equilibrium equations at the damped bearing are

$$(D_{11} - D_{13})y_1 + (D_{21} - D_{23)y2} + (D_{31} - D_{33})y_3 + (D_{41} - D_{43})y_4 = -F_{u1} + F_{u3}$$

$$(D_{12} - D_{14})y_1 + (D_{22} - D_{24})y_2 + (D_{32} - D_{34})y_3 + (D_{42} - D_{44})y_4 = -F_{u2} + F_{u4}$$

$$(D_{11} - D_{13})y_5 + (D_{21} - D_{23})y_6 + (D_{31} - D_{33})y_7 + (D_{41} - D_{43})y_8 = 0$$

$$(D_{12} - D_{14})y_5 + (D_{22} - D_{24})y_6 + (D_{32} - D_{34})y_7 + (D_{42} - D_{44})y_8 = = 0 \tag{10}$$

$$(D_{11} - K_{fr})y_1 + D_{21}y_2 + (D_{31} + K_{fr})y_3 + D_{41}y_4 + \Omega B_{fr}(y_5 - y_7) = -F_{u1}$$

$$D_{12}y_1 + (D_{22} - K_{fs})y_2 + D_{32}y_3 + (D_{42} + K_{fs})y_4 + \Omega B_{fs}(y_6 - y_8) = -F_{u2}$$

$$\Omega B_{fr}(-y_1 + y_3) + (D_{11} - K_{fr})y_5 + D_{21}y_6 + (D_{31} + K_{fr})y_7 + D_{41}y_8 = 0$$

$$\Omega B_{fs}(-y_2 + y_4) + D_{12}y_5 + (D_{22} - K_{fs})y_6 + D_{32}y_7 + (D_{42} + K_{fs})y_8 = 0$$

The first four equations define the equilibrium conditions across the film; the second four equate the forces on the shaft to the response of the film.

Although solution of unbalance response as outlined above would be of interest as final confirmation of particular engine design, calculation of critical speed may be of greater use as a design tool. Here the number of equations is cut in half and the amplitude is chosen. Critical speeds may then be avoided, or at least predicted, before the more extensive analysis needed to determine sensitivity to unbalance is attempted. An interesting characteristic that could be obtained is the variation of critical speed with amplitude. A multi-valved amplitude might predict that operation at a speed reached by acceleration through a critical speed so as to attain the lowest possible amplitude would be subject to a sudden jump. The engine running described in this paper did exhibit such a jump at the highest speed reached.

R. L. Ammon
L. R. Eisenstatt
G. O. Yatsko

Westinghouse Electric Corporation,
Advanced Energy Systems Division,
Pittsburgh, Pa.

Creep Rupture Behavior of Selected Turbine Materials in Air, Ultra-High Purity Helium, and Simulated Closed Cycle Brayton Helium Working Fluids

Five turbine materials, IN100, 713LC, MAR-M-509, MA-754 and TZM were selected as candidate materials for use in a Compact Closed Cycle Brayton System (CCCBS) study in which helium served as the working fluid. The suitability of the alloys to serve in the CCCBS environment at 927 C (1700 F) was evaluated on the basis of creep-rupture tests conducted in air, ultra-high purity helium (>99.9999 percent), and a controlled impurity helium environment. Baseline reference creep rupture properties for times up to 10,000 hr were established in a static ultra-high purity helium environment.

Introduction and Background

The creep-rupture work reported in this paper was conducted in support of a compact closed cycle Brayton System feasibility study [1]. In the proposed compact closed cycle Brayton system (CCCBS), the highest combination of stress and temperature occurs in the first row turbine blades [1]. First stage stator vanes and blades are expected to operate at elevated temperatures for a system life in the range of 10,000 to 40,000 hr. The working fluid is an inert gas, helium, with equilibrium concentrations of various impurities. Based on past helium turbine design technology from the Westinghouse closed Brayton turbomachinery development with the United States Maritime Administration [2, 3], and based on expected materials properties, it was concluded that a turbine inlet temperature on the order of 927°C (1700°F) pushes but does not exceed the state-of-the-art for uncooled turbine blades and stators in inert gas. This conclusion regarding materials capability was based on engineering extrapolation of materials properties data obtained in inert gas at lower temperatures and on properties data at comparable temperature in air for shorter test time periods. However, to demonstrate material performance feasibility, additional material testing was necessary at or near expected service conditions to confirm materials properties and to provide baseline data for the feasibility evaluation [1].

Historically, superalloy development has been aimed at problems associated with aviation and land gas turbines where thermal fatigue, hot corrosion, and oxidation are the primary factors which limit component life. While creep-rupture behavior is an important design consideration in such systems, hot component life is limited to a large degree by materials compatibility with combustion products, including fuel impurities such as sulfur compounds and catalytic agents, like vanadium pentoxide, from fuel processing. In the case of CCCBS turbine components, creep behavior is expected to be a primary design consideration. Minor amounts of active contaminants in the inert working fluid are expected to produce surface reactions which may or may not influence creep behavior.

The objective of the materials test program described in this paper was to determine the feasibility of potential turbine materials to function under CCCBS operating conditions for the design life of the system. To achieve this objective, the creep-rupture behavior of five selected alloys were evaluated at 927°C (1700°F) in air, in static ultra-high-purity helium (UHP-He) and in a dynamic simulated CCCBS helium working fluid. Creep-rupture properties were also compared to available published data obtained from the Mechanical Properties Data Center, Traverse City, Mich. The five alloys chosen for evaluation were In100, 713LC, MAR-M509, MA754 and TZM. To characterize the creep-rupture behavior of each particular heat of material obtained for evaluation, a limited number of creep-rupture tests were carried out in air. The TZM alloy was not tested in air due to its reactive nature with oxygen at elevated temperatures. Creep-rupture tests were conducted under a static ultra-high purity helium (UHP-He) (≥99.9999 percent) atmosphere to establish long-term baseline data under test conditions, which minimizes environmental effects. Because superalloys, while under development, are normally tested in air for creep-rupture behavior, they are naturally optimized for use in an air environment. There exist data that indicate that an air test environment, particularly at elevated temperatures can have a beneficial or deleterious effect on creep-rupture behavior of certain superalloys [4–7].

Test Equipment and Procedures. Creep-rupture tests were carried out in air, UHP-He and simulated CCCSB helium working fluid. Creep tests were conducted in conventional lever arm units under static air conditions. The air test equipment and procedures were conventional and routine in nature, thus a description is not included in this paper. Since the static UHP-He and dynamic simulated CCCBS environmental test equipment are considered to be

Contributed by the Gas Turbine Division of THE AMERICAN SOCIETY OF MECHANICAL ENGINEERS and presented at the Gas Turbine Conference and Products Show, New Orleans, La., March 10–13, 1980. Manuscript received at ASME Headquarters, January 9, 1980. Paper No. 80-GT-173.

unique, a brief description of the test equipment and procedures used is included.

Ultra-High Purity Helium Test System and Procedure. Creep-rupture testing was carried out in five ultra-high vacuum creep test units modified for ultra-high purity helium atmosphere operation. The creep units are illustrated schematically in Fig. 1. Ultra-high vacuum creep test operation of these units is described in detail elsewhere [8]. The cogent system characteristics which made these units ideally suited for ultra-high-purity helium atmospheric testing are

- The all metal system construction utilizes crushable copper gasket seals which permits evacuation to pressures below 1×10^{-7} torr while the entire system is baked at 204°C (400°F). This operation removes adsorbed moisture and gases from all internal surfaces.
- The specimen is heated by radiation from a split tantalum resistance heating elements insulated by tantalum radiation shields. Tantalum at temperatures above 538°C (1000°F) is an active "getter" of oxygen, thus the test specimen is exposed to an environment with a very low oxygen level.
- The specimen is deadweight loaded internally by weights contained in the system. External loads are transmitted to the specimen through a stainless steel bellow seal.
- Specimen strain is measured optically directly off the gage section. This feature plus deadweight loading eliminates systematic error.

Helium gas used for the creep testing atmosphere was Matheson Purity 99.9999 percent min. helium. Gas analysis was conducted using a one liter sample bottle which was attached to the system through a bakeable valve. The sample bottle, which was baked out under dynamic vacuum conditions, was permitted to equilibrate with the static helium environment within the test chamber. The helium in the sample bottle was analyzed using a concentration technique developed at the Westinghouse Research and Development Center [9, 10].

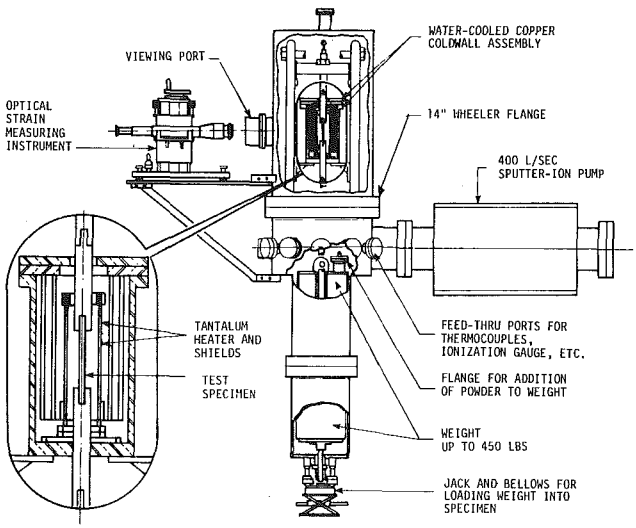

Fig. 1 Schematic diagram of modified ultra-high vacuum creep units

Table 1 Typical helium gas analysis

	Typical He Analysis (ppm)						
	H_2	O_2	N_2	C_0	CO_2	THC	Ar
Final	1.0	0.04	0.9	ND	0.2	0.04	1.4
Initial	0.3	ND	0.07	ND	0.2	0.04	0.01
Initial	0.5	0.1	0.2	ND	0.4	0.10	0.01
Final	4.0	ND	ND	1.3	0.2	0.05	0.1
Initial	2.2	ND	ND	0.1	2.3	0.2	0.1

Final analyses were taken from tests run for >1000 hours. It must be noted that reported values at or below the 1 ppm level are at the limits of detectability and most likely represent background levels of the sampling and analytical equipment.

ND - Not Detected

THC - Total Hydrocarbons

Gas samples were taken at the beginning and at the conclusion of a creep test. Typical analytical results are reported in Table 1. Hydrogen was the most prominent active gas with concentration levels which varied from initial values of 0.35 ppm to maximum values as high as 4.0 at the end of testing. All other active gases were either not detected or were present in levels which were consistently less than 1.0 ppm.

Test Procedure. A suitably prepared and thermocoupled test specimen was inserted into the test chamber shown previously in Fig. 1. The grips were attached to the upper support member and weight train by means of pinned joints. The thermocouple leads were fed to the outside by means of a ceramic feed-through assembly. Extreme care was exercised during loading of the system to prevent the introduction of any foreign matter, such as dirt, oil, etc., which would compromise system operation. After the test specimen was placed in the load train, the system was sealed, evacuated and baked out.

Once the test specimen was installed into the load train, the metal bell jar was sealed in place. The system was baked under dynamic vacuum at 204°C (400°F). The specimen was also heated during the bakeout cycle to remove adsorbed moisture and gases from all internal surfaces. The bakeout cycle was programmed to be carried out overnight. After the system cooled to ambient temperature, the test chamber was backfilled with UHP helium through vacuum purged and baked lines. The specimen was then heated to test temperature and the load was applied. Strain measurements were taken at frequent intervals during the primary creep stage.

Simulated CCCBS Helium Test System and Procedure. Creep rupture testing in simulated CCCBS helium working fluid was carried out in five test units equipped with a specially designed simulated CCCBS helium working fluid environmental supply system.

Each unit consisted of a resistance wound radiation heater mounted so that the specimen was in the center of the hot zone. The creep chamber was a clear quartz tube with pyrex fused at each end; several transition zones separated the 100 percent quartz from the 100 percent pyrex. Crushable copper gasket seals were used in the metal-to-metal interfaces. The glass-to-metal seals were kovar. The thermocouple leads were introduced into the system through conventional vacuum feedthroughs. Strain was measured by a dial gage detecting lever arm motion. This measurement included deflections in the entire load train. This led to large indicated primary creep strains. However, secondary creep rate and rupture life were unaffected. Optical measurements were also used to measure strain.

Test Procedures. Thermocouples were attached to the test specimen at three places along the gage length. The specimen was connected to the load train by means of either button head or threaded joints. This assembly was then placed inside the quartz tube. The thermocouple leads were led out of the tube by way of a ceramic feedthrough assembly. The quartz tube was attached to the frame of the creep machine, and the load train was connected to the loading apparatus. The load train emerged from the tube through a bellow seal and was connected to the load by means of a threaded joint.

Evacuation of the creep chamber was accomplished by a mechanical and diffusion pump. The pressure was reduced to 1×10^{-5} to 1×10^{-6} torr. The system was checked for leads. Once it was determined that the system had no leaks, the chamber was baked to remove adsorbed gases and moisture from the internal surfaces. This was accomplished by heating the chamber to 260 to 316°C (500 to 600°F) and then cooling to room temperature.

The test chamber was made a part of the impure helium loop. The test specimen was heated to temperature, and once thermal equilibrium was established, the load was applied by means of a lever assembly. Periodically during the creep test the change in length, $\Delta\ell$, was measured by a dial gage. To determine the strain-time curve, ℓ_0 was taken to be the length of the gage section at a room temperature.

Simulated CCCBS Helium Environmental Supply System.

Figure 2 is a schematic of the impure helium loop creating the CCCBS environment. In the actual system the five creep-chambers were arranged in parallel. For simplicity, only one is shown in the figure. A full flow purification system was utilized to remove all impurities from the recirculating helium. The desired levels of each impurity species in the helium was attained by an injection system prior to distribution of the helium gas to the test chambers. In this way, the species and concentration levels were precisely controlled.

The purification section of the loop consisted of a copper oxide bed operating at 371°C (700°F). The bed was filled with copper ribbon which was oxidized to CuO at 649°C (1200°F) by passing air through the bed. The CuO bed operating at 371°C (700°F) removed CO and H_2 by the following reaction:

$$CO + CuO \rightarrow Cu + CO_2$$

$$H_2 + CuO \rightarrow Cu + H_2O$$

After passing through the CuO bed, the helium gas was permitted to cool to ambient temperature prior to passing through a type 5A molecular sieve bed. The molecular sieve bed, which was maintained at ambient temperature, removed CO_2 and H_2O by adsorption. Following the molecular sieve bed was a silica-gel trap cooled by a refrigeration system to −40°C (−40°F). The silica gel trap removed N_2, CH_4 and traces of CO, CO_2 and H_2O from the helium gas stream. The final step in the purification process was a titanium sponge bed operating at a temperature of 649°C (1200°F). Titanium is an active "getter" of oxygen at elevated temperatures. The calculated equilibrium partial pressure of oxygen over titanium at 649°C (1200°F) is $<1 \times 10^{-45}$ atmospheres. The oxygen level in the helium under flow conditions of 5 liters-per-minute through the titanium sponge bed was well below the limits of detectability.

The continuous injection of the impurity gases was accomplished through microflow rate needle valves. The gases were supplied by cylinders of high purity CO, CH_4 and H_2. In parallel to the impurity injection line was an oxalic acid bed to supply moisture to the carrier gas as required to maintain the desired level in the recirculating helium. The impurity injection system was isolated by two "normally closed" solenoid operated valves in the event of an electrical outage. This possibility was minimized as the system electrical power was supplied through an uninterruptable power supply (UPS). Accumulators were used to smooth out pressure surges in the loop and to serve as a mixing chamber for blending impurities in the helium carrier gas. Quartz wool was included in the supply side accumulator for this purpose.

Helium Gas Analysis. The identity and concentration level of impurities in the simulated CCCBS helium working fluid test environment was determined by a Varian Aerograph gas chromatograph, Model 2732. This instrument utilizes a helium ionization detector which makes it ideally suited for analyzing trace impurities in inert gases. A 457 cm (15 ft) 13X MS column operating at 121°C (250°F) was used to separate the impurity constituents in the gas sample being analyzed. Calibration curves for H_2, CO and CH_4 were generated using helium doped with individual impurity species in the range of interest. The calibration curves were rechecked using a single helium source containing all of the impurity species at concentrations within the ranges of interest for each impurity species. This helium gas source was used to periodically check the calibration of the gas chromatograph during loop operations. Sampling lines permitted the helium stream to be analyzed after passing through the purification system, after the impurity injection system and after passing through the test chambers.

Selection of Simulated CCCBS Helium Composition. Based on the review of the data from other materials test programs involving the use of simulated reactor helium and gas-cooled reactor experience around the world [11–14], it was decided that the CCCBS materials test environment would be operated in the following impurity ranges:

H_2—400 to 500 μ atmos.

H_2O—1 to 3 μ atmos.

CO—40 to 50 μ atmos.

CO_2—permitted to establish equilibrium levels

CH_4—40 to 50 μ atmos.

Alloy Selection and Procurement

The alloys selected for the initial phase of the materials testing program are listed in Table 2. The first three alloys were selected on the basis of their commercial status and their particular applicability to the Compact Closed Brayton System requirements. Alloys 713LC, IN100 and MAR-M509 are commercially available alloys which have

Table 2 Selected alloys and nominal compositions

ALLOY	DENSITY (lbs/in^3)	COMPOSITION (wt. %)
1. Alloy 713LC	0.289	Ni-12Cr-4.5Mo-2Cb-5.9Al-0.6Ti-0.05C
2. IN100	0.280	Ni-10Cr-15Co-3Mo-4.7Ti-5.5Al-0.9V-0.18C
3. MAR-M509	0.320	Co-23.5Cr-10Ni-7.0W-3.5Ta-0.2Ti-0.5Zr-0.6C
4. MA 754	0.300	Ni-20Cr-0.5Ti-0.3Al-0.6Y_2O_3-0.05C
5. TZM	0.368	Mo-0.5Ti-0.08Zr-0.02C

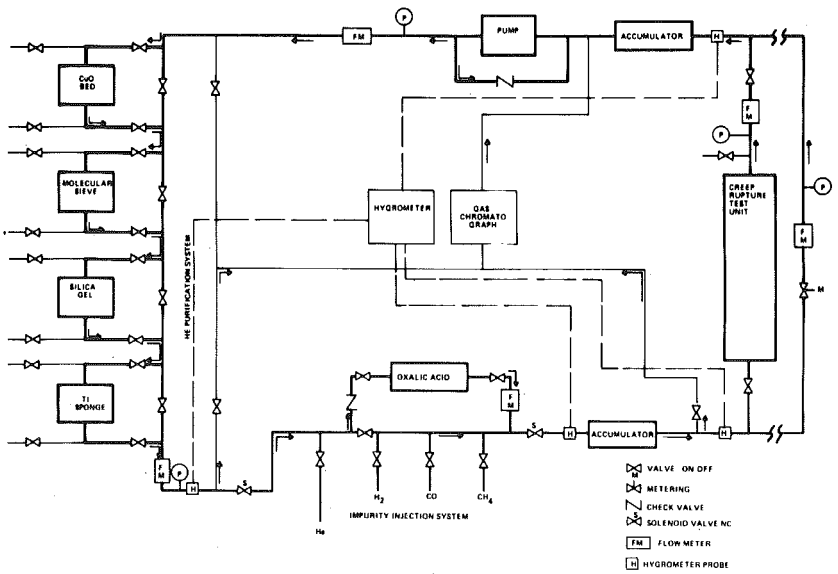

Fig. 2 Schematic of CCCBS helium supply system

Table 3 Chemical analysis of test material* (percent)

ALLOY	HEAT NO.	C	Mn	P	S	Si	Ni	Cr	Mo	Co	Fe	Ti	Al	B	Zr	Other
713LC	B553	.06	<.1	<.01	.003	<.1	bal.	11.4	4.0	.1	.05	.6	5.75	.015	.13	Cu-.04; Cb-1.99
IN 100	B747	.16	<.01	-	.004	.01	bal.	8.9	3.0	14.1	.2	.91	4.75	5.44	.001	V-.91
MAR-M509	B716	.621	.042	<.005	.005	.058	10.51	23.39	-	bal.	.408	.205	-	.0073	.467	Ta-3.47; W-7.24
MA 754**	DT0074B2-2	.02	-	-	-	-	bal.	20.00	-	-	-	.44	.3	-	-	Y_2O_3-.6
TZM	7502	.01	-	-	-	-	-	-	bal.	-	-	.5	-	-	.1	O_2-.002; N_2-.01; H_2 - .001

* Certified analysis by supplier.

** Typical analysis.

Alloy 713LC, IN 100, and MAR-M509 supplied by Jet Shapes, Inc., MA 754 by INCO, and TZM by AMAX.

been used extensively in gas turbine applications over the past 10 to 15 yr. Their history of metallurgical development and mechanical behavior is well documented. Thermal stability as determined by microstructural behavior on thermal exposure at elevated temperature is also well known and recorded. Alloy 713LC is one of a few nickel-base superalloys which does not contain cobalt as an intentional alloying addition. IN100 is a "workhorse" turbine blade material designed to have a relatively low density combined with excellent creep resistance up to 1038°C (1900°F). The alloy has been successfully cast and utilized in a variety of shapes from turbine blades, vanes, and nozzles to integral wheels. Cobalt alloys are generally used as vanes, nozzles and other static hot structures because of their excellent hot corrosion (sulfidization) resistance. Cobalt alloys however, are not generally used for rotating parts due to their lower creep and oxidation resistance compared to nickel-base alloys. MAR-M509 has good creep strength, resistance to thermal stressing, and resistance to crack propagation. It can be successfully welded and joined both to itself and to many dissimilar metals by conventional techniques.

MA754 is a recently developed nickel-chromium alloy produced by mechanical alloying which uniformly disperses yttrium oxide for dispersion strengthening at temperatures to the alloy is melting point. MA754 exhibits excellent stress-rupture properties which are equivalent to or superior to cast alloys. MA754 is currently being used as vanes in gas-turbine engines where high temperature strength is required. The superior creep-rupture properties of MA754 provides high temperature growth potential for CCCBS turbine components.

TZM, a molybdenum-base alloy, is a refractory metal alloy which has demonstrated compatibility with inert gases at elevated temperatures and has superior creep strength at 982°C (1800°F) and above. TZM provides system growth to higher temperature capability.

Alloy 713LC, IN100 and MAR-M509 were obtained as "as-cast" creep specimens from Jet Shapes, Inc., of Rockleigh, N. J. Alloy 713LC was purchased according to a Westinghouse specification, since no formal published specification for the alloy could be found in open literature. The specification was modeled after AMS 5391 for alloy 713C. The only difference being a lower carbon level, 0.05 percent for the LC version vs. 0.12 percent for the "C" alloy designation. IN100 specimens were cast according to AMS 5397 and MAR-M509 to a Pratt and Whitney specification, PWA 647E. Cast specimens were examined by x-ray analysis to insure sound porosity-free gage sections.

MA754 test material was procured from Huntington Alloys as solution annealed bar stock 8.9 cm × 3.2 cm × 12.7 cm (3½ in. × 1¼ in. by 5 in. long). No specification exists at this time for this material. A Huntington data sheet supplied with the material indicated the solution annealing heat treatment to be ½ hour at 1316°C (2400°F) followed by air cooling.

The TZM test specimens were machined from forged and stress relieved material which was part of a NASA sponsored creep test program. Processing information and chemical analysis were supplied by TRW, Cleveland, Ohio, the contractor to NASA [15]. The TZM alloy was obtained from Climax Molybdenum of Michigan (now AMAX) in the form of 27.9 cm (11 in.) dia disk forging. The material was vacuum arc-melted to 29.2 cm (11½ in.) dia ingot, extruded to a

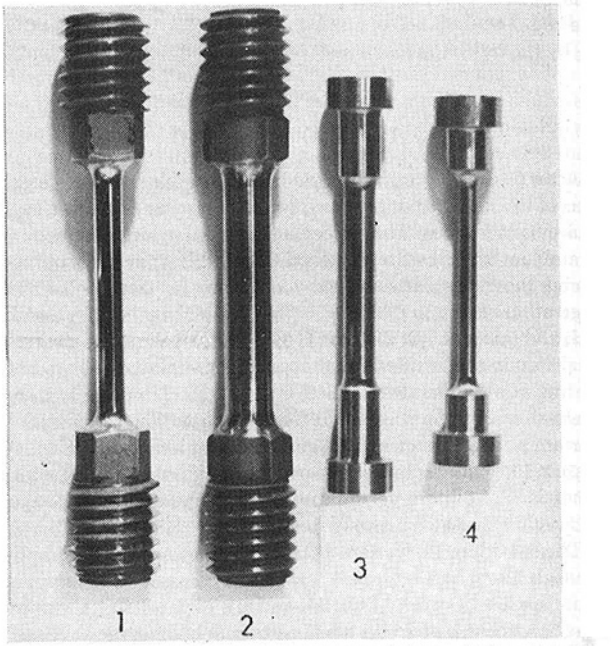

Fig. 3 Photographs of creep-rupture specimens: (1) Ultra-high purity helium test specimen for ascast Alloy 713LC, IN100 and MAR-M509 material. (2) Air test specimens for as-cast alloy 713LC, IN100 and MAR-M509. (3) MA 754 creep-rupture test specimen. (4) TZM creep-rupture test specimen.

15.9 cm (6¼ in.) dia then upset forged to final size at 1204°C (2200°F) after heating to 1482°C (2700°F). The material was then stress relieved one hour at 1482°C (2700°F). Creep specimens were cut in a radial direction from the forged disk with the gage section parallel to the wrought microstructure. Chemical analyses of the test materials are given in Table 3.

Test Specimen Geometry

The creep-rupture test specimen geometries, which were used, are shown in Fig. 3. The cast materials, Alloy 713LC, IN100 and MAR-M509, were received as cast-to-size specimens. The specimens had a nominal 0.64 cm (¼ in.) dia gage section 3.2 cm (1¼ in.) long with ½-13 threaded ends. The as-cast specimens were machined to produce a round, uniform diameter along the gage length as shown by specimen 2 in Fig. 3. These specimens were used for the air tests because the cross-sectional area was compatible with the load capacity of the lever arm test machines. For the dead-weight loaded tests in ultra-high purity helium, the cross-sectional area of the gage section was reduced to a diameter of 4 mm (0.160 in.) as illustrated by specimen 1 in Fig. 3. The gage diameter for each material was adjusted to accommodate the physical volume of the load required to achieve the desired stress levels and remain within the equipment limitations. Double shoulder-type creep specimens with differing gage diameters were used for the MA754 and TZM materials as shown by specimens 3 and 4 in Fig. 3. The MA754 specimen gage diameter was 4.6 mm (0.180 in.), and the TZM specimen diameter was 2.5 mm (0.1 in.).

Creep-Rupture Test Results and Evaluation

Creep-rupture testing of five selected turbine materials was conducted in ultra-high purity helium and simulated CCCBS helium working fluid environment. Supplementary creep-rupture tests were

Table 4 Creep-rupture data for selected CCCBS materials at 930°C (1700°F)

Material	Test Atmos.	Stress (MPa)	Stress (ksi)	Time to % Strain (Hours) 0.5%	1.0%	3.0%	Total Strain (%)	Rupture Time (Hrs)	Reduction in Area (%)
Alloy 713LC	UHP He	138	(20.0)	84	192	268	6.4	269	16.7
		138	(20.0)	260	495	691	8.0	755	22.0
		124	(18.0)	128	943	1522	4.8	1527	8.4
		103	(15.0)	1060	2500	3150	5.6	3182	10.2
	Air	138	(20.0)	212	395	572	9.6	623	25.8
		138	(20.0)	8	86	324	10.4	397	8.7
		124	(18.0)	29	119	405	9.6	476	8.3
		103	(15.0)	100	740	1870	5.6	1959	8.1
	CCCBS*	117	(17.0)	575	820	1130	8.0	1268	26.8
IN 100	UHP He	155	(22.5)	700	1170	1982	16.0	2272	17.6
		124	(18.0)	1217	-	-	-	1448	- (1)
		110	(16.0)	3000	4300	7950	10.4	9452	34.5
	Air	207	(30.0)	8	70	211	6.4	271	6.7
		207	(30.0)	22	93	285	7.2	334	8.5
		172	(25.0)	1	7	490	7.2	685	4.3
		155	(22.5)	110	550	1130	7.2	1347	6.0
		124	(18.0)	1460	2890	2985	7.2	3110	12.1
		110	(16.0)	200	3800	4900	8.0	5244	16.1
	CCCBS*	124	(18.0)	1550	2000	2810	7.2	3338	23.7
		110	(16.0)	-	-	-	-	1316	- (1)
		110	(16.0)	1000	2650	3920	13.5	6304	24.2
MAR M509	UHP He	103	(15.0)	2350	2440	2460	4.0	2537	0.1
		86	(12.5)	1900	5050	7900	12.8	11615	44.4
	Air	124	(18.0)	2	5	264	21.6	618	34.1
		103	(15.0)	1	570	1910	16.8	2507	19.6
		86	(12.5)	5	25	2750	7.2	4652	0.9
MA 754	UHP He	152	(22.0)	-	-	-	-	8751	- (1)
		138	(20.0)	-	-	-	-	17626	- (3)
	Air	152	(22.0)	-	-	-	-	2100	- (2)
		138	(20.0)	70	3480	15440	12.0	15712	10.4
	CCCBS*	165	(24.0)	20	100	230	5.0	289	9.2
		155	(22.5)	40	110	636	3.0	636	7.6
		155	(22.5)	100	600	1445	4.0	1445	1.9
		152	(22.0)	1	500	2640	4.4	2660	9.4
TZM	UHP He	414	(60.0)	220	425	1095	12.0	1483	98.0
		379	(55.0)	450	1010	2000	14.5	2256	98.0
		362	(52.5)	790	2000	5200	10.2	5592	76.0
		331	(48.0)	1850	4650	-	-	7818	-

*Simulated CCCBS He Working Fluid, 400 to 500 μ atmos. H_2, 40 to 50 μ atmos. CH_4, 40 to 50 μ atmos. CO, 1 to 3 μ atmos. H_2O, CO_2 equilibrium levels.

1 Temperature Controller Malfunctioned
2 Specimen Failed in Grips
3 Test Stopped

also conducted in static air for alloy 713LC, IN100, MAR-M509 and MA754. The test data generated are listed in Table 4. A total of 40,035 hr were accumulated in air, 76,583 hr in ultra-high purity helium, and 11,350 hr in a dynamic simulated CCCBS helium working fluid. Termination of the program by the customer prevented completion of the tests involving the dynamic stimulated CCCBS helium working fluid environment. Test results for each alloy are described and evaluated individually in the following discussions.

Alloy 713LC. Four creep-rupture tests of Alloy 713LC were conducted in ultra-high purity helium for a total of 5733 test hours. Test times ranged in duration from 269 to 3182 hr. Four air tests at corresponding stress levels were also conducted. One test in the dynamic simulated CCCBS environment was conducted at a stress of 117 MPa (17 ksi). The test results, rupture life versus stress level, are plotted in Fig. 4. In order to provide a basis for comparison, a computer printout of creep-rupture data for Alloy 713LC was obtained from the Mechanical Property Data Center (MPDC), Traverse City, Michigan. The MPDC is a DOD supported materials information center. The Alloy 713LC printout contained data for 831 creep-rupture tests, which were carried out in air in the temperature range 732 to 1204°C (1350 to 2200°F). The data were gathered from Government-sponsored programs. Of the 831 creep-rupture test results reported, 507 were carried out at 982°C (1800°F) at a stress level of 152 MPa (22 ksi). These test conditions are apparently used for heat qualification. Only three tests of >10,000 hr were reported, and they were conducted at 816°C (1500°F) or lower. Sixteen creep-rupture tests of greater than 1000 hr were reported. The data illustrate the dearth of long-term high temperature creep-rupture data available in the open literature for a widely used, relatively old, commercial superalloy.

The solid reference curve in Fig. 4 was generated from a Larson-Miller plot of the MPDC data. Logarithmic curve fit and linear regression analysis were used to produce a best-fit curve for 61 data points representing the rupture life of Alloy 713LC in the stress range 86 to 207 MPa (12.5 to 30 ksi) and test temperatures in the range 871 to 982°C (1600 to 1800°F). The air, UHP-He, and the CCCBS environment test data for material evaluated on this program compare favorably with the reference curve. At the 138 MPa (20 ksi) stress level, four tests were conducted, two under each environmental condition. The test results for both conditions, however, fall within a reasonable scatter band. Insufficient test data prevent definitive conclusions to be drawn, although a trend to improved rupture life of Alloy 713LC in UHP-He appears as a possibility. Additional tests preferably at times of 10,000 hr or longer, are required to definitely establish the validity of the observed trend. The one simulated CCCBS helium working fluid environmental test had a rupture life of 1268 hr at a stress level of 117 MPa (17 ksi). This data point fell on the reference curve.

One additional comment regarding the stress-rupture behavior of Alloy 713LC relevant to CCCBS requirements involves the projected stress required to give a 10,000 hr rupture life. Initial data published by INCO in which a limited number of rupture tests of less than 3500 hr, indicated an extrapolated rupture life of 10,000 hr at a stress of slightly higher than 103 MPa (15 ksi) at 927°C (1700°F) [16]. Data from MPDC involving many more test results indicate that the extrapolated 10,000 hr rupture life may be closer to 83 MPa (12 ksi) at 927°C (1700°F).

Alloy IN100. A total of ten IN100 creep-rupture tests were completed including six in air, two in UHP-He, and two in CCCBS helium working fluid environment. The rupture life data are given in Fig. 5. The reference curve was generated from a Larson-Miller plot of data received from the Mechanical Property Data Center. As pointed out in the discussion of Alloy 713LC, the number of long-term tests conducted at temperatures above 871°C (1600°F) was very limited. Of the 473 reported test results, only 22 tests of greater than 1000 hr were reported. There were no test results in the 871 to 982°C (1600 to 1800°F) test temperature range greater than 4700 hr. A total of 52 data points were used to develop a Larson-Miller curve from which the

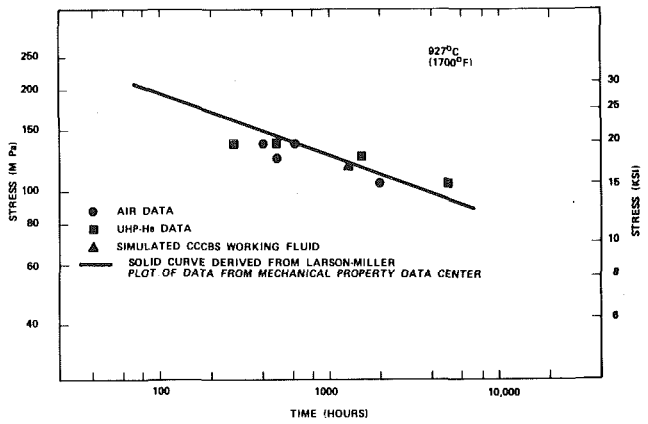

Fig. 4 Creep-rupture life of alloy 713LC

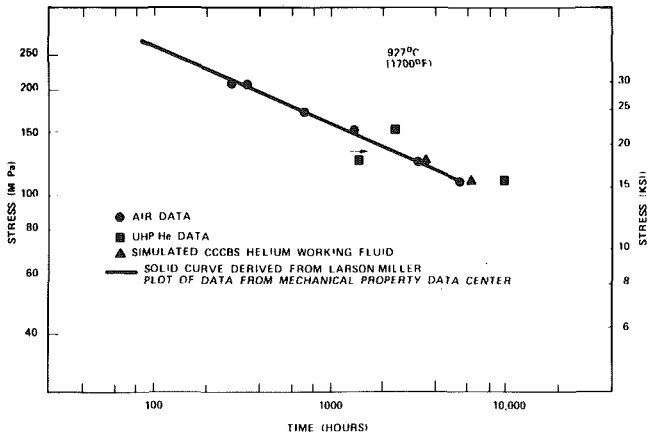

Fig. 5 Creep-rupture life of as-cast IN100

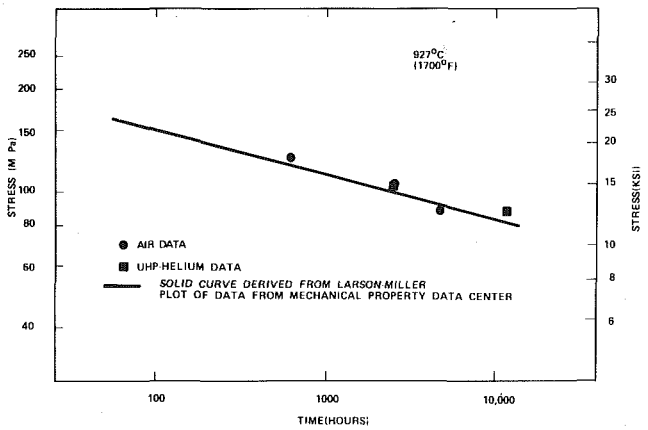

Fig. 6 Creep rupture life of as-cast MAR-M-509

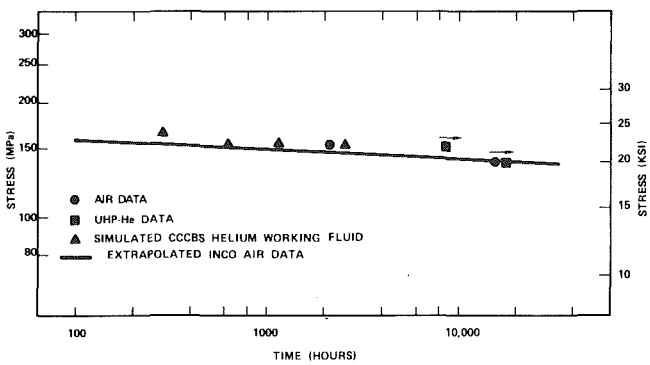

Fig. 7 Creep-rupture life of MA754

reference curve in Fig. 5 was produced. The air data show excellent correlation with the reference data. The two tests carried out under UHP-He environment conditions displayed rupture life values which were significantly greater than the reference air data. The third test which was not completed was approaching the air data curve. From the amount of strain (<1.0 percent) accumulated at the time of controller malfunction, it appears that this test would have achieved a comparable rupture life. The two tests carried out in the CCCBS environment had rupture life values comparable to the air data. Although the data are meager, Alloy IN100 appears not to be deleteriously affected by the change in test environment.

It should be noted that the reference curve in Fig. 5 derived from MPDC data varies from other published data regarding the expected stress to produce 10,000 hr rupture life at 927°C (1700°F) [17]. The extrapolated stress to produce a 10,000 hr rupture life at 927°C (1700°F) is reported to be approximately 83 MPa (12 ksi).

Alloy MAR-M509. A total of five creep-rupture tests of Alloy MAR-M509 were conducted, three in air and two in UHP-He. All tests were completed, and the data are shown in Fig. 6. The reference curve was produced from MPDC data and represented 90 creep-rupture tests in the temperature range 871 to 1093°C (1600 to 2000°F). The longest test time reported was 3200 hr at 982°C (1800°F) at 70 MPa (10 ksi). The remainder of the reported tests were carried out at higher stress levels for test times of less than 800 hr in duration. Both the air and ultra-high purity helium data for this particular heat of MAR-M509 compared quite well with the MPDC derived curve. Rupture life values for both ultra-high purity helium tests were slightly greater than the air data curve. While the limited data preclude conclusive proof as to the beneficial influence of UHP-He test environment over air, it can be stated that the UHP-He test environment does not produce a gross deleterious effect on the creep-rupture behavior of MAR-M509. MAR-M509 was not tested in the dynamic simulated CCCBS helium working fluid environment.

Alloy MA754. A total of eight creep-rupture tests of MA754 were conducted, two in air, two in UHP-He, and four in simulated CCCBS helium working fluid. The creep-rupture life data are given in Fig. 7. The reference curve was produced from rupture life data at 1093°C (2000°F) published by INCO [18]. A Larson-Miller plot of the INCO data was used to obtain the reference curve in Fig. 7. Air tests were conducted at 152 and 138 MPa (22 and 20 ksi) stress levels. The 152 MPa (22 ksi) failed in the threaded portion of the specimen after 2100 hr while the 138 MPa (20 ksi) test failed after 15,712 hr. Both air test results agreed quite well with the reference curve. The two UHP-He tests were conducted at the same stress level.

The test at 152 MPa (22 ksi) was halted by a malfunctioning controller which overtemperatured the specimen after 8751 hr. The test at 138 MPa (20 ksi) was stopped after 17,626 hr. Both specimens when halted exhibited no measurable strain. The 138 MPa (20 ksi) air test failed with 12 percent fracture strain and also produced three percent strain after 15,440 hr and 1.0 percent strain after 3480 hr. A potential effect of test environment is indicated. Four tests were conducted in the dynamic simulated CCCBS helium working fluid environment at stress ranging from 152 to 165 MPa (22 to 24 ksi). While recognizing the short time duration of the CCCBS environmental creep-rupture tests, there appears to be no gross deleterious influence of the CCCBS test environment on the creep-rupture life of MA754 for those tests that were completed.

Alloy TZM. A total of four TZM creep-rupture tests were conducted. Three were completed and the fourth was stopped after 7818 hr. The creep-rupture life test data are given in Fig. 8. The reference curve in Fig. 8 was produced by the extrapolation of shorter term test results for stress relieved TZM generated at higher stress levels and temperatures under ultra-high vacuum test conditions [19]. Tests of TZM were not conducted in air due to the incompatibility of molybdenum with oxygen at temperatures above 300°C (600°F). The UHP-He test results show good agreement with the reference curve, indicating that the UHP-He test environment was comparable to an ultra-high vacuum of 1×10^{-8} torr or better. TZM was not tested in the dynamic simulated CCCBS helium working fluid environment.

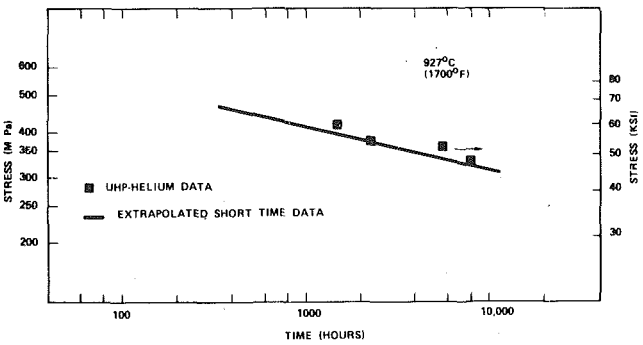

Fig. 8 Creep-rupture life of stress relieved TZM

Summary of Results

- Creep-rupture data obtained from the Mechanical Property Data Center for the three relatively standard gas turbine superalloys, 713LC, IN100 and MAR-M509, confirmed the dearth of published creep-rupture data that exists for materials at temperatures above 871°C (1600°F) and for test times greater than 1000 hr.
- The air test data at 927°C (1700°F) for Alloys 713LC, IN100 and MAR-M509 indicate that the materials evaluated in this program were typical of commercially available heats of the respective alloys. Air test data for MA754 appeared to agree with the limited available data supplied by the producer of the alloy.
- The ultra-high purity helium environmental creep-rupture test results indicated that all five materials were not adversely affected by the ultra-high purity helium test environment. Creep-rupture life times at 927°C (1700°F) were comparable to or exceeded life times for material tested in air. The TZM alloy being a refractory metal alloy was not tested in air due to reactivity with oxygen. TZM creep-rupture life data were comparable to extrapolated data obtained under ultra-high vacuum test conditions.
- Limited creep-rupture data obtained in a dynamic simulated helium working fluid containing 400 to 500 micro-atmospheres hydrogen, 40–50 micro-atmospheres carbon dioxide, 40–50 microatmospheres methane and 1 to 3 micro-atmospheres moistures, at a test temperature of 927°C (1700°F) for three alloys, 713LC, IN100 and MA754, indicated no effect of the test environment on material rupture life for times up to 4000 hr.

Acknowledgment

The work reported in this paper was conducted as part of a compact closed cycle Brayton system feasibility study sponsored by the Office of Naval Research under Contract N00014-76-C-0706.

References

1 Thompson, R. E., et al., "Compact Closed Cycle Brayton System Feasibility Study," WAES-TNR-237, Final Report to be released.

2 Wall, F. J., "Metallurgical Development for 1500°F MGCR Gas Turbine Maritime Gas-Cooled Reactor," Project Engineering Report, EC-193, Feb. 1964.

3 Wall, F. J., "Final Metallurgical Report of 1300°F MGCR Gas Turbine Maritime Gas-Cooled Reactor," Project Engineering Report, GTM-123, Apr. 1961.

4 Chaku, P. N., and McMahon, C. J., Jr., "The Effect of an Air Environment on the Creep and Rupture Behavior of a Nickel-Base High Temperature Alloy," *Metallurgical Transactions*, Vol. 5, No. 2, Feb. 1974, p. 441.

5 Widmer, R., and Grant, N. J., "The Role of Atmosphere in the Creep-Rupture Behavior of 80 Ni-20 Cr Alloys," ASME, *Journal of Basic Engineering*, Dec. 1960, p. 882.

6 Shahinian, P., and Acheter, M. R., "Temperature and Stress Dependence of the Atmosphere Effect on a Nickel-Chromium Alloy, *Transactions ASM 51*, 1959, p. 244.

7 Shahinian, P., "Effect of Environment on Creep-Rupture Properties of Some Commercial Alloys," *Transactions ASM 49*, 1957, p. 862.

8 Buckman, R. W., Jr., and Heatherington, J. S., "Apparatus for Determining Creep Behavior Under Conditions of Ultra-High Vacuum," *The Review of Scientific Instruments*, Vol. 37, No. 8, Aug. 1966.

9 Hickman, W. M., *Proceedings of the 9th Annual Conference of Mass Spectrometry*, ASTM Committee E-14, Chicago, Illinois, 1966.

10 Hickan, W. M., "Cryogenics Applied to Mass Spectrometric Trace Gas Analysis," *Analytical Chemistry*, Vol. 45, Feb. 1973, p. 315.

11 "Advanced Gas Cooled Nuclear Reactor Materials Evaluation and Development Program," DOE Contract EY-76-C-02-2975 A002, General Electric Co., Energy Systems Program Dept., Schenectady, NY.

12 Graham, L. W., et al., "Environmental Conditions in HTRS and the Selection and Development of Primary Circuit Materials," *International Symposium on Gas-Cooled Reactors with Emphasis on Advanced Systems*, Julich, Federal Republic of Germany, Oct. 1975.

13 Kondo, T., *Annual Review of the High Temperature Metals Research for VHTR at JAERI*, Jan. 1977.

14 Schuster, H., and Jakobeit, W., "High Temperature Alloys for Power Conversion Loops of Advanced HTRS," International Symposium on Gas-Cooled Reactors with Emphasis on Advanced Systems, Julich, Fed. Rep. of Germany, Oct. 1975.

15 Sawyers, J. C., and Stiegerwald, E. A., "Generation of Long Time Creep Data on Refractory Alloys at Elevated Temperatures," Final Report NASA Contract NAS3-2545, June 1967, TRW, Cleveland, Ohio.

16 INCO Data Brochure, "Alloy 713LC—Low Carbon Alloy 713C, Preliminary Data," 1M6-68-4290, July 1964.

17 INCO Data Brochure, "Engineering Properties of IN100 Alloy," 2M9-69-5073.

18 Huntington Alloys Data Sheet, "Inconel Alloy MA754," 3M-9-75S-51.

19 Salley, R. L., and Kovacevick, E. A., "Materials Investigation, SNAP 50/SPUR Program, Creep-Rupture Properties of Stress Relieved TZM Alloy," APL-TDR-64-116, Part 1, Oct. 1964, Garrett Corporation, AiResearch Manufacturing Division.

W. S. Y. Hung[1]
Mem. ASME

W. H. Dickson
Assoc. Mem. ASME

S. M. DeCorso
Mem. ASME

Combustion Turbine Systems Division,
Westinghouse Electric Corporation,
P.O. Box 251
Concordville, PA 19331

Preliminary Design Analysis of a Catalytic Ceramic Structure in a Turbine Combustor

Analysis and design of a catalytic ceramic element and its support structure in a turbine combustor for low emission application have been performed. Preliminary analysis including a survey of literature has helped identify certain design considerations and conceptual designs of the catalytic ceramic element. A thermo-mechanical analysis of the major components in these conceptual designs has been performed for both steady-state and transient (shut-down) situations. Consequently, an arrangement to build a viable catalytic ceramic combustor element has been identified which is expected to perform its mechanical functions.

Introduction

Based upon evolving conditions within the marketplace, there is sufficient reason to proceed with development of a low-emission, high performance combustion turbine to meet future needs. For instance, air quality requirements are in the process of being regulated on federal, state and local levels. In particular, Southern California has enacted rules to limit emissions for stationary power sources and the U.S. Environmental Protection Agency (EPA) has proposed emission regulations for stationary gas turbines with particular emphasis on the levels of nitrogen oxides. These constraints are occurring at a time when energy conservation is motivating a move towards higher performance through improved combustion. The use of catalytic materials has the potential to satisfy the need for a low emission, high performance combustion system.

In the development of a catalytic combustor for large industrial combustion turbine applications, the problems relating to the design of the full size catalytic element and its support structures have to be identified and solved. At this stage of the development, it is necessary to perform the conceptual design of the full size catalytic element and its supporting metal structure. Then thermal, mechanical, and stress analyses must be made to determine its expected structural performance in the combustion turbine transient and steady-state operating environment.

The objectives of this study are to establish a conceptual reference design arrangement for a catalytic ceramic combustor element to be used in large industrial combustion turbines for low emission application and to evaluate the catalytic reactor structural performance through thermal and mechanical analyses of the catalytic ceramic elements and supporting metal structures over the operating range of the combustion turbine.

Background

The historical background leading to the development of the catalytic combustor in its present form has been reviewed in a recent paper [1]. A major breakthrough (CATATHERMAL reaction) in the catalytic combustion concept (2) and the increasing need of a clean, energy-efficient combustion system paved the way that leads to the recent increase in activity in catalytic combustor development.

The potential of the catalytic combustor to be a low emission, energy-saving and high combustion efficiency system for combustion turbines has been demonstrated in small scale laboratory tests [3–7]. These preliminary results were encouraging and led to additional laboratory testing [8–12], development [13–14] and analytical [15–17] efforts. From a review of the open literature, it is evident that while increased efforts in catalytic combustor development have already taken place, experimental work has been limited to small scale testing in the laboratory and considerably more development is needed before a production catalytic turbine combustor can be realized.

A typical catalytic element employs a monolithic structure or substrate made up of a ceramic cylinder in which many small parallel channels are formed. These parallel channels or cells can be made in a variety of shapes and sizes. In order to provide a uniform high surface area, a thin oxide layer or washcoat such as alumina (Al_2O_3) is normally applied to the substrate. The catalytic material is then impregnated on the washcoat to insure its exposure to the main flow of reactants. The substrate is generally supported inside a tubular metallic housing which also serves the function of guiding the flow of reactants in and products out of the catalytic reactor.

It has been pointed out in [1] that the catalytic combustor is basically a device to burn mixtures of air and vaporized fuel. The mechanisms that occur in the catalytic reactor have been discussed in references [5, 18]. The reactants diffuse to the catalyst and at least one of the reactants must be absorbed. Oxidation reactions take place at the catalyst surface. Desorption and diffusion of the products into the bulk flow then follow. The temperature of the fuel-air mixture in the bulk flow is increased as it flows down the catalytic reactor through the transport of thermal energy from the surface reactions. At a critical temperature of about 1000°C [1], homogeneous gas phase reactions take place. This catalytically supported thermal combustion process is the key in achieving high combustion efficiency and low emissions.

The primary variable that influences the generation of thermal NO_x is the peak temperature at which nitrogen and oxygen co-exist. In a

[1] Presently at Solar Turbines Int., 2200 Pacific Highway, San Diego, Ca. 92138.

Contributed by the Gas Turbine Division and presented at the Winter Annual Meetings, December 10–15, 1978, San Francisco, California, of THE AMERICAN SOCIETY OF MECHANICAL ENGINEERS. Manuscript received at ASME Headquarters August 24, 1978. Paper No. 78-WA/GT-10.

conventional combustor where there is a diffusion flame, this peak temperature, at which NO_x is formed, as in the order of the flame temperature [19]. In mixing the cold dilution air with the hot combustion products to achieve a temperature below the threshold temperature of significant NO_x production (say 1600°C), a definite mixing time is required and significant NO_x can be generated in this post-combustion, pre-quenched time interval. In the catalytic combustor on the other hand, the equivalence ratio of the fuel-air mixture entering the reactor can be maintained at sufficiently low level that the peak temperature in the reactor never exceeds this threshold temperature of 1600°C. Consequently, no significant thermal NO_x can be generated in a catalytic combustor.

In order to provide a fairly-uniform, highly-vaporized fuel-air mixture for the catalytic reactor, the design of a satisfactory fuel/air carburetion system is essential. In the laboratory tests conducted so far, idealized fuel preparation systems have been used. For industrial combustion turbine applications, the ability to design a satisfactory fuel preparation system is limited on the one hand by the available space and the operating compressor discharge temperature, and on the other hand, by the autoignition characteristics of the fuel which provides a time limit for the vaporization and mixing processes.

Experimental evaluation of the autoignition characteristics of No. 2 fuel oil and JP4 in a moving airstream has been reported in [20]. Using these data, a semi-empirical equation has been developed in [21]. At any given combustor inlet air temperature and pressure, one can determine from this correlation equation the autoignition time. In order to avoid autoignition, the residence time in the fuel preparation system should be kept at a level below the autoignition time.

In the design of catalytic elements, the space velocity is a parameter that needs to be considered. The space velocity is the inverse of the contact time defined by the length of the catalytic element divided by the reference velocity, which is defined as the ratio of the volume flow rate based on combustion inlet conditions to the total area of inlet face of catalytic element. The time available for catalytic reaction varies inversely as the space velocity. For a given length of a catalytic element, the space velocity or contact time is a function of the reference velocity and the relationship has been plotted as shown in Fig. 1. In order to meet a given space velocity requirement, one can determine from Fig. 1 the minimum length of catalytic element required for any design reference velocity.

Another area of design is the pressure loss of the catalytic combustor. The percent pressure loss across a 7 in. (178 mm) catalytic element as a function of the reference velocity has been measured and plotted, as shown in Fig. 2 [7]. These results indicate that the pressure loss is proportional to the reference velocity raised to the power of 1.6. This is in good agreement with results reported in [10]. It can be observed from Fig. 2 that in order to minimize the pressure loss across a given catalytic element the reference velocity has to be kept at a low level. For industrial combustion turbine applications, the minimum reference velocity is likely to be limited by the space available. Hence, in selecting the size of a catalytic element, one has to take into consideration the requirements for space velocity, reference velocity and pressure loss.

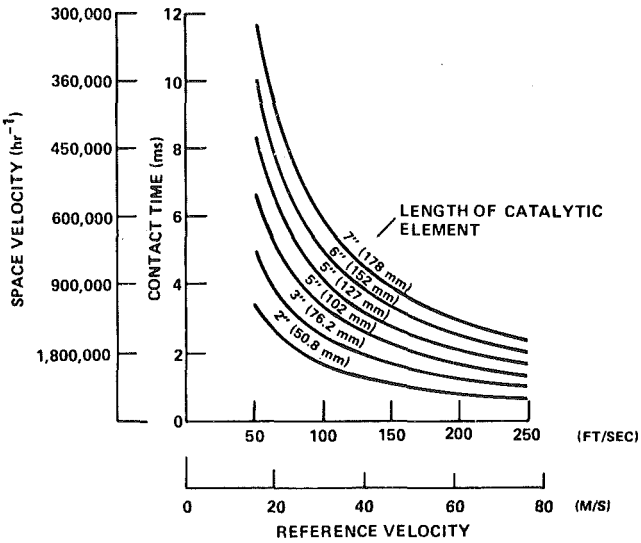

Fig. 1 Space velocity or contact time in catalytic elements as a function of reference velocity

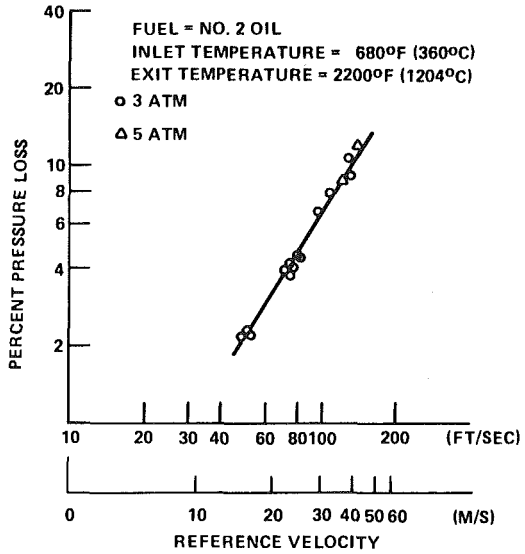

Fig. 2 Pressure loss as a function of reference velocity for a 7 in. catalytic element

Conceptual Design

Total Combustion System. Based on the small scale test experience in the past [7], a conceptual design arrangement of a catalytic combustor in an industrial combustion turbine has been envisioned as shown in Fig. 3. In this conceptual design, multiple fuel nozzles are used to provide direct fuel injection just upstream of the fuel preparation zone. The conventional fuel nozzle has the dual function of allowing the startup of the turbine and providing control of the preheat temperature to the fuel preparation zone downstream. Ideally, this conventional nozzle should produce a short and uniform-temperature flame in order to avoid preignition of the fuel injected through the multiple fuel nozzles. Fine sprays are to be produced by these multiple fuel nozzles such that significant amounts of the liquid fuel will be vaporized in the fuel preparation zone without causing autoignition. Adequate mixing in the fuel preparation zone should

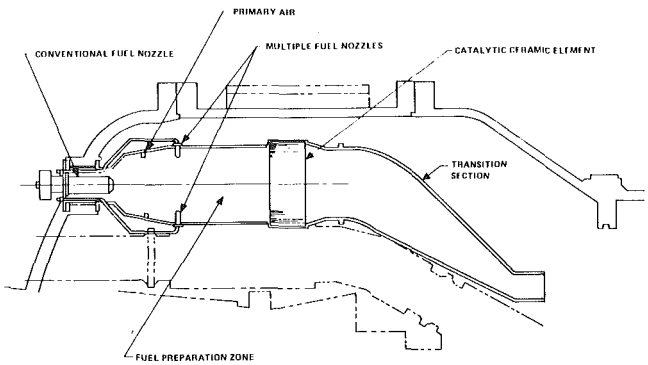

Fig. 3 A conceptual design arrangement of a catalytic ceramic element in an industrial combustion turbine

also be provided to produce a fairly uniform fuel-air mixture prior to entering the catalytic element.

The catalytic element should be sized to provide sufficient contact time for good combustion efficiency and its length should be short to minimize the pressure drop to an acceptable level. Preliminary analyses have indicated that the diameter of the catalytic ceramic element is expected to be larger than that of a conventional combustor currently in production. Downstream of the catalytic element, the reacted products are mixed with dilution air in a transition section which leads to the turbine inlet.

Catalytic Ceramic Element. From a preliminary analysis of the available information on contact time, reference velocity, pressure loss, combustor operating conditions and space limitation, including a consideration of the structural integrity, a 7 in. (178 mm) length by 15 in. (381 mm) dia ceramic substrate has been selected for the present study.

The substrate is to be supported by a metallic cylinder. Preliminary analyses have shown that, if unprotected, the metal cylinder will reach temperature higher than those allowed for the materials currently used. Hence, an intermediate layer between the substrate and the support metal cylinder is required to provide cooling and/or insulation. Further analysis showed that the difference in thermal growth between the ceramic substrate and the metallic cylinder was sufficiently large that some provision must be included in the design to absorb these movements and to hold the substrate.

The recommended conceptual design utilizes an air-cooled coiled wire to provide the flexibility and conformity as shown in Fig. 4. The coil is compressed in assembly. A layer of castable ceramic on the outer cylindrical surface of the substrate is required to provide a smooth surface for contact with the coil and to act as a thermal barrier. In the design, two outer layers of cells in the substrate has been made inactive to provide the desired temperature gradient and structural stiffness. Two rows of corrugations have been incorporated in the design to provide film cooling air to the conical and cylindrical portions of the support structure downstream of the ceramic substrate as shown in Fig. 4. A conceptual method of providing cooling air to the coil wire is illustrated in Fig. 5. The coil cooling air is metered through holes in the metal cylinder. It flows upstream and meets the main flow at the inlet to the ceramic substrate. This design feature is to prevent any fuel-air mixture from reaching the coil wire.

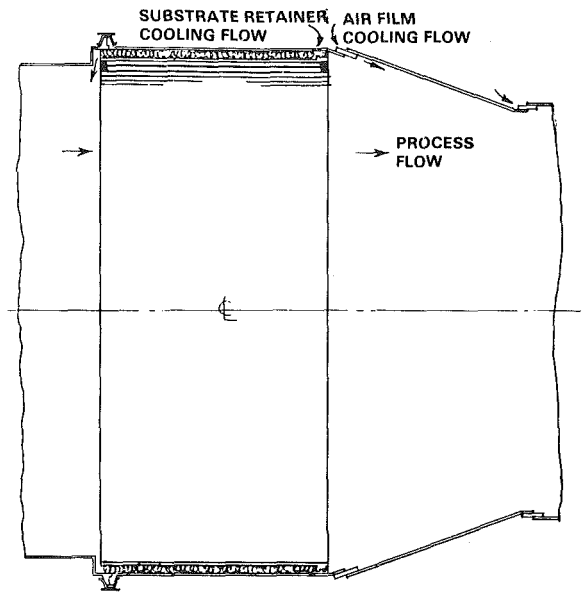

Fig. 4 A conceptual design with film cooling of metal support structure

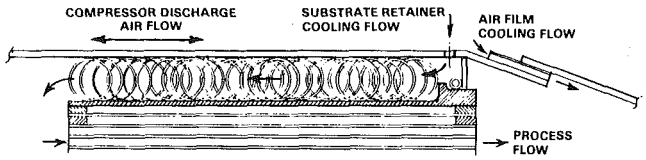

Fig. 5 A conceptual coil wire design with cooling

Thermo-Mechanical Analysis

The thermo-mechanical analysis was performed for both the steady-state and the transient conditions. One dimensional analogs are utilized in the preliminary steady-state analysis to allow a quick evaluation of the mechanical performance of the catalytic element. The analysis was extended to consider the transient condition in order to determine the effects of different loading on the structural components over the entire operating cycle. The effects of two dimensionality was introduced in the transient solution which also included the steady-state case.

Steady-State Analysis. In performing the analysis, the catalytic element is divided into its three components: the ceramic substrate, its metal support cylinder and an intermediate compliant layer between them.

Substrate. Since the conceptual design of the total combustion system is still preliminary at this stage, it is sufficient to select a typical material for analysis. A survey shows that cordierite ($2\,MgO{\cdot}2Al_2O_3{\cdot}5\,SiO_2$) is the substrate material used in catalytic converters on automobiles. Most of its material properties are readily available. On this basis, it was selected as the substrate material in the present study.

The ceramic material when used as a support for catalyst takes the form of cellular tubes. It follows that the bulk mechanical properties will depend on such features as cell shape, cell size, cell wall thickness and manufacturing techniques in addition to the mechanical properties due to the pure material. For instance, depending upon cell count, proportions and load direction, the allowable compressive loading on one square inch of bulk surface of the substrate profile varies considerably [22].

Cordierite has the capability to withstand thermal shock due to its very low coefficient of thermal expansion [22] and a low modulus of elasticity, $4 - 18 \times 10^6$ psi ($28 - 124$ G Pa) depending upon porosity [23]. According to [22], it can also withstand continuous duties at temperatures of 1350°C (2462°F) and transients as high as 1500°C (2738°F).

For the present analysis, a uniform temperature of 750°F at the inlet and a nominal temperature of 2300°F (1260°C) at the exit of the reactor are assumed. The temperature rise from inlet to discharge is considered linear. An analysis of the thermal expansions showed that the temperature gradient will cause a thermal distortion to occur in the substrate disk. Hence, it is important that no axial restraints be applied across the face of the disk.

The pressure drop across the substrate is influenced by the size and shape of the cells and the wall thickness used. For a typical substrate structure as that used in [7], the pressure loading is well within the allowable limit.

Support Cylinder. The metal support system of a catalytic combustor will experience similar pressure and thermal loadings as the secondary dilution zone of a conventional turbine combustor. It is convenient, therefore, to select the material used for the conventional combustor as the material for the support system. There has been extensive experience in the use of Hastelloy X, a nickel base alloy, as the material for combustor components. For the purpose of the present analysis, Hastelloy X is selected as the candidate material for the metal support system. Its mechanical properties are readily available from [24].

The metals are film cooled by air at the compressor discharge temperature. In the design, adequate film cooling will be provided such that the catalytic combustor shell can be expected to perform its duty, namely, withstand the external loads caused by gravity, airflow, fluid pressure and temperature.

The fundamental stress in the cylindrical elements is the hoop stress due to the pressure differential across the wall. The maximum pressure loading is associated with the pressure drop due to flow losses in the combustor. Assuming a pressure loss of 5 percent, the calculated hoop stress for a 0.050 in. (1.27 mm) thick wall is at a reasonable stress

level. A thicker wall can be used to reduce this stress, if necessary.

As with the substrate, there can be thermal stresses resulting from restraints that prevent thermal growth occurring freely. For continuous shells, fortunately, most temperature jumps will not be greater than 100°F (55.6°C) because axial heat flow will tend to mitigate the differences. The cooled downstream shell, however, will need some special consideration to prevent high temperature differences.

The cylinder will experience dimensional changes resulting from temperature changes. The differential thermal growth between the cylinder and the substrate will likely be the parameter that defines the design. These differentials must be accommodated if high stresses are to be avoided. The accommodations for these relative movements, either completely or partially, suggest an intermediate layer of high compliancy.

Compliant Layer. Its primary function is to absorb the relative movements across the layer between the cylinder and the substrate. An additional requirement is that it must distribute the restraints it applies to the substrate uniformly and lightly. This requirement stems from the allowable loading of the substrate, particularly in transverse directions [22].

One promising scheme is to use a metallic mesh layer as possible support of the substrate. With cooling flow through the wire mesh, the metal temperatures will be low enough for the coils to survive. The wire mesh, of proper wire size and density, could provide flexibility, good capability for conformity and a large number of support points. Therefore, a metallic coiled wire compliant layer will be capable of following the differential growths, conforming to the surface of the substrate, having a multitude of contact points, resisting shearing and operating at high temperatures.

Another aspect of the design is the contact between the coils and the hot substrate. Two techniques can be applied. The first is a coating of hydraulic-setting castable alumina insulation on the outer cylindrical surface of the substrate. This smooths the surface of the substrate and insulates the coils. Additional temperature reduction can be provided by preventing the catalytic reactions from taking place in the outer two or three layers of substrate cells. These inactive cells plus the coating will provide sufficient resistance to heat flow into the wires. Additionally, controlled air flow around the substrate through the compliant layer will also conduct heat away to further cool the wire. A sketch of the above concept is shown in Figure 5. Ultimately, the proof of this design will be established by experimental situations.

Transient Analysis. In reviewing the operating cycle of a combustion turbine, it has been determined that the most severe transient loading occurs during the shut-down process. Hence, the present analysis is aimed at evaluating the stresses that can be developed during this critical period.

A one-dimensional time dependent analysis of the heat transfer at various stations along the combustor was performed. The change in pressure with time after shut-down was determined based on actual engine data. These calculated temperatures and pressures as a function of time after shut-down are then the input to an existing computer code to perform the stress analysis. In this way, a time history of stresses was developed with temperatures along the combustor at simulated operating conditions at various times following shutoff of the device.

Thermal Analysis of Support Cylinder. The metal support system must be kept at temperature levels which will result in acceptable life. This temperature was taken to be 1400°F (760°C).

The conical and cylindrical portions of the support structure which are downstream of the catalytic reactor are exposed to the 2300°F (1260°C) gaseous products leaving the reactor and therefore, must be cooled. This will be accomplished by introducing film cooling air at the upstream portion of the cone as shown in Fig. 4. The film cooling airflow requirement is estimated to be 6.6 percent and 5.2 percent of the total combustor airflow for the conical and cylindrical portions, respectively.

The cylindrical portion of the metal support surrounding the catalytic reactor will be cooled because combustor shell air will be flowing over both the outer and inner surface as shown in Fig. 5.

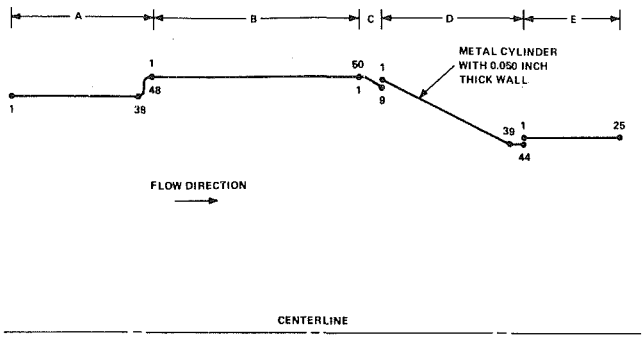

Fig. 6 Catalytic combustor support cylinder model for finite element analysis

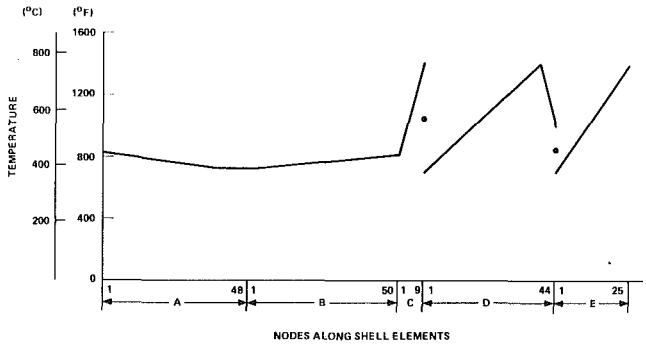

Fig. 7 Steady-state (time = 0 s) temperature distribution along metal support cylinder

The steady-state temperatures at various stations along the entire metal support structure were calculated. Starting at these levels, transient temperatures for the various stations were calculated to simulate the shut-down process. Actual engine data were used to determine airflows and combustor shell temperatures as a function of time. This information was then used to calculate internal convective heat transfer coefficients as a function of time. The heat transfer coefficients and air temperature were then used to determine the metal temperature at the various stations through the use of an existing transient heat transfer computer code.

Stress Analysis of Support Cylinder. In order to perform a finite element stress analysis of the metal support cylinder, the structure has been divided into five elements with each element further subdivided into nodes as shown in Fig. 6. The steady state shell temperature pattern at time $t = 0$ is shown in Fig. 7. Based on this temperature and on estimated pressured loading, the steady-state stresses and elongations have been calculated and the results have been plotted as shown in Figs. 8, 9, and 10. The horizontal axis in these figures represents the nodes along the contour of the shell. The higher stresses occur at the locations where there are structural and/or thermal changes.

These high calculated stresses result from the 700°F temperature difference between the shell elements in the analytical model; actual stresses are considerably lower. The type of construction proposed for the cooling air slots, a corrugate strip between the adjoining rings, is used in conventional combustors at the same temperature loading with satisfactory performance. The corrugated strip and the staggered spotweld attachment between rings offers more flexibility and lower stresses than the analytical model provides. Improved modelling in the vicinity of the air slots with a more elaborate element type is required before accurate stresses can be determined.

The transient analysis of the support cylinder is based on the changes in the metal temperatures and the pressure loading after the fuel supply is turned off. The heat transfer analysis yields the temperature decay with time. The temperature decay at node 39, element D, is plotted as shown in Fig. 11. The calculated stresses and deflections at any time interval would appear similar in shape to the steady-state results except for magnitudes.

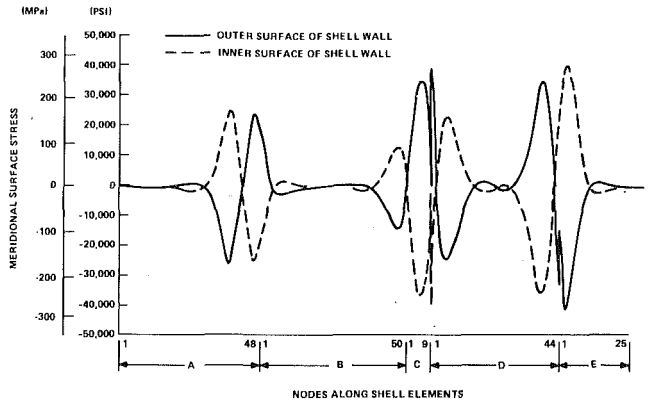

Fig. 8 Catalytic combustor support cylinder meridional surface stress at time = 0 s (steady-state)

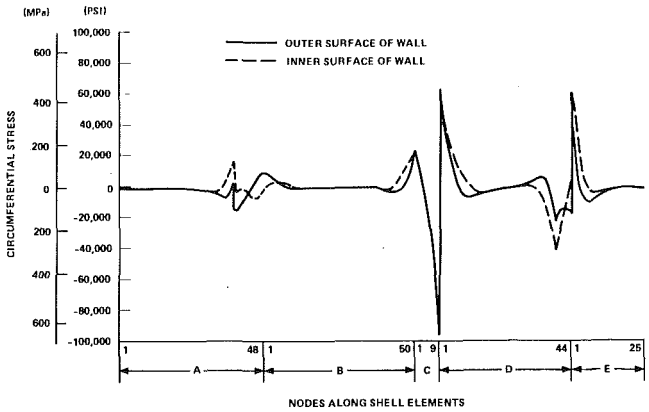

Fig. 9 Catalytic combustor support cylinder circumferential stresses at time = 0 s (steady-state)

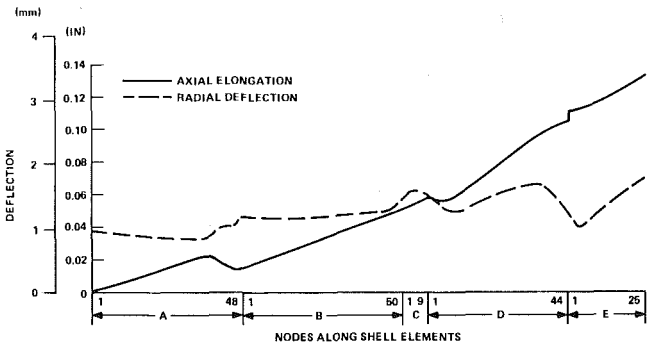

Fig. 10 Catalytic combustor support cylinder deflections at time = 0 s (steady-state)

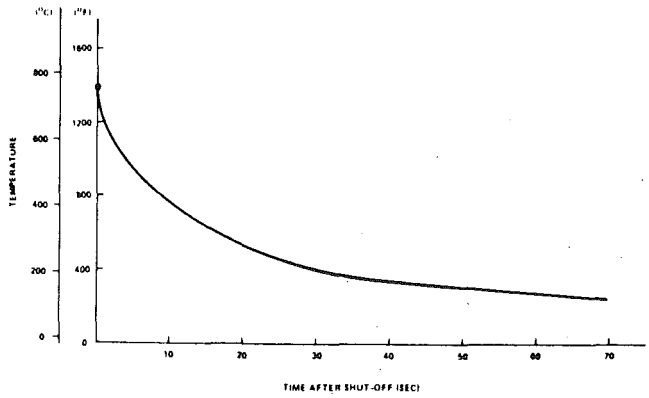

Fig. 11 Temperature decay at node 39, element D

The transient stress response at three selected locations are plotted as shown in Figs. 12–14. The typical decay of stresses in an initially low stress region is illustrated in Fig. 12. In all transient stress plots, it was observed that all initial high stresses tend to decay rapidly to low values with the cool-down as illustrated by the hoop stresses shown in Fig. 13. The only stresses that show a temporary increase are those in shell elements C and D. The meridional stresses at node 9, element C increase for about 30 s and then start a gradual reduction. The inner hoop stress at node 44, element D increases for about 5 s and then decreases in a typical manner as shown in Fig. 14. The maximum value reached is less than 30,000 psi (207 MPa) which is low in comparison with the steady-state hoop stresses.

Substrate. In comparison with the thin walled, flexible shell, the substrate is a three-dimensional device, which can be considered a solid element in some aspects. The most refined elements of a finite element program, namely iso-parametric three dimensional solid elements are recommended for use in the calculation of stresses in bulky structures such as the substrate. There is favorable experience with these elements, but their limitations have to be recognized. The first restraint is associated with modelling which involves a design of the elements to represent the substrate. Since the substrate is supported along the outer surface by the compliant layer, a set of reaction nodes (discrete load points along the outer edges of the outer elements by which loading and/or attachment to adjacent elements is secured) must be specified. The calculation procedure and the characteristics of this element are such that when the reactions at these nodes are developed during the calculation, the stress fields are inaccurate through two or more layers of elements in the model. This makes it necessary to use a larger number of elements and layers. Also, the representation of the contact of the compliant layer with the substrate makes a large number of surface modes desirable.

Theoretically, the iso-parametric element is designed to replace the need for a large number of smaller, simpler elements. The distributed nature of the reaction forces, generated by the compliant layer, however, retains the need to use many smaller elements to represent the substrate. The ideal number of elements has to be established by trial and error; a confirmation procedure to assure the validity of the model. The use of a large number of elements, particularly iso-parametric elements, extends the computing time.

An additional problem relating to the compliant layer also exists. The above discussion considers the reaction nodes to position the substrate in space, but they are nodes at the flexible compliant layer and frictional forces position the substrate. Additional layers of elements must be applied at each support node to represent the compliant layer. This increases the element count further.

Friction is another feature which must be considered in the solution. With friction considered to be the restraint for holding the substrate in its axial location in the support cylinder, a more elaborate calculation is required to recognize slippage. The slippage is due to both differences in the elastic properties of the substrate and the compliant layer, and different thermal growths at the boundary between the compliant layer and the substrate. Friction requires an interactive calculation scheme and based on comparable experiences as many as 20 iterations are required before equilibrium is reached in the friction elements.

In addition, a problem exists in defining the properties of the substrate; usually, when material properties are quoted, such as Young's modulus, density, thermal coefficients of expansion etc., the values do not recognize the existence of the details, such as holes and cell structure. The results of the stress and other mechanical calculations, therefore, are bulk stresses and deflections, good enough to see if the substrate will fit the space, or be crushed due to the distributed loading on the surface, but not fine enough to determine stresses through or along cell walls. With brittle material, it is these small, local stress details that can cause failure much as flaw details in metallic parts affect performance. Thus, modelling of the cellular construction may eventually be required, but such an increase in model complexity will make the number of finite elements very large.

So far, only the pressure loading on the outer contours of the sub-

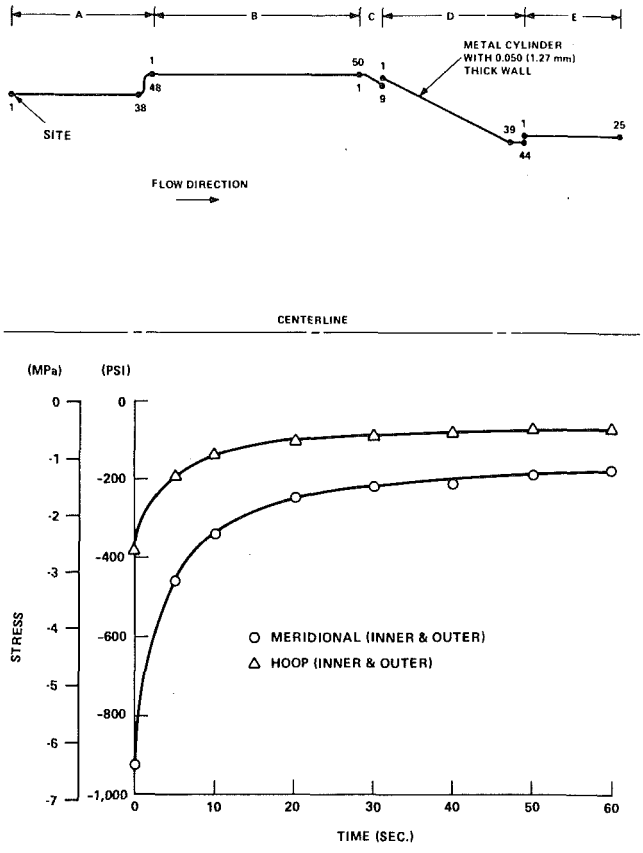

Fig. 12 Transient stress response—shell element A, node 1

strate has been considered. Another loading mode is that of temperature. The bulk-model elements with soft temperature gradients will probably yield results compatible with the function describing the stress within an element; the solution will be accurate. However, if steep gradients or temperature steps are to be imposed, then bulk model elements may become unstable and will generate inaccurate stress variations. Again, a trial-and-error process will be required to confirm the model unless appropriate prior experience can be utilized.

Hence, while the substrate is simple in shape and some simple calculations indicate acceptable performance, the device, when considered in more detail, rapidly becomes very complex for the available methods of handling it. Presently, therefore, the performance of substrates can better be judged based on their performance in prior tests and applications. Future designs can be better judged only after operational and test procedures are applied. The most elaborate calculation does not seem to be able to offer a greater assurance.

In summary, detailed stress analysis of a substrate/compliant layer/shell system under the expected thermal and mechanical load situations in a catalytic combustor will be an extremely time consuming task. As the thermal conditions to which the cell walls will be exposed are not well known as yet, it does not seem to be prudent to perform in-depth investigations when the input data are not available to the extent necessary to run finite element programs. On the other hand, this investigation indicates that the design of catalytic combustors can be viable. Consequently, the most cost-effective approach appears to be the testing of the concept described in the paper and the use of the sophisticated finite element methods to investigate the design after the tests provide the necessary thermal and flow input.

From the present study, the following conclusions have been reached:

1 The analyses have identified a conceptual arrangement to build a viable catalytic ceramic element and its support structure for combustion turbine application.

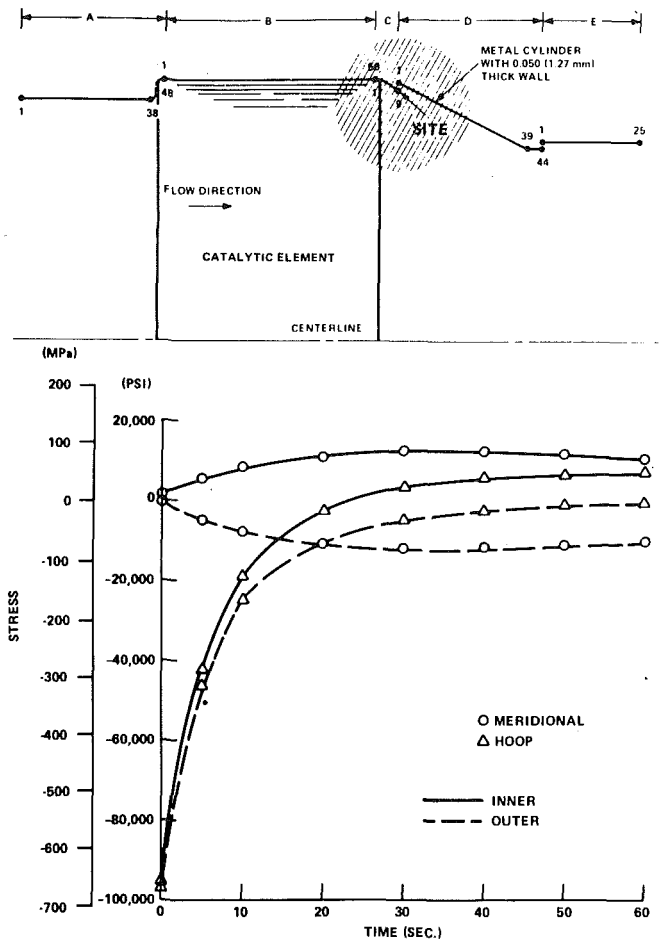

Fig. 13 Transient stress response—shell element C, node 9

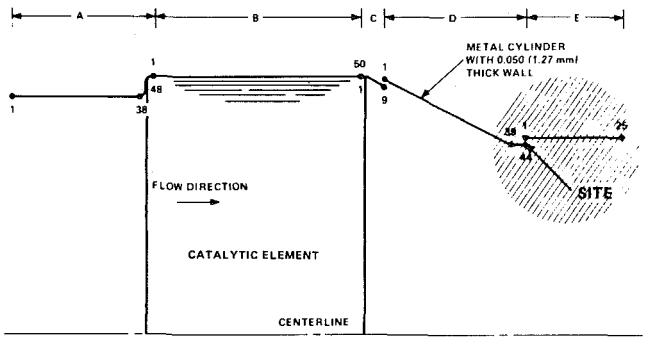

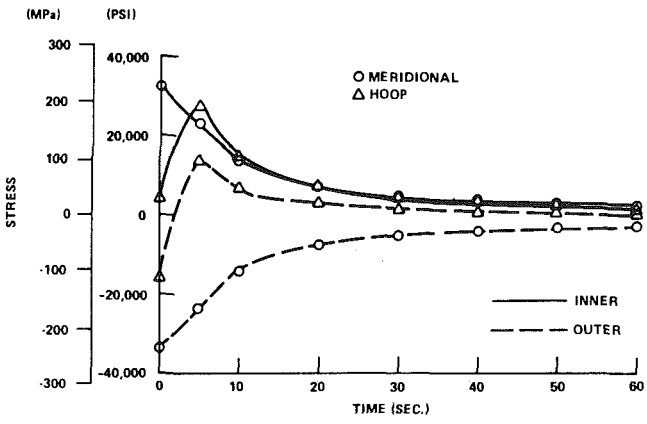

Fig. 14 Transient stress response—shell element D, node 44

2 This design as currently conceived is expected to perform its functions from the mechanical standpoint.

3 At this stage, additional experimental input is needed so that more sophisticated computer analysis can be applied for future designs.

4 The analyses suggested that a reasonable amount of experimental work in conjunction with analytical methods discussed in the report will provide the necessary design information.

Acknowledgment

This work was performed with the support of the Electric Power Research Institute under Contract No. RP 421-1 with Dr. Arthur Cohn as Program Manager. The authors wish to thank R. G. Glenn, E. W. Tobery and S. E. Mumford for their contributions in performing this task.

References

1 Pfefferle, W. C., "The Catalytic Combustor-A Look Back, A Look Forward," Paper 77-31, Western States Section, The Combustion Institute, Oct., 1977.

2 Pfefferle, W. C., "Catalytically Supported Thermal Combustion," Belgium Pat. 814,752, Nov. 8, 1974 and U.S. Pat. 3,938,961, Dec. 30, 1975.

3 Blazowski, W. S. and Bresowar, G. E., "Preliminary Study of the Catalytic Combustor Concept as Applied to Aircraft Gas Turbines," AFAPL-TR-74-32, Air Force Aero Propulsion Lab., Wright-Patterson AFB, Ohio, May, 1974.

4 Wampler, F. B., Clark, S. W., and Gaines, F. A., "Catalytic Combustion of C_3H_8 on P_T Coated Monolith," Paper No. 74-36, Western States Section, the Combustion Institute, Oct., 1974.

5 Anderson, D. N., Tacina, R. R., and Mroz, T. S., "Performance of a Catalytic Reactor at Simulated Gas Turbine Combustor Operating Conditions," NASA TM X-71747, 1975.

6 Pfefferle, W. C., et al., "Catathermal Combustion: A New Process for Low-Emissions Fuel Conversion," ASME Paper No. 75-WA/Fu-1, Nov.–Dec., 1975.

7 DeCorso, S. M., et al, "Catalysts for Gas Turbine Combustors—Experimental Test Results," ASME Paper No. 76-GT-4, Mar., 1976.

8 Anderson, D. N., "Preliminary Results from Screening Tests of Commercial Catalysts with Potential Use in Gas Turbine Combustors. Part I: Furnace Studies of Catalyst Activity," NASA TM X-73410, 1976.

9 Anderson D. N., "Preliminary Results from Screening Tests of Commercial Catalysts with Potential Use in Gas Turbine Combustors. Part II: Combustion Test Rig Evaluation," NASA TM X-73412, 1976.

10 Anderson, D. N., "Emissions and Performance of Catalysts for Gas Turbine Catalytic Combustors," ASME Paper No. 77-GT-65, Mar., 1977.

11 Heck, R. M., "Final Report Part I. Durability Testing at 1 atm of Advanced Catalysts and Catalyst Supports for Automotive Gas Turbine Engine Combustors," NASA CR-135132, June, 1977.

12 Anderson, D. N., "Performance and Emissions of a Catalytic Reactor With Propane, Diesel and Jet A Fuels," NASA TM-73786, Sept., 1977.

13 Roffe, G., "Development of a Catalytic Combustion Fuel/Air Carburetion System," AFAPL-TR-77-19, Wright Patterson, AFB, Ohio, Mar., 1977.

14 Siminski, V. J. and Shaw, H., "Development of a Hybrid Catalytic Combustor," ASME Paper No. 77-GT-84, Mar., 1977.

15 Cerkanowicz, A. E., Cole, R. B. and Stevens, J. G., "Catalytic Combustion Modeling; Comparisons with Experimental Data," ASME Paper 77-GT-84, Mar. 30, 1977.

16 Kelly, J. T., et al., "Development and Application of the PROF-HET Catalytic Combustor Code," Paper No. 77-33, Western States Section, The Combustion Institute, Oct. 1977.

17 Kesselring, J. P., Krill, W. V. and Kendall, R. M., "Design Criteria For Stationary Source Catalytic Combustors," Paper No. 77-32, Western States Section, The Combustion Institute, Oct., 1977.

18 Rosfjord, T. J., "Catalytic Combustors for Gas Turbine Engines," AIA/Paper No. 76-46, Jan., 1976.

19 Hung, W. S. Y., "An Experimentally Verified NO_x Emission Model For Gas Turbine Combustors," ASME Paper No. 75-GT-71, 1975.

20 L. J. Spadaccini, "Autoignition Characteristics of Hydrocarbon Fuels at Elevated Temperatures and Pressures," ASME Paper 76-GT-3, 1976.

21 DeZubay, E. A., "A Note on the Autoignition of Liquid Fuel," *Combustion and Flame*, Vol. 32, pp 313–315, 1978.

22 Anon., "CELCOR Cellular Ceramics," Corning Glass Works, Corning, N.Y.

23 Boyer, W. A., Corning Glass Works, private communication, Dec., 1977.

24 Anon., "Hastelloy Alloy X," Haynes Stellite Co., Kokomo, Ind., Aug., 1961.

Averaging Methods for Determining the Performance of Large Fans from Field Measurements

P. M. Gerhart
Associate Professor of Mechanical Engineering,
The University of Akron,
Akron, Ohio 44325

When testing large fans in the field, it is often necessary to make measurements at locations where the distributions of gas velocity, pressure, and temperature are highly irregular. When this occurs the fan pressure rise or fan specific energy is usually expressed in terms of average values of pressure, density, and temperature. This paper proposes criteria for the definition of such averages and develops defining equations for them. The averages proposed allow the continuity, energy, and ideal gas state equations to be written in simple one-dimensional form without correction factors. Performance variables such as total pressure are defined in the customary way from the averages of the fundamental flow properties.

Introduction

The performance of a flow machine such as a fan is expressed in terms of the quantity of fluid passing through it in unit time (measured in either mass or volume terms), some measure of the "useful," "ideal," or mechanical specific (per unit mass or volume) energy imparted to the fluid by the machine, and the power transferred to the fluid by the rotor (possibly including power dissipated in bearings or other elements of the drive train). In some instances, the power may be replaced by the efficiency; however, the equation

$$\text{Efficiency} = \frac{\text{quantity} \times \text{specific energy}}{\text{Power}}$$

is always true, being the definition of efficiency.

It has been customary practice in fan engineering in the U.S. to express fan performance in terms of a Fan Volume Flow Rate, a Fan Pressure Rise (pressure being a type of "energy per unit volume"), and a Fan Input Power [1]. In Europe, the mass flow is favored over the volume flow and the fan specific energy, defined by

$$y_F \equiv \int_1^2 \frac{dP}{\rho} + e_{K2} - e_{K1} + e_{P2} - e_{P1},^1 \tag{1}$$

often replaces the pressure rise [2, 3]. Since the pressure-density integral in equation (1) is impossible to evaluate in practice, it is usually approximated by the use of an (arithmetic) mean density:

$$y_F \simeq \frac{P_2 - P_1}{\frac{\rho_2 + \rho_1}{2}} + e_{K2} - e_{K1} \tag{2}$$

The values of pressure and density in equation (2) and in the definition of fan pressure rise are generally conceived of as uniform across the fan inlet and outlet planes; they are equivalent one-dimensional values.

The flow at the inlet, and especially the outlet, of large fans is often highly disturbed, with highly nonuniform distributions of velocity, static pressure, temperature, and density. In order to overcome this problem in laboratory testing of fans, measurements are often made at planes removed from the fan boundaries [1] at which the flow has "mixed" or "recovered." When measurements are made under field conditions, it is usually not possible to locate ideal measurement planes; in fact, it is often more feasible to make measurements very near the fan boundaries. Recent work indicates that it is possible to make reliable measurements of fan flow rate by velocity traversing in such regions [4]; and, of course, fan input power measurements are not affected by the selection of a location for making flow measurements. The velocity traverse also includes data on the values of the static pressure at the traverse points. The major problem to overcome when making measurements in regions of nonuniform flow near fan inlet or outlet is the determination of appropriate values of gas pressure and density for expressing fan performance. The obvious solution to the problem is to employ appropriate average values. There are several methods of defining such averages, all involving the integration of the quantity to be averaged over the cross section. The simplest average is the geometric or area average, which for pressure for example would be

$$(\bar{P})_A = \frac{\int_A P dA}{A} \tag{3}$$

When using measurement methods which employ measurements made at the centers of a number of equal elemental areas, the area average is approximated by a simple arithmetic average

$$(\bar{P})_A \simeq \frac{\sum_{j=1}^{N} P_j}{N} \tag{4}$$

Such averages are the easiest to calculate and, indeed, are the suggested averages for some current test methods [5]; however, for

[1] It is customary in fan engineering to neglect changes of potential energy.

Contributed by the Power Division and presented at the Joint Power Generation Conference, Phoenix, Ariz., Sept. 28–Oct. 2, 1980 of THE AMERICAN SOCIETY OF MECHANICAL ENGINEERS. Manuscript received at ASME Headquarters January 28, 1980. Paper No. 80-JPGC/Pwr-1.

purposes of performance rating these simple averages are unsatisfactory, due to the fact that they do not reflect the nature of the fan flow process or appropriately reflect the terms in the basic dynamic equations of motion. Such averages do not accurately express the amount of momentum or energy added to the gas by the fan and thus cannot form the basis of a fair performance rating. To overcome this difficulty, various weighted averages are necessary. The weighting usually involves the local mass or volume flow rate; however, other methods have been proposed [6]. The purpose of this paper is to suggest proper weighted averages for expressing fan performance.

Analysis

The main purpose of employing average quantities is to reduce a complex nonuniform flow situation to an equivalent one-dimensional flow; thus the average quantities should, as far as possible, represent the flow rate of the physical entities involved. The average quantities should permit the writing of the dynamical equations governing the fan flow process in a simple one-dimensional form.

The equations of interest in fan analysis are the continuity equations:

$$\int_{A_1} \rho_1 V_{1n} dA = \int_{A_2} \rho_2 V_{2n} dA, \tag{5}$$

the momentum equation:

$$\mathbf{F} - \int_{A_1} P_1 \, \mathbf{dA} - \int_{A_2} P_2 \, \mathbf{dA} = \int_{A_2} \rho_2 \, \mathbf{V}_2 \, V_{n2} \, dA - \int_{A_1} \rho_1 \, \mathbf{V}_1 \, V_{n1} \, dA \tag{6}$$

and the total energy equation:[2]

$$\mathcal{P} = \int_{A_2} \left(\frac{P_2}{\rho_2} + u_2 + e_{K2} \right) (\rho_2 V_{n2}) \, dA - \int_{A_1} \left(\frac{P_1}{\rho_1} + u_1 + e_{K1} \right) (\rho_1 \, V_{n1}) \, dA \tag{7}$$

For nonuniform flow, the equations involve integration over all streamlines of flow crossing the inlet and outlet planes.

Averages may be defined which permit *each* of these equations to be reduced to its one-dimensional form; but it is not possible to find a single averaging method which will reduce all of them to such a form. As an example, the area average will permit the pressure force term in the momentum equation to be written in the one-dimensional form

$$\int_A P dA = (\overline{P})_A A \tag{8}$$

however, the energy equation suggests an average pressure defined by

$$\int (P/\rho) \, (\rho V_n) \, dA = \int P V_n \, dA = (\overline{P})_V Q \tag{9}$$

i.e.,

$$(\overline{P})_V = \frac{\int P V_n \, dA}{\int V_n \, dA} \tag{10}$$

would be necessary for the accurate expression of the energy equation in one-dimensional form.

At this point, two important facts must be noted:

1 The various averages are different for nonuniform flow

$$(\overline{P})_A \neq (\overline{P})_V \tag{11}$$

2 Familiar equations may not be valid when using averages. For example, while it is true that each fluid particle obeys the ideal gas law

$$P = \rho R T \tag{12}$$

it may not be true that the average quantities obey the ideal gas law

$$\overline{P} \stackrel{?}{=} \overline{\rho} R \overline{T}. \tag{13}$$

Obviously, there is some room for choice as to how averages are defined. The contention of this paper is that averages should be defined in such a manner that:

1 Averaging should be performed on fundamental physical entities such as *static* pressure and *static* temperature.

2 The most useful or critical equations appear in their one-dimensional form without correction factors.

3 The basic physical nature of a given quantity is preserved by averaging.

4 In a flow with uniform static pressure, temperature, and density, but nonuniform velocity, the average values of P, T, and ρ should be the actual values. This seems almost obvious, but the averages proposed in reference [6] do not meet this criterion.

5 Secondary (defined) quantities, such as fan specific energy or total pressure, are obtained by writing the usual defining equation employing the average quantities rather than attempting to average the quantity itself.

As an example of the latter, the average total pressure is *defined* by

$$(\overline{P}_0) \equiv (\overline{P}) + \overline{\rho} \overline{e}_K \tag{14}$$

rather than by taking an average of the actual total pressures.

A consequence of these principles is that different types of averages are used for different quantities.

Probably the most useful equations in fan performance analysis are the continuity and energy equations, with the momentum equation being of secondary importance. Additionally, the ideal gas law is of considerable use. The averages proposed herein permit these equations to be written in the simple one-dimensional forms:

$$\dot{m} = \overline{\rho} Q = \overline{\rho} \overline{V} A$$

$$\mathcal{P} = \dot{m} \left[\frac{\overline{P}_2}{\overline{\rho}_2} - \frac{\overline{P}_1}{\overline{\rho}_1} + C_v \, (\overline{T}_2 - \overline{T}_1) + \overline{e}_{K2} - \overline{e}_{K1} \right] \tag{15}$$

$$\overline{P} = \overline{\rho} R \overline{T}$$

From the continuity equation, the average density is

$$\overline{\rho} = (\overline{\rho})_V = \frac{\int \rho V_n \, dA}{\int V_n \, dA} = \frac{\dot{m}}{\overline{V} A} \simeq \frac{\sum_1^N \rho_j V_{nj}}{\sum_1^N V_{nj}} \tag{16}$$

[2] The process is assumed to be adiabatic.

Nomenclature

A = duct cross-sectional area
C_v = Constant volume specific heat
e_K = specific kinetic energy ($V^2/2$)
e_p = specific potential energy (gz)
$\mathbf{F}$ = force
g = acceleration of gravity
$\dot{m}$ = mass flow rate
N = number of measurement points
P = pressure (absolute or gage, as appropriate)
P_0 = total pressure
$\mathcal{P}$ = power
Q = volume flow rate
R = specific gas content
T = absolute temperature
u = specific internal energy
V = fluid velocity
V_n = fluid velocity normal to area A
y_F = fan specific energy
z = elevation above specified datum
ρ = fluid mass density

Subscripts and Superscripts

$(\bar{})$ = average
$(\bar{})_A$ = area average
$(\bar{})_V$ = volume flow average
$(\bar{})_m$ = mass flow average
1 = fan inlet
2 = fan outlet
i = value at measurement point

where the latter term is an approximation for measurements made at the center of N equal elemental areas.

From the energy equation, the average pressure is

$$\overline{P} = (\overline{P})_V = \frac{\int PV_n\, dA}{\int V_n\, dA} \simeq \frac{\sum_1^N P_j V_{nj}}{\sum_1^N V_{nj}} \tag{17}$$

the average temperature is

$$\overline{T} = (\overline{T})_m = \frac{\int T(\rho V_n)\, dA}{\int \rho V_n\, dA} = \frac{\int T(\rho V_n)\, dA}{\dot{m}} \simeq \frac{\sum_1^N T_j \rho_j V_{nj}}{\sum_1^N \rho_j V_{nj}}, \tag{18}$$

and the average specific kinetic energy is

$$\overline{e}_K = (\overline{e}_K)_m = \frac{\int \frac{V^2}{2}(\rho V_n)\, dA}{\int \rho V_n\, dA} = \frac{\int \frac{V^2}{2}(\rho V_n)\, dA}{\dot{m}} \simeq \frac{\frac{1}{2}\sum_1^N V_j{}^2 \rho_j V_{nj}}{\sum_1^N \rho_j V_{nj}}. \tag{19}$$

Since each fluid particle has $P = \rho RT$

$$\overline{T} = \frac{\int \frac{P}{\rho R}(\rho V_n)\, dA}{\int \rho V_n\, dA} = \frac{1}{R}\frac{\int PV_n\, dA}{\int \rho V_n\, dA} = \frac{1}{R}\frac{\overline{P}Q}{\overline{\rho}Q} \tag{20}$$

and hence

$$\overline{P} = \overline{\rho} R \overline{T} \tag{21}$$

Having defined the averages for all of the elemental quantities, the derived or defined quantities are

$$\overline{P}_0 = \overline{P} + \overline{\rho}\overline{e}_K \text{ and} \tag{22}$$

$$y_F = \frac{\overline{P}_2 - \overline{P}_1}{\left(\frac{\overline{\rho}_2 + \overline{\rho}_1}{2}\right)} + \overline{e}_{K2} - \overline{e}_{K1} \tag{23}$$

Discussion

The proposed averages have the disadvantage of employing different types of average for different quantities; however, the advantages of the averages are felt to far outweigh the disadvantages.

The major advantages are:

1 The most important equations, i.e. continuity, energy, and state, all appear in simple, expected form in which the straightforward multiplication of averages yields the correct flows of mass and energy.

2 The averages are taken on the fundamental quantities such as static pressure and temperature rather than on derived quantities such as total pressure or total temperature.

3 The averages preserve the basic physical characteristics of the averaged quantity.

In regard to this last point, consider the fact that the average static pressure is defined by a volume flow weighted average rather than a mass flow weighted average. The pressure appears in the energy equation as a mechanical work term, *not* as an energy flow term. Thus, while it is appropriate to average energies via mass flow since mass carries energy, it is more appropriate that the pressure appear as a force-diaplacement term rather than a mass related term.

In regard to the definition of the average total pressure using the averages of basic quantities rather than taking an average of the local total pressures, one should recall that the total pressure is itself a defined quantity, being a mixture of a thermodynamic quantity (pressure) and a dynamic quantity (specific (per unit volume) kinetic energy). The so-called total pressure is not really a pressure at all! Similar arguments may be applied to the fan specific energy.

In closing, it is reiterated that the averages suggested in this paper are not unique. Reference [6] discusses averages based on the accurate representation of the continuity and momentum equations (rather than the continuity and energy equations). While this approach is undoubtedly appropriate for certain applications, the present approach is more appropriate for fan performance determination.

References

1 Anon., "Laboratory Methods of Testing Fans for Rating Purposes," ASHRAE Standard 51-75/AMCA Standard 210, American Society of Heating, Refrigerating and Air Conditioning Engineers and Air Moving and Conditioning Association.

2 Anon., "Fan Pressure and Fan Air Power Where ρ_2 Differs from ρ_1," ISO/TC 117/SC1, Paris, France, 1978.

3 Anon., ASME Performance Test Code No. 11—Large Industrial Fans, Draft copy, 1979.

4 Gerhart, P., Nuspl, S., Wood, C. & Lovejoy, S., "An Evaluation of Velocity Probes for Measurement of Non-Uniform Gas Flow in Large Ducts," ASME Paper No. 78-WA-PTC-1, 1978.

5 Anon., *AMCA Fan Application Manual—Part 3—A Guide to the Measurement of Fan-System Performance in the Field,* AMCA Publication 203, Air Moving and Conditioning Association, 1976.

6 Gilbert, G. B., "Average Pressure Measurement in Low Velocity Non-Uniform Gas Flows," ASME JOURNAL OF ENGINEERING FOR POWER, Apr. 1972, pp. 91–97.

B. C. Studley
Burns and Roe, Inc.,
Oradell, N.J.
Assoc. Mem. ASME

Utility Operations: An Effective and Economic Approach to Operator Training

There is no question that, with the increasing costs of Fossil-Fuels, overall production of electricity, and replacement energy costs, the need to develop an operator's complete familiarity with the specific plant he will be required to operate is a necessity. The major benefit is that of reduced operator errors which maximizes unit availability as dictated to by the operating staff. The approach presented utilizes the concept of developing an operator's understanding of each system within the plant through the use of a visual tool called an operational schematic. Coupled with the use of condensed word instructions to explain both normal and abnormal operator actions in addition to a system's control logic, the operator experiences an environment very similar to his working atmosphere. Finally, the effectiveness of this approach, considering that classroom training is coupled with continual control room and in-plant inspections, can be seen to be competitive with that obtainable from the use of a simulator but for a fraction of the cost.

Introduction

Realizing that the need for training is essential, the means by which an operating staff is made completely familiar with the specific plant that they will be responsible for operating becomes a problem. Although generic training programs are successful in developing basic skills, they are not effective in educating a staff on the actual equipment and controls that will be used in the operation of the unit. Therefore, it is natural and to the benefit of the operators to train using material which is *specific* to the unit in question. Presented properly, the trainees become proficient in the operation of the actual unit while developing the necessary basic understanding for equipment and personnel safety. To accomplish such a task, certain training tools are required together with their integration into a program that will be both effective and economical.

Operator Training Tools

The primary visual tool to be implemented in the program is the *operational schematic.* A schematic will exist for each system within the plant and defines the contents functionally and displays to the operator what must be operated in that particular system in addition to the available indication and alarms that must be responded to during the operation of the system. Typically, the schematic presents in one place

- control switch positions
- system annunciators
- CRT inputs
- power sources
- indicators including baseline data for future reference
- system setpoints
- auto/manual control stations
- backup record inputs (if applicable)
- a control logic which explains in sufficient detail *how* the particular components of that system function

Figure 1 is a typical operational schematic for a condensate system in which shading has been incorporated to show the operator exactly what control stations, handswitches and instruments exist within the control room.

Having presented what is to be operated, a tool is required to establish the proper sequence of operator actions required for startup, normal and shutdown operation of each system. To accomplish this, an *operational outline* is developed with the assistance of the operational schematic. As Figs. 2(*a*), 2(*b*) and 2(*c*) illustrate the operational outline becomes a graphic representation of a system, depicting its valve line-up, required switch positions, and flowpath for the startup, normal and shutdown modes of operation coupled with the necessary operating instructions. The operating instructions which are located on the far right of each outline

- provide the operator with the correct sequence of events
- inform the operator *how* and *when* to perform each event
- inform the operator *where* each event is performed, locally or in the control room
- provide a system verification (output) for each operator action (input) to prove input did occur

The operational outline has, therefore, presented the necessary information for operator familiarization with what is to be operated as well as how to operate the system.

The previous tools have dealt with the normal operation of a system and have not considered the operator actions required upon receipt of an alarm. To address pertinent alarm conditions within a system, *alarm responses* are generated to permit expeditious operator response to evaluate, curtail and/or correct the alarm condition to prevent unnecessary trips and failure of equipment or injury to personnel as a result of improper operator action. Typical alarm responses are shown in Appendices I–IV.

Contributed by the Power Division and presented at the Joint Power Generation Conference, Phoenix, Ariz., September 28–October 2, 1980 of THE AMERICAN SOCIETY OF MECHANICAL ENGINEERS. Manuscript received at ASME Headquarters January 28, 1980. Paper No. 80-JPGC/Pwr-2.

Having defined the three training tools which couple the visual with the necessary word instructions, their integration into a training program which is capable of effectively training a variety of operating personnel is absolutely essential. All of us, at one time or another, have attended lectures, training programs or seminars and are aware of the importance that the overall presentation plays in obtaining and retaining the proper understanding of the subject material. Naturally, the program must also be structured to initiate and maintain a strong desire on the part of the trainees to *want to learn*. This desire is enhanced by the realization that it is management's responsibility to provide proper recognition and the possibility of advancement, both in responsibility and financially, to those individuals who, through their training, have maximized their contribution to maintaining a high unit availability. As the purpose of this paper is to define an effective and economic approach to operator training, it will be assumed that the necessary classroom and support facilities (audio-visual aids, etc.) exist to properly portray the training material.

As the training tools explain what there is to operate, where it is to be operated from and how and when it is operated, the training program must effectively portray these tools in addition to sufficiently explaining why a system was designed to be operated in a certain fashion. The why ingredient is essential in any program, because once you understand a system, you automatically become more effective in operating it, both under normal and abnormal conditions. The system understanding referred to is one of a general nature concerned with how the particular components of a system function as well as how the system supports the overall operation of the unit. By eliminating the theoretical aspects and considerating the practical only, the operator is confronted only with the essentials required for safe and reliable operation.

Operator Training Program

Realizing that the overall scope of the program is to present the training material specific to the unit on a system-by-system basis, the material must first be organized in such a manner as to inform and guide the training instructor on the technical details he is to present. Prior to defining the specifics of the program, the importance of a qualified training instructor must first be realized. If at all possible, the instructor should be an experienced member of the owner's staff and a working member on the unit in which training will be performed. This immediately establishes an amiable relationship between instructor and trainees as well as developing a sense of personal respect. This type of relationship, coupled with the instructor's ability to present the training material in clear and concise terms, along with the guidelines listed below, will contribute to the maximum absorption of the material.

- Instruct at a pace consistent with the learning ability of the class.
- Maintain a workload on trainees to insure progress.
- Acknowledge your unfamiliarity with certain subjects and return with answers at the next session.
- Attempt to maintain a common level of understanding between all trainees.
- Instruct trainees to always question an unclear action.
- Follow lesson plans and react to questionable looks, repeating as necessary.
- Prepare yourself by reviewing the system material in advance.
- Maximize the use of visual aids such as operational schematics, handouts, video tapes.
- Always present the training material with the plant (physical) to enable the relationship to be retained.
- Attempt to pair the trainees in knowledge/unknowledgeable groups.
- Do not use abbreviations.

The training program is oriented to initially present the trainee with the *basic* technical practices that will be implemented in all systems. This general instruction is given prior to specific system instructions to allow the individual to relate to their own operating knowledge of equipment in general. This should minimize or eliminate one's initial fear of being confronted with completely unfamiliar material (i.e., the fear of being overwhelmed). These basic practices are listed below realizing that modifications will be necessary as a function of an organization's position on department interfacing.

- Operate systems in accordance with operating instructions.
- At all times, observe plant safety and tagging policy.
- Be aware of all interfacing technical policies.
- Do not start any pump without first verifying a flow path and then verifying discharge pressure after start.
- Start all large pumps with discharge valve cracked and slowly go to full open.
- Always verify indicating light agreement with switch position change or with handswitch flag.
- Warm steamlines with by-passes supplying steam and removing condensate.
- Do not use "check valves" as isolation on high energy piping.
- For series valve service on high energy piping, always throttle with downstream valve and unisolate/isolate with upstream valve. Do not throttle upstream valve.
- Do not throttle gate valves.
- Do not fill tanks without continuously monitoring level especially for chemicals/oils.
- Mark normal indications on gauge glasses for easy reference.
- Do not drain chemicals/oil without proper ventilation and equipment.
- Do not operate a cavitating pump or control valve.
- Equalize equipment run times.
- Do not use manual valve operator extensions.
- Do not leave an annunciated condition without notifying the supervisor and recording the status in log book.
- Report abnormal noises and vibration.

Having presented the basic practices, the training instructor is informed and guided on the technical details he is to present on each system through the use of a *course outline* and *lesson plan*. A course outline exists for each system and is a summary of the material to be presented, it can be divided into lesson plans as a function of the amount of information to be transmitted. The number of lesson plans will be a function of the complexity of the system and will guide the instructor in portraying the three previously presented training tools and allow the trainees to arrive at a complete understanding of the system. To conserve total training time, only complex systems should be divided into more than one lesson plan. This will allow the majority of systems to be presented in one day.

Each course outline will consist of eight typical divisions which will be applicable to all systems. These eight divisions are listed below with the appropriate training tools shown in parentheses, indicating the interface that exists with the visual exhibits.

1.0 General Introduction
2.0 Functions of System (Operational Schematic, Fig. 1)
3.0 Description of System (Operational Schematic, Fig. 1)
4.0 Description of Major Components (Operational Schematic, Fig. 1)
5.0 Control Logic Descriptions (Operational Schematic, Fig. 1)
6.0 System Operating Instructions (Operational Outline, Figs. 2(*a*–*c*)
7.0 Alarm Responses (Alarm Responses, Appendices I–IV)
8.0 System Examinations

Appendix V is a typical course outline for a condensate system which has been divided into two lesson plans. Although the division of the course outline into lesson plans may appear to be rather flexible, it considers the amount of classroom training per day against the daily time spent in the plant and control room relating the material presented in the class to the physical arrangement of the system. In addition, the outline is geared to first present the overall function of the system along with its components followed by what automatic and manual control, indication and alarms exist and concluded with the necessary instruction on system operation including how to respond to alarms.

As defined earlier, the lesson plan guides the training instructor

in portraying the training tools thereby allowing the trainees to arrive at the level of understanding required for safe and reliable system operation. By definition alone, the importance of the lesson plan as the one device that integrates all essential information into an *effective* training program can be readily seen. With the information available through the operational schematics, operational outlines, and the alarm responses, an experienced individual, the training instructor, can develop the lesson plans following the course outlines. This will complete his orientation with the material to be presented and provide him with a thorough understanding of why the systems were designed to be operated in a certain fashion. With this background coupled with the experience gained by being a working member of the plant staff, the instructor is in a position to maximize the trainee's ability to obtain and retain a proper understanding of the material through his overall presentation.

Each lesson plan will consist of eight categories arranged in the following order

1.0 Review Questions from Previous Session(s)
2.0 Introduction to the New Lesson
3.0 Discussion of Lesson Material
4.0 Summary of Handouts
5.0 System Examinations
6.0 Recommendations For Vendor or Specialist Presentations
7.0 Assignment For Next Lesson
8.0 Instructor's/Trainee's Comments and Suggestions For Improved Training

Appendix VI is a typical lesson plan developed for the condensate system which is summarized in the course outline (Appendix V). The final lesson plan has been exhibited and also implements the system examinations which are given at the conclusion of a system's training material presentation. Again, the order that the lesson plan categories are presented in is important as it allows the trainees to resolve any past questions, be introduced to the purpose of the new lesson and to be presented with the lesson material in sufficient detail. To conclude the daily lesson plan, the handouts distributed are summarized, examinations distributed, the need for a separate session involving a vendor representative discussed, and the following lesson's assignment issued. All suggestions for improving the training program, whether initiated through the trainees or the instructor, will be recorded, analyzed, and implemented, if appropriate.

All good training programs incorporate a series of examinations to determine the understanding the operators (trainees) have of the material presented and if additional training is necessary. These examinations are developed for the purpose of confirming the trainee's knowledge of the direct and indirect functions of a system, along with the system's operating characteristics. In addition, the physical location of a system's major components, significant instrumentation and controls is validated to ascertain that the trainees have properly related the material presented in the class to the physical arrangement of the system. To accomplish the above, two types of examinations are required. A *software examination* will be given in the classroom for each system presented and consists of 20 questions of the composition, completion or multiple choice type. Appendix VII is a typical software examination for a condensate system realizing that question difficulty may be adjusted to suit the overall level of understanding of the class. A *hardware examination* will be given at the conclusion of daily classroom training in the form of logically developed assignments and will combine hands on orientation in the plant with an evaluation of the trainee's understanding of the system. The assignments are organized to complement that specific day's training and by division of the class into small working groups the system can be physically walked by all. A time limit is imposed on the assignments to allow an oral examination to be given at the end of each day. This requires that the small working groups rejoin in the classroom allowing all trainees to benefit from the discussion. These exams may take the form of an oral presentation by the various working groups regarding their findings during the assignment or be a series of questions asked by the Instructor. Testing in this manner should maintain a fairly relaxed atmosphere allowing the trainees to concentrate on maximum absorption of all material. Appendix VIII is a typical hardware examination for a condensate system.

Having discussed the specifics of the program, the approximate cost to prepare the training material should be identified. Realizing that a typical power plant may consist of up to 60 systems, the owner is in the position of selecting those systems which directly relate to continual operation of the unit. By doing this and being aware that normally the turbine and steam generator manufacturers provide training on their equipment, the number of systems to have training material developed is reduced substantially. Based upon past experience, the total cost of preparing the training material will be less than 300,000 dollars for the systems selected (approximately 35 systems). At today's prices for replacement energy, the program presented is economical since it should substantially reduce operator errors.

Summary

In summary, the operator training program presented develops the complete familiarity of the operators with the specific plant they are required to operate. This is accomplished through the use of training material formulated in a manner to allow the Operators to experience an environment very similar to their working atmosphere. In addition, the learning experience was optimized by building on those human factors which make all of us want to learn. Finally, the program can be justified realizing that the cost of the training material has been determined to be less than 10 percent of the initial investment of a simulator designed to duplicate the unit's control room. Even more important, in an age when human error[1] is responsible for approximately 22 percent of power plant failures, the program pays for itself by reducing this error, therefore, resulting in higher unit availability. To be specific, assuming a replacement energy cost of $15/MWhr, the prevention of one unit trip on a 600MW station in which electrical generation is interrupted for 32 hr would completely pay off the money expended for the training program material.

APPENDIX I

Condensate Pumps Discharge Header Press Low (Alarm Response No. 17.1, Condensate System, Initiating Device PS-470, Setpoint 450 PSIG)

A Possible Cause(s) of Alarm. (1) loss of a running condensate pump, (2) ruptured condensate system piping.

B Automatic Action(s). A nonrunning condensate pump will start if its handswitch is in "normal-after-stop" position.

C Control Room Observation(s). Annunciation: alarm on cabinet 1AM. CRT display: FD 107. CR indication: PI-472. local observation(s) indication: PI-412.

D Immediate Operator Action. (1) Verify alarm is valid through control room/local observations; (2) verify automatic start of standby condensate pump; (3) start a condensate pump if not done in D. 2 above; (4) verify that a pipe rupture does not exist.

E Effect On Plant. (1) Running condensate pump could run off its pump curve or overload; (2) decreasing deaerator level (prior to starting standby pump); (3) shutdown of plant if ruptured pipe cannot be isolated.

APPENDIX II

Loss of Condensate Minimum Flow One Pump (Alarm Response No. 17.3, Condensate System, Initiating Device FS-422A, Setpoint 1300-gpm)

A Possible Cause(s) of Alarm. (1) Loss of a condensate pump, (2) FCV-422, condensate minimum control valve fails close, (3) FCV-422 is isolated.

B Automatic Action(s). None.

C Control Room Observation(s). Annunciation: alarm on cabinet 1am. CRT Display: FD 128. CR indication: FCV-422 indi-

[1] "The Role of Personnel Errors in Power Plant Equipment Reliability," AF-1041, Technical Planning Study 77-715 prepared by Failure Analysis Association for Electric Power Research Institute.

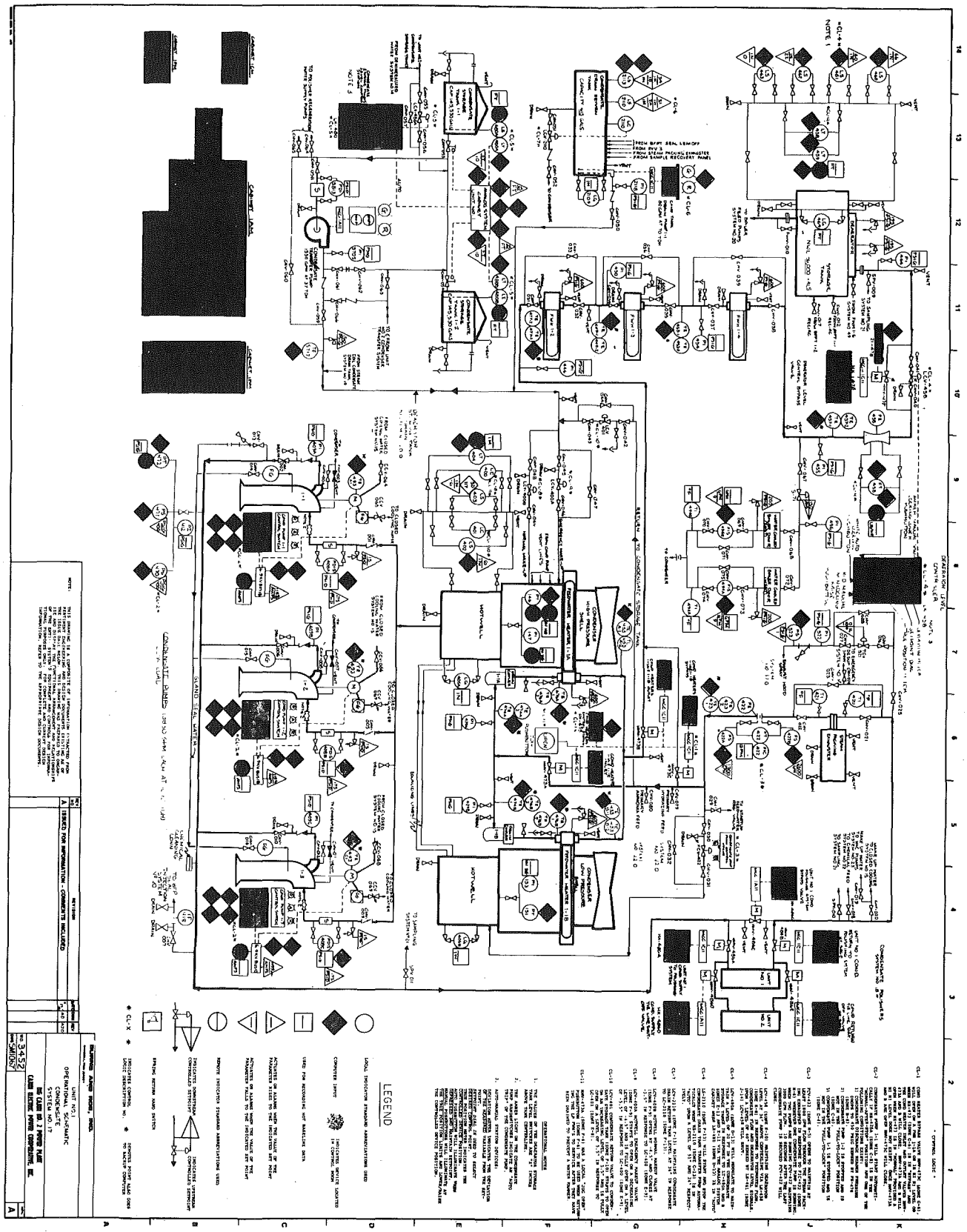

Fig. 1 Operational schematic

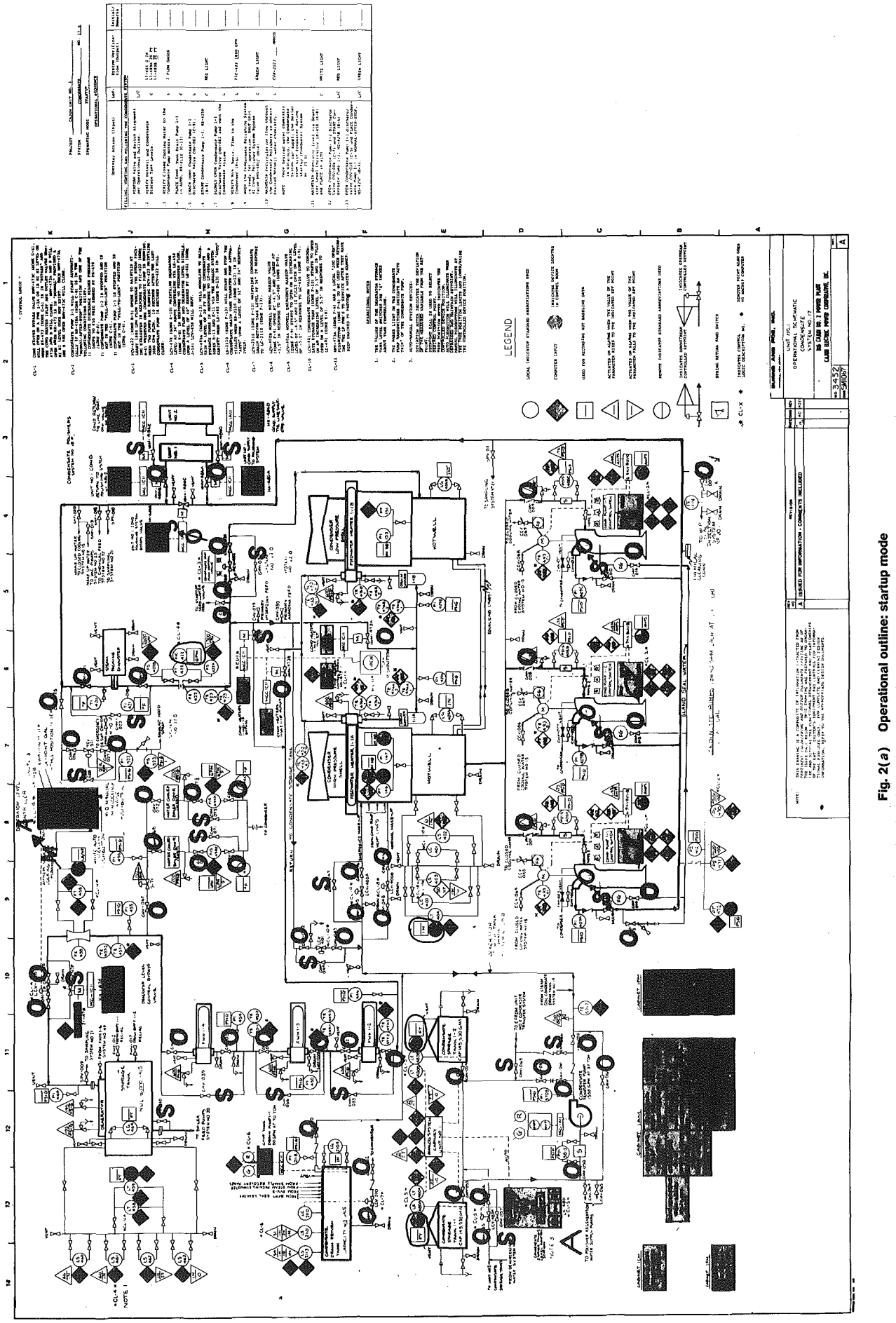

Fig. 2(a) Operational outline: startup mode

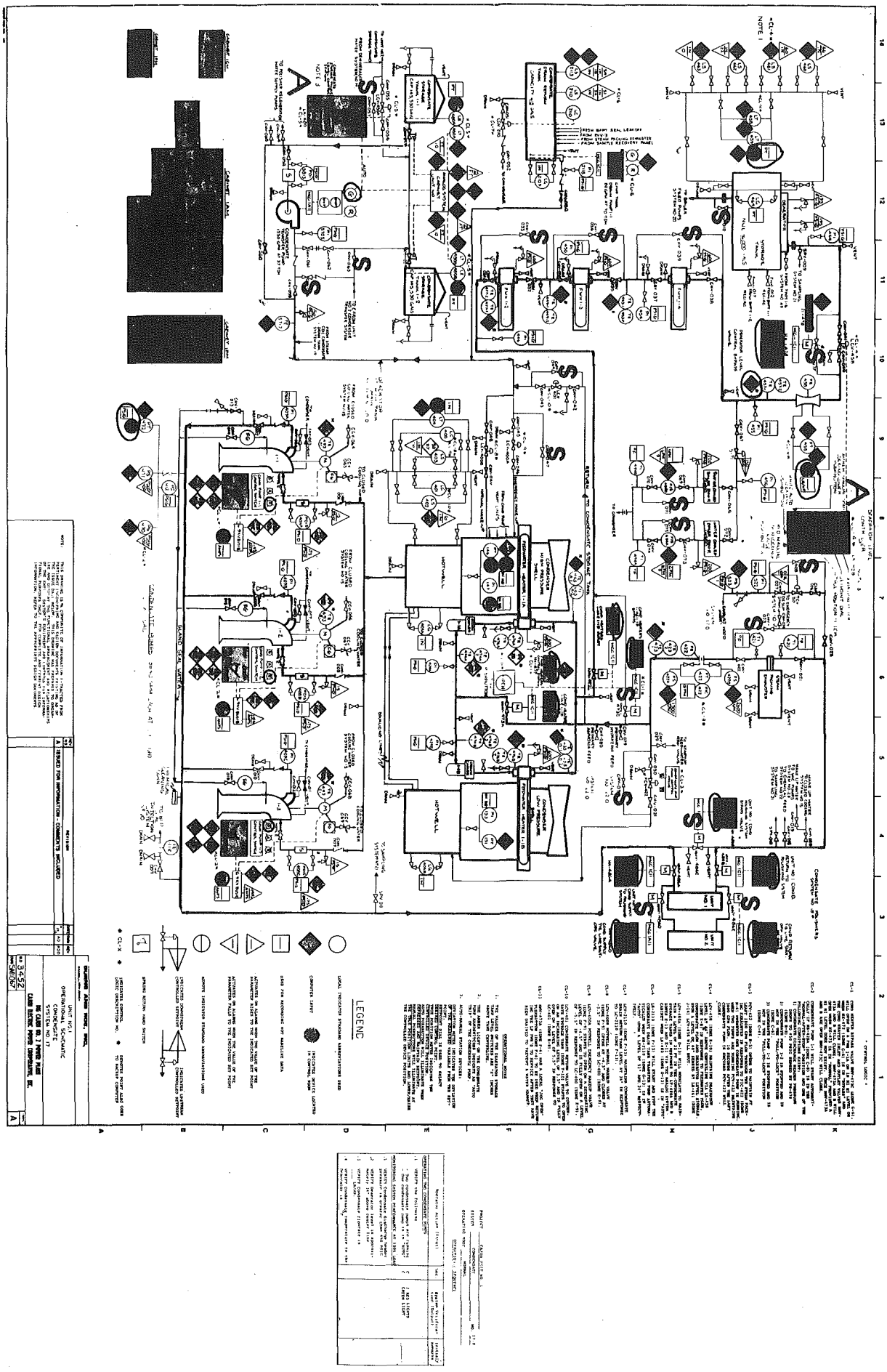

Fig. 2(*b*) Operational outline: normal mode

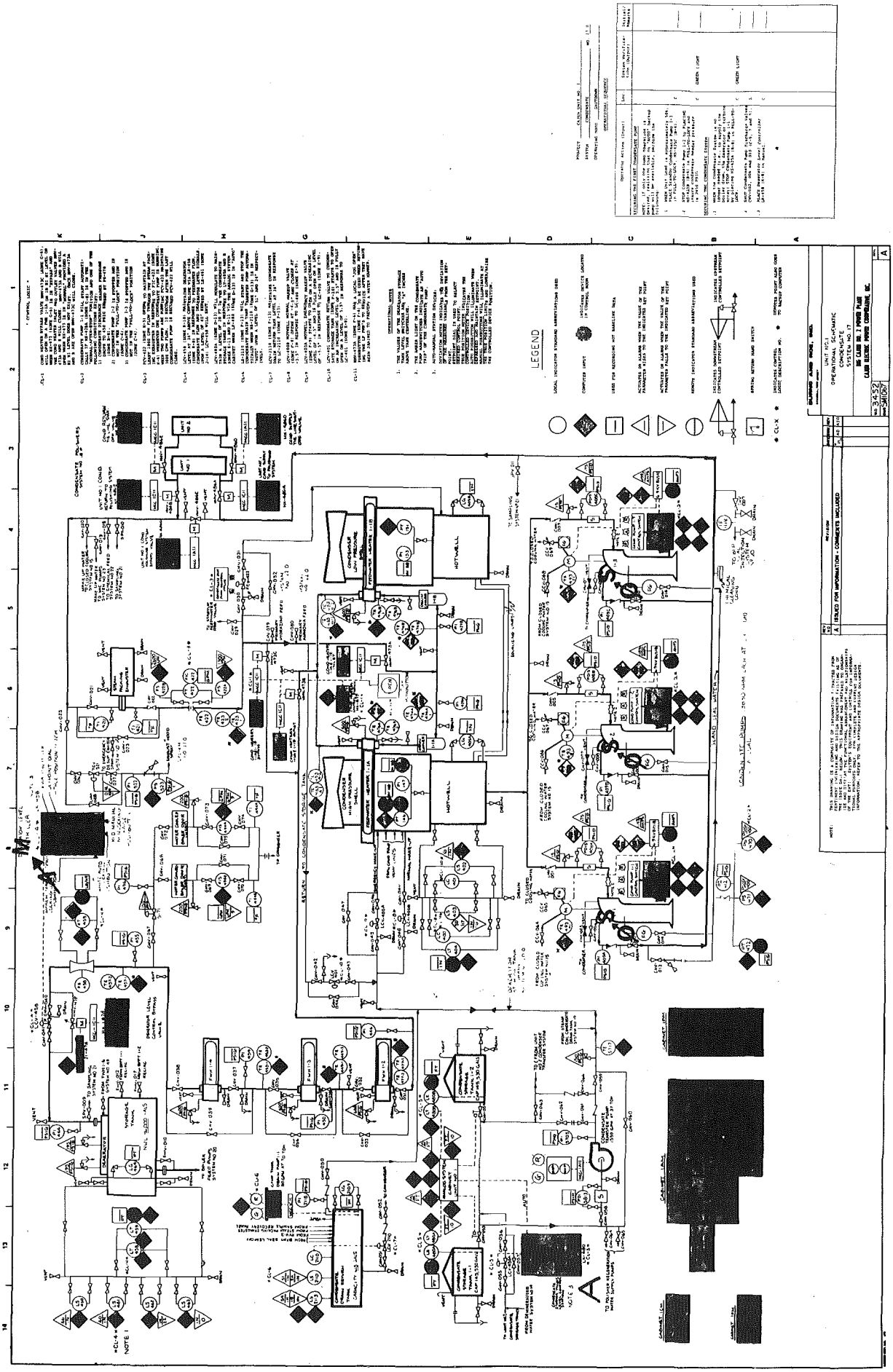

Fig. 2(c) Operational outline: shutdown mode

cating lights. local observation(s) indication: FIC-422.

D Immediate Operator Action. (1) Verify alarm is valid through control room/local observations; (2) have auxiliary operator bypass FCV-422 and call control room.

E Effect On Plant. (1) Overheat steam packing exhauster, (2) overheat condensate pump due to insufficient recirculation flow.

APPENDIX III

Deaerator ST Tank Level Hi-Hi Extraction Line Trip (Alarm Response No. 17.10, Condensate System, Initiating Device LS-460, Setpoint 47 in.)

A Possible Cause(s) of Alarm. (1) Deaerator level controller LK-458 failure, (2) deaerator level control valve LCV-458 failure, (3) deaerator level control valve bypass valve HMV-478 open.

B Automatic Action(s). (1) FWH-1-6 normal level control valve LCV-206A closes, (2) bleed steam 5 drain valves HCV-160-5A1, and 5A3 open, (3) bleed steam 5 nonreturn valves FV-160-5A1 and 5A2 close, (4) bleed steam 5 isolation valve HMV-160-5 closes.

C Control Room Observation(s). Annunciation: alarms on cabinet 1bm. CRT display: FD 127. CR indication: LI-459. local observation(s) indication: LG-464.

D Immediate Operator Action. (1) Verify alarm is valid through control room/local observations; (2) verify automatic actions occurred; (3) take manual control of LK-458 and return deaerator level to normal; (4) verify HMV-478 is shut; (5) when deaerator level is returned to normal, have auxiliary operator reset FV-160-5A1 and 5A2; (6) open HMV-160-5 and close HCV-160-5A1, 5A2 and 5A3.

E Effect on Plant. (1) Loss of low pressure steam (bleed steam) to boiler feed pump turbines; (2) loss of bleed steam to the deaerator and air preheater steam coils (auxiliary steam will supply these users); (3) damage to main turbine by water backing up if the automatic actions did not occur.

APPENDIX IV

Condensate Pump Motor Overload/Overcurrent (Alarm Response No. 17.15, Condensate System, Initiating Device 49 or 50 or 51 Relay, Setpoint N/A)

A Possible Cause(s) of Alarm. (1) Thermal overload on any condensate pump (49 relay), (2) instantaneous overcurrent on any condensate pump (50 relay), (3) time delayed overcurrent on any condensate pump (51 relay), (4) locked rotor, (5) runout of pump.

B Automatic Action(s). (1) Associated condensate pump, will trip, (2) A nonrunning condensate pump will start if its handswitch is in "normal-after-stop" position.

C Control Room Observation(s). Annunciation: alarms on cabinet 1am: CRT display: FD 111, FD 117, FD 122. CR indication: auto trip amber, light illuminates. local observation(s) indication: relay shutter opens.

D Immediate Operator Action. (1) Verify alarm is valid through control room/local observations, (2) verify automatic start of standby condensate pump, (3) start a condensate pump if not done in D.2 above.

E Effect on Plant. (1) Decrease in condensate header pressure (prior to starting another pump), (2) decrease in deaerator level (prior to starting another pump).

APPENDIX V

Course Outline and Lesson Plan for Condensate System No. 17

Course Outline

Lesson Plan No. 1 of 2

1.0 Introduction

2.0 Functions of System

3.0 Description of System

4.0 Description of Major Components. (4.1) Condenser, (4.2) Condensate Pump and Motor, (4.3) Steam Packing Exhauster, (4.4) Condensate Polishers, (4.5) LP Feedwater Heaters, (4.6) Deaerator, (4.7) Condensate Storage Tanks.

5.0 Control Logic Descriptions. (5.1) Hotwell Level Control—Alarms and Indications, (5.2) Condensate Pump Control—Alarms and Indications, (5.3) LP Feedwater Heaters by Pass Controls—Alarms and Indications, (5.4) Deaerator Level Control—Alarms and Indications, (5.5) Condensate Storage Tank Controls—Alarms and Indications, (5.6) Condensate Pump Minimum Flow Control—Alarms and Indications

Lesson Plan No. 2 of 2

6.0 System Operating Instructions. (6.1) Interfacing Systems, (6.2) Prerequisites, (6.3) Limitations and Precautions, (6.4) Startup, Normal and Shutdown.

7.0 Alarm Responses. (7.1) 18 Alarm Responses.

8.0 System Examinations. (8.1) Software Examination (8.2) Hardware Examination.

APPENDIX VI

Course Outline and Lesson Plan for Condensate System No. 17: Instructor's Lesson Plan—Lesson No. 2 of 2

1.0 Review Questions: (a) Student questions from previous assignment, (b) Review control, indication and alarm for the system shown on the operational schematic. (see Lesson Plan No. 1 as required).

2.0 Introduction. (a) To review system functions, flow paths, and control, alarm, and indication to insure student understanding prior to system operating procedure training. (b) To develop student understanding of system operating procedure by discussing: systems which support the condensate system, prerequisites for startup, limitations and precautions, startup mode, normal operating mode, and shutdown mode.

3.0 Discussion of Lesson Material. (a) *System Operating Procedure:* Use Handout No. 1—Condensate System Operational Schematic. Discuss the overall functions of the system to maintain hotwell and deaerator Levels at a flow rate of 6400 gpm. (b) *Interfacing Systems:* Discuss the following systems which support the condensate system from the following list:

Supporting Systems	Supporting Function
6900V power	condensate pump power source
480V power	motor operated valves power source
d-c power	instrumentation/control power source
control/service air	air users source
demineralized water	source to condensate storage tank
heater drain	control to LP heater by-pass
bleed steam	source to deaerator heater
sampling	chemistry control
condensate polishing	regeneration of mixed beds
closed cooling water	condensate pump motor oil coolers

(c) *Prerequisites for Startup:* Prior to condensate system startup, the following items must be insured: (1) All interfacing systems identified above are operating to support the condensate system. (2) condensate system status: (A) hotwell at normal level, (B) condensate storage tank at normal level, (C) condensate system valve lineup per operational outline, (D) instrumentation and control lined up for operation, (E) closed cooling water is supplying condensate pump motor oil coolers. (d) *Limitations and Precautions:* Observe the following: (1) observe all chemistry requirements, (2) do not operate gland seal exhauster without condensate flow, (3) monitor pumps on start as appropriate. (e) *Startup Mode.* Use Handout No. 12—System Operational Outline. (f) *Normal Mode:* Use Handout No. 12—System Operational Outline. (g) *Shutdown Mode.* Use Handout No. 12—System Operational Outline. (h) *Alarm Responses:* Use Handout No. 13—Alarm Responses.

4.0 Summary of Handouts.

Handout No.	*Description*
1	Condensate System Operational Schematic

12	Condensate System Operational Outlines
13	Alarm Responses
14 and 15	System Examinations

5.0 System Examinations. (a) *Software Examination:* Use Handout No. 14—System Examination. (1) administer examination, (2) record grades. (b) *Hardware Examination.* Use Handout No. 15—System examination, (1) Review hardware examination, (2) assign working groups, (3) give oral examination, (4) grade individuals on their responses.

6.0 Recommendations for vendor or Specialist Presentations. None.

7.0 Assignment for Next Lesson. Review the next system operational schematic.

8.0 Instructor's/Trainee's Comments and Suggestions for Improvements.

APPENDIX VII

Condensate System No. 17: Software Examination

1 A shutdown condensate pump will start automatically upon an operating pump trip only if its handswitch is in the, (a) "stop" position, (b) "start" position, (c) "standby" position, (d) "normal-after-stop" position.

2 If condenser hotwell level falls below normal, makeup water is furnished (a) from the deaerator storage tank via gravity drain, (b) via the LP feedwater heater bypass line, (c) from the condensate storage tank via gravity flow, (d) from the condensate pump recirculation lines.

3 LP heaters 1-1A and 1-1B will be automatically bypassed, (a) if deaerator storage tank level is too high, (b) when LP heater 1-1A & B condensate flow is too high, (c) on LP heater 1-1A and B high outlet temperature signal, (d) on LP heater 1-1A or B high level.

4 Gland sealing water for the condensate pump shaft seals is supplied from the _____.

5 Briefly describe the operation of the condensate pump minimum flow recirculation line control.

6 List two reasons why there is a condensate pump minimum flow recirculate line.

7 What condition(s) will cause LP heaters 1-1A and 1-1B to be automatically isolated and bypassed?

8 During normal plant operation, a high hotwell level will be automatically corrected by bypassing condensate to the _____.

9 Briefly describe how you would refill LP feedwater heaters 1.1A and 1-1B if they were isolated and drained for maintenance.

10 The condensate polishing system may be bypassed, (a) automatically during high temperature conditions, (b) remotely by pushbutton control on MBB, (c) automatically during high flow conditions, (d) only manually.

11 List two components or systems which are supplied water from the condensate storage tank. Do not include the condenser(s).

12 The condensate pump motor lube oil coolers are cooled by _____.

13 List the automatic actions which take place if "Deaer ST tank level hi-hi extraction line trip" alarm annunciates.

14 Two condensate pumps must be operated at _____ percent or greater load.

15 LP heaters 1–2, 1–3 and 1–4 may only be isolated and bypassed (a) by remote-manual operation from the MBB, (b) simultaneously by hand operated control valves, (c) individually, (d) automatically.

16 The purpose of the relief valve on the suction of the condensate pumps is to prevent overpressurization during pump _____.

17 Deaerator level control is maintained by comparing what three parameters?

18 What conditions will automatically start a condensate pump?

19 LP heater isolation will *increase/decrease* deaerator heater inlet temperature?

20 While starting a condensate pump in the system for the first time, one must throttle its discharge valve because _____.

APPENDIX VIII

Condensate System No. 17: Hardware Examination

Assignment No. 1. With a condensate system operational schematic in hand, line-walk the condensate system piping and identify key components for the gravity flow makeup line from the condensate storage tank to the hotwell and from the hotwells through the condensate pumps up to their discharge valves. Include (1) individual condensate pump recirculation lines and gland seal supply (2) all supply or return connections from interfacing systems (3) all instruments which you consider to be significant (4) identify all components by their respective floor location.

Assignment No. 1 Questions (Typical Examples). (1) The condensate storage tank is chemically contaminated and must be dumped and refilled. Describe where you would go and what valves you would operate to accomplish isolation and draining of the tank. (2) Where are the local hotwell level indicator and level gauges located? (3) The gravity flow makeup control valve between the condensate storage tank and the hotwell has malfunctioned and must be manually bypassed. Describe where in the plant the manual bypass is located. (4) The instructor should choose an instrument which the students did not include as "significant" per the assignment above and request the students to justify its exclusion. (5) What effect, if any, would a high hotwell level have on plant operations?

Assignment No. 2. With a condensate system operational schematic in hand, line-walk the condensate system piping from the discharge valves of the condensate pumps to the deaerator storage tank. Include the following: (1) minimum flow recirculation line to the condenser, (2) condensate polishing system bypass and LP feedwater 1-1A and 1B valves and controls, (3) steam packing exhauster (4) exhaust hood spray line, (5) all supply or return connections from interfacing systems, (6) all instruments or local controls (not excluded above) which you consider to be significant. (7) Identify all components by their respective floor locations.

Assignment No. 2 Questions. (1) You are preparing to place the boiler feed pumps in service and find that their gland seal water is not available at the pump(s). The condensate system is pressurized and recirculating. Describe your actions including the location of any equipment to be operated. (2) You are informed by the control room that the MBB controls for LP heater(s) 1-1A & B bypass valve are inoperative. Can you operate the bypass locally/manually? Describe where you would go in the plant to accomplish this and how you would operate the valve. Assume the plant is at full load and the valve must be shut. (3) Why does the minimum flow recirculation line tap off the condensate pump discharge line where it does? Where is the flow which controls that line measured? Why? (4) Where in the plant must you go to read the indication for condensate pump discharge flow? (5) The steam packing exhauster has suffered a tube failure. Where will the water leaking from the condensate system be found? What action could be taken to minimize the consequences of the failure?

Assignment No. 3. With a condensate operational schematic in hand, line-walk the condensate system piping associated with LP Heaters 1-1A and 1B, 1–2, 1–3 and 1–4. Address only that equipment between the heaters' respective isolation valves. Include: (1) all instruments or local controls which you consider to be significant. (2) Identify all components by their respective floor locations.

Assignment No. 3 Questions. (1) The control room reports that the inlet temperature to the deaerator has been slowly decreasing over the past several shifts of full load operation. How could you tell locally which heater(s) might be malfunctioning? (2) In regard to the above questions, how could you tell from the control room which heater(s) might be malfunctioning? (3) Where in the plant are the LP Heaters 1-1A & B inlet and outlet pressure gauges located? (4) Where in the plant is the local jog pushbutton for LP heaters 1-1A and 1B inlet valve HMV-473A? (5) What is the purpose of the local jog pushbutton for HMV-473A?

Assignment No. 4. With a condensate system operational schematic in hand, line-walk the deaerator and deaerator storage tank including all instrumentation and accessories mounted on the tank.

Show all connections including their identification by floor location.

Assignment No. 4 Questions. (1) Where would you be standing to read the local deaerator storage tank level? (2) What is the normal deaerator storage tank level which you would expect to see at full load? (3) The deaerator shell local pressure indicator PI-82 is broken. From the vicinity of the deaerator, how could you tell what the shell pressure is during full load operation?

Assignment No. 5. With a condensate system operational schematic in hand, line-walk the condensate drain return tank including: inputs and outputs, instrumentation, identification of components by floor location.

Assignment No. 5 Questions. (1) What are the inputs into the condensate drain return tank? (2) Where do the outputs from the condensate drain return tank go?

W. J. Heilker
Section Manager,
Analytical Engineering, NCE,
Mem. ASME

R. Q. Vincent
Supervisor,
Component Engineering Test Laboratory,
Assoc. Mem. ASME

Combustion Engineering, Inc.,
Chattanooga, Tenn 37402

Vibration in Nuclear Heat Exchangers Due to Liquid and Two-Phase Flow

In order to optimize a steam generator tube bundle support system, it is necessary to understand the differences in vibration behavior of tube arrays subjected to a two-phase flow regime as compared to a single phase flow regime. The relationships discussed in this paper are based on findings derived from a comprehensive vibration testing program which included both water and simulated two-phase (air-water) flow regimes. Tube bundles of various configurations and spacings were tested in crossflow using $^3/_4$ in. (1.9 cm) and $^7/_8$ in. (2.2 cm) o.d. tubes with 36 in. (91 cm) span lengths and as many as 40 tubes per array. Sufficient test loop capacity was provided to drive most test array configurations up to and beyond fluid-elastic instability. Parameters obtained included displacement, effective force coefficients, damping coefficients, Strouhal numbers, and instability constants for various tube array configurations in both liquid and simulated two-phase flow mediums.

Introduction

The primary cause of tube vibration in a heat exchanger is the propensity for the tubes to extract energy from the shell side flow and convert it into tube motion. The extent of movement experienced by the tubes is dependent on the velocity, density and relative orientation of the flow regime as well as tube bundle geometric parameters such as tube diameter, pitch and span stiffness.

In a typical inverted U-tube steam generator, of the type found in the majority of PWR nuclear power plants, there are, for vibrational assessment purposes, three types of shell side flow. The first, bundle entrance flow is composed of either subcooled or saturated water of high density which enters the lower type bundle in cross-flow at various orientations to the pattern of the tube array. The second, bundle exit flow is composed of a water and steam mixture traveling in a more or less vertically upward direction and subjecting tube spans in the U-bend region to crossflow. While this flow does not possess the density of entrance flow, it may be capable of exciting tube spans in the upper region which are normally not as well supported as tube spans in the entrance region. The third type of shell side flow is axial flow which does not possess nearly as much potential for exciting tube spans as crossflow. Therefore, it has not been included as a subject of this study.

The purpose of this study was to examine several tube bundle configurations in a parametric manner to determine their susceptibility to flow-induced vibration caused by either liquid or simulated two-phase cross-flow.

Experimental Facility

Test Loop. The experimental data presented in this paper were obtained from a water flow loop (Fig. 1) capable of delivering room temperature water at a maximum flow rate of approximately 5000 gpm (0.32 m^2/s). The loop consisted of a holding tank, centrifugal pump, flow control valves, flow meters, approach section, test section, air supply system and related piping. The holding tank had a capacity of 2000 gal (7.6 m^3) and contained an inner tank which acts as an air-water separator for two-phase tests. A centrifugal pump powered by a 100 hp (75 kW) moter (mounted on a sand lined concrete pedestal to dampen pump vibrations) provided water flow to the loop with manual globe valves used to set the desired flow rate. Venturi meters in the piping measured the flow rate of air and water separately.

The approach section to the model consisted of a diverging-converging rectangular transition section to provide a uniform fully developed turbulent velocity profile to the test model. The loop was designed to accept test models up to 7 ft (2.13 m) in height with rectangular mating flanges giving a cross-sectional flow area 36 in. × 8.75 in. (91 cm × 22 cm). A downstream transition section converted the loop from rectangular back to a circular cross-section pipe which returns to the holding tank. Main loop piping was 12 in. (30 cm) schedule 10 with a 4 in. (10 cm) by-pass for setting low flow rates, up to 1000 gpm (0.06 m^3/s).

Air supply for two phase testing was delivered to the loop at 100 psig (0.69 MPa) where it in turn was filtered and the pressure reduced through a regulator before being exhausted into the test section. Optional manual or air controlled valves were used to set the desired air flow rate.

Test Model. Models covered in this paper simulated areas in heat exchangers were the tubes experience cross flow such as entrance and exit regions. The models measured 3 ft (0.91 m) in height (flow direction) with the tube bundle span length fixed at 3 ft (0.91 m) (Fig. 2). Tubes were supported in a horizontal position by O'rings at each end in removable end plates with the flow being upward across the tube bank. Tube bundle sizes ranged from 4 tubes for row test array 13 to 41 tubes for full bundle test array 8. Acrylic material was used on the front wall and one end plate for observing the vibrations and

Contributed by the Nuclear Engineering Division of THE AMERICAN SOCIETY OF MECHANICAL ENGINEERS and presented at the Century 2 Nuclear Engineering Conference, San Francisco, Calif., August 19–21, 1980. Manuscript received at ASME Headquarters March 6, 1980. Paper No. 80-C2/NE-4.

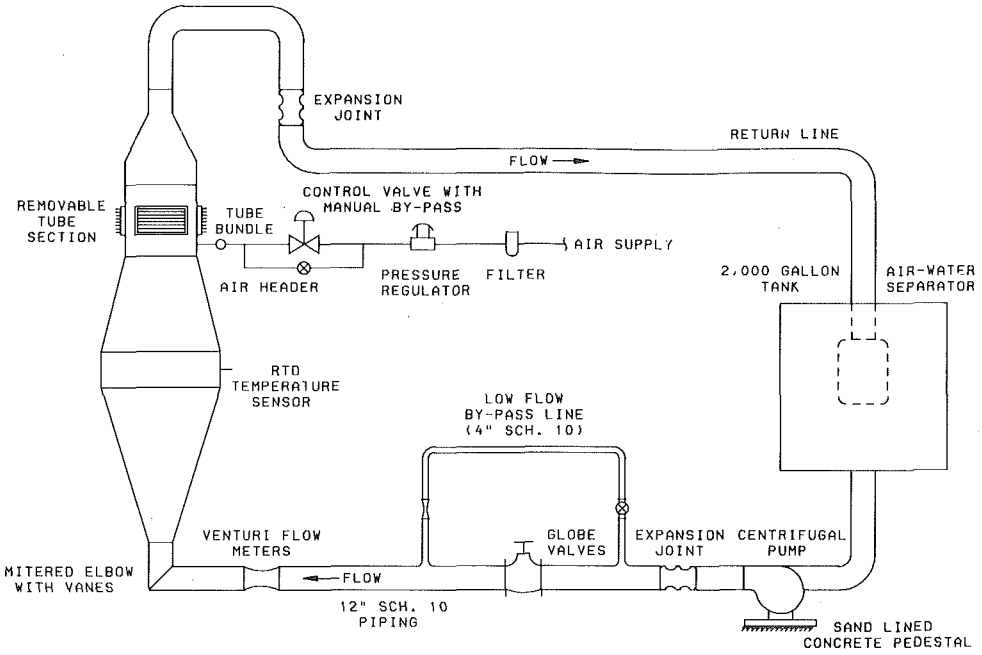

Fig. 1 Test loop

two phase mixture. Half rounds were attached to the front and back walls to prevent any by-pass flow. Velocity profiles upstream of the tube bundle were obtained from pitot tube traverses in two perpendicular directions in the plane transverse to the flow which showed the velocity to be essentially constant over the cross-sectional flow area. Tubes were dry on the inside to simplify instrumentation with the effect of primary side fluid being handled analytically as additional mass.

Air was injected below the tube bundle through mixer tubes perforated with 0.094 in. (0.24 cm) dia holes along the length every 0.5 in. (1.3 cm). Mixer tubes were sized and located to provide a homogeneous two phase mixture to the tube bundles with minimum slip between the phases.

Instrumentation and Data Acquisition. Selected tubes were instrumented internally to measure the mid-span vibration motion in two directions—with the flow (drag direction) and transverse to the flow (lift direction). A bi-axial piezoelectric accelerometer and semi-conductor strain gages were mounted inside the tubes to determine mid-span deflections under flow conditions and to generate frequency content. The majority of tests included four strain gaged tubes and one tube equipped with an accelerometer. Data were recorded simultaneously on a 14 channel FM tape recorder for post test analysis. Figure 3 is a diagram of the instrumentation-data acquisition system. A real time analyzer and digital signal analyzer were used on-line to monitor the vibration amplitudes in the frequency and time domains to insure that a resonant condition was not overlooked in going from no flow to maximum flow conditions. In addition, a two channel x-y oscilloscope was used to observe the orbital motion of two adjacent tubes. Samples of the CRT displays are shown in Fig. 4. Off line analysis included generating power spectral density, coherence,

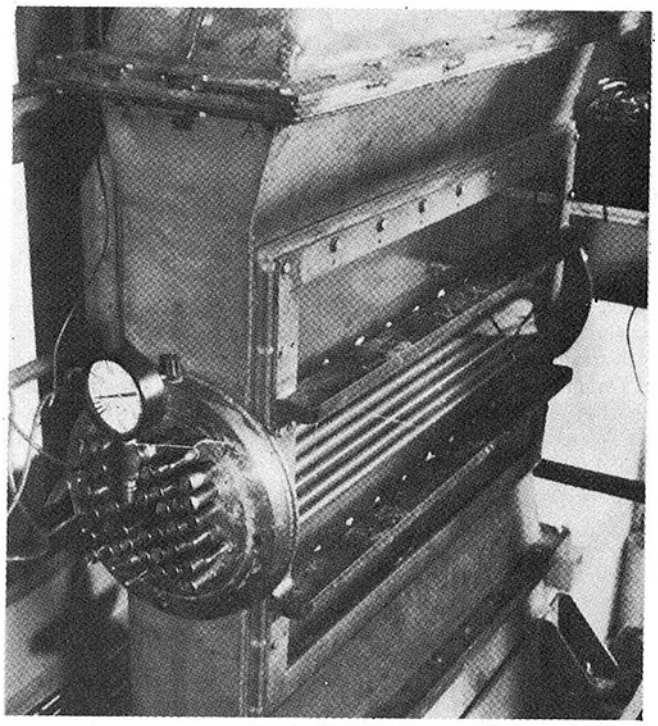

Fig. 2 Model I

Nomenclature

C_F = effective force coefficient
d = tube outside diameter, in. (cm)
F_f = effective fluid force, lb/ft (N/m)
f_n = fundamental frequency, H_z
f_v = vortex shedding frequency, H_z
g = gravitational constant, ft/s^2 (m/s^2)
H_z = analysis bandwidth frequency, H_z
K = fluid-elastic instability constant
M_0 = reference tube density, lb/ft (N/m)
P = pitch, distance between centerline of tubes, in. (cm)
P_f = fluid pressure = $\rho V_g{}^2/2g$, lb/ft^2 (Pa)
S = Strouhal number = $f_v d/V_G$
t = time, s
U = displacement, in. (cm)
V_c = critical instability velocity, ft/s (m/s)
V_g , gap velocity = $[P/(P - d)]V\alpha$, ft/s (m/s)
V_α = freestream velocity, ft/s (m/s)
α = void fraction
δ_0 = logarithmic decrement = $2\pi\zeta$
δ_R = resultant deflection = $(\delta_x{}^2 + \delta_y{}^2)^{1/2}$, in. (cm)
δ_x = deflection transverse to flow direction, in. (cm)
δ_y = deflection in flow direction, in. (cm)
ζ = critical damping ratio
ρ = fluid density, lb/ft^3 (Kg/m^3)
ω = frequency, radians/s

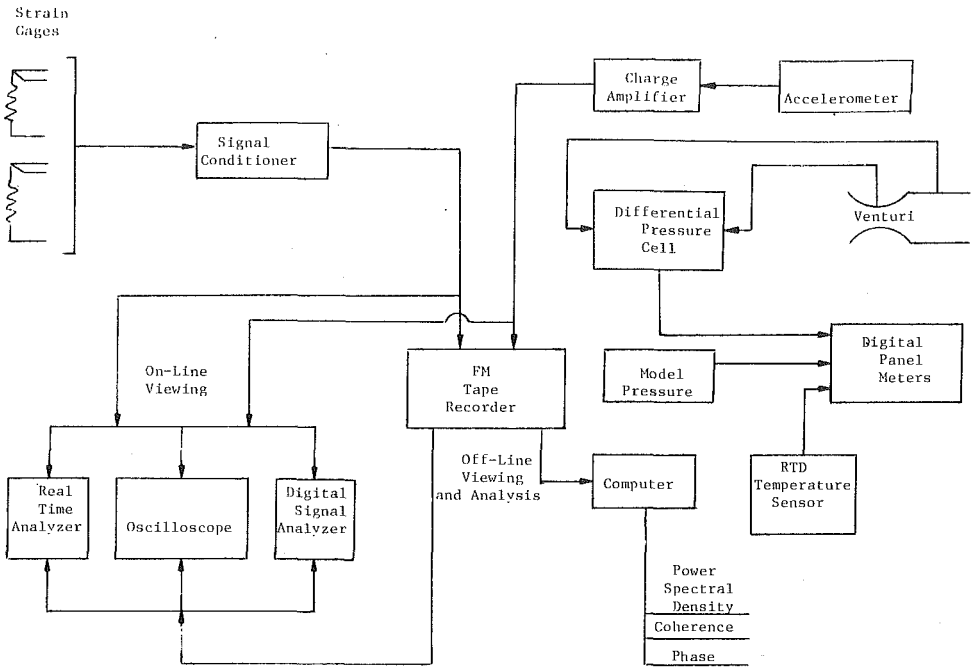

Fig. 3 Instrumentation diagram

and phase plots from a computer analysis of the FM tape, samples of which are shown in Fig. 5. Signals were also root mean square averaged on a RMS voltmeter for approximately one minute to give an average displacement or acceleration level for each instrumented tube for each run.

Flow rates were determined by differential pressure cells which measured the head produced across venturis and the fluid temperature was monitored by a RTD. Model pressure was obtained from a pressure transducer located in the back wall of the test models.

Tube Arrays

Liquid Flow. Table 1 is a compilation of test configurations reported in this paper. Pertinent geometric parameters are included therein. Four models were tested in liquid flow, two with a triangular pitch arrangement and two with a square pitch arrangement (see Fig. 6). Tests for models I, III and IV also examined the flow approach angle (layout angle) where the tube arrangements varied from in-line to staggered. In addition to the full bundle test models I, III, and IV were also tested with only a single row of tubes for comparison with published data [1].

Water tests were conducted by incrementing the flow rate from zero up to the point where large amplitude vibrations (instability, tubes impacting) were encountered or the flow capacity of the loop was reached. Data were recorded at the incremental steps with the tube motion being monitored on-line in going from one step to the next. Model 1 velocity was driven past the point of instability by a factor of 3 to determine if amplitudes would decrease as typified by vortex shedding resonance. Amplitudes remained large with tubes impacting violently.

Two-Phase Flow. Two-phase cross-flow occurs in the upper bend region of a U-tube heat exchanger where the flow direction is essentially fixed. For this reason only two models (Table 1) were tested (one triangular pitched and one square pitched) at fixed layout angles.

Void fractions expected in the upper bend region of U-tube heat exchangers were generated using the Martinelli-Nelson Correlation which was applied for various power levels of operation. These volumetric ratios were established experimentally by metering the air and water flows prior to mixing at the model pressure. The quantities of air and water were varied to give a range of mixture velocities, which bracketed the average velocities generally anticipated for operating nuclear heat exchangers. Results obtained are of interest, since higher than average local velocities may be expected for complex tube bundle arrangements.

Test Results

Some Basic Terms. Before discussing specific details of the test results, it is useful to mention some of the concepts used in processing the test data in terms of the general findings.

In order to have a uniform method for determining the gap velocity of the fluid flowing through the various tube arrays, the convention established by Pettigrew [2] was used which is

$$V_g = \frac{P}{(P-d)} V_\alpha \tag{1}$$

This convention was applied to both triangular and square pitch arrays regardless of the orientation of the flow relative to the array.

A general observation which was made with regard to tube motion, for either water or air-water flow media and for both small and large amplitude displacements, was that movement tended to be orbital with no preference for the apogee to be oriented in the direction of flow or perpendicular to the direction of flow. Sometimes the orbit would remain steady but at other times it appeared to be revolving as indicated in Fig. 4. As fluid velocity was systematically increased by increments, tubes exhibiting steady orbits would sustain orientation changes in their orbits or the orbits would become unsteady. For these reasons, it could be misleading to plot the increase in RMS tube displacement as a function of increased fluid velocity in either the drag (direction of flow) or life (perpendicular to direction of flow) directions. An increase or decrease in displacement in a particular direction could as easily be caused by a change in orbital orientation as by a change in the magnitude of excitation. Therefore the concept of a resultant RMS deflection was used in this study which is as follows.

$$\delta_R = (\delta_x{}^2 + \delta_y{}^2)^{1/2} \tag{2}$$

Accordingly the term effective force coefficient (C_F) was used to describe the relationship between deflection (δ_R) and fluid pressure regardless of the direction of deflection.

Tube Bundle Response to Flow. In presenting the primary data of this study, tube excitation as a function of flow rate, it was found useful to plot tube deflection versus fluid pressure where fluid pressure is defined as

$$P_f = \frac{\rho V_G{}^2}{2g} \tag{3}$$

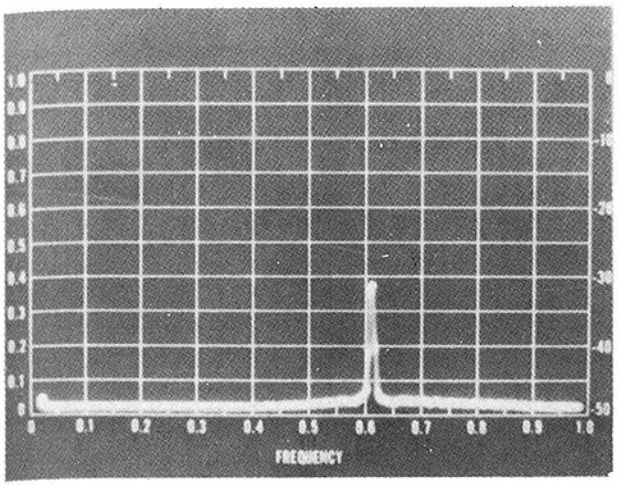

Fig. 4(*a*) Real time analyzer spectrum, $\delta = 0.038$ in.

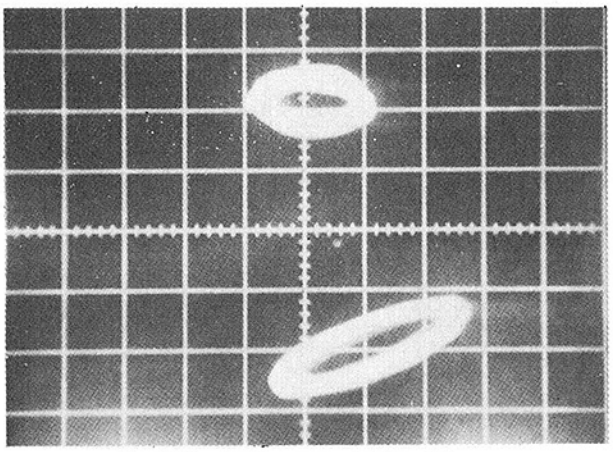

Fig. 4(*d*) Oscilloscope—steady orbits

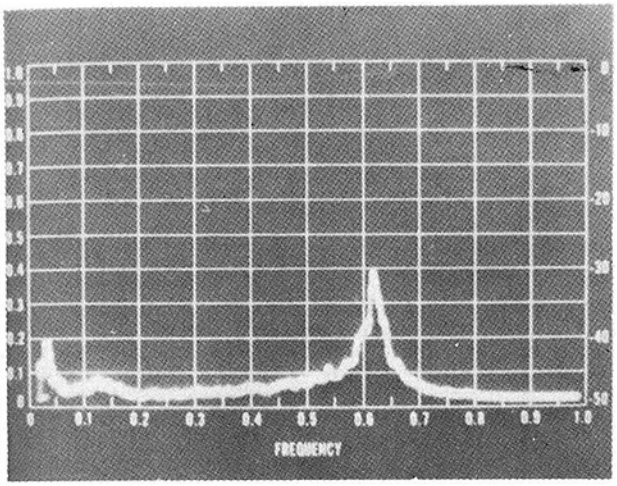

Fig. 4(*b*) Real time analyzer spectrum, $\delta = 0.001$ in.

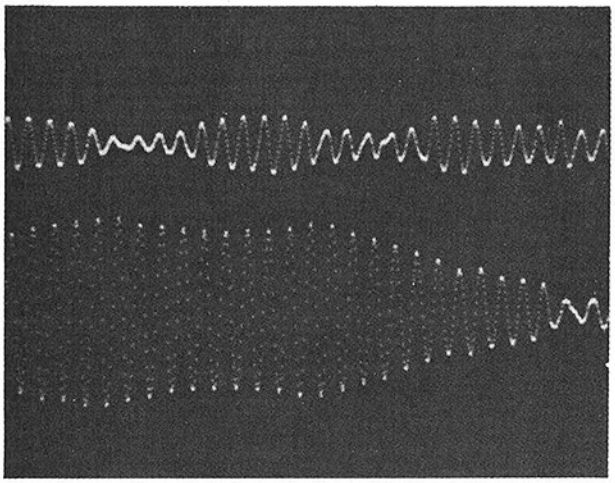

Fig. 4(*e*) Digital signal analyzer—$\delta = f(t)$

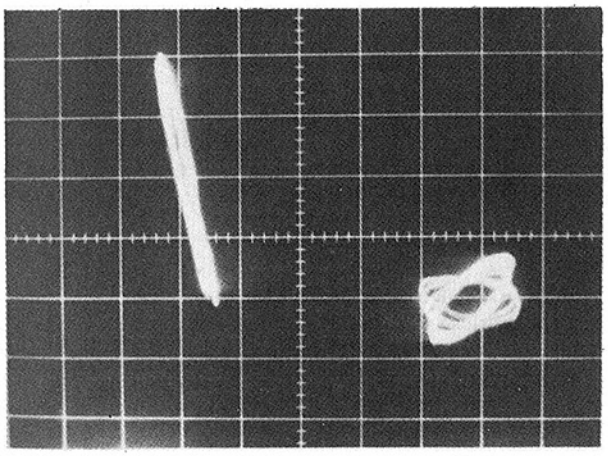

Fig. 4(*c*) Oscilloscope—revolving orbit

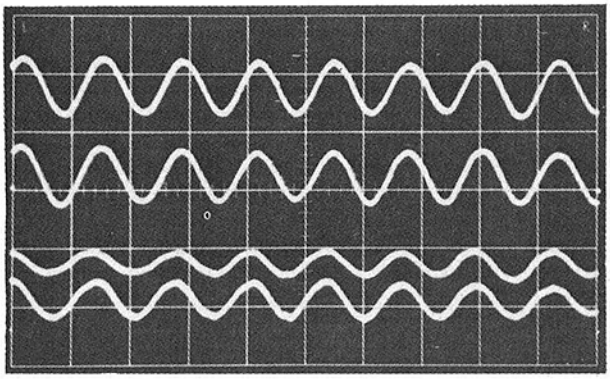

Fig. 4(*f*) Digital signal analyzer—constant amplitude time traces

Fig. 4 Cathode ray tube displays

This was convenient for several reasons. First, it seemed intuitively correct that tube response would be linearly proportional to the dynamic head of the fluid medium and was, up to the point at which the amplitude of vibration gave rise to the feedback mechanism that led to fluid-elastic instability. Secondly, it facilitated the comparison of displacement caused by flowing fluids of different densities, specifically the comparison of water flow to simulated two-phase (air-water) flow. Finally, it led directly into the calculation of effective force coefficients.

By inspection of the plots found in Fig. 7(*a*)–(*e*) it was readily apparent that array configuration had a significant bearing on the susceptibility of that array to flow induced excitation. Also of importance was the flow orientation relative to the array. In discussing flow orientation in this study the convention adopted by Chenoweth [3] was adhered to, but even this system was not without its pitfalls. Notice the confusion among array No. 6 of triangular pitch, and arrays No. 8 and 10, having square pitch.

The triangular pitch bundle arrays were not prone to vortex

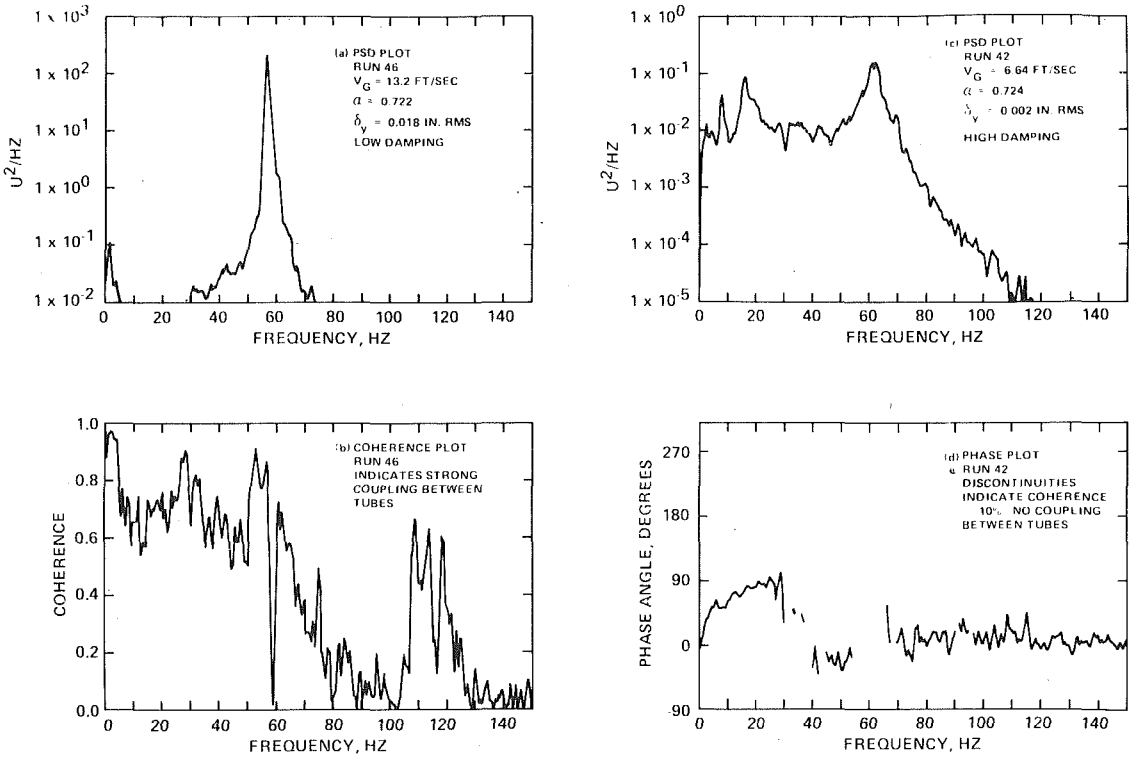

Fig. 5 Off-line computer processed data

shedding resonance, but the row array for Model 1 displayed a pronounded resonance peak before it began its ascent to instability. In the case of both Models I and III, the 60 deg orientation (tubes in-line) demonstrated the strongest tendency toward instability. By contrast in both models the 30 deg orientation showed the least tendency toward instability, in fact, they showed little more susceptibility than the row arrays. One might think of the 30 deg array orientation as a series of row arrays constructed in a staggered fashion. Differences in performance between flow orientations of 30 deg and 60 deg are somewhat academic, however, in the vibratory evaluation of nuclear heat exchangers. Since flow normally enters the bundle all around the periphery, a complete spectrum of flow approach angles exist and the controlling orientation of 60 deg must be considered in the support design. Of particular interest was Fig. 7(*d*), which demonstrated that tube vibration instability can occur in the presence of two-phase flow with only slightly greater fluid pressure required. It should be noted that this phenomenon occurred over a wide range of void fractions, from 0.65 to 0.87, the range normally found in the upper bundle regions of steam generators in nuclear service. The fluid pressure required for tubes to approach instability was somewhat proportional to α. An α of 0.87 caused the tubes to approach instability at a fluid pressure of only 40 percent more than required for water flow. It was presumed that the air-water flow media used in Model II would have eventually caused fluid-elastic instability had sufficient loop capacity existed. Due to the large spacing which was represented in Model II, the tube bundle was just approaching instability for water flow when the maximum pump capacity was reached.

The square pitch bundle, Model IV, indicated various degrees of susceptibility to both vortex shedding resonance and fluid-elastic instability. The potential for vortex shedding resonance induced tube damage in tube bundles was first recognized by Chen [4]. The pertinent relationship is:

$$S = \frac{f_v d}{V_G} \tag{4}$$

Chen's work indicated that higher Strouhal numbers exist for tube bundles than the classical value of $S = 0.2$ for single tubes. The data from Model IV yielded Strouhal numbers as high as $S = 0.5$ for the 90 deg orientation. Practical design limitations make it difficult to design above this value, so there might be come concern for square pitch arrays. It should be remembered, however, that vortex shedding resonance was not found in the triangular pitch tube bundle arrays nor was vortex shedding resonance found in the two-phase flow tests of Model II (two-phase flow tests were not performed for Model IV).

Table 1 Tube and array geometry

MODEL NO.	ARRAY NO.	ORIEN-TATION (REF. 9)	TUBE d IN.*	TUBE PITCH DIMEN. IN.*	SQUARE OR TRI.	FLOW MEDIUM WATER OR AIR-WATER
		TUBE BUNDLE ARRAYS				
I	1	60°	0.750	1.000	Triangular	W
I	2	50°	0.750	1.000	Triangular	W
I	3	40°	0.750	1.000	Triangular	W
I	4	30°	0.750	1.000	Triangular	W
III	5	60°	0.866	1.181	Triangular	W & A-W
III	6	45°	0.866	1.181	Triangular	W
III	7	30°	0.866	1.181	Triangular	W
II	8	45°	0.750	1.123	Square	W & A-W
IV	9	90°	0.875	1.234	Square	W
IV	10	45°	0.875	1.234	Square	W
		TUBE ROW ARRAYS				
I	11	Row	0.750	1.000	--	W
IV	12	Row	0.875	1.234	--	W
III	13	Row	0.866	1.181	--	W

*NOTE - 1 in. = 2.54 cm

The square pitch bundle arrays in both Models II and IV displayed less inclination toward fluid elastic instability than did the triangular pitch tube bundle arrays. One reason for this difference could be the generally tigher spacings employed in triangular pitch bundles. When sufficient fluid pressure was applied, however, all arrays tested could be forced to become unstable.

Fluid-Elastic Instability. The concept of fluid elastic instability was introduced by Connors in 1970 [1] and further developed in 1977 [5]. Additional studies were conducted by Pettigrew and Gorman [2, 6, 7] and by Blevins [8]. Each of these authors contributed additional data points on the cumulative stability diagram. The instability relationship can be expressed as follows.

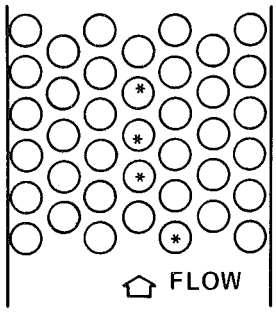

Fig. 6(*a*) Array 1

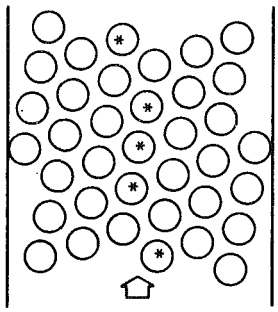

Fig. 6(*b*) Array 2

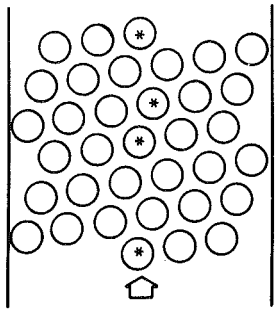

Fig. 6(*c*) Array 3

* DENOTES INSTRUMENTED TUBES

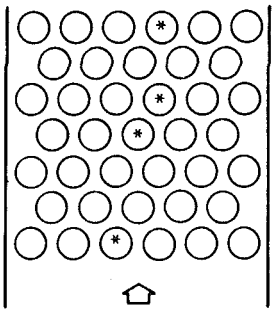

Fig. 6(*d*) Array 4

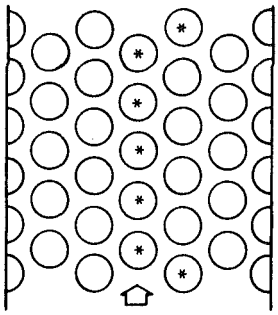

Fig. 6(*e*) Array 5A

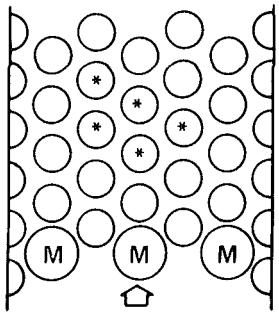

Fig. 6(*f*) Array 5B

(M - AIR MANIFOLD PIPES)

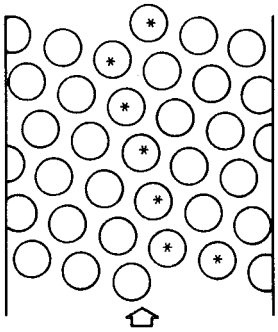

Fig. 6(*g*) Array 6

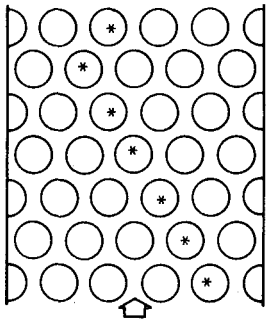

Fig. 6(*h*) Array 7

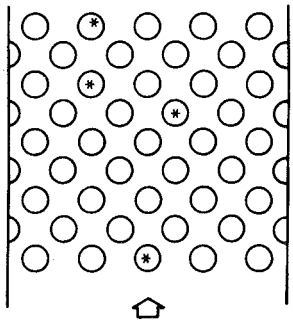

Fig. 6(*i*) Array 8A

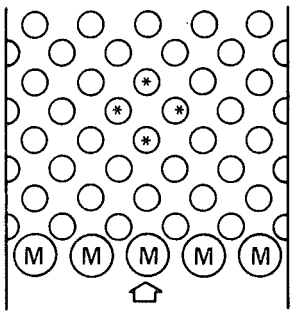

Fig. 6(*j*) Array 8B

(M - AIR MANIFOLD PIPES)

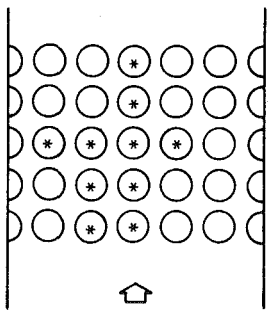

Fig. 6(*k*) Array 9

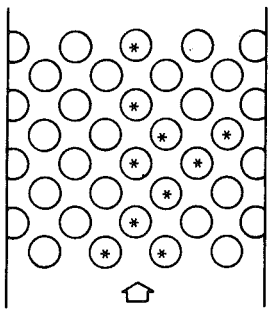

Fig. 6(*l*) Array 10

Fig. 6(*m*) Array 11

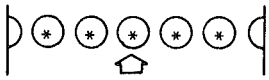

Fig. 6(*n*) Array 12

Fig. 6(*o*) Array 13

Fig. 6 Tube arrays tested

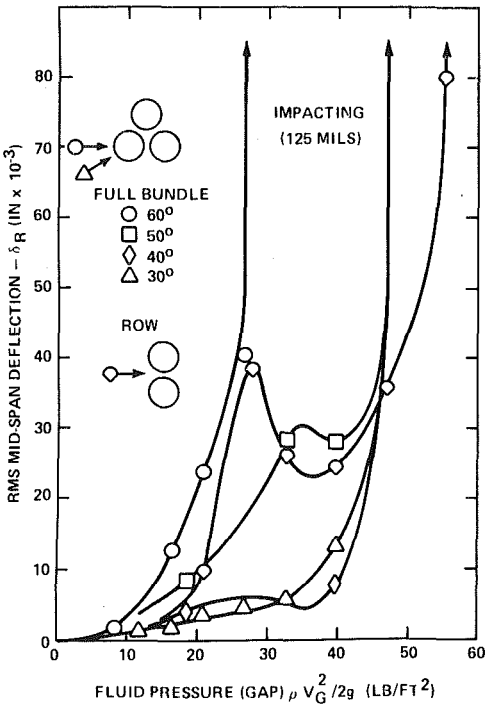

Fig. 7(*a*) Model I—water flow

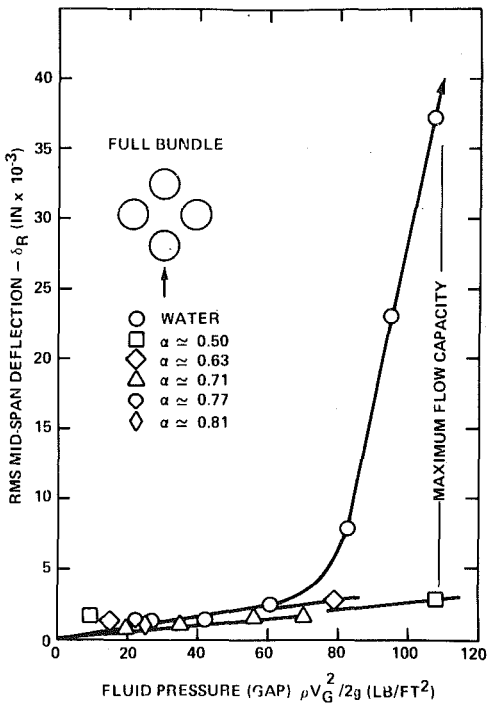

Fig. 7(*b*) Model II—water and 2 phase flow

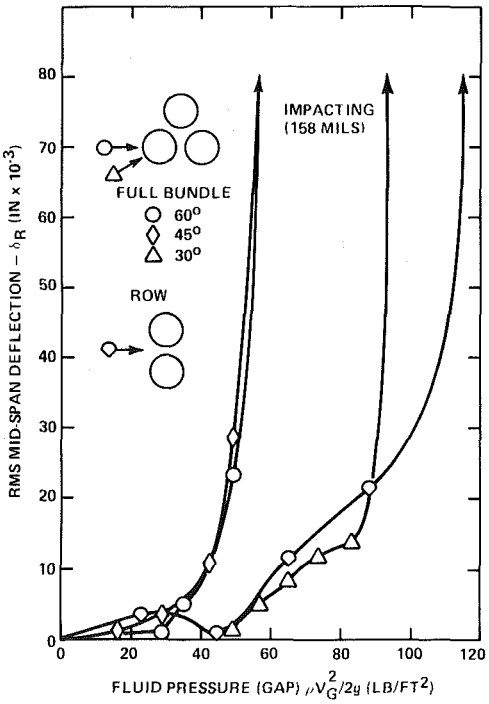

Fig. 7(*c*) Model III—water flow

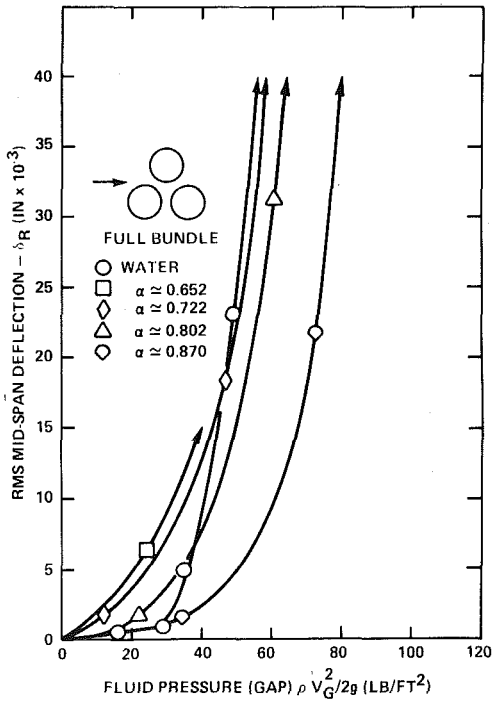

Fig. 7(*d*) Model III—water and 2 phase flow

Fig. 7 Tube deflection versus fluid pressure

$$\frac{V_c}{f_n d} = K\left[\frac{M_0\delta_0}{\rho d^2}\right]^{1/2} \tag{5}$$

The relationship can also be expressed graphically by means of a stability diagram such as Fig. 8. In this study, the criteria for instability was either impacting between tubes or rattling within supports accompanied by large deflections in the case of widely spaced tube arrays.

The contribution of this study to the existing body of knowledge in the area of fluid-elastic instability is two-fold. First, some data points representing tube bundle configurations common in nuclear heat exchanger service, but previously unreported, have been contributed. Second, the simulated two-phase flow data points were the first generated by a large scale test wherein the tube bundle models were subjected to two-phase flow along the entire span length (36 in.) (91 cm) at prototypical fluid velocities. It should be pointed out that Pettigrew [6] studied the effects of subjecting a portion of the tube span of a small tube bundle to simulated two-phase flow.

Examining Fig. 8 revealed several interesting points. The instability data point for array Number 12 (row array) was very close to the

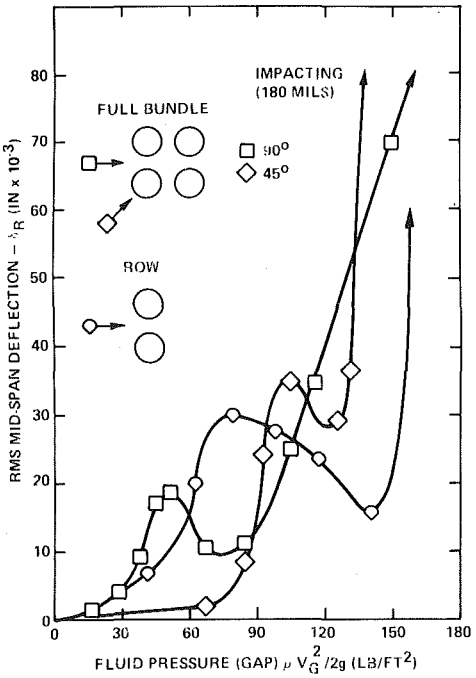

Fig. 7(*e*) Model IV—water flow

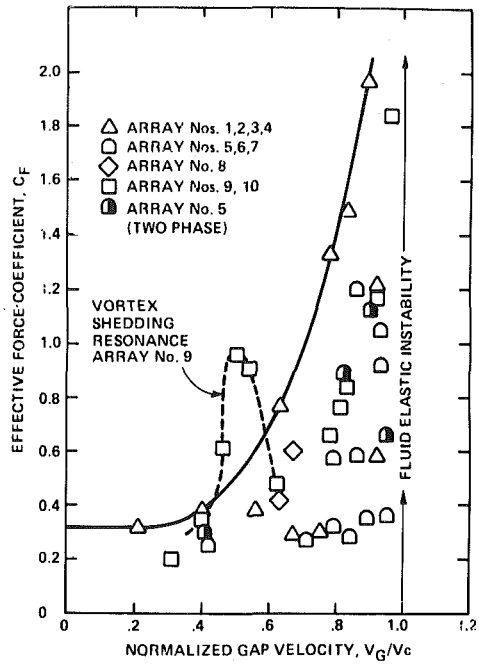

Fig. 9 Upperbound effective force coefficient

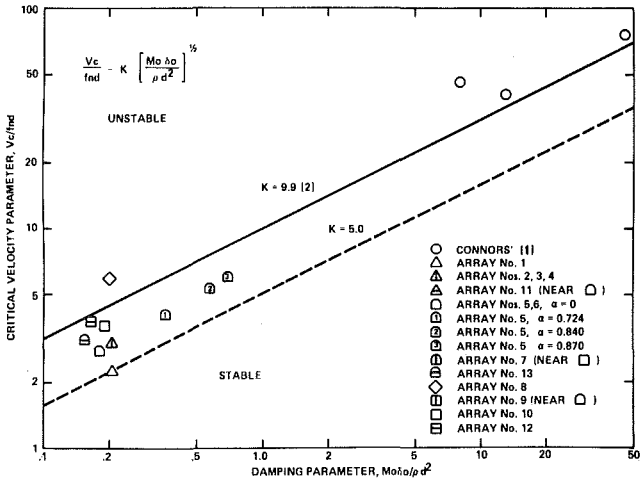

Fig. 8 Stability diagram

original instability line suggested by Connors [1]. Array Number One established the lowest instability line for this study ($K = 5.0$), while the widely spaced array Number Eight was the highest as might have been expected. Note that for array Number Five, air-water mixtures possessing void fractions of 0.724, 0.840 and 0.870, as well as 100 percent water flow, all fell on essentially the same instability line.

Effective Force Coefficient. In an effort to enhance the use of this study a design tool, an attempt was made to find some common ground among the tube bundle arrays tested in quantifying the parameter, effective force coefficient. This parameter, not to be confused with the lift coefficient associated with vortex shedding, is a measure of the tube's ability to extract energy from the flowing fluid. Assuming that instability has been prevented in the design process, it might be useful to make predictions of actual amplitudes expected so that some assessment of tube performance with regard to high cycle fatigue and fretting could be made. The outcome of the aforementioned effort is Fig. 9. The following expression was used to calculate the effective force coefficient.

$$F_f = C_F d \frac{\rho V_G^2}{2g} \sin \omega t \tag{6}$$

where F_f is a function of resultant deflection, tube span geometry and damping. If a designer were to measure or obtain through the literature the critical instability velocity for a particular tube bundle array and flow medium, he could utilize Fig. 9 to obtain an upper bound effective force coefficient for a gap fluid velocity of interest. However, corrections for differences in damping would need to be made. With the notable exception of the vortex shedding resonance peak experienced by array Number Nine, which was discussed earlier, the solid line curve upper bounds all of the data points for each tube bundle array tested, of which only a representative sample is shown. It might be noted that a design which maintained a separation factor of two from the critical velocity should experience no significant tube vibration provided a thorough check was made to preclude the possibility of a vortex shedding resonance.

Damping. A prediction of a fluid-elastic instability coefficient is only as valid as the damping measurements used to obtain it. There are basically two methods which are generally used to calculate damping, the log decrement technique and the half-power point method. Detailed descriptions of these methods are contained in reference [9]. Damping measurements were made in stationary water using the log decrement method and in flowing fluid (both water and two-phase) using the half-power point method. Obviously a stationary two-phase medium could not be maintained in an air-water simulation of two-phase flow (see Fig. 10). Therefore, the half-power point method was used exclusively for the measurement of damping in two-phase flow. There was agreement between stationary water and slowly flowing water damping measurements, but as the flow rate was increased, the damping values decreased. The range was $\zeta = 0.4$–1.5 percent for water. Damping also decreased with increasing flow rate for two-phase flow with the measured range being $\zeta = 0.8 - 4.0$ percent. Figure 5 illustrates the variance of damping with flow rate. Comparing the PSD plots 5(*a*) and 5(*c*), which have in common a similar void fraction and $f_n = 56$–62 Hz, run 46 had double the flow velocity of run 42. The great difference in amplitude for run 46 (a factor of 9) is attributable in part to much lower damping as characterized by the more slender response peak.

Damping values used in this study to plot and establish fluid-elastic instability were taken from flowing fluid using the half-power point method. This damping was predominantly viscous and some additional structural damping might be expected in actual heat exchangers.

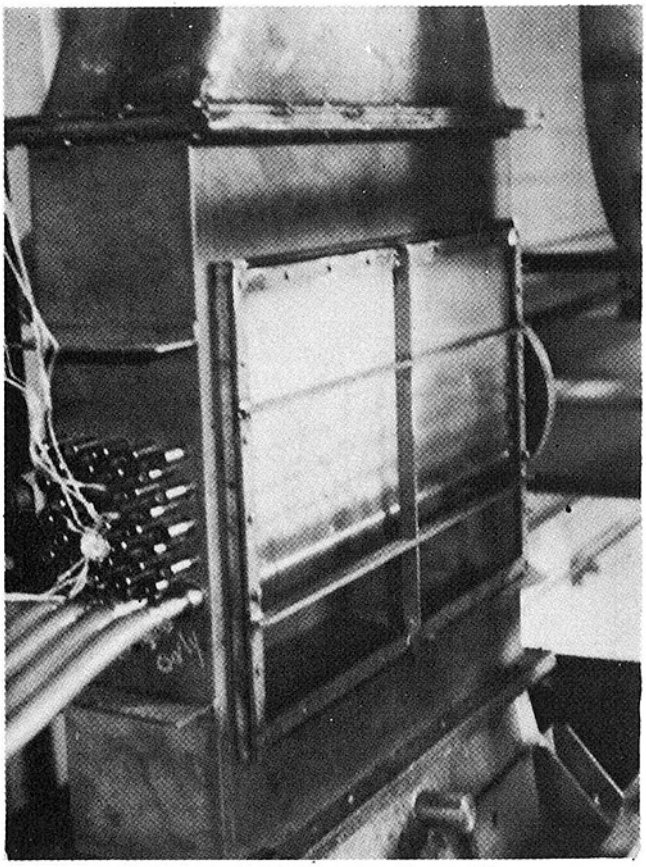

Fig. 10(*a*) Model II—front view two-phase test in progress

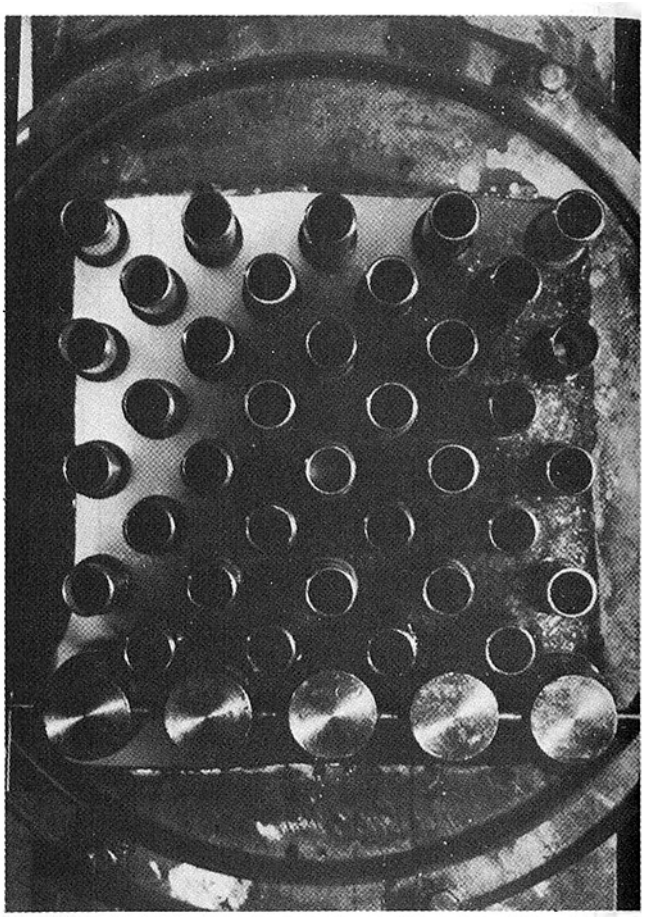

Fig. 10(*b*) Model II—side view two-phase mixture viewed through transparent end plate

Conclusions

In tube bundle arrays representative of those most commonly used in inverted U-tube steam generators for PWR nuclear power plants, experiments were carried out to determine the susceptibility of those arrays to flow-induced vibration. The concepts of gap velocity $V_G = (P/(P - d))V_\alpha$, resultant deflection $\delta_R = (\delta_x{}^2 + \delta_y{}^2)^{1/2}$ and fluid pressure $P_f = \rho V_G{}^2/2g$ were used to process the data from the 13 tube arrays tested. Conclusions reached were:

1 All arrays were shown to be prone toward fluid-elastic instability according to the relationship $V_c/f_n d = K\,(M_0\delta_0/\rho d^2)^{1/2}$. The tightly packed triangular pitch arrays were the most susceptible, the 60 deg flow orientation controlling, with an instability constant $K = 5.0$. The square pitch arrays demonstrated a propensity for vortex shedding resonance according to the relationship $S = f_v d/V_G$. The highest Strouhal number was measured for the 90 deg orientation at $S = 0.5$.

2 It was shown that fluid-elastic instability could be induced by simulated two-phase flow. Only 40 percent more fluid pressure was required of flow possessing a void fraction of 0.870 to cause tubes to approach instability than was required of water flow.

3 A concept for upper bounding the effective force coefficient was introduced. An observation was made that by maintaining a separation factor of two from the critical instability velocity, most arrays would experience no significant tube vibration.

References

1 Connors, H. J., Jr., "Fluidelastic Vibration of Tube Arrays Excited by Cross Flow," *Flow-Induced Vibration of Heat Exchangers,* ASME, Dec. 1970, pp. 42–56.

2 Pettigrew, M. J., Gorman, D. J., "Vibration of Heat Exchanger Components in Liquid and Two-Phase Cross-Flow," Paper No. 2:3, *International Conference on Vibration in Nuclear Plant,* Keswick, U. K., 1978.

3 Chenoweth, J. M., "Flow-Induced Tube Vibrations in Shell-and Tube Heat Exchangers," Final Report, ERDA Contract No. EY-76-C-03-1273, 1977.

4 Chen, Y. N., "Flow-Induced Vibration and Noise in Tube-Bank Heat Exchangers due to Von Karman Streets," ASME Paper 67-VIBR-48, 1967.

5 Connors, H. J., Jr., "Fluidelastic Vibration of Heat Exchanger Tube Arrays," *Journal Mechanical Design,* Vol. 100, 1978, pp. 347–353.

6 Pettigrew, M. J., Gorman, D. J., "Experimental Studies on Flow Induced Vibration to Support Steam Generator Design, Part III–Vibration of Small Tube Bundles in Liquid and Two-Phase Cross-Flow," Paper No. 424, *International Symposium on Vibration Problems in Industry,* Keswick, U. K., 1973.

7 Gorman, D. J., "Experimental Development of Design Criteria to Limit Liquid Cross-Flow-Induced Vibration in Nuclear Reactor Heat Exchange Equipment," *Journal of Nuclear Science and Engineering,* Vol. 61, 1976, pp. 324–326.

8 Blevins, R. D., "Fluid Elastic Whirling of a Tube Row," *Journal of Pressure Vessel Technology* Vol. 96, 1974, pp. 263–264.

9 Harris, C. M., Crede, C. E., *Shock and Vibration Handbook,* Second Edition, 1976, McGraw-Hill, New York.

J. Moore[1]
J. G. Moore[1]
Rolls-Royce, Aero Division,
Bristol, England

Calculations of Three-Dimensional, Viscous Flow and Wake Development in a Centrifugal Impeller

A partially-parabolic calculation procedure is used to calculate flow in a centrifugal impeller. This general-geometry, cascade-flow method is an extension of a duct-flow calculation procedure. The three-dimensional pressure field within the impeller is obtained by first performing a three-dimensional inviscid flow calculation and then adding a viscosity model and a viscous-wall boundary condition to allow calculation of the three-dimensional viscous flow. Wake flow, resulting from boundary layer accumulation in an adverse reduced-pressure gradient, causes blockage of the impeller passage and results in significant modifications of the pressure field. Calculated wake development and pressure distributions are compared with measurements.

Introduction

Flows in the impellers of centrifugal compressors are among the most complex in turbomachinery. They occur in rotating passages of complex geometry usually with a stationary shroud wall. They are often transonic with shocks in the inducer, they have significant viscous and secondary flows, they can be unsteady and include regions of separation, and there are known mechanisms by which the structure of their turbulence can be modified by both the rotation and curvature of the passage.

It is just over ten years since Dean [1] gave a comprehensive review of the experimental observations supporting this complex picture. The timing is of interest, for among Dean's statements were the following: "the prediction of the effect of secondary flow upon separation patterns in the impellers is truly a complex matter which will not be amenable to analysis . . . because the secondary flow alone does not affect the separation pattern, but many other things do too . . ." and "the hope of putting together a complete theory is rather dim now and would seem to be so for ten years at least into the future." Now is, therefore, an appropriate time for a brief review of our attempts in the last decade to develop calculation methods for secondary flows and separation patterns in centrifugal impellers.

Ten years ago, boundary layer blockage and separation in impellers were predicted using standard two-dimensional boundary layer models with pressure gradients prescribed by inviscid hub-to-shroud or blade-to-blade analyses. Secondary flow calculations were performed, if at all, using methods based on the inviscid flow analysis of Smith [2]. It was possible therefore to estimate the amount of boundary layer fluid at the impeller exit and also to predict the probable location of its accumulation. However, this method was clearly approximate as no complete three-dimensional inviscid flow solution was possible, so the pressure distributions were not well known, and there was no data available on boundary layer growth in rotating passages with which to compare boundary layer theories developed for flows on nonrotating surfaces.

To fill this gap in experimental data, Moore [3, 4] made measurements of boundary layer development in a rotating radial-flow passage. From the measured values of free stream velocity, momentum thickness and friction coefficient, Moore calculated velocity profiles using Moses [5] two-parameter family of two-dimensional turbulent boundary layer profiles and these were found to be in good agreement with the measured profiles. Moore [3, 6] then extended Moses method for two-dimensional boundary layer calculations to include three-dimensional flow in rotating coordinates and found that in combination with a simple potential flow theory this standard boundary layer method was capable of describing the observed boundary layer development. In fact combining the analysis of the boundary layers on all four walls to allow the accumulation of boundary layer fluid on the suction side wall gave a procedure for accurate calculation of the wake development.

Moore's measurements suggested that there was little or no backflow in the passage even in the wake region and a simple marching integration of the boundary layer equations combined with continuity for the whole passage was found to be adequate. Indeed a further simplification suggested by the observed constant shape of the wake velocity profile allowed the method to successfully calculate the growth of the wake as well. This flow was therefore found to be parabolic with elliptic effects due to the pressure distribution only occurring close to the exit of the passage, after the formation and subsequent growth of the wake.

At that time, a combined potential flow/boundary layer theory was all that was available for calculating the three-dimensional flow which is so important in controlling the accumulation of low momentum fluid in the wake. Later, in 1972, Patankar and Spalding [7] published their marching-integration procedure for three-dimensional parabolic

[1] Presently Mechanical Engineering Department, Virginia Polytechnic Institute Blacksburg, Va.

Contributed by the Gas Turbine Division for publication in the JOURNAL OF ENGINEERING FOR POWER. Manuscript received at ASME Headquarters May 27, 1980.

flows. This method allowed the calculation of the whole flow field which was covered with a finite-difference mesh, but it used a collateral, logarithmic wall function model for the important boundary layer region near the walls. Moore, et al. [8] appreciated the possible significance of secondary flows within the logarithmic region and recognized that the flow in this region was unlikely to be collateral. They therefore wrote a parabolic flow program using the Patankar method but allowing small grid spacing near the walls and not using the logarithmic wall function. This duct-flow program, written using orthogonal curvilinear coordinates, again showed that a simple viscosity model (the Prandtl mixing-length model) could be used to give a good description of the flow in Moore's [3, 4] rotating passage. In the calculations the wake developed on the suction side wall as in Moore's earlier [3, 6] boundary layer calculation. But now, most significantly, the temporary accumulation of low stagnation pressure fluid in the pressure-side/top-wall corner appeared in the calculated results at the same location as it was observed in the experiment. The calculation allowed the eventual migration of this fluid to the suction side to be followed.

The three-dimensional parabolic method allows no elliptic influence of the pressure field; thus downstream effects cannot influence the upstream flow. This restriction was removed by Pratap and Spalding [9] who treated this class of partially parabolic flows; using pressure-correction methods they gradually improve the three-dimensional pressure solution until marching integration through the flow field gives the three-dimensional flow. Clearly this class of flow has many features found in cascade flows. Moore and Moore [10] therefore extended their parabolic duct-flow method for the analysis of partially-parabolic duct flows.

In the present paper, the modifications necessary to further extend the method to handle flows in general geometries, not described by orthogonal coordinates, are described, together with the procedures required for the calculation of flow entering and leaving a blade row. This general marching-integration method for cascade flows is then used to calculate steady, developing, three-dimensional, viscous, incompressible flow in a De Havilland Ghost impeller [11] which Johnson and Moore [12, 13] have tested with a rotating shroud wall. Comparisons of calculated and measured wake flow development are presented.

The present flow calculations omit effects due to compressibility, shock waves, unsteadiness, turbulence modification, tip leakage and a stationary shroud wall, but they describe flow in a general geometry with viscous and secondary flow and they show the accumulation of boundary layer fluid to form a wake flow. The method described is capable of handling compressible flow and is being extended in an attempt to handle tip leakage and a stationary shroud wall. The present work therefore represents a major step towards "putting together a complete theory" which Dean saw as ten years away at least. But if fully elliptic and unsteady flow calculations are necessary to adequately model the loss mechanisms in impellers, then we are still ten years away from our goal.

The Flow Model

Geometry. For the Ghost impeller and other complex geometries, we need to be able to perform calculations over a general three-dimensional (i, j, k) grid without the restriction of orthogonality between the grid lines. The grid index directions for the Ghost impeller are shown in Fig. 1.

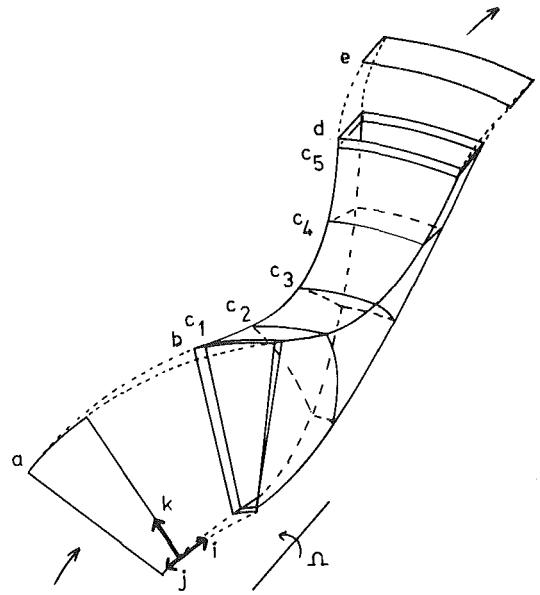

Fig. 1 The calculation field for the Ghost impeller showing the grid directions and a selection of constant i surfaces: a—flow inlet, b—leading edge, c_1-c_5—five measurement stations within the impeller, d—trailing edge, e—flow exit

The i index increases in the approximate bulk flow direction, covering the flow from flow inlet, upstream of the blade row, to flow exit, downstream of the blade row. The j index goes from blade to blade or repeating boundary to repeating boundary and the k index from hub to shroud.

Governing Equations. The continuity and momentum equations are written for steady flow—steady relative to a reference frame rotating with constant angular velocity, Ω. They are for a fluid with an isotropic effective viscosity μ and compressibility effects are retained in all but the viscous terms.

Continuity.

$$\nabla\cdot\rho u = 0 \tag{1}$$

Momentum.

$$(\nabla\cdot\rho u)u - (\nabla\cdot\mu\nabla)u = \nabla\cdot\mu\overline{\nabla u}^T - \nabla p - \rho(2\Omega \times u + \Omega \times (\Omega \times R)) \tag{2}$$

Velocity Components. For momentum to be satisfied it is sufficient to satisfy the momentum equation resolved in any three independent directions. However, because the flow field is to be solved over a finite-difference grid with assumed linear or stepwise profiles between the grid points the selection of the three directions is limited. In particular, to ensure that the profile assumption between the grid points never gives flow through the blades, the u_2 velocity direction is taken normal to surfaces of constant j. Similarly, the u_3 component

Nomenclature

C = factor in abbreviated momentum equation (11)
e = pressure-correction scaling factor
E_n = gradient transformation vectors equation (6)
F^p = momentum equation force residual vector
i, j, k = three-dimensional grid indices
L = mixing length
m_n = unit vectors in velocity component directions
p = static pressure.
p_a = estimated static pressure
p_c = pressure correction
p_d = elliptic pressure correction
P_r = reduced static pressure, $p_r = p - \frac{1}{2}\rho\omega^2 r^2$
p_r = dimensionless reduced static pressure, equation (16)
p^* = rotary stagnation pressure, $p^* = p + \frac{1}{2}\rho u^2 - \frac{1}{2}\rho\omega^2 r^2$.
P^* = dimensionless rotary stagnation pressure, equation (17)
$\overline{P}^*$ = mass averaged dimensionless rotary stagnation pressure
ΔP^*_L = local dimensionless rotary stagnation pressure
r = radial coordinate
R = position vector
u = velocity vector
u_n = velocity components (nonorthogonal)
μ = effective viscosity
μ_ℓ = laminar viscosity
ω = angular speed of rotation of the impeller
Ω = angular velocity vector of rotating impeller
ρ = density

is taken normal to surfaces of constant k to avoid flow through the hub and shroud. This gives the boundary condition as simply, $u_2 = 0$ on the blades and $u_3 = 0$ on the hub and shroud. The remaining component may be chosen more arbitrarily, and we take u_1 in the i direction, normal to both u_2 and u_3.

The unit vectors in the directions of the velocity components are m_1, m_2 and m_3. Therefore

$$u_n = m_n \cdot u, \qquad n = 1,2,3. \tag{3}$$

This set of equations may be inverted to write

$$u = G_n u_n, \tag{4}$$

where G_n are vectors determined from the unit vectors. Here the repeated subscript implies summation (n = 1, 2, 3,).

Components of Momentum. The components of the momentum equation in each of the three velocity component directions are obtained by the dot product of the unit vectors with the momentum equation

$$m_n \cdot (\text{momentum equation (2)}), \qquad n = 1, 2, 3.$$

Expanding this, retaining the spatial variation of m_n in the convection term but approximating m_n as a constant vector in the viscous terms yields

$$(\nabla \cdot \rho u) u_n - (\nabla \cdot \mu \nabla) u_n = \nabla \cdot \mu (m_n \cdot \nabla) u - m_n \cdot \nabla p - \rho m_n \cdot (2\Omega \times u + \Omega \times (\Omega \times R)) + u \cdot (\rho u \cdot \nabla) m_n, \quad n = 1, 2, 3. \tag{5}$$

To obtain useful finite-difference forms of the momentum equations, they are integrated over a control volume for each grid point using the divergence theorem. Furthermore, the operator ∇ is expressed conveniently as

$$\nabla = E_1 \frac{\partial}{\partial i} + E_2 \frac{\partial}{\partial j} + E_3 \frac{\partial}{\partial k}. \tag{6}$$

The vectors E_1, E_2, and E_3 are determined from vectors spanning a unit change in i, j and k. Finally we use the parabolic flow assumption of negligible gradients of velocity in the bulk flow direction ($\partial u_n / \partial i \simeq 0$) when evaluating the viscous terms.

Pressure Corrections. The momentum equations may be easily linearized and decoupled except for the pressure term. The pressure used in the momentum equations consists of an a priori estimated pressure, p_a, and pressure corrections. The purpose of the pressure corrections is to obtain velocity components which satisfy continuity. Because the grid lines are not orthogonal, separated pressure corrections—as used in the earlier duct flow calculations [10]—are inconvenient. However the essence of separated pressure corrections is retained by using the pressure correction, p_c, as follows:

to calculate the rotary stagnation pressure (and density when the flow is compressible), use

$$p = p_a + p_c; \tag{7}$$

to obtain the derivatives of p for the momentum equations, use

$$\frac{\partial p}{\partial i} = \frac{\partial p_a}{\partial i} + \frac{\partial p_c}{\partial i}, \tag{8}$$

$$\frac{\partial p}{\partial j} = \frac{\partial p_a}{\partial j} + \frac{1}{e} \frac{\partial p_c}{\partial j} \tag{9}$$

and

$$\frac{\partial p}{\partial k} = \frac{\partial p_a}{\partial k} + \frac{1}{e} \frac{\partial p_c}{\partial k} \tag{10}$$

where $e = -0.01$. The small magnitude of e essentially separates the pressure correction. That is, large revisions to the cross-stream pressure gradient ($1/e\ \partial p_c/\partial j$ or $1/e\ \partial p_c/\partial k$) are not reflected as large variations in the bulk-flow direction pressure gradient ($\partial p_c/\partial i$), rather they appear a factor of 100 smaller. e is negative to insure numerical stability.

As for the duct flow calculations [10], the equation used to solve for the pressure correction is obtained by substituting an abbreviated momentum equation relating velocity and pressure corrections,

$$C u_c = -\nabla p_c, \tag{11}$$

into continuity.

The Calculation Procedure. The calculation procedure differs only slightly from the earlier duct-flow work. It remains a marching integration of the equations through the flow field using an estimated pressure distribution followed by the solution of a three-dimensional elliptic pressure-correction equation. It may be summarized as follows.

1 A priori, estimate the three-dimensional pressure distribution. This estimate need only be accurate at the flow inlet.

2 Starting with specified flow inlet conditions upstream of the blade row, perform a marching integration of the momentum equations from the flow inlet to the flow outlet downstream of the blade row. Over each step of the marching integration: (a) the momentum equations are solved for the downstream velocity components using an estimated pressure distribution; (b) the pressure correction, p_c, is calculated together with the corresponding changes to the velocity components which would result in the velocity components satisfying continuity; (c) the estimated pressure distribution for the step is updated using p_c and (a) and (b) are repeated up to five times; (d) velocity components satisfying continuity are substituted into the momentum equations together with the original estimated pressure (omitting the pressure correction) to obtain Force Residuals, F^P.

3 Convert the Force Residuals to a three-dimensional elliptic pressure correction using

$$\nabla \cdot \left(\frac{1}{\rho |u|} (\nabla p_d + F^P) \right) = 0 \tag{12}$$

to obtain a new improved three-dimensional estimated pressure distribution, $p_a + p_d$ [10].

4 If the pressure corrections are large, (2) and (3) may be repeated. In general fewer than five passes will be required. In the present calculations we have used three inviscid passes to build up the pressure solution followed by 1 or 2 viscous passes.

Turbulent Viscosity Model. The viscosity model is a direct extension of the mixing-length model used in reference [14]. The effective viscosity, μ, is given by

$$\mu = \mu_\ell + \rho L^2 \text{“}du/dy\text{”}. \tag{13}$$

The mixing length, L, is the smaller of 0.08 times the boundary or shear layer width and 0.41 times the distance to the nearest point on the wall. The van Driest correction is used in the “0.41y” region and logarithmic averaging is used to obtain the viscosity next to the wall. du/dy is approximated by

$$\text{“}\frac{du}{dy}\text{”} = \left[\left(|E_2| \frac{\partial u_1}{\partial j} \right)^2 + \left(|E_3| \frac{\partial u_1}{\partial k} \right)^2 + \left(|E_2| \frac{\partial u_3}{\partial j} + |E_3| \frac{\partial u_2}{\partial k} \right)^2 \right]^{1/2}. \tag{15}$$

To determine the edges of the boundary or shear layers we define a local dimensionless stagnation pressure

$$\Delta P^*_L = \frac{p^* - p_r}{p^*_{\max_i} - p_r}, \tag{15}$$

where, for incompressible flow, p^* is the rotary stagnation pressure ($p^* = p + \frac{1}{2}\rho u^2 - \frac{1}{2}\rho\omega^2 r^2$), p_r is the reduced static pressure ($p_r = p - \frac{1}{2}\rho\omega^2 r^2$) and $p^*_{\max_i}$ is the maximum value of p^* on the current i surface of the flow calculation. ΔP^*_L then ranges from a maximum of 1 where $p^* = p^*_{\max_i}$, to a minimum of 0 when the velocity equals zero at the viscous walls. Boundary or shear layers are regions in which the gradient of ΔP^*_L exceeds one over a characteristic passage width.

Flow in the Ghost Impeller

We will compare the calculated flow in the Ghost impeller with the data of Johnson and Moore [12, 13]. The impeller rotates at 500 rpm and the Mach numbers are low so that the flow is incompressible with

a density, $\rho = 1.225$ kg/m^3. Johnson and Moore measured flow velocities and rotary stagnation pressures at five measuring stations in one impeller passage. These stations correspond closely with i surfaces $c_1 - c_5$ in Fig. 1. The calculations are for two flow rates, design and high, with mass flow rates of 0.14 and 0.17 kg/s respectively for the single passage.

Johnson and Moore define a dimensionless reduced static pressure,

$$P_r = \frac{p_r - p^*_{\min}}{p^*_{\max} - p^*_{\min}} \tag{16}$$

and a dimensionless rotary stagnation pressure

$$P^* = \frac{p^* - p^*_{\min}}{p^*_{\max} - p^*_{\min}} \tag{17}$$

For the design and high flow rates, $p^*_{\max} - p^*_{\min}$ is 315 and 400 N/m^2, respectively.

Calculation Details. The a priori estimated pressure distribution was one-dimensional with uniform static pressure across each i surface varying from inlet to outlet with the mean change in $\frac{1}{2}\rho\omega^2 r^2$.

Three inviscid passes were used to build up the three-dimensional pressure solution. The absolute velocity at inlet was uniform and axial. The calculations used $\mu = 0$ and a boundary condition of zero shear at the walls. For the inviscid calculations a 17 by 8 by 8 grid was used. In the i direction there were 3 steps from inlet to leading edge, 11 steps through the impeller passage and three steps downstream of the trailing edge. In the j and k directions the relative blade-to-blade and hub-to-shroud spacings of the grid points were 0., 0.05, 0.2, 0.4, 0.6, 0.8, 0.95 and 1.0. Each inviscid flow pass required 3 minutes computer time on the Cambridge University IBM 370/165.

For the design flow rate two viscous passes were made. The difference between the calculated profiles near the trailing edge for the first and second passes was negligible. Therefore at the high flow rate only one viscous pass was made. The inlet profiles for the viscous flow included turbulent boundary layers on the hub and shroud each covering 5 percent of the hub-to-shroud width. (This estimate was based on the limited data available for the inlet flow.) A boundary condition of zero relative velocity was used on the walls, i.e. zero relative to the rotating impeller and the attached rotating shroud, and zero relative to the stationary outer duct wall extending upstream of the impeller shroud. For the viscous calculations additional grid points were required near the walls. These had relative blade-to-blade and hub-to-shroud spacings of 0.0008, 0.0031, 0.0125, 0.9875, 0.9969 and 0.9992, giving a maximum 14 by 14 grid on each i surface. Each viscous pass required 11 minutes of computer time.

Throughout the calculations the static pressure at inlet was unchanged and a boundary condition of uniform static pressure at outlet was maintained.

The Design Flow. The calculated and measured reduced static pressures for the design flow rate are compared in Fig. 2. Figure 2(a) shows good agreement along the hub. Figure 2(b) shows good agreement along the shroud for the first part of the impeller. However, at measurement stations 3 and 4, the calculations markedly overestimate the impeller loading at the shroud. The viscous calculation predicts slightly less loading on the impeller than the inviscid calculation, but the difference is not dramatic.

The reduced static pressures at station 4 are shown in more detail in Fig. 3. It can be seen that the calculated and measured contours agree well except over the suction-side/shroud quarter of the passage. Here the measured reduced static pressure is nearly uniform. The calculated P_r continues to decline towards the suction-side/shroud corner becoming uniform only over a very small region in the corner.

Measured contours of dimensionless rotary stagnation pressure are shown in Fig. 4(a) for the five measuring stations. At station 1, P^* is high and nearly uniform. At station 2 there is a large region of low P^* fluid in the suction-side/shroud corner. The fluid with P^* less than 0.8 covers about $\frac{1}{6}$th of the passage. This region of low P^* fluid remains in the suction-side/shroud corner and continuously grows until at station 5 it covers just over $\frac{1}{4}$th of the passage.

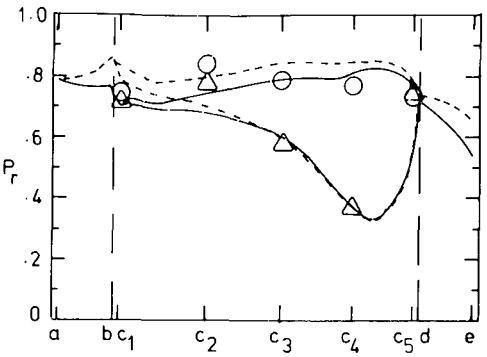

Fig. 2(a) P_r at the hub/suction and hub/pressure side corners

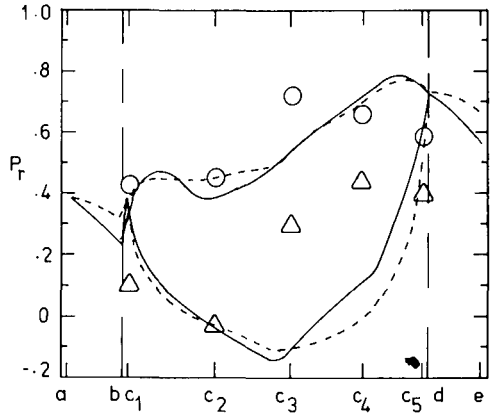

Fig. 2(b) P_r at the shroud/suction and shroud/pressure side corners

Fig. 2 Comparison of measured and calculated dimensionless reduced static pressure, P_r, for the design flow rate. Constant i surface: a—flow inlet, b—leading edge, c_1—c_5—measurement stations, d—training edge, e—flow exit. - - - - inviscid calculation. —— viscous calculation. ○—measured, pressure side corner. △—measured, suction side corner.

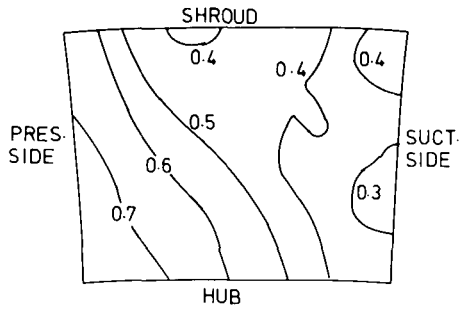

Fig. 3(a) Measured

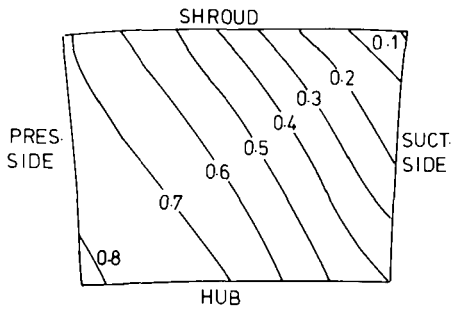

Fig. 3(b) Viscous flow calculation

Fig. 3 Comparison of measured and calculated contours of dimensionless reduced static pressure, P_r, for the design flow rate at station 4

Contours of dimensionless rotary stagnation pressure from the viscous calculation are shown in Fig. 4(*b*). A narrow band of fluid with P^* less than 0.8 appears along the shroud at station 1. This region grows slowly extending along the suction side until at station 5 it covers a modest portion of the passage—about $\frac{1}{10}$th—mostly along the shroud towards the suction side.

Comparing the calculated and measured P^*'s, the measured wake at station 5 is obviously much bigger than the calculated wake. However, the location of the lowest P^* fluid, at the shroud towards the suction side, is well predicted. The dramatic departure of the calculations from the measurements occurs between stations 1 and 2. From station 2 to station 5, the calculated growth of the region with P^* less than 0.8 from 3 to 10 percent of the passage area compares well with the measured growth from 17 to 25 percent of the passage area.

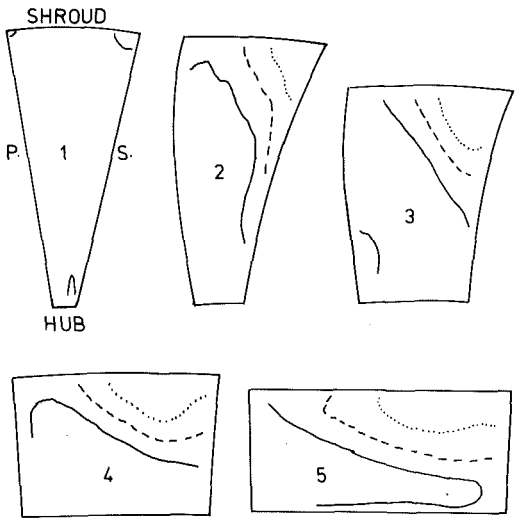

Fig. 4(*a*) Measured

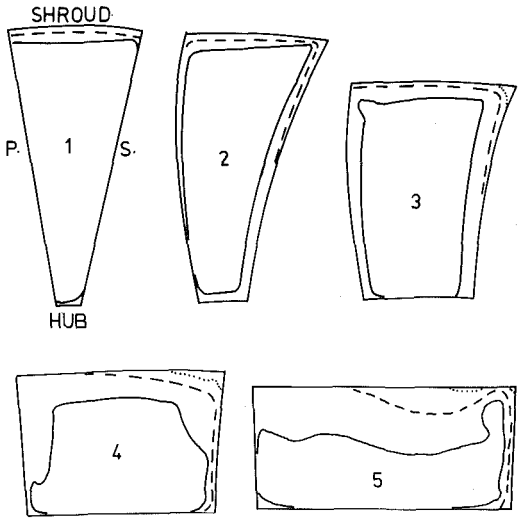

Fig. 4(*b*) Viscous flow calculation

Fig. 4 Contours of dimensionless rotary stagnation pressure, P^*, for the design flow rate, at the five measuring stations. —— $P^* = 0.95$, - - - - $P^* = 0.8$, ····· $P^* = 0.6$.

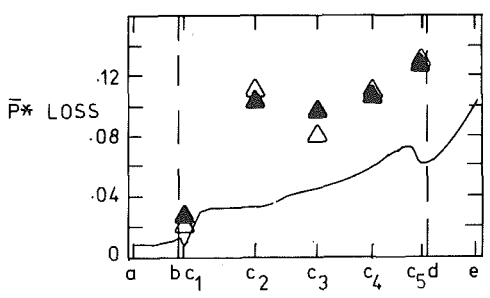

Fig. 5 Loss in dimensionless rotary stagnation pressure mass-averaged across *i* surfaces. △—measured ($1 - \bar{P}^*$) ▲—measured ($P^*_{max_i} - \bar{P}^*$), —— calculated ($\bar{P}^*_{inviscid} - \bar{P}^*_{viscous}$).

The rate at which rotary stagnation pressure is lost is shown more directly in Fig. 5. Here the decrease in dimensionless rotary stagnation pressure mass-averaged across the i surfaces is shown. The data are given in two different ways. First simply as $1 - \bar{P}^*$. Secondly, to try to eliminate any systematic errors in the data, it is assumed that the maximum P^* follows an inviscid streamline and should therefore be the same at all measuring stations. Thus the loss is estimated by $P^*_{max_i} - P^*$. Either way, the data show a large rise between stations 1 and 2 and a fall from stations 2 to 3. Since a fall in the loss is not physically possible, this indicates a level of accuracy for the data. Johnson suggests much wider error bands of ±0.06 for $\bar{P}^*$.

To eliminate any systematic numerical errors, the calculated loss in $\bar{P}^*$ is shown as the difference between $\bar{P}^*$ calculated for the inviscid flow and $\bar{P}^*$ calculated for the viscous flow. This rises smoothly except near the leading and trailing edges of the impeller. $\bar{P}^*$ for the inviscid calculation varies from 0.987 to 1.035 with the worst variation occurring near the leading edge.

The High Flow. The flows at the design and high flow rates were very similar. The measured and calculated contours of dimensionless rotary stagnation pressure for the high flow at station 5 are compared in Fig. 6. Again the measured wake is considerably larger than the calculated wake. The location of fluid with lowest P^*—slightly more towards the center of the shroud than for the design flow—is well calculated.

Figure 7 shows the angle the high flow makes with the radial direction at station 5. The vectors plotted are a projection of unit vectors in the flow direction onto the surface which is normal to the radial direction. Thus the length of the vectors gives the flow angle. Both the measured and calculated angles show the same secondary flow pattern—movement of fluid near the pressure and suction side surfaces around onto the shroud wall.

Discussion and Conclusions

The flow model adequately calculates the growth of the wake due to secondary flow movement of low P^* fluid.

A large portion of the measured wake occurs early in the flow. Secondary flow cannot have a large influence in the early portion of the impeller passage; therefore this portion of the wake must arise for some other reason. Figure 2 shows the reduced pressure gradient to be favourable in the suction-side/shroud corner between stations 1 and 2; therefore the wake cannot be the result of two-dimensional separation. It is probable then that a large portion of the measured wake arises from some unsteady and/or leading edge phenomenon, such as a horseshoe vortex, which is beyond the scope of a steady partially-parabolic model.

In both the calculations and the measurements, for the design flow at station 4 (see Figs. 3 and 4), the wake region corresponds to a region of uniform reduced static pressure. The calculated reduced static pressure in the suction-side/shroud corner being much lower than the measured P_4 at stations 3 and 4 (Fig. 2) is then consistent with the difference between the calculated and measured wake sizes. The formation of a large wake obviously has a significant influence on the static pressure.

In summary, the flow model should be of considerable use in calculating impeller flows other than those in which leading-edge effects dominate. It may be used to assess the relative importance of secondary flows due to rotation and curvature and is a significant step towards the calculation of losses within the impeller.

Acknowledgments

The authors wish to thank Rolls-Royce, Aero Division, for their financial support of this project as part of the Rolls-Royce/Cambridge University Whittle Laboratory collaboration, and especially Mr. P. H. Timmis of the Rolls-Royce Helicopter Group and Mr. P. Clark of Rolls-Royce, Bristol, for their encouragement.

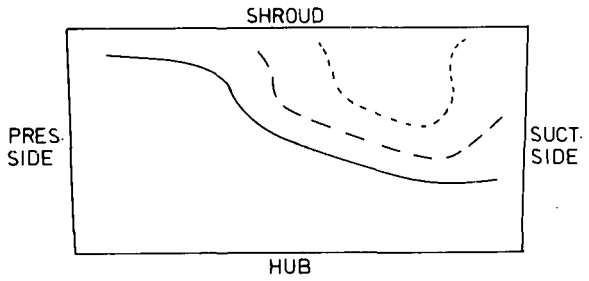

Fig. 6(*a*) Measured

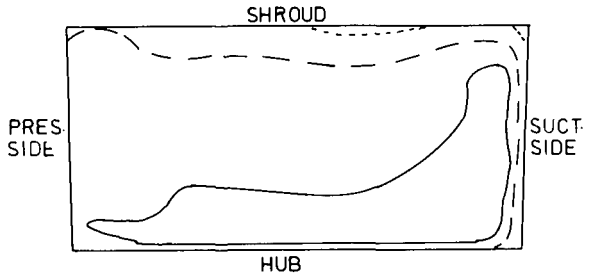

Fig. 6(*b*) Viscous flow calculation

Fig. 6 Comparison of measured and calculated contours of dimensionless rotary stagnation pressure, P^*, for the high flow rate at station 5. —— $P^* = 0.95$, - - - $P^* = 0.8$, - - - - $P^* = 0.6$

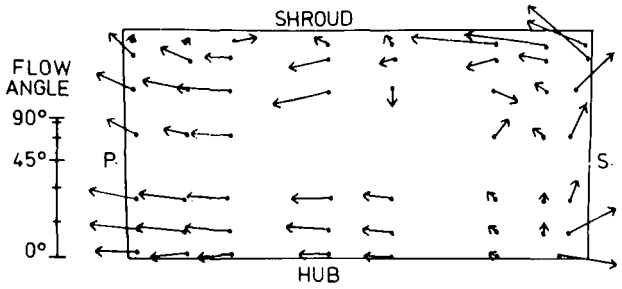

Fig. 7(*a*) Measured

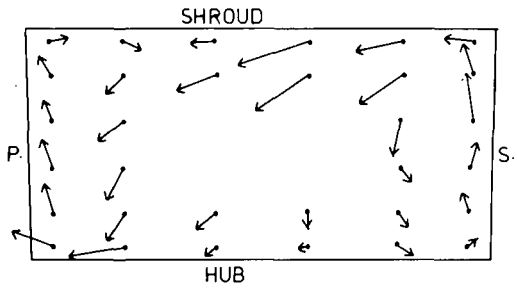

Fig. 7(*b*) Viscous flow calculation

Fig. 7 Comparison of measured and calculated angles of the flow to the radial direction, for the high flow rate at station 5

References

1 Dean, R. C., Jr., "On the Unresolved Fluid Dynamics of the Centrifugal Compressor," Creare TN-68 Vol. I, Mar., 1968 also *Advanced Centrifugal Compressors*, ASME, Special Publication, 1971, pp. 1–55.

2 Smith, A. G., "On the Generation of the Streamwise Component of Vorticity for Flows in a Rotating Passage," *Aeronautical Quarterly*, Vol. 8, 1957, pp. 369–383.

3 Moore, J., "The Development of Turbulent Boundary Layers in Centrifugal Machines," Gas Turbine Laboratory Report No. 99, M.I.T., June 1969.

4 Moore, J., "A Wake and an Eddy in a Rotating, Radial-Flow Passage, Part 1: Experimental Observations," ASME JOURNAL OF ENGINEERING FOR POWER, Vol. 95, July 1973, pp. 205–212.

5 Moses, H. L., "A Strip-Integral Method for Predicting the Behavior of Turbulent Boundary Layers," Symposium on Turbulent Boundary Layers, Stanford U., Aug. 1968.

6 Moore, J., "A Wake and an Eddy in a Rotating, Radial-Flow Passage, Part 2: Flow Model," ASME JOURNAL OF ENGINEERING FOR POWER, Vol. 95, July 1973, pp. 213–219.

7 Patankar, S. V., and Spalding, D. B., "A Calculation Procedure for Heat, Mass and Momentum Transfer in Three-Dimensional Parabolic Flows," *International Journal of Heat and Mass Transfer*, Vol. 15, 1972, pp. 1787–1806.

8 Moore, J., Moore, J. G., and Johnson, M. W., "On Three-Dimensional Flow in Centrifugal Impellers," Cambridge Univ. Eng. Dept. Rep. Turbo/TR 85, 1977 also Aeronautical Research Council Current Paper CP No. 1384, 1977.

9 Pratap, V. S., and Spalding, D. B., "Fluid Flow and Heat Transfer in Three-Dimensional Duct Flows," Int. J. Heat and Mass Transfer, Vol. 19, 1976, pp. 1183–1188.

10 Moore, J., and Moore, J. G., "A Calculation Procedure for Three-Dimensional, Viscous, Compressible Duct Flow, Part I Inviscid Flow Considerations", to be published, ASME J. of Fluids Eng., Dec. 1979.

11 Moore, J., "Eckardt's Impeller—A Ghost from Ages Past," C.U.E.D./A-Turbo/TR83/1976.

12 Johnson, M. W., and Moore, J., "The Development of Wake Flow in a Centrifugal Impeller," ASME Paper No. 79-GT-152, to be published, ASME J. of Eng. for Power.

13 Johnson, M. W., and Moore, J., "Wake Flows in a Centrifugal Impeller," submitted to the Worthington competition, Jan. 1979.

14 Moore, J., and Moore, J. G., "A Calculation Procedure for Three-Dimensional, Viscous, Compressible Duct Flow, Part II—Stagnation Pressure Losses in a Rectangular Elbow," to be published, ASME J. of Fluids Eng., Dec. 1979.

PREFACE

Measurement Methods in Rotating Components of Turbomachinery

B. Lakshminarayana and P. Runstadler, Jr.

Techniques for making measurements in turbomachinery—fluid dynamic, structural, and thermal measurements—continue to be improved. Over the past decade, optical, noncontact methods, in particular, have been rapidly developed for measuring structural and fluid dymanic properties within the rotating components of turbomachines. Hot wire technique has been applied to both rotating and stationary reference frames to make flow measurements inside and at the exit of the rotor. Microprocessors and computers have revoluntionized data acquisition, processing and display techniques. These innovative approaches to measurement and data processing have provided new and/or supplemental information to that obtained using more conventional instrumentation. A symposium was held at the Joint Gas Turbine/Fluids Engineering Conference, New Orleans, March 9–13, 1980, to display the wide range of instrumentation methods available today for taking measurements on the rotating components of turbomachines by demonstrating the use of these techniques to obtain information needed by the research, development, and design engineer. The emphasis was on the development of new techniques, improvements in existing techniques, as well as new applications of conventional techniques of measurements.

Measurements made on turbomachinery rotors are among the most difficult fluid dynamic, structural, or thermal measurements performed today. These difficulties arise due to the complexity of the flow and the complicated nature of the stress, vibration, and heat transfer phenomena. The flow itself may be unsteady, with subsonic, supersonic, and transonic regions and associated shock phenomena. It is certainly viscous and usually turbulent with appreciable three dimensionality. Laminar, transition, and turbulent boundary layers with separated regions along the blade are often encountered. Almost invariably it is rotational with concentrated combined vortices due to blade tip leakage and induced secondary flow. The flow is noisy. Blade vibration and flutter cause many additional complications in designing high performance hardware. Good structural measurements are essential for the design of reliable machinery. Temperature and heat transfer measurements in turbine rotors where the environment is very hostile are both complicated and difficult. Above all, the transmission of mechanical, pressure or electrical data from a rotor presents a situation which is almost unique to turbomachinery. This symposium covered all of these aspects while addressing measurements on fluid flow (pressure, velocity, density, turbulence intensity and stress, wall shear stress, unsteady blade pressure) and temperature, vibration, strain and flutter measurements. Some of the world's newer facilities where these techniques have been incorporated were also described.

B. Lakshminarayana wrote the keynote paper for the sessions on Aerodynamics Measurements; in it he reviewed all of the non-optical techniques for the measurement of aerodynamic properties in a rotor. In addition, one paper describing a facility for rotor flow measurements and two papers on the use of high frequency response probes (hot wire and sphere probes) for exit flow measurement were presented. The sessions on Aerodynamic Measurements also had four papers dealing with flow measurement and blade flow visualization inside low speed rotor passages, using both conventional probes and hot wire/film probes.

The keynote paper for the sessions on Optical Flow Measurement was written by H. Weyer. He reviewed the state of the art of the laser velocimeter for flow measurement in rotor passages as well as discussing other optical methods of flow visualization, velocity and fluid property measurement. Use of LV systems in measuring two and three-dimensional flows in centrifugal and axial turbomachinery, marine propulsor as well as an improved LV data processing system were described in the eight papers in this session.

In the session on Unsteady Aerodynamic Measurements, F. Carta and R. L. O'Brien reviewed the techniques applicable to unsteady aerodynamic measurements in a rotor. Three papers in this session dealt with the use of laser systems, unsteady blade pressure on the rotor blade, and a system for measurement of blade static pressure undergoing flutter.

M. J. Hartmann wrote the keynote paper for the session on Vibration, Stress and Flutter Measurements. Two papers in this session dealt with a strain gage and a telemetry system. Two other papers dealt with vibration and flutter measurements using optical and pressure probes, respectively. Two of the papers covered the measurement of vibration and temperature in aero engines. In addition, there was one paper each on aerodynamic damping, a digital system for blade displacement, and on steady stress measurements.

The last session was on instrumentation systems for temperature and heat transfer measurements in turbomachines; the keynote was written by R. W. Graham. Two of the papers in this session described high temperature facilities and their instrumentation while the other papers dealt with disk cooling and pyrometry for the high speed turbine.

Thirty-six papers were presented at this symposium and published in the symposium volume *Measurement Methods in Rotating Components of Turbomachinery*, ASME, New York, Edited by B. Lakshminarayana and P. Runstadler Jr., March 1980. Fourteen of these papers, considered to be of permanent interest, are published in this issue of the *Journal of Engineering for Power*. Four of the remaining papers appeared in the December 1980 issue of the *Journal of Fluids Engineering*.

B. Lakshminarayana

Director of Computational Fluid Dynamics Program and Professor of Aerospace Engineering, The Pennsylvania State University, University Park, Penn. 16802

Techniques for Aerodynamic and Turbulence Measurements in Turbomachinery Rotors[1]

The objective of this paper is to review the techniques employed for the measurement of flow in turbomachinery rotors. Only nonoptical techniques are included. Measurement of the following properties are covered: three-dimensional mean velocity, turbulence intensity and Reynolds stresses, static and stagnation pressures, and blade surface measurement. Both the conventional as well as the hot-wire/film techniques, including both the rotating- and the stationary-probe measurements, are reviewed. A brief description of various rotating-probe traverse mechanisms and rotor flow data transmission systems in use is also included.

Introduction and Scope

A knowledge of three-dimensional mean and turbulent flow fields in rotors is essential in developing new analytical, numerical, and design techniques that incorporate all essential features of real and ideal fluid effects in turbomachinery. In the early days of jet engine development, cascade testing was responsible for improved design and performance. In modern turbomachinery, three-dimensional viscous, shock, as well as other three-dimensional effects underscore the need for the generation of knowledge of the rotor flow field, as two-dimensional cascade data and correlation are no longer sufficient. Pressure, velocity, temperature, and wall shear stress are the basic aerodynamic parameters that enter into the design process.

A considerable amount of work has been carried out during the last decade in the development of new techniques for the measurement of rotor flow field. Among the major developments are: (1) a laser doppler velocimeter for relative flow measurement [1], (2) a three-sensor hot-wire and ensemble averaging technique for the measurement of rotor exit flow [2], a single hot-wire technique [3] for the measurement of wake transport through a multistage compressor, (3) measurement of unsteady and steady rotor flow using high response probes at the exit [4, 5], (4) a rotating three-sensor hot-wire technique for three-dimensional mean and turbulent flow field [6], (5) unsteady lift, moment, and pressure measuring techniques for a rotor blade [7, 8], and (6) a telemetry system for electrical data transmission from the rotor of a stationary frame of references [9, 10].

Several symposia held during the last decade covered various applied aspects and techniques related to turbomachinery flow measurement [11–14] as well as basic aspects of flow measurement techniques [15, 16].

The objective of this keynote paper is to review techniques and instrumentation used in the measurement of flow in turbomachinery rotors. Only nonoptical methods will be covered, since Weyer [17] has reviewed the state-of-the-art of all optical methods. Weyer's paper, as well as Carta and O'Brien's [18] review on unsteady aerodynamic measurements and Graham's [19] paper on turbine flow and temperature measurement, will complement the author's review.

Measurement of the following properties are presented: three-dimensional mean velocity, three-dimensional turbulence intensity, three-dimensional Reynolds stress, static and stagnation pressure, blade static pressures, wall shear stress, and blade-limiting streamline angle. A summary of the techniques covered in this paper is tabulated in Table 1.

Finally, this is a review of only recent material or techniques not covered in earlier reviews on this topic.

Rotating-Probe Traverse Mechanisms

One of the prerequisites for the measurement of rotor passage flow using hot-wire or conventional probes is the need for a traverse mechanism that can move the probe across the blade passage during rotation. The probe, mounted on this device, should be rotating at the same speed as the rotor. The mechanism should enable movement of the probe relative to the rotor blade as precisely as possible. The devices that have been built so far are classified according to operational features and described below. Devices which can perform only tangential (or blade to blade) traverse are described in the next two sections.

Mechanisms for Tangential Traverse (Mechanical). Weske [20] was one of the first investigators to measure blade pressure distributions on a rotor blade and traverse a rotating pitot probe across a rotor blade wake. His device consisted of a series of pulleys and sliding blocks. A somewhat improved version of this technique was developed by Shnee, et al. [21]. This device, shown in Fig. 1, is built for traversing a rotating pitot probe. Rotation of the hand wheel sets in motion the drive screw made integral with a worm wheel. The screw sets in progressive motion a slide block and a longitudinal rod which has, at the other end, two cylindrical pins that fit into the slanting groove of the shaft of the probe holder marked 2. A longitudinal change in the position of the rod in the slanting groove leads to a turning of the holder through a certain angle relative to the disk of the moving blade row. The relative motion between the probe and the blade, both of which are rotating, is thus achieved. The pressure transfer device is an integral part of the mechanism. The pressures

[1] Contributed by the Gas Turbine Division as a keynote paper to the symposium volume, *Measurement Methods in Rotating Components of Turbomachinery*, ASME, New York, 1980. Manuscript received for publication in the JOURNAL OF ENGINEERING FOR POWER May 22, 1980.

Table 1 Nonoptical flow measurement systems and techniques

ROTATING PROBES FOR PASSAGE AND EXIT FLOW

Technique	System	Properties Measured
Three-Sensor Hot Wire/Film	Rotating-Probe Traverse (Mechanical & Electrical) and Data Transmission Systems	3D Mean Velocities, Turbulence Intensities, and Stresses
Single-Sensor Hot Wire/Film	Rotating-Probe Traverse (Mechanical & Electrical) and Data Transmission Systems	Resultant Velocity
Five-Hole Pressure Probe	Rotating-Probe Traverse Mechanism--Pneumatic/Electrical Data Transmission System with or without a Scanivalve	3D Mean Flow Field, Stagnation, and Static Pressures
Static Pressure Probe	Rotating-Probe Traverse Mechanism--Pneumatic/Electrical Data Transmission System	Static Pressure
Pitot Probe	Rotating-Probe Traverse Mechanism--Pneumatic/Electrical Data Transmission System	Stagnation Pressure
Blade Static Pressure Blade Pressure Transducers	Pneumatic/Electrical Data Transmission System with Scanivalve	Steady Static Pressure on the Blade Unsteady Static Pressure on the Blade
Ammonia-Ozalid Technique	Ammonia Transfer Device	Blade-Limiting Streamline Angle, Visualization of Flow Near Blade Surface
Surface Hot Film	Electrical Data Transmission System	Wall Shear Stress

STATIONARY PROBES FOR EXIT FLOW

Techniques	Properties Measured
Hot Wire/Film	
(a) 3-Sensor Hot Wire/Film	3D Mean Velocities, Turbulence Intensities, and Stresses
(b) Single Slanted Wire	3D Mean Velocities
Fast Response Pressure Probes	
(a) Pitot Probe	Stagnation Pressure
(b) Five-Hole Probe	Mean Flow Field; Stagnation and Static Pressures

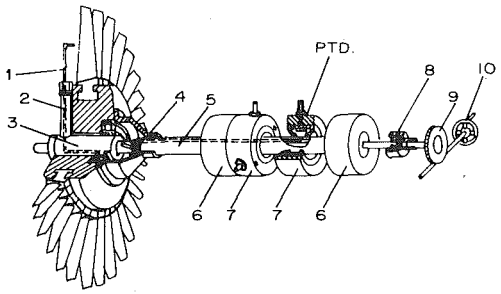

Fig. 1 Rotating probe traverse mechanism of Shnee, et al. [21] (1) pitot tube, (2) holder, (3) turning shaft, (4) longitudinal rod, (5) shaft, (6) bearing, (7) sealing section, (8) slide block, (9) worm wheel, and (10) hand wheel

from the probe are transferred through a seal, shown in Fig. 1, to a stationary manometer or transducer.

Shnee, et al. used the device to measure relative flow at 20 points along two passages in a turbine rotor with an inlet Mach number of 0.35. The device has been rotated at a maximum speed of 5000 rpm. Both the conventional Pitot tube and the five-hole probe have been employed to measure the flow field and losses in the rotor. Devices similar to those of Shnee, et al. have been employed by other Russian scientists [22, 23].

Mechanisms for Tangential Traverse (Electrical). Ushakov, et al. [24] were probably the first ones to design a rotating-probe actuating mechanism driven by an electric motor. They employed a 10 W electric d-c motor, which drives a probe through a worm gear train. An elaborate control system enabled the probe traverse to be made during rotation. The entire mechanism was located within the hub of the rotor. Only a cobra probe and a Kiel probe were employed in this investigation. Ufer [25] built a probe mechanism for traversing a single-sensor hot-wire probe, both inside and downstream of the rotor passage. The mechanism was driven by a d-c motor (20,000 rpm)

Nomenclature

A = hot-wire constant
B = number of blades/hot-wire constant
a_{ik}, a_{jk} = direction cosines between sensor and coordinate directions
C = chord length
C_f = skin friction coefficient
E = voltage (instantaneous)
e = fluctuating voltage
$\overline{e_i e_j}$ = fluctuating voltage correlation
k = error due to deviation from cosine law
n = exponent in hot-wire equation/sample number
N = number of samples
P = stagnation pressure
p = static pressure
Q = cooling velocity for the hot wire
q = fluctuating component of hot-wire cooling velocity
R = nondimensionalized radius (r/r_t)
r, θ, z = cylindrical coordinate system (radial, tangential and axial coordinates, respectively) $z = 0$ at the trailing edge
s, n, r = streamwise, normal and radial directions, respectively
t, T = time and period, respectively
U = instantaneous flow velocity (relative velocity for rotating probes, absolute velocity for stationary probes)
u = fluctuating flow velocity
U_t = blade tip speed
$\overline{u_i u_j}$ = fluctuating velocity correlation ($i = j$ for intensity)
x = distance from leading edge
Y = tangential distance normalized by blade spacing
τ_w = wall shear stress
ν = kinematic viscosity
ϵ = limiting streamline angle/error
$Z = z/c$

Subscripts

i, j, k = components in three coordinate directions (tensor notation $i, j, k = 1, 2, 3$)
s, n, r = components in streamwise, normal and radial directions, respectively
r, θ, z = components in radial, tangential and axial directions, respectively
ℓ = designates wire number (= 1, 2, 3)
0 = free stream value

Superscripts

$\hat{}$ = ensemble average
$\bar{}$ = time average (periodic component for stationary probe)

with a speed reducer system consisting of spur and worm gears. The power supply was a three-volt battery which enabled stopping, starting, and reversal of the motor. A device was built for measuring the movement of the probe. Similar traversing can be done much more easily now using stepping motors.

Several rotating-probe traverse mechanisms have been developed at The Pennsylvania State University [26–30]. One of the earlier models was used for the measurement of the boundary layer on the rotor blade of an inducer. A good description of this mechanism is given in reference [27] and will not be repeated here. A modified version of this mechanism is used in the axial-flow compressor facility [26] of 0.932 m dia with maximum speed range of 2000 rpm. It has been operated at 1000 rpm [26, 28]. This unit is shown in Fig. 2 and will be referred to as PSU-Unit 1. The mechanism, driven by a slo-syn motor and a planetary gear, is capable of providing precision traverse of 0.09 deg interval and is ideally suited for measurement in thin shear layers (boundary layer and wake of a rotor blade). The probe holder is designed to hold conventional as well as hot wire probes. The traverse motor is controlled by an indexing device located externally. The motor is powered and controlled by a slo-syn preset index unit in the stationary instrumentation panel through an eight-channel slip-ring unit. The index has provision for the variation of the motor step size from 1 (0.09 deg) to 1000 (90 deg). The motor can also be jogged and reversed.

The probe can be traversed across several passages during rotation. The device is simple and has very few parts. Most importantly, the motor and shaft are along the axis, which considerably simplifies the balancing problem. The entire assembly is inside the rotating hub, thus providing least interference to the flow. The probe can be traversed inside or outside the rotor passage. A scanivalve assembly is also mounted inside the traverse gear (Fig. 2) to enable consecutive measurement of pressures from rotor blade static taps or a five-hole probe. Devices similar to these have been used by Johnson and Moore [31] and Murakami, et al. [32].

Mechanisms for Probe Rotation about Its Axis. In many instances, the probe has to be aligned in the direction of the flow to derive the flow angle, static pressure, and stagnation pressures. This

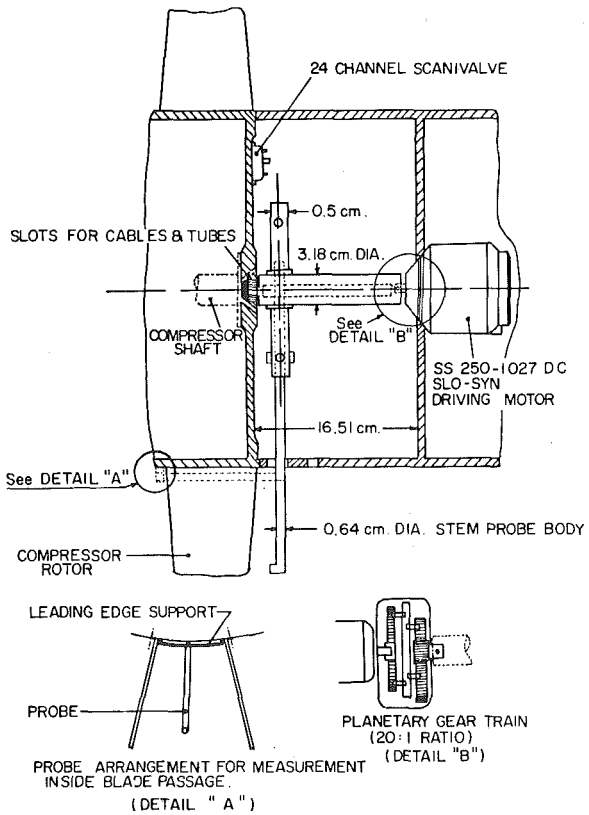

Fig. 2 Rotating-probe traverse mechanism of The Pennsylvania State University-PSU Unit 1

provision, referred to as "nulling" in this paper, has been incorporated in the mechanisms employed in references [33–35]. Mechanisms that are used to perform only the null operation are described in this section. The device used by Klein [35] is an improved version of that developed by Muesmann [34], who employed a rotating pitot probe and a camera to measure the rotor wake and visualize the flow inside a rotor passage. The device is good only for the nulling operation; all other traverses (including tangential) are carried out while the rotor is stationary. The null motion is achieved by a device similar to Fig. 1, through a hand crank, bevel gears, and a spindle. Klein used the device to measure the stagnation pressure distribution at the exit of a rotor and compare this with corresponding measurements from a stationary probe.

Mechanisms for Null, Tangential, Radial, and Axial Traverses. Devices described in this section have provision for more than one traverse (tangential and null, tangential and radial, etc.) during the rotation.

The earliest and most elaborate device built in this category was developed at The Pennsylvania State University [29, 30]. A detailed description of this device, which was not provided in earlier references [29, 30] is given here. The mechanism has two degrees of freedom (null and tangential traverse) and was built for rotor wake and passage flow measurement inside an axial-flow fan facility of 55 cm dia with a maximum speed of 3000 rpm. A detailed drawing of this facility is shown in Fig. 3 and a photograph is given in reference [26]. This device, referred to as PSU-Unit 2 in this paper, is designed and built to rotate the probe with the rotor, to traverse the probe (remotely) in the tangential direction, and to null the probe about the radial direction, while the rotor is in operation. The probe movement in the axial and radial directions is achieved manually, while the rotor is stationary. The traverse mechanism can be used to traverse a three-sensor hot-wire probe or a five-hole probe. The electrical signals from the probe are transferred to the stationary frame of reference through a mercury slip-ring unit. The traverse mechanism is mounted immediately downstream of the rotor and rotates with it.

The traverse mechanism—PSU Unit 2—shown in Fig. 3 consists of a slo-syn step motor (A) driving the worm gear (C) through a gear train (B). The worm gear in turn drives the worm wheel (D), which is attached to the probe-carrying hub-segment (G). Thus, the segment (G) and the probe (F) are traversed in small steps. The step size of 0.0192 deg is small enough to obtain an accurate description of the flow in the rotor wake and the end wall region of the rotor blade. The probe can be traversed 60 deg in the tangential direction. The worm wheel sits on bearings on the shaft (E), which is coupled to the rotor shaft. The step motor is controlled by a stationary slo-syn indexer through the brush slip-ring. The nulling motion of the probe is achieved by means of another step motor (J). The step motor drives a worm (K), which in turn drives the worm wheel (L). The worm wheel drives the bevel gear train (M), which rotates the probe about the radial direction through a spur gear train (not shown in Fig. 3). The nulling motion is achieved in steps of 0.02 deg. A limiting switch driven by the step motor through the spur gear train (N) controls the extent of nulling motion of the probe. The null mechanism is not yet operational. The axial movement of the probe is achieved through a lead screw mechanism and the probe can be fixed at various axial stations ranging from the trailing edge of the rotor blade to 1.5 chord downstream of the trailing edge of the rotor blade. A worm (P) drives the worm gear (Q), which is fixed to the lead screw (R). The nut (T) moves the lead screw axially through an axial slot on the shaft (E), thus providing axial movement of the probe. A lever attached to the worm (P) facilitates easy axial motion of the entire probe-transversing mechanism.

The traverse mechanism in the high-speed (9500 rpm) compressor facility (0.42 m tip dia) at the University of Aachen [36–39] has been used for exit flow measurements using rotating pitot probes. The mechanism is shown in Fig. 4 and described below [36]. It consists of a planetary gear system attached to the compressor shaft (b). This system and the gear train (A) drives the satellite carrier (a). The gear (d) of the gear train set (C) is attached to the hollow tube (D) on which the probe is mounted. The tube (D) rotates at the same speed as the

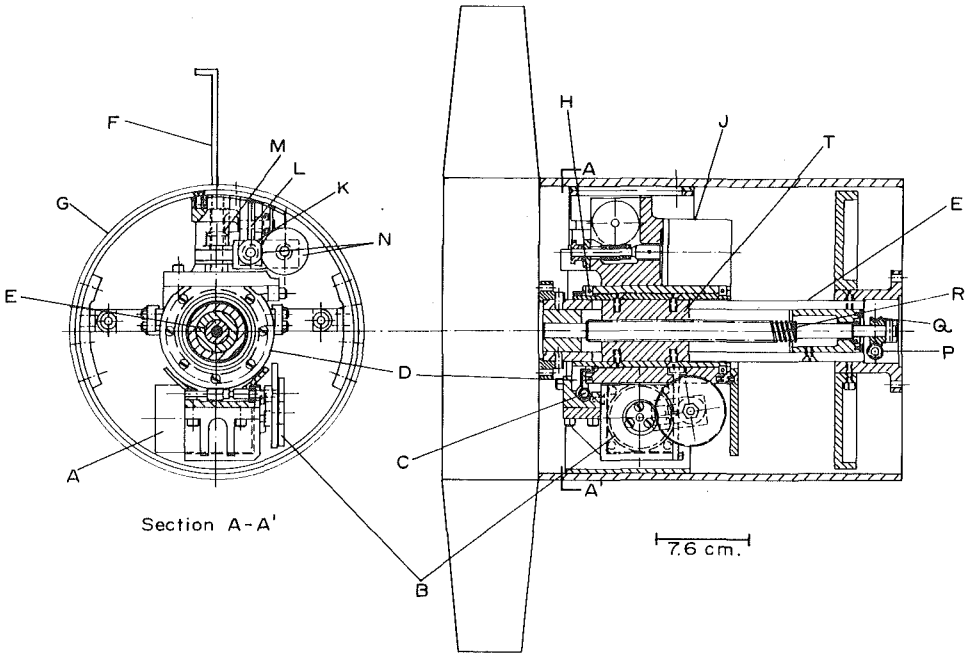

Fig. 3 Rotating-probe traverse mechanism of The Pennsylvania State University-PSU Unit 2

rotor. If the outside wheel (e) of the wheel set (C) is turned in the circumferential direction by the worm gear (E), the tube (D) moves relative to the rotor shaft. The gear train set between the sets (A) and (C) serves to move the probe in the radial direction. The relative motion of tube (F) by this set provides the radial traverse. The latter arrangement is not yet operational.

At the United Technologies Research Laboratory [40, 41], a traverse mechanism is mounted inside a large-scale, low-speed facility which is used to study various aspects of axial-flow compressor and turbine aerodynamics and heat transfer. Because of its large-scale (1.5 m dia) engine, Reynolds number levels are obtained at low rotational speeds, typically less than 1000 rpm. Some of the data from this facility are given in reference [41]. The traverse system can move circumferentially over 25 deg, radially from hub to tip on the 0.8 hub/tip ratio models, and can yaw a probe over ±90 deg. It is mounted inside a circumferential ring which forms part of the rotor hub and through which the probe protrudes. The ring moves circumferentially relative to the rotor hub on a series of rollers. The radial motion is obtained by mounting the probe holder in a device which is driven radially by a ball screw and is guided by a ball bushing. The probe holder can pivot (yaw) in this device and is driven by a radially oriented spline, along which it slides. The radial and yaw drive motors and their location-sensing potentiometers are positioned close to the rig axis. The circumferential drive motor and its potentiometer are located closer to the rotor hub. This provides the circumferential motion of the traverse ring relative to the hub. The entire system is controlled by a dedicated online Interdata 8/16 mini-computer.

Larguier and Sievers [42] developed a rotating-probe actuating mechanism using hydraulic actuators. Two hydraulic actuators, one for the tangential traverse and one for the null is employed. This device is shown schematically in Fig. 5. The probe displacements are recorded on the control panel through a marked potentiometer. The tangential and null traverse are automated, but the radial movement is carried out manually. The mechanism has been used for rotating a pitot probe. The pressure outlets of the probe are connected to a rotating pneumatic manifold at the end of the rotor shaft.

In addition, Tombult [43] describes an electronic device for indicating the position of the probe with respect to the blade.

It is evident from these discussions that the devices operational at The Pennsylvania State University [26, 28–30], Aachen [36, 37], and United Technologies [40, 41] are most suitable when extensive flow measurement (blade to blade, hub to tip, and downstream) are required inside the rotor passages and at the exit.

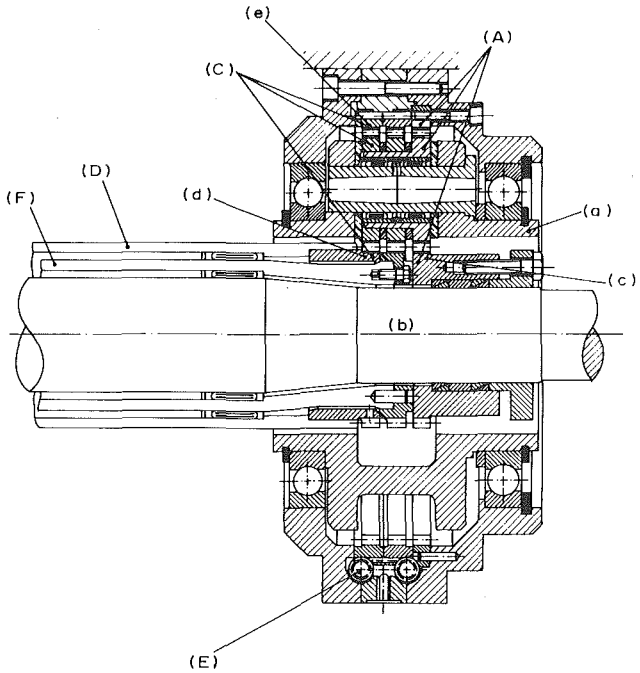

Fig. 4 Rotating-probe traverse mechanism at the University of Aachen [36]

Rotor Flow Data Transmission Systems

This chapter deals with systems used for transmitting the electrical and pneumatic probe data from the rotor frame of reference to the stationary frame. A discussion of on-the-shaft microelectrical signal conditioners as well as the telemetry system are also included. The data in a rotor frame of reference may originate from a hot wire, pitot, or other probes as well as pressure, shear stress, strain, and temperature gauges on the blade.

Transfer of Pressure Data. These devices are mainly used to transfer the pressures from a rotating blade, cooling passage, or pressure probes (Prandtl, three-hole or five-hole probes) to a stationary system. The pressure may be transferred directly to a stationary transducer or a manometer, or the pressure may be converted into an electrical signal in the rotor frame of reference using a rotating transducer. Both of these techniques are described below.

Pressure Transfer Device (PTD) and Scanivalve. Some of the earlier PTD systems were built by Weske [20] and Runkel and Davey [44]. Weske employed a selector switch, which is similar to the scanivalve described later, and a seal to transfer the blade static pressure and pressure from probes. Runkel and Davey built a PTD which employs mercury to provide the necessary seal between the rotating shaft and the stationary housing. The device was found to be adequate up to 6000 rpm and was cooled by water at speeds in excess of 2000 rpm. Leakage of mercury was found to be a major problem in these earlier devices.

The group at Keio University [45] utilized carbon ring spacers, springs and "O" rings to provide a sealed channel for transmitting pressures from a rotating blade. Klein [35] employed "O" rings to provide the seal between the channels of a seven-channel PTD unit built for transferring pressures from a rotating pitot tube. Shaw [46] built a 24-channel PTD with sealed bearings and "O" rings for the measurement of the rotor blade static pressure in an axial-flow compressor facility at the Liverpool University. Shnee, et al. [21] used an oil-cooled gland-type sealing element, shown in Fig. 1, to transmit pressures from a rotating shaft to a stationary manometer. This device was used up to 5000 rpm. Many others [27–43, 47–50] have used devices similar to the ones described above.

The device built at The Pennsylvania State University [51] and used in the inducer [52] and the compressor facilities is shown in Fig. 6. It is a three-channel system and utilizes sealed ball bearings (MRC-R-1622) mounted on a teflon-coated shaft attached to the rotor shaft. The "O" rings and spacers provide additional sealing. The pressures from the rotating blade or the probe are brought through the hollow shaft to sealed channels, then on to a stationary transducer or manometer. The device is tested statically and dynamically for leakage through channels. This unit has been used for flow measurement in inducers [51] operating at 450 rpm and compressor rotor [26] operating at 1060 rpm.

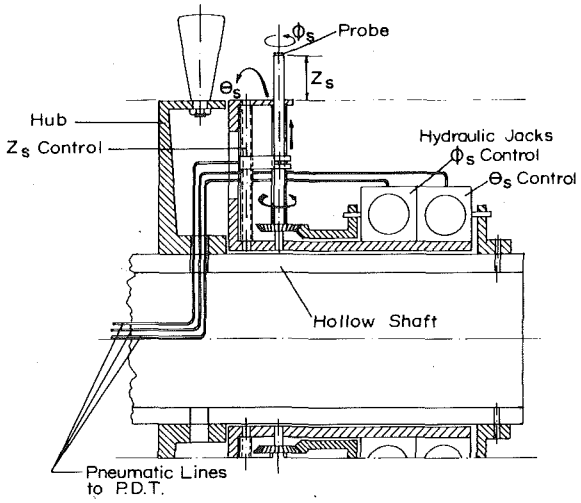

Fig. 5 Rotating-probe traverse mechanism at ONERA (France) [42]

The pressures from a rotating probe or a blade transmitted through a PTD have to be corrected due to centrifugal forces. This correlation can be calculated by using the radial equilibrium equation for the flow between r and r_0 of the rotating-probe system

$$P_A = P_M \exp\left[\frac{\omega^2}{2RT}(r^2 - r_0^2)\right], \tag{1}$$

where P_A = actual pressure, P_M = pressure measured from *PTD*, T = absolute temperature, ω = angular velocity, r = radius at the probe or blade static location, r_0 = radius of channel in PTD, and R is the gas constant.

If the density inside the rotating probe is constant,

$$P_A = P_M + \rho\frac{\omega^2}{2}(r^2 - r_0^2). \tag{2}$$

In many instances, multi-pressures (as in blade static and five-hole probe) have to be transmitted from a rotor frame of reference. Instead of employing a large number of PTD channels, it is more covenient to employ a switching unit such as a scanivalve [47], which is commercially available. Another type of switching unit developed by Howells and Lakshminarayana [53, 54] is described in the next section.

Rotating Transducer. It is convenient to convert the mechanical pressures (e.g., blade static, five-hole probe pressures, etc.) into electrical signals through a transducer in the rotating frame of reference and transmit the electrical signal through a slip ring. This is the technique used by Howells and Lakshminarayana [53, 54], and Johnson and Moore [31], Dring and Joslyn [41], Pollack and Liebert [55, 56], and Lakshminarayana [26].

The unit built by Howells and Lakshminarayana [53, 54] is shown in Fig. 7. The instrumentation package attaches to the face of the rotor hub and rotates with the blade system. Pressures from rotor are transmitted by the stationary part, or the plate, of the 20-channel switching unit. The movable part of the switching unit, or the wiper arm, is controlled by a slo-syn HS-25E precision stepping motor. A copper bellows with adjustable compression is located between the motor shaft and wiper arm, and holds the arm firmly against the plate. Rubber O-rings in the wiper arm and the teflon-coated face of the plate form a pressure seal. The wiper arm may be positioned over any hole in the plate by stepping the motor, and then the pressure of the corresponding static orifice may be read. The pressure signal is passed to the pressure transducer. A slip-ring unit is used to transmit the electrical signal. Since the use of a pressure transducer mounted in the rotating system was a new technique, some questions about the effect of centrifugal force on the transducer existed. Thus, it was necessary to investigate the output of a rotating transducer and to develop calibration curves, if required. A test jig was built [54] to spin the transducer over a range of speeds (0 to 3750 rpm) and eccentricities (0 to 1.3 cm). Eccentricity is the distance between the axis of rotation and the center of the transducer diaphragm. The results show

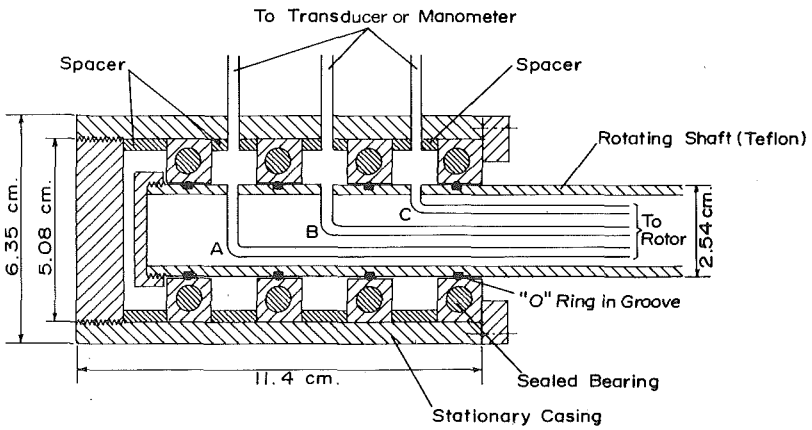

Fig. 6 Pressure transfer device at The Pennsylvania State University

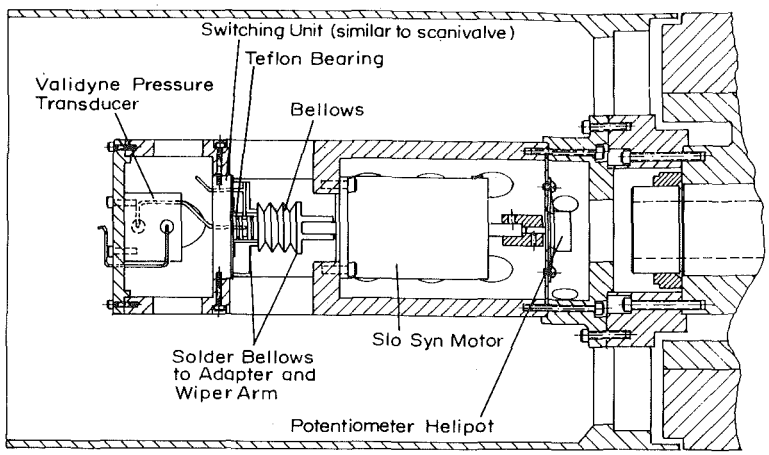

Fig. 7 Pressure transfer device-scanivalve-rotating transducer assembly at The Pennsylvania State University [53, 54]

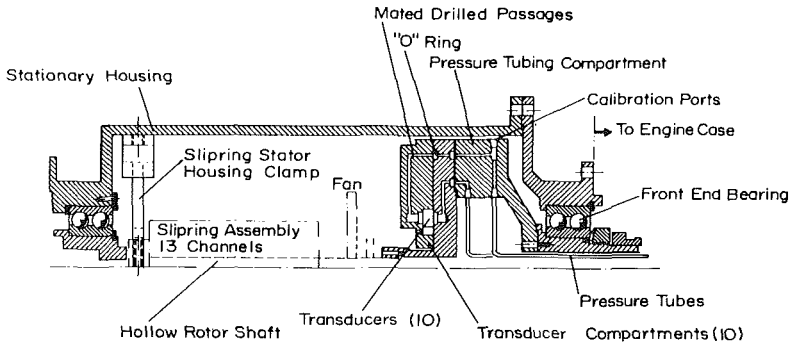

Fig. 8 Pressure transfer device-rotating transducer assembly at NASA Lewis Research Center [55, 56]

that for all speeds and eccentricities tested, the deviation between the stationary and rotating output signal from the transducer was less than 18×10^{-2} mm of H_2O (2.56×10^{-4} psi). Hence, the effect of rotation on the transducer, as used with this instrumentation, is negligible and no calibration was required.

Pollack and Liebert [55, 56] developed a ten-channel rotating pressure-measuring system capable of operation to shaft speeds of 9000 rpm and environmental temperatures of about 320 K (120°F). The assembly shown in Fig. 8 consists of transducer compartments, a mounting plate, and a pressure tubing compartment. Each transducer is mounted in a separate transducer compartment, so that the transducer diaphragm is in the plane of rotation. The pressure tubing compartment contains ten pairs of inlet ports, one pair for each transducer. The pressure tubing inlet ports are connected to the transducers by means of a series of mating drilled passages through the bulkhead assembly as shown in the figure. The transducers selected by Pollack and Liebert [55] are the variable reluctance pressure difference type described in reference [57]. These variable reluctance transducers are capable of measuring pressure when operating up to 5000 g centrifugal force and temperatures up to 370 K. Rotating performance tests on a spin rig showed that the output data from seven to the ten transducers tested were within a system error of 3 percent. However, the error of the output data from three other transducers was as large as 8 percent at 9000 rpm. This system has now been modified [58] to include transmission of data from temperature sensors.

Bragg [59] describes a rotating manometer system for reading the pressure directly from a rotor frame of reference. This system is suitable for low speeds.

At low speeds (up to 5000 rpm) either PTD's or rotating transducers can be utilized for transmission of pressure, but at higher speeds it may be desirable to employ a rotating transducer and a telemetry system (described later), since the heat generated by PTD and slip-ring units may be excessive.

Transfer of Electrical Data. The electrical data from rotating transducers such as hot wire, strain gauge, thermocouple, and stress gauge have to be transferred from a rotating system to a stationary system without distortion in frequency or amplitude. In many instances the signals are weak, and hence one of the important requirements of an electrical data transmission system is the low noise/signal ratio. The systems are available for use and are described below.

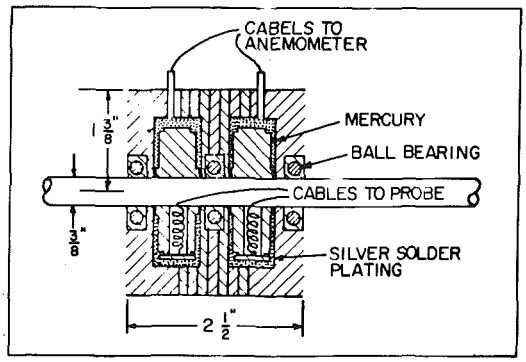

Fig. 9 Mercury slip-ring unit [51]

Mercury Slip-Ring Unit. A schematic of the two-channel unit built at The Pennsylvania State University [51] is shown in Fig. 9. Each channel consists of a thin disk rotating in a small housing filled partially with triple-distilled mercury. During rotation, the shear pumping effect of the disk carries mercury to the gap between the housing and the disk. This thin layer of mercury acts as a conductor. The signals are transferred from the inner shaft through the rotating disk and the mercury pool to the stationary conductors on the casing of the slip-ring unit. This system provides noiseless contact between the rotating and stationary conductors and is ideally suited for transferring weak (a-c and d-c) signals from the rotating system to the stationary instrument. The mercury has to be changed at regular intervals as contamination of the triple-distilled mercury introduces

a higher noise/signal ratio. Similar units have been used by Ufer [25], who reports a change in maximum resistance of 6 mΩ between 0-3000 rpm. Mercury slip-ring units are commercially available now (Rotocon Meridian Laboratory, Inc.) from 2 to 150 terminals for operation from very low speeds to 30,000 rpm. They have a very low stable and contact resistance (5 mΩ) and can be operated from −25 to 60°C.

Both the brush type and mercury slip-ring units are suitable only in situations where the alignment can be maintained and speeds are not excessive. Hence, many engine manufacturers are now embarking on the development of a telemetry system for transmitting strain gauge, thermocouple, and blade pressure data. This system is described below.

Telemetry System. In a telemetry system, data is transmitted without physical contact, which is an attractive feature. There are basic differences in this system, depending on the application. The systems used for strain and pressure measurements are similar [9, 10] and are characterized by frequency response. Of all the telemetry systems employed, only those due to O'Brien, et al. [9], Heller and Widnall [60], and Light [61] were used for blade static (steady and unsteady) pressure measurements. All other systems [62–68, 10] are used either for strain or temperature measurements. Some systems are most suitable for research environments [9, 60, 61] while others [10, 62–68] are suitable for severe environmental conditions that exist in jet engines.

O'Brien, et al. [9] developed a six-channel direct FM telemetry system adapted for fluctuating and steady pressure measurements on a rotor blade. A schematic of the system is shown in Fig. 10. Each channel of the telemetry instrument incorporated functional blocks including transducer (0.31 cm dia embedded on rotor), amplifiers with 20 kHz frequency response, VCO (voltage controlled oscillators) transmitters, antenna system, and receiver elements. The circuit on the rotor side was battery charged. Information was transmitted by 6 FM carriers in the range of 1 to 12 mHz, and received and amplified by a single antenna system. VCO converted the information to a frequency modulated carrier. A simple capacitance was used to conduct the FM signal from the rotor to the stator without contact. Six receivers, employing the phase-lock loop principle of demodulation, separated frequency multiplex into the six carriers, and reproduced the transducer information. The functional unit of the receiver demodulator was a NE 560 B integrated circuit. The output from this demodulator was recorded on a tape recorder with zero suppression of d-c. The telemetry package was fitted within a housing at the end of the test compressor and transmission occurred between antenna segments, across an axial gap. This device was later modified by light [61] for high-speed and high-frequency (50 kHz) operation. Heller and Widnall [60] used a similar device to transmit fluctuating pressures from a rotor blade. The frequency range was 20–10,000 Hz.

Other telemetry systems used for the transmission of strain and temperature data are described by Donato and Davis [66] and Colangelo and Schlerth [67], who had 16 channels for the strain and 30 channels for temperature. Lesco, et al. [64] had 69 channels for the thermocouple data, with less than 0.5 percent error, from a turbine at 9000 rpm and 72 channels for the strain data. Adler and Hoeks [63] used a phase-locked transmitter and developed a system capable of operating at 175°C at 50,000 g acceleration. Worthy [68] developed a system capable of operating in an in-flight and test-stand engine environment for the Rolls-Royce RB211 aircraft engine.

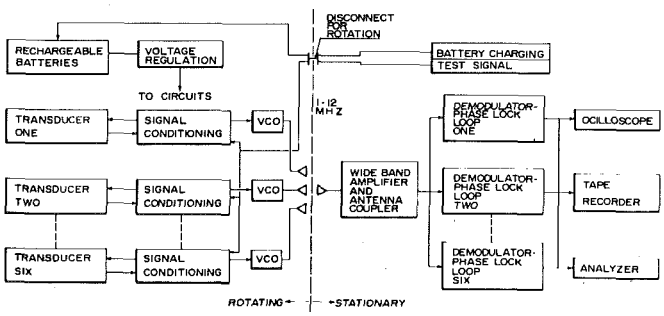

Fig. 10 Telemetry system [9]

It is thus evident that telemetry has been successfully used for strain, temperature, and fluctuating and steady blade static pressure measurements. The same system could be used for wall shear stress data from hot films. Extension of a telemetry system to transmit signals from high-frequency probes (hot wire, etc.) would be very useful.

Hot-Wire Technique for Three-Dimensional Mean and Turbulence Flow Field

The hot-wire technique is based on the principle of heat transfer between a cylinder and the flow around it, governed by the relationship

$$\mathrm{Nu} = A + B(\mathrm{Re})^n, \tag{3}$$

where Nu is the Nusselt number, Re is the Reynolds number, A and B are constants for a particular fluid, cylinder, and temperature. The principle element of a hot-wire probe is a thin sensor of 1 to 5 μm dia made of platinum, platinum-iridium, or tungsten. The wire is heated by an electric current and cooled by the flow, causing the temperature to drop. In a constant-temperature hot-wire anemometer system, which is widely used now, the temperature of the sensor is kept constant and the voltage is measured. The relation between the voltage (E) and the flow velocity (Q) is given by

$$E = A + BQ^n. \tag{4}$$

The exponent n is found to be 0.45 to 0.5. The frequency response of the hot-wire probe is very high (10 to 15 kHz).

Basic aspects of hot-wire/film techniques for described in references [69] and [70], and an up-to-date review of the literature is given by Comte-Bellot [71, 16]. Since the rotor flow field (both mean and turbulence quantities) is three-dimensional, the application of the hot-wire technique to turbomachinery involves considerable complication. In addition, the flow is rotating and is steady only in the relative frame of reference. If a probe is used in the stationary frame of reference, the flow field sensed by the probe is unsteady, with both periodic and random components. One has to resort to some averaging technique in decomposing the two.

Early application [72–74] of the hot wire technique to turbomachinery was mostly qualitative and was utilized to detect wake and stall regions, and rotating stall.

Raj and Lakshminarayana [75] made extensive use of a hot-wire in the quantitative study of cascade wakes. Railly and Sharma [76] used it to measure the "apparent stresses" caused by the blade-to-blade variation in flow properties.

The hot-wire techniques available for turbomachinery rotor flow measurement can be classified as follows.

1 Rotating Hot-Wire Technique. In this method a three-sensor hot wire is rotated inside a rotor passage and traversed from blade to blade using a rotating-probe traverse mechanism described in an earlier section. This method is due to Gorton and Lakshminarayana [6].

2 Stationary Hot-Wire Technique. There are two methods available for measuring the flow at the exit using a stationary hot-wire probe. The first method utilizes a three-sensor wire and is due to Lakshminarayana and Poncet [2, 77]. The second method utilizes a single sensor, rotated twice about its own axis. This method is due to Whitfield, et al. [78]. Both methods employ a periodic sampling and averaging technique to decompose the periodic and random components from the measured signal.

A detailed discussion of both techniques follows.

Rotating Hot-Wire Technique for Rotor Passage and Exit Flow Measurements. If the flow properties inside a blade passage are to be obtained, the most useful method is the rotating hot-wire technique. In this technique, the hot wire is rotated with the rotor, and traversed across the passage, using the traverse mechanisms and data transmission systems described earlier. Ufer [25, 79] employed a single-sensor hot-wire probe and measured the flow near the tip of a fan rotor, with and without tip clearance. Since the flow is three-dimensional, the single sensor at best can provide qualitative information. The same criticism applies to rotating hot-wire probe data

at the exit of a Francis Turbine by Gerich [80]. Day [81], using a large (22 m dia), low-speed (4.3 rpm) turbine facility, rode with the rotor and measured the flow in a rotor passage using three orientations of an X wire. The skew angles near the blade surface were found to be large.

Gorton and Lakshminarayana [6] employed a three-sensor hot wire inside an inducer passage. This technique provides comprehensive information on the mean and turbulence flow field and has enabled verification of the existing computer codes for three-dimensional flows [82, 83]. This technique has subsequently been improved and simplified for three-dimensional boundary-layer measurement in a flat-plate inducer [84, 85]. The hot-wire error due to rotation has been found to be negligible [86]. This technique has also been widely used by the Penn State group [26, 28, 30, 87–89] to study the endwall flow and rotor blade wake characteristics. This has provided not only a great insight into the structure of rotor wake flow, but also enabled the verification of numerical techniques and turbulence models [90, 91]. A summary of the technique developed at Penn State is given below. It represents a description of the latest technique, rather than a historical evolution of the method.

Three-Sensor Hot-Wire Probe, Instrumentation and Equations. The most commonly employed three-sensor hot-wire probe is shown in Fig. 11. The sensors are 3 μm dia tungsten wire with a length-to-diameter ratio of 300. The sensor is located inside the pasage or at the exit such that the relative mean velocity vector is inside the cone formed by the sensor. The hot wire is mounted on a rotating traverse mechanism, such as the one shown in Figs. 2 or 3. Gorton and Lakshminarayana [6] did not have an automated tangential traverse, and Anand and Lakshminarayana [84, 85] used a device similar to Fig. 2. The traverse mechanism shown in Fig. 3 was used in references [30] and [87]. The hot-wire electrical signal is brought through a mercury slip-ring unit into a stationary anemometer system. A schematic of the instrumentation used for the rotating-probe system is shown in Fig. 12. The three electrical signals from the hot wire are brought into three anemometers. Final output from the instrumentation system consists of three mean voltages $(\overline{E}_1, \overline{E}_2, \overline{E}_3)$ and rms values of six fluctuation voltages $(\overline{e_1^2}, \overline{e_2^2}, \overline{e_3^2}, \overline{e_1e_2}, \overline{e_2e_3}, \overline{e_1e_3})$ where 1, 2, 3 refers to the wire number. A spectrum analyzer was also used to determine the energy spectra of each of the six fluctuating voltages.

The equations relating the mean and fluctuating voltages to the three mean velocities and six stress components in an arbitrary coordinate system are given by Gorton and Lakshminarayana [6]. The equations are valid for a nonorthogonal hot-wire system. A summary of the equations is given below [84].

In this analysis, the fluctuating and mean velocities are separated and the equations are simplified neglecting the second-order terms. The following equations (in matrix form) for the mean velocities and turbulence stresses relating them to the corresponding voltages are derived.

$$\{Q_{\ell n}\}_{(3,N)} = \{\alpha_{\ell i}\}_{(3,3)} \times \{U_{in}\}_{(3,N)} + \{\beta_{\ell ij}\}_{(3,3)} \times \left\{\frac{U_{in}U_{jn}}{U_{1n}}\right\}_{(3,N)} \tag{5}$$

and equation (4) for this system is

$$\{E_{\ell n}{}^2\}_{(3,N)} = \{E_{0\ell}{}^2\}_{(3,N)} + \{B_\ell(n)\}_{(1,3)} \times \{\sqrt{Q_{\ell n}}\}_{(3,N)}, \tag{6}$$

where subscripts ℓ, n, and i denote the wire, the observation point, and the velocity component in the reference coordinate system, respectively. U_{1n} is the principal component of mean flow velocity, which in the present coordinate system is in the streamwise direction. $\alpha_{\ell i}$ and $\beta_{\ell ij}$ are functions of direction cosines of the ℓth wire, which includes the correction factor for deviation from the Cosine Law. E_0 is the output d-c voltage at zero flow velocity. $E_{\ell n}$, $B_\ell(n)$ and $Q_{\ell n}$ are the measured values of voltage, slope of the hot wire calibration curve, and effective mean cooling velocity, respectively, for the ℓth wire at nth observation point. U_i is the mean velocity component (e.g., U_r, U_θ, U_z). The numbers in parentheses outside of a matrix represent its dimensions; e.g., $(Q_{\ell n})_{(3,N)}$ is a matrix with three rows and N columns. N is the total number of observation points in a measuring set.

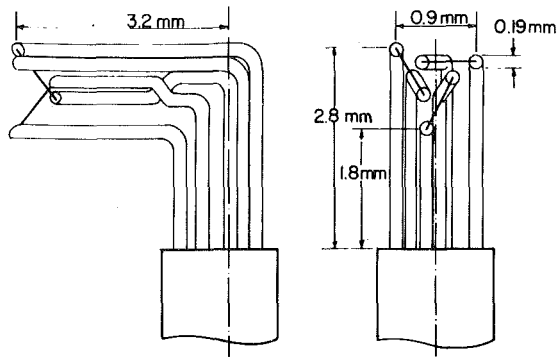

Fig. 11 Three-sensor hot-wire probe

Indices i, j, ℓ can take values 1, 2 and 3. For $\ell = 1$, α_{11}, α_{12}, and α_{13} correspond to Gorton and Lakshminarayana's [6] terms α_5, α_6, and α_7, respectively. Similarly, for $\ell = 1$, $\beta_{122} = \alpha_8$, $\beta_{133} = \alpha_9$, and $\beta_{123} = \alpha_{10}$, and all other values of β_{1ij} are zero.

All of the six components of Reynolds stress tensor $(\overline{u_iu_j})$ at any point in the rotor passage, in the rotating coordinate system, are obtained from the six measured values of the fluctuating voltage correlations $\overline{e_ie_j}$ and the three mean d-c voltages $\overline{E}_i(i, j = 1 \text{ to } 3)$. The velocity correlations are related to fluctuating cooling velocities as follows.

$$\{\overline{q_{\ell n}q_{mn}}\}_{(6,N)} = \{\gamma_{\ell i}\gamma_{mj}\}_{(6,6)} \times \{\overline{u_{in}u_{jn}}\}_{(6,N)}$$

$$\gamma_{\ell i} = \left(\alpha_{\ell i} + \Gamma_{\ell ij}\frac{U_{in}}{U_{1n}}\right) \tag{7}$$

where quantity $(\overline{q_{ln}q_{mn}})$ is the correlation between fluctuating cooling velocities of ℓth and mth wires at the nth observation point and is related to output a-c and d-c voltages as follows

$$(\overline{q_{\ell n}q_{mn}}) = \frac{16\overline{E}_{\ell n}\overline{E}_{mn}}{B_\ell(n)B_m(n)}\sqrt{Q_{\ell n}Q_{mn}}\,(\overline{e_{\ell n}e_{mn}}). \tag{8}$$

The coefficients $\alpha_{\ell i}$ and $\beta_{\ell ij}$ are the same as those occurring in equation (5) for mean effective cooling velocity Q. u is the fluctuating velocity, and U_{1n} is the mean velocity in the principal direction at the measuring point n. The superscript (—) denotes the time-averaged quantity. The coefficients $(\alpha_{\ell ij})$, for $\ell = 1$ in Gorton and Lakshminarayana's [6] notation are

$$\Gamma_{122} = a_{11}, \quad \Gamma_{133} = a_{12}, \quad \Gamma_{123} = \Gamma_{132} = a_{13}$$

$$\Gamma_{222} = b_{11}, \quad \Gamma_{233} = b_{12}, \quad \Gamma_{223} = \Gamma_{232} = b_{13}$$

$$\Gamma_{322} = c_{11}, \quad \Gamma_{333} = c_{12}, \quad \Gamma_{323} = \Gamma_{332} = c_{13}$$

Expressions for a_{11}, a_{12}, a_{13}, etc. are given in reference [6]. All other Γ values are zero. The quantities $\overline{E}_{\ell n}$, $B_\ell(n)$, and $Q_{\ell n}$, etc., are, respectively, mean d-c voltage, slope, and mean effective cooling velocity of the ℓth wire at the nth data point and N is the total number of data points in a measuring set. The matrix equations (5–8) are solved successively using the known values of voltages and calibration data, by using the Newton-Raphson convergency scheme until the convergency criterion given below is reached.

$$|U_i^{(p)} - U_i^{(p-1)}| \le 0.005U_{bt} \tag{9}$$

where $U_i^{(p)}$ and $U_i^{(p-1)}$ are values of a mean velocity component U_i at pth and $(p-1)$th iteration, respectively, and U_{bt} is the peripheral velocity of the rotor blade at the tip.

The velocity components and shear stresses can be derived in any arbitrary coordinate system. A cylindrical coordinate system was used in references [6, 28] and [30] and an intrinsic coordinate system was used in references [84] and [85]. The computer program, reproduced in reference [82], incorporates many of the errors discussed later. This program was subsequently modified by Anand and Lakshminarayana [84, 85] and Ravindranath [88]. The latest computer program [88] incorporates corrections due to many of the errors. Among the most important corrections incorporated are: (1) effect of change in the

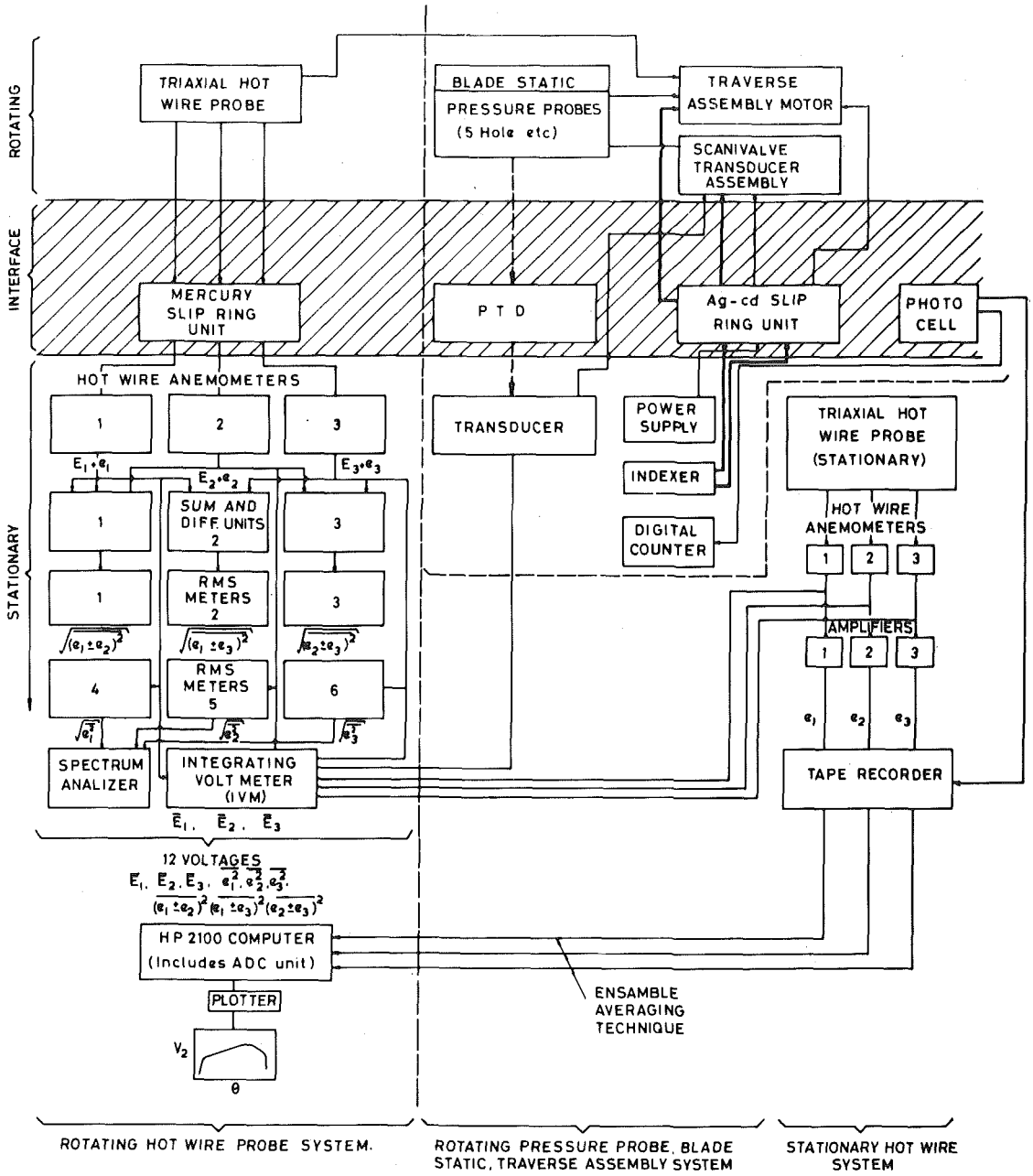

Fig. 12 Schematic of control and instrumentation system for rotating and stationary three-sensor hot-wire techniques, and other rotating probes [26]

ambient fluid temperature during the course of the experiment and in calibration, included at each step and for every data point, (2) spatial error, incorporated by interpolating measurements from adjacent points, (3) error due to deviation from the Cosine Law, (4) effect of change in slope B in the calibration curve. Local slope is used to alleviate this problem, and (5) in-site calibration was carried out to determine the value of E_0 at $Q = 0$. This value is used in a new calibration curve.

Gaulier [92] has recently suggested a three-term equation of the following type for the hot wire:

$$E^2 = A + BQ^n + CQ, \tag{10}$$

where C is an additional constant. This calibration equation can be easily incorporated in equations [5–8]. The use of the computer program can be eliminated by designing an analog device to carry out some of the computations as was done by Zimmerman and Abbott [93].

It is beyond the scope of this paper to discuss the data from rotating hot-wire measurements. This can be found in references [6, 25, 26, 28, 30, 79–91]. Typical data obtained by this technique inside an axial-flow inducer are shown in Fig. 13. The data are at 0.9 chord length from the leading edge and at various radii. Appreciable radial velocity, boundary layer growth, and interaction near the tip is evident.

A detailed discussion of the probe errors is given in a later section. The hot-wire Equations [5–8] can also be solved by the use of an on-line data processing technique. This capability exists at the Aerospace Engineering Department of The Pennsylvania State University.

Stationary Hot-Wire Technique for Rotor Exit Flow Measurement. A stationary hot-wire probe at the exit of a rotor blade senses unsteadiness which consists of both the periodic component, at the blade passing frequency, and the random component due to turbulence. There are several ways of extracting the information on the periodic (or blade-to-blade distribution) component as well as turbulent stresses and intensities.

In these techniques, the blade-to-blade flow is acquired using an analog signal enhancement [78] or digitized signals [2]. In both cases, a once-per-revolution signal is used to ensure conditional averages (time mean) for the same location relative to a specific blade. A brief discussion of the averaging method is followed by a description of the three-sensor and the single-sensor hot-wire techniques.

Averaging Technique. The instantaneous signal from a hot wire can be decomposed into

$$U_i(t) = \overline{U}_i(t) + u(t), \tag{11}$$

where $\overline{U}_i(t)$ is the signal obtained by periodically sampling the signal $U_i(t)$ of ith wire with period $T(= 60/NB, B$ = number of blades, N = rpm) and averaging,

$$\overline{U}_i(t) = \sum_{n=1}^{N} U_i(t + nT), \tag{12}$$

since the contribution due to $u_i(t)$ as $N \to \infty$ is zero. $\overline{U}_i(t)$ and $u_i(t)$ can be separated by obtaining a reference signal from a photocell or an electromagnetic pulse generator at the blade passing frequency. This pulse can be used as a reference for determining the phase of the signal. The averaging can then be carried out using a digital [2, 77] or analog technique [78]. The former will be termed phase-locked ensemble-averaging technique (PLEAT) and the latter will be referred to as phase-locked averaging technique (PLAT) in this paper. A detailed discussion of signal-averaging techniques can be found in reference [94].

Since PLEAT, employed by the Penn State Group, is used in conjunction with a three sensor hot wire, they are combined together for convenience and will be discussed in the next section. PLAT was first used by Whitfield, et al. [78] employing a single-slanted wire rotated successively through 120 deg increments. Most others who utilized this technique also used the PLAT method of averaging. Hence, description of the single-sensor technique and discussion of the phase-locked averaging technique will be combined in one section. It should be emphasized here that either of the averaging techniques could be employed with a single wire, an "X" wire, and a three-sensor hot wire.

The most accurate technique for deriving the entire mean and turbulence flow field is the three-sensor technique described in the next section. If the interest lies only in mean-velocity components, the single-slanted wire technique, described later, is adequate.

Three-Sensor Hot-Wire Technique and Phase-Locked Ensemble-Averaging Technique (PLEAT). This technique was developed by Lakshminarayana and Poncet [77, 2] in 1970 and was used in measuring the flow at the exit of an axial-flow inducer. It was subsequently improved by Raj and Lakshminarayana [95] and Reynolds and Lakshminarayana [96]. Hah [97] recently adopted this technique for use in an on-line data processing technique employing the HP 2100S digital computer. All of these investigators utilized a three-sensor hot wire and derived three components of velocity and six components of Reynolds stresses across the entire blade passage, as well as from hub to tip, of a turbomachinery rotor. A detailed discussion of these data can be found in references [95–100]. Following is a description of the latest technique.

Several three-sensor probes, some custom made, were employed in this investigation. Lakshminarayana and Poncet [2, 77] employed an "X" and a single-wire combination. Figure 11 shows the miniature tri-axial probe employed in references [95] and [96]. The tri-axial hot-wire probe was located downstream of an inducer rotor [2, 77], fan rotor [95, 96] or compressor rotor [97] such that the absolute mean velocity was inside the cone formed by the sensors. The angle between the probe axis and the rotor axis was noted. The fluctuating signals were amplified and memorized in a tape recorder and the d-c voltages integrated in an integrating voltmeter. A one pulse per revolution signal from a photo cell on the rotor shaft was simultaneously recorded in one of the tape recorder channels to enable averaging by the PLEAT method. The center frequency was high enough (43 kHz) to capture both the mean and fluctuating voltages in the 0–10 kHz range.

An analog-to-digital converter which was used could convert data at a maximum rate of 2465 samples per second for each of the simultaneously digitized channels. Thus, a real-time analog-to-digital conversion was not possible. So that approximately 388 digital points would represent the blade-to-blade variation in measured quantities, the analog signal was digitized at a tape speed 1/30 of real time. Digitized data were in a form whereby each coded word contained a

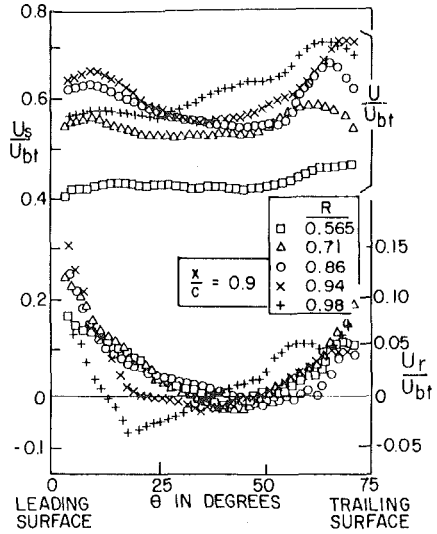

Fig. 13 Velocity profile inside the inducer passage (flow coefficient 0.065, rpm = 450, 4 blades, θ is the tangential location in degrees [84])

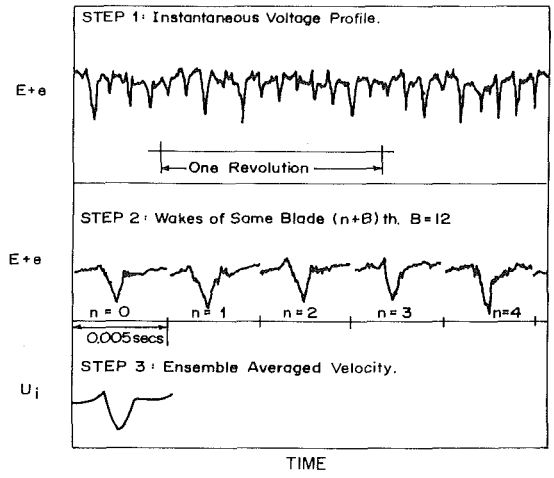

Fig. 14 Procedure involved in phase-locked ensemble-averaging technique (PLEAT)

four-bit channel number, a six-bit identification number, a four-bit synchronization nibble, and a ten-bit integer data value. To adjust the digitized data to represent the characteristics of flow across one blade passage, only every $(n + B)$th wake ($n = 0$ to N) was saved. The value of N in this investigation varied from 80 to 200. A one spike per revolution signal peak was used to determine every $(n + B)$the wake. A sample input and output of this phase of data processing is shown in Fig. 14.

The digitized electrical data ($3 \times N \times 388$ bits) corresponding to instantaneous voltages was converted to corresponding cooling velocities using King's equation, with a varying exponent.

$$Q_\ell = \left[\frac{E_\ell{}^2 - E_{0\ell}{}^2}{B_\ell}\right]^{1/n_\ell}, \tag{13}$$

where subscript ℓ denotes the wire. Orthogonality of the wires was assumed in reference [95], and no such assumption was made in the formulation employed in references [96] and [97].

The values of B_ℓ, n_ℓ and $E_{0\ell}$ were obtained from the calibration of each hot-wire sensor. In many instances [97], the exponent n_ℓ was varied for low, medium and high fluid velocities. The following procedure was used to get the instantaneous velocity from the tri-axial hot-wire probe, whose three sensors are non-orthogonal. The direction cosines of three sensor directions (k) to the reference orthogonal coordinates (i) were first measured. This is similar to the procedure used by Gorton and Lakshminarayana [6] for a rotating wire described earlier in this paper. The angles between hot wires $[(\theta_{ij})$ are derived from the following equation (in tensor notation),

$$\cos\theta_{ij} = \sum_{k=1}^{3} a_{ik}a_{jk}, \tag{14}$$

where θ_{ij} is the angle between wires i and j, and a_{ik} is the direction cosine between sensor direction k and the reference coordinate i. The effective cooling velocity (instantaneous) can then be expressed in terms of instantaneous velocity components as follows.

$$Q_\ell{}^2 = \sum_{j=1}^{3} (k_\ell{}^2 \cos^2\theta_{\ell j} + \sin^2\theta_{\ell j}) V_j{}^2, \tag{15}$$

where V_j is the instantaneous velocity component in the direction of sensor j, Q_ℓ is the instantaneous cooling velocity of the wire ℓ and k_ℓ is the correction factor due to deviation from the Cosine Law for the wire ℓ. This is a function of the length-to-diameter ratio of the wire and other parameters. The three linear equations (ℓ = 1, 2, 3) are solved simultaneously knowing θ_{ij} from equation (14). The instantaneous velocity in coordinate directions can be derived from

$$U_i = \sum_{j=1}^{3} a_{ij}V_j, \tag{16}$$

where a_{ij} is the direction cosine of the angle between ith coordinate direction and the jth wire, and U_i is the instantaneous velocity in the coordinate direction i.

Using these instantaneous velocity components in three coordinate directions, three components of mean velocities, turbulence intensities and shear stresses are statistically calculated using the PLEAT method described below.

The processed data contain instantaneous velocity in three chosen coordinate directions sampled at M number of points (M = 50 in [2], 388 in [95] and [96]) across the passage in N (N = 80 in [2], 200 in [97]) number of consecutive signals of period ($2\pi/\Omega B$). Thus, the data belong, physically, to the same passage at different intervals of time. The ensemble average at any passage location $\theta = \theta_m$ is given by

$$\hat{U}_i(\theta_m) = \frac{1}{N}\sum_{n=1}^{N} U_{in}(\theta_m), \quad \begin{matrix} m = 1 \cdots M \\ i = 1, 2, 3 \end{matrix} \tag{17}$$

where $U_{in}(\theta_m)$ represents the instantaneous velocity at the passage location $\theta_m (m = 1 \cdots M)$.

The turbulence intensity is given by

$$[u_i(\theta_m)]^2 = \sum_{n=1}^{N} \{[U_{in}(\theta_m) - \hat{U}_i(\theta_m)]^2\}/N, \tag{18}$$

and the velocity correlation at θ_m location is given by ($i \neq j$)

$$\overline{u_i u_j} = \sum_{n=1}^{N} [U_i n(\theta_m) - \hat{U}_i(\theta_m)][U_j n(\theta_m) - \hat{U}_j(\theta_m)]/N, \tag{19}$$

where i, j = 1, 2, 3 represent the coordinates of 1, 2, and 3, respectively.

The ensemble-averaged value ($\hat{U}_i$) approaches the time-averaged value,

$$\overline{U}_i = \lim_{T\to\infty} \frac{1}{2T}\int_{-T}^{T} U_i dt \tag{20}$$

for large values of N. The error involved in finite sampling is given by references [94, 2]

$$E\left[\frac{(\hat{U} - \overline{U})^2}{\overline{U}^2}\right] = \epsilon = \frac{T}{\sqrt{N}}, \tag{21}$$

where T is the turbulence intensity and E is the expected value. For example, with 10 percent turbulence intensity and N = 120, the error in mean velocity is less than 1 percent.

The error in turbulence intensity, assuming the probability density of velocity is Gaussian [2, 77, 94], is given by

$$\epsilon = \sqrt{2/N}\,. \tag{22}$$

Detailed discussion of the data and error analysis of random signals can be found in reference [94]. The error associated with the hot-wire sensor and instrumentation is discussed in a later section. Equations (21) and (22) are errors associated with ensemble averaging alone.

The earlier computer program reproduced in reference [77] was intended to calculate the three mean velocities and turbulence intensities in a cylindrical coordinate system [2]. Raj and Lakshminarayana [29, 95] utilized a three-sensor wire and modified the computer program to derive three mean velocity components and six components of Reynolds stresses in an intrinsic (streamwise, principal normal, and radial directions) coordinate system, and reported extensive rotor wake data at several axial and radial stations. Reynolds and Lakshminarayana [96, 30] modified these programs to include arbitrary wire geometry (e.g., nonorthogonal) corrections due to wire aging and temperature changes. They provided rotor wake data at various blade loadings. Hah [97] has adopted these programs to an online computer (Fig. 12). His experiment was performed at the exit of the compressor [26] with differing entry turbulence.

Typical wake data obtained by this method are shown in Fig. 15. The axial velocity component (U_z) normalized by freestream axial velocity (U_{z0}) is plotted across the passage ($Y = \pm 0.5$ represent the mid passage) at various axial locations (Z). Rapid decay near the trailing edge region is evident from this data. For detailed discussion of the rotor flow data derived from this technique, refer to references [28, 30] and [95–100].

Bennett [101, 102] utilized some of these techniques to measure the flow at the exit of a compressor [101] and a propeller [102]. The data from the latter were acquired using a three-sensor hot wire at a rotor speed of 10,900 rpm. PLAT, explained in the next section, was utilized. The data were analyzed using a Saicor correlator and probability analyzer with 2048 samples averaged for each time increment. The signal was triggered once per revolution using an optical pick-up. The data at 7500 rpm indicate that the axial and the tangential velocities are of the same order of magnitude at the exit of this propeller. A three-sensor hot film was employed by Bennett [101] for the measurement at the exit of the compressor. The advantage of hot film is the increased operating life, but the frequency response, especially for a noncylindrical sensor, is not good [103]. He found that the k_ℓ factor in equation (15) is not constant, varying with both pitch and yaw angle. Hence he employed a modified equation for the hot-wire/film equation given by

$$E^2 = A + F(\alpha)\sqrt{U}\,,$$

where $F(\alpha)$ is a function of α, the angle between the total velocity vector (U) and the hot wire. Empirical values of $F(\alpha)$ versus α were used for each of the wires.

Evans [104] used the ensemble-averaging technique and an "X" configuration probe at the exit of a compressor. The anemometer signal was fed directly to an analog-digital interface of the PDP 12

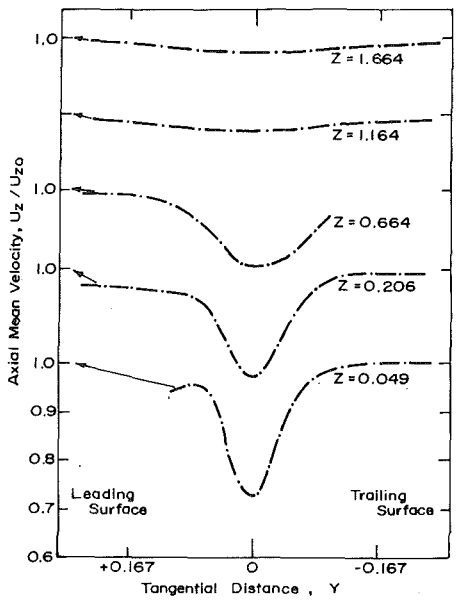

Fig. 15 Axial mean velocity profile inside the wake of an axial-flow fan rotor at mid-radius and at 15 deg incidence (speed 1060 rpm, flow coefficient = 0.6, 12 blades [96])

computer, which, after digitizing, ensemble-averaged in a real time. The sampling was initiated by a synchronizing pulse from a magnetic pick-up on the rotor. The data processing technique is the same as in references [77] and [2], but the neglection of the radial velocity and the assumption of isotropic turbulence in the data analysis casts some doubt on the accuracy of the data (see discussions by Hirsch and Lakshminarayana in reference [104]).

Some of the improvements that can be carried out to increase the accuracy of the three-sensor hot-wire technique are as follows: (1) improved calibration technique to include the effects of yaw and pitch angle as well as the vicinity of a wall, (2) inclusion of corrections for the nonuniform temperature distribution along the wire, (3) incorporation of the periodic sampling device such as the one described in the next section, (4) On-line data (digital) processing in real time, and (5) processing the instantaneous signals, in a real time, by a network of high-speed analog devices.

The analog computer such as the one developed in reference [93] is designed to apply the corrections for deviation from the Cosine Law and carry out the coordinate transformation. The mean and fluctuationg velocities can also be separated to provide the necessary information.

Items (3) and (4) or (3) and (5) should provide real-time digital or analog data processing techniques, respectively.

Single-Sensor Hot-Wire and the Phase-Locked Averaging Technique (PLAT). Many investigators [105–108] have employed a single-sensor hot wire for the measurement of three-dimensional flow field and the resultant stress. Extension of this technique to turbomachinery exit flow, where the flow is three-dimensional, unsteady, and turbulent was carried out by Whitfield, et al. [78], Hirsch and Kool [109–112], Larguier and Sievers [42], Okiishi and Schmidt [3, 113, 114], Lakshminarayana and Davino [115], Raj and Swim [116] and Favier, et al. [117]. Kool [118] has recently made attempts to extend these techniques to the measurement of turbulence quantities at the exit of a rotor.

The analog technique, termed the phase-locked averaging technique in this paper, was first utilized by Whitfield, et al. [78] in combination with a single sensor hot-wire probe, shown schematically in Fig. 16. In this technique, the hot-wire signal is triggered by a revolution frequency pulse at a fixed point during each revolution. Corresponding points in successive wave forms are then averaged with one another so that only components repeating every rotor revolution are retained. The procedure [110] is illustrated in Fig. 16. In this system, the signal is sampled during a finite time ϵ, a fixed delay τ_d after each occurrence of a synchronous trigger pulse, the latter occurring with a period T. All of these samples are added in an analog memory. Those that come from the periodic signal $\overline{U}(t)$ (equation (11)) will add coherently and the turbulence part $[u(t)]$ will add incoherently. After N samples are averaged ($N = 1024$ in [110]) the time delay τ_d is changed to derive an average at another point in the period of the signal averaged. If τ_d is made to scan the whole period, signal $\overline{U}(t)$ in one period will be recovered.

The instrumentation system used by Schmidt and Okiishi [113] is shown in Fig. 17. This set-up was used in connection with a single-wire technique and is thus limited to mean velocity measurement only. The signal from the single wire is processed through a hot-wire anemometer, linearizer, and a periodic sample and hold circuit. Details of this circuit are given in reference [3].

A 5 μs(ϵ) sample of the linearized output voltage is obtained each time a photoelectric pick up was activated (one per revolution). The time delay (τ_d) in Fig. 16, between the synchronous signal and the sample pulses, was varied to permit control of the rotor blade sampling position relative to the fixed blade rows. A sample and hold circuit was used to make the analog to digital conversion. About 700 samples were obtained using this system, and electronically smoothed with the low-pass filter. Of these, 180 samples were digitized and averaged using the calculator.

The single-sensor hot-wire technique is illustrated in Fig. 16. The sensor wire is slanted at an angle of β to the axis (radially oriented) of the wire. The stem is rotated through successive 120 deg increments. This provides three mutually orthogonal directions of the wire.

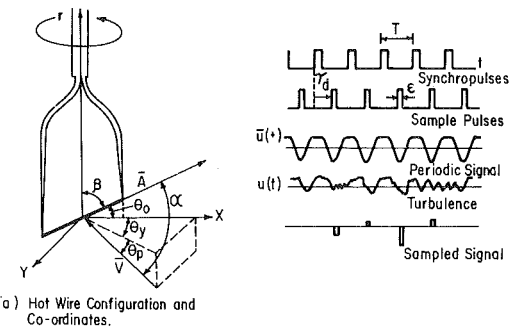

Fig. 16 Hot-wire configuration and phase-locked averaging technique (PLAT) [110, 113]

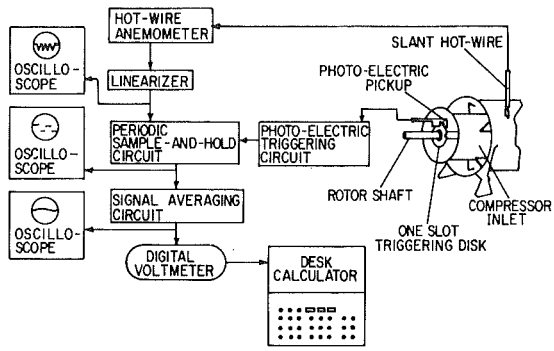

Fig. 17 Schematic diagram of instrumentation for the single-sensor technique [113]

The technique described below is a summary of the procedure outlined in references [3] and [110].

The hot-wire sensor is represented in Fig. 16 by the unit vector A slanted at the angle θ_0 to the axis; the velocity vector is denoted by $\overline{V}$. The probe coordinates y and r are fixed to the probe. The probe yaw θ_y will change by the amount of turning while the pitch angle θ_p will remain constant as the probe is rotated about its axis. The sensor yaw angle α can be expressed in terms of the angles θ_0, θ_p, and θ_y as follows.

$$\cos\alpha = \cos\theta_0 \cos\theta_p \cos\theta_y + \sin\theta_0 \sin\theta_p. \tag{23}$$

Schmidt and Okiishi [113] developed a second-order empirical correlation to express the effective cooling velocity as a function of the sensor yaw angle, pitch angle, and velocity as follows:

$$Q/U = b_0 + b_1\alpha + b_2\theta_p + b_3U + b_4\alpha^2 + b_5\theta_p{}^2 + b_6U^2 + b_7\alpha\theta_p + b_8\alpha U + b_9\theta_p U. \tag{24}$$

The coefficients b_0–b_9 were determined by a least squares fit of the effective cooling velocity data. Measurements are obtained at the flow field measurement points by positioning the hot-wire sensor at three probe angle orientations (a, b, and d). These orientations correspond to probe yaw angles of $\theta_{y,a}$, $\theta_{y,b}$, and $\theta_{y,d}$ which are

$$\theta_{y,a} = \theta_y$$

$$\theta_{y,b} = \theta_y - \tau_b$$

$$\theta_{y,d} = \theta_y - \tau_d, \tag{25}$$

where τ_b and τ_d are constant probe turning angle increments. For every wire orientation, an expression for the yaw angle α similar to equation (23) and a relationship for the effective cooling velocity similar to equation (24) can be expressed (Q_a, Q_b, Q_d). Since the effective velocities are measured values, six unknown variables (α_a, α_b, α_d, θ_p, θ_y, U) remain, and the six nonlinear equations (equations (23–24)) could be solved simultaneously by using the Newton-Raphson numerical method. With U, θ_p, and θ_y determined, the velocity vector is completely specified with respect to the probe coordinate system. The velocity vector with respect to compressor coordinates could be determined when the relationship between the probe and compressor coordinate system is known.

Whitfield, et al. [78] and Hirsch and his group [109–112] used this technique to measure the flow at the exit of a compressor rotor. Okiishi and his group [3, 113, 114] employed this technique to measure the wake production, transport, and interaction in a multistage compressor. Favier [117] recently employed this technique and a single-sensor hot film to measure the wake of a propeller blade. Lakshminarayana and Davino [115] oriented the wire such that the probe axis (r in Fig. 16) is in the streamwise direction, which provides least aerodynamic interference, and measured the flow at the exit of a stator. In most cases, $\beta = 57.3$ deg., $\tau_a = \tau_b = 120$ deg.

One major advantage of this method compared to a three-sensor hot-wire technique is simplicity. Only a single calibration needs to be performed, and the wire replacement is simple. Major disadvantages of this technique are: (1) greater time is required to perform the experiment; (2) turbulence measurements are not accurate; and (3) the technique is not suitable for measurements inside a rotor passage.

Kool [118] recently extended the single-wire technique to include the measurement of turbulence intensity and stress. The technique is based on the linearized hot-wire response relating the fluctuating voltage to the fluctuating velocity component (in tensor form),

$$e_k = A_i u_i. \tag{26}$$

Summation is implied in this equation. For example,

$$\overline{e_a{}^2} = A_1{}^2\,\overline{u_1{}^2} + A_2{}^2\,\overline{u_2{}^2} + A_3{}^2\,\overline{u_3{}^2} + 2A_1A_2\,\overline{u_1u_2} + 2A_1A_3\,\overline{u_1u_3} + 2A_2A_3\,\overline{u_2u_3} \tag{27}$$

This equation has six terms and contains both the intensity and stress components. By employing six wire orientations, it is possible to find six components of stresses. Six orientations, and the associated complexity and data handling, as well as large yaw and pitch angle errors in coefficients (A_i, A_j) in equation (27), makes this technique much less attractive than a three-sensor hot-wire technique, where the stresses and intensities are derived from simultaneous measurement of the fluctuating voltages of the wire.

Errors in Hot-Wire Measurements. In the case of measurements with a three-sensor hot-wire probe, the following sources of errors may occur: (1) inclination of the wire to the flow streamline (deviation from the Cosine Law), (2) geometry of prongs and probe body (inviscid flow and heat transfer effects), (3) finite distances between wires (spatial resolution of the probe), (4) finite dimensions of individual wires (ℓ/d, end effect, spatial resolution, etc.), (5) temporal resolution or thermal inertia of the wires, (6) aging, oxidation and contamination of the wires, (7) ambient temperature drift, (8) proximity of wire to the wall, (9) probe body vibration due to rotation and flow-induced excitation, (10) spurious signals from the power line (60 Hz) and blade-passing frequency, (11) finite sampling time, (12) measurement of wire angles with respect to the reference coordinate system, and (13) mis-alignment of the probe with respect to the reference axis.

Errors (1, 7) and (8) are eliminated by using correction factors from available hot-wire literature and calibration in a wind tunnel. The probe and sensor errors (2–6) are minimized by proper selection of the probe dimensions, support needles, and sensors. Error (9) is eliminated by proper clamping, and error (10) is minimized by reducing the number of ground loops to a minimum. Error (11) is inherent and can only be reduced by increasing the sampling time. Errors (12) and (13) depend on the accuracy of the angle-measuring equipment and aligning devices, respectively.

A detailed discussion of the methods of estimating and minimizing the above-mentioned errors, and methods of correcting the data are described in Anand and Lakshminaryaana [84, 85]. Most of the important errors have been incorporated in the rotating three-sensor hot wire [88] and the stationary three-sensor hot-wire [29] data reduction computer programs. A brief discussion of many of these errors are given in earlier sections.

Pressure Probes for Pressure and Velocity Field

The pitot probe, conceived in 1732, still remains one of the simplest and most widely used instruments for measuring pressure. There is an extensive amount of literature as well as several good reviews on pressure probes. Hence, this section will be confined to the application aspects of pressure probes in the measurement of rotor flow and pressure fields. An excellent review of various pressure probes employed for the steady flow measurement is given by Chue [119]. High-response probe techniques for unsteady flow are reviewed by Weyer in reference [12] and Carta and O'Brien in reference [18]. Specific application of pressure probes to turbomachinery are reviewed by Fleeger and Seyb, and Sieverding, et al. [12]. The review covered in this section is designed to compliment the earlier reviews [12, 119, 120] on this topic. The techniques employed for the rotor flow measurement can generally be classified as: (1) rotating pressure probes for rotor passage and exit flow, and (2) stationary high-response pressure probes for exit flow.

The probes available for flow measurement in incompressible as well as compressible flow can be classified as:

1 *Impact or Pitot Tube.* This is used for measuring the stagnation pressure and usually has a wedge, spherical, or flat nose. The Kiel probe is ideally suited for total pressure measurements in situations where the exit flow direction is unknown.

2 *Static Pressure Measurement.* The wall piezometer or an orifice is used for surface pressure measurements. The probes employed for static pressure measurements in the flow are: Prandtl probe, knife edge, wedge, and conical probes. A spherical stagnation-static pressure probe insensitive to the flow direction was developed and used in reference [28]. Details are given in reference [121].

3 *Dynamic Pressure Measurements.* Prandtl tube, conical, and cantilever probes.

4 *Flow Direction and Vector Velocity Measurement.* The claw probe, wedge probe, conrad yaw meter, and cobra probe are widely used in two-dimensional flows. The five-hole pressure probe, prism probe, conical probe, and spherical probe are employed for three-dimensional flow measurement. A thin disk probe [27, 121] is suitable for measurement of two-dimensional flow within a boundary layer.

Detailed discussion of most of these probes, including constructional features, calibration procedure, limitations, and effects of Reynolds number and Mach number are described in detail in reference [119]. Sieverding, et al. and Fleeger and Seyb [12] provide details on the probes used in turbomachinery research.

Some of the errors involved in these measurements are as follows: (1) effects of Reynolds number and Mach number, (2) effects of velocity and pressure gradients, (3) effect of turbulence, (4) effects of probe interference, blockage, and size, (5) effects of yaw and pitch angles, and (6) effects of wall interference and nose shape. Many of these errors have been investigated thoroughly. A detailed account of these errors and methods of incorporating them in the data analysis are given in reference [119].

Any of these probes can be employed in the rotor frame of reference, where the flow is steady. For absolute flow, which is unsteady, these probes have to be employed in combination with a high-frequency response pressure transducer. Both techniques are described below.

Rotating Pressure Probes for Rotor Passage and Exit Flow. In this technique, a pressure probe (pitot, claw, five-hole probe, etc.) is rotated inside the passage, traversed across the passage using mechanisms described in the section on the "Rotating-Probe Traverse Mechanisms." The data are transmitted through a PTD or a rotating transducer or slip ring unit using one of the systems described in the section on "Rotor Flow Data Transmission System."

Some of the earlier applications of this technique are described in references [20–24, 33–35, 44] and [47]. Most of these investigations were concerned with the stagnation pressure measurements at the exit of a rotor blade row. Flow losses were calculated from these data. Klein [35] compared the measurements from rotating and stationary probes.

Shnee, et al. [21] utilized the probe traversing mechanism shown in Fig.1 and evaluated the performance and losses in a turbine rotor. Ushakov, et al. [24] measured the pressure field in an axial-flow fan

rotor. Dring and Joslyn [41] rotated a Kiel probe utilizing a traversing mechanism and derived loss contours at the exit of a turbine blade row. Larguier and Sievers [42] utilized total and static pressure probes in combination with the traversing mechanism shown in Fig. 5 and reported some discrepancy between these measurements and those from a stationary hot-wire probe.

Lakshminarayana [52] rotated a pitot probe and measured the blade static and flow static pressures to derive the total velocity distribution at various chordwise and radial positions inside an axial-flow inducer passage operating at 450 rpm.

In many situations, the flow can be considered as two-dimensional. For example, the velocity vector inside the blade boundary layer is nearly parallel to the surface. Hence, only the pitch angle needs to be measured. Lakshminarayana, et al. [122] used a boundary-layer pitot probe and a yaw probe to measure the chordwise and the radial velocity profiles inside the boundary layer of a rotor blade. The effect of rotation on the structure of boundary layer was studied. Anand and Lakshminarayana [27] employed a thin disk probe of 6.34 mm dia and 1.59 mm thickness to measure the rotor blade boundary layer and showed good agreement between the experimental and the predicted values of the boundary-layer parameters. Gallus, et al. [39] utilized a truncated cone type three-hole probe to measure the exit flow at the mid-radius (where the flow is nearly two-dimensional) of a compressor rotor at 9500 rpm. The traverse mechanism shown in Fig. 4 was utilized for traversing the probe. The results were corrected for spatial errors, as the distance between the outer holes of the probe was appreciable compared to the wake width. Murakami, et al. [32] also employed a three-hole probe to measure the flow field inside a centrifugal pump impeller.

The flow in most rotors is three-dimensional; hence, the most useful probe for the rotor flow measurement is a five-hole probe. In supersonic flow, the conical probe is desirable because of its analytical advantage. The prism type and the hemispherical type are suitable for subsonic flow. References [121] and [123–127] contain the basic information on five-hole probes. The procedure and data reported by Sitaram, et al. [121] represent the latest on three-dimensional flow measurements techniques for rotors using the conventional probes.

A five-hole probe is shown schematically in Fig. 18. Sitaram, et al. [121] utilized the traverse mechanism shown in Fig. 2, and the PTD-Transducer-Scanivalve combination shown in Fig. 7, and measured the five pressure (P_1, P_2, P_3, P_4, P_5). The calibration curves are of the form shown in Fig. 2 of reference [121]. Pressures are related to yaw and pitch angles through the relationships (Fig. 18):

$$(C_p)_{\text{total}} = (P_1 - P)/D = f_1(\alpha, \beta)$$

$$(C_p)_{\text{static}} = (P_1 - p)/D = f_2(\alpha, \beta)$$

$$(C_p)_{\text{yaw}} = (P_2 - P_3)/D = f_3(\alpha, \beta)$$

$$(C_p)_{\text{pitch}} = (P_4 - P_5)/D = f_4(\alpha, \beta), \qquad (28)$$

where $D = P_1 - \overline{P}$, and $\overline{P} = (P_2 + P_3 + P_4 + P_5)/4$.

The calibration curves provide these relationships. These equations are iteratively solved from the measured values of P_1, P_2, P_3, P_4, and P_5 to derive the values of P, p, α, and β. These properties provide all the information on the flow field. It should be cautioned here that the five-hole probe is sensitive to the Reynolds number, wall vicinity, blockage, and turbulence effects. Bennett [127] carried out an analysis to determine the effects of velocity fluctuations on mean pressure measurements for a hemispherical probe. The analysis indicates, for example, that with 10 percent in streamwise turbulence intensity, the errors in yaw and pitch angles are 2 and 0.2 deg, respectively, and the error in stagnation pressure is 3.5 percent. Sitaram, et al. [121] investigated the wall vicinity and Reynolds number effects. Furthermore, it is essential to apply the centrifugal force correction, as implied by equations (1) and (2), allowing for difference in the radial location of holes 1–5 in Fig. 18. Typical data derived from a rotating five-hole probe inside a compressor rotor passage, near the end wall, are shown in Fig. 5 of reference [121]. This clearly indicates the extent of three-dimensionality and the blade boundary layer. Johnson and Moore [31] also used a five-hole probe and carried out extensive flow

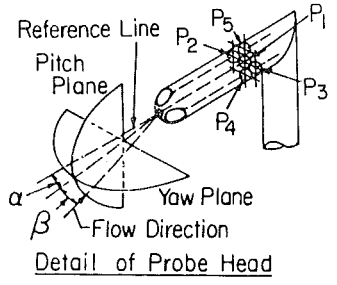

Fig. 18 Five-hole pressure probe

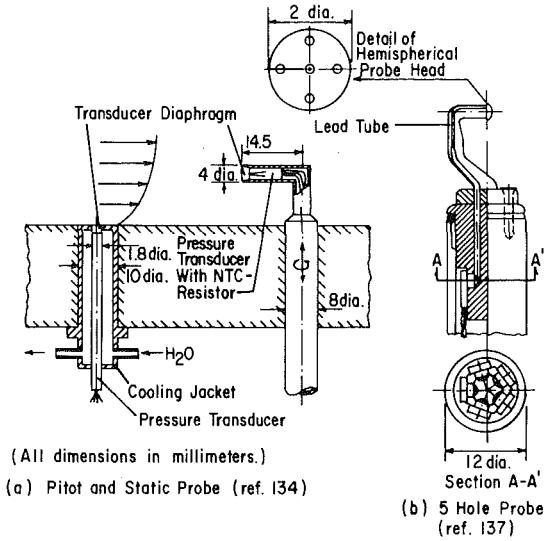

Fig. 19 Fast-response static, pitot, and five-hole probes

measurement in a centrifugal impeller passage. Dring [128] measured the wake of a compressor rotor blade using this technique.

Ravindranath and Lakshminarayana [28] developed a spherical static-stagnation pressure probe, which is insensitive to angle changes. They utilized the traverse mechanism shown in Fig. 2 to measure the static pressure and total velocity across a rotor wake and showed good agreement between this and the rotating hot-wire measurements. Further details on this probe, including calibration techniques, error evaluations are discussed in reference [121]. A comparison between a spherical static pressure probe, which is insensitive to yaw and pitch angles, and the conical, wedge, and Prandtl probes is given in reference [129]. A theoretical analysis of some of these angle-insensitive probes is carried out by Smith and Bauer [130].

When measurements are carried out in a wake or a boundary layer, it is essential to include the effect of pressure and velocity gradients [131].

Stationary High-Response Pressure Probes for Rotor Exit Flow. The velocity and pressure at the rotor exit are unsteady, with both periodic and random components. Many of the early attempts were aimed at the measurement of time-average pressures (e.g., [132]). There have been several attempts in recent years to develop high-response pressure probes for the measurement of unsteady flow at the exit of a rotor [4, 5, 11, 12, 14, 38, 133–138]. Weyer [12] and McNally [14] reviewed the state-of-the-art of these techniques as of 1977. Hence, the following review covers only those techniques that are recent, and that cover both the velocity and the pressure measurements at the exit.

Earlier techniques, concerned with the instantaneous stagnation and static pressure measurements, were developed by Eckhardt [135] and Weyer [4, 133]. Eckhardt measured the instantaneous total velocity and pressure at the exit of a centrifugal compressor operating at 27,000 rpm. His probe is shown schematically in Fig. 19. The frequency response and the maximum operating range were 120 kHz and 80°C, respectively. With the probe mounted on a compressor casing, the velocity and pressure contours derived from this probe confirmed the existence of the jet-wake type of flow structure at the exit. Ker-

rebrock, et al. [5] and Shreeve, et al. [136] developed probes for measuring the yaw angle, static pressure and stagnation pressure at the exit of a transonic compressor.

High-frequency response five-hole probes are most useful in turbomachinery rotor flow measurement. One of the earlier probes was built by Castorph and Raabe [134]. Matsunaga, et al. [137] and Kerrebrock, et al. [138] have built similar probes. Castorph and Raabe used a probe similar to a six-hole conrad tube and utilized six micropressure transducers (kulite with a natural frequency of 60 KHz) mounted inside each of the six tubes. The nose of the probe was a hemispherical shape. Four of these pressure-transducer channels were meant for the velocity vector determination (yaw and pitch angle), and one each for stagnation and static pressures. The pressure transducer had a diaphragm of stainless steel and a full bridge at the back. The probe (8 mm) was used to measure the exit flow in a water turbine of Kaplan type with a 612 mm tip dia runner.

Matsunaga, et al.'s [137] probe construction is shown in Fig. 19. The diameter of the spherical head is 2.00 mm and has five holes of 0.2 mm dia, each making an angle of 37 deg with the center hole. The five pressure lead tubes are individually connected to a small semi-conductor pressure transducer with a frequency response of 100 KHz. The lead tube is made as short as possible for fast response and is filled with 20×10^{-6} m^2/s silicon oil as the damper to eliminate the peak resonance. The probe was used at the exit of a mixed flow pump. The frequency response of the entire system was evaluated using a water vessel and hydrophone. The gain was near unity up to 500 Hz and the phase angle was constant up to 200 Hz, the differences between the five-probe cavity systems being very small. For a five-hole probe in unsteady flow, the pressure coefficient (equation (28)) may be written as

$$C_p = C_p' + C_p'' \tag{29}$$

where C_p' is the steady term and C_p'' is the unsteady term. The former is identical to those defined in equation (28). Matsunaga, et al. made use of the steady-state calibration curves and adopted an iterative technique to calculate C_p''.

Kerrebrock, et al.'s probe [138] probably has the best frequency response, but the probe is much larger (5 mm) than Matsunaga, et al.'s. The spherical probe has surface-mounted silicon pressure sensors with an overall frequency response of 30 KHz. It has been used at the exit of the MIT blowdown compressor facility [5] to measure the pitch and yaw angles, Mach number, and stagnation pressure.

Blade Surface Measurements

The aerodynamic properties near or at the blade surface that are of interest are: (1) qualitative nature of transition and separation, and quantitative measurement of limiting streamline angle, usually derived from a flow visualization experiment, (2) steady and unsteady blade static pressures, (3) wall shear stress, (4) skin temperature, and (5) strain. The last two properties have been covered by Graham [19] and Carta and O'Brien [18], respectively. Techniques for the measurement of items (1–3) are described below.

Flow Visualization. Some of the important parameters and characteristics of the three dimensional boundary layer on a rotor blade are: the limiting streamline angle (ϵ), which is the angle between the external streamline, and the limiting streamline, which is the limiting position of the streamline as the surface of the blade is approached, transition, and separation. Since any intrusive probe would alter these characteristics, flow visualization is the only means by which they can be measured. Many of the visualization techniques, which are useful for a stationary body, cannot be adopted for rotor flows. Hence, the rotor aerodynamicist has a limited choice of flow visualization techniques.

The ammonia technique is useful for the measurement of the limiting streamline angle. Johnston [139] used this technique for a centrifugal impeller blade, and Lakshminarayana, et al. [122] made extensive use of it to determine the limiting streamline angle on an inducer type of blading [27, 52, 82, 83, 85]. Recently Dring and Joslyn [41] employed this technique for a turbine rotor blade. In this application, extremely small amounts of ammonia gas is injected through very small holes (static pressure holes if available), and allowed to react with a sheet of ozalid paper pasted immediately downstream of the injection hole. The ammonia gas is injected during rotation through an ammonia transfer device [122], and reacts with the ozalid paper to form streaks or streamlines. The angle of this streamline represents the limiting streamline angle.

The smoke visualization method, useful only at very low speeds, has been widely explored by Lakshminarayana [140]. The most suitable smoke is the one generated by titanium tetrachloride and carbon tetrachloride (both are toxic). The liquid is smeared on the surface and the rotor set in motion. With suitable arrangement of a stroboscope and a camera, the flow is visualized not only near the blade surface (including the detection of transition, laminar, and turbulent regions), but also in the passage. This technique is also suitable for the limiting streamline angle measurement.

Bomelburg, et al. [141] utilized a series of electric sparks at high frequency to visualize the flow near the trailing edge of a rotor blade. This principle is based on the ionization of the gas in the spark gap.

As regards the detection of the transition zone, Lakshminarayana, et al. [122] found the sublimation technique developed by Richards and Burstall [142] to be most suitable. Larguier and Sievers [143] used a similar method. Surface-mounted hot films and pressure transducers can also be used for detecting the transition region. These techniques are described later.

Blade Static Pressure. The steady blade static pressures are measured using the rotor-flow data transmission systems described earlier. A scanivalve system or multi-channel PTD or rotating transducer is employed for the data transmission. The centrifugal force correction is applied using equation (1) and (2). Rotor blade static pressure measurements are reported in references [20, 26, 27, 41] and [44–54].

The unsteady blade static pressure measurements are crucial to the development of the theoretical approaches to the problems of aeroelastic flutter and flow-induced noise. Several attempts have been made to measure the unsteady pressure distribution on a stator or cascade blade [144–146].

One of the earlier attempts to measure the unsteady total lift and moment on a rotor blade is due to Bruce [8], who utilized a strain gage sensor and a floating blade element near the mid-radius. The measurements are reported by Bruce and Henderson [144]. Hanson, Peacock and Overli, Saxton, et al. [144] reported unsteady static pressure measurements on a rotor blade. Earlier measurements were carried out by Carroll [7], O'Brien, et al. [9], and Heller and Widnall [60]. Carroll and Hanson utilized strain gage pressure transducers in flat configuration. Heller and Widnall used a piezoelectric and film type capacitance transducer.

Englund, et al. [147] and Grant and Lanati [148] carried out a systematic study of the techniques for rotor blade unsteady pressure measurements and developed a system capable of surviving gas turbine engine operating conditions, which include high centripetal acceleration. They tested different configurations, and one of these is shown in Fig. 20. Parameter ranges covered by this work include oscillatory pressure amplitudes as low as 1 kPa, absolute pressure to 310 kPa, temperature to 150°C, static strain to 1680 microstrain, oscillatory strain to ±1000 microstrain, centripetal acceleration to 90,000 g, and oscillatory normal acceleration to 650 g. The blade-mounted transducers tested were the miniature semi-conductor strain gauge type with natural frequencies above 100 kHz. The diaphragm sensing area was one millimeter in diameter.

The unsteady pressure signals can be transmitted either through a slip-ring unit or a telemetry system described in the section on the "Rotor Flow Data Transmission System." Hanson [144] used a slip ring unit, while O'Brien et al. [9], Saxton et al. [144], and Heller and Widnal [60] utilized telemetry systems.

Wall Shear Stress. A knowledge of the wall shear stress is essential in understanding the characteristics of the three-dimensional boundary layer on a rotor blade and losses in turbomachinery. An excellent review of various techniques applicable to a stationary body is given by Winter [149]. Techniques available for direct shear-stress

measurements are almost impossible to implement on a rotor. The techniques based on the Preston tube [150] and the heated element [151] seem to be most attractive for the rotor blade shear-stress measurement.

The Preston tube technique is based on the existence of the law of the wall near the surface. A thin pitot probe (say, 1 mm o.d.) is placed on the surface such that the tube is in the direction of flow. The stagnation pressure from this tube as well as the static pressure on the surface is measured to derive the wall shear stress (τ_w) from the following equation,

$$\frac{(\Delta P)d^2}{\rho U^2} = F\left(\frac{\tau_w d^2}{\rho \nu^2}\right), \tag{30}$$

where d is the outside diameter of the pitot tube, and ΔP is the difference between the stagnation pressure measured by the Preston tube and the wall static pressure. The function F can be generated by either the calibration of the probe or by the use of the law of the wall and wake. Lakshminarayana, et al. [52, 83, 122] and Anand and Lakshminarayana [27, 85] made extensive use of this technique and measured the wall shear stress on a rotor blade. A skin-friction stress correlation [27, 122] which includes the effect of rotation was also developed.

Even though the relationship between the local skin-friction coefficient and the heat transfer from the wires embedded on a surface was long known, the first practical instrument using the analogy between the skin-friction stress and the heat transfer was designed by

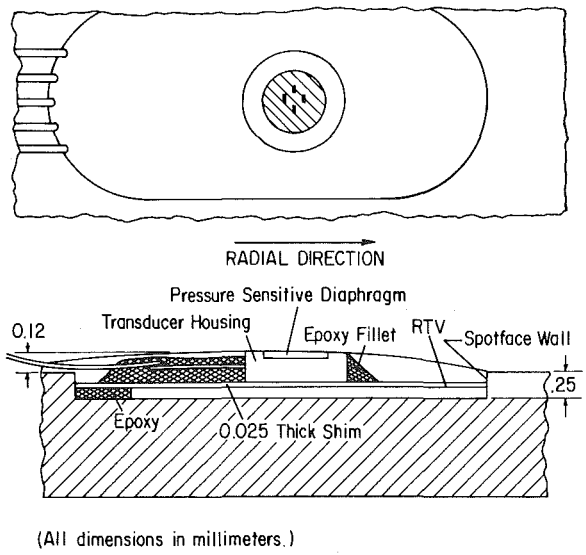

Fig. 20 Transducer mounting configuration for unsteady blade pressures [147, 148]

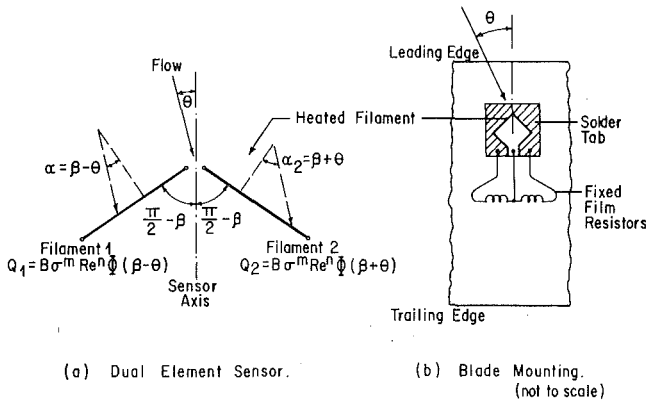

Fig. 21 Geometry and mounting configuration of the wall shear-stress gauge

Ludwieg [151]. He developed the following empirical correlation,

$$\frac{Q\ell}{K(\Delta T)} = 0.807\frac{(\ell^2\rho\sigma\tau_w)^{1/3}}{\mu^2}, \tag{31}$$

where Q = heat transfer per unit area; k = thermal conductivity of the fluid; ΔT = temperature difference between the heated element of length l and the unheated surface; σ = Prandtl number; and μ = viscosity. McCroskey and Durbin [152] extended this technique for the measurement of the flow angle and the shear stress on the surface of a helicopter rotor blade. Their sensor consisted of two nickel film gauges on a thin (0.025 mm thick) plastic, which is glued to a surface, thus producing very little flow disturbance. The sensor configuration is shown in Fig. 21. The gauges were 5.6 mm long, 0.05 mm wide, and 0.005 mm thick, made of pure nickel foil and arranged in a mutually perpendicular layout. The resistance of each wire was 4Ω. They developed a double-bridge constant temperature feedback system using a differential power input to measure the sum ($Q_1 + Q_2$) and difference ($Q_1 - Q_2$) of the convective heat transfer rates (Q) of these wires accurately. The heat transfer rate is proportional to electric power; hence, equation (31) can be expressed in the form

$$\frac{I^2R}{\Delta T} = a + b(\tau_w)^{1/3}, \tag{32}$$

where I = current; R = resistance; and a and b are calibration constants. The calibration constants were determined from measurements in a known flow. This calibration data were utilized to derive the values of shear stress by measuring the voltage or current across the bridge.

In can also be proved that [152]

$$\frac{Q_1 - Q_2}{Q_1 + Q_2} = K\theta,$$

where K is a constant. This principle was utilized in evaluating the flow angle (limiting streamline angle) on the rotor blade surface. Six stress gauges were mounted on a helicopter blade, at various chordwise locations, to determine the flow angle and the wall shear stress [153].

The shear stress gauge employed by Murthy and Rose [154] can be manufactured easily and the signal from the gauge can be processed using commercially available constant-temperature anemometers. This device is difficult to use on a rotor blade.

Data Processing

The turbojet test cells and turbomachinery test and research facilities involve the acquisition and processing of a large amount of data. Thus, the data management is now an integral part of any research or test program. The on-line data acquisition, processing, analysis, display, and management systems vary depending on the complexity of the system, type of data acquired, and whether it is a research or a test facility.

It is not the intention of the author to cover all aspects of data processing in this section, but to highlight one such system in use for turbomachinery research in the Department of Aerospace Engineering at The Pennsylvania State University. The system, shown in Fig. 22, consists of a seven-channel tape recorder, Hewlett Packard HP 2100 S Computer system, a digital plotter and printer, graphic display equipment, and a remote terminal to the IBM 370/3033 computer at the University. The method of interfacing this data processing system with the instrumentation and data acquisition system at the Turbomachinery Laboratory is shown in Fig. 12. The data processing system has the main computer with 32 K words memory size, two memory disks, a magnetic tape unit to store the experimental data, and an ADC unit. This system is presently used in processing the stationary three-sensor hot-wire data using the phase-locked ensemble averaging technique, explained in an earlier section. Plans are underway to expand this capability to include on-line processing of all the rotating hot-wire, five-hole probe, and stationary probe data, including the computation of turbulent quantities such as intensity, correlation, spectrum, length scale, etc.

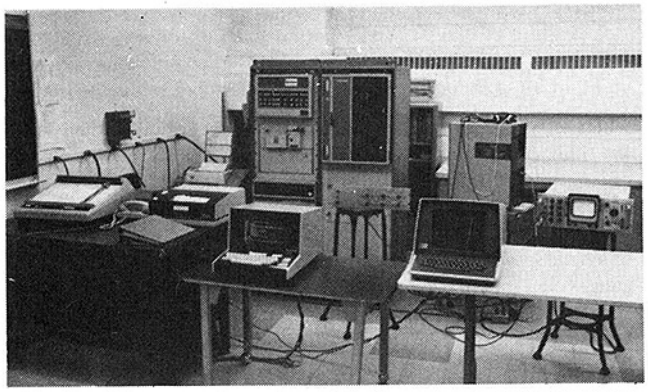

Fig. 22 Data processing system at The Pennsylvania State University

Concluding Remarks

It is evident from this review that rotor flow measurement techniques have reached a high level of sophistication. Extensive use of these techniques, not only in the research environment but also in actual engine and component testing, can be anticipated during the next decade. The ever-increasing demand for accurate data on all aspects of the rotor flow, by computer code developers as well as turbomachinery aerodynamicists and designers, will be met by the conventional probe and hot-wire techniques described in this paper and optical methods covered in Weyer's review [17].

The rotating-probe measurements are suitable for low- and moderate-speed turbomachinery, while the stationary fast response probes (hot-wire and pressure probes) can be employed in low- as well as high-speed turbomachinery.

Increased use of hot-wire probes, blade pressure transducers, and telemetry systems will provide the urgently needed basic information on the steady and unsteady flow through a blade passage, including blade boundary layer, wakes, hub and annulus wall boundary layers, shock configuration, leakage, and secondary flows.

Acknowledgments

The author wishes to acknowledge the support for his research by the National Aeronautics and Space Administration during the last 15 years (Grants NGL 39-009-007, NsG 3012, NsG 3032) during which many of the techniques described in this paper were developed. Part of the research was supported by the Applied Research Laboratory (ARL). Participation by the author's many former and present graduate students was valuable in the development of these measurement techniques. G. Gurney and ARL provided much needed assistance in the design and manufacture of some of Penn State's hardware (Figs. 3 and 8) described in this paper.

References

1 Wisler, D. C., and Mossey, P. W., "Gas Velocity Measurement Within a Compressor Rotor Passage Using the Laser Doppler Velocimeter," ASME JOURNAL OF ENGINEERING FOR POWER, Vol. 95, Apr 1973, p. 91.

2 Lakshminarayana, B., and Poncet, A., "A Method of Measuring Three-Dimensional Wakes in Turbomachinery," ASME *Journal of Fluids Engineering,* Vol. 96, No. 2, June 1974, pp. 87–91.

3 Okiishi, T., and Schmidt, D. P., "Measurement of the Periodic Variation of Turbomachine Flow Fields," *Proceedings of Dynamic Flow Conference,* edited by E. W. Hansen, 1979, pp. 249–270.

4 Weyer, H., "Determination of Time Weighted Average Pressures in Strongly Fluctuating Flow, Especially in Turbomachines," *Deutsche Forschungs und Versuchsanstalt fur Luft and Raumfahrt,* Report DLR-FG 74-34 (Technical Translation by European Space Research Organization ESRO TT-161, 1974).

5 Kerrebrock, J. L., Epstein, A., Haines, D., and Thompkins, W., "The M.I.T. Blowdown Compressor Facility," ASME JOURNAL OF ENGINEERING FOR POWER, Vol. 96, No. 4, 1974, pp. 394–405.

6 Gorton, C. A., and Lakshminarayana, B., "A Method of Measuring Three Dimensional Mean Flow and Turbulence Characteristics Inside a Rotating Turbomachinery Passage," ASME JOURNAL OF ENGINEERING FOR POWER, Vol. 98, No. 2, 1976, pp. 137–146.

7 Carrol. J. T., "Dynamic Flow Studies by Application of Pressure and Velocity Sensors on Axial Flow Fan Blades," in *Instrumentation for Air Breathing Propulsion,* edited by A. E. Fuhs and M. Kingery, AIAA Series on Progress in Aeronautics, Vol. 34, M.I.T. Press, 1974, pp. 115–130.

8 Bruce, E. P., "ARL Axial Flow Research Fan—A new Facility for Investigation of Time Dependent Turbomachinery Flows," ASME Paper No. 74-FE-27, 1974.

9 O'Brien, W., et al., "A Multi-Channel Telemetry System for Flow Research on Turbomachines," ASME Paper No. 74-GT-112, 1974.

10 Lesco, D. J., et al., "Rotating Shaft Mounted Microelectronic Data System," NASA TN D 5678, 1970.

11 Fuhs, A., and Kingery, M., (Eds), *Instrumentation for Air Breathing Propulsion,* AIAA series on Progress in Aeronautics, Vol. 34, M.I.T. Press, 1974.

12 Pianko, M. (Ed.) "Modern Methods of Testing Rotating Components of Turbomachines (instrumentation)," AGARD-AG-207, 1975.

13 AGARD, "Laser Optical Measurement Methods for Aero Engine Research and Development," AGARD-LS-90, 1977.

14 McNally, W. D., "Review of Experimental Work on Transonic Flow in Turbomachinery," *Transonic Problems in Turbomachinery,* editors, T. C. Adamson, M. F. Platzer, Hemisphere Publishing, New York, 1977, pp. 457–484.

15 Hansen, E. W. (Ed.), "Dynamic Measurements in Unsteady Flows," *Proceedings of the Dynamic Flow Symposium,* Baltimore, 1979.

16 Richards, B. E. (Ed.), *Measurement of Unsteady Fluid Dynamic Phenomena,* Hemisphere Publishing, New York, 1977.

17 Weyer, H., "Optical Methods of Flow Measurement and Visualization in Rotors," *Proceedings of the Symposium on Measurement Methods in Rotating Components of Turbomachinery,* Edited by B. Lakshminarayana and P. Runstadler, ASME, New York, 1980, pp. 99–110.

18 Carta, F., and O'Brien, R. L., "Unsteady Aerodynamic Measurement Techniques for Turbomachinery Research," *Proceedings of the Symposium on Measurement Methods in Rotating Components of Turbomachinery,* Edited by B. Lakshminarayana and P. Runstadler, ASME, 1980, p. 177–185.

19 Graham, R., "Impact of New Instrumentation on Advanced Turbine Research," *Proceedings of the Symposium on Measurement Methods in Rotating Components of Turbomachines,* Edited by B. Lakshminarayana and P. Runstadler, ASME, 1980, p. 289–302.

20 Weske, J. R., "An Investigation of the Areodynamic Characteristics of a Rotating Axial Flow Blade Grid," NACA TN 1182, 1947.

21 Shnee, Ya. I., Ponomarev, V. N., and Bondarenko, G. A., "Investigation of a Turbine Stage With the Aid of a Rotating Pitot Probe," *Teploenergitika,* Vol. 18, No. 5, 1971, pp. 83–85 (English Translation in *Thermal Engineering,* Feb. 1972, p. 121).

22 Dovzhik, S. A., and Ginevskii, A. S., *Promshlennaya Aerodynamika,* Vol. 20, 1961.

23 Somoilovich, G. S., and Pislmin, I. N., *Proceedings of the Moscow Power Institute, Power Machinery Construction Section,* 12d-vO, MEI, 1967.

24 Ushakov, K. A., et al., "Investigation Into the Annular Cascade of the Rotating Impeller of an Axial Flow Fan," *Promyshlennaya Aerodynamika,* Sb No. 10, 1958, pp. 43–60 (Translated by British DSIR, Russian Translation Program-RTS-No. 1080, 1960).

25 Ufer, H., "On the Influence of the Rotor Clearance on the Exit Velocity Field of a Rotating Axial Flow Turbomachinery Blade Row," Dr. Ing. Thesis, Faculty of Maschinenwesen, Technical University of Berlin, 1968.

26 Lakshminarayana, B., "An Axial Flow Compressor Facility with Instrumentation for Relative Flow Measurement," *Proceedings of the Symposium on Measurement Methods in Rotating Components of Turbomachinery,* ASME, 1980, p. 31–41 (to be published in *Journal of Fluids Engineering*)

27 Anand, A. K., and Lakshminarayana, B., "Three Dimensional Turbulent Boundary Layers in a Rotating Helical Channel," ASME *Journal of Fluids Engineering,* Vol. 97, No. 2, 1975, pp. 197–210.

28 Ravindranath, A., and Lakshminarayana, B., "Mean Velocity and Decay Characteristics of the Near and Far Wake of a Compressor Blade of Moderate Loading," ASME JOURNAL OF ENGINEERING FOR POWER, Vol. 102, No. 3 1980 pp. 535–548.

29 Raj, R., and Lakshminarayana, B., "On the Investigation of Cascade and Turbomachinery Rotor Wake," NASA CR 134680, Feb. 1975.

30 Reynolds, B., Lakshminarayana, B., and Ravindranath, A., "Characteristics of the Near Wake of a Compressor Rotor," *AIAA Journal,* Vol. 17, No. 9, Sept. 1979, pp. 959–967.

31 Johnson, M. W., and Moore, J., "The Development of a Wake Flow in a Centrifugal Impeller," ASME JOURNAL OF ENGINEERING FOR POWER, Vol. 102, No. 2, 1980 pp. 382–390.

32 Murakami, M., et al., "Velocity and Pressure Distributions in the Impeller Passages of Centrifugal Pumps," *Proceedings of the Symposium on Measurement Methods in Rotating Components of Turbomachinery,* ASME, 1980, pp. 81–90.

33 Muhlemann, E., "Experimental Studies in Axial Blower Stage," Mitteilungen Institute Aerodynamik der Eidgen. Techn. Hochschule. Zurich, No. 12, 1946.

34 Muesmann, G., "Relation of the Flow Properties of the Rotor of an Axial Blower with Those of a Single Blade," *Zeitschrift fuer Flugwiss,* Vol. 6, No. 12, 1958, pp. 345–362 (also see Bericht, 57/A/36, 57/A/31, and 57/A/21 of the *Aerodynamische Versuchsanstalt,* AVA, Gottingen, 1957).

35 Klein, A., "Comparative Measurement Behind a Compressor Rotor with a Space Bound and Corotating Cylindrical Probes," *Forschung in Ingenieurwesen,* Vol. 40, No. 1, 1974, pp. 25–34 (English translation in NASA TT-F-15833, 1974).

36 Gallus, H. E., Private communication, 1979.

37 Gallus, H. E., Lambertz, J., and Wallmann, Th., "Experimentalle

Untersuchung der Relativstromung in Laufrad Einer Axial Verdichterstufe," *Forschungsbericht des Landes,* NRW No. 2711, 1978, Verlag G.M.B.H. (West Germany), Leverkusen-Opladen.

38 Gallus, H. E., "Results of the Measurement of the Unsteady Flow in Axial Subsonic and Supersonic Stages," AGARD CP 177, Sept. 1975, pp. 10-1 to 10-17.

39 Gallus, H. E., Lambertz, J., and Wallman, Th., "Blade Row Interaction in an Axial Flow Subsonic Compressor Stage," ASME JOURNAL OF ENGINEERING FOR POWER, Vol. 102, No. 1, 1980, pp. 169–177.

40 Dring, R. P., Private communication, 1979.

41 Dring, R. P. and Joslyn, H. D., "Measurements of Turbine Rotor Blade Flows," ASME JOURNAL OF ENGINEERING FOR POWER, this issue, pp. 400–405.

42 Larguier, R., and Sievers, A., "Unsteady Flow Measurements in Turbomachines," ONERA (France) Report T.P. No. 1975-107E.

43 Tombult, W., "Electronic Indication of the Position for Rotating Measuring Probes," *Wissenschaftliche Gessellschaft fur Luft-und Raumfahrt,* WGLR Report No. 1, 1963, Aachen (English Translation NASA TTF-11096).

44 Runkel, J. F. and Davey, R. S., "Pressure Distribution Measurements on the Rotating Blades of a Single Stage Compressor," NASA TN 1189, 1947.

45 Watanabe, I., Private communication, 1972.

46 Shaw, R., "The Construction and Testing of a Large Axial Flow Compressor," British ARC CP 620, 1962.

47 Pemberton, J. C. and Ellis, G. O., "Flow Measurement in Rotating Machinery," *Instruments and Control Systems,* March 1964.

48 Leist, K. and Dettmering, W., *Test Models for Measuring the Pressure Distribution on Rotating Vanes,* No. 422, Kiln and Opladen, Westdeutscher Press, 1968.

49 Leist, K., "An Experimental Arrangement for the Measurement of the Pressure Distribution on High Speed Rotating Blade Rows," ASME Paper No. 56-GTP-13, 1956.

50 Michel, D. J., et al., "Experimental Investigation of Flow in Rotating Passages of a 48 Inch Impeller at Low Speeds," NACA RM E51D20, 1951.

51 Poncet, H., Yamaoka, H., and Lakshminarayana, B., "Investigations and Analysis of Flow Phenomena of Secondary Motions in Axial Flow Inducers," NASA CR 107267, July 1970, 115 pgs.

52 Lakshminarayana, B., "Three-Dimensional Flow Field in Rocket Pump Inducers, Part 1: Measured Flow Fields Inside the Rotating Blade Passage and at the Exit," ASME *Journal of Fluids Engineering,* Vol. 95, No. 4, 1973, pp. 567–578.

53 Howells, R., and Lakshminarayana, B., "Three Dimensional Potential Flow and Effects of Blade Dihedral in Axial Flow Propeller Pumps," ASME *Journal of Fluids Engineering,* Vol. 99, No. 1, March 1977, pp. 167–175.

54 Howells, R., and Lakshminarayana, B., "Instrumentation for Measuring the Steady State Static Pressures on a Rotating Blade in the Axial Flow Research Fan," The Pennsylvania State University, Applied Research Laboratory, Technical Memorandum TM 74-201, 1974.

55 Pollack, F. G., et al., "Rotating Pressure Measurements System for Turbine Cooling Investigations," NASA TM-X-2621, 1972.

56 Liebert, C. H., and Pollack, F. G., "Flow Measurement in Base Cooling Air Passages of a Rotating Turbine Blade," NASA TN D-7697, June 1974.

57 Patterson, J. L., "A Miniature Electrical Pressure Gauge Utilizing a Stretched Flat Diaphragm," NACA TN 2659, 1952.

58 Pollock, E. G., "Temperature and Pressure Measurement Techniques for an Advanced Turbine Test Facility," *Proceedings of the Measurement Methods in Rotating Components of Turbomachinery,* ASME 1980, p. 319–326.

59 Bragg, G. M., "Manometers for Rotating Systems," *Instruments and Control Systems,* March 1969, p. 105.

60 Heller, H., and Widnall, S. E., "The Role of Fluctuating Forces in the Generation of Compressor Noise," NASA CR 2012, 1972.

61 Light, R. W., "Development of a Rotating to Stationary Data Transfer System Based on FM Telemetry," M.S. Thesis, Mech. Eng., Virginia Poly. Inst. and State Univ., August 1975.

62 Kemp, R. E., "Close Coupled Telemetry for Measurements in Gas Turbines," *Instrumentation Technology,* Sept. 1978.

63 Adler, A., and Hoeks, B., "Phase Locked Telemetry System for Rotary Instrumentation of Turbomachinery," NASA CR 15943, Acurex Final Report 78-284, Sept. 1978.

64 Lesco, D. J., et al., "On the Shaft Data Systems for Rotating Engine Components," published in reference [11], p. 131–140.

65 Adler, A., "Telemetry for Rotating Measurements on Turbomachinery," ASME *Mechanical Engineer,* Mar. 1979, pp. 30–35 (also ASME Paper 78-GT-105).

66 Donato, V., and Davis, S. P., "Radio Telemetry for Strain Measurement in Turbines," *Sound and Vibration,* Vol. 7, No. 4, April 1973, pp. 28–34.

67 Colangelo, D., and Schlerth, F., "Special Purpose Telemeter for Jet Engine Environment," *Telemetry Journal,* Feb. 1971, pp. 15–18.

68 Worthy, J. G. B., "The Design, Development and Operation of Gas Turbine Radio Telemetry System," ASME JOURNAL OF ENGINEERING FOR POWER, this issue, pp. xxx–xxx.

69 Bradshaw, P., *An Introduction to Turbulence and its Measurement,* Pergamon Press, 1971.

70 Hinze, J. O., *Turbulence,* McGraw Hill, 1975.

71 Comte-Bellot, G., "Hot Wire Anemometry," *Annual Review of Fluid Mechanics,* Vol. 8, 1976, p. 209.

72 Weske, J. R., "Measurement of Arithmetic Mean Velocity of a Pulsating Flow of High Velocity by the Hot Wire Method," NACA TN 990, 1946.

73 Fessler, T. E., and Hartmann, M. J., "Preliminary Survey of a Compressor Rotor Blade Wake and Other Phenomena with a Hot Wire Anemometer," NACA RM E56 A13, 1957.

74 Walker, G. J., and Oliver, A. R., "The Effect of Interaction Between Blade Rows in an Axial Flow Compressor on the Noise Generated by Blade Interaction," ASME JOURNAL OF ENGINEERING FOR POWER, Vol. 94, 1972, pp. 241–248.

75 Raj, R., and Lakshminarayana, B., "Characteristics of the Wake Behind a Cascade of Aerofoils," *Journal of Fluid Mechanics,* Vol. 61, Dec. 1973, pp. 707–730.

76 Railly, J. W., and Sharma, P. B., "Treatment of the Annulus Wall Boundary Layer Using Secondary Flow Hypothesis," ASME JOURNAL OF ENGINEERING FOR POWER, Vol. 98, 1976, pp. 29–36.

77 Poncet, A., and Lakshminarayana, B., "Three Dimensional Analysis and Measurement of the Flow in a Three Bladed Rocket Pump Inducer," NASA CR 72750, 1970 (reissued as NASA CR 2290 in 1973).

78 Whitfield, C. E., et al., "A Three Dimensional Analysis of Rotor Wakes," *Aero Quarterly,* Vol. 23, Part 4, 1972.

79 Ufer, H., "Analysis of the Velocity Distribution on the Blade Tips of Axial Blowers," *Technische Mitteilungen Krupp,* Vol. 26, No. 2, pp. 33/45, 1968 (technical translation as NASA TTF 16366, 1975).

80 Gerich, R., "A Study of Non-Stationary Relative Velocities at the Outlet of Francis Turbine Impeller Using Rotating Hot Film Probe," *DISA Information,* No. 19, pp. 19–25, Mar. 1976.

81 Day, W. H., "Boundary Layer Characteristics of the Buckets of a Large Scale Turbine Stage," Part 1, ASME Paper 70-GT-59, 1970.

82 Gorton, C. A., Lakshminarayana, B., "Analytical and Experimental Study of the Three-Dimensional Mean Flow and Turbulence Characteristics Inside the Passages of an Axial Flow Inducer," NASA CR 140976, 1974.

83 Lakshminarayana, B., Gorton, C. A., "Three Dimensional Flow Field in Rocket Pump Inducers—Part 2: Three Dimensional Viscid Flow Analysis and Hot Wire Data on Three Dimensional Mean Flow and Turbulence Inside the Rotor Passage," ASME *Journal of Fluids Engineering,* Vol. 99, No. 1, 1977, pp. 176–186.

84 Anand, A. K., and Lakshminarayana, B., "An Experimental Study of Three Dimensional Boundary Layers and Turbulence Characteristics Inside a Rotating Channel," ASME JOURNAL OF ENGINEERING FOR POWER, Vol. 100, No. 4, 1978, pp. 676–690.

85 Anand, A. K., and Lakshminarayana, B., "An Experimental and Theoretical Investigation of Three Dimensional Turbulent Boundary Layer Inside an Axial Flow Inducer," NASA CR 2888, 1977, pp. 1–209.

86 Hah, C., and Lakshminarayana, B., "Effect of Rotation on a Rotating Hot Wire," *Journal of Physics E.: Scientific Instruments,* Vol. 11, 1978, pp. 999–1001.

87 Lakshminarayana, B., and Reynolds B., "Turbulence Characteristics in the Near Wake of a Compressor Rotor Blade," *AIAA Journal,* Nov. 1980.

88 Ravindranath, A., "Three Dimensional Characteristics of the Wake of a Moderately Loaded Compressor Rotor Blade," M.S. Thesis, Dept. of Aerospace Engr., The Pennsylvania State University, 1979. (also: NASA CR 159518, 1980).

89 Ravindranath, A., and Lakshminarayana, B., "Structure and Decay Characteristics of Turbulence in the Near and Far Wake of a Moderately Loaded Compressor Rotor Blade," ASME Paper 80-GT-95 (to be published in the ASME JOURNAL OF ENGINEERING FOR POWER).

90 Hah, C., and Lakshminarayana, B., "Numerical Analysis of Three Dimensional Turbulent Wakes of Rotor in Axial Flow Turbomachinery," ASME *Journal of Fluids Engineering,* 1980.

91 Hah, C., and Lakshminarayana, B., "The Prediction of Two- and Three-Dimensional Asymmetric Turbulent Wakes—A Comparison of Three Turbulence Models for the Effects of Streamline Curvature and Rotation," *AIAA Journal,* Oct. 1980.

92 Gaulier, C., "Measurement of Air Velocity by Means of Triple Hot Wire Probe," *DISA Information,* No. 21, 1977, pp. 16–20.

93 Zimmerman, D. R., and Abbott, D. E., "An Experimental Investigation of Three Dimensional Turbulent Boundary Layer," ASME Paper No. 77-WA/FE-22, 1977.

94 Bendat, J. S., and Piersol, A. G., *Measurement and Analysis of Random Data,* John Wiley, New York, 1966.

95 Raj, R., and Lakshminarayana, B., "Three Dimensional Characteristics of Turbulent Wakes Behind Rotors of Axial Flow Turbomachinery," ASME JOURNAL OF ENGINEERING FOR POWER, Vol. 98, 1976, pp. 218–228.

96 Reynolds, B., and Lakshminarayana, B., "Characteristics of Lightly Loaded Fan Rotor Blade Wakes," NASA CR 3188, 1979.

97 Hah, C., "Numerical and Experimental Study of Turbulent Wakes of Turbomachinery Rotor Blade, Isolated Airfoil and Cascade," Ph.D. Thesis, Dept. of Aerospace Engr., The Pennsylvania State University, 1980.

98 Lakshminarayana, B., "Nature of Flow Distortions Caused by Rotor Wakes," *Proceedings of the NATO-AGARD Symposium on Unsteady Phenomena in Turbomachinery,* AGARD CP 177, 1976, pp. 4-1 to 4-13.

99 Lakshminarayana, B., and Reynolds, B., "Rotor Wake Data at 0°, 5°, 10° and 15° Incidence," (in preparation).

100 Reynolds, B., and Lakshminarayana, B., "Blade Loading and Spanwise Effects on the Near and Far Wake Characteristics of Compressor Rotor Blade," AIAA Paper 80-0201, 1980.

101 Bennett, J. C., "Measurement of Periodic Flow in Rotating Machinery," AIAA Paper 77-713, 1977.
102 Bennett, J. C., "High Response Measurements of Prop-Fan Flow Fields," presented at the Dynamics Flow Symposium, John Hopkins University, Baltimore, Maryland, Sept. 1978.
103 Young, M. F., "Calibration of Hot Wires and Hot Films for Velocity Fluctuations," Mech. Eng. Dept. Report TMC-3, Stanford University, 1976.
104 Evans, R. L., "Turbulence and Unsteadiness Measurements Downstream of a Moving Blade Row," ASME JOURNAL OF ENGINEERING FOR POWER, Vol. 97, No. 1, 1974, pp. 131–139.
105 Hoffmeister, M., "Using a Single Hot Wire Probe in Three Dimensional Turbulent Flow Fields," *DISA Information,* Vol. 13, 1972, pp. 26–28.
106 Fujita, H., Kovasznay, L. S. G., "Measurement of Reynolds Stress by a Single Rotated Hot Wire," *Review of Scientific Instruments,* Vol. 39, 1968, p. 1351.
107 Bissonnette, L. R., and Mellor, G. L., "Experiments on the Behavior of an Axisymmetric Turbulent Boundary Layer With a Sudden Circumferential Strain," *Journal of Fluid Mechanics,* Vol. 63, Part 2, 1974.
108 Moussa, Z. M., and Eskinazi, S., "Directional Mean Flow Measurements Using a Single Inclined Hot Wire," *Physics of Fluids,* Vol. 18, No. 3, 1975.
109 Hirsch, Ch., and Kool, P., "Application of a Periodic Sampling and Averaging Technique to Flow Measurements in Turbomachines," Vrije Universiteit Brussel, Rept. No. VUB-STR-4, Sept. 1973.
110 Hirsch, Ch., and Kool, P., "Measurement of the Three-Dimensional Flow Field Behind an Axial Compressor Stage," ASME JOURNAL OF ENGINEERING FOR POWER, Vol. 99, 1977, p. 168.
111 Kool, P., "Experimental Investigation of the Three Dimensional Flow Field Downstream of Axial Compressors," Ph.D. Thesis, Vrije Universiteit Brussel, Dept. of Fluid Mechanics, Jan. 1977.
112 Kool, P., DeRuyck, J., and Hirsch, Ch., "The Three Dimensional Flow in an Axial Plane Downstream of a Compressor Rotor," ASME Paper No. 78-GT-66, 1978.
113 Schmidt, D. P., and Okiishi, T. H., "Multistage Axial Flow Turbomachine Wake Production, Transport and Interaction," *AIAA Journal,* Vol. 15, 1977, pp. 1138–1145 (also see Iowa State University Rept. ISU-ERI-AMES 77 130, TCRL-7, AFOSR-TR-77-0720, Nov. 1976).
114 Wagner, J. H., Okiishi, T. H., and Holbrook, G. J., "Periodically Unsteady Flow in an Embedded Stage of a Multi-Stage Axial Flow Turbomachine," ASME JOURNAL OF ENGINEERING FOR POWER, Vol. 101, 1979, pp. 42–51.
115 Lakshminarayana, B., and Davino, R., "Mean Velocity and Decay Characteristics of the Guide Vane and Stator Blade Wake of an Axial Flow Compressor," ASME JOURNAL OF ENGINEERING FOR POWER, Vol. 102, No. 1, 1980, p. 50–60.
116 Raj, D., and Swim, W. B., "A Sampling Technique to Measure the Mean Flow Velocity and Velocity Fluctuations at the Exit of the Rotor," ASME JOURNAL OF ENGINEERING FOR POWER, this issue, pp. 393–399.
117 Favier, D., et al., "An Experimental Study of Three Dimensional Characteristics of Propeller Wakes Under Stall Conditions," ASME *Journal of Fluids Engineering,* Vol. 99, 1977, p. 745.
118 Kool, P., "Determination of the Reynolds Stress Tensor With a Single Slanted Wire in Periodically Unsteady Turbomachinery Flow," ASME Paper No. 79-GT-130, 1979.
119 Chue, S. H., "Pressure Probes for Fluid Measurement," *Progress in Aeronautical Science,* Vol. 17, 1975, pp. 147–223.
120 Dean, R. C., "Aerodynamic Measurements," Gas Turbine Lab, MIT, 1953.
121 Sitaram, N., Lakshminarayana, B., and Ravindranath, A., "Conventional Probes for the Relative Flow Measurement in a Rotor Blade Passage," ASME JOURNAL OF ENGINEERING FOR POWER, this issue, pp. 406–414.
122 Lakshminarayana, B., Jabbari, A., and Yamaoka, H., "Turbulent Boundary Layer on a Rotating Helical Blade," *Journal of Fluid Mechanics,* Vol. 51, 1972, pp. 554–569.
123 Hunt, R. R., "Five Hole Pitot Probe Instrumentation," Naval Ship Research and Development Center, Hydro. Lab, TN 92, 1967.
124 Wright, M. A., "The Evaluation of a Simplified Form of a Presentation for Five Hole Spherical and Hemispherical Pitometer Calibration Data," *Journal of Physics E.: Scientific Instruments,* Vol. 3, 1970, pp. 356–362.
125 Dau, K., McLeod, M., and Surry, D., "Two Probes for the Measurement of the Complete Velocity Vector," *Aeronautics Journal,* Vol. 72, 1968, pp. 1006–1008.
126 Treaster, A. L., and Yocum, A. M., "The Calibration and Application of Five Hole Probes," *Proceedings of the 24th International Instrumentation Symposium,* Inst. Soc. of America (ISA), Albuquerque, May 1978.
127 Bennett, J. C., "Use of Five-Hole Pneumatic Probe in Unsteady Flows," *Progress in Aeronautics and Astronautics,* Vol. 53, 1977, p. 77.
128 Dring, R. P., "Experimental Investigation of Compressor Rotor Wakes," Final Report to U. S. Air Force APL, Rept. R79-914183-15, 1979.
129 Huey, L. J., "A Yaw-Insensitive Static Pressure Probe," ASME *Journal of Fluids Engineering,* Vol. 100, 1978, p. 229.
130 Smith, A. M. O., and Bauer, A. B., "Static Pressure Probes That are Theoretically Insensitive to Pitch, Yaw, and Mach Number," *Journal of Fluid Mechanics,* Vol. 44, 1970, p. 513–528.
131 Ikui, T., and Inoue, M., "Pressure or Velocity Gradient Error in the Flow Direction Measurement," Memoirs of Faculty of Engineering, Kyushu University, Vol. 29, No. 3, 1970.
132 Johnson, R. C., "Averaging of Periodic Pressure-Pulsations by a Total Pressure Probe," NACA TN No. 3568, Washington, 1955.
133 Weyer, H., and Schodl, R., "Development and Testing of Techniques for Oscillating Pressure Measurements Especially Suitable for Experimental Work in Turbomachinery," ASME *Journal of Basic Engineering,* Vol. 93D, 1972.
134 Castorph, D., and Raabe, J., "Measurement of Unsteady Pressure, Unsteady Relative Velocity Field of a Kaplan Runner by Means of an Electronic Multi-miniature Probe as a Basic Contribution to Research on Unsteady Runner Load," *Proceedings of the 7th IAHR Symposium,* Vienna, 1974.
135 Eckhardt, D., "Instantaneous Measurements in the Jet-Wake Discharge of a Centrifugal Impeller," ASME JOURNAL OF ENGINEERING FOR POWER, ASME Paper No. 74-GT-90, 1974.
136 Shreeve, R. P., et al., "Determination of Transonic Compressor Flow Field by a Synchronized Sampling of Stationary Fast Response Transducers," in *Nonsteady Fluid Dynamics,* editors D. E. Crow and J. A. Miller, ASME 1978, p. 91–102.
137 Matsunaga, S., et al., "Accurate Measurement of Nonsteady Three Dimensional Incompressible Flow by Means of a Combined Five-Hole Probe," in *Nonsteady Fluid Dynamics,* editors E. Crow and J. A. Miller, ASME, 1978, p. 65–72.
138 Kerrebrock, J. L., et al., "A Miniature High Frequency Sphere Probe," *Proceedings of ASME Symposium on Measurement Methods in Rotating Components of Turbomachinery,* editors B. Lakshminarayana and P. Runstadler, ASME 1980, p. 91–98.
139 Johnston, J. P., "A Wall Trace Flow Visualization Technique for Rotating Surfaces in Air," ASME *Journal of Basic Engineering,* 1964.
140 Lakshminarayana, B., "Visualization Study of Flow in Axial Flow Inducers," ASME *Journal of Basic Engineering,* D94, 1972, pp. 777–787.
141 Bomelburg, H. J., Herzog, J. and Weske, J. R., "The Electric Spark Method for Qualitative Measurements in Flowing Gases," *Zeitschrift fuer Flugwiss,* 7–11, 1959, p. 322.
142 Richard, E. J. and Burstall, F. H., "The China Clay Method of Indicating Transition," Brit ARC R & M 2126, 1945.
143 Laguier, R. and Sievers, A., "Methodes de Measures Instantionnaires Dans les Turbomachines," *L'aeronautique et L'astronautique,* No. 46, 1974 (Translation NASA TTF 16082).
144 AGARD, "Unsteady Flow Phenomena in Turbomachinery," AGARD CP 177, 1975.
145 Fleeter, S., "Time Variant Aerodynamic Response of a Stator Row Including the Effects of Camber," ASME JOURNAL OF ENGINEERING FOR POWER, Vol. 102, No. 2, 1980, pp. 334–343.
146 Henderson, R. E., and Franke, G. F., "Investigation of the Unsteady Pressure Distribution on the Blades of an Axial Flow Fan," Applied Res. Lab., The Pennsylvania State University Report ARL TM 78-54, 1978.
147 Englund, D. R., Grant, H. P., and Lanati, G. A., "Measuring Unsteady Pressure on Rotating Compressor Blades," 25th International Instrumentation Symposium of ISA, Calif., May 7–10, 1979 (NASA TM 79159).
148 Grant, H. P., and Lanati, G. A., "Instrumentation for Measuring the Dynamic Pressure on Rotating Compressor Blades," NASA CR 159466 (also Pratt and Whitney Aircraft Rept. No. PWA 5558-12), Sept. 1978.
149 Winter, K. G., "An Outline of the Techniques Available for the Measurement of Skin Friction in Turbulent Boundary Layers," *Progress in Aeronautical Sciences,* Vol. 18, 1977, pp. 1–57.
150 Preston, J. H., "The Determination of Turbulent Skin Friction by Means of a Pitot Probe," *Journal of the Royal Aeronautical Society,* Vol. 58, 1954, pp. 109–121.
151 Ludwieg, H., "Instrument for Measuring the Wall Shear Stress of Turbulent Boundary Layers," *Ingenieur Archiv,* Vol. 17, 1949, pp. 207–218 (Translation as NACA TM 1284, 1950).
152 McCroskey, W. J., and Durbin, E. J., "Flow Angle and Shear Stress Measurements Using Heated Films and Wires," ASME *Journal of Basic Engineering,* Vol. 94, 1972, pp. 46–52.
153 McCroskey, W. J., and Fisher, R. K., "Detailed Aerodynamic Measurements on a Model Rotor in the Blade Stall Regime," *Journal of the American Helicopter Society,* 1972, p. 20.
154 Murthy, V. S., and Rose, W. C., "Buried Wire Gauge for Wall Shear Stress Measurement," AIAA Paper 78-798, 1978.

Measurements of the Mean Flow Velocity and Velocity Fluctuations at the Exit of an FC Centrifugal Fan Rotor

D. Raj
Research Engineer,
Babcock and Wilcox,
Research and Development Center,
Alliance, Ohio 44601

W. B. Swim
Professor,
Tennessee Technological University,
Department of Mechanical Engineering,
Cookeville, Tenn. 38501

The flow from a small forward curved fan rotor was studied to provide guidance for fan design. The single width fan had a 0.23 m rotor containing 48 blades. It is typical of the centrifugal fans used in small air-conditioning units. Visualization techniques and hot wire measurements showed the rotor flow to be highly turbulent and strongly three-dimensional. The inlet flow was found to fill only 3/4 of the blade span. The shroud end of the rotor was an inactive or separated region. A jet-wake pattern occurred at the blade exit in the active flow region. The inlet flow separated at the leading edge of the blade suction surface. Design changes are offered to improve the performance of FC fans.

Introduction

Interest in improved centrifugal fans has increased recently. The improvements sought, reduced noise level and increased efficiency, require an improved design method based on good models of the fans' internal flow. The first step in developing the new design tools is to obtain a good understanding of the flow, mean velocity, and velocity fluctuations occurring in the fan.

The flow field in a forward curved (FC) centrifugal fan is, indeed, very complex and there appears to be very little published literature in that area. The textbook on fans by Eck [1] has some information on the theory of flows in FC centrifugal fans, but it does not give much detail of the actual internal flows. Gessner [2] measured the velocities at the rotor inlet of an FC centrifugal fan. His measurements showed the flow near the shroud to be nearly axial and slowly changing to radial at the back plate. The inlet flow was nearly axisymmetric. Gardow [3] measured the velocity at the exit of a backward inclined (BI) centrifugal fan. His measurements showed the exit flow in the region close to the shroud to be a highly fluctuating, low velocity flow, similar to a separated flow. This region was independent of the circumferential location.

Most of the work done in the past on flow in centrifugal devices has been on centrifugal compressors. Centrifugal compressor design cannot be used for FC centrifugal fans because of the compressors' high pressure ratios. A similarity between the flows in compressors and FC centrifugal fans is the presence of a high velocity, high energy "jet" type flow on the pressure surface of the blade passage and a low velocity, low energy "wake" type flow on the suction surface of the blade passage. BI centrifugal fans, on the other hand, based on Gardow's measurements, do not exhibit this flow behavior.

The objective of this project was, therefore, to study the flow at the exit of an FC centrifugal fan rotor. This was achieved (1) by using flow visualization techniques to get an idea of the gross flow behavior and (2) by using a single hot wire probe to measure the mean velocity and the velocity fluctuations at the various locations at the exit of the rotor.

Experimental Program

The fan selected for the study was a single inlet FC centrifugal fan having a squirrel cage rotor. Its specifications and operating conditions for the velocity measurements were as follows.

Rotor outlet diameter	0.269 m (10.6 in.)
Rotor inlet diameter	0.226 m (8.9 in.)
Rotor width	0.142 m (5.6 in.)
Number of blades	48
Blade inlet angle	6 deg
Blade outlet angle	154 deg
Fan inlet throat dia.	0.223 m (8.8 in.)
Housing width	0.187 m (7.35 in.)
Fan discharge area	0.187 m × 0.288 m (7.35 in. × 11.35 in.)
Area at cut-off	0.187 m × 0.178 m (7.35 in. × 7 in.)
Blade thickness	0.76 mm (0.03 in.)
Design flow rate	354 1/s (750 cfm)
Operating speed	900 rpm

Two different operating conditions were selected for the study: the design and 150 percent design flow.

Fan Performance. Much of the metal housing of the fan was replaced by a Plexiglas housing of the same shape and size to permit visual observation of the interior flow.

The operating characteristics of the fan with the plexiglas housing was measured and compared with the manufacturer's data as shown in Fig. 1. The curves are quite close, indicating negligible changes introduced by the plexiglas housing. The difference is attributed to

Contributed by the Gas Turbine Division and published in the symposium volume, *Measurement Methods in Rotating Components of Turbomachinery*, ASME, New York, 1980. Manuscript received for publication in the JOURNAL OF ENGINEERING FOR POWER May 22, 1980.

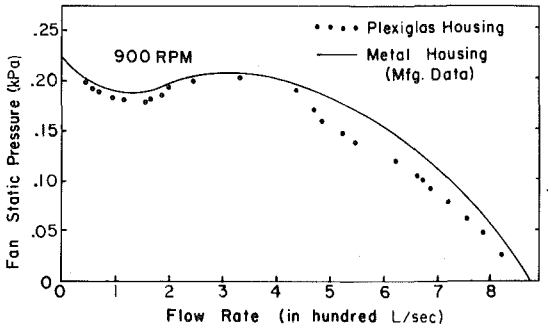

Fig. 1 Comparison of the performance curve of the fan with the plexiglas housing and the manufacturer-supplied performance curve

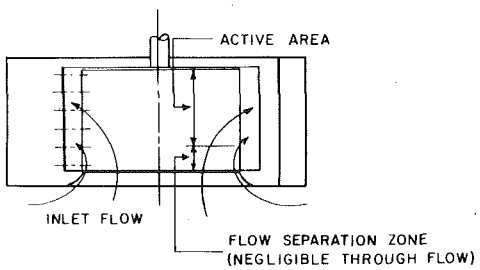

Fig. 2 Active area and the separation zone at the rotor inlet

measurement errors and possible inaccuracies in the manufacturer's data.

Flow Patterns throughout the Fan. The flow patterns throughout the fan were studied using flow visualization techniques. Tufts, tuft probes and smoke were used to "see" the flow. The flow visualization experiments gave a gross picture of the flow in the fan. The important points that were noted are:

1 The flow entering the fan changed from axial at the shroud to radial at the back plate. This was in agreement with Gessner's data.

2 The rotor inlet flow did not fill the entire rotor width. A no-flow or inactive separation zone extended from the shroud end of the blades towards the back plate or hub end, as illustrated in Fig. 2. The axial length of this flow separation zone was found to be a strong function of circumferential position around the inlet as well as fan flow rate. The inlet flow was observed to be highly asymmetric, contrary to Gessner's findings.

3 The flow entered the blade passage with an extremely high angle of attack. It separated from the suction surfaces of the blades, as shown in Fig. 3. The suction surface flow was always stalled.

4 There was very little through flow near the shroud—the inactive zone.

5 In regions where through flow existed, the axial component of the absolute flow exit velocity was small. This indicated that part of the turning of the flow from axial, at the rotor inlet, to radial, at the rotor exit, was accomplished in the blade passage.

Rotor Exit Velocity and Velocity Fluctuation Measurement. The flow velocities at the rotor exit are three-dimensional and highly fluctuating. However, the flow visualization experiments showed that the axial component of flow velocity at the rotor exit was small. Hence, a single hot wire probe in the r–θ plane was used to measure the exit velocity. This simplification obviously introduces some errors in the measurement but these errors are small for small axial velocity components. For example, replacing the true total velocity by just the r and θ components for a flow in which the axial component is 10 percent of the total velocity introduces an error of only 0.5 percent. For an extreme case where the axial component is 25 percent of the total velocity, the error is only 3 percent. Even though the magnitude of the total velocity at the rotor exit can be easily measured with a single hot wire probe, the direction cannot be measured. Only the

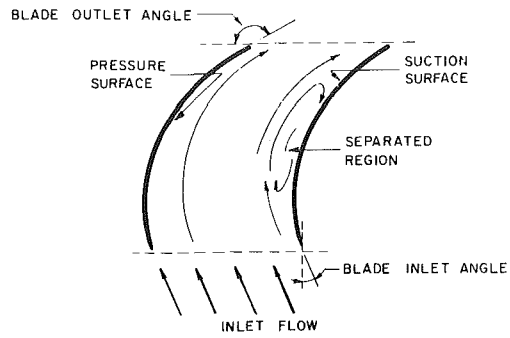

Fig. 3 Blade passage flow

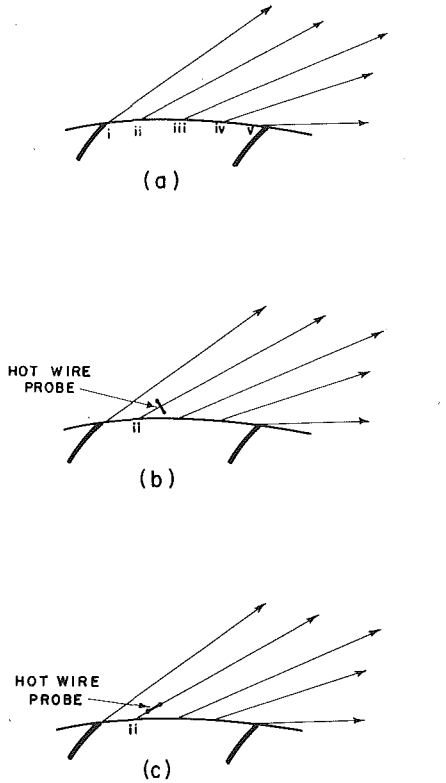

Fig. 4 Hot wire probe orientations for the velocity measurements

direction of the r–θ component can be measured. This is quite adequate for the case of FC fan rotor exit velocity measurements. For cases where a significant axial component of velocity exists, two probes could be used.

Sampling Technique. A typical mean absolute flow velocity distribution at the exit of a blade passage of a centrifugal fan is shown in Fig. 4. The figure shows that both the direction and the magnitude of the exit velocity for a blade passage are not constant. If, along with the nonuniform mean velocity, the flow is very turbulent, then the mean velocity distribution and the velocity fluctuations cannot be directly measured. Hence, a periodic-average sampling technique was used. This measurement technique has been used successfully by several researchers (e.g., Evans [4], Raj and Lakshminarayana [5], Hirsch and Kool [6], Okiishi and Schmidt [7], and Gostelow [8]).

The principle of the sampling technique is as follows: A number of points are selected at the exit of a blade passage (points i, ii, iii, etc., as shown in Fig. 4(a)). To measure the mean velocity and the velocity fluctuations at any point (ii, for example), the hot wire is placed at right angles to the velocity direction at point ii (see Fig. 4(b)). Each time the point ii passes the hot wire, the output from the anemometer is sampled. Once a large enough number of samples are obtained, they

are averaged to give the mean velocity at point ii. The fluctuation in the sampled values and, thus, the fluctuations in the velocity at point ii, are obtained by finding the AC rms value of the samples.

Figure 5 shows the system used to sample the exit velocity.

The mean velocity and velocity fluctuation measurements for the absolute velocity at the blade passage exit were made as follows:

1 A desired location in the blade passage (e.g., point ii) was selected by adjusting the time delay in the data acquisition circuit.

2 To find the velocity direction at point ii, the hot wire was rotated (in the r–θ plane) until a minimum in the periodic averaged signal was obtained. The hot wire was thus aligned with the velocity direction at point ii, as shown in Fig. 4(c). The hot wire direction (and, therefore, the velocity direction) was noted.

3 The hot wire probe was rotated through 90 deg so that the hot wire was at right angles to the velocity at ii (see Fig. 4(b)).

4 The output from the averaging circuit gave the mean velocity at point ii.

5 The fluctuations in the signal from the sample and hold amplifier, as measured by the AC rms voltmeter, gave the velocity fluctuations in the direction of the velocity at point ii.

6 A different point (e.g., iii) was selected by adjusting the time delay, and the same procedure was repeated. Once the velocities for all the points in the blade passage were measured, the probe was moved to a new axial location.

The location of the minimum velocity in the rotor exit flow velocity profile was assumed to occur at the blade. This assumption is true for FC centrifugal fans where the exit velocity is always greater than the blade velocity. However, the measurements have to be made at the rotor exit. This was not possible because of the diameter of the probe support. The center of the probe could only be placed 0.3 mm (1/8 in.) from the rotor exit. The mixing of the jet-wake flow makes it extremely difficult to specify the exact blade location from the hot wire trace. The precise location of the blade and the hot wire were known, however, from the fan and probe geometry.

Velocity measurements were made at three circumferential locations (1, 2, and 3) and six axial locations 1 in. apart (a, b, c, d, e, and f) at a radius ratio of 1.02, as shown in Fig. 6. This figure also shows the location of pressure taps used to measure the circumferential pressure distribution. The miniature probe used for the measurements had a platinum-plated tungsten wire with a diameter of 5 μm (0.0002 in.) and a length of 1.25 mm (0.05 in.). The probe support has a diameter of 4 mm (0.157 in.) and a length of 235 mm (9.25 in). The probe and the probe holder were introduced into the housing through Teflon bushings placed in the housing at locations 1, 2, and 3. The probe support was clamped to a traversing mechanism whose base in turn was fastened to the front of the housing. A scale and protractor on the traversing mechanism permitted the hot wire to be located at any axial location and any angular direction in the r–θ plane.

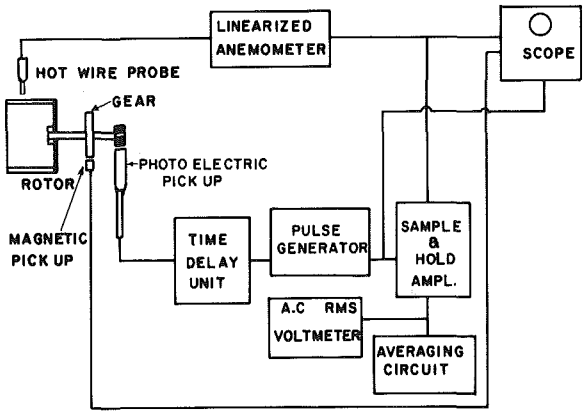

Fig. 5 Rotor exit velocity measurement system

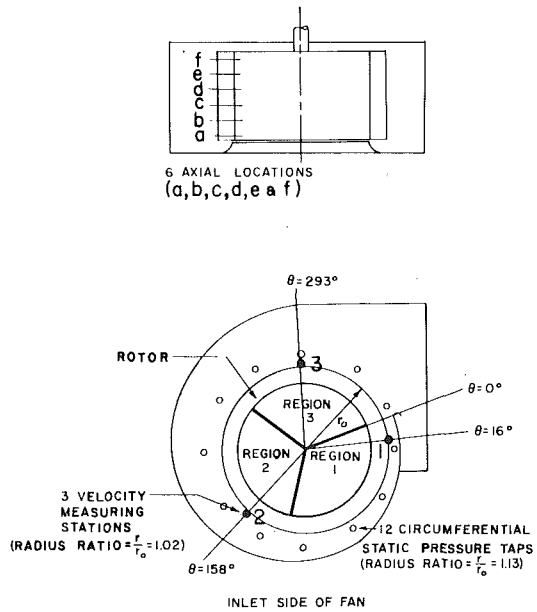

Fig. 6 Pressure and velocity measurement locations

Results

Static Pressure Distribution. The static pressure distributions around the outlet side of the rotor for the two different flow rates are presented in Fig. 7. The figure also shows the variation of the scroll flow area with circumferential location.

Velocity at the Rotor Exit. Preliminary measurements of the flow velocity at the rotor exit were made with a single hot wire in the r–θ plane without the sampling circuit. The hot wire was rotated in the r–θ plane until a maximum of the mean anemometer output was obtained. The anemometer output did not represent the actual velocity profile because of the varying exit flow angles. However, since hot wire probes are not very sensitive to small changes in the velocity direction, the anemometer output did not vary much (3 to 4 percent) from the actual velocities. Photographs of the repeated anemometer traces, for a reference blade, were taken from the oscilloscope screen. These traces gave the velocity magnitude as well as an indication of the fluctuation in the velocities. Figure 8 shows the rotor exit flow velocities for circumferential location 3 and the six lettered axial locations. In this and the following figures, the traces represent the exit flow velocity variation across a blade passage. Each photograph contains three sets of traces, each set representing the velocity at a particular axial location. The two photographs in Fig. 8, therefore, show the velocities at all six axial locations (a–f) for the given circumferential location 3. The axial locations are identified at the right-hand side of the traces. Each set of traces is offset with respect to the others to prevent overlapping. The zero velocity level for each is, therefore, different and is shown on the left-hand side of the pho-

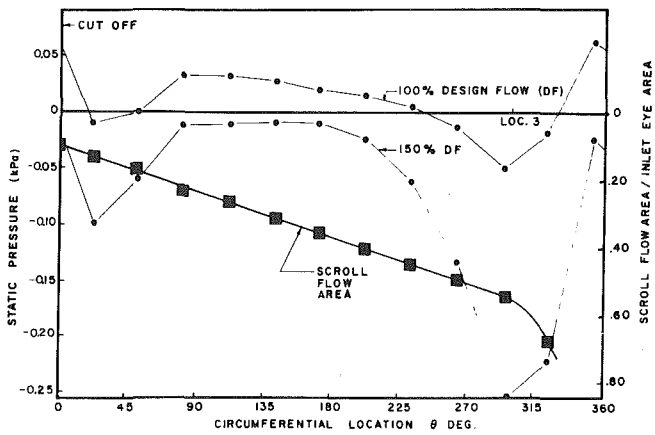

Fig. 7 Circumferential variation of the static pressure in the housing

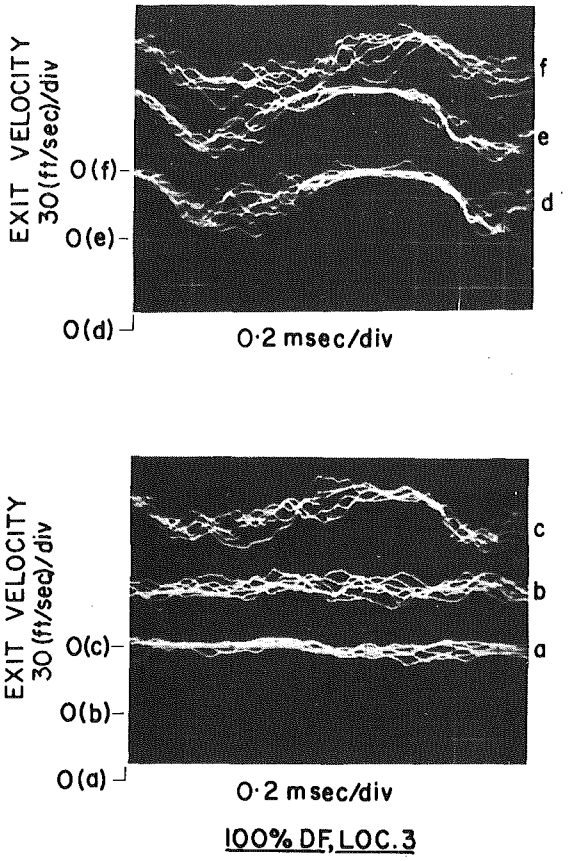

Fig. 8 Absolute flow velocity at the rotor exit—location 3, 100 percent design flow

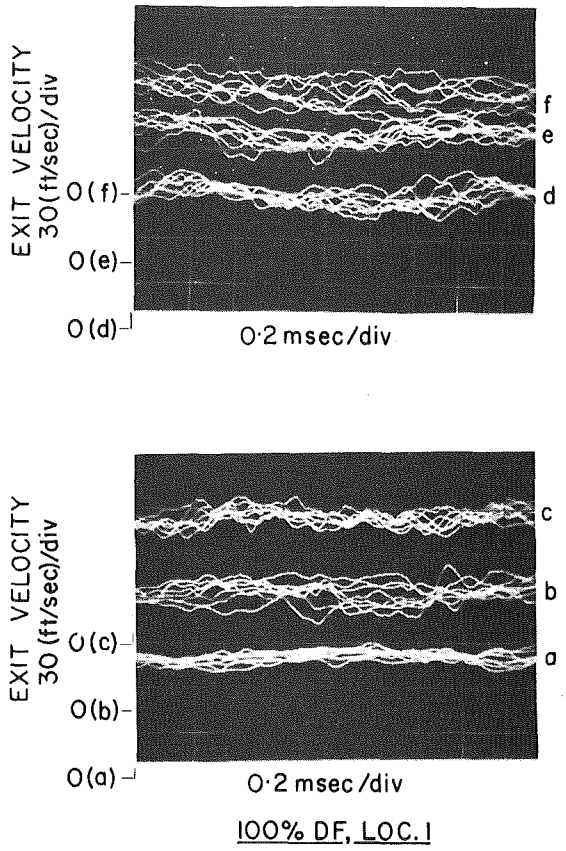

Fig. 10 Absolute flow velocity at the rotor exit—location 1, 100 percent design flow

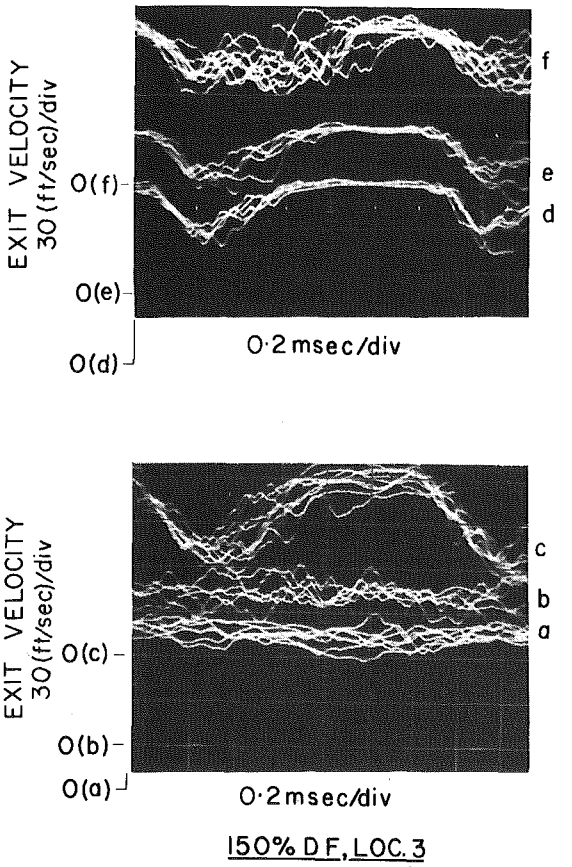

Fig. 9 Absolute flow velocity at the rotor exit—location 3, 150 percent design flow

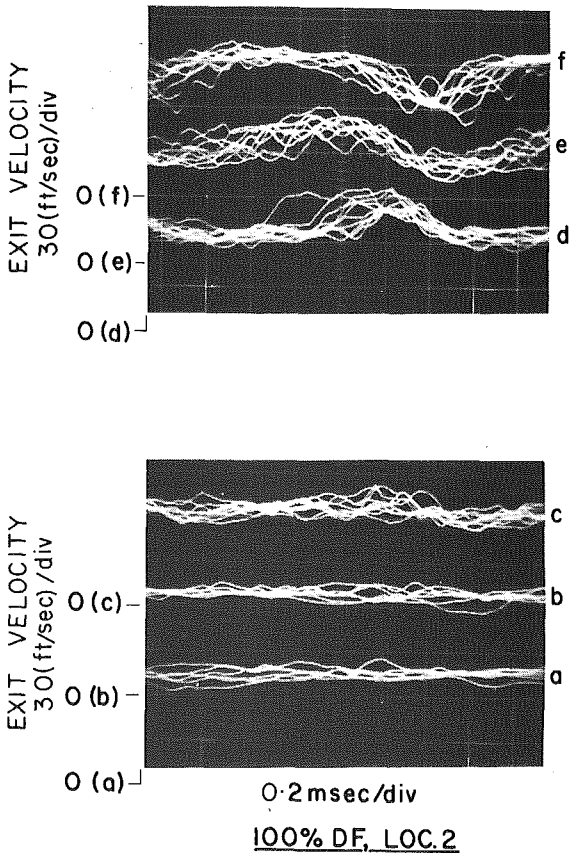

Fig. 11 Absolute flow velocity at the rotor exit—location 2, 100 percent design flow

tograph. The rotor exit flow velocities for circumferential locations 1 and 2 at 100 percent design flow as well as location 3, 150 percent design flow, are shown in Figs. 9–11.

The absolute flow velocities at the rotor exit (magnitude, direction and fluctuation level) were measured using the sampling technique. Figure 12 shows the mean absolute velocity profiles at location 3 for the design flow rate. In this figure, the data represent the mean exit flow velocity for one blade passage. In the figures, the blade locations correspond to the beginning and the end of each velocity profile. The suction surface and the pressure surface of the blade passage and the velocity profiles at axial locations a through f are shown in the figure. The velocity profiles for the different axial locations are labeled a–f and are offset with respect to each other to prevent overlapping of the curves. Since the figures are too small to show the zero velocity levels for all the profiles, a higher reference velocity level (25 m/s) for each is shown on the left-hand side of the figures. The numbers above the data points along the curves indicate the rms velocity fluctuations in m/s at the different locations in the blade passage exit.

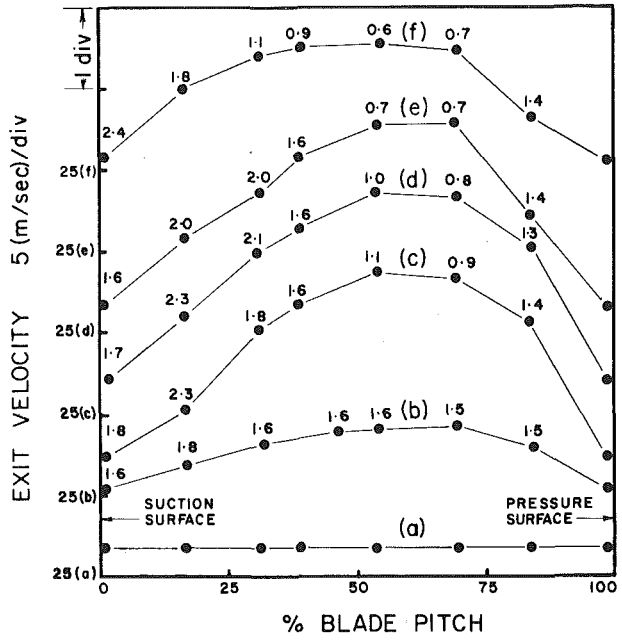

Fig. 12 Mean flow velocity and velocity fluctuations at the rotor exit—location 3, design flow (Numbers above the data points denote rms velocity fluctuations.)

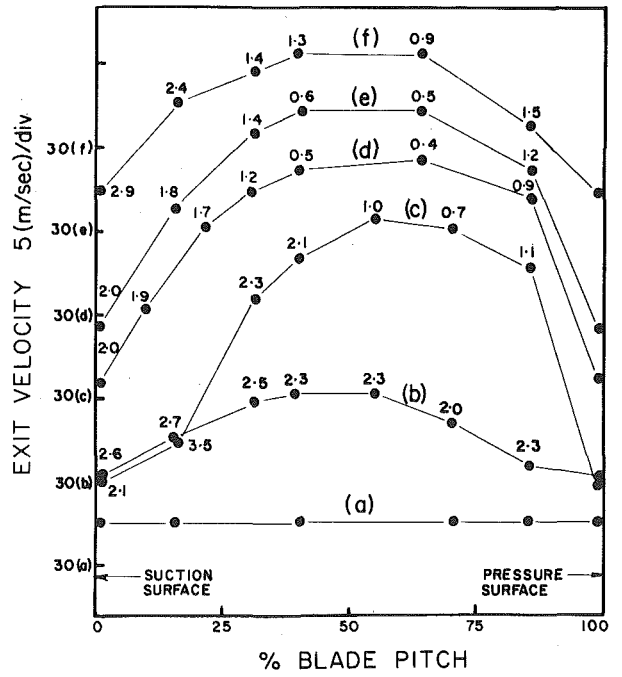

Fig. 13 Mean flow velocity and velocity fluctuations at the rotor exit—location 3, 150 percent design flow (Numbers above the data points denote rms velocity fluctuations.)

Figure 13 shows the velocity profile data for circumferential location 3 and 150 percent design flow.

The relative velocity in the blade passage exit can be calculated from the absolute velocity at the blade passage exit by vectorial subtraction of the blade velocity U. Figure 14 shows the relative velocity at the blade exit at location 3 for the design flow rate. In the figure, the relative velocities at axial locations a–f are shown. For each location, the figure shows a blade passage exit, where PS represents the pressure surface and SS represents the suction surface of the blade passage. The tail of the arrow represents the location in the blade passage of a particular relative velocity. The length of the arrow represents the magnitude of the relative velocity and the direction of the arrow represents the direction of the relative velocity.

The relative velocity profiles for circumferential location 3 and 150 percent design flow are shown in Fig. 15.

Discussion of Results

The following observations were made based on the flow visualization experiments and the velocity measurements.

1 The static pressure distribution around the rotor was not uniform, as can be seen from Fig. 7. There was a pressure drop following the cut-off. The pressure increased and stayed uniform over a portion of the wheel, following which there was a rapid drop to a minimum just before the cut-off ($\theta = 0$ deg). The plot of the scroll flow area with circumferential location showed a linear increase from the cut-off to location 3 (see Fig. 6). Beyond that, there was a rapid increase in the area. This region was, thus, a high diffusion zone and a rapid increase in the static pressure occurred. Flow visualization experiments showed this high diffusion zone to be highly turbulent and to contain regions of flow reversals.

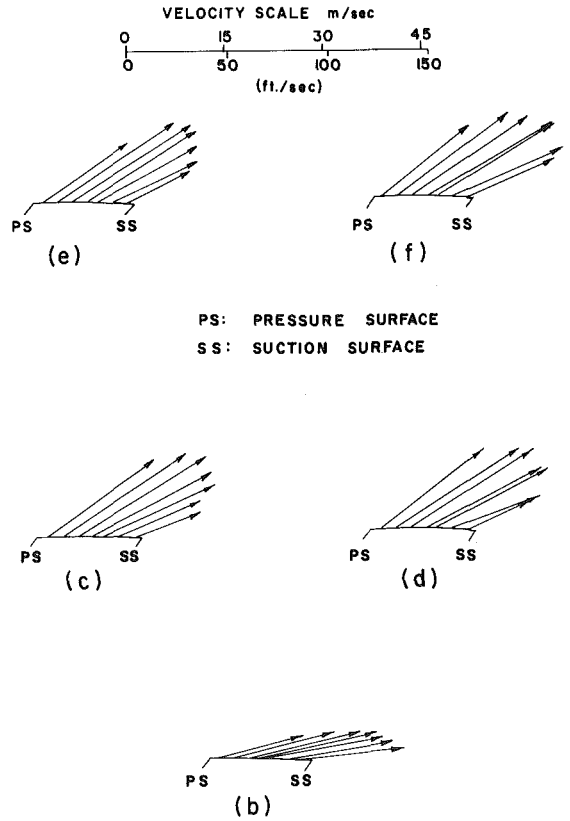

Fig. 14 Relative flow velocity at the rotor exit at axial locations b, c, d, e, and f—location 3, design flow

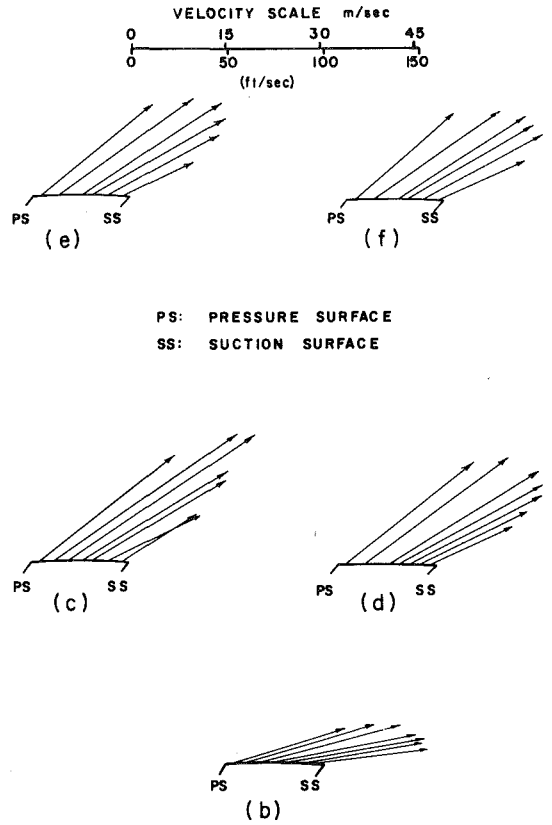

Fig. 15 Relative flow velocity at the rotor exit locations b, c, d, e, and f—location 3, 150 percent design flow

2 The assumption that the absence of a minima in the velocity traces indicates an absence of through flow can be used to estimate the extent of the inlet shroud separation zone (see Fig. 2) from the velocity traces of Figs. 8–11. For example, in Fig. 11, the presence of flow through the blade passage is first observed in trace (d). The inlet shroud separation zone extends, for this condition, from the inlet shroud to axial location d. The separation zone, therefore, covers about 60 percent of the rotor width. This approach can be used to calculate the active flow area for each flow rate.

Flow visualization and the velocity measurements show that the active flow area at design flow is 75 percent of the total area. This area drops to 70 percent of the total area when the flow rate is raised to 150 percent design flow. It has to be noted that the above assumption is only completely true when the probe is at the rotor exit. For any other radial location, the scroll through flow complicates the interpretation of the results. Also, small through flows cannot be detected, as can be seen from Fig. 10. At location 1, the presence of through flow, shown to exist by the flow visualization experiments, is not evident from the traces.

3 The velocity traces show that at every location where appreciable blade passage through flow exists, the velocity exhibited the jet-wake profile. The jet was next to the pressure surface and the wake next to the suction surface. The extent of the jet and the wake regions depended on the axial location as well as the flow rate. The jet-wake ratio increased in going from the shroud to the back plate. The larger velocity fluctuations in the wake region are apparent from Figs. 8, 9, 12, and 13. The jet-wake ratio in the regions where through flow existed also increased with the flow rate, as can be seen for location 3 in Figs. 8 and 9.

4 It is difficult to calculate the flow velocities at the blade passage exit from the absolute velocities when the through flow is small. This is evident from the calculated relative velocity profiles at location b, in Fig. 14. The through flow at location b was small and, hence, the velocity measured at the blade exit was mainly due to the scroll flow and not the blade passage flow. The profiles for location b are, therefore, unreliable.

5 The exit flow velocity, like the static pressure, was a function of the circumferential location. If only the velocities near the back plate are considered (region where appreciable through flow exists), then it was seen that regions of low static pressures were accompanied by high exit velocities.

Conclusions

Based on the measurements made, the following conclusions were reached.

1 The sampling technique using a single hot wire probe, described in this paper, is quite effective in measuring the mean velocity and velocity fluctuations at the exit of FC rotors where the flow is extremely turbulent but essentially two-dimensional. This method can be used effectively to measure the flow in other turbomachines with two-dimensional flows where large variations, magnitude and/or direction, in the blade to blade velocities occur.

2 The flow through the rotor is a function of three variables: The axial location on the rotor, the tangential position in the housing, and the through flow rate. There are large flow separation zones near the inlet shroud. Negligible through flow occurs in these separation zones. The presence of the no-flow separation zones reduces the active rotor flow area. Thus, the loading on the active portion of the blades is increased. The active rotor area decreases with the flow rate so that higher flow rates utilize less of the rotor area.

3 Flow visualization and velocity measurements at the rotor exit show the flow along the blade suction surface to be highly separated. The high angle of attack of the inlet flow guarantees that the flow will separate on the suction surface. The strong diffusion in the inlet region of the blade passage prevents the reattachment of the separated flow to the suction surface. The flow along the pressure surface is smooth and closely follows the blade profile.

4 The rotor exit velocity measurements show the presence of a jet-wake velocity profile. The wake fluctuations are high as compared to those in the jet. The ratio of the jet area to the wake area depends on the flow velocity at the rotor inlet. Higher rotor inlet velocities yield higher jet-wake ratios. The velocity profiles at the blade exit improve going from the inlet shroud to the back plate. Here, an improved profile is one with a higher jet-wake area ratio. Increasing the flow rate improves the blade passage flow throughout the active rotor area. However, the active rotor area decreases with the flow rate.

5 Lower static pressures occur with the higher flow velocities at the blade exit near the back plate. Thus, an indication of the velocity magnitude near the back plate can be obtained directly from the static pressure distribution. The static pressure distribution can also show the presence of tangential velocity gradients and indicate regions where flow improvement is needed.

6 The factors responsible for the poor efficiencies and low performance of FC centrifugal fans are:

(i) The presence of tangential pressure gradients around the rotor. These gradients give rise to tangential variations in the flow rate and tangential variations in the inlet shroud flow separation zone. Both variations make the design of a rotor blade capable of efficient operation at all locations in the housing virtually impossible.

(ii) The axial variation of the flow along the rotor axis. The flow varies from a highly separated flow near the inlet shroud to a reasonably smooth high velocity flow near the back plate.

(iii) The unsteady blade passage flow. The flow over most of the blade suction surface is highly separated.

These three problem areas must be dealt with to design improved FC centrifugal fans.

Recommendations

1 More complete measurements of the flow should be made by selecting more circumferential locations.

2 Three-dimensional flow measurements, using a suitable probe, should be made and compared with the two-dimensional flow mea-

surements to evaluate the errors introduced by assuming two-dimensional flow.

3 The housing should be redesigned to eliminate the tangential pressure gradients.

4 Narrower rotors and a redesigned housing inlet should be used to reduce the inlet flow separation zone.

5 Profiled blade designs should be selected to eliminate or reduce the blade suction surface flow separation. A two-dimensional aerofoil blade shape with a convergent blade passage to guarantee an accelarating flow should reduce the flow separation. The blade inlet should be aligned with the inlet flow direction.

References

1 Eck, B., *Fans*, 1st ed., Pergamon Press, New York, 1973.

2 Gessner, F. B., "An Experimental Study of Centrifugal Fan Inlet Flow and Its Influence on Fan Performance," ASME Paper No. 67-Fe-21, 1967.

3 Gardow, E. B., "On the Relationship Between Impeller Exit Velocity Distribution and Blade Channel Flow in a Centrifugal Fan," Ph.D. Thesis, Feb., 1968, State University of New York at Buffalo.

4 Evans, R. L., "Turbulence and Unsteadiness Measurements Downstream of a Moving Blade Row," ASME JOURNAL OF ENGINEERING FOR POWER, Vol. 97, 1975.

5 Raj. R., and Lakshminarayana, B., "Three-Dimensional Characteristics of Turbulent Wakes Behind Rotors of Axial Flow Turbomachinery," ASME JOURNAL OF ENGINEERING FOR POWER, Vol. 98, 1976.

6 Hirsch, C., and Kool, P., "Measurement of the Three-Dimensional Flow Field Behind an Axial Compressor Stage," ASME JOURNAL OF ENGINEERING FOR POWER, Vol. 99, 1977.

7 Schmidt, D. P., and Okiishi, T. H., "Multistage Axial-Flow Turbomachine Wake Production, Transport and Interaction," *AIAA Journal*, Vol. 15, 1977.

8 Gostelow, J. P., "A New Approach to the Experimental Study of Turbomachinery Flow Phenomenon," ASME JOURNAL OF ENGINEERING FOR POWER, Vol. 99, 1977.

Measurement of Turbine Rotor Blade Flows

R. P. Dring
Supervisor, Gas Turbine Technology.

H. D. Joslyn
Reserach Engineer.

United Technologies Research Center
East Hartford, Conn. 06108

Measurement methods for obtaining various types of experimental data on a turbine rotor blade are discussed in this paper. A variety of different types of measurements have been taken in the rotating frame of reference, including: airfoil surface static pressure distributions, the radial distribution of total pressure in the incident flow, flow visualization of surface streamlines, and radial-circumferential traversing of a pneumatic probe aft of the rotor. Typical results are presented showing interesting flow phenomena present on the rotor. In particular, results are shown which demonstrate the various viscous and inviscid mechanisms that give rise to strong radial flows.

Introduction

The level of performance obtained in turbomachinery is a direct reflection of the degree of understanding of the flow mechanisms occurring in the blade rows. Stationary cascades have been of great value in studying many of these mechanisms. The advances in the areas of improved potential flow prediction techniques, better understanding of airfoil boundary layers and heat transfer, and finally of airfoil loss and deviation are to some degree attributable to the broad range of cascade experiments that have been carried out by numerous researchers. The cascade, however, is unsuitable for the study of a variety of mechanisms which are present in turbomachinery. Mechanisms which, for example, are related to the rotating frame of reference are most suitably studied in an actual turbomachine environment.

Certain types of information about the flows in the rotating frame of reference may be obtained by making high response measurements in the stationary frame. It is clear, however, that there is a distinct advantage in being able to conduct detailed measurements using instrumentation in the rotating frame of reference. The United Technologies Research Center Large Scale Rotating Rig (LSRR) was designed to have rotating frame instrumentation capabilities which are no less elaborate than its stationary frame instrumentation. The value of the rotating frame radial-circumferential traverse system was demonstrated by Greitzer, et al. [1] in their study of the effects of compressor rotor casing treatment. Rotating frame total pressure surveys showed clearly the influence of casing treatment and blade solidity on the relative total pressure defect at the blade trailing edge plane. The value of rotating frame measurements is also evident in the work of Dring, et al. [2] where measurements of rotor blade surface pressures and temperatures and rotating frame flow visualization were used in a study of blade film cooling. It was demonstrated that the film coolant trajectory can have a strong radial component, independent of the coolant-to-freestream density ratio. It was also demonstrated that the film effectiveness on a rotating blade can be considerably different from that on a very similar blade in a stationary cascade.

These studies demonstrate the value of a strong rotating frame measurement capability. The present paper describes the applications of such a measurement capability to the three-dimensional flow over the turbine rotor blade used in reference [2]. A variety of rotating frame pressure measurements and flow visualizations have been carried out in order to better understand the aerodynamic mechanisms present in the flow over this blade.

Experimental Facility

The United Technologies Research Center Large Scale Rotating Rig (LSRR) is 5 ft (1.52 m) in diameter and can accept a variety of turbine and compressor models ranging in hub/tip ratio from 0.5 to 0.8. Figure 1 shows the partially assembled 0.8 hub/tip ratio turbine model. This model has three rows of airfoils: first vane, first blade and second vane, all with aspect ratios (span/axial chord) of approximately 1.0. The airfoil chords are approximately five times engine scale. The large scale of the rig is a distinct advantage because it permits the use of instrumentation which is small relative to the phenomena under study. The large scale also has the advantage of giving Reynolds numbers which are typical of high pressure turbines at nominal rig running conditions (for the turbine model) of 405 rpm and a test section average axial flow velocity of 75 ft/s (23 m/s). The various absolute and relative flow angles and the airfoils that produce them are also typical of current high pressure turbine stages. The major departure from actual engine aerodynamic parameters is that the flow is virtually incompressible. The airfoil exit Mach numbers are approximately 0.2. Thus, the facility is limited to the study of phenomena which are insensitive to compressibility effects.

Rotating Frame Instrumentation

Compared to an actual turbine or a high speed engine scale rig, the LSRR has a relatively benign environment of ambient temperature air and low rotational and flow speeds. This makes possible the application of a wide variety of instrumentation, especially in the rotating frame. The rotating frame pneumatic instrumentation package is mounted as an assembly on the rotor axis. All of the pressure transducers (Druck, model PDCR22, 1 psia) are located very close to the axis of rotation. On-board fluid switches are used to switch the transducers to the various probes that may be in use and to calibration pressures. In addition, a 48 channel Scanivalve (Scanivalve, model 48J9-1290) is used to obtain airfoil surface static pressures as well as the pressures from a rotor mounted total pressure rake.

The traverse probes can range from simple Kiel total pressure

Contributed by the Gas Turbine Division and published in the symposium volume, *Measurement Methods in Rotating Components of Turbomachinery*, ASME, New York, 1980. Manuscript received for publication in the JOURNAL OF ENGINEERING FOR POWER May 22, 1980.

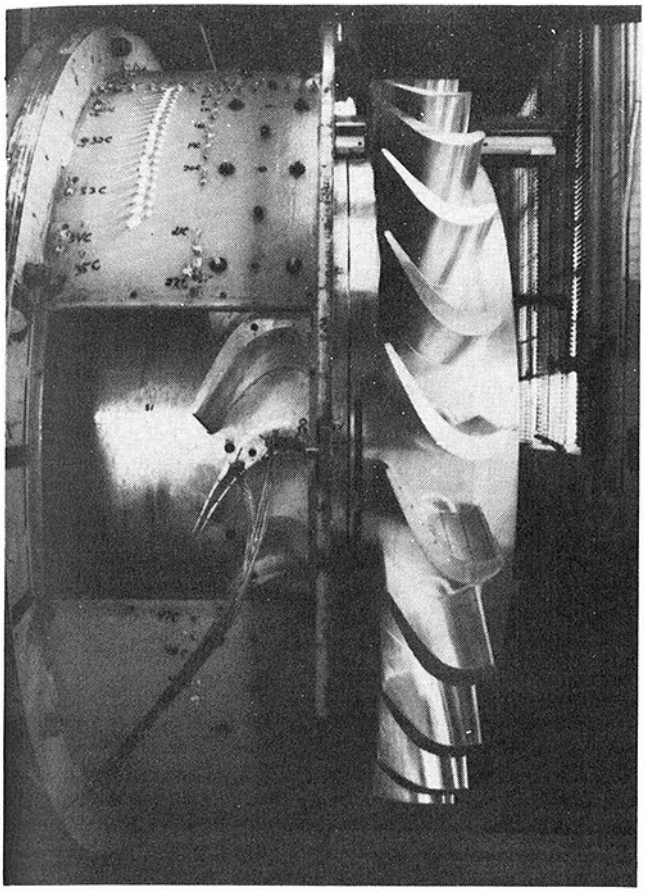

Fig. 1 Large scale rotating rig 1½ stage turbine configuration (first vane and rotor case removed)

probes (United Sensors model KBC-12) to combinations of five Hole and Cobra probes (United Sensors model USC-F-152). For the present work, only Kiel data will be discussed. In all cases, however, the probes are small relative to the airfoils, having diameters of less than 2 percent of the blade pitch. The probes may be traversed radially from hub to tip, within the limits of specific probe geometry, and circumferentially over approximately two blade pitches. When it is required, as with multi-element probes, they can also be driven in yaw to obtain a pressure null condition. The radial and circumferential probe positioning as well as the yaw nulling is controlled by a dedicated on-line minicomputer (Interdata 8/16). Electrical communication with the rotating frame transducers, probe position drive motors, and location sensing potentiometers is through a slip-ring assembly (Fabricast, model 1273). Calibration of the rotating frame transducers is also controlled by the minicomputer. Various combinations of reference pressures are applied to each transducer to obtain five point calibrations covering the range of interest. The pressures are brought onto the rotating frame through a two channel rotary union thus permitting on-line calibration of the transducers with the rig at its running conditions. The accuracy in terms of long-term repeatability of the entire system is typically 1 percent of reading where the reading is the difference between the measured pressure and the reference pressure (usually inlet absolute total pressure).

Parenthetically, it should also be mentioned that temperature measurements in the rotating frame of up to 144 thermocouple channels have been carried out [2] using a voltage scanning device (Dynatech, model 6200). Finally, it should also be pointed out that all of the instrumentation capabilities in the rotating frame are also available in the stationary frame.

The remainder of this paper describes the application of these measurement capabilities to the study of the three-dimensional flow over a turbine rotor blade. Specifically, the present work was motivated by a desire to a gain a better understanding of the three-dimensional flow observed in reference [2].

Results

It had been demonstrated in earlier studies of this rotor [2] that there were strong spanwise flows on the pressure surface of the airfoil. This was evident from the trajectory of film coolant discharged from the airfoil pressure surface at midspan and 16 percent axial chord from the leading edge. The flow visualization indicated that the surface flow had a strong radial displacement (roughly 30 deg radially outward). It was demonstrated that the surface flow direction was independent of the nature of the film coolant fluid for coolant to freestream density ratios up to 4. This insensitivity of the flow trajectory to density ratio strongly suggests that the radial flow was not a result of centrifugal pumping in the boundary layer. This observation appears, on the surface at least, to contradict conclusions by Lakshminarayana, et al. [3–6] about the importance of centrifugal pumping as seen in their studies of the rotating helical channel of a high solidity inducer. This, however, is not the case. It was observed that the shear forces dominated the flow in the inducer, causing boundary layers usually of the order of 25 percent of the blade passage width, and that centrifugal effects produced large radial velocities on the blades. The flow coefficient of the inducer, however, was smaller by a factor of 12 than that of the turbine model of the present study. In addition, the turbine airfoil boundary layer thickness is a very small fraction of the blade passage width. As a result of differences such as these (and as pointed out by Lakshminarayana in references [3] and [5]), the flow in the inducer is entirely different from what one would expect in typical axial compressors or turbines which have much higher flow coefficients and much smaller shear dominated zones.

In order to gain a more complete picture of the nature of the pressure surface flows, two more flow visualizations were carried out. The technique used was developed by Ruden [7] and by Johnston [8]. It consists of attaching a piece of Ozalid paper onto the airfoil surface immediately downstream of a pressure tap location. When ammonia is slowly discharged from the tap, it reacts with the paper leaving a dark streak line. The advantage of this approach is that it can be employed conveniently in the rotating frame. In addition, it is uninfluenced by centrifugal effects. It may be feared that the nature of the orifice thru which the ammonia is injected or the injection velocity can strongly influence the direction of the streak line. In fact, however, as was demonstrated in reference [2], the direction on the streak line was invariant over a wide range of injection velocities. Also, the direction was the same for relatively large film cooling holes as it was for very small pressure taps as used in the present work. Thus, it is felt that the streak lines of the present study truly represent the actual flow directions. In the present program, the ammonia was brought onboard the rotor through the rotary union and discharged at various spanwise arrays of blade surface static pressure taps. The results are shown in Fig. 2. The airfoil has strong radial out-flow near the leading edge, and it tends to turn more axial as the flow proceeds aft. There is relatively little radial flow near the hub (and even some radial inflow), but the radial component increases rapidly toward the tip. Day's results [9] also indicate strong radial flow on the pressure (and suction) surface of his turbine rotor blade. The data indicated radial flow both

Nomenclature

B_x = airfoil axial chord
C_x = axial component of flow velocity
U = wheel speed
X = axial distance
P_s = static pressure
P_T = relative total pressure ($P_s + \frac{1}{2}\rho W^2$)
P_R = rotary total pressure ($P_s + \frac{1}{2}\rho\,(W^2 - U^2)$)
W = relative flow speed
Q_U = dynamic pressure based on midspan wheel speed ($\frac{1}{2}\,\rho U_m^2$)
β = relative flow angle from tangential
ρ = fluid density

Subscripts

1 = rotor inlet
2 = rotor exit
m = midspan

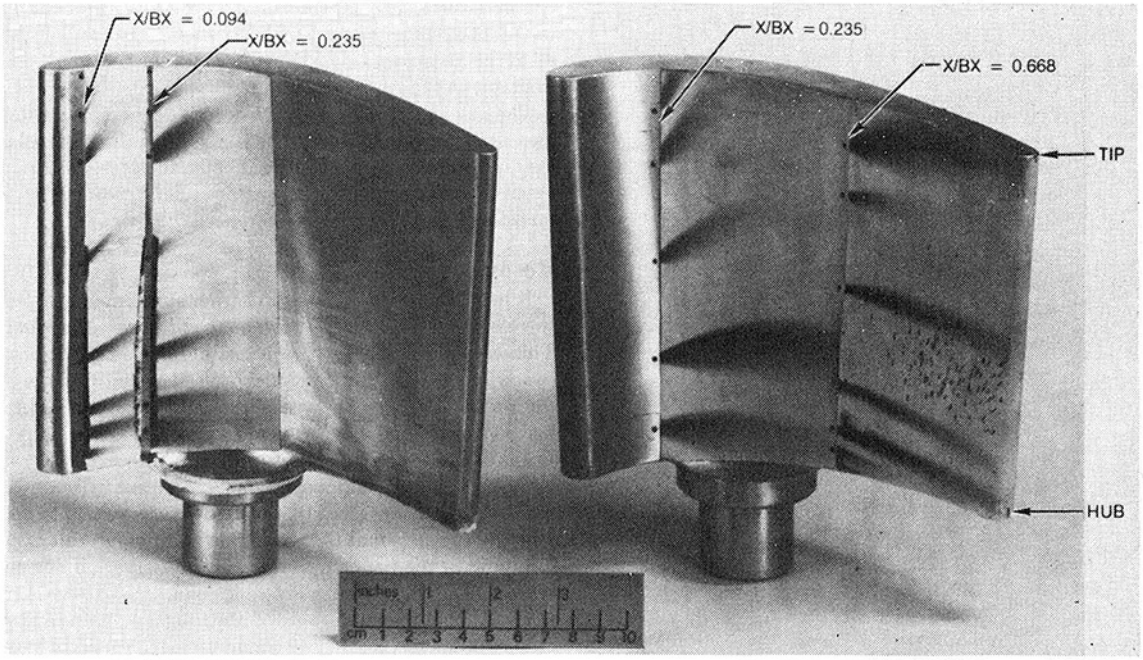

Fig. 2(*a*) 0.005 in. tip clearance

Fig. 2(*b*) 0.085 in. tip clearance

Fig. 2 Pressure surface flow visualization results (ammonia/ozalid technique)

in the blade boundary layer as well as in the flow outside the boundary layer.

It was suspected that the strong radial flows shown in Fig. 2 might have been due to leakage flow over the unshrouded tip of the airfoil; however, as can be seen, back-to-back flow visualizations indicated that this was not the case. When the clearance was reduced from 0.085 in. (2.2mm) to 0.005 in. (0.013mm), the flow near the tip did indicate a somewhat reduced radial component, but there was no influence at midspan. Thus, tip clearance can contribute to radial flow in the immediate vicinity of the tip of an airfoil, however, radial flow can also come about as a result of other mechanisms.

One such possible mechanism is inviscid secondary flow. As Hawthorne [10] pointed out, secondary flows are produced in the rotating frame by gradients in rotary total pressure. A gradient in rotary total pressure in the rotating frame is analogous to a gradient in total pressure in the nonrotating frame. In order to determine whether or not a rotary total pressure gradient was present in the incident flow, a total pressure rake was mounted on the rotor hub with five Kiel probes between 8 and 92 percent span. The relative total pressures measured are shown in Fig. 3, and the corresponding rotary total pressures are also shown. The spanwise distribution of rotor inlet rotary total pressure is relatively uniform, varying by approximately ±5 percent of the rotor inlet relative dynamic pressure, and it has no monotonic gradient from hub to tip as one might have expected from the flow visualization. Thus, it seems unlikely that the radial flows are an inviscid secondary flow effect.

In an attempt to better understand the blade flows, the pressure distribution was measured around the perimeter of the airfoil and at five spanwise locations from 12.5 percent span (near the hub) to 87.5 percent span (near the tip). The data are shown in Fig. 4 (the symbols) in terms of a pressure coefficient versus percent axial chord. It is convenient here to use a pressure coefficient based on the blade exit static pressure ($P2$) as a reference pressure and the difference between the inlet relative total pressure and the exit static pressure ($P\mathrm{T}1-P2$) as a normalizing pressure difference. The exit static pressure was determined by applying an adjustment to the static pressure measured on the rig casing at the rotor exit. This adjustment was based on the assumption of free vortex flow and is approximately 1 percent of the exit relative dynamic pressure. Also indicated in Fig. 4, are potential flow predictions based on the analysis of Caspar, et al. [11]. This is a two-dimensional calculation based on finite area techniques,

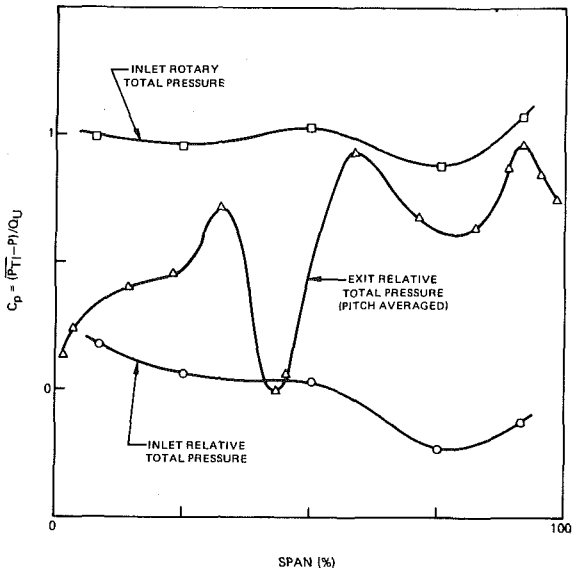

Fig. 3 Spanwise distribution of the rotor inlet and exit total pressure

and it includes the effect of radial stream tube contraction. The predictions were carried out by varying the inlet and exit flow angles until best agreement had been obtained. The resulting angles are tabulated in Fig. 4 and are shown in Fig. 5. In the calculation, the stream tube radial contraction or divergence was obtained from a through-flow calculation carried out for this turbine rig. In all cases, it was found that the measured pressure surface maximum pressures were slightly lower than one would have expected from the measured rotor inlet total pressures. The difference was about 1 percent of the rotor exit relative dynamic pressure. This may be related to the radial flows occurring between the Kiel probe (at 0 percent chord) and the maximum pressure location at (30 percent chord).

Generally speaking, excellent agreement was obtained between the measured and computed pressure distributions at all span locations. One might question how a two-dimensional calculation could do so well in such a clearly three-dimensional flow. This is not so surprising when one considers that the pressure surface dynamic head on the

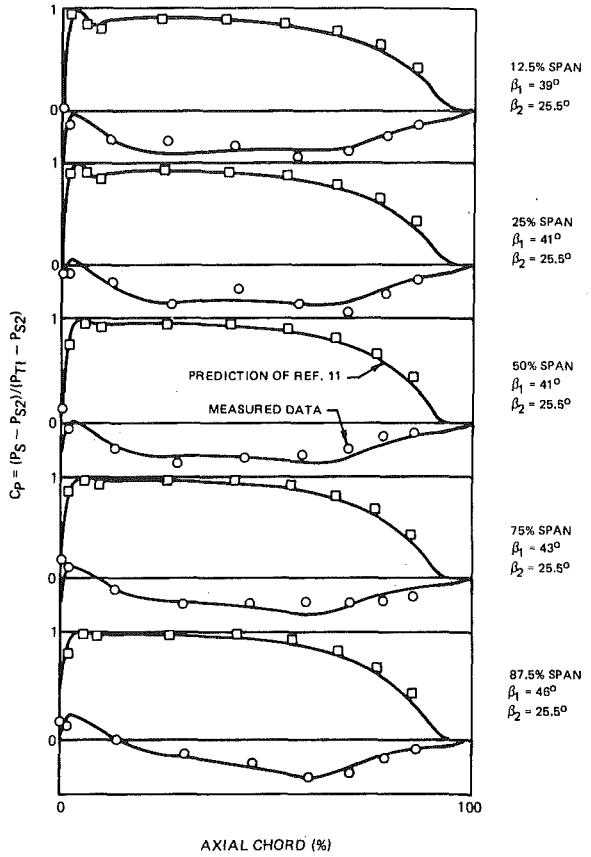

Fig. 4 Spanwise distribution of the blade pressure distribution

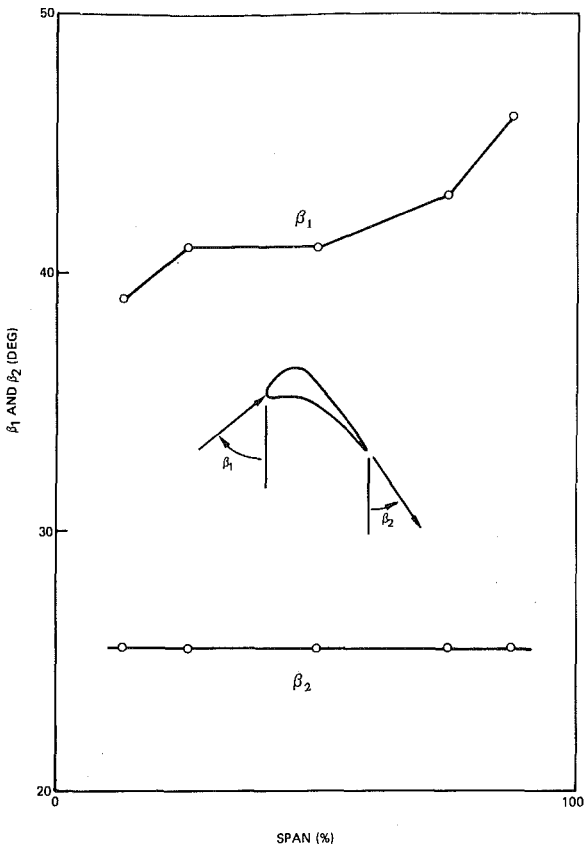

Fig. 5 Deduced relative inlet and exit flow angles

forward half of the airfoil is a very small fraction of the exit dynamic head. In addition, the radial flow component comprises a relatively small portion of the local pressure surface dynamic head. Thus, it would not be expected to have a significant effect on the airfoil pressure distribution.

The rotor pressure surface static pressure distribution was examined to provide some insight into the source of the radial flow. Contours of rotary static pressure coefficient are shown in Fig. 6 for a region on the pressure surface near the leading edge. The arrow indicates the local flow direction at the pressure surface blowing site of [2]. The flow is almost normal to the contours and in the direction of increasing rotary static pressure. This would tend to rule out any explanation such as the flow simply following a pressure gradient.

Since the pressure surface radial flow does not appear to be caused by either centrifugal effects, tip clearance effects or by secondary flow, one is left with the possibility that its source is in the three-dimensional inviscid flow over the airfoil. Without a fully three-dimensional flow analysis, it would be difficult to say with certainty what aspects of the airfoil design might have produced the radial flow. It seems safe to say that they are in part a result of the very low pressure surface velocities and that if the local flow velocity was increased in this area, the radial component would be reduced.

Having considered the nature of the three-dimensional flow on the pressure surface, let us now turn our attention to the suction surface. Surface flow visualizations of the suction surface leading and trailing edge regions are shown in Fig. 7. Here again, the ammonia/ozalid technique has been used. In the leading edge region, the ammonia was injected close to the stagnation point which is in fact located on the pressure surface (Fig. 4). The flow rapidly accelerates around the leading edge to the suction surface where it negotiates the suction surface leading edge over-speed (Fig. 4) without the occurrence of a separation bubble. It can be seen that the suction surface leading edge flow has practically no radial component. This is due to the fact that the flow speed here is very high, approximately five times the speed on the forward portion of the pressure surface.

In the trailing edge region of the suction surface, the picture is quite

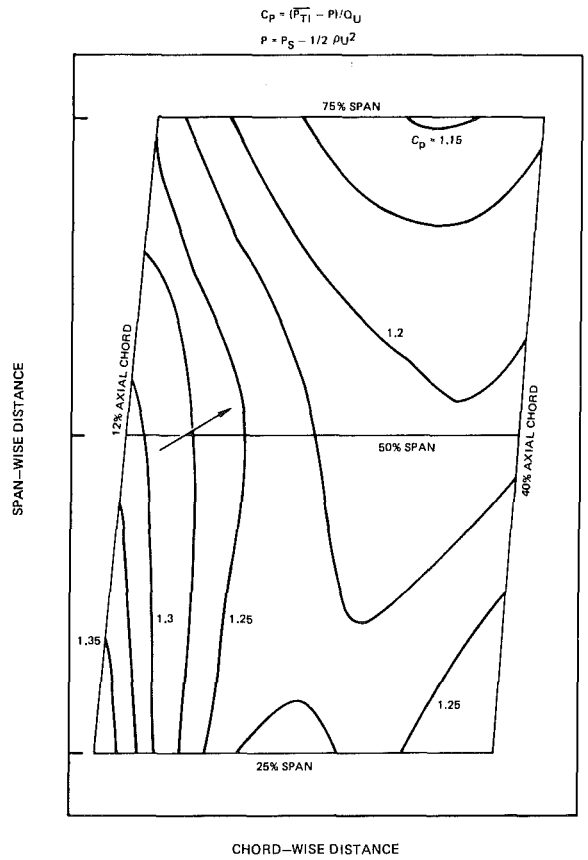

Fig. 6 Contours of rotary static pressure on the blade pressure surface

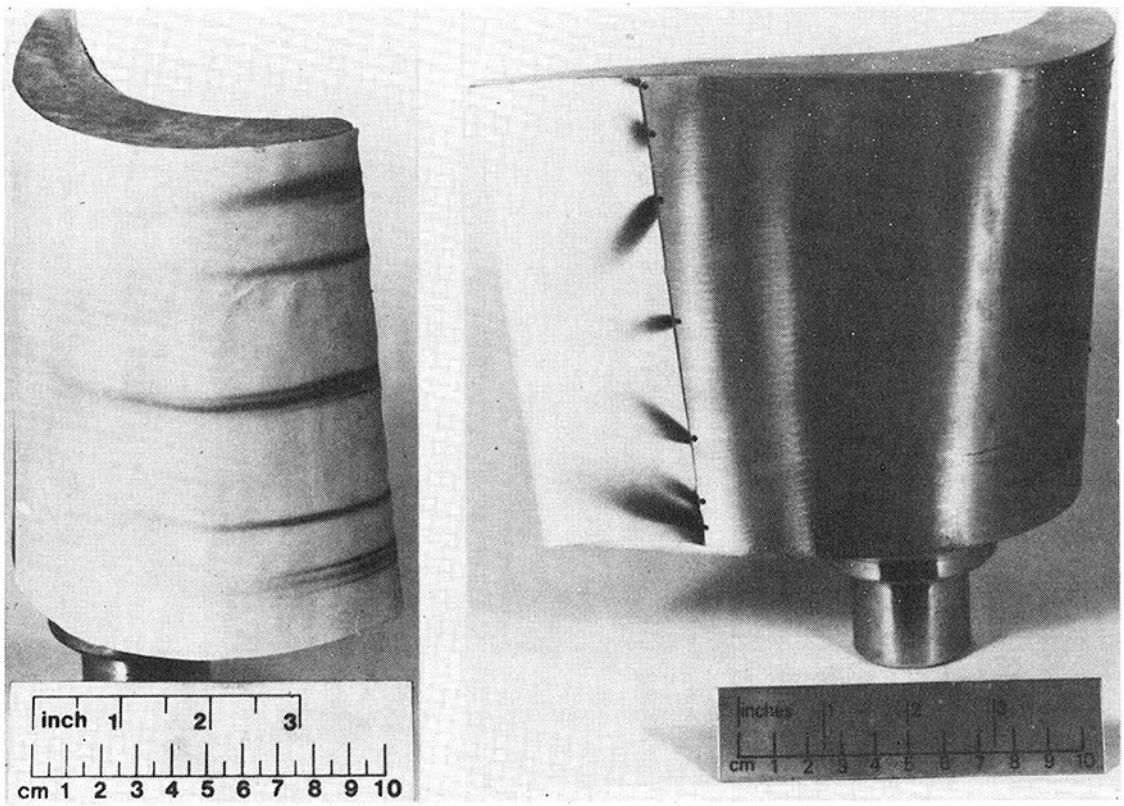

Fig. 7(*a*) Leading edge region

Fig. 7(*b*) Trailing edge region

Fig. 7 Suction surface flow visualization results

different. The ammonia here has been injected just downstream of the channel throat. The surface flows here have a large radial component toward the midspan region. These are a result of the hub and tip endwall vortices [12]. The ammonia injected at midspan had a slight radial component toward the hub, indicating that the vortex pattern is symmetric about approximately the 45 percent span location. It is also apparent that the tip flow is somewhat different from that at the hub. This is due to the tip leakage vortex. The pressure driven flow that leaks through the tip gap (0.085 in., (2.2mm) clearance) produced a tight vortex at the tip of the opposite sign to the tip endwall vortex. This can be seen to cause the surface flow very near the tip to be moving radially outward. Thus, in contrast to the pressure surface where the source of the radial flow appears to be inviscid three-dimensional flow, the radial flows on the suction surface are due to tip leakage and endwall secondary flow. In this respect, they are the same as what one would have expected from cascade results such as those of Langston, et al. [12]. It is interesting to note, however, that reasonably good agreement for the computed pressure distributions was obtained with a constant exit angle (Fig. 5), i.e., without any influence of over-turning and/or underturning due to the endwall vortices.

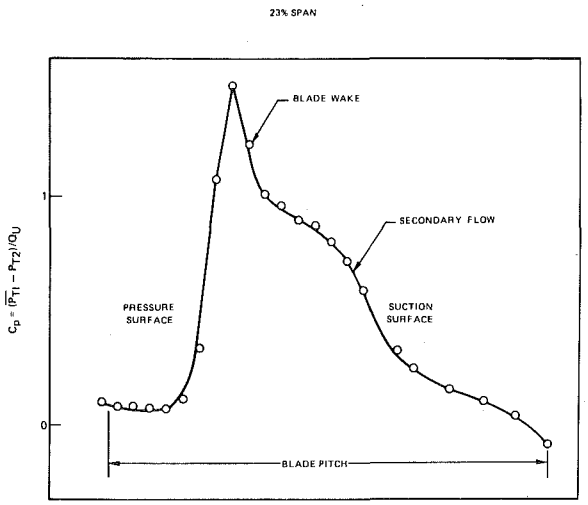

Fig. 8 Circumferential variation in relative frame total pressure at blade exit

Another clear indication of the three-dimensional nature of the flow over the rotor blade can be seen in the measurement of the relative total pressure at the rotor exit. A Kiel probe was traversed over a radial/circumferential array of locations to provide a detailed picture of the rotor wake. Fourteen circumferential traverses were carried out from 2 percent span to 98 percent span with typically 22 measurements across a blade pitch. The traversing was carried out close to the blade trailing edge (6.8 percent axial chord aft) with a probe that was small relative to the blade pitch (Kiel shroud diameter 2 percent of pitch). The result is a rather detailed picture of the rotor wake. A typical circumferential traverse is shown in Fig. 8. The data show the narrow blade wake as well as an accumulation of low relative total pressure fluid in the suction surface endwall vortex. The nature of the flow becomes clearer when all of the circumferential traverses are combined to form a composite contour plot (Fig. 9). The dominant feature of the flow is the hub and tip endwall vortices. They virtually fill the passage, and they are approximately symmetric about the 45 percent span location. The high loss fluid has moved off the end-walls toward midspan and has been replaced by relatively low loss fluid. In addition, there is a concentrated region of high loss fluid near the tip due to the tip leakage flow. These measured rotor exit flow patterns of high and low loss fluid correspond closely to what was observed in the suction surface flow visualization. These results also compare well with those of reference [12] (Fig. 7) for a plane cascade of very similar geometry. However, comparison with the annular cascade results of Goldman and McLallin ([13], Fig. 11) for a turbine inlet guide vane shows significant differences. Doubtless, much of the difference is tied to the fact that the present airfoil has an inlet angle of typically 42 deg whereas the vane of reference [13] has axial inlet (90 deg) and, hence, a much higher flow convergence in the cascade. Due to the high absolute swirl (high radial static pressure gradient) in the flow leaving

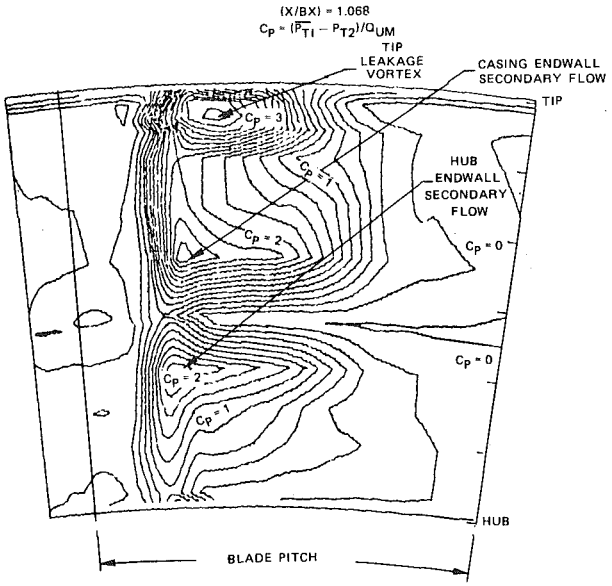

Fig. 9 Relative frame total pressure contours downstream of tubine rotor blade (X/BX) = 1.068

the annular cascade, the hub and tip end-wall loss regions migrate toward the hub. In contrast, the endwall loss region aft of the rotor is nearly symmetric about midspan due to the low absolute swirl there (low radial static pressure gradient). In fact, the rotor exit endwall loss regions are very similar to those in the plane cascade of Ref. 7 where there was no exit radial (spanwise) static pressure gradient.

The exit plane data have been circumferentially area averaged in order to more clearly illustrate the nature of the spanwise variation of relative total pressure. The results are shown in Fig. 3. Again, it can be seen that the endwall loss concentrations are symmetric about approximately 45 percent span and that the tip leakage loss is concentrated at 90 percent span. The fluid near the hub and that at 45 percent span has relatively high total pressure, and in fact, it is higher than that of the inlet flow at these radial locations. This is probably a result of radial redistribution of the flow in the channel (Fig. 2). These pitch averaged results may be contrasted with those of the annular cascade of reference [13] (Fig. 13). Even ignoring the effect of the rotor tip leakage loss, there is a considerable difference between the spanwise loss distributions of the rotor and the stator due primarily to the different levels of absolute swirl.

Conclusions

This study has pointed out (1) the value of large scale low speed rotating rig testing and (2) the value of an extensive rotating frame measurement capability. The ability to carry out rotating frame flow visualization, pressure measurements, and traverse measurements has led to a better understanding of the nature of the three-dimensional flow over a turbine rotor blade. It was demonstrated that two-dimensional potential flow calculations can give a reasonably accurate prediction of the blade pressure distribution even in the presence of strong three-dimensional effects on both the suction and pressure surfaces. Finally, it has been shown that spanwise migration of high loss fluid can be considerably different in the rotating and stationary frames of reference.

References

1 Greitzer, E. M., Nikkanen, J. P., Haddad, D. E., Mazzawy, R. S., and Joslyn, H. D., "A Fundamental Criterion for the Application of Rotor Casing Treatment," ASME *Journal of Fluids Engineering*, Vol. 101, No. 2, 1979, p. 237.

2 Dring, R. P., Blair, M. F., and Joslyn, H. D., "An Experimental Investigation of Film Cooling on a Turbine Rotor Blade," ASME JOURNAL OF ENGINEERING FOR POWER, Vol. 102, No. 1, pp. 81–87.

3 Lakshminarayana, B., "Visualization Study of Flow in Axial Flow Inducer," ASME *Journal of Basic Engineering*, 1972, p. 777.

4 Lakshminarayana, B., Jabbari, A., and Yamaoka, H., "Turbulent Boundary Layer on a Rotating Helical Blade," *Journal Fluid Mechanics* Vol. 51, Part 3, 1972, pp. 545–569.

5 Lakshminarayana, B., "Three-Dimensional Flow Field in Rocket Pump Inducers, Part 1: Measured Flow Field Inside the Rotating Blade Passage and at the Exit," ASME *Journal of Fluids Engineering*, 1973, p. 567.

6 Anand, A. K., and Lakshminarayana, B., "Three-Dimensional Turbulent Boundary Layer in a Rotating Helical Chennel," ASME *Journal of Fluids Engineering* 1975, p. 197.

7 Ruden, P., "Investigation of Single Stage Axial Fans," NACA RM No. 1062, Apr. 1944.

8 Johnston, J. P., "A Wall-Trace Flow Visualization Technique for Rotating Surfaces in Air," ASME *Journal of Basic Engineering*, 1964, p. 907.

9 Day, W. H., "Boundary Layer Characteristics on the Buckets of a Large-Scale Turbine Stage Part 1: Profiles of Mean and Turbulent Velocity Vectors," ASME Paper No. 70-GT-59, 1970.

10 Hawthorne, W. R., "Secondary Vorticity in Stratified Compressible Flow in Rotating Systems," Cambridge University, CUED/A—Turbo/TR 63, 1974.

11 Caspar, J. R., Hobbs, D. E., and Davis, R. L., "The Calculation of Two-Dimensional Compressible Potential Flow in Cascades Using Finite Area Techniques," *AIAA Journal*, Vol. 18, No. 1, 1980, p. 103.

12 Langston, L. S., Nice, M. L., and Hooper, R. M., "Three-Dimensional Flow Within a Turbine Cascade Passage," ASME JOURNAL OF ENGINEERING FOR POWER, 1977, pp. 21–28.

13 Goldman, L. J., and McLallim, K. L., "Cold-Air Annular-Cascade Investigation of Aerodynamic Performance of Core-Engine Cooled Turbine Vanes. I—Solid Vane Performance and Facility Description," NASA TM X-3224, Apr. 1975.

N. Sitaram
Graduate Assistant.

B. Lakshminarayana
Professor.

A. Ravindranath
Graduate Assistant.

Department of Aerospace Engineering,
The Pennsylvania State University,
University Park, Penn. 16802

Conventional Probes for the Relative Flow Measurement in a Turbomachinery Rotor Blade Passage

This paper reports the measurement of the relative flow in the rotor blade passages of an axial-flow compressor and an axial-flow inducer using conventional probes such as five-hole, disk, and spherical pitot-static probes. The five-hole probe provides an inexpensive, yet accurate, method of deriving the three-dimensional flow field in a rotor; the disc probe is suitable for the blade boundary-layer measurement; and the pitot-static probe is useful for obtaining the static and stagnation pressures and the total velocity across the rotor passage. Typical data obtained from each of these probes demonstrate the complex nature of the turbomachinery rotor flow. A detailed discussion of various sources of probe errors and methods of estimating these errors is also included.

Introduction

Lack of understanding of flow structure in the rotor blade passage of a turbomachinery is a serious handicap for turbomachinery analysis and design. The flow in the rotor blade passage is complex due to the effects of coriolis and centrifugal forces, viscosity in the annulus wall and blade boundary layers, and secondary and tip clearance flows in the endwall regions. Theoretical analysis of flow in the rotor blade passage is complicated due to strong interaction of boundary layers on the rotor blade with the annulus wall boundary layer, and with secondary and tip clearance flows. Hence, experimental information on the flow in the rotor blade passage is essential for improvements in the three-dimensional analysis, design, and efficiency of the turbomachinery. The laser doppler anemometer (LDA) has been successfully used to measure these flows. The advantages of LDA (such as measurements of velocities and turbulence quantities using a stationary system) are offset by its inability to measure flow in the blade "shadow" region and blade boundary layer, its inability to measure pressures, and its high cost. Hence, for measurement of flow in the rotor blade passages, conventional and hot-wire probes in the rotating system are suitable. The conventional probes have an added advantage of measuring velocities and pressures, whereas the hot-wire probes cannot measure static and stagnation pressures. Moreover, the conventional probes are rugged and withstand vibrations. This method requires development of a sophisticated rotating probe traverse mechanism, data transmission system, and suitable probes. In this paper, this method is described and measurements taken in the endwall and wake region of an axial-flow compressor with conventional probes (rotating with the rotor) are presented. Also, errors involved due to various sources are recognized, and necessary corrections to be applied to the experimental results are discussed.

Contributed by the Gas Turbine Division and published in the symposium volume, *Measurement Methods in Rotating Components of Turbomachinery*, ASME, New York, 1980. Manuscript received for publication in the JOURNAL OF ENGINEERING FOR POWER May 22, 1980.

Experimental Equipment and Methods

The single-stage axial-flow compressor facility of the Department of Aerospace Engineering at The Pennsylvania State University is used in the present experimental investigation. A detailed description of the facility, along with its unique rotating-probe traverse mechanism to measure relative flow inside and at the exit of the rotor blade passage, is provided in reference [1]. Only a brief description of the rotating-probe traverse mechanism, along with modifications necessary for rotor endwall flow measurement, is given here.

The rotating-probe traverse mechanism, described and shown in Fig. 2 of reference [2], traverses the probe in the tangential direction in steps of 0.09 deg and is controlled remotely. The axial and radial movements of the probe are manual. For measurements inside the passage, the probe head length becomes long. Hence, the probe is supported at the leading as well as at the trailing edge of the blade. This arrangement avoids the radial displacement of the probe due to centrifugal forces. The support consists of a bracket fastened to the hub near the blade leading edge. This arrangement allows flow measurement from leading to trailing edge of the blade, from suction surface to pressure surface, and from hub to tip. Measurements in successive blade passages can be made to determine the nonperiodic nature of the flow. Since the rotating-probe traversing mechanism is not capable of aligning the probes with the flow direction, which is varying across the rotor blade passage, only pre-calibrated probes (such as hot-wire probes, five-hole probes and three-hole probes) and probes insensitive to flow direction (such as sphere probes) can be used.

The pressure signals from the conventional probes are converted into electrical signals by means of a rotating pressure transducer (Fig. 8 of reference [2]). This transducer, which is a part of the data transmission system, is used to simplify the measurement of the pressure from a multi-tube probe (such as a five-hole probe) or blade static or wall static pressure. A rotating scanivalve allows the use of the same output channel for the measurement of multi-tube pressures.

The other components of the data transmission system (reference

[1]) consist of an eight-channel brush slip-ring unit used for power transmission and control of the step motor inside the rotating traverse mechanism; a three-channel pressure transfer device (PTD) for transferring rotating pressures through a scanivalve to a stationary transducer or manometer; a ten-channel mercury slip-ring unit used for distortion-free transmission of electrical signals from pressure transducers, hot wire probes or wall shear stress gages; and a photocell unit for the accurate measurement of the rotor speed.

The data transmission system along with the rotating-probe transverse mechanism is used to measure the relative flow inside and exit of the rotor blade passage by means of a five-hole probe and a sphere probe. This paper also reports measurement of the boundary layer on a rotating blade of an axial-flow inducer, using a disk probe. The probe traverse and transmission of pressure signals are achieved by means of a rotating-probe traverse mechanism and data transmission system similar to those described above. Details of the inducer facility are given in reference [3].

Five-Hole Probe

Five-hole probes are extensively used for measuring three-dimensional flows. The relative ease of acquiring data and its reduction, and non-nulling mode of operation of the probe, makes it very useful. Various methods of reducing the five-hole probe data are available [4, 5]. Basically, the calibration technique consists of measuring pressures from the five tubes at various pitch and yaw angles. The pressures are presented in nondimensionalized coefficients, and these calibration curves are used for interpolation and determination of static and stagnation pressures, total velocity, and yaw and pitch angles. Typical application of five-hole probes (nonrotating) in the measurement of flow at the compressor exit are described in references [6] and [7]. Recently a five-hole probe was used to measure the nonsteady three-dimensional flow downstream of an impeller [8]. The five-hole probe had not been used earlier, in rotating mode, inside a rotor passage to measure the relative flow.

When a pressure probe (three-hole, five-hole, etc.) is used to measure flow with a steep velocity or pressure gradient (e.g., boundary layers on rotor blades and annulus walls, and tip leakage and secondary flow vortices), the holes of the probe measure pressure at different locations. A simplified analysis of this error, and a method of correction is given for a three-hole probe in reference [9] and for a five-hole probe in the last section of the paper.

The response of a pressure probe is affected by the fluctuations (turbulence and unsteady flow) in the flow due to the nonlinear response of the probe. Ignoring these effects introduces errors in the results. A simplified analysis to take this into effect in pitot probe measurements is given in the last section of the paper.

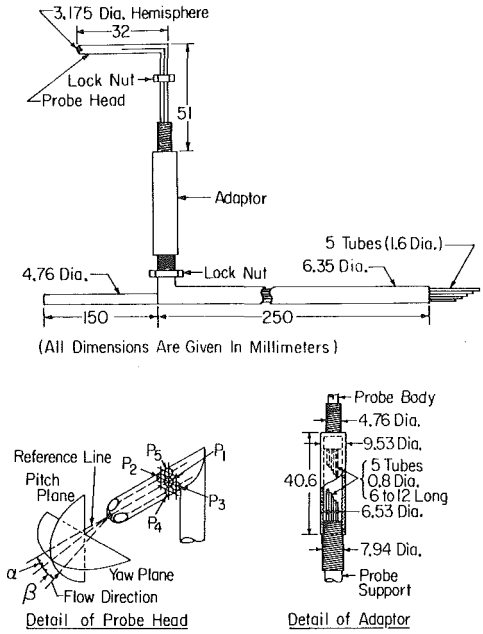

Fig. 1 Hemispherical five-hole probe

Probe Description, Calibration and Errors. The details of the five-hole probe used for the rotor endwall flow measurements is shown in Fig. 1. The probe is manufactured by the United Sensor Corporation. The probe head is a 3.17 mm (0.125 in.) dia hemisphere and has four holes at 45 deg to the axis of the probe head in two mutually perpendicular planes. A central hole is drilled along the axis. The pressures measured by these five holes are used to determine the three-dimensional flow field (i.e., stagnation and static pressures, total velocity, and yaw and pitch angles) by interpolation of calibration curves.

The probe is calibrated in the 30.5 cm dia open-jet facility of the Garfield Thomas Water Tunnel of The Pennsylvania State University. While calibrating the probe, it is kept in the uniform region of the jet. The probe is calibrated in intervals of 10 deg from −20 to 20

Nomenclature

c = blade chord, m(ft)
C_{p_0} = stagnation pressure coefficient, $(P_{0_2} - P_{0_1})/\frac{1}{2}\rho U_t^2$
$C_{p_{\text{pitch}}} = (P_4 - P_5)/D$
C_{p_s} = static pressure coefficient, $(p_2 - p_1)/\frac{1}{2}\rho U_t^2$
$C_{p_{\text{static}}} = (\overline{P} - p)/D$
$C_{p_{\text{total}}} = (P_1 - P_0)/D$
$C_{p_{\text{yaw}}} = (P_2 - P_3)/D$
$D = P_1 - \overline{P}$
d = diameter of five-hole probe, m(ft)
d_h = hole diameter, m(ft)
K = calibration constant for sphere probe
K_1, K_2, K_3, K_4, K_5 = calibration constants in the error analysis (equations (4–7))
L = nondimensional distance from the centerline of the wake, $2Z/s$
P_0 = stagnation pressure, m(ft) of water
P_1, P_2, P_3, P_4, P_5 = pressures indicated by five-hole probe tubes (see Fig. 3) m(ft) of water
$\overline{P} = (P_2 + P_3 + P_4 + P_5)/4$
p = static pressure, m(ft) of water
p_w = pressure behind the sphere of the sphere probe, m(ft) of water
q = turbulent velocity fluctuation
r = radius, m(ft)
r_0 = radius of pressure transfer device, m(ft)
R = nondimensionalized radius, r/r_t
R_d = Reynolds number based on probe diameter
s = blade spacing, m(ft)
U = blade velocity, m/s (ft/s)
V = velocity, m/s (ft/s)
W = relative velocity, m/s (ft/s)
W_0 = maximum relative velocity, m/s (ft/s)
x = distance from blade leading edge along chordline, m(ft)
Y = distance from pressure surface of blade, m(ft)
z = distance from flat plate, m(ft)
z = normalized distance from blade trailing edge $(x/c - 1)$
Z = distance from the center line of the wake, m(ft)
α = pitch angle, deg
β = yaw angle, deg
ϵ = error in the pitch or yaw angle due to the effects of pressure and velocity gradients
ϵ_v = error in velocity
ω = angular velocity of rotor, radians/s
ρ = density, gm/cm^3 (lbm/ft^3)
ψ_0 = relative stagnation pressure coefficient normalized by the dynamic head based on tip velocity, $(P_0 - P_{\text{atm}})/\frac{1}{2}\rho U_t^2$
ψ_s = static pressure coefficient normalized by the dynamic head based on tip velocity, $(p - p_{\text{atm}})/\frac{1}{2}\rho U_t^2$

Subscripts

a = actual
atm = atmospheric
p, s = pressure and suction sides, respectively
r, θ, z = radial, tangential and axial directions
t = tip
1, 2 = rotor inlet and exit, respectively

Superscript

— = values in the absence of turbulence, velocity and pressure gradients

deg in both the yaw and pitch planes. The calibration and interpolation methods are described in reference [6]. Typical calibration curves of this probe in a jet velocity of 34 m/s are shown in Fig. 2.

While calibrating the probe, it was observed that the calibration characteristics vary with Reynolds number. Hence, the probe is calibrated at various jet velocities. Figure 3 shows a plot of various coefficients at a yaw angle $\beta = -10$ deg and various pitch angles, and at various Reynolds numbers (based on jet velocity and spherical probe head diameter). For this particular probe, the variation of the calibration coefficients with the Reynolds number is negligible. For the prism probe, the calibration coefficients, especially $C_{p_{static}}$, varies considerably. Typical variation of calibration coefficients for the prism probe is given in reference [6]. The prism probe is very sensitive to the Reynolds number compared to the spherical head probe employed in this paper for relative flow measurement.

This probe (Fig. 1) is also used to measure flow near the rotor blade. Hence, the probe readings are affected by the interaction of the probe and the blade surface. This effect, known as wall vicinity effect, gives inaccurate results near solid surfaces such as blade surface and annulus wall encountered in turbomachinery. In order to evaluate this effect, measurements are made with the probe axis parallel to a knife-edged plate in a jet. The probe is moved normal to the plate. The velocity and pressure data derived from these measurements are compared with those obtained from a very small (0.59 mm dia) pitot probe. Since the thickness of the boundary layer is small, the flow is uniform over the plate. Wall static pressure is atmospheric and is used to compare with the static pressure obtained from the five-hole probe. The results of the experiment on the wall vicinity effect are shown in Fig. 4. The stagnation pressure is fairly constant. The flow accelerates, resulting in increased velocity, due to the presence of the probe near the wall. Hence, the probe measures higher than actual velocity. The error in velocity is less than 1 percent when the probe is two or more diameters away from the wall. The error in velocity is defined as

$$\epsilon_v = \frac{V}{V_a} - 1$$

Discussion and estimation of other sources of errors are described in the section on "Sources of Errors and Estimation of Their Magnitude."

Measurement of Relative Flow in Rotor Blade Passage. The non-nulling mode of operation of the five-hole probe makes it very suitable to measure the relative flow in an axial-flow compressor rotor blade passage, where nulling of the probe in either yaw or pitch plane is very difficult. The method of measuring relative flow in a rotor blade passage is described in the previous section. This method is used to measure relative flow in the rotor blade endwall flow region at various axial and radial stations tabulated in Table 1. The blade profiles are modified from the NACA 65-010 basic profile with a circular arc camber. The blade has varying stagger angle and chord along its span. The blading details are given in reference [2]. The rotor was operated at a flow coefficient of 0.56.

The measurements taken at $R = 0.959$ are shown in Fig. 5. A slight jump in the data near the mid-passage may have been caused by a small radial displacement of the probe, when the probe was traversed from the pressure surface to mid-passage and from the suction surface to mid-passage. This measurement procedure was necessitated due to the rotor blade twist. All five-hole pressures are corrected for the effect of rotation by taking the actual radii of the holes into account. The correction is as follows.

$$P_i = P_i' + \frac{1}{2}\rho\omega^2(r_i^2 - r_0^2) \qquad (1)$$

where P_i' = pressure of the i^{th} hole of five-hole probe measured by the rotating pressure transducer, m(ft) of water. P_i = pressure of i^{th} hole of five-hole probe corrected for effect of rotation, m(ft) of water. r_i = radius of rotation of i^{th} hole of five-hole probe, m(ft). r_0 = interface radius of the pressure transfer device (when a rotating pressure transducer is used, $r_0 = 0$). ω = angular velocity of rotor, rad/s.

After the pressures P_i are obtained applying the correction for the effect of rotation, these values are used to determine static and stag-

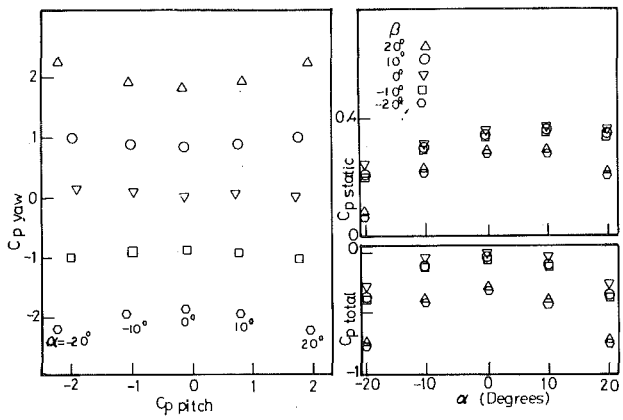

Fig. 2 Calibration curves of the hemispherical five-hole probe (velocity V = 34 m/s)

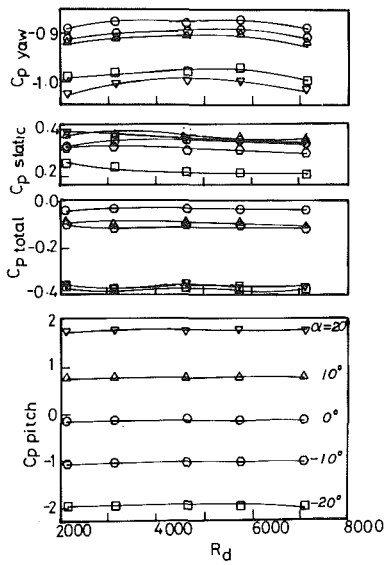

Fig. 3 Reynolds number effect for the hemispherical five-hole probe (yaw angle $\beta = -10$ deg)

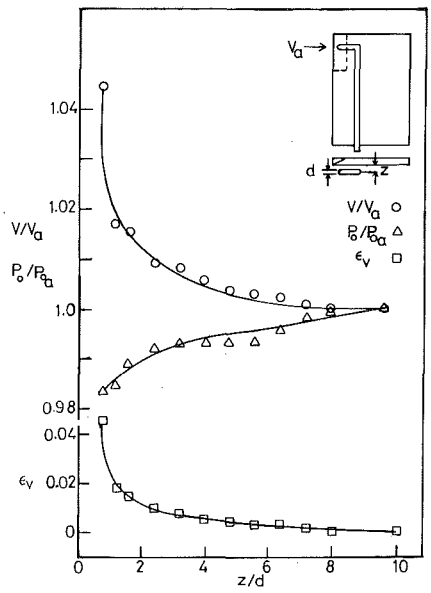

Fig. 4 Wall vicinity effect for the hemispherical five-hole probe (velocity V = 34 m/s)

nation pressures, and relative total, axial, relative tangential, and radial velocities using the interpolation scheme described in reference [6]. During the experiment, the probe was monitored for vibrations by means of a stroboscope. The probe vibration was found to be negligible.

Blade-to-blade distribution of pressures and velocities at radius $R = 0.959$ are shown in Figs. 5(a) and 5(b). Strong endwall flow effects (secondary flow and tip leakage vortex) are seen at this radius, especially at axial stations $x/c = 0.5$, 0.75 and 1.01. At axial stations $x/c = 0$ and 0.25, the potential flow effects persist. The leakage vortex formation takes place between $x/c = 0.5$ and 0.75. This results in defect in the stagnation pressure and total velocity in the blade mid-passage region (Fig. 5(a)). The stagnation pressure is nearly uniform at $x/c = 0$. The distribution at $x/c = 0.25$ shows a tendency towards lower values near the mid-passage, similar to the effect observed in reference [3] for an inducer. Drastic changes take place beyond $x/c = 0.5$. The formation of the vortex near the suction surface and wake at the trailing edge is clearly seen. The stagnation pressure losses are also high. The static pressure distribution shown in Fig. 5(b) seems to be mainly influenced by the inviscid effect, except at the trailing edge, where an increase in the static pressure across the wake is observed. This trend is similar to those reported in references [10] and [11]. A qualitative analysis of of the reasons for the increase in static pressure across the wake is given by Reynolds [10].

Table 1 Five-hole probe endwall flow measuring stations

R	Percent Span	Axial location from leading edge, x/c				
0.986	97.2	—	0.25	0.5	—	—
0.973	94.6	0	0.25	0.5	0.75	—
0.959	91.8	0	0.25	0.5	0.75	1.0
0.946	89.2	0	0.25	0.5	0.75	1.0
0.918	83.6	0	0.25	0.5	0.75	—

The wake at $R = 0.959$ is quite thin and is well defined, the total velocity from $x/c = 0$ to $x/c = 0.5$ is rather well behaved (Fig. 5(a)). The interaction effect at mid-passage is clearly seen in Fig. 5(a). The complex interaction of the blade boundary layer, the secondary flow, and the leakage flow result in a wake type of profile at the mid-passage [3, 12]. The radial velocity is outward and nearly uniform across the passage at most locations (Fig. 5(b)).

Comparison with Tri-Axial Hot-Wire Probe Measurements. The total velocity and the velocity components obtained from the five-hole probe and a rotating tri-axial hot-wire probe [13] very near the trailing edge of the rotor blade ($x/c = 1.01$) and $R = 0.959$ are compared in Figs. 5(c) and 5(d), respectively. The agreement between the total velocity distributions obtained from the five-hole probe and hot-wire probe measurement is very good. This is quite surprising in view of the fact that neither set of data is corrected for various possible sources of errors discussed later. The hot-wire data are corrected only for deviation from the cosine law and calibration changes due to wire

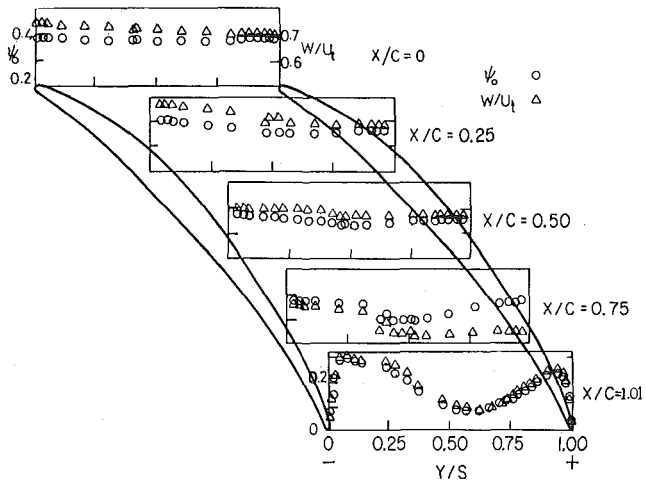

Fig. 5(a) Relative stagnation pressure coefficient, ψ_0 and relative total velocity, W/U_t

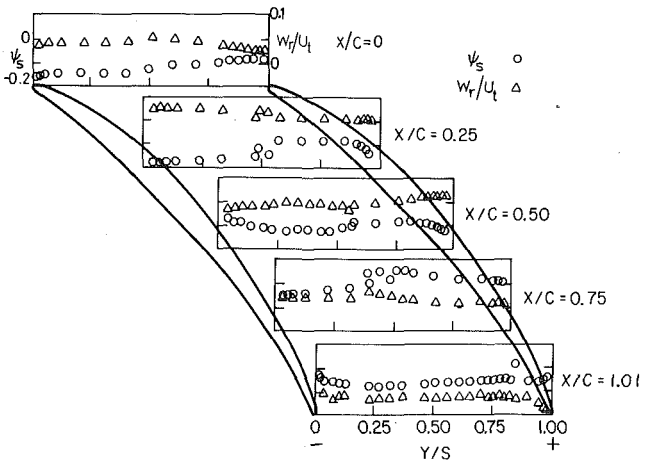

Fig. 5(b) Static pressure coefficient, ψ_s and radial velocity, W_r/U_t

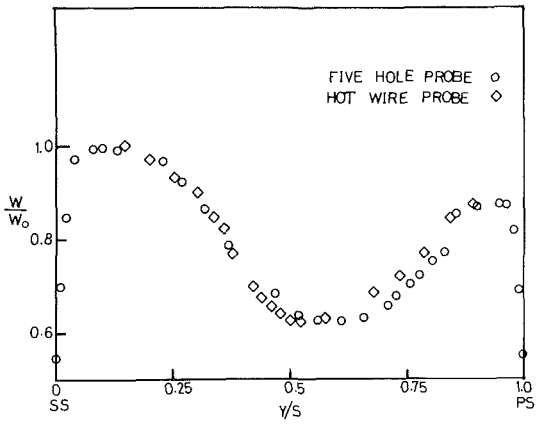

Fig. 5(c) Comparison between tri-axial hot-wire probe and five-hole probe—relative total velocity at $x/c = 1.01$

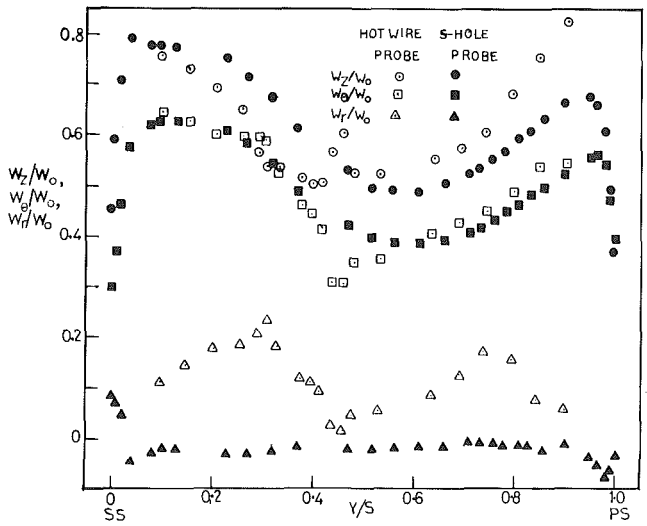

Fig. 5(d) Comparison between tri-axial hot-wire probe and five-hole probe—relative velocity components at $x/c = 1.01$

Fig. 5 Blade-to-blade distribution of flow properties in the rotor blade passage of an axial-flow compressor at $R = 0.959$ and $\phi = 0.56$

aging and temperature drift. The agreement between the two measurements is quite good for axial and tangential relative-velocity distributions. The hot-wire probe is very sensitive to both the random and periodic fluctuations in the flow, and thus measures the mean velocities more accurately compared to the five-hole probe, whose response to the fluctuating flow is slow. However, major discrepancy is observed in the radial velocity measured by the two probes. The radial velocity measured by the five-hole probe is uniform except in the wake region, whereas the hot-wire probe measurements indicate a nonuniform radial-velocity profile. One possible reason for this discrepancy may be the inaccuracy in measurement of orientation of both the probes and angles of the hot-wire probe sensors. The inaccurate measurement of probe orientation shifts the flow angles in both yaw and pitch planes by a constant amount for all the measuring stations.

Disk Type Boundary-Layer Probe

Probe Description and Calibration. A three-hole disk probe (Fig. 6) is used to measure the total pressure and pitch angle. This probe is suitable for boundary layers, where the flow vector is nearly parallel to the surface and deviates only in the spanwise or radial direction. The method of traversing the probe and transmitting the probe signals is very similar to those described in the earlier section and described in detail in reference [3]. The disk probe is 6.35 mm (0.25 in.) in diameter and 1.6 mm (0.063 in.) thick. Three holes 0.8 mm (0.032 in.) diameter each were drilled circumferentially on the disk and 45 deg to each other form the sensing area (Fig. 6). The central hole measures stagnation pressure (approximately) and the top and lower holes determine the static pressure and the pitch angle. The disk probe has a number of advantages over a conventional five-hole probe for measurements close to the blade. It can be easily aligned parallel to a blade surface, produces less flow distortion, and the response is linear in the range of angle ±30 deg.

Extensive study of boundary layers on the blade surfaces of an axial-flow inducer rotor has been carried out using this probe. In order to evaluate the accuracy of the disc probe in such flows, the following experimental study is undertaken. The disk probe is calibrated in the open-jet facility of the Garfield Thomas Water Tunnel of The Pennsylvania State University at various yaw angles and jet velocities. The pitch angle is varied from −30 to 30 deg and all of the three-hole pressures are measured. These pressures are plotted in a normalized form and are used to determine the static and stagnation pressures, and the total streamwise and radial velocities. A typical calibration curve (pitch coefficient ($C_{p_{\text{pitch}}}$) versus pitch angle (α)) at various yaw angles at a jet velocity of 34 m/s is shown in Fig. 7. It is clear that the pitch coefficient at a particular pitch angle is practically constant at all yaw angles. Note that $\beta = 0$ degrees corresponds to disc probe in two-dimensional flow, and $\beta \neq 0$ deg corresponds to the disc probe in three-dimensional flow.

Since the probe is used at conditions other than those employed for calibration, an error estimate was carried out using the data plotted in Fig. 7. One of the cases chosen was that of using the calibration curve at $\beta = 0$ and at $V = 34$ m/s in a flow where β and V are different. The data plotted in Fig. 8 shows that the error is small for mild three-dimensional flow (β variation ±10 deg). In most cases, the rotor boundary-layer flows are nearly parallel to the blade surface, with little variation in yaw angle inside the boundary layer. Hence, the probe is extremely useful in such situations.

A discussion of various sources of probe errors is given in a subsequent section.

Typical Results. Some typical data from a disk probe, obtained in a rotor blade passage of an axial inducer, are shown in Fig. 9. The velocities measured by the disc probe are compared with those obtained by a rotating three-sensor hot-wire probe. Description of the hot wire probe, measurement technique, and facility are given in references [3] and [14]. No attempt is made to correct the disc probe data or the hot-wire probe near the leading and trailing surfaces, where the probe readings are affected by the presence of blades and gradients in the flow. In general, there is good agreement between the disk probe and the hot-wire probe, especially for the radial velocity W_r. Major differences occur near the leading surface.

Spherical Head Static-Pitot Pressure Probe

Probe Description and Calibration. One of the main problems in the measurement of static pressure in the rotor passage and the wake is that the direction of the velocity vector is varying continuously across the wake and the passage, and it is therefore impossible to obtain an accurate measurement of the static pressure. To overcome this difficulty, a spherical head static-pitot probe, insensitive to direction, was built at The Pennsylvania State University.

Main features of the probe are illustrated in Fig. 10. It consists of a 3.175 mm (0.125 in.) brass sphere with trips around it to stabilize the wake region. The sphere has a total-pressure hole at its center and the stem at the back carries four static-pressure holes which actually measure the pressure behind the sphere (p_w). Knowing the total pressure (P_0) and the wake pressure, p_w, it is possible to get the static pressure upstream of the flow using the equation

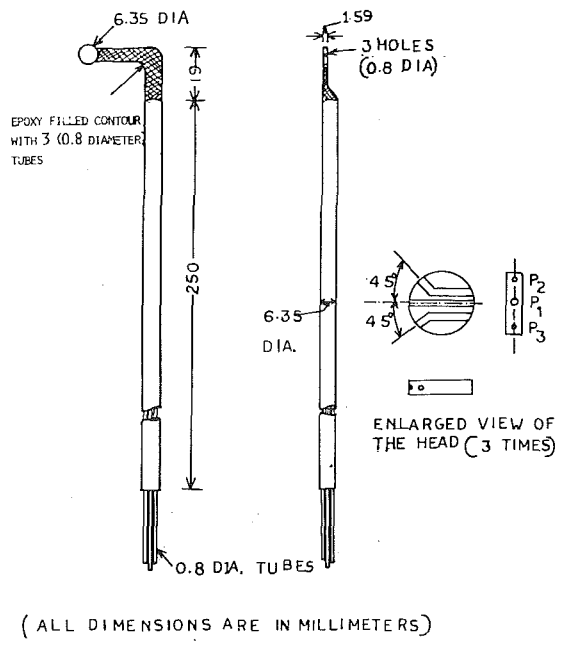

Fig. 6 Disk type boundary-layer probe

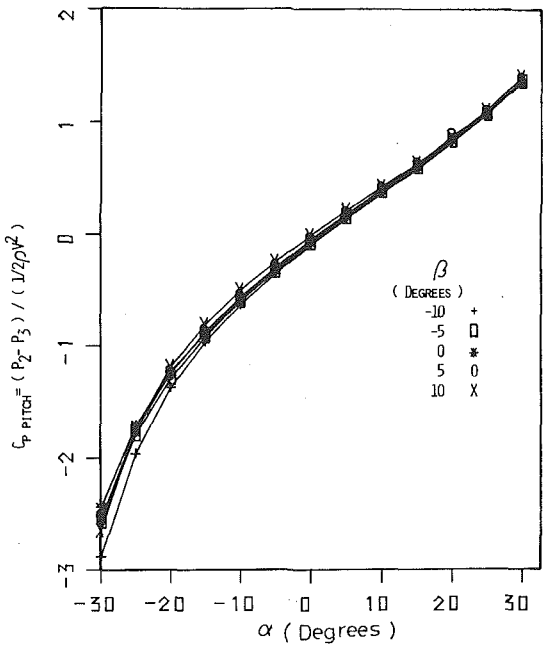

Fig. 7 Calibration of disk probe (velocity $V = 34$ m/s)

$$p = \frac{p_w + KP_0}{1 + K}. \tag{2}$$

The spherical static-pitot probe has been so designed that the factor K, which is known as the probe factor, is substantially constant at a value near 0.411 over the entire range of yaw and pitch angles.

The sphere probe is calibrated in the open-jet facility of the Department of Aerospace Engineering at The Pennsylvania State University. Typical calibration curve for the stagnation pressure is shown in Fig. 11. The asymmetry about yaw angle $\beta = 0$ and pitch angle $\alpha = 0$ is due to the fact that the probe cannot be aligned exactly with the flow. From the calibration curve, it is seen that the stagnation pressure measured by this probe lies within 5 percent of the dynamic head in the yaw and pitch angle range of −8 to 8 deg. The static pressure is measured accurate to 2 percent within ±10 deg change in yaw angle at zero pitch angle, and the accuracy is within 3 percent for ±10 deg change in pitch angle at zero yaw angle.

The percentage error in velocity, obtained by the sphere probe measurement, is shown for various yaw and pitch angles in Fig. 12. The percentage error is within 4 percent for most of the yaw and pitch angle range. This is due to the fact the error in static pressure measured by the sphere probe compensates for the error in stagnation pressure measured by the probe. Hence, the sphere probe is useful for the measurement of total velocity and static pressure in a three-dimensional flow, where the flow direction changes rapidly.

Wall vicinity effects might affect the accuracy of this probe. Experimental evidence has shown that a distance of at least three sphere diameters should be maintained between the center of the sphere and the walls, and no obstacle should be placed in the wake of the sphere closer than seven sphere diameters to the probe, to insure accuracy of the probe reading. The probe is calibrated in a known uniform flow and, therefore, the calibration curve shown in Fig. 11 would include the aerodynamic interference effects. However, the errors due to the probe being immersed in shear gradients are not included. A discussion of other sources of error is given in the section "Sources of Errors and Estimation of Their Magnitude."

The comparison of the velocity profiles across the rotor wake derived from this probe and those obtained from triaxial hot wire probe measurements show excellent agreement [11].

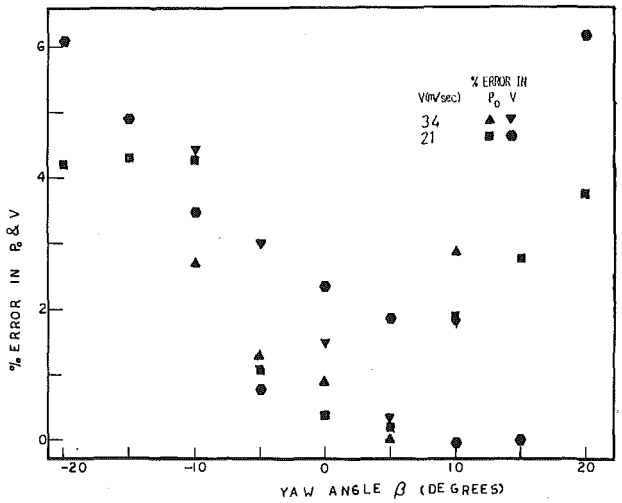

Fig. 8 Accuracy of disk probe in three-dimensional flow

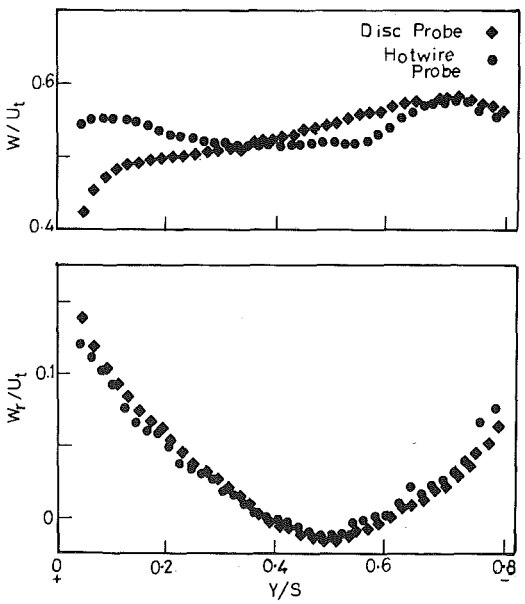

Fig. 9 Blade-to-blade distribution of velocities in an axial-flow inducer rotor at $R = 0.717$, $x/c = 0.9$ and $\phi = 0.065$

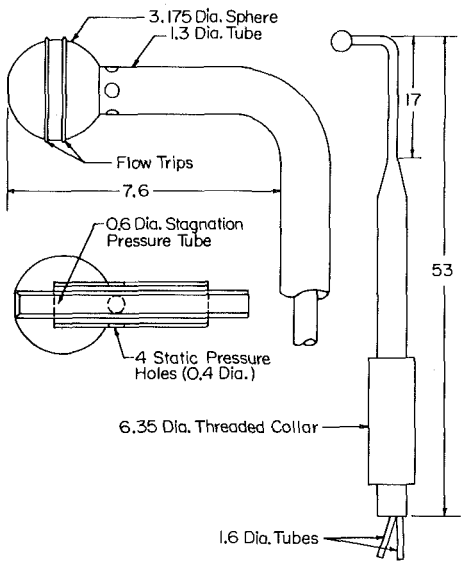

Fig. 10 Spherical head static-pitot pressure probe

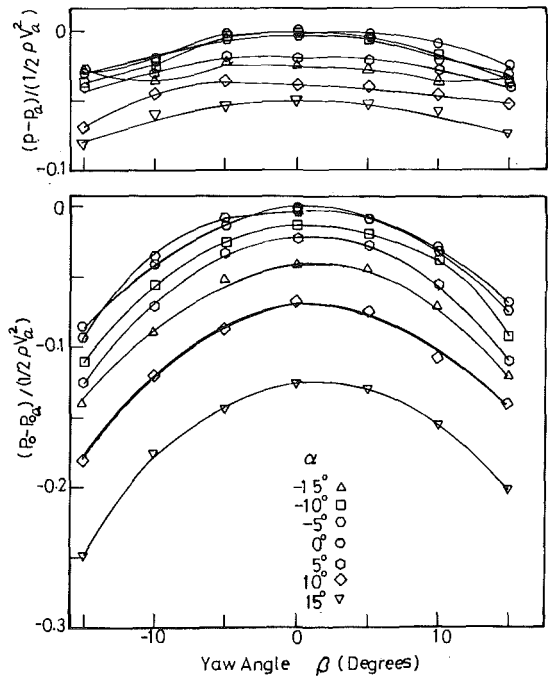

Fig. 11 Calibration curve of spherical static-pitot probe (velocity $V = 34$ m/s)

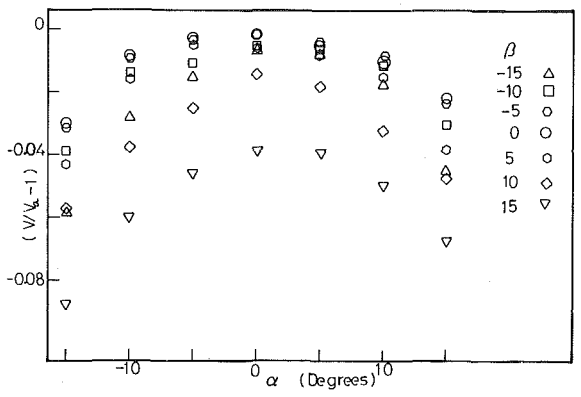

Fig. 12 Accuracy of sphere probe for velocity measurement

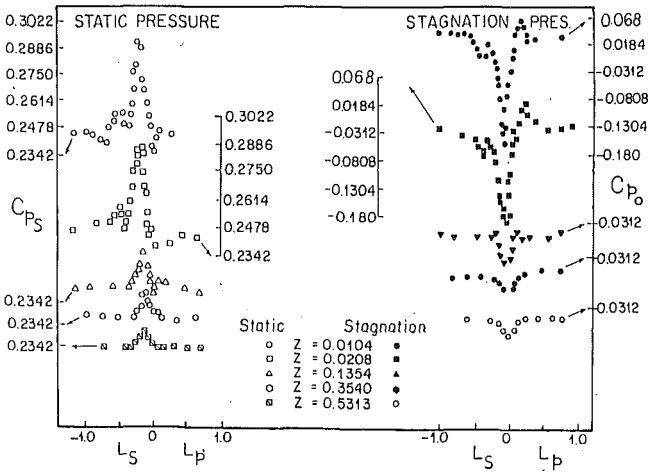

Fig. 13 Static and stagnation pressure variation across the rotor wake of an axial-flow compressor at $R = 0.792$ and $\phi = 0.56$

Typical Data. The data reported in this section are obtained at the exit of a compressor rotor wake using the rotating probe traverse mechanism, described earlier. Plots of static and stagnation pressures normalized by tip speed of the rotor is plotted in Fig. 13. Some of the traditional models of an inviscid core flow and a viscous wake appear in these plots. Static pressure not only varies across the wake, but also shows the inviscid effects in the trailing-edge region, which is not reflected in the stagnation pressure plots.

In the trailing-edge region, the static pressure variation is as large as 40 percent, and drops off to about 5 percent half a chord downstream. In the present case, the first measurement station is very close to the trailing edge and very large static-pressure gradients as reported were measured. The static pressure increases towards the wake center, and the peak pressure lies outside the center of the wake towards the pressure surface. It is also observed that the minimum stagnation pressure and the maximum static pressure are off-set by a small tangential distance. At this point, it is difficult to comment on whether the error arises from the spatial error of the static-stagnation ports or whether it is because of the nature of the flow itself.

Sources of Errors and Estimation of Their Magnitude

Sources of errors in the conventional-probe measurement of the relative flow in turbomachinery rotor blade passages are: (1) turbulence effects, (2) Reynolds number and Mach number effects, (3) effect of rotation, (4) effects of pressure and velocity gradients, (5) wall vicinity effects: (*a*) probe near the annulus wall, (*b*) probe near the blades, (*c*) probe near the blade trailing edge, and (6) effects of probe blockage and probe stem.

A brief description of these sources of errors and an estimate of their magnitude are given below.

Turbulence Effect. The conventional probes are usually calibrated in a well-controlled calibration tunnel where the flow turbulence is very low. They are used to measure relative flow in turbomachinery rotors, where the turbulence fluctuations are large and cause error in pressure probes. Goldstein [15] has theoretically investigated the direct effect of the turbulent velocity components on the pressure probe measurement. This analysis is modified here to estimate the error due to turbulence for various probes employed in this investigation.

Five-Hole Probe. The pressure sensed by each hole can be written as

$$P_i = p + \alpha_i \left(\frac{1}{2}\rho V^2\right) + K_i \left(\frac{1}{2}\rho\overline{q^2}\right), \tag{3}$$

where P_i refers to the ith hole ($i = 1, 2, 3, 4, 5$), α_i and K_i are constants for a particular hole, with their values less than unity. For example, for the center hole $\alpha_i \approx 1$, $K_i < 1$ for moderate pitch and yaw angles. The term $\frac{1}{2}\rho\overline{q^2}$ is the kinetic energy in turbulent fluctuation. The value of D can be expressed as

$$D = \overline{D} + \frac{1}{2}\rho\overline{q^2}[K_1 - 0.25(K_2 + K_3 + K_4 + K_5)]$$

$$= \overline{D} + \frac{1}{2}\rho\overline{q^2}\,A, \text{ where } A = K_1 - 0.25(K_2 + K_3 + K_4 + K_5). \tag{4}$$

Similarly, neglecting terms of small order (e.g., $\overline{q^2 q^2}$),

$$C_{p_{\text{pitch}}} = \frac{P_4 - P_5}{D} = \overline{C_p}\left(1 - \frac{\frac{1}{2}\rho\overline{q^2}A}{\overline{D}}\right), \tag{5}$$

where $\overline{D}$, $\overline{C_p}$ refer to values in the absence of turbulence (i.e., during calibration). Using similar procedure expressions for $C_{p_{\text{yaw}}}$, $C_{p_{\text{total}}}$ can be derived.

An estimate of the errors due to turbulence is carried out below assuming that the central hole senses mostly total pressure and the others, mostly the static pressure. Reasonable assumptions for K_1 is 1.0 and K_2, K_3, K_4, K_5 are 0.33 since the central hole senses, approximately, the total turbulent kinetic energy, while the static holes sense the normal component. Hence, $A = 0.33$, and assuming $\overline{D} \approx \frac{1}{2}\rho V^2$, the error in $C_{p_{\text{pitch}}}$ is 0.67 percent for 10 percent turbulence intensity and 2.68 percent for 20 percent turbulence intensity. There will be corresponding errors in angles and pressures. Thus, for a 10 percent turbulence intensity the estimated value of the error in total velocity is approximately 0.33 percent, while the errors in velocity components vary depending on the pitch and yaw angles. This may account for part of the discrepancy (Fig. 5(*d*)) observed in the radial velocity measured by the hot-wire and the five-hole probes. The deviations near the blade surface (Fig. 5(*c*), 5(*d*)) may be due to high turbulent intensity in this region as well as wall vicinity effects.

Disk Probe. The error in the disk probe measurement in turbulent flow can be estimated using the above analysis. Some of the discrepancy between the hot-wire probe and the disk probe data in the blade passage of an axial inducer, where the flow is highly turbulent, is probably due to the error in disk probe measurements in turbulent flow (Fig. 9).

Spherical Head Static-Stagnation Pressure Probe. The static pressure measured by the spherical static-pitot pressure probe is not affected by the turbulence in the flow, since the trips around the sphere generate turbulence when the probe is calibrated in a uniform flow. Goldstein's analysis for the pitot probe error in the turbulent flow shows the percentage error in the stagnation pressure of about 0.5 times turbulence intensity. The same magnitude may be assumed for the error in the stagnation pressure measured by the central hole of the sphere probe. Hence, the sphere probe measures slightly higher stagnation pressures and velocities in a turbulent flow.

Reynolds Number and Mach Number Effects. Calibration of the probes used in this paper (e.g., Fig. 3) does not show appreciable variation with Reynolds number in the calibration characteristics at high Reynolds number. However, the effects of low Reynolds numbers (based on probe head diameter) may be appreciable. For the probes used in this paper, calibrations were carried out approximately at a Reynolds number equal to that in the measured flow; hence, the Reynolds number effects are accounted for in the calibration.

In the calibration and interpolation of the probe characteristics, the flow is assumed to be incompressible, and the incompressible Bernoulli equation is used. The error caused by neglecting the effect of compressibility for the Prandtl probe amounts to about 1 percent at Mach 0.28, and the same magnitude of error may be assumed for the five-hole, disk, and sphere probes. These probes can be used in highly subsonic flows (up to Mach 0.7), if the first two terms of the binominal expansion of the isentropic Bernoulli equation is used in the calibration and interpolation of these probe characteristics. All the measurements reported in this paper were carried out at $M < 0.3$; hence, this error estimate is irrelevant.

Effect of Rotation. Since the pressures measured by the rotating probes are subjected to the centrifugal forces, the correction given by equation (1) is applied. But the actual radii of the side holes of the probes are different and difficult to measure, as they vary with the probe orientation. The maximum error in the radial position of the side holes is equal to 0.35 times the probe diameter (for the five-hole and disk probes). The estimated maximum error for the probes used in the present investigation is negligibly small (0.5 percent of the centrifugal force correction).

Effects of Pressure and Velocity Gradients. The probes used in this investigation are calibrated in a uniform flow, but they are used to measure relative flow in turbomachinery rotors where steep gradients in pressure and velocity exist (e.g., rotor wakes, boundary layer, and tip leakage flow). These gradients affect the probe performance in the following ways:

1 The probe indicates the reading at a location different from the geometric center of the probe. This effect, known as the displacement effect, has been investigated extensively for the pitot tube [16, 17] and a three-hole probe [9].

2 In multi-hole probes, each hole is located in a differing pressure field; hence, an additional error is introduced. This will be called spatial error in this paper, and may be the dominant error for a five-hole probe.

3 The presence of the probe in a velocity gradient causes deflection of the streamlines toward the region of lower velocity. This deflection causes the probe to indicate pressures in excess of that existing at the same location in the absence of the probe.

An estimate of the spatial error due to gradients in the flow for a five hole probe is given below.

Assuming the pressure gradient in the flow is known (dP_0/dn), the following relationships may be written for the five-hole probe used in this investigation.

$$P_1 = K_1 P_0$$
$$P_i = K_i \left(P_0 - \frac{dP_0}{dn} 0.35d \right) \quad i = 2, 5 \tag{6}$$
$$P_i = K_i \left(P_0 + \frac{dP_0}{dn} 0.35d \right) \quad i = 3, 4,$$

where P_0 is pressure at the geometric center of the probe. Hence, the calibration coefficient for the five-hole probe is given by

$$\begin{aligned} D &= P_1 - 0.25(P_2 + P_3 + P_4 + P_5) \\ &= K_1 P_0 - 0.25 \left\{ (K_2 + K_3 + K_4 + K_5) P_0 \right. \\ &\qquad \left. + (K_3 + K_4 - K_2 - K_5) \frac{dP_0}{dn} 0.35d \right\} \qquad (7) \\ &= \overline{D}(1 + A), \end{aligned}$$

where A depends on the pressure gradient, orientation and geometry of the probe. Hence, to the first approximation,

$$C_{p_{\text{yaw}}} \simeq \overline{C_{p_{\text{yaw}}}} (1 - A).$$

Similarly, other coefficients are modified. In the absence of the experimental or theoretical data for the coefficient A, the error due to the gradient in the flow is difficult to estimate. The results of reference [9] for a three-hole probe may be assumed to be valid for each set of holes, in the yaw and pitch planes. Accordingly, the yaw and pitch angles are to be corrected as follows.

$$\epsilon = 13.2 \frac{d}{P_0} \left(\frac{dP_0}{dn} \right), \tag{8}$$

where ϵ is error in degrees.

The disk and sphere probes are not subjected to the above error, since the holes are either along the same axis as in the sphere probe or not subjected to pressure gradients as in the disk probe. All three probes are subjected to the displacement effect, which may be assumed to be the same as that of a pitot tube.

$$\frac{\delta}{d} = 0.021 \frac{d_h}{d}, \tag{9}$$

where δ is the displacement of probe measuring point from the probe geometric and d_h center, is the diameter of the probe hole.

Wall Vicinity Effects. Whenever a probe is located near a solid surface, the flow acceleration in that region introduces an additional error. In the measurement of relative flow in a turbomachinery rotor, the probe is placed close to many solid surfaces, such as annulus wall and blades. A discussion of these errors follow.

Experimental results of reference [6] (for a prism type five-hole probe) indicate an increase in velocity measured by the probe close to a solid surface.

Figure 4 shows the error in velocity measured by the five-hole probe, when the probe is adjacent to a blade. The error is negligible, when the distance between the probe and the blade is more than two probe diameters. Similar magnitude of error in velocity measured by the disk probe and the sphere probe may be anticipated.

When a probe is very near a blade trailing edge, it is subjected to the following effects: (1) viscid and inviscid interference between the probe and the trailing edge, (2) area blockage, and (3) velocity and pressure gradients discussed earlier.

The complexity of the interaction between the probe and trailing edge prohibits an estimate of the error in the probe measurements, and the results very near the trailing edge are to be viewed with caution.

Effects of Probe Blockage and Probe Stem. Probes used for the flow measurement effectively block the flow area. For the probes used in this investigation, the probe blockage is about 2 to 3 percent of blade spacing. Hence, the axial velocity increases by this amount, so the measured velocities are to be decreased by the same amount.

The probe stem supporting the probe causes interference with the flow near the tip. Experimental results for the pitot and static probes indicate that this effect is negligible when the distance between the probe tip and the axis of stem is more than four times the stem diameter. All three probes have the probe tips located more than four times the stem diameter from the stem axis. Hence, this error is negligible.

Conclusions

A method of measuring the relative flow in the rotor blade passage using conventional probes, such as the five-hole, disk, and spherical static-pitot probes, is described in this paper. A discussion of the probe error and the calibration procedure is given. Some typical data obtained from the probes are also presented. Some of the major conclusions are:

1 The five hole probe provides an easy means of obtaining useful data on the three-dimensional flow field inside a rotor passage. Reynolds number effect on the probe accuracy is small. The error due to wall vicinity effect is less than 1 percent up to and beyond 2 diameters clearance between the probe and the wall.

2 The endwall flow data (at $R = 0.959$) derived from the five-hole probe reveal the presence of three-dimensional viscid and inviscid effects and the leakage flow. The leakage flow seems to originate about half a chord downstream of the leading edge.

3 The disk probe described is suitable for boundary-layer measurements in situations where yaw angle change is less than ±10 deg. It can measure velocities (two components) quite accurately. It is a

useful probe for acquiring the rotor blade boundary-layer data.

4 The spherical head static-pitot probe is suitable for measurement of the total velocity and the static, stagnation pressures in flows with changes in velocity vector, as well as in situations where nulling (as in a rotor frame of reference) is not possible. It provides the only means of acquiring accurate static pressure data across the passage in a rotor.

5 The static pressure measurements across a rotor indicate substantial pressure gradients across the rotor blade wake.

Acknowledgments

This work was carried out under the National Aeronautics and Space Administration (NASA) Grant NSG 3032, with technical management by P. Sockol. Partial support from the NASA Grant 3012, with M. F. Heidmann as the technical monitor, is also acknowledged. The authors wish to thank George Gurney for helpful suggestions in the development of the probes used in this program.

References

1 Lakshminarayana, B., "An Axial Flow Compressor Facility Designed for Flow Measurement in Rotor Passages," *Proceedings of ASME Conference on Measurement Methods in Rotating Component in Turbomachinery*, edited by B. Lakshminarayana and P. Runstadler, Jr., ASME, New York, 1980, to be published in the ASME *Journal of Fluids Engineering*.

2 Lakshminarayana, B., "Techniques for Aerodynamic and Turbulence Measurements in Turbomachinery Rotors," ASME JOURNAL OF ENGINEERING FOR POWER , Vol. xxx, No. x, pp. xxx–xxx.

3 Anand, A. K., and Lakshminarayana, B., "Three Dimensional Boundary Layer in a Rotating Helical Channel," ASME *Journal of Fluids Engineering*, Vol. 97, No. 2, 1975, pp. 197–210.

4 Wright, M. A., "The Evaluation of a Simplified Form of Presentation for Five-Hole Spherical and Hemispherical Pitotmeter Calibration Data," *Journal of Physics E., Scientific Instruments*, Vol. 3, 1970, pp. 356–362.

5 Shreeve, R. P., et al., "Calibration and Application of Multiple Sensor Pneumatic Probes Determination with Corrections for Boundary Effects," AIAA Paper No. 76-373, 1976.

6 Treaster, A. L., and Yocum, A. M., "The Calibration and Application of Five-Hole Probes," *Institution Society Am. Transactions*, Vol. 18, No. 3, 1979, pp. 23–34.

7 Bennett, J. C., "Use of Five-Hole Pneumatic Probe in Unsteady Flows," United Technologies Research Center Report No. UTRC 76-41, 1976.

8 Matsunaga, S., et al., "Accurate Measurement of Nonsteady Three-Dimensional Incompressible Flow by Means of a Combined Five-Hole Probe," *Proceedings ASME Conference on Nonsteady Fluid Dynamics*, edited by D. E. Crow and J. A. Miller, ASME, New York, 1978, pp. 65–72.

9 Ikui, T. and Inoue, M., "Pressure or Velocity Gradient Error in the Flow Direction Measurement," *Memoirs of the Faculty of Engineering*, Kyushu University, Vol. 29, No, 3, 1970.

10 Reynolds, B. D. and Lakshminarayana, B., "Characteristics of Lightly Loaded Fan Rotor Blades," NASA CR 3188, Oct. 1979.

11 Ravindranath, A. and Lakshminarayana, B., "Mean Velocity and Decay Characteristics of the Near- and Far-Wake of a Compressor Rotor Blade of Moderate Loading," ASME JOURNAL OF ENGINEERING FOR POWER, Vol. 102, No. 3, 1980.

12 Lakshminarayana, B., and Gorton, C. A., "Three Dimensional Flow Field in Rocket Pump Inducers—Part 2," ASME *Journal of Fluids Engineering*, Vol. 99, No. 1, Mar. 1977, pp. 176–186.

13 Ravindranath, A., "Three Dimensional Mean and Turbulent Characteristics of the Near Wake of a Compressor Rotor Blade," M.S. Thesis, Department of Aerospace Engineering, The Pennsylvania State University, Nov. 1979, also NASA CR 159518, 1980.

14 Anand, A. K., and Lakshminarayana, B., "An Experimental Study of Three-Dimensional Boundary Layer and Turbulence Characteristics Inside a Rotating Channel," ASME JOURNAL OF ENGINEERING FOR POWER, Vol. 100, Oct. 1978, p. 676.

15 Goldstein, S., "A Note on Measurement of Total and Static Pressure in a Turbulent Stream," *Proceedings of the Royal Society*, 155, 1936, p. 570.

16 Lighthill, M. J., "Contribution to the Theory of the Pitot Tube Displacement Effect," *Journal of Fluid Mechanics*, Vol. 2, 1957, p. 493.

17 Hall, I. M., "The Displacement Effect of a Sphere in a Two-Dimensional Shear Flow," *Journal of Fluid Mechanics*, Vol. 1, 1956, p. 142.

Experimental Analysis Methods for Unsteady Flows in Turbomachines

R. Larguier

Head, Engines Research Group, Aerodynamics Department, Office National d'Etudes et de Recherches Aérospatiales (ONERA), 92320 Châtillon, France

This paper describes the measuring methods developed at the ONERA Aerodynamics Department for the characterization of unsteady flows in turbomachines. They mainly concern the flow in the rotor, its wake, and boundary layers on stator or rotor blades. The means used consist of: • measurements using pressure probes or short response time pressure transducers, • measurements with hot wire probes or hot film gauges, and • direct measurements using laser velocimeter.

1 Introduction

This paper describes methods, recently developed at ONERA, for measuring unsteady flows in turbomachines and concerning, in particular, the flow within the rotor, the wake behind it, and the flow in the following stator.

The means of investigation at the experimenter's disposal, and usable in a fixed reference frame mainly consists of:

- measurements by fast response time pressure probes or wall pressure transducers,
- measurements by hot wire probes or hot film gauges,
- direct velocity measurements by laser.

Whatever the type of measurement considered, its implementation in a flow periodically modulated at the frequency of the rotor blade passage implies the use of broadband transducers and data processors, and the determination of the rotor position at the time of measurement.

Fast response time pressure probes generally used in industrial turbomachines have the disadvantage of disturbing the flow field under study, hence the necessity of their miniaturization.

This drawback is far less perceptible with hot wire probes, which are very small; but they are so fragile that their use in an industrial environment can only be considered if the incoming air is thoroughly filtered.

Laser velocimetry, which avoids the introduction of any material probe within the flow, requires, however, a special design of the machine casing (windows), as well as particular techniques for seeding the flow.

The use of unsteady measurement means to define experimentally a periodically variable flow can be avoided if this flow is explored with instruments bound to the rotor and rotating with it, and consequently working in a permanent velocity field (relative reference frame). This is absolutely true if the upstream disturbances of support struts are neglected and without downstream stator blades. This process, inapplicable to industrial machines, can be used with great advantage in a research set-up, as it only requires classical steady-flow probes, whose miniaturization raises no major problems. In this case, the difficulty is transferred to the information transmission devices (pneumatic or electric measurement collector—slip rings).

Work similar to that described here is underway in other laboratories [1–15].

Most measuring methods which are presented are new: in particular, all those concerning three-dimensional analysis of rotor wakes (rotating pressure probes solid with the rotor, laser velocimeter, slanting hot wire, revolving pitot probe), analysis of a rotating stall, and determining the nature of boundary layer on mobile blades. Other referenced methods can complete this paper; for example, determination of the shock-wave configuration for the rotor of a supersonic compressor and analysis of boundary layers on a stator vane using hot-wire or hot-film gauges.

2 Test Set-Up

A special set-up for aerodynamic studies on rotors has been created at ONERA for the implementation of the afore mentioned methods and devices [16–17].

It is designed to make the experimentation and development of measuring methods easier. One feature is a hollow shaft which can be equipped with either a pneumatic collector [18] or an electric collector, permitting the transmission of measurements such as:

- pressure distribution on rotor blades,
- analysis of the blade-to-blade flow or the flow behind a rotor, by means of rotating probes solid with the rotor,
- implementation of the wall hot film technique, or of rotating hot wire probes.

Moreover, a division of the casing into interchangeable parts allows the adaptation of special elements, such as windows for laser velocimetry.

3 Rotor Wake Analysis

The aerodynamic field behind the rotor of the aerodynamic study device described above is not considered as a subject of study per se, but constitutes essentially a reference flow, periodically variable and reproducible at will, where the measuring devices intended for use in industrial machines can be experimented on. Such a reference flow must be known with the greatest possible accuracy, and this knowledge is often acquired through measuring means which are ill-adapted for industrial use.

3.1 Measurement of Flow Parameters by Means of Rotating Pressure Probes Solid with the Rotor: Reference Test. Several probes are necessary to explore the flow: directional probes, pitot probe, static pressure probe (Fig. 1(*a*)). These are successively installed on a mechanism enclosed in the machine hub, allowing the adjustment of the probe azimuthal position related to the rotor, as well as its orientation around its own axis; it is thus possible to set the probe in a well defined position in the frame of reference solid with

Contributed by the Gas Turbine Division and published in the symposium volume, *Measurement Methods in Rotating Components of Turbomachinery*, ASME, New York, 1980. Manuscript received for publication in the JOURNAL OF ENGINEERING FOR POWER May 22, 1980.

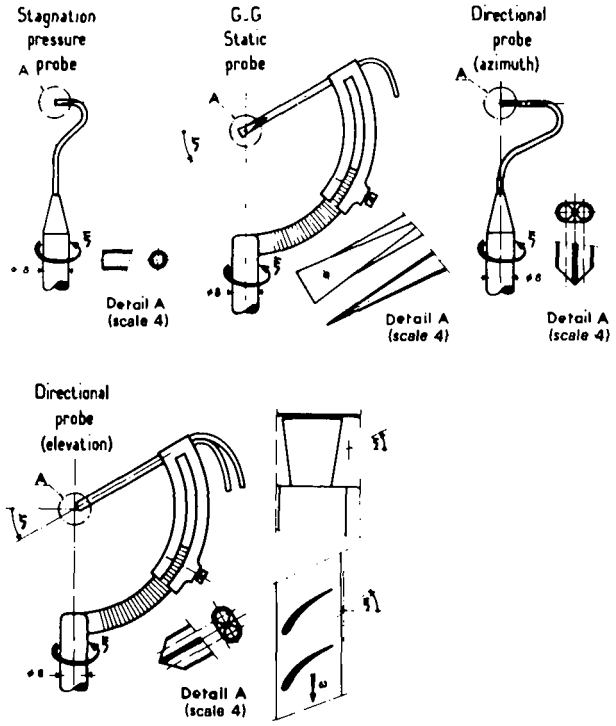

Fig. 1(*a*) Probes used on the support solid with the rotor (all dimensions in mm)

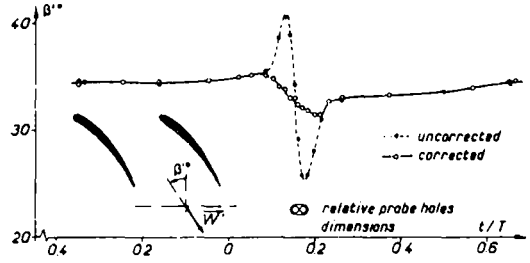

Fig. 1(*b*) Azimuthal directional probe used on the support solid with the rotor. Influence of correction for geometrical position of the probe holes

the rotor. The pressure transducer, external to the machine, is connected to the probe through a pneumatic collector at the end of the machine shaft; consequently, the rough measurements must be corrected, in order to take into account the centrifugal effect on the column of air included in the rotating piping.

This correction is expressed by the correction factor

$$k = \exp \frac{\omega^2 r^2}{2R_0 T_0} \text{ such that } p = kp_m$$

With the test-conditions given in this paper (N = 3000 rpm; r/R = 0.852): $k \approx 1.027$.

Directional measurements are based on the equality of pressures measured by the two holes of the probe when its axis is in the wind direction, after correction for geometrical position of the probe holes, which is necessary in the case of a strong velocity gradient (Fig. 1(*b*)). Static pressure measurement is performed with the probe axis in the local direction of the velocity **W** obtained from previous measurements.

The results thus obtained in the mobile reference frame by means of classical probes can easily be transferred by calculation into the fixed reference frame; in this form, they will serve as bases of comparison with those obtained by the various methods of unsteady measurements, directly performed in the fixed reference frame, which will be presented later.

All the measurements, whose results will be presented, have been made at 23.4 percent rotor blade chord, at r/R = 0.852.

3.2 Three-Dimensional Exploration by Laser Velocimetry. The technique used is based on a one-directional argon laser, emitting 1.8 W on the green line (5145Å) [19]. The beam of coherent light is split, and the two resulting beams, made convergent by appropriate optics, cross at the measuring point, giving rise to an interference fringe pattern (Fig. 2). The measure consists in measuring the time needed by a particle, immersed in the flow and crossing the pattern, to run through a given number of fringes. The passage of this particle in the alternately bright and dark zones of the pattern is detected by the light scattered by the particle.

Obviously, the measurement performed only defines the projection of the velocity on the normal to the fringe pattern. Consequently, if the measurements are repeated using different orientations of the

Nomenclature

E_Θ = response of hot wire anemometer set at an angle Θ to the wind
E_0 = hot wire anemometer response without wind
ℓ = chord length
M = mach number
N = rotor rotation speed (rpm)
p = pressure at the measurement point
p_m = pressure measured by the transducer
P = stagnation pressure
r = local radius
R = radius of external casing
Ro = perfect gas constant
t = time
T = blade passage time (time interval between the passage of two adjacent blades in front of the probe)
To = ambiant temperature at time of test
u = velocity in the boundary layer
u_e = velocity outside the boundary layer
V = modulus of velocity in the fixed reference frame
V' = modulus of the projection of v on the XOY plane
v,v' = velocity vectors of modulus V, V'
V_v = voltage output of the hot-film wall gauge
V_{ov} = voltage output of the hot-film wall gauge in the absence of flow (natural convection and conduction)
w'_1, w'_2 = axial and transversal turbulent components, referred to **W'**, on the XOY plane
$\mathbf{w}_1'$, $\mathbf{w}_2'$ = velocity vectors of modulus w_1', w_2'
W = velocity in the rotating reference frame
W' = modulus of the projection of **W** on the XOY plane
W, **W'** = velocity vectors of modulus W, W'
$\Delta W = W - \overline{W}$
x = abscissa of a point on the profile, measured along the normalized chord (leading edge to trailing edge)
y = distance from a point in the flow to the profile, measured along the normal to the profile
α = direction of velocity **V** relative to the local meridian plane (> 0 in the direction of rotation of the rotor)
α' = direction of velocity **V'** in the XOY plane
β = direction of velocity **W** relative to the local meridian plane (> 0 in the direction opposite to the rotation of the rotor)
β' = direction of velocity **W'** in the XOY plane
$\Delta\beta = \beta - \overline{\beta}$
γ_v = angle between **V'** and **V**
γ_w = angle between **W'** and **W**
$\Delta\gamma_w = \gamma_w - \overline{\gamma}_w$
Θ = angle of orientation of the unsteady probe around its axis
φ = (in hot wire probe measurement) slant angle of the wire relative to the plane normal to the probe holder
ω = rotor angular velocity
ξ = (in measurements by rotor-connected probe) a geometric orientation angle of the probe, relative to the local meridian plane
ζ = (in measurements by rotor-connected probe) probe elevation angle
OX = direction parallel to the rotor axis
OY = direction tangent to the blading
OZ = direction parallel to the rotor radius

beam splitter, we obtain the projections of the particle velocity in different directions of a plane; this plane is perpendicular to the bissectrix of the angle formed by the two beams converging at the measuring point.

Two different orientations are sufficient to define the modulus and orientation of the projection on the plane considered, of the mean velocity vector of a supposedly ergodic flow. On the other hand, it is necessary to repeat the measurements along a third direction in the plane to obtain the components of the turbulent fluctuations. The measurements along these three directions must be repeated many times, to allow statistical estimates of the mean velocities, and standard deviations of the fluctuations which, in the considered plane, characterize turbulence.

In order to obtain the modulus and orientation in space of the velocity vector, its projections must be measured on two different planes including the measuring point.

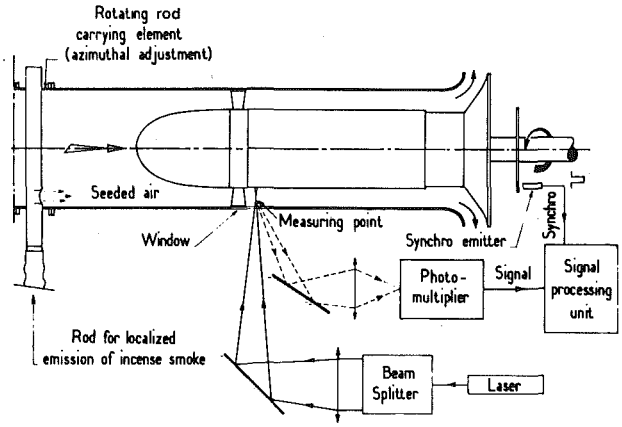

Fig. 2(*a*)

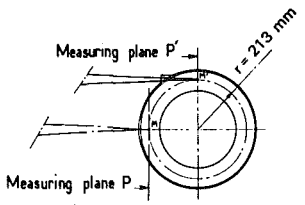

Fig. 2(*b*)

Fig. 2 Three-dimensional analysis of rotor wakes by laser velocimetry. Experimental set-up

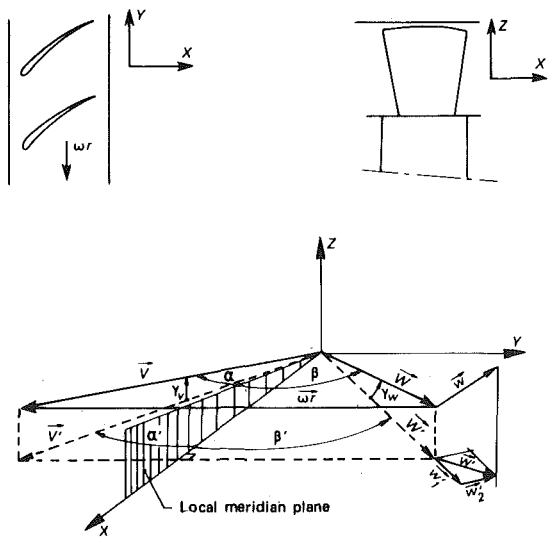

Fig. 3 Three-dimensional flow behind a rotor. Notations and sign conventions

The measurement of these projections would require the rotation of the whole optical system around the air duct, which would be very cumbersome indeed. That is why we used the expedient described below.

Assuming that the flow is truly periodic, the measurements are first performed on a tangential plane, such as P of Fig. 2(b). Then, the optical system is translated so as to sight the radial plane, such as P'; if the pulse generator triggering the measurement is shifted by the duration of a quarter turn, points M and M' are at the same location related to the rotor blading.

The two measuring planes, mutually perpendicular, are noted XOY and XOZ in Fig. 3. The local periodic velocity vector, noted **W** in the reference frame solid with the rotor, has as a projection on the XOY plane, a vector **W'**, defined by its orientation β' in this plane. The angle between **W** and **W'**, is noted γ_w.

Axial and transversal components, referred to **w'**, of the projection on the XOY plane of turbulent components **w** of the velocity **W** are w_1' and w_2' (Fig. 3).

An example of measurement results, is given in Figs. 4(a)–4(d). In Figs. 4(a)–4(c), the results are compared with those deduced from surveys of pressure probes rotating solid with the rotor. The agreement is quite good; in particular the evolution of the radial velocity, expressed by the angle γ_w, reveals the existence of a swirling flow between the blades.

Although it is not possible to determine all terms of the Reynolds tensor, from measurements performed in only two planes, some characteristic terms of turbulent fluctuations have been calculated and given, as examples, in Fig. 4(d).

3.3 Three-Dimensional Investigation by a Fixed Slanting Hot Wire Probe. The method is based on the directional properties of the hot wire. The probe used is equipped with a platinum coated tungsten wire, 5μm in diameter and 1.25 mm long. This wire, held by two thin antennae, makes a $\varphi = 45$ deg angle with the plane normal to the probe holder axis.

The experimental technique consists in introducing the probe into the flow through an orifice in the machine casing, the holder axis being set along the local radius. The wire response is recorded for three different orientations Θ of the probe around its axis.

To process the measurements it is assumed that the wire response follows King's law,

$$E_\Theta{}^2 = E_0{}^2 + k\, V_{\text{eff}}{}^m \tag{1}$$

with

$$V_{\text{eff}} = \sqrt{k_1{}^2 v_{1f}{}^2 + k_2{}^2 v_{2f}{}^2 + k_3{}^2 v_{3f}{}^2} \tag{2}$$

k_1, k_2, k_3 being the probe sensitivity coefficients for the three particular orientations of the flow relative to the wire (Fig. 5):

- flow parallel to the wire axis (k_1, v_{1f}).
- flow perpendicular to the wire, in the plane defined by the wire and the holding antennae (k_3, v_{3f}).
- flow perpendicular to this same plane (k_2, v_{2f}).

The unknown coefficients are determined through a calibration operation performed in a small wind-tunnel, by varying the flow velocity modulus and orientation related to the wire.

Equation (1), complemented by (2), can be written as a function of the components u_{1f}, u_{2f}, u_{3f}, of the velocity V in the fixed reference frame related to the turbomachine:

- u_{1f}: axial component, along OX,
- u_{2f}: tangential component, along OY,
- u_{3f}: radial component, along OZ (also the probe holder axis).

By repeating the measurements for three values of Θ, a system of three homogeneous equations of the second degree in u_{1f}, u_{2f}, u_{3f} is obtained. It is solved by a method of successive approximations, called gradient method.

In practice, the recording of a response is performed each time for 100 values distributed over one elementary time T, corresponding to the time between the passage of two successive blades in front of the probe. These values are obtained from 900 added measurements in the same interblade channel. These values are directly stored in the memory of a programmable computer providing the solutions of the 100 systems of equations.

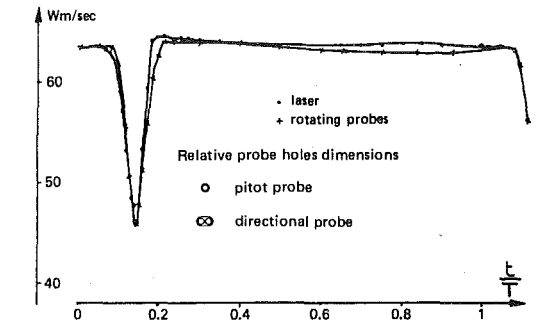

Fig. 4(*a*)

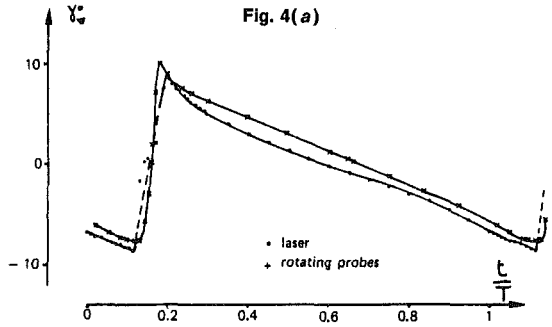

Fig. 4(*b*)

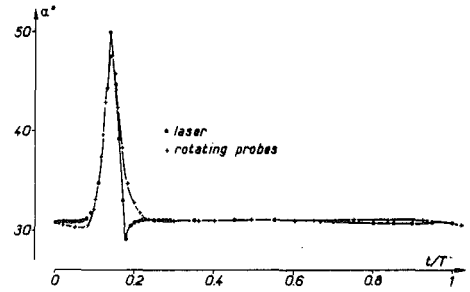

Fig. 4(*c*)

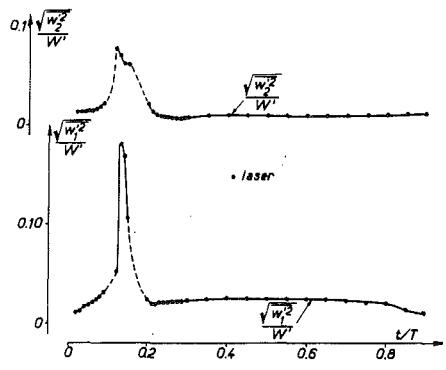

Fig. 4(*d*)

Fig. 4(*a–d*) Three-dimensional analysis of rotor wakes by laser velocimetry

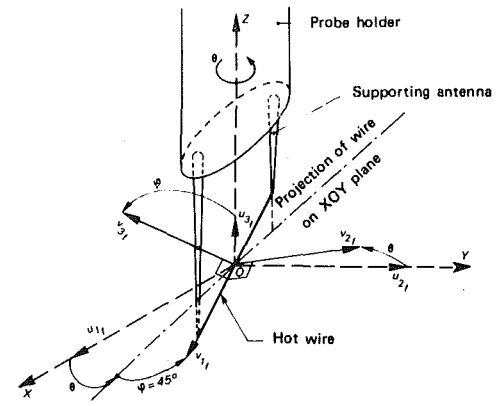

Fig. 5 Slanting hot wire probe. Notations and conventions

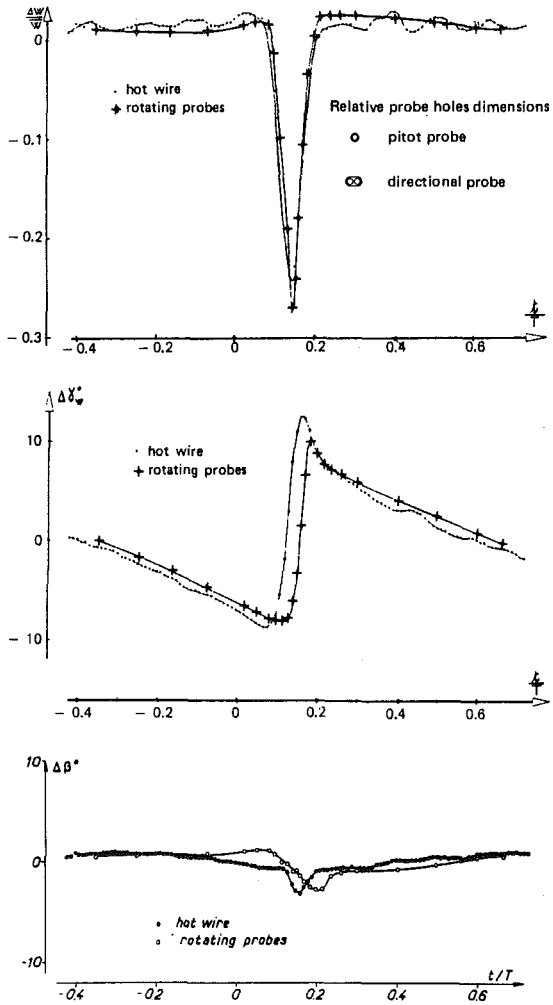

Fig. 6 Three-dimensional analysis of rotor wakes by slanting hot wire probe

As an example, results obtained in this way, transferred into the mobile reference frame, are presented in Fig. 6, compared with those obtained directly from rotating probes. As can be seen, the agreement is good.

The above experimental method is a convenient means of obtaining the periodic components of the modulus and angles of orientation of the velocity, whose measurement constitutes the essential problem in the experimental study of the unsteady flow in a turbomachine. However, experience shows that the mean values of the quantities measured this way are not very much accurate, and that it is better to obtain them by classical instrumentation if needed.

Indeed, mean values $\overline{\alpha}$, $\overline{\gamma}_v$ and $\overline{V}$ in the fixed reference frame, measured on a blade passage time, respectively by the hot wire probe and by the rotating pressure probes solid with the rotor are:

$$\overline{\alpha} = 30.07 \text{ and } 31.85 \text{ deg}$$

$$\overline{\gamma}_v = -1.72 \text{ and } -0.2 \text{ deg}$$

$$\overline{V} = 67.9 \text{ m/s and } 61.1 \text{ m/s}$$

3.4 Exploration by Revolving Unsteady Pitot Probe. This type of probe, schematically represented in Fig. 7(*a*), is intended for

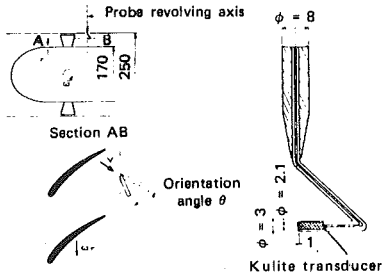

Fig. 7(*a*)

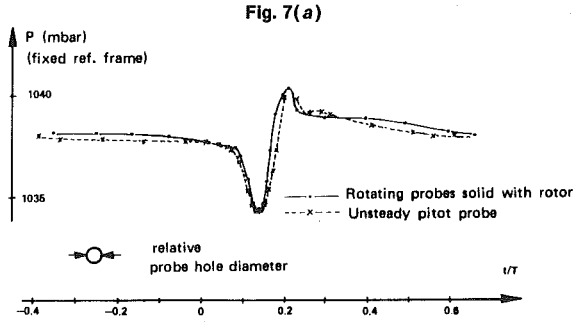

Fig. 7(*b*)

Fig. 7 Analysis of rotor wakes by revolving unsteady stagnation pressure probe (all dimensions in mm)

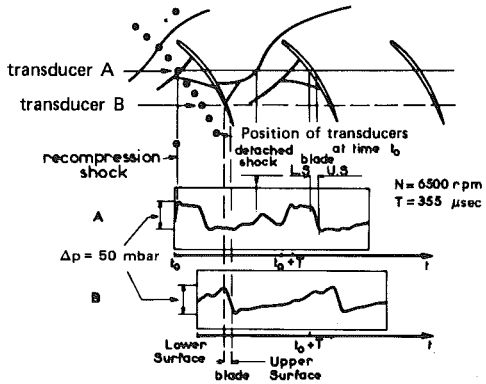

Fig. 8(*a*) Transducer arrangement and relative position of rotor at time of measurement triggering. Examples of recordings

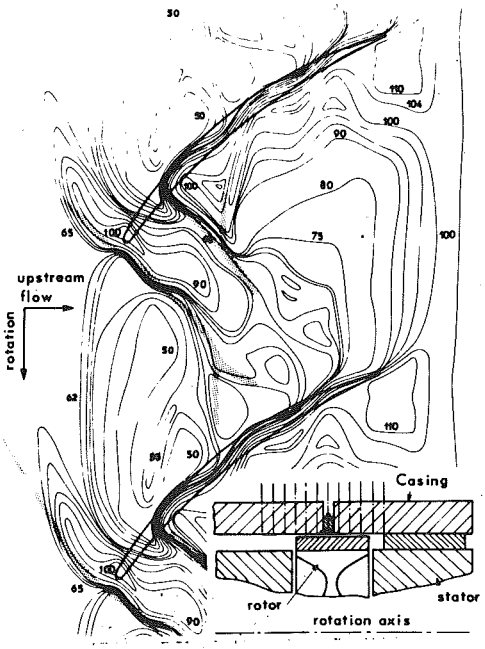

Fig. 8(*b*) Chart of isobars along the casing wall (mbar). Comparison with shock waves observed by schlieren photography (shaded zones)

measuring the periodic variations of stagnation pressure at one point of the flow. To this end, the sensitive face of the pressure transducer is placed facing directly the flow. Furthermore, the transducer is surrounded by a thin protruding tip which, in steady flow, insures a uniform pressure on the transducer face, and this in a broad range of angles of attack.

The transducer is mounted in such a way that the centre of its sensitive face remains on the probe holder axis whatever its orientation Θ around it.

The steady component is deduced from a measurement with a stagnation pressure probe of the same shape as the unsteady pressure probe but without short response time transducer and connected to an usual differential manometer with sufficiently long time constant.

Assuming that the flow orientation is unknown, the experimental procedure consists in representing, as a function of Θ (referenced relative to the machine meridian plane, for instance), the pressure measured at a given time of the elementary period. Obviously, we in fact record the response of the probe set at a given angle Θ as a function of time. The results of tests repeated for various values of Θ provide a network, in which the locus of maxima represents the distribution of the stagnation pressure as a function of the relative temporal abscissa t/T.

The final result of such a processing of data measured on the rotor test rig compares well (Fig. 7(*b*)) with results deduced from measurements with rotating probes, after transfer by calculation to the fixed reference frame.

4 Analysis of the Unsteady Pressure Field on the Casing Wall

4.1 Transducers Used. These transducers, equipped with a piezoelectric ceramic, have a sensitivity of the order of 1 millivolt per millibar, with a bandwidth up to 500 kHz. They can be mounted behind a pressure hole 0.8 mm in diameter, without resonant cavity between the orifice and the transducer's sensitive face; this can be avoided by filling this cavity with an elastomer that does not increase the response time. The use of these transducers is well adapted to measurements in industrial installations, as they do not suffer from dust, oil, etc.

4.2 Determination of the Shock-Wave Configuration for the Rotor of a Supersonic Compressor. Measurements were made on a model of a supersonic compressor, operating in freon [20, 21], and belonging to the ONERA test installation at Palaiseau.

A removable door, located in the casing of the rotor section, was equipped with 12 piezoelectric ceramic pressure transducers [22, 23] making it possible to produce, through a digital averaging unit [24], pressure diagrams as a function of time (Fig. 8(*a*)). The isobar chart corresponding to one blade pitch, which was produced from pressure recordings, is superimposed on the drawing of the shock waves as detected by schlieren photographs (Fig. 8(*b*)).

It is found that the shock waves correspond approximately to the zones where the close spacing of the isobar curves reveals high pressure gradients. This agreement is of great interest because, as schlieren photography is not easily carried out on production engines, such pressure measurements on the casing can indirectly provide shock wave locations.

4.3 Study of Rotating Stall. Rotating stall appears suddenly in a compressor when the flow rate decreases beyond a certain limit, which depends on the rotor geometry [25, 26]. It is characterized by the formation, within the mobile blading, of one or several cells where flow rate is practically zero. These cells, more or less extended, rotate uniformly around the compressor axis, in the same sense but with a lower angular velocity.

The experiment, whose results will be presented later in this paper, was carried out on the rotor test rig described in Section 2, equipped with an isolated rotor; a casing zone located in the rotor section was equipped with 26 piezoelectric ceramic pressure transducers (see Section 4.1).

When there are no rotating stall cells, each of these transducers emits a signal periodically modulated by the passage of the mobile

blades (Fig. 9(*a*)). When rotating stall occurs, its passage in front of a transducer is expressed by an important change of response, as shown in Fig. 9(*b*), where it can be seen that the passage of the separated zone is accompanied by a reduction of the amplitude of the modulation due to the blade passage, while the mean pressure level varies. The oscillograms shown concern a transducer placed in the section of the rotor leading edges.

Two characteristic results of the spectral analysis of the signal of this same transducer are represented, at logarithmic scale, Figs. 10(*a*) and 10(*b*). The first of these figures concerns the 0–500 Hz frequency range in order to emphasize the lines of the rotating stall. The second figure concerns a wider frequency range (0–20 kHz) to show the lines pertaining to moving blade passage. Logarithmic scale reveals the importance of the random part of the signal.

A description of the rotating stall configuration has been attempted from the instantaneous pressure charts on the casing; from these successive charts, we can deduce the evolution of the pressure distribution on the tip profiles of the mobile blades at various times during the passage of the rotating stall cell. Figure 11 represents the proposed pattern, as well as the corresponding pressure distribution on the surrounding blade tip profiles. Considering the relative motion between rotor and separation bubble, blade No. 1 comes out of the disturbed zone while blade No. 6 enters it. On the pressure distribution corresponding to these two blades, it can be seen that lift and angle of attack of blade 6, are much higher than those of blade 1: indeed, the flow deviation caused by the bubble actually provokes a decrease of the angle of attack for blade 1 and an increase for blade 6.

The reverse flow which, within the bubble, attacks blades 3 and 4 by the trailing edge, provokes a very strong lifting effect, except in the region of their leading edges, which now act as trailing edges, as can be seen by the pressure distribution concerning these two blades.

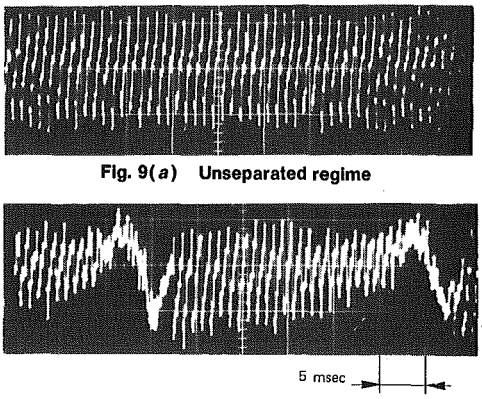

Fig. 9(*a*) Unseparated regime

Fig. 9(*b*) Rotating stall regime

Fig. 9 Oscillograms of the response of a transducer in the leading edge section

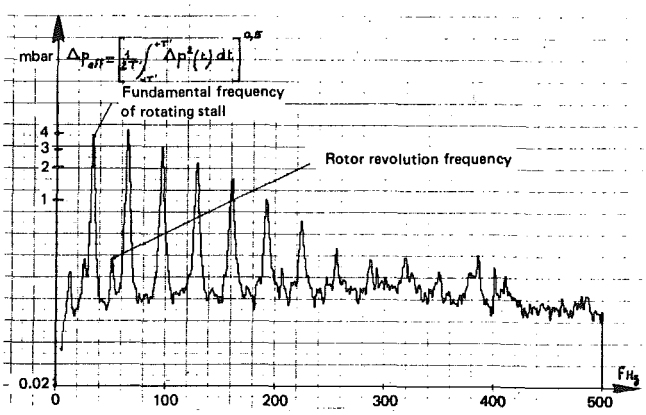

Fig. 10(*a*) Rotating stall analysis $\Delta f = 1$ Hz

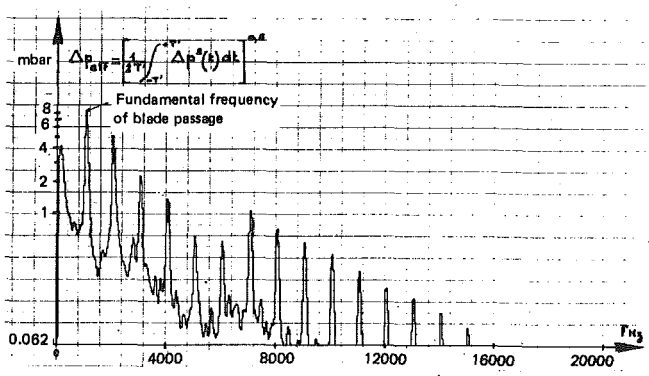

Fig. 10(*b*) Blade passage analysis $\Delta f = 40$ Hz

Fig. 10 Spectral analysis of the response of a transducer close to the leading edge section in the presence of a rotating stall

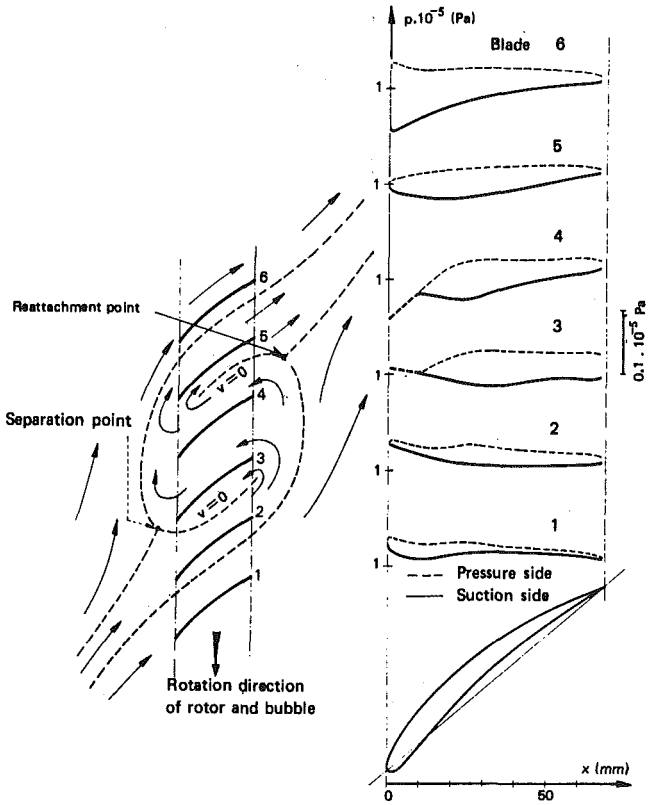

Fig. 11 Assumed sketch of the flow in a rotating stall bubble and instantaneous pressure distribution of the rotor blade tip profiles

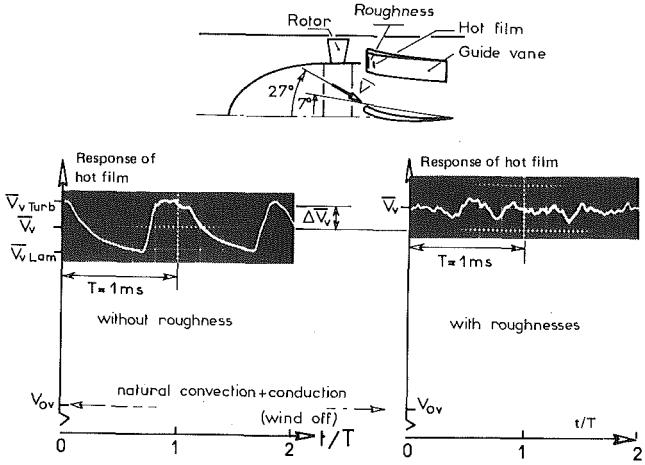

Fig. 12 Detection of boundary layer transition on a stator vane

5 Analysis of Fixed or Mobile Blade Boundary Layers

5.1 Determining the Nature of the Boundary Layer on a Stator Vane by Means of Hot Film Wall Gauges. The hot film transducer used consists of a film of nickel bonded to the wall. It is thin enough so that its presence is unlikely to disturb the flow. The low thermal inertia of the film makes it possible to follow rapid changes in the heat exchange with the flow [27].

These gauges have been used on a stator vane to check whether, when the vane is swept at high frequency by rotor blades wakes, the boundary layer can present, during a fraction of the blade passage time, a laminar nature over a certain portion of the suction side or whether, on the contrary, it remains permanently turbulent.

The oscillogram shown on the left-hand side of Fig. 12 corresponds to the response of a gauge located on the suction side and at about 10 percent of the chord. This response is periodic, but it is not possible to assert whether it is a question of variations linked with the periodic velocity modulation, or whether the observed variations of the signal express the periodic changes in the local convection coefficient, as a result of changes in the condition of the boundary layer.

In order to settle this point, it seemed simple to eliminate the possibility of changes in the nature of boundary layer, by artificially fixing the transition upstream of the detector. The corresponding oscillogram is shown on the right-hand side of Fig. 12. It is found, in fact, that in the presence of roughness the signal produced by the hot film loses its periodic nature, and displays almost random fluctuations. We can therefore attribute the periodic fluctuations on the oscillogram obtained with the smooth blade to changes in the nature of the boundary layer and conclude that, in this case, the turbulent condition on the gauge only occurs during the period when the rotor blade wake passes across it.

5.2 Analysis of the Instantaneous Velocity Profiles In the Boundary Layer on a Stator Vane, Using a Hot Wire Anemometer. Contrary to the experimental method based on hot film gauges, whose application to industrial compressors is envisaged, the hot wire anemometer method does not seem to be usable on industrial test rigs for boundary layers survey.

However, hot wire anemometer provides a very efficient method for detailed analysis of boundary layers on experimental rigs; that is why its use was developed, firstly in order to study the problems of interaction between rotor wakes and stator vane boundary layers, and secondly to check the matching between the time abscissae corresponding to the wake detected by the hot wire and that of the increase in the local convection coefficient detected by the hot film wall gauge.

The measurements consisted of time-recording of the response of the hot wire at different heights of the probe above the suction side of the vane, in particular in the same casing section as that of the hot film gauges described in section 5.1. During a blade passage time T, these recordings were made by using a digital averaging unit with the technique described earlier. Some characteristic aspects of these recordings are shown in Fig. 13(a), on which the signal from the hot film wall gauge (Fig. 13(b)) is plotted.

The shape of the observed phenomena is complex, but presents a characteristic which varies with the change in height of the probe.

Close to the wall, we observe a very marked minimum velocity. This is caused by the passing of a rotor blade wake. Comparison of this recording with the signal from the hot film gauge shows that the increase in the convection coefficient and the start of the reduction in velocity due to the wake, are simultaneous.

As we move away from the wall, this minimum velocity is attenuated, but a second minimum appears, with a lower value of t/T. This second minimum increases as the probe is moved away from the wall of the vane, and remains visible outside of the boundary layer, while the first one disappears.

The time abscissa of each of these two minima remains the same for all heights. Similar explorations of the boundary layer, carried out on the other points of the vane profile, also reveal the presence of the same minima, varying with the height in a similar way.

However, as we move away from the leading edge, the time interval

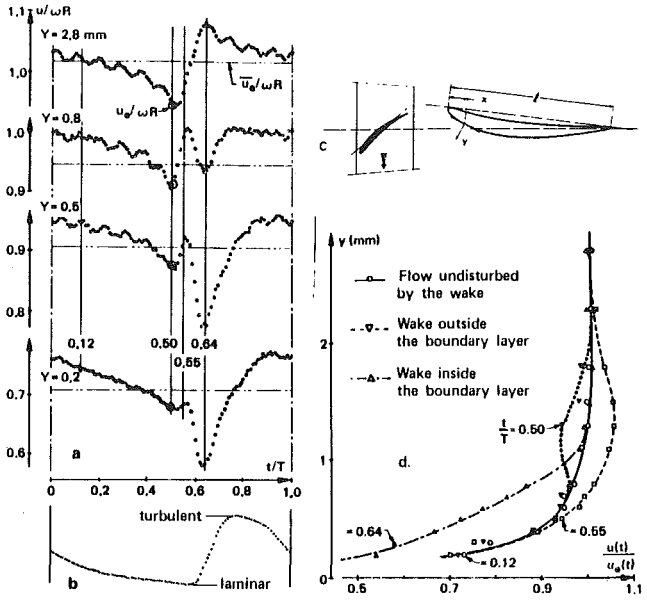

Fig. 13 Direct exploration of a stator vane boundary layer, N = 3000 rpm (a) hot wire—results at several heights, (b) hot film wall gauge, (c) stage schematics (20 rotor blades, 8 stator vanes), (d) instantaneous velocity profiles at x/l = 0.091

observed between the two minima gradually increases: this may be attributed either to the delay in propagation of the wake in the boundary layer, or to the highly three-dimensional nature of the flow in the channel between the stator vanes [28].

By interpolation in the network of curves $u/\omega R = f\,(t/T, y)$, instantaneous velocity profiles in the boundary layer, corresponding to characteristic values of t/T, have been plotted (Fig. 13(d)).

With the exception of the profile measured at the dip on the wake in the boundary layer (t/T = 0.64), all the other profiles share in common a part of the line near the wall. But beyond a height of the order of 0.5 mm, some profiles show singularities, which are apparently due to the disturbance caused by the passing of the wake outside the boundary layer.

5.3 Determining the Nature of the Boundary Layer on Mobile Blades. The visualization process of boundary layer transition by the classical method of sublimating coating is justified in the case of the first rotor, where the incident flow is practically permanent.

However, during short intervals of the period, the upstream flow is disturbed by the wake of the supporting struts of the front bearing (three streamlined radial struts, located about two chords before the rotor).

The passing effects of these disturbances on the nature of the boundary layer of a rotor blade has been detected by means of a hot film gauge bonded on the mobile blade and connected to the measuring unit by a slip ring at the end of the rotor shaft.

The gauge is located on the blade so as to lie at the limit of laminar flow when the rotor is driven at 3000 rpm, the exhaust throttle being wide open (maximum flow rate). This position is deduced from the visualization of the boundary layer transition by the sublimating coating method.

It is thus possible, for a given position of the exhaust throttle, to move the position of the transition backwards by reducing the rotation speed, and so the Reynolds number. By throttling, and thus reducing the compressor flow rate, it is also possible to increase the blade angle of attack, and consequently to move the position of the transition forwards.

The oscillograms shown in Fig. 14 illustrate these two processes. On the first one, rotation speed is less than 3000 rpm, and the boundary layer is laminar on the detector, except during the time of passage of the blade in the strut wakes; this passage is visible twice on the first oscillogram. On the second oscillogram no change of thermal exchange level at the crossing of these wakes can be seen: in this case, because of the reduction of compressor flow rate by throttling, the gauge is immersed in a turbulent boundary layer.

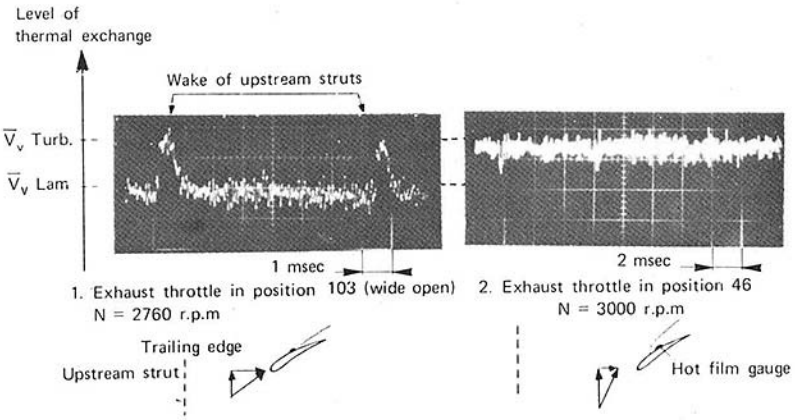

Fig. 14 Detection of the variations of the nature of the boundary layer on the suction side of a rotor blade by means of a hot film wall gauge

6 Conclusions

Most measurements made on industrial test rigs and analysed by engine manufacturers consisted, until recent years, of readings of the mean pressure and temperature at various points of the turbomachine. The information likely to be derived from these measurements could thus only concern the overall characteristics of the machine component investigated.

However, the presence in the flow of periodic or random unsteady components is the origin of disturbances which cause losses in efficiency, structural vibration, and constitute sources of noise.

The analysis of these disturbances is therefore essential to know their causes, and possibly to remedy them. The few experimental results presented in this article, although still needing development and improvement, show that it is now possible to perform unsteady measurements on industrial test rigs.

The means described in this paper are obviously not the only ones and among those developed at ONERA in the Aerodynamics Department some are being used on industrial aeronautic turbomachines.

- Two-dimensional survey of rotor wakes by unsteady pressure cylindrical probes [16] has been carried out in transonic compressors [29] and in high temperature turbines [30].
- It has been shown that laser velocimetry for two-dimensional analysis of rotor wakes of a transonic compressor, can be used.
- Determination of shock wave configuration of supersonic compressor rotor, by means of wall pressure transducers, is currently used [31]. Besides, the application of the hot film measurement technique for characterizing the nature of the boundary layer on mobile blades in an industrial compressor is under study.

Other methods are also under development, for example:

- study of an unsteady pressure probe with five pressure transducers for three-dimensional instantaneous analysis of a distorsion due to air intake-engine interaction,
- study of an unsteady static pressure probe for rotor wake analysis.

Acknowledgments

Work performed with the financial support of DRET, the Research Directorate of the Defence Ministry.

The author appreciated the cooperation of A. de Siévers in this research work, as well as the technical assistance of Ch. d'Humières.

References

1 Weyer, H. B., and Hungenberg, H. G., "Analysis of Unsteady Flow in a Transonic Compressor by Means of High-Response Pressure Measuring Techniques," AGARD-CP 177 (1976).

2 Raj, R., and Lakshminarayana, B., "Three-Dimensional Characteristics of Turbulent Wakes behind Rotors of Axial Flow Turbomachinery," ASME JOURNAL OF ENGINEERING FOR POWER, Vol. 98, Apr. 1976, pp. 218–228.

3 Gorton, C. A., and Lakshminarayana, B., "A Method of Measuring the Three-Dimensional Mean Flow and Turbulence Quantities inside a Rotating Turbomachinery Passage," ASME JOURNAL OF ENGINEERING FOR POWER, Vol. 98, Apr. 1976, pp. 137–146.

4 Wagner, J. M., Okiishi, T. H., and Holbrook, G. J., "Periodically Unsteady Flow in an Imbedded Stage of a Multistage, Axial-Flow Turbomachine," ASME JOURNAL OF ENGINEERING FOR POWER, Vol. 101, Jan. 1979, pp. 42–51.

5 Kool, P., De Ruyck, J., and Hirsch, Ch., "The Three-Dimensional Flow and Blade Wake in an Axial Plane Downstream of an Axial Compressor Rotor," ASME Paper No. 78-GT-66, 1978.

6 Wisler, D. C., "Shock Wave and Flow Velocity Measurements in a High Speed Fan Rotor Using the Laser Velocimeter," ASME JOURNAL OF ENGINEERING FOR POWER, Vol. 99, Apr. 1977, pp. 181–188.

7 Leist, K., "An Experimental Arrangement for the Measurement of the Pressure Distribution on High-Speed Rotating Blade Rows," ASME, Vol. 79, No. 3, Apr. 1957, pp. 617–626.

8 Evans, R. L., "Boundary-Layer Development on an Axial-Flow Compressor Stator Blade," ASME JOURNAL OF ENGINEERING FOR POWER, Vol. 100, Apr. 1978, pp. 287–293.

9 Kerrebrock, J. L., Epstein, A. H., Haines, D. M. and Thompkins, W. T., "The MIT Blowdown Compressor Facility," ASME JOURNAL OF ENGINEERING FOR POWER, Vol. 96, Oct. 1974, pp. 394–406.

10 Weyer, H., and Schodl, R., "Development and Testing of Techniques for Oscillating Pressure Measurements Especially Suitable for Experimental Work in Turbomachinery," ASME *Journal of Basic Engineering*, Vol. 93, Dec. 1971, pp. 603–609.

11 Smith, Jr. L. H., "Wake Dispersion in Turbomachines," ASME *Journal of Basic Engineering*, Vol. 88, Sept. 1966, pp. 688–690.

12 Lakshminarayana, B., and Poncet, A., "A Method of Measuring Three-Dimensional Rotating Wakes behind Turbomachinery Rotors," ASME *Journal of Fluids Engineering*, Vol. 96, June 1974, pp. 87–91.

13 Whitfield, C. E., Kelly, J. C., and Barry, B., "A Three-Dimensional Analysis of Rotor Wakes," *The Aeronautical Quarterly*, Vol. 23, Nov. 1972, pp. 285–300.

14 Walker, G. J., and Oliver, A. R., "The Effect of Interaction between Wakes from Blade Rows in an Axial Flow Compressor on the Noise Generated by Blade Interaction," ASME JOURNAL OF ENGINEERING FOR POWER, Vol. 94, Oct. 1972, pp. 241–248.

15 Walker, G. J., "The Unsteady Nature of Boundary Layer Transition on an Axial-Flow Compressor Blade," ASME Paper No. 74-GT-135 (1974).

16 De Sievers, A., and Larguier, R., "Dispositif d'Étude de l'Écoulement Aérodynamique Interne d'une Turbomachine Axiale," *Bulletin de L'ATMA*, No. 73, 1973, pp. 459 483, and ONERA T.P. No. 1238, 1973.

17 Larguier, R., and De Sievers, A., "Méthodes de Mesures Instationnaires dans les Turbomachines," *Aéronautique et Astronautique* No. 46 (1974-3), pp. 9–18, English translation: NASA TT-F-16082 and Royal Aircraft Establishment, Library Translation No. 1835.

18 Rollin, G., and Suif, F.,"Perfectionnements Apportés aux Moyens pour la Mesure de Pression en Plusieurs Points d un Élément Tournant de Turbomachine," French patent application No. 71-25707, 1971.

19 Boutier, A., Fertin, G., Larguier, R., Lefevre, J., and De Sievers, A., "Laser Anemometry Applied to a Research Compressor," ISL Report, No. 117, 1976, pp. 553–565, and ONERA T.P. No. 1976-43.

20 Fabri, J., and Reboux, J., "Similitude des Performances de Compresseurs Utilisant des Gaz à Thermodynamiques Différentes," *Bulletin de L'ATMA*, No. 71, 1971, pp. 201–220, and ONERA T.P., No. 966, 1971.

21 Fabri, J., "La Visualisation de l'Écoulement dans un Compresseur Axial Supersonique," *Aéronautique et Astronautique* No. 17, 1970–1.

22 Lambourion, J., and Larguier, R., "Description, Étalonnage et Exemple d'Utilisation d'un Capteur de Pression à Court Temps de Réponse," *Recherche Aerospatiale*, No. 133 (Nov.–Dec. 1969), pp. 53–54.

23 Lopez, J., and d'Humières, Ch., "Etalonnage Dynamique des Capteurs de Pression par Créneaux Périodiques," *Recherche Aerospatiale*, No. 1970-3, pp. 175–176.

24 Larguier, R., Fasso, G., and Scherer, M., "Etude des Fluctuations Pér-

iodiques de Pression sur les Aubes Fixes d'un Compresseur Axial de Grande Puissance," *Bulletin de L'ATMA,* No. 71, 1971, pp. 177–199, and ONERA T.P., No. 967, 1971.

25 Le Bot, Y., *Etude du Phénomène de Décollement Tournant. Aéro-Hydro-Élasticité,* Ed. Eyrolles, Paris, 1973.

26 Werle, H. and Gallon, M., "Ecoulement dans une Maquette Hydraulique de Turbomachine Axiale," *Recherche Aerospatiale,* No. 1977-5, pp. 267–288.

27 McCroskey, W. J., and Durbin, E. J., "Flow Angle and Shear Stress Measurements using Heated Films and Wires," ASME *Journal of Basic Engineering,* Vol. 94, March 1972, pp. 46–52.

28 Larguier, R., and De Sievers, A., "Mesures Instationnaires dans les Turbomachines," *Recherche Aerospatiale,* No. 1975-5, pp. 267–277, English translation: European Space Agency, Technical translation, ESA TT-298, May 1976.

29 Larguier, R., and Ruyer, C., "Méthodes d'Analyse Experimentale de l'Écoulement Instationnaire Interne d'un Compresseur Aéronautique Transsonique," *Recherche Aerospatiale,* No. 1972-6, pp. 353–354.

30 Le Bot, Y., Charpenel, M., and Michard, P., "Techniques de Mesure dans les Turbines à Hautes Températures," AGARD-CP 229 (1978), and ONERA T.P., No. 1977-92.

31 Paulon, J., and Veuillot, J., "Etude Théorique et Experimentale d'une Grille d'Aubes Supersonique Annulaire Mobile," ICAS-Paper, No. 76-31 (1976), and ONERA T.P., No. 1976-105.

Efficient Laser Anemometer for Intra-Rotor Flow Mapping in Turbomachinery

J. A. Powell
A. J. Strazisar
R. G. Seasholtz

NASA-Lewis Research Center,
Cleveland, OH 44135

Innovative features of the anemometer include: (1) a rapid and efficient data acquisition process, (2) a detailed real-time graphic display of the data being accumulated, and (3) input laser beam positioning that maximizes the size of the intra-rotor region being mapped. Results are presented that demonstrate the anemometer's capability in flow mapping within a transonic axial-flow compressor rotor. Typically, a velocity profile, derived from 30,000 measurements along 1000 sequential circumferential positions covering 20 blade passages, can be obtained in 30 s. The use of fluorescent seed particles allows flow measurements near the rotor hub and the casing window.

Introduction

In order to improve the understanding of flow phenomena in turbomachinery, and to verify flow models used in analysis, detailed measurements of the internal flow field of the rotating components are needed. Increasingly, laser anemometry is being used to answer this need [1]. Several approaches to laser anemometry have been applied to turbomachinery. Among these, are the fringe-type anemometer (sometimes called a laser Doppler velocimeter) [2, 3] and the time-of-flight anemometer [4–6].

Since turbomachinery research facilities often consume large amounts of energy, there is an additional need that flow measurements be made as quickly as possible. In each of the systems described in [2, 4–6], the laser was time-gated so that velocity measurements were accepted only during a small fraction of each revolution of the rotor. The reason for this is as follows: The probe volume, fixed at some axial and radial position, sweeps out a circumferential path within the rotating blade row. In each case, the circumferential path in a given blade passage was divided into a fixed number of line segments and the velocity for each segment was determined, one segment at a time. This was accomplished by turning the laser beam on (i.e. time-gating the laser) only when the desired line segment was in the field of view. In the system of [5, 6], measurements from corresponding segments in successive blade passages were averaged in order to speed up the data taking rate. However, in all of the time-gated systems, the data acquisition process is very wasteful of facility run time. In the system described in [3], data are continuously collected from a circumferential path covering two blade passages. The individual measurements are then presented as marks on an oscilloscope display such that the vertical position of each mark represents the velocity and the horizontal position represents the circumferential location of the measurement. Measurements are recorded by photographing the oscilloscope display. This approach also does not lend itself to rapid and efficient data taking.

This paper describes a fringe-type laser anemometer (LA) with a data acquisition process which is much more efficient. In this system, velocity measurements, at any given time, are accepted from any of 1000 line segments along the circumferential path. Each velocity measurement is tagged with the location of the line segment in which it occurred and the resulting data sorted out with a minicomputer. Also adding to the efficiency of the anemometer is a real-time graphic display that allows the evaluation of data being accumulated. The anemometer also makes use of techniques that minimize the portion of the intra-rotor region that cannot be mapped because of shadowing due to blade twist.

The anemometer was used to map the intra-rotor region of a transonic axial-flow compressor rotor. The rotor contained 52 blades and had an overall diameter of 50.8 cm. It was operated at a maximum speed of about 16,000 rpm. Sufficient results are presented to demonstrate the capability of the anemometer. This particular application is discussed in detail in another paper [7].

Description of System Hardware

Brief Overall Description. Figure 1 shows the basic optical components of the LA. It is a fringe-type, on-axis, backscatter system that uses the 514.5 nm line of an argon-ion laser. In a fringe-type LA, the flow velocity is determined by measuring the transit time required for a seed particle to traverse laser fringes of known spacing. The fringes occur at the intersection (called the probe volume) of the two laser beams. The particular velocity component being measured lies in the plane of the two beams and is perpendicular to the bisector of the two beams. The component is selected by rotating the splitter to the required angle. Optical access to within the rotor blade row is made along an approximately radial path through a window in the casing around the rotor. The motorized-goniometer mirror mount, shown in the figure, allows the converging beams to be positioned so as to minimize shadowing due to the twisted rotor blades. This ability to position the bisector of the input laser beams in an off-radial direction also allows, at least in principle, the measurement of the radial component of velocity. Fluorescent seed particles coupled with an orange-pass optical filter in the receiving optics reduce detection of unwanted scattered light. This allows measurements near the rotor hub and casing window.

Contributed by the Gas Turbine Division and published in the symposium volume, *Measurement Methods in Rotating Components of Turbomachinery*, ASME, New York, 1980. Manuscript received for publication in the JOURNAL OF ENGINEERING FOR POWER May 22, 1980.

Figure 2 is a simplified block diagram of the complete laser anemometer system. Velocity measurements occur randomiy along the measured circumferential path since a measurement depends upon a seed particle passing through the probe volume when it is in the field of view of the optics. At any given time, the system accepts measurements from any of 1000 sequential angular positions along this circumferential path. The position information for each velocity measurement is provided by an electronic shaft angle encoder that was developed for this system. When a measurement is obtained, the transit time and rotor position are recorded and processed by the minicomputer. In this way, velocity measurements are accumulated along a circumferential path. In this paper, velocity measurements along a circumferential path covering up to twenty blade passages is called a velocity profile. A complete velocity map is obtained by determining velocity profiles at a sequence of axial and radial positions. After each profile is obtained, the data are stored on a magnetic disk.

Overall control of the anemometer is maintained through a CRT (i.e., video) terminal. During each data run, a CRT display of the accumulated data is updated as often as every 5 s. The display contains: (1) alphanumeric information on operating conditions, (2) a plot of the velocity profile for an ensemble-averaged blade passage, and (3) a histogram showing the distribution of measurements over the 1000 angular positions.

Optics. The anemometer uses the 514.5 nm line of an argon ion laser operating in the TEM_{00} mode at a power level of 1.5 W. The laser beam (see Fig. 1) is turned through 180 deg before passing through two mode matching lenses. The function of these lenses is to insure that a beam waist is located at the probe volume and that the waist diameter is the desired value, in this case, 125 μm, based on the $1/e^2$ intensity points. Using two lenses, instead of one, allows this to be accomplished with off-the-shelf lenses [8].

The optical path through the beam splitter is shown in Fig. 3. The splitter is rotated about the optical axis to select a particular velocity component. The two optical flats are selectively coated to minimize losses. This particular splitter configuration yields equal path lengths for the two beams and symmetrical placement of the two beams about the optical axis. The splitter flats are coated for "S" polarization which means that the electric vector of the incident laser beam must be perpendicular to the plane of incidence, that is, the plane containing the surface normal and the incident beam. A $\lambda/2$ retardation plate, placed in front of the splitter, rotates the normally vertical polarization of the laser beam to follow the splitter rotation. However, a characteristic of the $\lambda/2$ retardation plate is that it rotates the direction of polarization twice the angle through which it turns. So, the retardation plate is rotated at half the angle of the beam splitter.

After passing through the 50 mm dia, 200 mm focal length focusing lens, the two beams are turned 90 deg by a mirror mounted on a motorized goniometer cradle. The angle, θ, between the two converging beams was determined to be 2.825 deg by projecting the beams on a wall at a distance of about 3 m and measuring the distance to the wall and the separation of the projected spots. Because the spots were blurred, multiple measurements of the spot separation were made with the beam splitter set at different angles. The resulting standard deviation in θ from these measurements was 0.02 deg. With this angle θ and a wavelength of 514.5 nm, the fringe spacing is 10.4 μm.

Some of the light scattered from seed particles passing through the probe volume is collected and directed to a 100 μm dia pinhole in front of the photomultiplier (PM) tube. The focusing lens in front of the PM tube is 50 mm in diameter, with a focal length of 160 mm. The combination of the 160 mm and 200 mm focal lengths of the two focusing lenses yields a pinhole image diameter of 125 μm at the probe volume. These lenses are commercially-available cemented doublets corrected to obtain negligible spherical aberration (to third order) for an object-to-image ratio of infinity. A 25 mm dia mask over the central part of the 160 mm lens is used to reduce the effective length of the probe volume to about 2 mm.

All of the optics, including the laser, are located on a large horizontal x-y traversing table. With this table, the probe volume can be located at a particular axial and radial position within 0.05 mm. The beam

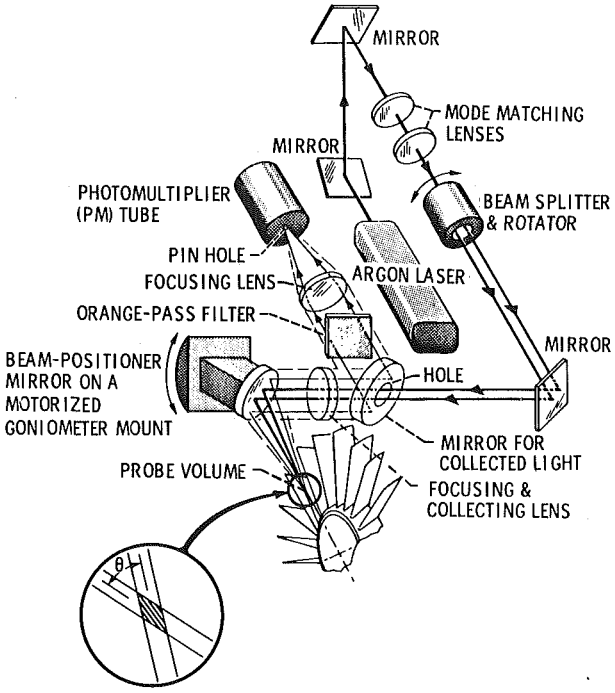

Fig. 1 Optical layout of anemometer

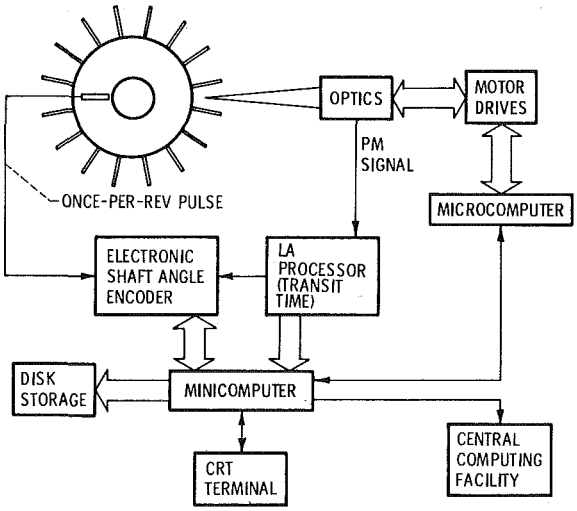

Fig. 2 Block diagram of complete anemometer

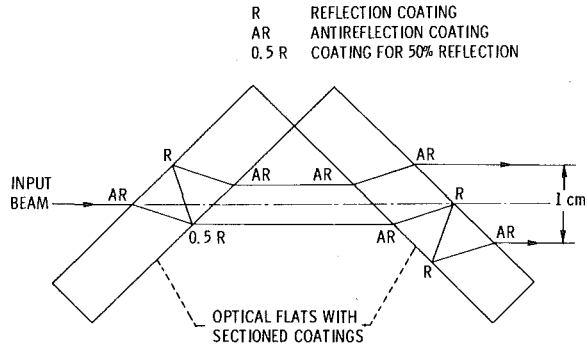

Fig. 3 Optical path through beam splitter

splitter can be rotated to within 0.03 deg and the direction of the input beams (i.e., the bisector of the two beams) can be oriented to within 0.01 deg using the goniometer-mounted mirror.

System Computers and Electronics. In order to obtain efficient operation, a minicomputer is used to process the enormous amount of data generated and to provide the required system control. The

minicomputer, a 16-bit-word computer, has 32 k (k = 1024) words of core memory and hardware floating-point multiply/divide capability. These features allow large tables of data to be stored and processed quickly. It also has dual cartridge-type magnetic disk storage, with each disk having a capacity of 1.25 million 16-bit words. The minicomputer terminal has a CRT display for presentation of both alphanumeric and graphic information. Also, the minicomputer is connected by phone lines to a large central computer, to which data are transmitted for both further processing and curve plotting.

A commercial counter-type LA processor with a 500 MHz clock processes the signal bursts from the PM tube. The processor measures the transit time of a seed particle across eight fringes. It performs several tests on each signal burst from a seed particle passing through the probe volume to help insure measurement validity. One of these tests is the $^5/_8$ comparison test where the transit times for five and eight fringes are compared. The ratio of these two times must be sufficiently close to the value $^5/_8$ to be accepted. Another test is a sequence check such that during each signal burst, the signal must alternately rise above a threshold level and fall below the zero level at each fringe in order to be accepted.

For each validated measurement, the LA processor loads a digital representation of the transit time for the eight fringes into an output buffer register. Also, the electronic shaft angle encoder (to be described in the next section) is signaled and the current rotor angular position is loaded into the encoder output buffer register. The processor also interrupts the minicomputer which then records the transit time and the angular position. For the particular application described in this paper, measurement rates within a circumferential path being mapped were about 2500 measurements per second, and transit times were of the order of 50 ns per fringe across the fringe spacing of 10.4 μm.

In keeping with the design goal of efficient data taking, the motions required to position the probe volume and select the velocity component are controlled by the minicomputer. High-speed stepping motors provide the following four motions: the axial and the radial probe volume position (x-y traversing table), the beam splitter angle, and the input beam direction (goniometer cradle). An optical encoder attached to each motor shaft provides position feedback to each motor drive. The motor drives are of the accelerate-decelerate type (with regard to the output pulse train) and typically position the optics in about one second. Each motor has a "home" position to which it can be moved for remote position calibration.

An eight-bit-word microcomputer serves as the interface between the four motor drives and the minicomputer. The microcomputer and the motor drives are located in the test cell and the minicomputer is located in a control room. In order to minimize noise pickup in transmitting data back and forth between these two computers, a standard 20 mA asynchronous current loop is used.

Electronic Shaft Angle Encoder. This section describes the previously mentioned electronic shaft angle encoder. It was developed for the anemometer to simplify the task of tagging each velocity measurement with the proper angular position. The encoder that was developed is shown in Fig. 4. It produces the current angular position independent of rotor speed with the only required input being an accurate once-per-rev (OPR) pulse. Although the encoder involves the use of the minicomputer, a commercial stand-alone version is now available with the required computational logic circuits included. At this point, it should be mentioned that the encoder has applications beyond the anemometer described in this paper. Any application requiring the knowledge of the instantaneous angular position of a high-speed rotor could make use of the encoder. The encoded angular position of the rotor is produced by the counter that is clocked by the frequency synthesizer. The synthesizer frequency is adjusted as necessary by the minicomputer so that the number of counts for each revolution (selected by the operator) remains constant. An optical sensor, detecting a target on the rotor hub, provides the OPR pulse. At this pulse, the current count is read into the output buffer register of the counter, the counter is reset to zero, and the minicomputer is interrupted. The minicomputer then calculates a new synthesizer frequency using the equation

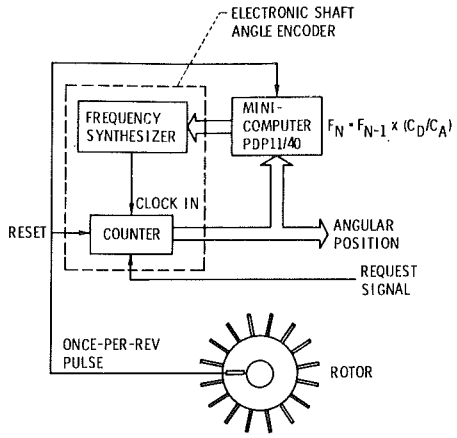

Fig. 4 Method for generating the rotor angular position

$$f_n = f_{n-1} \times \left(\frac{C_D}{C_A}\right)$$

where f_n = new frequency, f_{n-1} = frequency programmed on previous revolution, C_D = desired count for one revolution, and C_A = actual count for previous revolution. The synthesizer is then programmed with the new frequency. Thus, the number of counts for each revolution remains approximately constant, independent of rotor speed. At each velocity measurement, a request signal causes the current count to be transferred to the output buffer register where it can be recorded with the velocity.

An operational requirement of the angle encoder is that the fractional change in the angular velocity of the rotor for each revolution be small compared to the desired resolution in the angular position expressed as a fractional part of one revolution. Otherwise, it will be necessary to adjust the synthesizer frequency more than once during each revolution. This requirement was easily met in the research facility to which the anemometer was applied. For example, the 52-bladed research rotor was operated at speeds up to about 16,000 rpm. The desired count was chosen to be 200 counts per blade passage for a total count per revolution of 10,400. The long term (i.e., 1 s) speed drift in the facility was about 0.3 percent (30 counts out of 10,400), but the rev-to-rev speed changes were less than one count. For all results and examples cited in this paper, the encoder count was divided by four to yield a resolution of 50 angular positions (angles) per blade passage. However, the anemometer was set up so that it could operate with either 50, 100, or 200 angles per blade passage.

Description of System Software

General Comments. Increasingly, as instruments are being applied to more difficult and/or complex experiments, computers and their associated software are assuming a larger proportion of the development time. In the anemometer being described, more than half of the development time was spent on the software. Among the software design goals was the use of a high level language (e.g., Fortran) in those cases where operating speed is not important.

Figure 5 shows a block diagram of the measurement program for determining velocity profiles. The upper four modules are Fortran. Because of execution-speed requirements, the lower three routines are written in assembly language. After the required parameters are initialized, and appropriate tables are cleared, the main program determines the routing to the various subroutines. The following sections describe the functions of these subroutines.

Once-Per-Rev (OPR). There are two routines that are called for in response to a hardware interrupt signal, and the higher priority of the two is the OPR routine. Its primary function is to service the electronic shaft angle encoder. At the OPR pulse, this routine causes the current encoder count to be read, calculates the new synthesizer frequency, and then updates the synthesizer. If the current encoder count is not within some preset tolerance of the desired count, typically 0.1 percent, then the velocity data accumulated in the previous

revolution are discarded. This prevents velocity data from being assigned to the wrong angular position if the encoder is not properly tracking the rotor speed. The OPR routine requires about 200 μs which is about 5 percent of a revolution at 16,000 rpm.

Data Acquisition. This is the other interrupt routine. Its function is to respond to the anemometer's counter-type processor. When a validated measurement has been obtained by the LA processor, a "data ready" signal interrupts the minicomputer, which then reads both the transit time and the corresponding angular position (angle). If the angle is one of the 1000 angles being accepted, the data are put into one of two temporary buffers for further processing (see Fig. 6). If the angle is beyond the range of those angles being accepted, the routine is disabled until the next OPR occurrence. This allows data in the buffers to be processed for the rest of the revolution without interruption. This routine, the shortest of all the routines in execution time, requires about 40 μs. It essentially sets a limit on the rate at which velocity data can be accumulated.

Data Processing. This routine processes the data that have been placed in the temporary buffers. At any given time one of the buffers is being loaded with data and the other is being emptied as the data are processed. The reason for the two buffers is the following. As mentioned previously, after each revolution the total encoder count is compared with the desired count. If the count is within some preset tolerance and the buffer being emptied is empty, then the roles of the two buffers are exchanged. That is, the buffer being emptied in the previous revolution will now be the buffer being loaded with new data. This exchange is done in the OPR routine. However, if a spurious OPR pulse was detected during the previous revolution, the encoder may contain incorrect position counts. An indication of this problem will show up in the OPR routine where the total count will not be within tolerance. In this case, the data in the buffer being loaded in the previous revolution will be discarded.

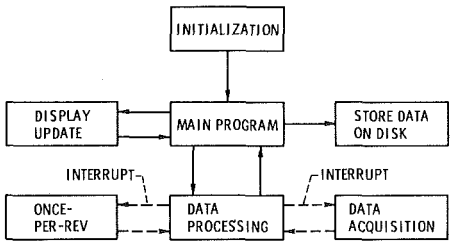

Fig. 5 Diagram of the minicomputer routines used in the anemometer measurement program

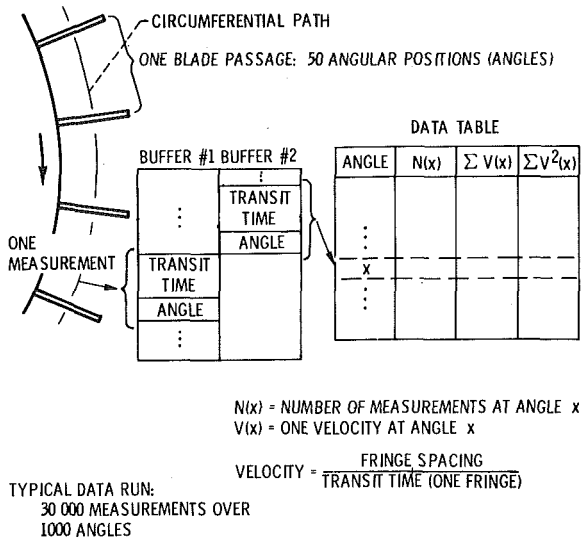

Fig. 6 Data aquisition and processing scheme

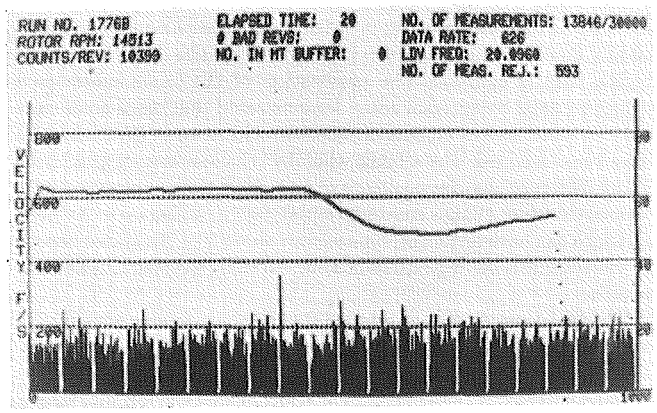

Fig. 7 CRT real-time presentation of accummulated data

An important consideration in the use of the minicomputer was the amount of available random access memory, in this case, the core memory. Recording all transit time-angle data pairs would quickly fill the available memory. For example, 30,000 measurements would require 60,000 words of storage, but there are only about 10,000 words available for storage. Also, the data would not be in a form that could easily be converted into a real-time display. In order to reduce the amount of storage required, the approach taken in recording data is shown in Fig. 6. At each rotor angular position (i.e., angle, x), the following information is stored: (1) the number of measurements at each angle, $N(x)$, (2) the sum of the velocities, $\Sigma V(x)$, and (3) the sum of the velocities squared, $\Sigma V^2(x)$. With this information, the mean velocity and standard deviation can be calculated for every angle.

To obtain the velocity from the processor data output, a number of data processing steps are taken. The processor output is actually a time measurement (transit time) in a special floating-point format (mantissa-exponent). The transit time is first transformed into an integer representation of the velocity. Since the velocity is inversely proportional to the transit time, this step involves taking the reciprocal of the transit time. In integer form, the velocity is used in the comparison test described below. The velocity is then converted to the two-word floating-point format compatabile with a real variable in Fortran. In this format, the quantities, $\Sigma V(x)$, and $\Sigma V^2(x)$ are calculated. The quantity, $N(x)$, is a one-word integer. The data table, thus, consists of five 16-bit words, $N(x)$, $\Sigma V(x)$, and $\Sigma V^2(x)$, for each angle. For 1000 angles, the data table takes up 5000 words of storage. The magnitude of the angle defines the location of the five words within the table.

A data run, consisting of two parts, is completed for each probe volume position and beam orientation. This enables an additional method for discarding "bad data". In the first part of the data run, velocity data from corresponding positions from all 20 blade passages are combined to form an "average" for each position (a total of 50 averages). As discussed in the next section these averages are used in the real-time display. In the second part of the data run, each measured velocity value is compared with the corresponding previously obtained average. If the difference is more than 25 percent, then that value is rejected as being bad data.

The data processing routine continues between interrupts until (1) the desired number of measurements has been obtained, or (2) it is time for a display update. In either case, control returns to the main program. If the desired number of measurements has been obtained, a routine is called that transfers the data to a magnetic disk.

Display Update. In order to be able to evaluate data being accumulated, a routine to provide a real time graphic display on the CRT was developed. An example of this display is shown in Fig. 7. The display is normally updated every 15 s, but the time between updates can be set to any value greater than 5 s. The display consists of three parts. The upper part is an alphanumeric presentation of some of the operating conditions. For example, it includes the elapsed time (in seconds) since the beginning of a data run to obtain a velocity profile.

The lower part is a histogram of the number of measurements over the 1000 angles covering the twenty blade passages. The abcissa ranges from 0 to 1000 and the ordinate ($N(x)$, listed on the right side of the histogram) ranges from 0 to 80 measurements.

The middle part is a plot of the velocity profile over an ensemble-averaged blade passage. The abcissa ranges over a circumferential segment with a length of one blade pitch. Note that the abcissa for the velocity profile covers only one blade passage, while the abcissa for the histogram covers 20 blade passages. The ordinate (listed on the left side) is in feet per second. It is obtained by averaging velocity data from corresponding positions from each of the 20 blade passages.

When a CRT update is required, data acquisition is suspended for about one second while the necessary graphic information is calculated. The transmission of the graphic information to the CRT terminal is interspersed with the data processing routine, so the three-second time for transmission has a small impact on the overall measurement rate.

Optics Position Control. When the optics needs to be reset, the minicomputer transmits a set of new motor positions to the microcomputer then calculates the direction and number of pulses each motor must receive to reach the new position. The correct pulse trains are then transmitted in parallel to the corresponding motor drives. If the number of pulses transmitted to each motor agrees with number of pulses returned by the encoder on each motor shaft, the optics are assumed to be at position and ready for measurements. The microcomputer then transmits an "at position" signal to the minicomputer and measurements resume. If the numbers don't agree, an error message is transmitted to the minicomputer and appropriate action taken. The software for the minicomputer for this operation is written in Fortran, except where assembly language is required in the transmission of data. The software for the microcomputer is written in PL/M [10] except for the transmission of pulses to the motor drives.

System Performance

Experimental Procedure. The initial application for the anemometer was in a single-stage transonic compressor research facility. The first test rotor had 52 blades, and inlet tip diameter of 50.8 cm, and a hub-tip radius ratio of 0.7. The 100 percent design tip speed for the rotor was 426 m/s, corresponding to a rotor speed of 16,000 rpm.

Optical access to the rotor was made along a nominally radial path through a window in the casing. The window was ordinary double-strength window glass (3 mm thick) that was contoured to match the inside wall of the casing. The contouring was accomplished by allowing the glass to sag onto a machined graphite form in a vacuum furnace. The window, which was not optically coated, had a clear aperture of 5.1 cm along a circumference and 10.2 cm in the axial direction.

When the probe volume is near a solid surface, scattered laser light from the surface tends to dominate the collected signal. As a result, measurements cannot be made near the casing window and the rotor hub. In order to minimize this problem, the fluorescent dye technique [9] was used. In this technique, fluorescent seed particles absorb the laser light and then emit light at a different wavelength. An optical filter in the receiving optics filters out the unwanted laser light scattered from surfaces near the probe volume. The selected seed material was a 0.02 molar solution of rhodamine 6G in a 50-50 mixture (by volume) of ethylene glycol and benzyl alcohol. This particular material fluoresces orange when it absorbs the green laser light. Thus, when the orange-pass filter is placed in the receiving optics, the extraneous green scattered light is filtered out. A commercial atomizer produced the seed particle aerosol by feeding the liquid into a high velocity jet (located within the atomizer). The mean size of the particles that were actually measured was estimated to be about 1.2 to 1.4 μm. This estimate is based on (1) particle lag in crossing shocks within the rotor, and (2) separate experiments involving particle acceleration through a nozzle with known flow conditions.

Results. Velocity measurements were taken over operating conditions ranging from 50 to 100 percent design speed. A detailed description and discussion of the results are given elsewhere [7]. However, sufficient discription is given here to illustrate the capabilities of the anemometer.

The encoder worked very well in providing the rotor angular position information. For example, at 16,000 rpm the average deviation of the actual encoder count from the desired count for a complete revolution was about three counts out of 10,400 (200 × 52 blades). Remembering that each rotor angular position is obtained by dividing the encoder count by four, the average error in the angular position was 0.75 at the end of a revolution. As the rotor speed drifts up and down, the position error generally is a minimum at the beginning of a revolution when the synthesizer update occurs and a maximum at the end. The 20 blade passages selected for measurements were normally in the first half of each revolution. Thus, the actual average error in the rotor angular position was less than 0.75 out of 50 for each of the twenty blade passages.

Velocity profiles along circumferential paths covering 20 consecutive blade passages (i.e., 50 angular positions per blade passage X20 blade passages) were determined and recorded. Axial and radial positions that were measured included the region upstream and downstream of the rotor as well as within the blade row. Typically, the profiles consisting of 30,000 measurements over 1000 angular positions were obtained in 15 to 45 s. At 90 to 100 percent design speeds, shocks were measured in front of and within the blade row.

The real-time display shown in Fig. 7 is a typical result and was obtained at 90 percent design speed (14,513 rpm) within the blade row. It shows the ensemble-average velocity profile for one blade passage at 20 s into the second part of a data run where 13,846 out of 30,000 measurements have been obtained. The *Data Rate* of 626 per second is only an approximate value since the time of 20 s is only an approximate value. The *LDV Freq* of 20.096 MHz is a typical value of the LA frequency calculated from the LA processor output. A total of 593 measurements have been rejected because they differed by more than 25 percent from the corresponding average obtained in the first part of the data run. The *Counts Per Rev* of 10,399 is a typical value of the encoder count for one rotor revolution. In this case, the desired count was 10,400. The *No. Bad Revs* is the number of revolutions since the beginning of part two of the data run where the total encoder count for one revolution differed from the desired count by more than the preset tolerance (in this case, 10). The *No. in MT Buffer* is the number of transit time-angle data pairs in the temporary data buffer being processed. If this number becomes large, it indicates the minicomputer is not keeping up with the data being collected. The knee of the profile is where a shock occurs. The gap at the right is where the blade for the ensemble-averaged blade passage occurs. The gaps in the histogram at the bottom are where the 20 individual blades occur. At the edge of the eighth gap from the left there is a spike in the number of measurements. This is probably caused by this particular blade becoming coated with the fluorescent dye material.

The accuracy of measurements made with a fringe-type anemometer is strongly dependent on each application. Pertinent factors include the flow conditions, signal-to-noise ratio of each signal burst, system noise, etc. In this particular application, it is estimated that the velocity profiles determined for the ensemble-averaged blade passage are accurate to within about 3 to 5 percent.

Conclusions

This paper has described an anemometer that was designed to make intra-rotor flow measurements in turbomachinery rapidly and efficiently. Another design goal was to maximize the size of the intra-rotor region that is mapped. The application of the anemometer to a transonic axial compressor rotor demonstrated that these goals were met. Detailed measurements of shocks and intra-rotor flow velocities have been obtained. The scheme whereby velocities are accepted from many different angular positions at any given time works very well. Velocity profiles along a circumferential path covering up to 20 blade passages can be determined, typically, in about 30 s. An added benefit of this scheme is the high spatial resolution along the resulting velocity profile.

The real-time display developed for the anemometer is helpful in achieving efficient operation. As an example, both the ensemble-averaged velocity profile and the histogram are useful indicators of extraneous velocity data due to light scattering by the rotating blades. When this problem is significant, corrective action can be taken (e.g.,

input laser beam direction can be changed).

The capability of changing the input laser beam direction allows an increase in the size of the intra-rotor region mapped. By operating at a calculated optimum input direction, the shadowing due to twisted rotor blades is minimized.

References

1 Durst, F., Melling, A., and Whitelaw, J. H., *Principles and Practice of Laser Doppler Anemometry,* Academic Press, New York, 1976.

2 Wisler, D. C., and Mossey, P. W., "Gas Velocity Measurements Within a Compressor Rotor Passage Using the Laser Doppler Velocimeter," ASME JOURNAL OF ENGINEERING FOR POWER, Vol. 95, No. 2, Apr. 1973, pp. 91–96. (Paper 72-WA/GT-2, Nov. 1972.)

3 Wisler, D. C., "Shock Wave and Flow Velocity Measurements in a High Speed Fan Rotor Using the Laser Velocimeter," ASME JOURNAL OF ENGINEERING FOR POWER, Vol. 99, No. 2, Apr. 1977, pp. 181–188. (Paper 76-GT-49, Mar. 1976.)

4 Schodl, R., "Laser Dual-Beam Method for Flow Measurements in Turbomachines," ASME Paper No. 74-GT-157, Mar. 1974.

5 Eckardt, D., "Detailed Flow Investigations Within a High-Speed Centrifugal Compressor Impeller," ASME *Journal of Fluids Engineering,* Vol. 98, No. 3, Sept. 1976, pp. 390–402. (Paper 76-FE-13, Mar. 1976.)

6 Dunker, R. J., Strinning, P. E., and Weyer, H. B., "Experimental Study of the Flow Field Within a Transonic Axial Compressor Rotor by Laser Velocimetry and Comparison with Through-Flow Calculations," ASME JOURNAL OF ENGINEERING FOR POWER, Vol. 100, No. 2, Apr. 1978, pp. 279–286. (Paper 77-GT-28, Mar. 1977.)

7 Strazisar, A. J. and Powell, J. A., "Laser Anemometer Measurements in a Transonic Axial Flow Compressor Rotor," presented at the *Symposium on Measurement Methods in Rotating Components of Turbomachinery,* Gas Turbine Conference and Products Show, New Orleans, Mar. 9–13, 1980.

8 Seasholtz, R. G., "Laser Doppler, Velocimeter System for Turbine Stator Cascade Studies and Analysis of Statistical Biasing Errors," NASA TN D-8297, 1977.

9 Stevenson, W. H., dos Santos, R., and Mettler, S. C., "Fringe Mode Fluorescence Velocimetry," AGARD CP-193, 1976, pp. 20-1 to 20-9.

10 "8008 and 8080 PL/M Programming Manual," Intel Corporation, Santa Clara, Calif., 1975.

Laser Anemometer Measurements in a Transonic Axial Flow Compressor Rotor

A. J. Strazisar
J. A. Powell

NASA-Lewis Research Center,
21000 Brookpark Road,
Cleveland, OH 44135

A laser anemometer system employing an efficient data acquisition technique has been used to make measurements upstream, within, and downstream of the compressor rotor. A fluorescent dye technique allowed measurements within endwall boundary layers. Adjustable laser beam orientation minimized shadowed regions and enabled radial velocity measurements outside of the blade row. The flow phenomena investigated include flow variations from passage to passage, the rotor shock system, three-dimensional flows in the blade wake, and the development of the outer endwall boundary layer. Laser anemometer measurements are compared to a numerical solution of the streamfunction equations and to measurements made with conventional instrumentation.

Introduction

Advances in the aerodynamic technology of turbomachinery are dependent on obtaining a comprehensive understanding of the complex physical phenomena which occur within the blade passages. Progress is being attained through improvements in both analytic and experimental techniques. With the increased availability of large scale computers significant advances in computational methods for compressor design and analysis are being made. As advances in numerical methods continue, there is an increasing need to make detailed flow measurements inside blade rows. Such measurements will determine flow phenomena such as the distribution of turning and losses which are required inputs for some numerical methods. They will also generate data for use in verifying numerical solutions.

Cascade tests and the use of rotating instrumentation in low-speed machines are two experimental approaches to the measurement of intra-blade flowfields. However, these approaches cannot provide data on the combined effects of high Mach number and high rotational speeds. High-response pressure measurements and nonintrusive optical measurement techniques such as laser anemometry and holographic interferometry are extending flow measurement capabilities in the high-speed testing regime beyond those available with conventional low-response instrumentation. Applications of laser anemometer (LA) systems to axial-flow turbomachinery employing fringe-type anemometers have been reported in [1–3]. Applications involving time-of-flight anemometers have been reported in [4].

This paper describes the application of a LA system to a transonic axial-flow compressor rotor. The results of several types of measurements which demonstrate the system's capability of measuring velocity and flow angle in a rotating blade row are discussed. However, a comprehensive evaluation of the flow in this transonic compressor is beyond the scope of the present paper. A detailed description of this LA system is contained in [5]. Since transonic compressor testing requires a significant expenditure of both manpower and energy, a rapid data acquistion technique has been developed in order to minimize running time. The incorpation of four degrees of freedom in the laser beam orientation enables measurement of the radial component of velocity in some cases and the minimization of regions blocked from optical access by the complex blade geometry.

Test Compressor and Instrumentation

The test rotor of the present study was designed as an inlet rotor for a core compressor. The rotor design pressure ratio and mass flow are 1.67 and 215 kg/m^2/s, respectively, at a tip speed of 426 m/s. The tip relative Mach number is 1.4 at design speed. The rotor has 52 blades, a tip chord length of 44.6 mm, and a tip solidity of 1.48. The inlet tip diameter is 508 mm and the hub-tip radius ratio is 0.7. For the LA application reported herein, the rotor was tested without inlet guide vanes and without a stator blade row. This configuration eliminates the circumferential variation in the flowfield induced by the stationary blade rows and thereby simplifies data acquistion and analysis.

Optical access is provided by a glass window which is 102 mm long in the axial direction and 51 mm wide (11 deg arc) in the circumferential direction. The window material is 3 mm thick commercial window glass formed to the outer endwall contour. Static blade tip clearance was set at 1 mm under the window. Window washing is performed about once an hour during compressor operation by injecting automative window washing fluid into the endwall boundary layer through a row of 0.5 mm holes located 230 mm upstream of the window.

Laser anemometer measurements were made along the design streamsurfaces shown in Fig. 1. Measurements are distributed at axial locations between $z = -25.4$ mm and $z = 50.8$ mm as shown along streamsurface 2. Conventional probe survey measurements were made at stations 1 and 2 using a 6.4 mm dia combination probe. The probe used contains a thermocouple, total pressure tube, and null balancing static pressure holes for measurement of total temperature, total pressure, and flow angle. Details of the conventional survey data acquisition and reduction system are given in [6]. The operating points at which LA surveys were performed are shown in the performance map for the rotor as measured using the conventional instrumentation (Fig. 2).

Contributed by the Gas Turbine Division and published in the symposium volume, *Measurement Methods in Rotating Components of the Turbomachinery*, ASME, New York, 1980. Manuscript received for publication in the JOURNAL OF ENGINEERING FOR POWER May 22, 1980.

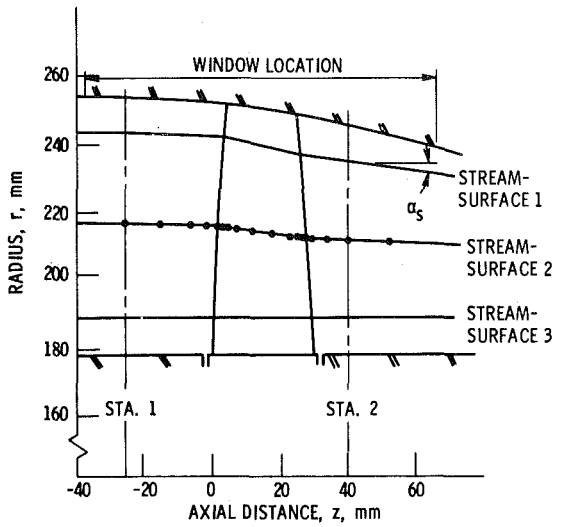

Fig. 1 Test compressor flowpath and streamsurface locations

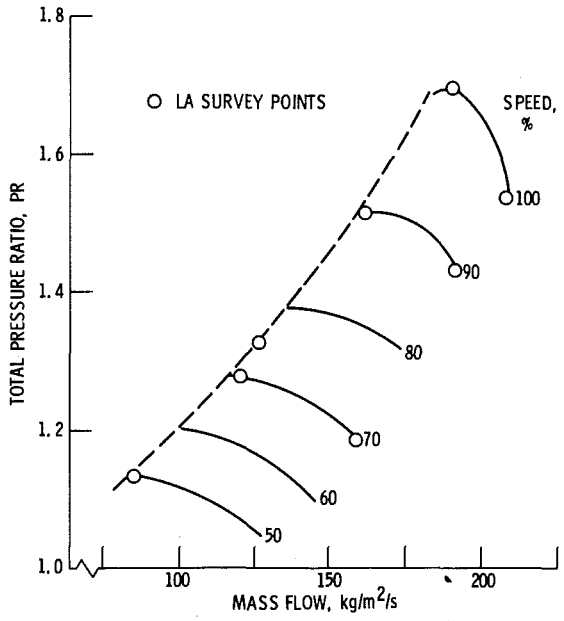

Fig. 2 Test compressor performance map

Laser Anemometer System

The laser anemometer is a single-channel, dual-beam system with on-axis backscatter light collection. The LA system optical layout is shown in Fig. 3. The laser light source is a 1.6 W argon-ion laser operating at 514.5 nm. The beam crossing angle is 2.825 deg and the fringe spacing is 10.4 μm. The probe volume diameter based on the $1/e^2$ intensity points is 125 μm. The length of common intersection of the crossing beams is about 4 mm. The effective length of the probe volume is reduced to about 2 mm by placing a mask on the central portion of the focusing lens located in front of the photomultiplier tube. Backscatter light is collected through an 11 deg cone angle.

The entire optical system is mounted on an x-y traversing table which is used to set the probe volume axial and radial position. A rotatable beam splitter is used to rotate the plane of the laser beams for measurement of velocity components at various angles from the axial direction. The beams nominally enter the compressor rotor in the radial direction. A beam director mirror is used to direct the beam away from the radial direction by ±10 deg to minimize shadowed regions caused by blade twist as shown in Fig. 4. Without variable beam direction, 20 to 30 percent of the blade-to-blade passage at the hub would be blocked due to blade twist at sections AA and BB. Another advantage offered by the variable beam direction is that it gives some capability of measuring radial velocity components.

Measurements to within 1 mm of the endwalls are made possible by using a fluorescent dye seed material and an optical filter. Without the fluorescent seed, reflected light from the endwall surfaces prevents measurements at radial positions less than 10 mm from either endwall. Seed particles are generated by spray-atomization and are injected into the inlet through a 6.4 mm dia tube located 460 mm upstream of the rotor face. The seed material consists of rhodamine 6G dye dissolved in a benzyl alcohol, ethylene glycol solution [7]. When a seed particle containing this dye crosses the LA fringe system the particle absorbs the green incident light and fluoresces orange. An orange-pass filter placed in front of the photomultiplier tube optically filters out green light reflected from blade and endwall surfaces and passes orange light scattered from the seed particles.

Data Acquisition

The data acquistion technique is efficient in that it allows free-running of the LA system. Unlike several other LA systems used in turbomachinery research [1, 3, 4], the optical system is not gated by a once-per-rev or once-per-blade signal, but is free to make velocity measurements whenever a seed particle crosses the probe volume. The technique is implemented by using a dedicated minicomputer to control data acquisition. The seed particle fringe crossing frequency (which is proportional to the particle velocity) is measured by a commercial counter-type processor. The rotor shaft position is gen-

Nomenclature

c = confidence interval
C_1 = pre-shock gas velocity normal to the passage shock in the (Z, θ) plane
C_2 = post-shock gas velocity normal to the passage shock in the (Z, θ) plane
D_p = seed particle diameter
f = seed particle fringe crossing frequency
k = confidence interval length
N = number of measurements
PR = total pressure ratio across the rotor
PS = blade pressure surface
r = radial distance
s = distance along circumferential measurement path
SS = blade suction surface
T_p = plenum temperature
T_s = standard day temperature, 518.7 deg Rankine
U = wheel speed
V = velocity
V_{ABS} = absolute flow velocity
V_n = particle velocity component normal to the passage shock in the (Z, θ) plane
V_{REL} = relative flow velocity
W = compressor mass flow
x_n = particle distance normal to the passage shock
z = axial distance
α, β, γ = laser beam orientation angles measured from the z, θ, r axes
α_s = streamline slope in the meridional plane
β_{ABS} = absolute flow angle
β_{REL} = relative flow angle
θ = circumferential distance
ν = kinematic viscosity
ρ = density
ϕ_r = angle between the beam bisector and the radial direction
ϕ_z = angle between the fringe normals and the axial direction

Subscripts

b = biased
c = corrected to standard day conditions
g = gas
i = denotes i^{th} measurement at a given shaft position
j = shaft position number
m = measured
p = particle
r = radial direction
z = axial direction
θ = tangential direction

Superscripts

$-$ = mean quantity
$'$ = fluctuating quantities

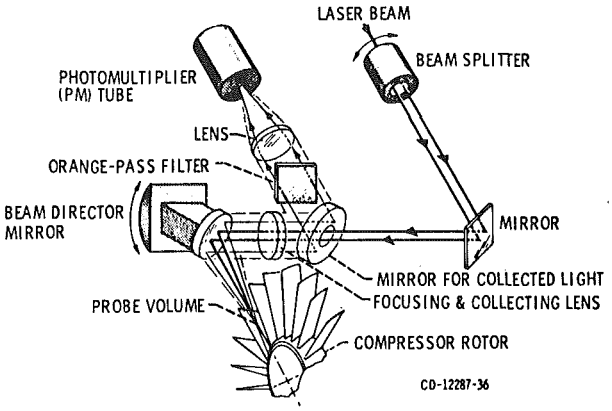

Fig. 3 Laser anemometer system optical layout

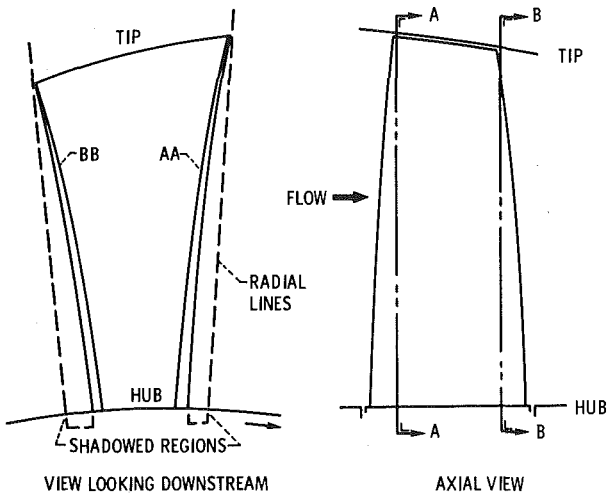

Fig. 4 Blade geometry showing shadowed regions due to blade twist

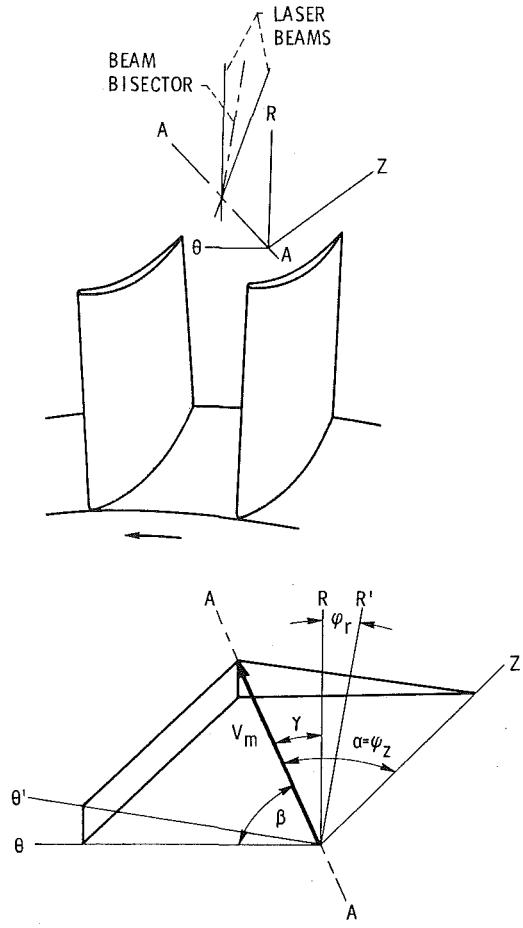

Fig. 5 Coordinate system and LA beam orientation

erated by an electronic shaft angle encoder which provides a continuous measure of the rotor shaft position relative to a once-per-rev signal obtained from the rotor disk. When a velocity measurement occurs the minicomputer records the frequency and shaft position as a data pair. At each axial and radial position surveyed, data are recorded at 1000 different shaft positions. These positions are typically distributed as 50 positions per blade passage across 20 consecutive blade passages.

It is significant that the velocity measurements do not really occur at a discrete shaft position, but rather are made anywhere within an interval between adjacent rotor shaft positions marked by the shaft angle encoder. With 50 intervals per blade passage, the interval length varies between 0.43 mm at the hub and 0.61 mm at the tip of the blade. In this paper the term shaft position is used with the understanding that measurements attributed to a shaft position actually occur in an interval about that position.

A typical run consists of collecting 30,000 measurements yielding an average of 30 measurements at each shaft position. Run times typically vary between 15 and 45 s. During data acquisition a graphics terminal is used to generate a graphic display which is typically updated every 15 s based on the data accumulated to that point in the run. The display consists of a histogram of the number of measurements at each shaft position and a blade-to-blade velocity distribution averaged across the 20 measured blade passages along the circumferential measurement path. This real-time display adds to the efficiency of the system since it enables the operator to monitor the data acquisition process and terminate a run if necessary. At the conclusion of each run, a data table of $N_j\ \Sigma_{i=1}^{N_j} f_i\ \Sigma_{i=1}^{N_j} f_i^2$ is stored on disk. Subscript j is the shaft position number which runs from 1 to 1000; N is the total number of measurements at position j; and f_i is the LA signal frequency of the i^{th} measurement at position j. Further details of the data acquisition system can be found in reference [5].

Data Reduction

The measured particle fringe crossing frequency is converted to velocity by multiplying by the fringe spacing. The velocity is corrected to standard day conditions using the relation

$$V_c = V\sqrt{T_s/T_p},$$

where V_c is the corrected velocity, T_p is the temperature measured in a plenum chamber upstream of the compressor inlet; and T_s is the standard-day temperature. For each measured component of velocity the mean and standard deviation at each shaft position are then calculated from

$$\overline{V} = \sum_{i=1}^{N} V_i/N$$

$$V' = \left[\left(\sum_{i=1}^{N} (V_i - \overline{V})^2\right)\Big/(N-1)\right]^{1/2}$$

$$= \left[\left(\sum_{i=1}^{N} V_i^2 - N\overline{V}^2\right)\Big/(N-1)\right]^{1/2}$$

The velocity magnitude and flow angle are calculated at each position using data from runs made at different beam orientations. The geometry of the beam orientation is shown in Fig. 5. The measured velocity component V_m lies along line AA which is in the plane of the beams and perpendicular to the bisector of the crossing beams. The beam bisector can be deflected in an off-radial direction by the beam director mirror. The beam bisector is restricted to the (R,θ) plane and the deflection angle is denoted by ϕ_r. The rotatable beam splitter is used to rotate the direction of the fringe normals about the R'-axis (which is alined with the beam bisector). The angle between the fringe normals and the Z-axis is denoted by ϕ_z and is measured in the (Z, θ') plane. The mean and standard deviation of the z, θ, r velocity components are calculated from the three equations

$$V_z \cos \alpha_i + V_\theta \cos \beta_i + V_r \cos \gamma_i = V_{m_i} \qquad i = 1, 2, 3$$

where the subscript i denotes each different beam orientation and

$$\cos \alpha = \cos \phi_z$$

$$\cos \beta = \cos \phi_r \sin \phi_z$$

$$\cos \gamma = \sin \phi_r \sin \phi_z$$

The two equations

$$V_z \cos \alpha_i + V_\theta \cos \beta_i = V_{m_i} \qquad i = 1, 2$$

can be used to calculate V_z and V_θ using data obtained during two runs made at different ϕ_z angles with $\phi_r = 0$. In practice the ϕ_r angles for the two runs are equal but are set to some nonzero value in the range ±4 deg to minimize the blade shadow regions. Thus the calculated, V_θ component of velocity actually lies along the θ' direction. However, the difference between the calculated velocity in the θ' direction and the velocity in the θ direction is small compared to the measurement error since the cosine of 4 deg is 0.9976.

The velocity distribution across the 20 measured blade passages is considered to be 20 separate observations of the flow in an average blade passage. Velocities at corresponding points relative to the blade in each individual blade passage are averaged together to yield a spatially-ensemble averaged blade-to-blade velocity distribution. The averaged velocity distribution may be compared to the velocity distribution in individual blade passages to assess passage-to-passage flow variations.

Measurement Errors

The error in axial and radial probe volume positioning is ±0.05 mm. The errors in setting the beam splitter and beam director angles are ±0.03 deg and ±0.01 deg, respectively. The error in a single LA measurement is a function of flow turbulence intensity and random noise in the photomultiplier tube signal. It is difficult to make an error estimate for an individual measurement since this noise is generated by background radiation which varies with each measurement. However, the statistical confidence in N individual measurements made at a given shaft position is

$$k = cV'/(\overline{V}\sqrt{N}),$$

where k is the length of the confidence interval and c is the confidence level. N is approximately 30 for each point in the velocity distribution across an individual blade passage. N is approximately 600 for each point in the ensemble-averaged velocity distribution, since the averaged distribution is calculated from the 20 individual blade-to-blade velocity distributions. All error bars which appear in this paper are for a 95 percent confidence level ($c = 2$). It should be noted that V' results from the sum of the flow fluctuation effects such as those caused by turbulence, velocity variations due to rotor speed drift, and velocity gradients in the tangential direction across the measurement shaft position interval, plus the previously mentioned random noise in the photomultiplier tube signal. The maximum velocity gradient in the tangential direction occurs across the passage shock during transonic operating conditions and is on the order of 1 percent per shaft position interval. Observations indicate that the rotor speed drift during a run is on the order of 0.3 percent.

Least squares polynomial curves are fit to the data prior to comparing velocity distributions from individual blade passages. One advantage to this approach is that the fitted curve contains information from all 1500 measurements made in a blade passage (30 measurements at each of 50 points), while the data at a single shaft position are based on only about 30 measurements. Typically the difference between the data and the fitted curve is 1 to 2 percent.

Two additional sources of measurement error are statistical and angle biasing. Statistical biasing arises because of the following. First, the velocity magnitude varies with time. Second, for a uniformly seeded flow more particles cross the probe volume per unit time when the velocity is higher than the mean than when the velocity is lower than the mean. An arithmetic average of measurements made over a given period of time therefore yields a calculated mean velocity which is higher than the true mean. Statistical bias can be removed using the relation [8]

$$\overline{V} = \overline{V}_b/[1 + (V'/\overline{V})_b^2]$$

where the subscript b denotes biased measurements. Typical values for $(V'/\overline{V})_b$ outside of blade wake and shock regions are 3 to 6 percent, which result in a 0.4 percent correction. Because this correction is small, the data have not been corrected for statistical bias.

Angle biasing [9] occurs because the flow direction fluctuates with time. More measurements per unit time occur when the flow direction is parallel to the fringe normal direction than when the flow direction fluctuates away from the fringe normal direction. The error in an arithmetic average of the velocity measurements made over a given time period is proportional to the angle between the fringe normals and the mean flow direction. This error is 1 percent or less when the angle between the fringe normals and the mean flow direction is less than 20 deg. In the present work the ϕ_z fringe orientation angle is set at ±15 deg from the average flow angle to minimize angle biasing error. However, the flow angle changes by 30 deg across wakes and passage shocks. Therefore there are regions in which the angle between the fringe normals and the velocity vector is on the order of 45 deg which could result in a 4 percent error in the measured velocity.

Seed Particle Dynamics

The rotor passage shock can be used to determine particle lag and seed particle size using the method described in [3]. A Stokes drag model is used to predict the velocity response downstream of the shock for a particle of diameter D_p. The resulting equation is

$$18\, \nu_g x_n/D_p^2(\rho_p/\rho_g) = (C_1 - C_2) - C_2 \ln[(V_n - C_2)/(C_1 - C_2)] - (V_n - C_2)$$

where C_1 = pre-shock gas velocity normal to the shock in the (Z, θ) plane; C_2 = post-shock gas velocity normal to the shock in the (Z, θ) plane; V_n = particle velocity component normal to the shock in the (Z, θ) plane; = $V_{\mathrm{REL}} \sin(\beta_{\mathrm{REL}} + \alpha)$; and x_n = particle distance normal to the shock = $s \cos \alpha$

The relative flow angle β_{REL} and the shock inclination angle α are defined in Fig. 6. The measured velocity component V_n as a function of x_n is determined from the ensemble-averaged blade-to-blade distribution of relative velocity V_{REL} using the geometry shown in Fig. 6, where s is the distance downstream of the shock along the circumferential measurement path. This procedure assumes that the distribution of V_n is uniform along the face of the shock over the distance $s \cdot \sin \alpha$. Typical values of s and α used in the above calculations are 14 mm and 10 deg, respectively, which yield $s \cdot \sin \alpha = 2.4$ mm.

The particle diameter D_p is determined in the following manner: For various values of D_p, V_n is calculated at given values of x_n using the known values of ρ_p, ρ_g, ν_g, C_1, and C_2. The particle diameter is then taken as the value of D_p which yields the best agreement between the calculated and measured distribution of V_n as a function of x_n. The results of two particle size determinations are shown in Fig. 7. Each data point in the figure is based on approximately 600 measurements. The data were obtained under identical flow and signal processor conditions at two different axial stations. The only change made in the LA system between the two runs was the removal of the orange filter used in the fluorescent dye technique. The agreement between the data obtained at axial stations $z = 10.2$ mm and $z = 12.7$ mm indicates that V_n is uniform along the face of the shock over distances of 2 to 3 mm. With the orange filter in place, the minimum diameter of the particles detected by the optics is about 1.4 μm, while the diameter of particles detected without the filter in place is 1.2 μm. This difference in diameter reflects the loss in signal strength in passing through the orange filter. With the LA counter-processor threshold level held constant, a larger particle diameter is necessary to trigger the counter circuitry when the filter is in place.

The results shown in Fig. 7 indicate that the distance required for the particle velocity to decay to within 5 percent of the post-shock gas velocity is about 12 mm normal to the shock. This is about 13 mm or 13 percent of the blade chord in the relative flow direction. Note that

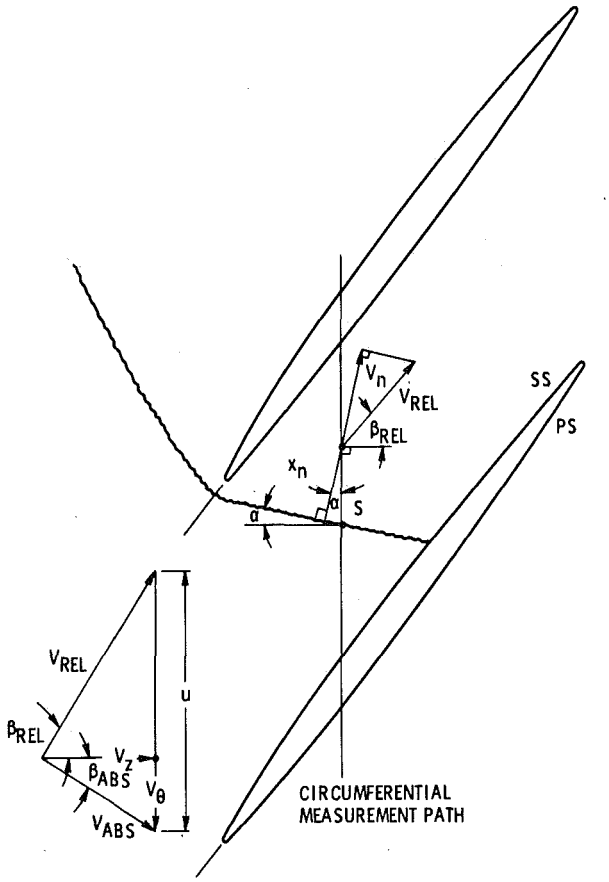

Fig. 6 Relation between the relative velocity V_{REL} and the shock normal velocity component V_n

the flow angle as well as the velocity magnitude is in error in the lag region. Additional particle size determinations performed with the orange filter in place yield particle sizes ranging from 1.2 to 1.5 μm. Although the minimum particle size detected by the optics increases with the orange filter in place, comparisons of blade-to-blade velocity distributions measured under identical flow conditions with and without the filter in place indicate no differences greater than the experimental error in the velocity distribution results due to the use of the filter.

The passage shock is not the only region in the blade passage where particle tracking may be a problem. Maxwell [10] analyzed seed particle flow in an axial-flow compressor rotor similar to the test rotor used in the present study. He obtained a numerical solution for the gas flowfield and then integrated the particle equation of motion to determine the particle path and velocity. The results indicate that for 1.5 μm dia particles the particle-to-gas velocity ratios are $0.90 < V_p/V_g < 0.96$ in the leading edge region and $0.98 < V_p/V_g < 1.02$ through the remainder of the blade passage. Particle angular deviation was found to be a maximum of 6 deg along the suction surface and across the blade passage at the trailing edge.

Results and Discussion

Flow phenomena studied during the initial application of the LA system include variations in flow from passage-to-passage, shock surface location, velocity changes across shock waves, three-dimensional flows in the blade wake, and the development of the endwall boundary layer. In addition, LA measurements were compared to numerical results within the blade row and to conventional probe measurements at stations outside of the blade row. The results obtained will be briefly discussed.

Passage-to-Passage Flow Variations. One advantage of the current data acquisition scheme is the ability to record velocity measurements across consecutive individual blade passages. Passage-to-passage variations in flow conditions can be observed and

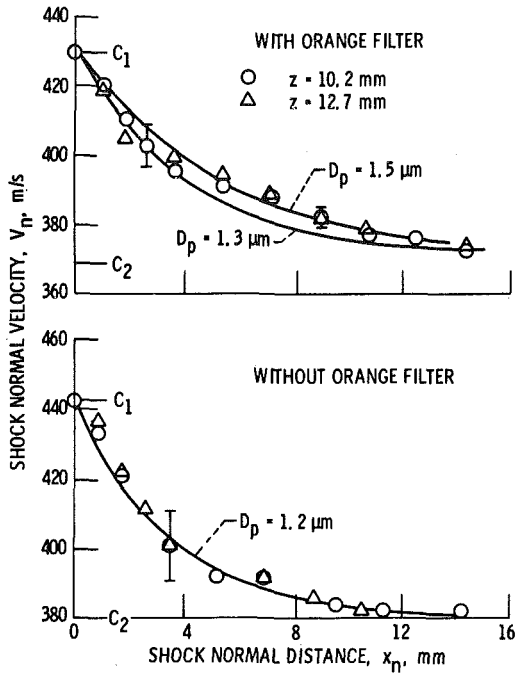

Fig. 7 Seed particle velocity lag downstream of the passage shock. Streamsurface 1, 100 percent speed, PR = 1.53, W = 205 kg/m²/s

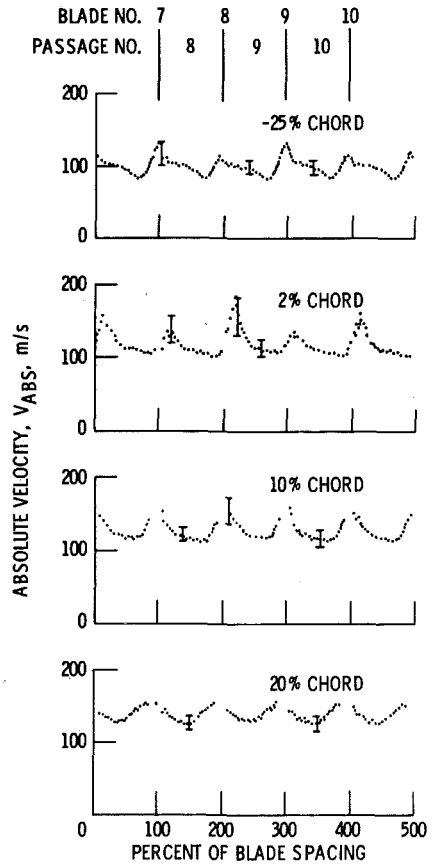

Fig. 8 Passage to passage variation in absolute velocity across five consecutive blade passages. Streamsurface 1.75 percent speed, PR = 1.33, W = 123 kg/m²/s

analyzed by using data from the individual blade passages. As an example, the distribution of absolute velocity across five consecutive blade passages is shown in Fig. 8 at four axial stations (given in percent axial chord) along streamsurface 1 (near the tip). The operating point is near stall at 75 percent of design speed. At −25 and 2 percent chord the flow in passage 9 is clearly different from that in passages 8 and

10. The variation in flow between passages at 2 percent chord may be caused by small variations in leading edge geometry and axial location. Least squares curve fits of the velocity distribution in passages 8 and 9 are compared to curve fits of the ensemble averaged velocity distribution in Fig. 9 where the blade locations are denoted by the cross-hatched areas. The error bars in Fig. 9 represent twice the standard deviation between the fitted curve and the data and therefore encompass 95 percent of the data points. Using the averaged curve fit as a reference, we see that the flow variation between passages 8 and 9 is a maximum of 20 percent near the leading edge. The data shown here represent the greatest passage-to-passage velocity variation observed in the present work. At operating points near maximum efficiency the incidence angles are small and there is less turning around the blade leading edge relative to that for the near stall case. Passage-to-passage flow variations at these operating points are on the order of 5 percent or less.

Blade-to-Blade Velocity Distributions. It is generally desirable to use the ensemble-averaged velocity distributions when performing data analyses because the ensemble-averaged data set, which contains 50 points in the averaged velocity distribution, is much smaller than the unaveraged data set which contains 1000 points in the velocity distributions across 20 blade passages. A possible source of error in using the averaged data is the tendency to smear out details of the velocity distribution by averaging across the 20 blade passages. However, comparison of the averaged and unaveraged distributions in Fig. 9, a worst-case example, indicates that velocity distribution details are not significantly modified by averaging.

Ensemble-averaged blade-to-blade distributions of velocity and flow angle measured on streamsurface 1 (near the tip) at 23 percent chord under transonic operating conditions are shown in Fig. 10. The operating point is at design speed near stall mass flow. The passage shock location is indicated by the rapid change in velocity and flow angle at mid-passage. Note that the absolute flow remains axial until it encounters the shock even though the measurement station is located well behind the leading edge. The shock turns the absolute flow by more than 30 deg which represents 75 percent of the turning measured at the blade trailing edge.

Rotor Shock Surface Mapping. The three-dimensionality of the rotor shock system is shown graphically in Fig. 11 where the shock location on streamsurfaces 1, 2, 3 (near-tip, mid-span, and near-hub, respectively) is plotted for the maximum mass flow condition at 100 percent design speed. The inlet relative Mach number varies from 1.16 on the near-hub streamsurface to 1.39 on the near-tip streamsurface. The blade sections and shocks are radially projected to eliminate the spanwise variation of blade spacing. The shock location is determined from velocity distributions of the type shown in Fig. 10. The flow behind the passage shock is supersonic on all three streamsurfaces. At mid-span and near the hub (streamsurfaces 2 and 3, respectively) the flow then diffuses to subsonic velocities within the blade passage without passing through another shock. However on streamsurface 1 (near the tip) the flow passes through a normal shock near the blade trailing edge.

The swept back blade leading edge creates a shock surface which leans back in the flow direction from hub to tip. Flow turning across the inclined shock in the meridional plane generates an increase in

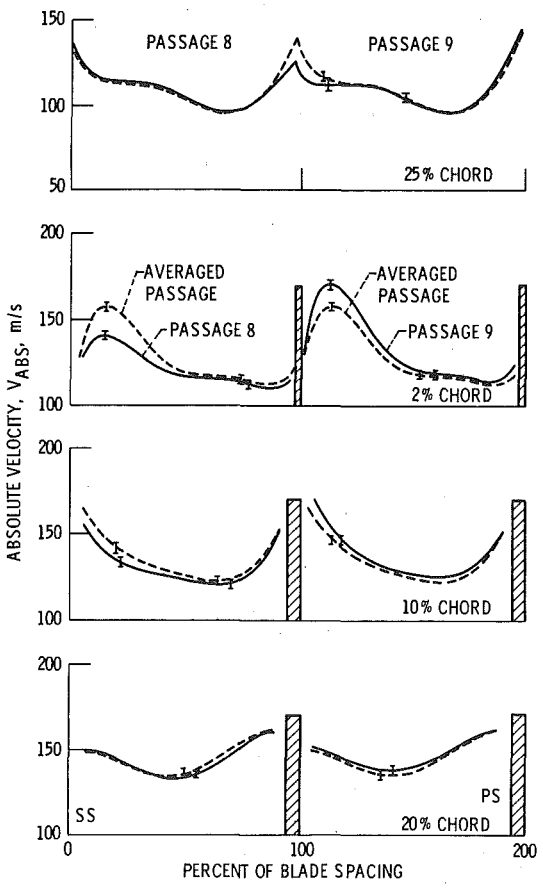

Fig. 9 Comparison between curve fits of the ensemble-averaged and individual blade passage distributions of absolute velocity. Streamsurface 1, 75 percent speed, $PR = 1.33$, $W = 123$ kg/m^2/s

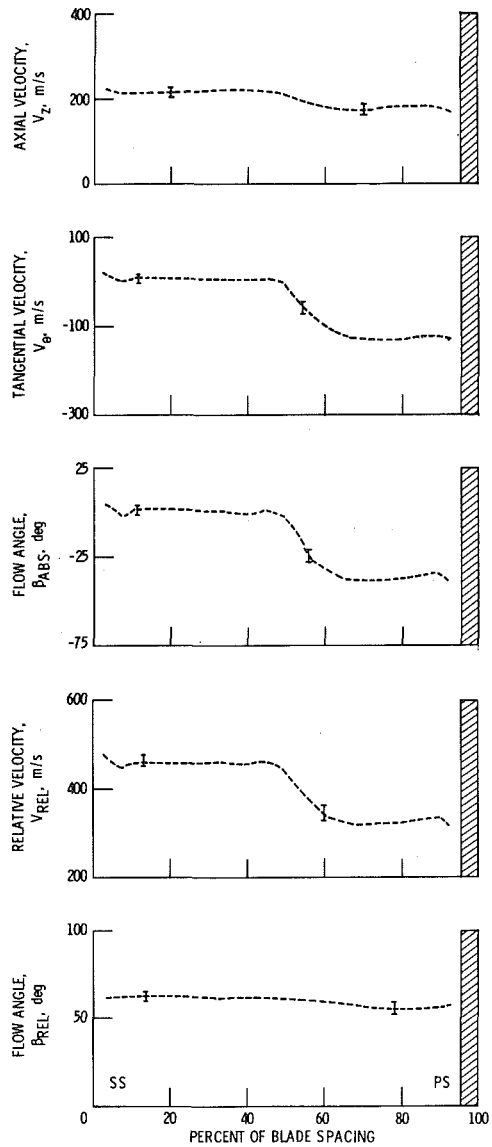

Fig. 10 Ensemble-averaged blade-to-blade distributions of velocity and flow angle across a passage shock. Streamsurface 1, 23 percent chord, 100 percent speed, $PR = 1.66$, $W = 190$ kg/m^2/s

the radial velocity component toward the tip downstream of the shock. As noted in [2, 4], the values of relative velocity and flow angle measured across the shock do not satisfy the isentropic normal shock relations even after correction for particle lag effects. Although attempts to measure the radial velocity component near the passage shock were not successful, a strong deposition of seed particles was observed on the window in the outer casing around the passage shock region. This may indicate that a radial outward flow is present in the vicinity of the shock.

Rotor Wake Measurements. Averaged velocity distributions measured downstream of the rotor at 70 percent design speed and at both maximum efficiency and near-stall conditions are shown in Fig. 12. The measurements were made on streamsurface 1 (near the tip), at station 2. The averaged velocity distribution is repeated so that the wake appears in the center of each plot. The radial velocity V_r and streamline slope in the meridional plane α_s are defined as positive outward toward the tip. The streamline slope outside of the wake agrees with the design streamline slope of −12 deg. Outward radial velocities in the blade wake are to be expected due to the radial pressure imbalance on the wake fluid. The radial outward flow, relative velocity defect, and wake width are all larger at the near-stall point than at the maximum efficiency operating point.

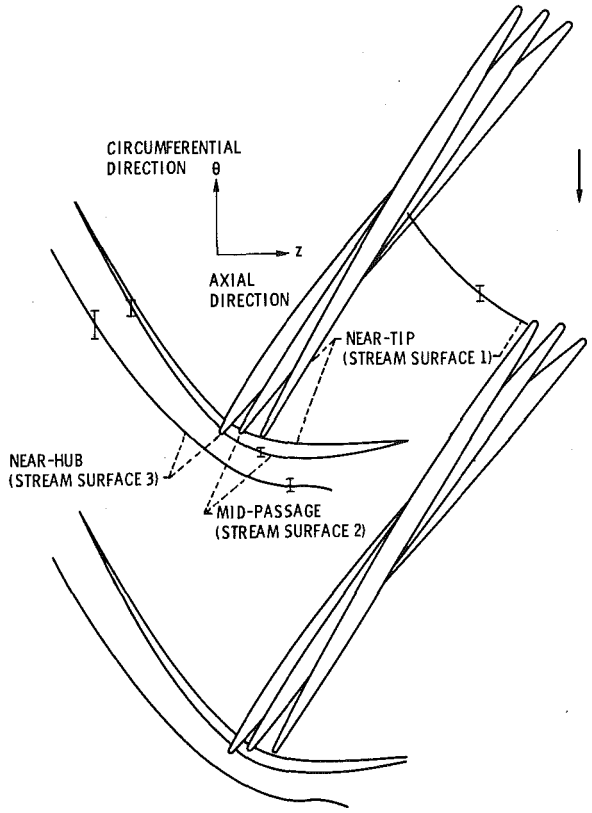

Fig. 11 Three-dimensional structure of the rotor shock system. 100 percent speed, PR = 1.53, W = 205 kg/m²/s

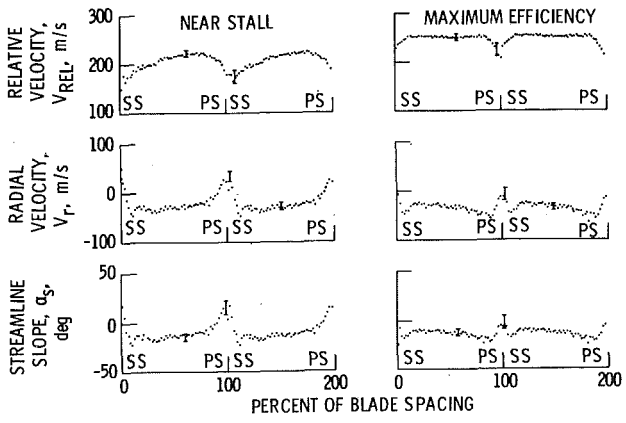

Fig. 12 Ensemble-averaged blade-to-blade distributions of velocity and flow angle in the blade wake. Station 2, streamsurface 1, 70 percent design speed. Operating conditions: near stall—PR = 1.27, W = 120 kg/m²/s; maximum efficiency—PR = 1.19, W = 156 kg/m²/s

Endwall Boundary Layer Development. The development of the outer endwall boundary layer at design speed and maximum mass flow is shown in Fig. 13. The effective probe volume length of 2 mm is indicated in the figure. The velocity at each data point is obtained by arithmetically averaging all 30,000 measurements obtained along the circumferential measurement path. The spanwise location of each point is the location of the probe volume center. Averaging across the finite probe volume length results in measured velocities which are higher than the true velocity, particularly near the wall. The boundary layer downstream of the blade is thinner than that upstream of the blade. This thinning of the boundary layer reflects the energy addition which occurs in passing through the rotor.

Comparison of LA Measurements and Numerical Results. The results of a finite difference solution [11] of the streamfunction equation on streamsurface 2 are compared to LA measurements in Fig. 14. The measurements were performed at 70 percent design speed near the maximum efficiency operating point. The cross-hatched areas near the blade surface denote regions in which no measurements were obtained. The numerical and experimental results display reasonable agreement in the expansion region around the blade leading edge, but the LA measurements indicate less diffusion than predicted by the numerical solution near the pressure side of the blade passage in the rear portion of the passage. This behavior may be due to the fact that the numerical model is inviscid and therefore cannot account for the displacement thickness effect of the blade wakes.

Comparison of LA and Conventional Probe Measurements. LA measurements are compared to conventional pressure survey measurements at stations 1 and 2 (see Fig. 1). The conventional instrumentation measures velocity and flow angle averaged along the entire circumference at a given axial and radial position. All 30,000 LA measurements obtained along a circumferential measurement path are therefore arithmetically averaged for comparison with the conventional survey measurements. The LA and conventional measurements are not made simultaneously since different compressor casings are used for the LA and survey runs, and measurement repeatability is therefore a factor to be considered in comparing results. The measurement repeatability of each instrumentation system when the compressor rig conditions are not changed is 1 percent. The repeatability in resetting the compressor rig conditions is 2 percent. Two additional factors which affect the comparison of results are the presence of a seed injection probe wake during LA measurements and

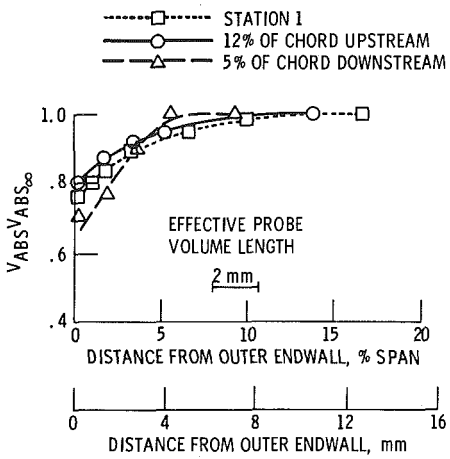

Fig. 13 Development of the outer endwall boundary layer. 100 percent speed, PR = 1.53, W = 205 kg/m²/s

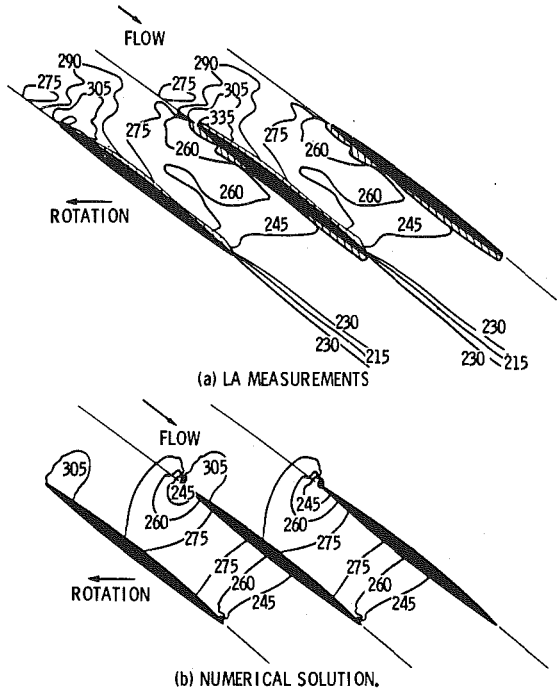

Fig. 14 Comparison of measured and calculated distribution of relative velocity. Stream surface 2, 70 percent speed, $PR = 1.19$, $W = 158$ kg/m²/s. Contours in m/s

probe blockage effects during pressure survey measurements. Although the seed injection probe is located 72 probe diameters upstream of station 1, a limited number of LA surveys made at station 1 in the θ-direction indicate that a 2 to 4 percent velocity defect from the seed injection probe is present at station 1. During pressure survey measurements there are four probes each at stations 1 and 2 and eight additional probes downstream of station 2. When the probes are fully extended for measurements near the hub, the total frontal area for the four probes at each station is 2 percent of the annulus area at the rotor face. An observed decrease in wall static pressures during probe injection indicates that throughflow velocity variations due to probe injection do exist.

The LA measurements of absolute velocity and flow angle at station 1 agree with the pressure survey measurements to within 4 percent. This is considered reasonable in view of the factors discussed above. The absolute velocities measured at station 2 by the LA and survey probe agree within 7 percent, but the flow angles measured by the two systems disagree by as much as 14 percent. The disagreement between the measured flow angles is due to differences in the measured V_θ velocity component. Agreement between the V_z velocity component measured by the LA and the survey probe is comparable to the agreement at station 1, but the V_θ component measured by the LA is 10 to 15 percent lower than that measured by the survey probe. The reasons for this difference require further study.

Summary and Concluding Remarks

The application of a laser anemometer system to the measurement of flow in a transonic axial flow compressor rotor is described. Use of a dedicated minicomputer to control data acquisition allows rapid accumulation of data with high spatial resolution in the blade-to-blade direction and the recording of data across 20 individual blade passages. A fluorescent dye technique reduces problems due to incident light reflection from metal blade passage surfaces and allows measurements to be made in the endwall boundary layers. The ability to direct the input laser beams away from the radial direction allows minimization of blade blockage effects and enables the measurement of radial velocity components.

Future research plans include holographic interferometric studies of the rotor shock system. Shock patterns measured by the holographic technique will be compared to those measured by the LA. Future LA research will involve measurements in compressor stages with stator blades present so that both rotor and stator flowfields and the extent of the circumferential variations in the rotor flowfield induced by the stator may be investigated. Survey probe and LA measurements will be made simultaneously to further investigate differences between the velocities measured by the two systems and to investigate the significance of survey probe blockage effects.

Acknowledgments

The authors wish to acknowledge the contributions of Genevieve Esgar for running the numerical stream-function solutions used in comparison with the LA data and of Mark Laessig for assisting in data reduction and analysis.

References

1 Wisler, D. C., and Mossey, P. W., "Gas Velocity Measurements Within a Compressor Rotor Passage Using the Laser Doppler Velocimeter," ASME JOURNAL OF ENGINEERING FOR POWER, Vol. 95, No. 2, Apr. 1973, pp. 91–96.

2 Wisler, D. C., "Shock Wave and Flow Velocity Measurements in a High Speed Fan Rotor Using the Laser Velocimeter," ASME Paper No. 76-GT-49, Mar. 1976.

3 Walker, D. A., Williams, M. C., and House, R. D., "Interblade Velocity Measurements in a Transonic Fan Utilizing a Laser Doppler Velocimeter," Minnesota Symposium on Laser Anemometry, E. R. G. Eckert, ed., University of Minnesota, Minneapolis, Minn., 1976, pp. 124–145.

4 Dunker, R. J., Strinning, P. E., and Weyer, H. B., "Experimental Study of the Flow Field Within a Transonic Axial Compressor Rotor by Laser Velocimetry and Comparison with Through-Flow Calculations," ASME JOURNAL OF ENGINEERING FOR POWER, Vol. 100, No. 2, Apr. 1978, pp. 279–286.

5 Powell, J. A., Strazisar, A. J., and Seasholtz, R. G., "Efficient Laser Anemometer for Intra-Rotor Flow Mapping in Turbomachinery," presented at the symposium on Measurement Methods in Rotating Components of Turbomachinery; Gas Turbine Conference and Products Show, ASME, New Orleans, La., Mar. 9–13, 1980.

6 Moore, R. D., Lewis, G. W., Jr., and Osborn, W. M., "Performance of a Transonic Fan Stage Designed for a Low Meridional Velocity Ratio," NASA TP-1298, 1978.

7 Stevenson, W. H., dos Santos, R., and Mettler, S. C., "Fringe Mode Fluorescence Velocimetry," *Applications of Non-Instrusive Instrumentation in Fluid Flow Research*, AGARD-CP-193, 1976, pp. 20-1-20-9.

8 Barnett, D. O., and Bentley, H. T., "Statistical Bias of Individual Realization Laser Velocimeters," *Second International Workshop on Laser Velocimetry*, Vol. 1, H. D. Thompson and W. H. Stevenson, eds., Purdue University, 1974, pp. 428–444.

9 Seasholtz, R. G., "Laser Doppler Velocimeter System for Turbine Stator Cascade Studies and Analysis of Statistical Biasing Errors," NASA TN D-8297, 1977.

10 Maxwell, B. R., "Tracer Particle Flow in a Compressor Rotor Passage with Application to LDV," *American Institute of Aeronautics and Astronautics, Journal*, Vol. 13, No. 9, Sept. 1975, pp. 1141–1142.

11 Katsanis, T., "FORTRAN Program for Calculating Transonic Velocities on a Blade-to-Blade Stream Surface of a Turbomachiner," NASA TN D-5427, 1969.

A. E. Smart
Spectron Development Laboratories, Inc.,
3303 Harbor Boulevard, Suite G-3,
Costa Mesa, CA 92626

D. C. Wisler
Manager, Turbomachinery Research,
Aircraft Engine Group,
General Electric Company,
Cincinnati, OH 45215

W. T. Mayo, Jr.
Spectron Development Laboratories, Inc.,
3303 Harbor Boulevard, Suite G-3,
Costa Mesa, CA 92626

Optical Advances in Laser Transit Anemometry

A Laser Transit Anemometer (LTA) system for measurement of velocity, flow angle and turbulence in the rotating blade rows of turbomachinery and for other applications has been developed by the authors (SDL). Advanced optical, electronic, and computer components make the system sensitive to submicron scatterers, provide automated data collection and permit probing close to blade and wall surfaces, in some cases without seeding the flow. This paper describes new and practical developments of the optical system and presents test results from axial compressor measurements. Based upon these test results, improvements were incorporated into the system and these improvements are discussed briefly.

Introduction

Laser Transit Anemometry (LTA) [1–8] has, in the last eight years, become a powerful technique for making measurements of velocity and turbulence in turbomachinery. It is less sensitive to wall flare than fringe anemometry [9, 10], while it retains many of the advantages. Schodl [3] perceived this potential advantage and constructed the first working instrument. Others [6, 7, 11] followed his lead and two of these authors have now constructed an instrument which has several innovations, some of which are discussed in this paper. This instrument is shown in Fig. 1.

Principle of Operation

The operating principle of laser transit anemometer systems is discussed in detail elsewhere [3, 7, 11, 12] and is reviewed only briefly here. Basically, a single laser beam is split into two equal power beams which are focused to form two intensely illuminated spots whose separation-to-size ratio may be between 20 and 40. Each spot is viewed with a separate photomultiplier to detect back-scattered light from particles crossing the spots. The suitably discriminated signals from these particles which move through the spots can be cross correlated to yield a histogram of transit times for the particles which may, with some careful considerations, be inverted to give speed probability in a chosen direction. The plane containing the spots may be rotated to explore different flow directions.

The spots must be free from aberrations and be closely parallel near the region of focus to avoid spurious broadening of velocity probabilities. Lenses used in the system must have good freedom from aberrations. Stops must be used to reject light from all places except from the region of the spots. The stops to achieve this are discussed in reference [7].

Optical System

The significant components of the optical system are shown in Fig. 2. Although this optical arrangement was conceived to solve the problem of measurements in the proximity of flare sources with no, or minimal, added particles, it proved to have other advantages not formerly obvious. One of these is superior sensitivity to submicron particles which are abundant in many test situations and which follow the gas flow well, even up to supersonic speeds. Another is the velocity information which is provided. The distribution of speeds in an accurately chosen direction may be plotted and, by exploring a number of angles, a complete velocity probability map may be constructed without the need for orthogonal or two-color systems.

Because of the sensitivity to smaller particles, the reduction in data rate which was predicted by those who were used to fringe systems need not occur, primarily because in most natural situations the number of particles per unit volume increases very rapidly with decreasing particle size.

Beamsplitter. The use of a Wollaston prism beamsplitter, shown in Fig. 2, enables the relative beam intensity to be adjusted and disposes the transmitted beams symmetrically about the optical axis. The focusing lens produce two spots from the diverging but almost collimated beams. The center of the beamsplitter is near to the back focal plane of this lens which acts as a Fourier transforming element. The transform planes are not exact and the focusing lens may be translated axially to make the final output spots of light parallel to each other and the axis. The beams will suffer divergence if there is

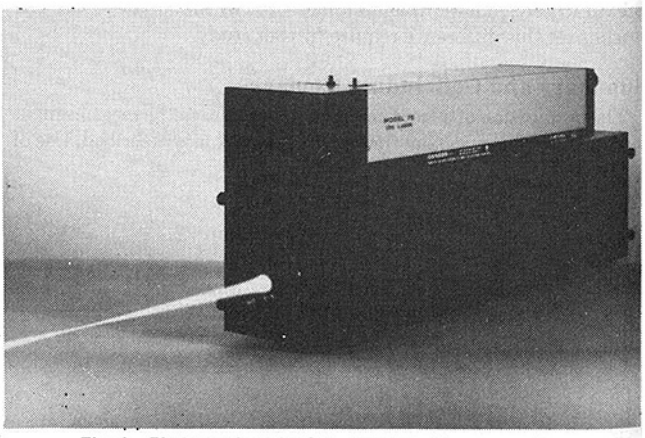

Fig. 1 Photograph of the SDL laser transit anemometer

Contributed by the Gas Turbine Division and published in the symposium volume, *Measurement Methods in Rotating Components of Turbomachinery*, ASME, New York, 1980. Manuscript received for publication in the JOURNAL OF ENGINEERING FOR POWER May 22, 1980.

not due allowance for the magnification variation with axial position for an extended object in the projection system.

Spot Rotation. The rotator prism was created for this system to achieve precise, computer controlled spot rotation about a common center [13]. This mirror Dove image rotator is designed to be aberrationless, short (F/4), efficient and easily and precisely rotated. Single pass optical efficiency is typically 87 percent with protected silver coated surfaces. The angular position is controlled by a digital command word and its final attained position is reported back to a control and data management system described below. Precision is typically 0.1 deg of arc in the spot orientation angle. The servo control circuitry is within the optical head to render it immune to electrical noise and interference. There is no significant run out in this unit as it is correctable by internal adjustments in the original alignment process.

The choice of such an image rotator was made to avoid possible differential drift between output beams and input stops when rotating by other methods. The position and size of stops is a critical factor.

Stops. A most important feature of an LTA system is the selection of stops that reject flare light. Included in the specification of stops is the extent to which the lenses achieve diffraction limited performance. The output lenses are most critical. Changing the relative sizes of stops allows more light and more flare or less light and less flare to be collected. Within a small band, it is not apparent where the best tradeoff is to be obtained and to some extent final design was empirical.

The nature of the basic optical stops is shown in Fig. 3. This figure illustrates the design of the center stop which limits the axial distance over which light may be received. A more detailed discussion is presented in Appendix A of reference [7].

Data Management System

An important property of any instrumentation system is the ease with which data collection and reduction may be automated [10]. In the case of turbomachinery, with the associated high cost of testing, it is further desirable to minimize the time necessary to obtain good data while providing some rapid near-real-time indication that the data is correct. Therefore the optical system is supported by a data management system based on a microprocessor and software having limited user programmability. This permits highly efficient use of the test time with a high degree of automation. The data management system, shown in Fig 4, controls the spot rotator to explore different flow directions automatically so that the velocity vector can be determined. The single-channel system, used in the tests reported here, observes only one space and time gate at once, reduces the data from a correlation processor and stores it on a floppy disk unit. All except the correlator is an integrated system.

Experimental Measurements

The prototype LTA system was transported to the Aircraft Engine Group of the General Electric Company at Evendale, Ohio, in December 1978 to demonstrate its capability for obtaining gas velocity measurements within the rotating blade rows of turbomachinery. This demonstration test was conducted in a compressor whose aerodynamic behavior was well-known so that the accuracy and reliability of the prototype LTA system could be evaluated before a commitment was made to an extensive and costly mapping of the flowfield within a transonic rotor such as those done by Wisler [14], Eckardt [5] and Schodl [15]. The test was conducted in a fashion similar to the feasibility study conducted in 1971 on the prototype fringe LV system developed by General Electric [9]. The total elapsed time from air freight delivery of the LTA system to air freight return was two weeks. This two-week period included uncrating, set-up, check-out, familiarization by GE personnel, test, disassembly, and shipment of the system.

Low Speed Research Compressor. The measurements were obtained in GE's Low Speed Research Compressor (LSRC), an ex-

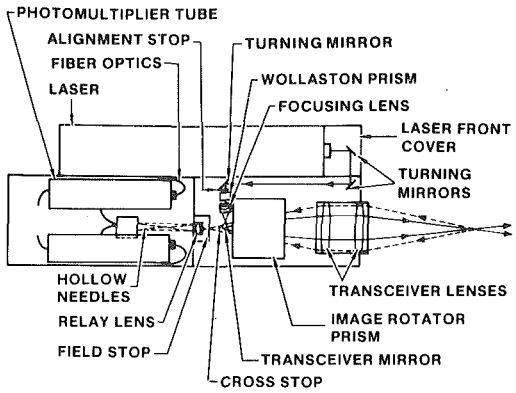

Fig. 2 Diagram showing components of optical system

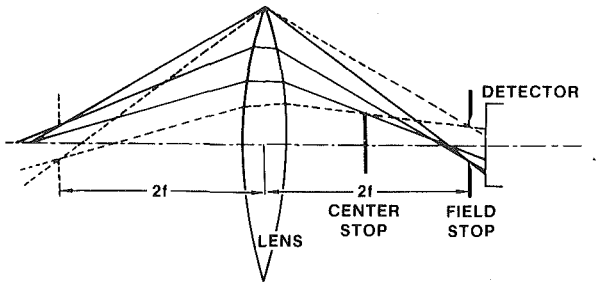

Fig. 3 General optical stops

Fig. 4 Photograph of LTA data management system

Nomenclature

C = absolute velocity
U_t = rotor tip speed
W = relative velocity
W_2 = far downstream velocity
β = relative air angle

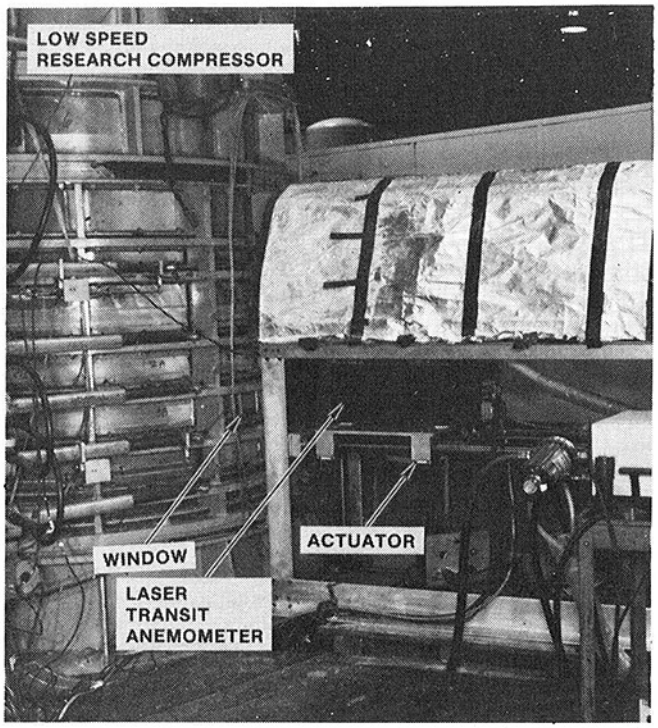

Fig. 5 Photograph of Low Speed Research Compressor and laser transit anemometer system

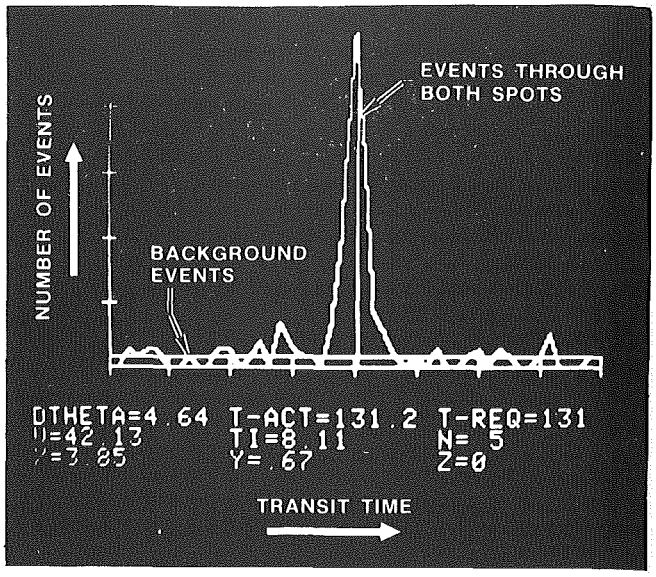

Fig. 6 Oscillogram showing a histogram of transit times

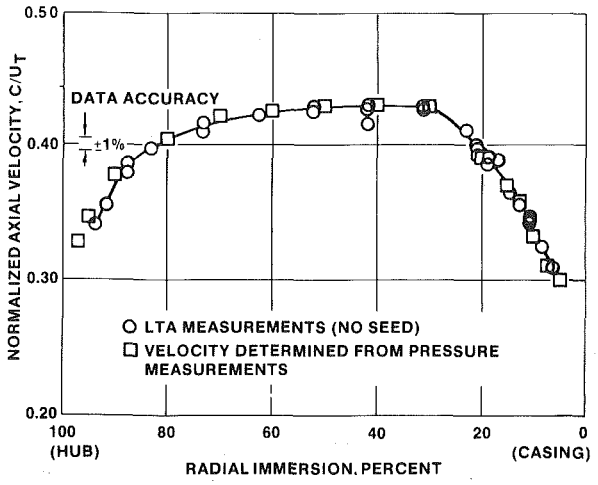

Fig. 7 Comparison of velocities determined from LTA and from pressure measurements, ahead of IGV's

perimental facility which is used for testing the aerodynamic characteristics of various compressor and fan designs. The LSRC duplicates many of the essential features of a high-speed compressor flow field in a large, low speed machine where very detailed investigations of fundamental aspects of turbomachinery aerodynamics such as airfoil surface boundary layer development, secondary flow phenomenon and leakage effects can be studied in detail.

The LSRC configuration for these tests consisted of a four-stage compressor having a constant casing diameter of 1.524 m (60.0 in.) and a radius ratio of 0.85. A photograph of the LSRC and the LTA system is shown in Fig. 5. The axis of rotation of the compressor is vertical and the flow enters from the top through a calibrated bellmouth inlet system. After passing through the blading, the air is exhausted through a throttle plate. The airfoils used in the test were 11.43 cm (4.5 in.) in span and approximately 9 cm (3.5 in.) in chord. The pitchline solidity, camber and stagger angle of the rotor were 1.163, 31.05 and 51.66 deg, respectively. Those of the stator were 1.426, 37.00 and 30.00 deg, respectively. The blading was hydraulically smooth at the test Reynolds number of 360,000 based on tip speed and blade chord. The average rotative speed was 790 rpm which gave an average tip speed of 62.56 m/s (205 ft/s).

Experimental Results. Laser Transit Anemometer measurements were obtained in the compressor annulus ahead of the inlet guide vanes (IGV's) and within the passage of the third-stage rotor. Optical access to the blading was provided by an anti-reflection window which was flat to $\lambda/10$. Time sequencing and triggering was provided by magnetic pickups which gave a one-per-rev signal and a one-per-blade signal on six selected blades. A typical oscillogram showing a histogram of transit times, from which speed probability in a chosen direction can be obtained, is shown in Fig. 6. Seeding, when required, was accomplished by use of a fluidized bed of titanium dioxide.

The measurements ahead of the IGV's were taken at the design point throttle setting to provide a comparison between velocities determined from total and static pressure measurements. This comparison, obtained without LTA seeding, is shown in Fig. 7 where the axial velocity normalized by the rotor tip speed is plotted as a function of percent immersion in the annulus. The agreement between the two measurement techniques is better than ±1 percent in most places across the annulus. The use of the computer-controlled rotator prism in the optical system greatly facilitated data taking.

Further evaluation of the LTA prototype system was done by comparing the LTA measurements taken ahead of and behind the third stage rotor with pitot-static and flow angle measurements. These absolute velocity and flow angle comparisons are shown in Figs. 8 and 9, respectively, for the design point and the near stall throttle. Again, in most instances there is good agreement between the various measuring techniques.

Tests were conducted to determine how close to the endwalls one could make LTA measurements. Successful velocity measurements were made within 5 mm (0.2 in.) of the hub and 7.6 mm (0.3 in.) of the casing. Wall flare prevented measurements from being made closer to the wall than this.

Rotor intra-blade flow angles and velocities were then measured. Data were taken ahead of the leading edge, behind the trailing edge and at five axial stations within the rotor passage for each radial immersion surveyed. At the design point throttle setting, surveys were made at 15, 30, 50 and 80 percent immersion and for the near-stall throttle a survey was made at 50 percent immersion. The relative velocities and flow angles were computed from the measured absolute values by using the standard turbomachinery equations involving wheel speed [9]. Velocity contour lines were drawn through the data points assisted by a knowledge of general isobar shapes typical of the potential flow-field about an airfoil. Dashed lines were used where data were extrapolated to the blade surface. The results are presented

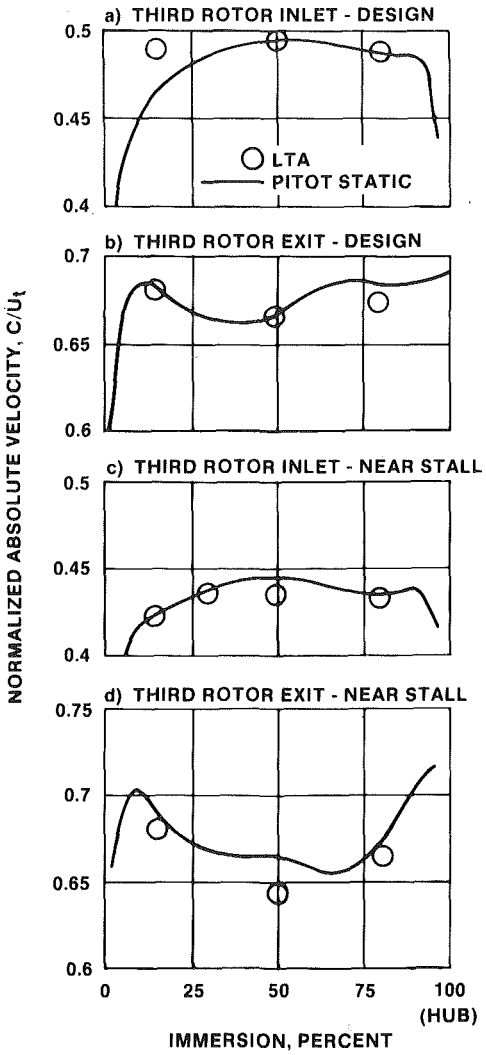

Fig. 8 Comparison of normalized absolute velocities from LTA and from pressure measurements, at third rotor inlet and exit

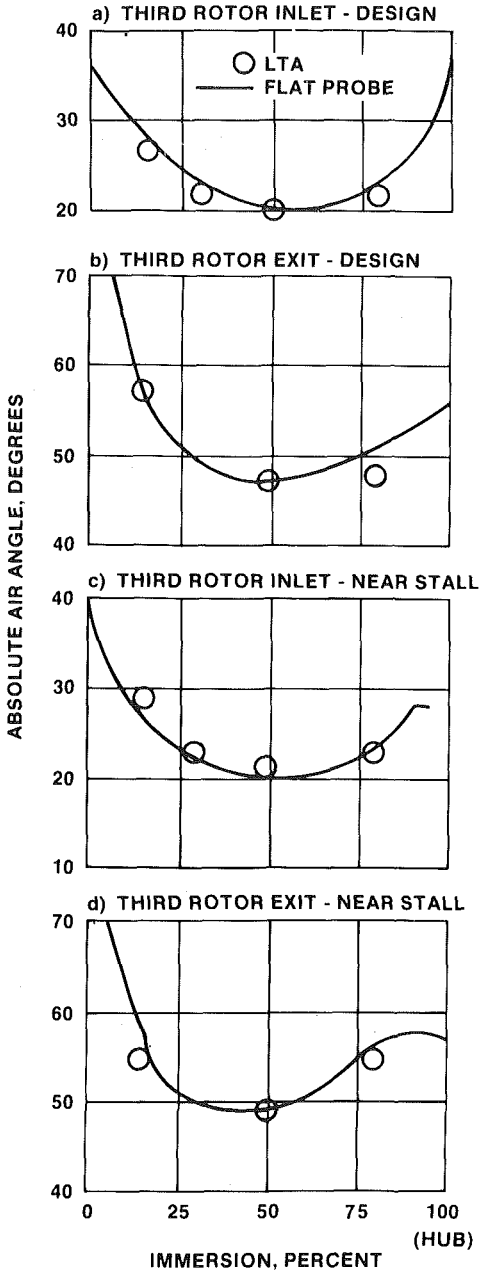

Fig. 9 Comparison of absolute air angles determined from LTA and flag probe measurements, at third rotor inlet and exit

in Figs. 10–12. The intra-blade relative flow angles presented in Fig. 10 for the design point throttle setting show a smooth turning of the flow from the entrance plane to the exit plane of the rotor. The flow turning of 14.3 deg inferred from the LTA measurements compares favorably with the value of 14.2 deg inferred from the flag probe measurements. Similar results, although not shown, were obtained for the other immersions.

The relative velocity measurements, seen as contour plots in Figs. 11 and 12, have several noteworthy features. First, the increased leading edge loading as the compressor is throttled from the design point (Fig. 11(c)) to the near stall point (Fig. 12) is evident as the location of the peak suction surface velocity moves from about 28 percent chord to about 13 percent chord. Secondly, at 15 percent immersion, Fig. 11(a), the peak suction surface velocity occurs at about 34 percent chord, which is about six percent chord further aft than at either 30 percent or 50 percent immersion. This velocity distribution on the suction surface results from the combined effects of the tip vortex/secondary flow phenomenon and of the blade design near the tip. These blade tip sections were designed to have their peak loading occur somewhat further aft than conventional. Thirdly, the rates of diffusion on the suction surface at design point indicate that the blade sections were operating without significant flow separation at all immersions tested. These results are supported by blade surface static pressure measurements which are discussed in the next section.

Comparison with Blade Surface Pressure Measurements. Two rotor blades were instrumented to determine the distribution of static pressure on the suction and pressure surfaces. Ten static taps were located on the pressure surface of one blade and 14 taps were located on the suction surface of the adjacent blade at each of five radial immersions. The pressures were read by a pressure transducer/slip ring device and then were converted to velocities by using Bernoulli's equation and a previously-determined total pressure. The velocity distributions obtained in this manner along the suction and pressure surfaces of the instrumented blades were compared with the velocity distributions obtained from the LTA measurements extrapolated to the blade surface and the results are shown in Figs. 13 and 14. The shapes of the velocity distributions determined from the LTA are for the most part in reasonable agreement with those determined from pressure measurements as can be seen by comparing the locations of the peak suction surface velocity and the rates of diffusion from the peak to the trailing edge. The substantial increase in leading edge loading from the design point (Fig. 13(c)) to the near stall point (Fig. 14) is recorded by both measurement techniques. The LTA results are not presented at the near stall point near the trailing edge in Fig. 14 because of the uncertainties in extrapolating the data to the blade surface.

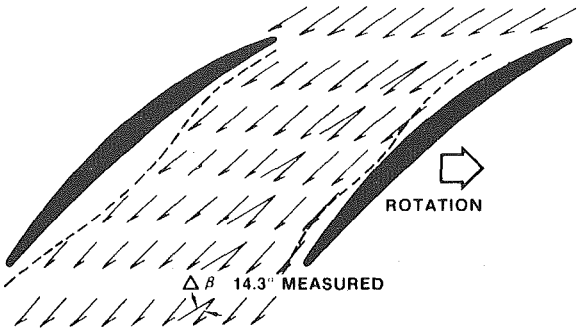

Fig. 10 Rotor intra-blade relative flow angles obtained from LTA measurements for the design point throttle and 50 percent immersion. $\Delta\beta$ indicates the flow turning.

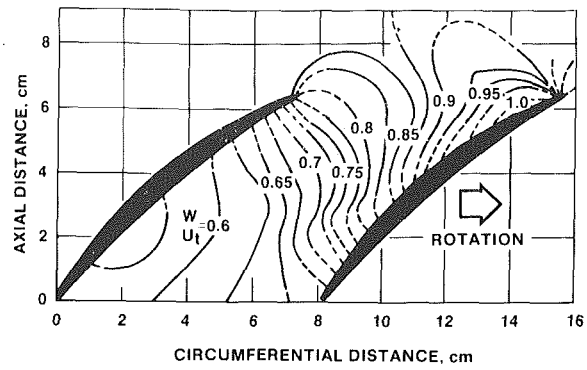

Fig. 12 Experimental velocity contours within the third rotor passage at the near stall throttle for 50 percent immersion

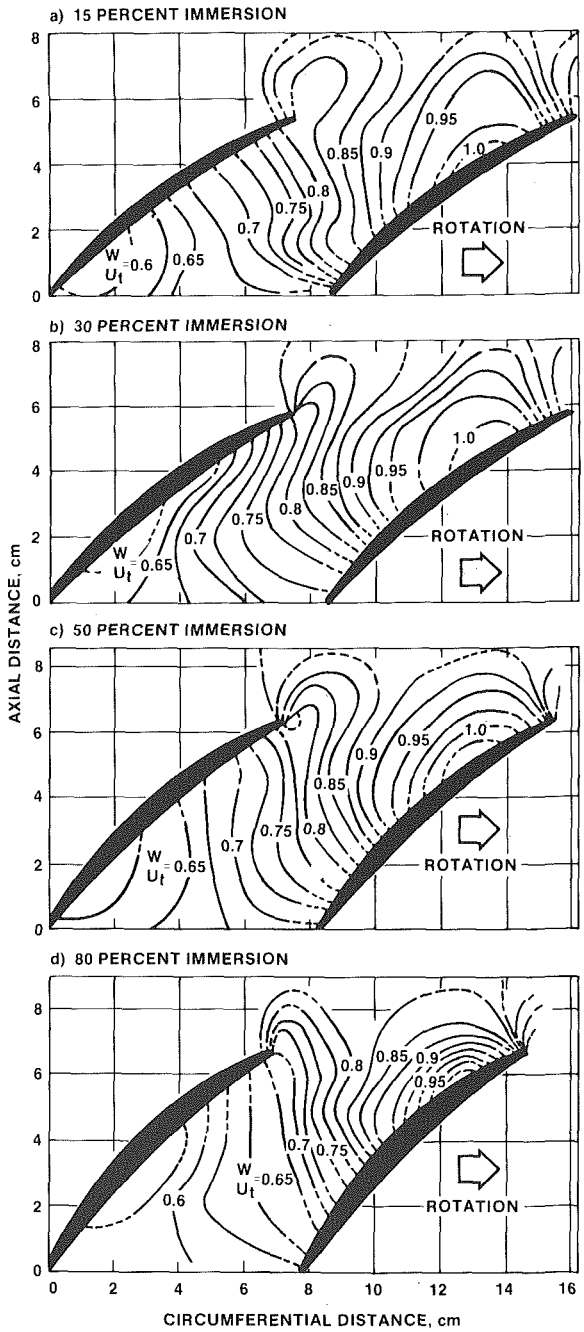

Fig. 11 Experimental velocity contours within the third rotor passage at the design point throttle, (*a*) 15 percent immersion, (*b*) 30 percent immersion, (*c*) 50 percent immersion, (*d*) 80 percent immersion

Theoretical Analysis

The flowfield in the rotor passage was analyzed theoretically by applying the Cascade Analysis by Streamline Curvature (CASC) computer program, a known blade-to-blade analysis tool developed by GE. The program solves the momentum and continuity equations in intrinsic coordinates to obtain the flow properties at the orthogonal-streamline intersections. The resultant velocity contour plots are shown in Fig. 15 for 50 percent immersion at the design point throttle. Comparison of these results with the LTA contours in Fig. 11(*c*) shows reasonably good agreement in velocity level through the rotor passage in rates of diffusion along the suction surface and in the location of the peak suction surface velocity.

LTA System Improvements

Based on the test results presented in this paper, it was concluded that two improvements in the system could be made. First, an increase in the number of time gates being observed could significantly reduce test time and secondly, an additional optical stop to reject flare could allow data taking closer to solid surfaces.

The system is being made more efficient by incorporating the capability to look at 32 time windows simultaneously instead of just one window. The speed of this multistation processor is also being raised from that currently available (50 ns) to an input time resolution of 10 ns for the 32 channels of 256 stores each. This will enable data to be sampled simultaneously, for example, across the entire circumferential extent of the rotor passage at a fixed angle and position making significantly more efficient use of test time.

An additional optical stop has been installed in the LTA system. This stop, which is called a cross stop because it eliminates channel cross talk, is a cross between a field stop and an aperture stop and is shaped like a cross. The improvement in flare rejection can be seen by examining the data in Fig. 16. These data were obtained by scanning an opaque Lambertian scatterer with texture of 1 or 2 μm through the active region of the LTA system for two cases: (1) with only the center and field stops in place and (2) with all stops including the cross stop in place. It is clear that a reduction of sensitivity to flare light is achieved by using the cross stop thus allowing good measurements closer to walls. Later measurements discussed in detail in reference [16] have indicated that this cross stop has reduced the distance for obtaining measurements close to a solid wall by a factor of two compared to the results reported in this paper.

Conclusions

A Laser Transit Anemometer system was developed for making measurements of velocity, flow angle and turbulence in rotating machines and in other applications. A compact backscatter optical system, whose optimal alignment is not affected by rotation of the sensitive direction, has been made possible by a new design of the image rotator. The two cylinders of light have controlled convergence so that they may be made parallel for different focal lengths of output lens. Optimal design of stops to reject flare light has assured a shorter sensitive volume than previously available.

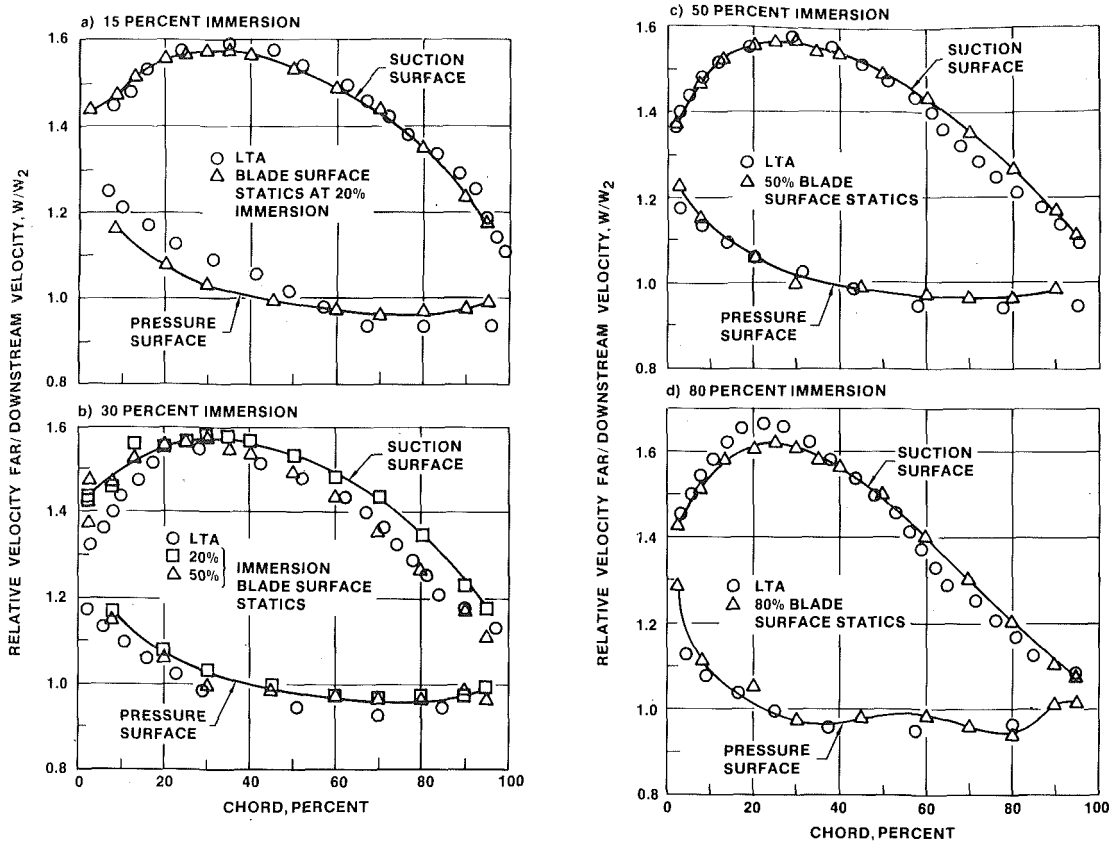

Fig. 13 Comparison of blade surface velocity distributions determined from the LTA and from pressure measurements at the design point throttle, (*a*) 15 percent immersion, (*b*) 30 percent immersion, (*c*) 50 percent immersion, (*d*) 80 percent immersion

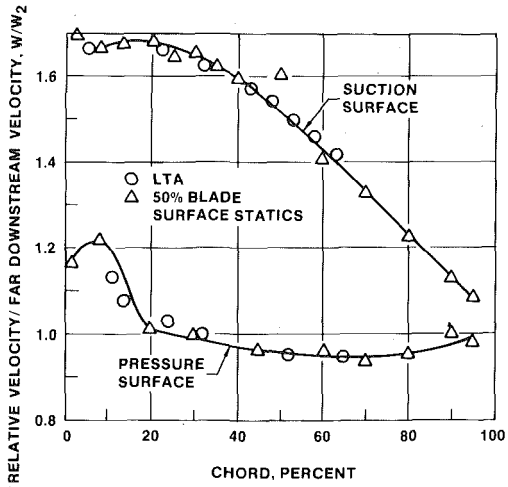

Fig. 14 Comparison of blade surface velocity distributions determined from the LTA and from pressure measurements at the near stall throttle and 50 percent immersion

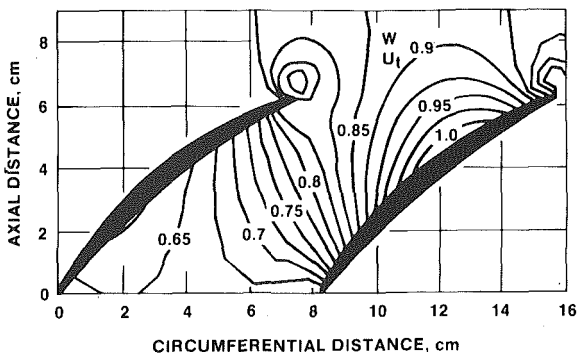

Fig. 15 Analytical velocity contours for the design point throttle at 50 percent immersion

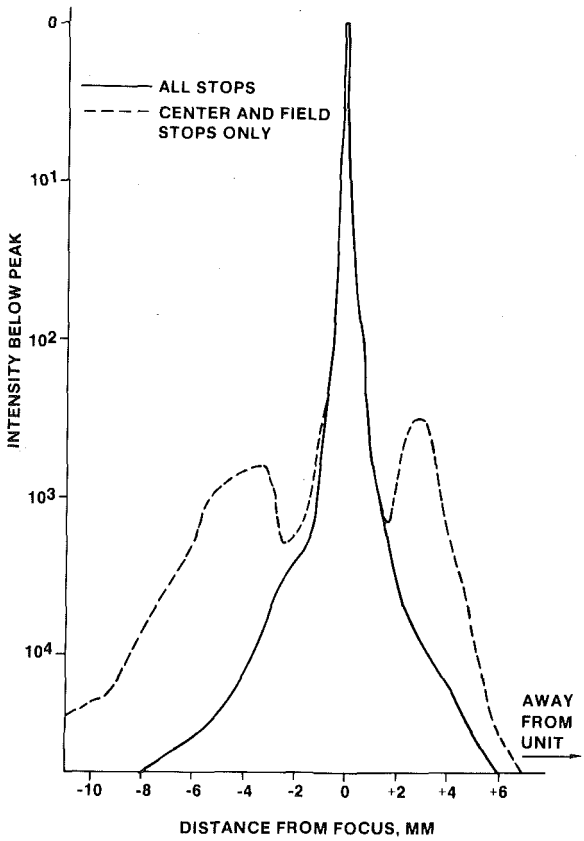

Fig. 16 Comparison of flare rejection between (1) center and field stops only and (2) all stops including cross stop

Detailed flowfield measurements within the rotating blade row of a low speed axial compressor were made with this advanced LTA system. The results of these measurements were consistent with the results obtained from pitot-static probes, flag probes, blade surface static taps and analytical modeling. Improvements in the system were made based upon the test results.

References

1 Thompson, D. H., "A Tracer Particle Fluid Velocity Meter Incorporating a Laser," *Journal of Physics, E, Journal of Scientific Instruments,* Series 2, Vol. 1, 1968, pp. 929–932.

2 Tanner, L. H., "A Particle Timing Laser Velocity Meter," *Optics and Laser Technology,* June 1973, pp. 108–110.

3 Schodl, R., "A Laser Dual Beam Method for Flow Measurement in Turbomachines," ASME Paper No. 74-GT-157, 1974.

4 Maxwell, B. R., "Particle Flow in Turbomachinery with Application to Laser Doppler Velocimetry," *AIAA Journal,* Vol. 12, No. 10, Oct. 1974, pp. 1297–1298.

5 Eckardt, D., "Detailed Flow Investigations Within a High Speed Centrifugal Compressor Impeller," ASME Paper No. 76-FE-13, 1976.

6 Smart, A. E., "Special Problems of Laser Anemometry in Difficult Applications," Lecture 6 in AGARD LS-90, Aug. 1977.

7 Smart, A. E., and Mayo, W. T., Jr., "Comparison of Data From the Transit Time Velocimeter with Other Systems Now in Use for Velocity Measurement," AEDC-TR-79-32, May 1979.

8 Runstadler, P. W., and Dolan, F. X., "Design Development, and Test of a Laser Velocimeter for High Speed Turbomachinery," LDA Symposium, Copenhagen 1975 (DISA).

9 Wisler, D. C., Mossey, P. W., "Gas Velocity Measurements Within a Compressor Rotor Passage Using the Laser Doppler Velocimeter," ASME Paper No. 72-WA/GT-2, 1972.

10 Mayo, W. T., Jr., Smart, A. E., and Hunt, T. E., "Laser Transit Anemometer with Microcomputer and Special Digital Electronics: Measurements in Supersonic Flows," 8th ICIASF to be held at Naval Postgraduate School, Monterey, Calif., Sept. 24–26, 1979.

11 Lading, L., "The Time-of-Flight Laser Anemometer," AGARD CP193, Paper 23.

12 Smart, A. E., "Data Retrieval in Laser Anemometry by Digital Correlation," *Laser Velocimetry and Particle Sizing,* ed. H. D. Thompson and W. H. Stevenson, Hemisphere Publishing, 1979 (presented at The Third International Workshop on Laser Velocimetry (LV-III), Purdue University, 11–13 July 1978).

13 Smart, A. E., "A Compact Wide Aperture Image Rotator Without Aberrations," submitted to *Journal of Physics, E, Journal of Scientific Instruments,* Apr. 1979.

14 Wisler, D. C., "Shock Wave and Flow Velocity Measurements in a High Speed Fan Rotor Using the Laser Velocimeter, ASME JOURNAL OF ENGINEERING FOR POWER, Vol. 99, No. 2, Apr. 1977, Paper No. 76-GT-49.

15 Schodl, R., "Laser-Two-Focus Velocimetry (L2F) for use in Aero Engines," Lecture No. 4 in AGARD LS-90, August 1977.

16 Smart, A. E., and Mayo, W. T., Jr., "Experimental and Analytical Development of the Application of a Transit Laser Velocimeter," Reported under AEDC Contract F40600-79-C-003, in press.

Mean Flow Measurements Near the Plane of an Open Rotor Operating with an Inlet Velocity Gradient

M. L. Billet

Research Associate
Applied Research Laboratory,
The Pennsylvania State University,
P.O. Box 30,
State College, PA 16801

As part of a study on the structure of a trailing vortex, laser doppler anemometer (LDA) measurements were made of the flow field near an open rotor having an inlet velocity gradient. The measurements were made in the 1.22 m dia water tunnel of the Applied Research Laboratory at The Pennsylvania State University. Velocity data were obtained for rotor inlet and outlet flow fields for several different inlet velocity gradients. Velocity data were also obtained downstream of the rotor plane that shows the vortex structure. Flow field measurements show the development of the downstream vortex motion. Small variations in the inlet velocity gradient near the rotor wall caused large differences in the structure of the trailing vortex. In addition, a measured downstream velocity profile is compared with a calculated velocity profile.

Introduction

The vorticity near the inner wall of a hydrodynamic rotor creates a trailing vortex. A theory has been developed from a study of this vortex [1] which shows that the magnitude and distribution of the blade exit streamwise vorticity near the inner wall determines the strength of the vortex. A set of vorticity equations are used in this theory to calculate the vorticity development along mean streamlines. These equations show the vorticity dependence on the mean loading (resultant V_θ) and the inlet vorticity (axial velocity gradient) near the inner wall. A calculation of the inviscid axisymmetric flow field through the rotor had to be made as input data to the vorticity calculations.

An accurate calculation of the mean flow field through an open rotor operating for several different inlet velocity gradients is a difficult problem. There are many investigators such as Novak [2], Davis, [3], and McBride [4] who have solved the indirect or design problem for an axisymmetric flow field; however, there is no simple method to calculate the flow field of an existing rotor operating at a specified flow condition. Difficulties arise in specifying the bounding streamline of the flow field, the blade deviation angles and the flow near the rotor inner wall which can be dominated by secondary flows.

The importance of secondary flows in a rotor has been discussed by many investigators, such as Hawthorne [5], the staff of NASA Lewis Research Center [6], Smith [7], and Lakshminarayana and Horlock [8]. Secondary flows are produced when the flow near the rotor wall which contains large velocity gradients does not have sufficient momentum to balance the pressure gradients imposed by the rotor. The result is a cross-flow component containing vorticity aligned in the streamwise direction which causes a deviation in the rotor outlet angles. This deviation depends on the velocity profile upstream of the rotor and on the amount of turning in the flow.

Mean flow measurements of the flow field were obtained in order to verify the mean flow calculation procedure. This procedure is outlined in detail in references [1] and [9]. Both inlet and outlet flow field measurements were made at several different operating conditions. In addition, flow field measurements were obtained at the end of the rotor cap which shows a vortex formation.

Most of the flow field measurements downstream of the rotor were obtained with a laser doppler anemometer (LDA). Application of the LDA to the 1.22 m water tunnel measurements was required due to the results of a preliminary test program.

This preliminary test program was conducted in order to visualize the structure of a trailing vortex. Dye was injected along the body surface and photographs were obtained. Figure 1 shows the vortex structure with and without a five-hole prism probe inserted into the vortex. These photographs were obtained at a reference velocity of 6.4 m/s in the water tunnel. As can be noted the probe caused diffusion of the vortex upstream of the probe.

This paper has two primary objectives. First, LDA application in the 1.22 m water tunnel for flow field measurements is discussed. Second, new experimental data are presented which show the rotor flow field and the trailing vortex structure for several different inlet velocity gradients. Some flow field calculations are given on the data plots as a comparison.

LDA Equipment and Water Tunnel Application

The flow field measurements were conducted in the 1.22 m dia water tunnel located in the Garfield Thomas Water Tunnel Building of the Applied Research Laboratory at The Pennsylvania State University. Details of the flow facility can be found in reference [8]. For the measurements a rotor was located near the end of a large body where the incoming velocity gradient to the rotor was due primarily to the boundary layer on the surface of the upstream body. The boundary layer thickness was larger than the rotor tip radius which is approximately 96 mm. The Reynolds number was 1.8×10^6 based on rotor diameter and the velocity at infinity. The rotor tip velocity (U_T) was approximately twice the velocity at infinity.

To reduce any effects produced by tunnel-wall interference, a "liner" was used in the test section. The resulting inner contour in the test section was determined by a potential flow solution for the body

Contributed by the Gas Turbine Division and published in the symposium volume, *Measurement Methods in Rotating Components of Turbomachinery*, ASME, New York, 1980. Manuscript received for publication in the JOURNAL OF ENGINEERING FOR POWER May 22, 1980.

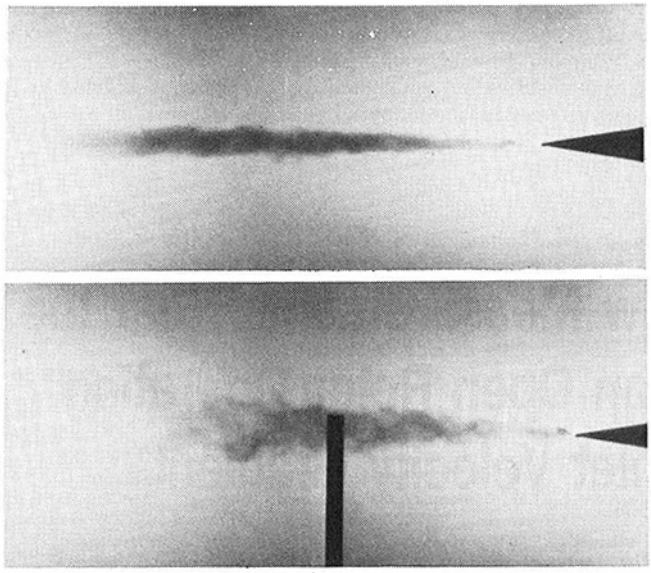

Fig. 1 Photographs of vortex structure with and without a probe in the flow field

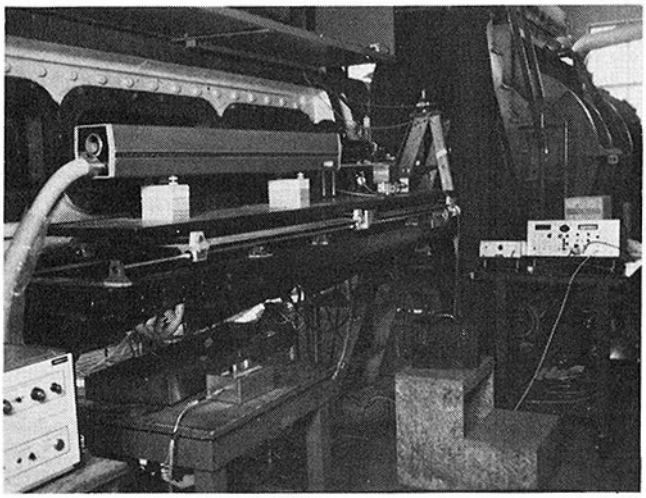

Fig. 2 Picture of LDA for 1.22 m water tunnel

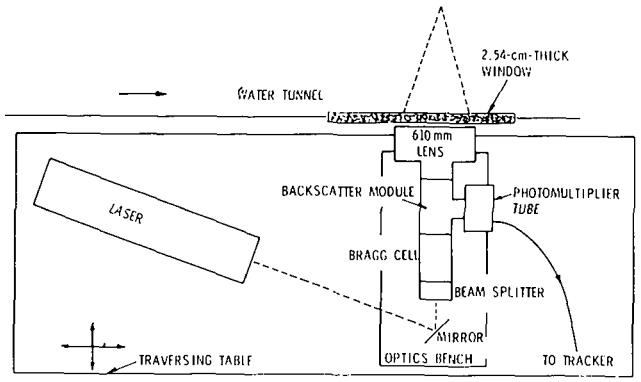

Fig. 3 Schematic of optics for 1.22 m water tunnel

which approximated a streamline surface where the body is in a flow of infinite extent.

Some of the flow field measurements were obtained using a five-hole probe. In other cases, total-pressure probes in conjunction with static-pressure probes were used. However, most of the measurements that were obtained downstream of the rotor plane were made using a LDA. Development of the LDA was necessary because preliminary flow field observations using dye showed that a probe could not be used to measure the vortex structure downstream of the rotor.

A photograph of the LDA used for the water tunnel measurements discussed in this paper is shown in Fig. 2. The system was mounted on a traversing table which could be moved parallel and perpendicular to the test section axis.

The dual beam-back scatter mode was used for the measurements because optics could not be mounted on both sides of the water tunnel. In the dual beam mode, the laser beam is separated into two parallel beams of equal intensity. These two beams cross and focus at the focal point of a lens. The scattered light originating from the focal point is collected through the focusing lens and is directed to a photomultiplier tube.

A schematic of the LDA is shown in Fig. 3. All of the beam conditioning components were obtained from Thermo-Systems. A Spectra Physics Model 164 Argon-ion laser was used as the coherent light source. The blue line of 488.0 nm was used at a power level of approximately 400 mw. The focusing lens has a focal length of 610 mm and the spacing of the two parallel beams is 100 mm. For some experiments, a 2.27 × beam expander was used to reduce the laser probe volume and was placed after the backscatter module. The resulting maximum probe size was approximately 0.48 mm × 5.7 mm without the beam expander and approximately 0.21 mm × 2.56 mm with the beam expander. A Thermo-Systems Model 1090 Tracker was used to process the signal.

A special flat lexan window of 25.4 mm thickness was inserted into the existing tunnel window. This was necessary because the existing windows are approximately 111.8 mm thick and are of poor optical quality. In addition to the special window, the body was painted with non-reflective black paint in order to reduce reflections and to measure the flow near the body surface. Data were obtained to within 5 mm of the surface.

The tangential velocity (V_θ) was obtained by rotating the probe volume 90 deg from the plane where the axial component of velocity (V_x) was measured. The data rate was approximately 500 data-samples/s without the Bragg cell in the system. This was obtained after seeding the 416.5 m^3 of water in the tunnel with approximately 20 cm^3 of silicon carbide particles having a mean diameter of 1.5 microns.

The Bragg cell was necessary when the tangential velocity was less than 10 percent of the axial velocity. One detrimental effect with using the Bragg cell was a significant decrease in the signal-to-noise ratio.

Results of Flow Field Measurements

The mean inlet velocity profile, outlet velocity profile, and downstream velocity profile were measured for several flow configurations. A schematic of the flow measurement locations is shown in Fig. 4. Each variation in inlet velocity gradient to the rotor at a constant Reynolds number was a basic flow configuration. Changes in the inlet velocity gradient were made by adding a screen and/or struts to the body upstream of the rotor. The screen placed against the body surface was approximately one meter in length and was three meters in front of the rotor inlet plane. The upstream struts consisted of four struts having chord lengths of 147 mm and maximum thickness of 10 percent. These were placed at 0, 90, 180, and 270 deg on the surface

Nomenclature

D = diameter of rotor
U_T = rotor tip velocity
V_m = meridional velocity
V_θ = tangential velocity
V_∞ = velocity at infinity
R = radius of rotor
R' = distance from surface in radial direction
Y = normal distance from surface
ν = kinematic viscosity of fluid

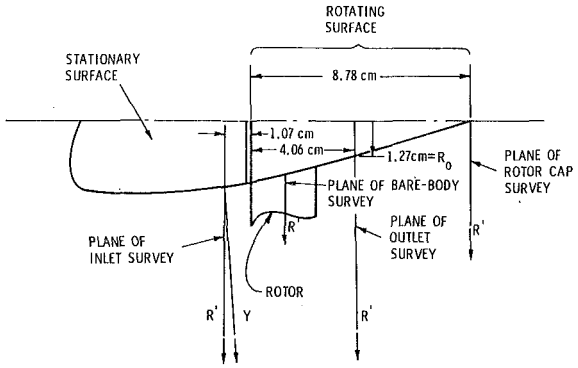

Fig. 4 Schematic of the flow measurements

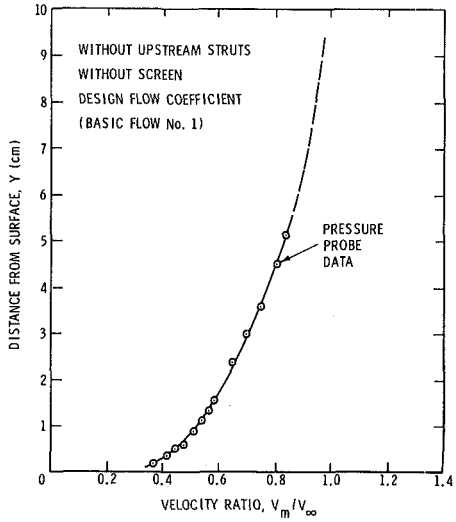

Fig. 5 Rotor inlet velocity profile for basic flow No. 1

and 38 mm before the rotor inlet plane. Four of the basic flow configurations are

Basic Flow No. 1. without upstream struts, without upstream screen, design flow coefficient,

Basic Flow No. 2. without upstream struts, without upstream screen, 0.9 design flow coefficient,

Basic Flow No. 3. without upstream struts, with upstream screen, design flow coefficient,

Basic Flow No. 4. with upstream struts, without upstream screen, design flow coefficient.

Some of the results for these four basic flows are given in Figs. 5–10. The instrumentation used to obtain the flow measurements is noted on the figures. In addition, the bare body velocity profiles were measured in the plane of the rotor without the rotor installed. These measurements were obtained for

Basic Flow No. 11. without upstream struts, without upstream screen, and without rotor,

Basic Flow No. 12. without upstream struts, with upstream screen, and without rotor,

Basic Flow No. 13. with upstream struts, without upstream screen, and without rotor.

The results are shown in Figs. 11–13. These data were obtained with total-pressure probes in conjunction with static-pressure probes. These probes were rotated around the surface in order to obtain a circumferential average.

The agreement between data obtained with a five-hole probe and LDA is shown in Fig. 6. A comparison shows good agreement between measurement techniques considering that the measurements were obtained at two different tunnel installations approximately one year apart. The results show an experimental accuracy of 3 percent of the reading.

The shape of the axial velocity profile at the end of the rotor cap is similar to that of the axial velocity profile measured near the rotor.

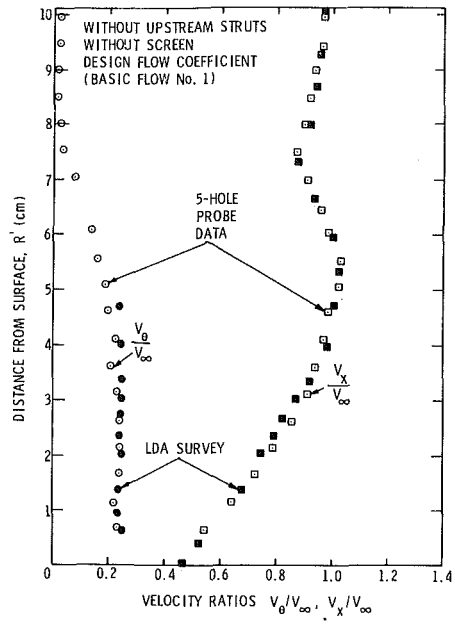

Fig. 6 Rotor outlet velocity profile for basic flow No. 1

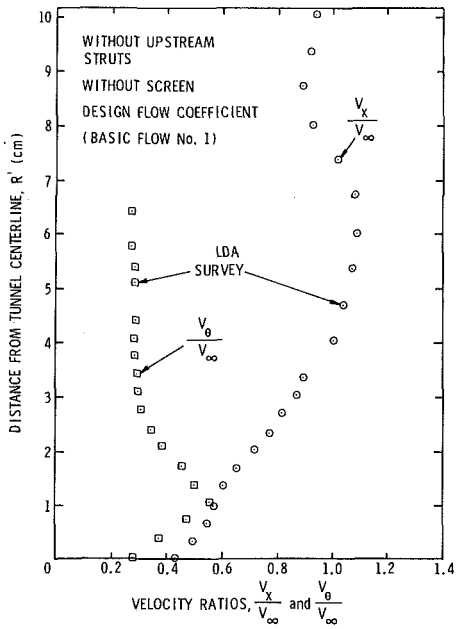

Fig. 7 Velocity profiles on rotor cap for basic flow No. 1

exit plane. However, the tangential velocity profile at the end of the rotor cap shows a well defined vortex which rotor outlet measurements do not show. It is important to note that the measured tangential velocity profile did not approach zero on the axis for the rotor cap measurements due to LDA measuring difficulties.

The effect of adding an upstream screen can be seen by comparing Fig. 11 to Fig. 12 for the bare body velocity profile and Fig. 7 to Fig. 9 for the rotor downstream velocity profiles. The screen essentially thickens the momentum deficit near the inner wall for the bare body velocity profile. By adding the screen, the resulting downstream velocity profile with the rotor shows a significant decrease in the maximum tangential velocity at the edge of the core.

The effect of adding upstream struts can be seen by comparing Fig. 11 to Fig. 13 for the bare body velocity profile. Figure 13 shows a circumferentially averaged profile obtained from profiles measured at 2 deg increments around the body. A comparision shows that the upstream struts add momentum to the deficit near the inner wall and increase the local velocity. This resulting deficit is controlled by the secondary flows created at the intersection of the struts and the inner

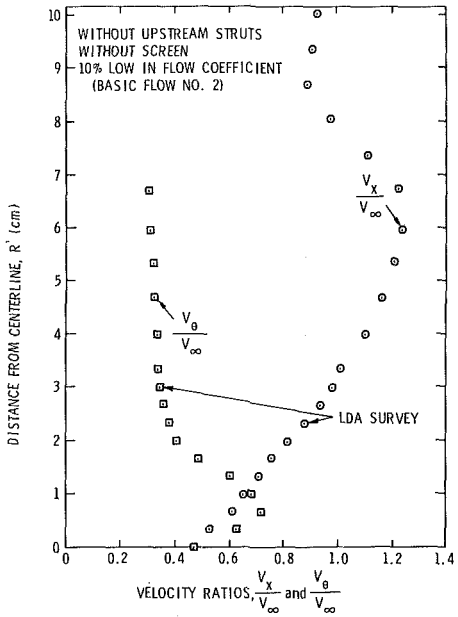

Fig. 8 Velocity profiles on rotor cap for basic flow No. 2

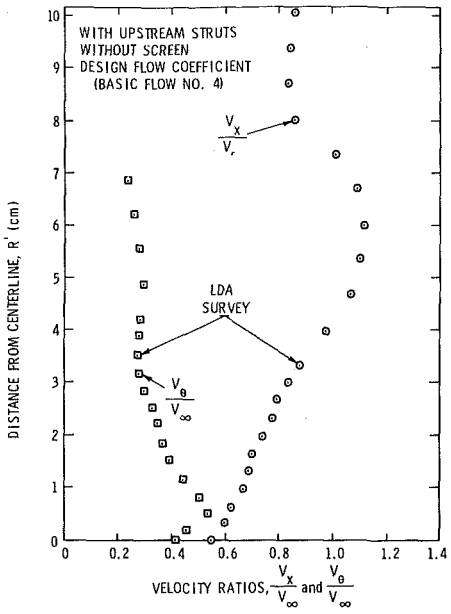

Fig. 10 Velocity profiles on rotor cap for basic flow No. 4

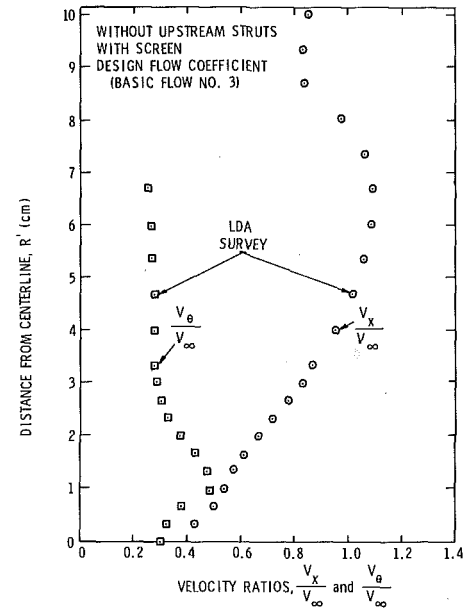

Fig. 9 Velocity profiles on rotor cap for basic flow No. 3

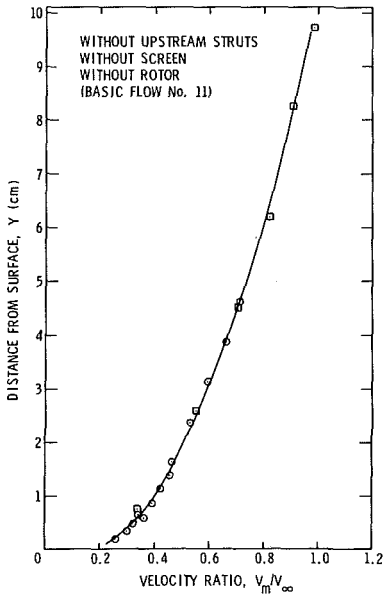

Fig. 11 Meridional velocity profile for basic flow No. 11

wall. A comparison between Fig. 7 and 10 for the rotor downstream velocity profile show a dramatic change in the tangential velocity profile due to the addition of upstream struts. The maximum tangential velocity at the edge of the core decreased slightly as the vortex core radius decreased significantly.

In Fig. 14, the inlet and outlet axial velocity profiles for basic flow No. 1 are compared to the profile that would exist on the body without the rotor. In this figure, the velocity profile without the rotor and the inlet velocity profile were corrected from the meridional velocity to the axial velocity. The change in velocity was small because the streamline angles were less than 8 deg. The acceleration of the flow to the rotor inlet plane can be noted in this figure in addition to the acceleration measured through the rotor.

Some Comparisons with Flow Field Calculations

An approximate calculation procedure was developed in order to determine the mean streamlines for each basic flow configuration. This involved a solution of the direct turbomachinery problem using the streamline curvature method. The flow field is assumed to be axisymmetric, inviscid and incompressible. The solution is an iterative one and brief outline will be given. More details can be found in references [1] and [9].

The streamlines were determined by using an iterative procedure in which the flow field is recalculated by using the streamline curvature equations for each estimate of the blade deviation angles. The boundary conditions for the flow field calculation using the streamline curvature equations are: (1) the flow outlet angles, (2) the velocity profile far upstream of the rotor plane, and (3) the bounding streamlines of the flow field. The flow outlet angles consist of the blade angles and a deviation angle.

To initiate the iterative procedure, the deviation angle correlation developed by Howell [11] is applied. This relationship considers only thin blade sections and assumes that each blade section operates near design incidence.

Once a convergent solution is obtained for the flow field using Howell's deviation rule, another estimate of the flow outlet angles can be made using the calculated flow field. For these deviation angles, the effects of acceleration, blade camber, and blade thickness are estimated. For the calculation of the deviation term due to axial acceleration through the rotor, an equation developed by Lakshmi-

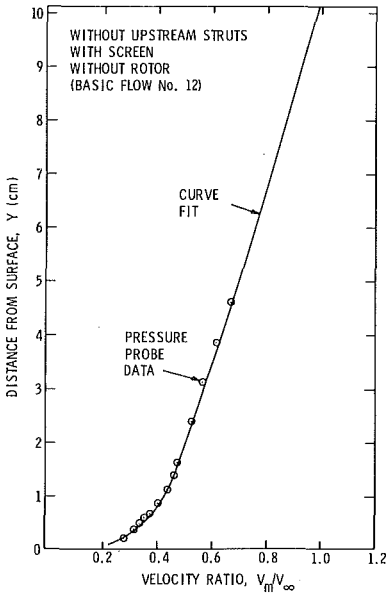

Fig. 12 Meridional velocity profile for basic flow No. 12

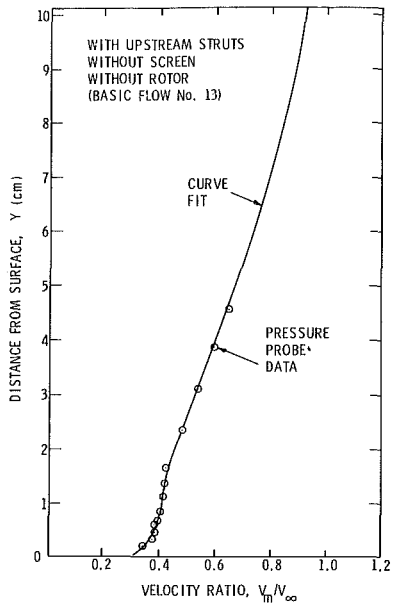

Fig. 13 Meridional velocity profile for basic flow No. 13

narayana [12] is applied. For the calculation of deviation terms due to camber and thickness effects, the data collected by Lieblein [13] are used. This improved deviation angle is used in the calculation of the flow field.

This improved estimation of the deviation angles and resulting calculation of the flow field is repeated until a convergent solution is found. The convergent solution of the flow field gives a calculation of the streamlines. Finally, the secondary vorticity equations are applied along the streamlines through the rotor. An additional deviation term is now calculated by solving Poisson's equation for the stream function in the rotor exit plane with the vorticity calculated by the secondary flow equations. Details of the secondary flow equations and the solution for the stream function to find the deviation term is given in reference [1]. Finally, the last calculation of the flow field is made with the secondary flow deviation term added to the deviation angle.

This calculation procedure was applied to several of the basic flow configurations. As an example, Figs. 15–17 show the calculated flow field and measured data for basic flow No. 1.

In Fig. 15, a comparison for the inlet velocity profiles to the rotor is shown. This figure shows quite good correlation except near the inner wall where the inviscid theory overpredicts the axial velocity.

A comparison between the calculated and measured rotor outlet profile is shown in Fig. 16. The agreement in the axial velocity profile is quite good including the effect of the rotor tip shown by the dip in the axial velocity. The tangential velocity profiles are also in good agreement. Near the inner wall, the calculated profile overpredicts the measured profile. This difference is primarily due to the secondary flow theory which assumes that the induced velocity field occurs in the rotor exit plane when, in fact, the secondary vorticity filaments extend downstream. Fig. 17 shows a comparison of the velocity profiles at the end of the rotor cap. The tangential velocity profiles are in good agreement outside of the vortex core. The mean structure of the vortex is close to the classical Rankine model.

Summary and Conclusions

Mean flow field measurements were obtained for a rotor operating with an inlet velocity gradient. The rotor was lightly loaded and had a low hub-to-tip ratio. Most of the flow measurements were made with a LDA in the 1.22 m water tunnel. The data obtained for the rotor outlet flow with a LDA compared favorably with previous data from five-hole probe measurements.

Comparisons of the axial velocity flow fields for the inlet, outlet, and rotor cap measurements for the same basic flow show the axial velocity acceleration. A significant amount of flow acceleration is seen

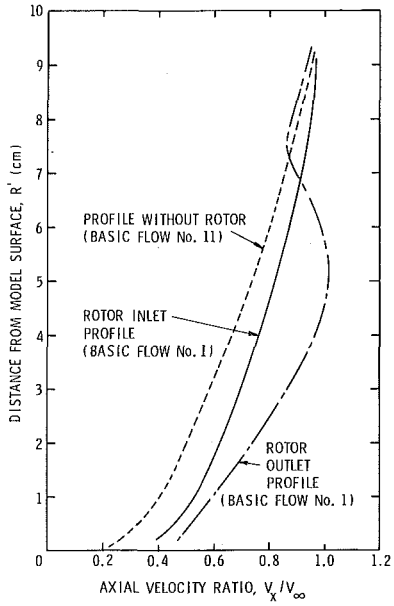

Fig. 14 Comparison of axial velocity profiles for basic flow No. 1

upstream of the rotor. Through the rotor plane the acceleration of the axial velocity reflects the loading of the rotor.

An analysis of the inlet velocity profile data shows that the largest changes in velocity occur near the rotor inner wall. As an example, at a position near the rotor inner wall, the largest change is an increase of 12 percent in velocity for basic flow No. 2 compared to basic flow No. 1. This can be compared to an increase of less than 4% at the rotor mid-radius for the same cases.

A more interesting comparison is found when analyzing the data obtained at the end of the rotor cap. The radius of the vortex core varies from 11.4 mm for basic flow No. 3 to 6.3 mm for basic flow No. 4. In contrast, the tangential velocity ratio outside of the vortex core varies from 0.72 for basic flow No. 2 to 0.50 for basic flow No. 4.

The calculated flow field using the streamline curvature equations with an iterative procedure for estimation of the blade deviation angles compares favorably with the measured profiles. In particular, the flow field measurements at the rotor cap correlate with the calculated profile.

The LDA adapted for rotor flow measurements in the 1.22 m water tunnel can measure the difficult rotor flow field. Special consideration

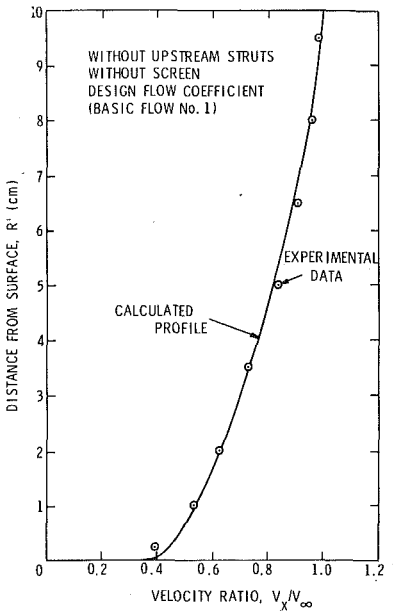

Fig. 15 Rotor inlet velocity comparison for basic flow No. 1

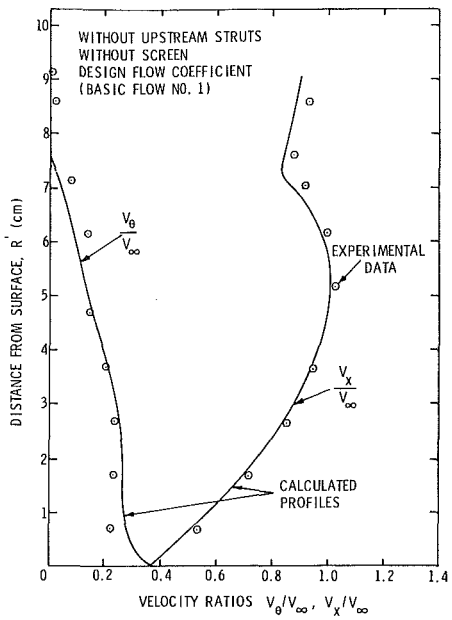

Fig. 16 Rotor outlet velocity comparison for basic flow No. 1

had to be given to laser power, seeding, windows, and surface preparation in order to obtain an acceptable signal. Measurements could be made within 5.0 mm of the surface. More consideration must be given in processing the LDA signal when measuring a vortex structure which is moving in the flow.

Acknowledgments

This investigation was sponsored in part by the Naval Sea Systems Command General Hydromechanics Research Program, Subproject SR 023 01 01, and by the Naval Sea Systems Command, Codes 05H and 63R. The General Hydromechanics Research Program is administered by the David W. Taylor Naval Ship Research and Development Center.

References

1 Novak, R. A., "Streamline Curvature Computing Procedures," ASME JOURNAL OF ENGINEERING FOR POWER, Vol. 89, No. 4, Oct. 1967, pp. 478–490.

2 Davis, W. R., "A Computer Program for the Analysis and Design of Turbomachinery—Revision," Carletion University, Report No. MEA/A 71-5.

3 McBride, M. W., "A Streamline Curvature Method of Analyzing Axisymmetric Axial, Mixed and Radial Flow Turbomachinery," Applied Research Laboratory, Technical Memorandum No. 77-217, July 21, 1977.

4 Hawthorne, W. R., "Secondary Circulation in Fluid Flow," *Proceedings of the Royal Society*, London, England, Series A, Vol. 206, May 1951, p. 374.

5 Staff of Lewis Research Center, "Aerodynamic Design of Axial-Flow Compressors," NASA SP-36, 1965.

6 Smith, L. H., "Secondary Flow in Axial-Flow Turbomachinery," *Trans. ASME*, Vol. 77, 1955.

7. Lakshminarayana, B., and J. H. Horlock, "Generalized Expressions for Secondary Vorticity Using Intrinsic Coordinates," *Journal Fluids Mechanics*, Vol. 59, 1973, pp. 97–115.

8 Lehman, A. F., "The Garfield Thomas Water Tunnel," ORL Report, Serial No. NOrd 16597-56, September 30, 1959.

9 Billet, M. L., "Secondary-Flow-Related Vortex Cavitation," Ph.D. Thesis, Dept. of Aerospace Engineering, The Pennsylvania State University, November 1978.

10 Billet, M. L., "An Appproximate Method for the Solution of the Direct Problem of an Open Rotor," Applied Research Laboratory, Technical Memorandum File No. 78-161, May 1978.

11 Horlock, J. H., *Axial Flow Compressors*, R. E. Krieger, New York, 1973, pp. 55–60.

12 Lakshminarayana, B., Discussion of Wilson, Mani, and Acosta's, "A Note on the Influence of Axial Velocity Ratios on Cascade Performance," NASA SP-304, Part 1, 1974, pp. 127–133.

13 Lieblein, S., "Experimental Flow in Two-Dimensional Cascades," NASA SP-36, 1965, pp. 209–222.

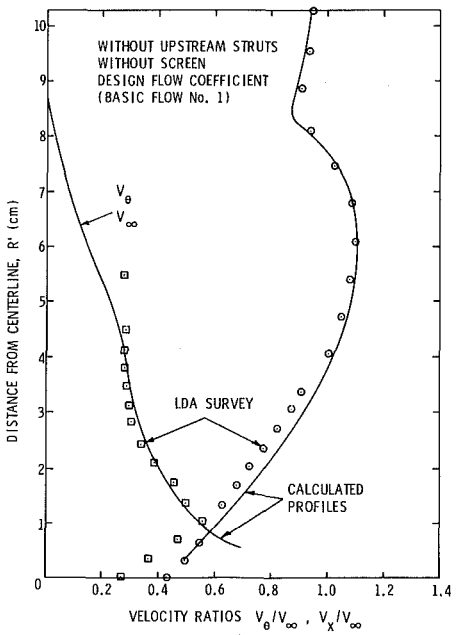

Fig. 17 Rotor cap velocity comparison for basic flow No. 1

Flow Instability at the Inlet of a Centrifugal Compressor

G. Flueckiger
A. Melling

Brown Boveri and Co. Ltd.,
CH-5401 Baden, Switzerland

Using laser Doppler anemometry, two components of the gas velocity have been measured at the inlet of a centrifugal compressor impeller, operated at speeds typical of service conditions for a medium-sized turbocharger. The flow was found to be unstable, especially adjacent to the suction side of the blades, such that two predominant conditions existed in the flow. The unstable flow is illustrated in the paper by distributions of relative velocity and relative flow angle, and the effects of different operating conditions on these distributions are examined. The instability is believed to be caused by a pre-stall condition as the compressor operating point approaches a fully stalled condition which occurs during surge.

Introduction

Efficient single stage centrifugal compressors having a broad operating range between choke and surge at a pressure ratio of 3 to 5 are needed to improve the performance of turbochargers and thereby contribute to a reduced fuel consumption of large Diesel engines. As part of the development of improved turbocharger designs at Brown Boveri [1], measurements of velocity distributions in a centrifugal compressor are being made using laser Doppler anemometry (LDA), both to provide a better understanding of the flow and to supply data for verification of a flow prediction procedure [2].

The present work relates to the flow at the inlet of a centrifugal compressor in a region extending up to a few mm downstream of the leading edge of the impeller blades. The measurements complement those made within the impeller flow by Eckardt [3] using a laser-two-focus (L2F or time-of-flight) anemometer [4], and more recent work reported in references [5] and [6] using laser Doppler anemometry. Of particular interest in this paper is a pronounced flow instability or bistability found in the flow at the impeller inlet.

The test compressor and the instrumentation are described in the next two sections. These are then followed by a presentation of the results and by a discussion of the flow features.

Test Compressor

A single stage centrifugal compressor with a vaned diffuser was used for the tests. The impeller had 14 radial blades and was driven by a d-c electric motor at a speed constant within 0.2 percent. Although the impeller was not representative of those in modern Brown Boveri turbochargers, it was satisfactory for measurement of details of the inlet velocity field.

The compressor was installed in a closed return circuit equipped with a heat exchanger to maintain a constant inlet air temperature. The mass flow rate was determined with a measuring nozzle constructed according to the standards prescribed by DIN 1952.

Important dimensions of the compressor and the measurement positions are given in Fig. 1 and Table 1. The axial positions, x, are referred to the impeller blade leading edge, where the channel width, h, is 70.3 mm; the radial positions, z, are referred to the shroud.

Contributed by the Gas Turbine Division and published in the symposium volume, *Measurement Methods in Rotating Components of Turbomachinery*, ASME, New York, 1980. Manuscript received for publication in the JOURNAL OF ENGINEERING FOR POWER May 22, 1980.

Values of rotational speed, pressure ratio, and mass flow rate at the operating conditions used for the present tests are marked on performance characteristics of the compressor in Fig. 2. Points 2 and 4 lay almost on the surge line, while point 1 lay 30 percent between the surge and choke limits in terms of the mass flow rate, i.e.,

$$\dot{m}_1 = \dot{m}_{\text{surge}} + 0.3\,(\dot{m}_{\text{choke}} - \dot{m}_{\text{surge}}).$$

Instrumentation

Optical System. The optical system of the laser Doppler anemometer was of the dual beam (differential Doppler) type, employing two intersecting beams of equal intensity. The beam from an argon ion laser, operated with a power of 150 mW at a wavelength $\lambda = 488$ nm, was divided by a prism splitter into parallel beams with a separation of 30 mm. These beams were focused into the measuring volume by a lens L (Fig. 1). Backscattered light from particles in the flow was collected by the same lens and detected by a photomultiplier. Because of space limitations imposed by the compressor discharge scroll, the optical system was mounted parallel to the intake duct of the compressor; a mirror deviated the parallel beams through 90 deg to the lens, L.

The optical system was mounted on a traversable support, allowing calibrated movements of the measuring volume in three mutually orthogonal directions. In addition, lens L could be separately traversed to allow more freedom in moving the measuring volume radially. Positions in the axial and radial directions were determined with respect to the shroud with a precision of ± 0.1 mm.

Characteristics of the optical system for two focal lengths of lens L are listed in Table 2.

Scattering Particles. Solid particles needed as scattering centers in the flow were generated from a simple fluidized bed and introduced into the flow through an 8 mm o.d. probe located 200 mm upstream of the impeller blade leading edges. A mixture based on magnesium oxide powder provided seeding particle agglomerates of 1 to 2 μm dia; larger agglomerates were removed by a cyclone.

To prevent contamination of the closed flow circuit, all seeding particles were removed by absolute filters located just after the compressor. The necessary quantity of seeding material was kept small by seeding the flow only locally upstream of the desired measurement position.

Signal and Data Processing. Doppler signals from the photo-

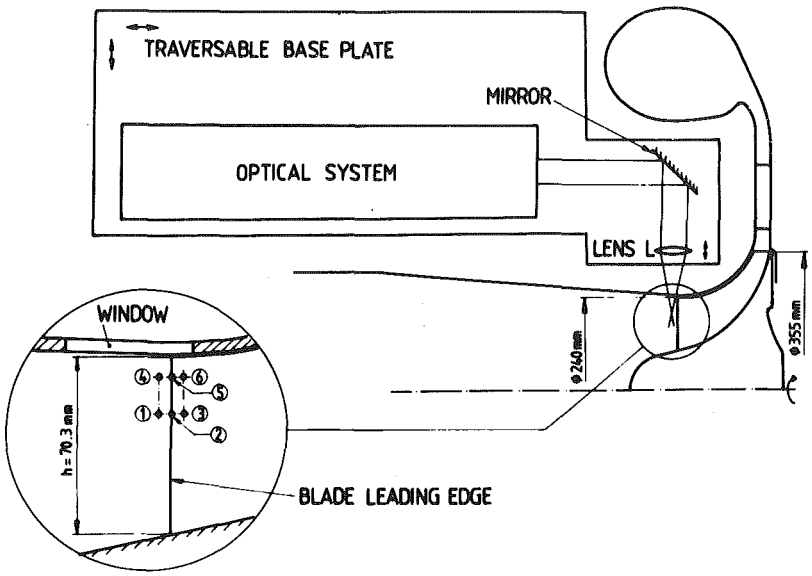

Fig. 1 Compressor geometry and measurement positions

Table 1 Measurement positions

$\frac{z}{h}$	$\frac{x}{h}$ = −0.068	0	+0.063
0.313	①	②	③
0.109	④	⑤	⑥

Table 2 Characteristics of optical system

Lens focal length, f	115.3 mm	153.3 mm
Semi-angle between beams, φ	7.4 deg	5.6 deg
Fringe spacing, λ^*	1.89 μm	2.51 μm
= velocity per unit Doppler frequency	1.89 (ms^{-1})/ MHz	2.51 (ms^{-1})/ MHz
Measuring volume dimensions ($1/e^2$ intensity)		
diameter, d	66 μm	87 μm
length, l	0.50 mm	0.89 mm

multiplier were processed with a sampling spectrum analyzer of the type described in reference [7]. Analog operation of the signal processor is shown by the oscilloscope display in Fig. 3(*a*).

The horizontal scale represents the time between passages of successive impeller blades past a reference position identified by a trigger pulse from an inductive proximity detector located in the shroud. The vertical deflection provided by the sweep voltage from the spectrum analyzer is proportional to the Doppler frequency, and hence to a velocity component, v, through the relationship

$$v = \lambda^* \nu_D. \tag{1}$$

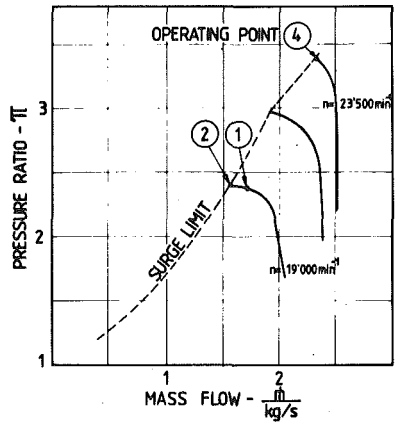

Fig. 2 Performance characteristics of compressor

A frequency range of 10 to 110 MHz (corresponding to a velocity range of 19 to 208 m/s) was normally used.

The oscilloscope was blanked except when detection of a Doppler signal produced a spot on the screen. After accumulating measurements for many impeller passages, a set of points was obtained which were most densely distributed near a curve representing the mean distribution of velocity across the blade passage. The scatter arises principally from turbulent velocity fluctuations, with a subsidiary (inseparable) contribution from flow differences from one blade passage to the next. The density of points along a vertical line describes the Doppler spectrum, i.e. the probability density function of signal frequencies $p(\nu_D)$.

For digital processing of the data, samples of the sweep voltages

Nomenclature

c = absolute velocity
c_{ax} = axial velocity component
c_u = circumferential velocity component
d = diameter of measuring volume
f = focal length
h = channel width at impeller blade leading edge
l = length of measuring volume
M = number of frequency samples per Doppler spectrum
$\dot{m}$ = mass flow rate
n = rotational speed
$p(v)$ = probability density function of velocity component
$p(\nu_D)$ = probability density function of Doppler frequency
S_k = sum defined in equation (4)
Tu = turbulence intensity
u = impeller velocity at radius of measuring station
v = velocity component
w = relative velocity
x = axial coordinate, relative to impeller blade leading edge
y/t = relative blade pitch
z = radial coordinate, relative to shroud
α = absolute flow angle
β = relative flow angle
θ = direction of measured velocity component
(with respect to circumferential direction)
$\Delta\nu_D$ = maximum error in Doppler frequency
Δv = error in measured velocity component
λ = wavelength
λ^* = fringe spacing
ν_D = Doppler frequency
$\tilde{\nu}_D$ = r.m.s. Doppler frequency fluctuation
π = pressure ratio (total-to-total)
φ = semi-angle between beams

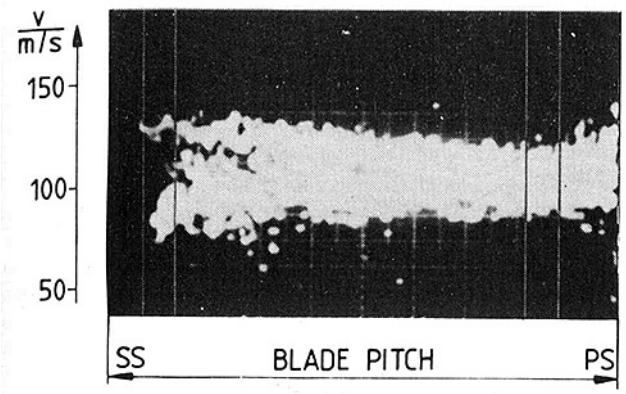

Fig. 3(*a*)

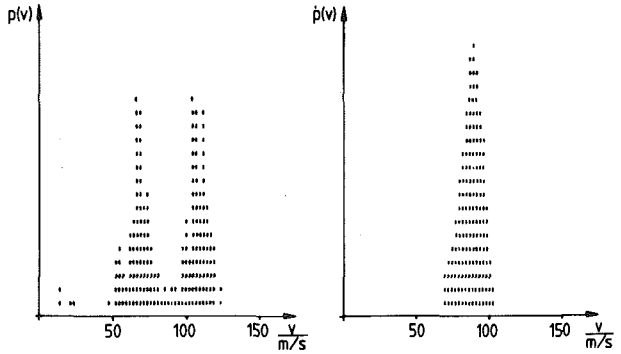

Fig. 3(*b*)

Fig. 3 Sampling spectrum analyzer output and typical Doppler spectra

from the spectrum analyzer and the oscilloscope were accepted by an interface upon detection of a Doppler signal, and digitized for input to a micro-computer. The blade passage was divided into 16 sectors by the digitization, and for each sector the statistics (mean, rms) of the Doppler spectrum were evaluated from M frequency samples, ν_i. A minimum of 100 samples was required to determine the mean frequency with acceptable accuracy. (See the section on accuracy below.)

Evaluation of Velocity Components and Absolute Velocity. The statistics of the Doppler spectrum, $p(\nu_D)$, were evaluated from the following formulae.

$$\text{mean: } \bar{\nu}_D = \frac{S_1}{M} \tag{2}$$

$$\text{rms: } \tilde{\nu}_D = \sqrt{\frac{S_2 - S_1^2/M}{M-1}} \tag{3}$$

where

$$S_k = \sum_{i=1}^{M} (\nu_i)^k \tag{4}$$

The mean velocity component corresponding to $\bar{\nu}_D$ was determined from equation (1). In general two velocity components, v_1 and v_2, were measured in directions θ_1 and θ_2, chosen by the orientation of the plane of the laser beams. The direction, α, and magnitude, c, of the absolute velocity, and the axial and tangential velocity components, c_{ax} and c_u, were found from the formulae below. These are based on formulae given in reference [8] but altered to use the tangential rather than the axial direction as reference for α.

$$\alpha = \alpha' + 90 \text{ deg} \tag{5}$$

where

$$\alpha' = \arctan\left[\frac{v_1 \cos\theta_2 - v_2 \cos\theta_1}{v_2 \sin\theta_1 - v_1 \sin\theta_2}\right] \tag{6}$$

$$c = \frac{v_1}{\cos(\theta_1 - \alpha')} \tag{7}$$

$$c_{ax} = c \sin\alpha \tag{8}$$

$$c_u = c \cos\alpha \tag{9}$$

The direction, β, and magnitude, w, of the relative velocity were determined as follows.

$$\beta = \arctan\left(\frac{c_{ax}}{u - c_u}\right) \tag{10}$$

$$w = \sqrt{(u - c_u)^2 + {c_{ax}}^2} \tag{11}$$

Accuracy. The accuracy of a single velocity measurement depends, according to equation (1), on the accuracy of ν_D and λ^*. The maximum error in ν_D is the round-off error of the analog-digital conversion, i.e., one half the frequency resolution of the six-bit digitization in the data processor; for a typical frequency ν_D = 50 MHz and a 100 MHz frequency range on the spectrum analyzer, this error is $\Delta\nu_D/\nu_D = \frac{1}{2}(100/64)/50 = 0.016$. The error in λ^* is an order of magnitude smaller.

The accuracy of a mean velocity component is, however, affected by the frequency resolution only when the Doppler spectrum is constructed from too few frequency intervals (according to an example in reference [9], a minimum of about six intervals could be accepted). The main limitation on the accuracy is the number, M, of frequency measurements on which the Doppler spectrum is based. The error in mean velocity at the 95 percent confidence limit is then approximately [9]

$$\frac{\Delta v}{v} \simeq \frac{2}{\sqrt{M}} Tu$$

For typical conditions (M = 100, Tu = 0.1), the error is $\Delta v/v$ = 0.02.

The accuracy achievable was also assessed using the spatially averaged absolute velocity from LDA measurements at the impeller outlet. In comparison with average radial and tangential velocity components evaluated from the mass flow rate and compressor work input respectively, the discrepancies in $\bar{c}$ lay between − 0.8 and + 1.3 percent and in $\bar{\alpha}$ between +0.2 and +0.7 deg.

Results

Detection of Flow Instability. The results of this paper are concerned with instability in the flow entering the impeller. At certain positions in the flow it was found that, after averaging out the velocity fluctuations due to turbulence, the mean velocity vector could take on two particular magnitudes and directions, rather than the unique magnitude and direction typical of a steady flow. How this instability was detected is explained briefly below, before the results are presented in detail.

The instability was revealed by the Doppler spectra $p(\nu_D)$ which are equivalent to probability density distributions of a velocity component $p(v)$. In turbulent flows these distributions are normally single-peaked as in Fig. 3(*b*), right; they are often, but not necessarily, roughly Gaussian in shape, with a maximum at the mean velocity and a width proportional to the turbulence intensity. In the present work, however, double-peaked Doppler spectra were also found, as in Fig. 3(*b*), left. The two peaks correspond to slightly separated bands of densely packed points on the oscilloscope display of Fig. 3(*a*). These bands merge near the middle of the channel, so that near the pressure surface normal single-peaked spectra were measured.

Bimodal spectra indicate a flow fluctuation between two rather well defined states with a very low probability of an intermediate state. Thus the distribution of a particular velocity component, v, across a blade passage could be represented by a pair of curves describing the mean velocity for each flow state; these coincided over that region where bimodal Doppler spectra were not detected. From such curves, vector plots and iso-Mach contours such as those in Figs. 4–9 could be constructed.

Vector Plots. Figures 4–6 show relative flow vectors along the stream surfaces, z/h = 0.109 and 0.313, for each of the operating points 1, 2 and 4. The length of each vector is proportional to the relative velocity existing at the tail of the arrow, according to the scale marked

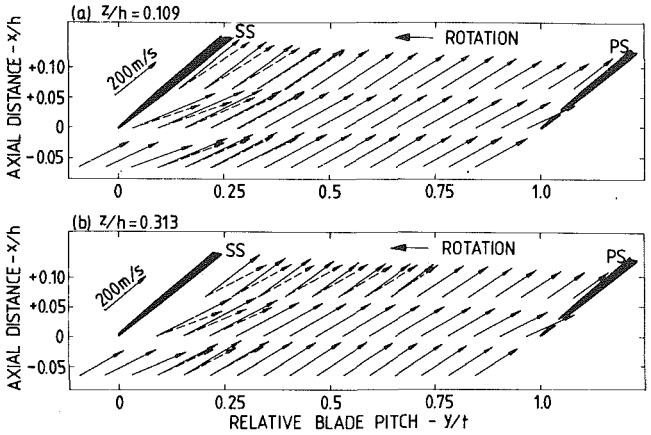

Fig. 4 Relative flow vectors at inlet: operating point 1. $\leq$, bistable velocities. *z/h:* distance from shroud normalized by channel width

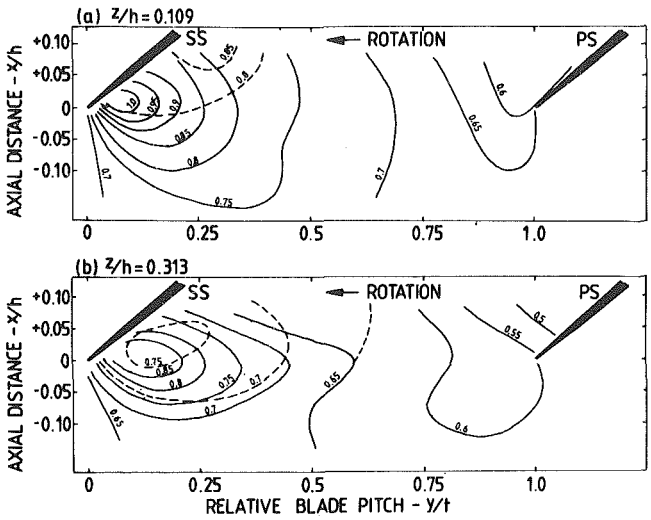

Fig. 7 Contours of constant relative Mach number at inlet, operating point 1

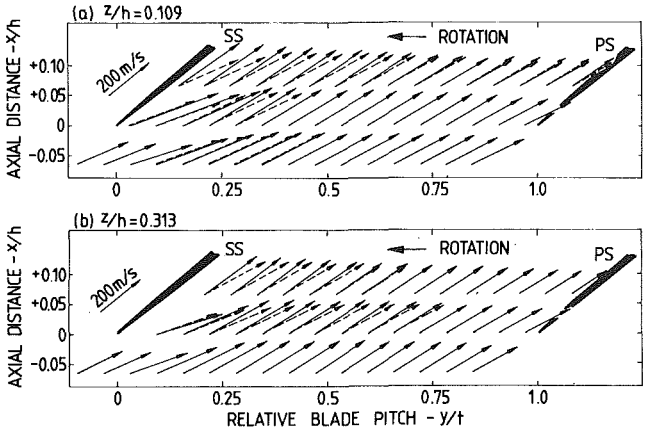

Fig. 5 Relative flow vectors at inlet: operating point 2. $\leq$, bistable velocities

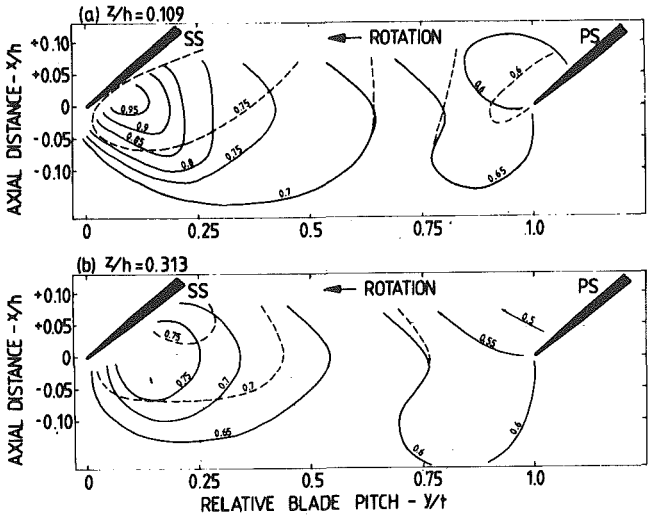

Fig. 8 Contours of constant relative Mach number at inlet, operating point 2

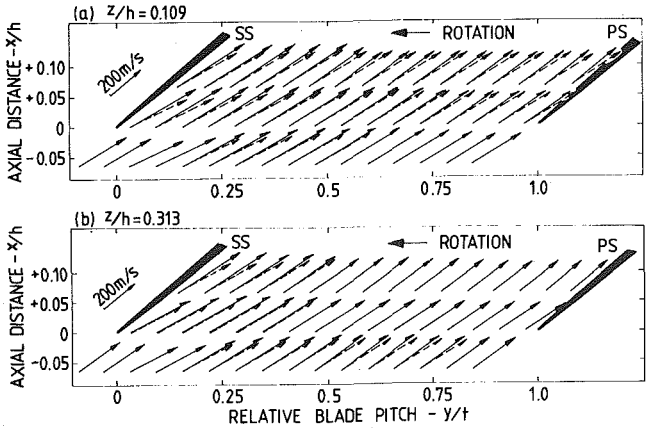

Fig. 6 Relative flow vectors at inlet: operating point 4. $\leq$, bistable velocities

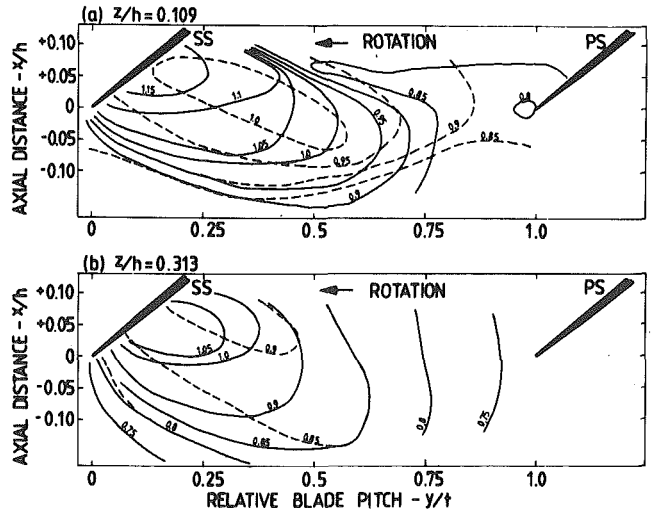

Fig. 9 Contours of constant relative Mach number at inlet, operating point 4

on each figure. Unstable flow exists in those regions where vectors of differing length and direction are drawn at the same point, representing the two possible flow states. The states corresponding to solid and broken vectors are denoted as S and B below, and are associated in most, but not all, cases with lower and higher incidence of the flow, respectively.

In Fig. 4 (operating point 1) a weak instability upstream of the impeller develops further at the impeller inlet. The unstable flow at $z/h = 0.109$ lies in the quarter of the blade passage nearest to the suction surface. Farther away from the shroud, at $z/h = 0.313$, the unstable region is of similar size at the blade leading edge, but spreads to the middle of the passage downstream of the leading edge. In all cases the B flow condition corresponds to a reduced relative velocity and a higher incidence of the relative flow to the blade surface (as much as 10 deg). In the leading edge plane, the flow is sharply inclined to the blades for both the S and B states; but downstream the flow adjusts itself better to the blade contour, particularly in the S state. The S and B flow states occurred with approximately equal probability.

The flow behavior at operating point 2 on the surge limit (Fig. 5) differs from that at operating point 1 in several respects. Firstly the portion of the flow affected by instability is enlarged, particularly for $x/h = +0.063$ at $z/h = 0.109$ where unstable flow occupies the entire passage and for $x/h = 0$ at $z/h = 0.313$. The intensity of the instability is similar to that at operating point 1, but regions of weak instability exist which are associated with a reduced rather than increased incidence angle for the B state. At this operating point state B appeared to be slightly more probable than state S.

The plots for operating point 4 at higher impeller speed in Fig. 6 show flow instability upstream of the impeller in the middle of the blade spacing. At $z/h = 0.109$ the unstable region fills the entire blade passage. The B state flow again shows increased incidence to the blades, but the maximum deviation is less than at operating points 1 and 2. Deeper into the flow, however, at $z/h = 0.313$, the region of unstable flow diminishes in the streamwise direction. The deviation of the flow in state B from that in state S is rather small, particularly in the leading edge plane. At operating point 4 state S was significantly more probable than state B at $z/h = 0.109$, but state B was more probable at $z/h = 0.313$. It is possible that the two more probable states occurred simultaneously such that the flow would be redistributed over the blade height in synchronism with the instability, but this could not be verified.

Contours of Constant Relative Mach Number. Contours of constant relative Mach number in Figs. 7–9 were interpolated from measurements at positions ① to ⑥ of Fig. 1. For operating point 1 in Fig. 7 the flow reaches a maximum velocity near the suction surface at the inlet to the impeller. In the S state at $z/h = 0.109$ the maximum velocity is marginally supersonic and lies just downstream of the blade leading edge, while further from the blade tip ($z/h = 0.313$) the flow remains subsonic. In the B state, the peak velocity is substantially reduced and lies about 4 mm downstream of the leading edge plane.

A similar trend is seen in Fig. 8 for operating point 2. The velocity levels are close to those for operating point 1 in both S and B states at $z/h = 0.109$, and also for the B state at $z/h = 0.313$. In the S state, however, the velocities near the suction side are substantially lower than for operating point 1. The peak velocity lies further from the suction surface upon transition from the S to the B state.

For operating point 4 (Fig. 9), a change from the S to the B condition reduces the peak velocity, but the maximum velocity remains just supersonic at $z/h = 0.109$ and is only slightly subsonic at $z/h = 0.313$. The peak velocity for both S and B states is located downstream of the leading edge at this operating condition, but in the B state the maximum is flat and displaced towards the centre of the channel. A high velocity gradient at $z/h = 0.109$ for the S condition, indicative of a shock, is smeared to a much gentler gradient in the B state.

Discussion

The principal feature of the unstable flow shown in Figs. 4–9 is a fluctuation in the magnitude and direction of the velocity vector at the impeller inlet, particularly near the suction side of the blade passages. The fluctuation occurs between two rather well defined states (S and B) with a very low probability of an intermediate state. The relative probability of the two states depends on the operating conditions; at operating point 4, one state (S or B, depending on z/h) is significantly more probable than the other, while at lower flow rate, pressure ratio and rotational speed (operating points 1 and 2) the two states occur with approximately equal probability. The possibility that the phenomena might be attributable to a variation in the flow field between one blade passage and the next was excluded by measurements in only one blade passage which showed the same instability.

Detailed inspection of Figs. 4–6 suggests that the unsteady flow may be associated with a separation zone just downstream of the blade leading edge. Evidence of separation is given by the especially high incidence angle of the velocity vectors nearest to the suction surface, particularly for operating points 1 and 2. It is noteworthy that the incidence angle across the blade passage is rather large (typically 10 deg), but this is in agreement with the angle of 9 deg reported by Linsi [10] at the most efficient operating point of a turbocharger compressor. Further evidence of a leading edge bubble is particularly well shown in Fig. 5 where the flow becomes unstable only at some distance from the leading edge; this behaviour is characteristic of free vortex layers. At operating point 4 the separation zone is much weaker, consistent with the smaller incidence angle existing at the higher Mach number. The flip-flop transition of the flow between two states would be consistent with the presence of two slightly different separation points on the rounded leading edge. At operating point 1, remote from the surge limit, the apparent spatial extent of the instability was less than at points near the surge limit; this trend was confirmed by measurements at an operating point on the constant speed characteristic through points 1 and 2 but 60 percent from the surge limit to the choke limit which showed no instability.

Evidence from the present work is supported by literature which suggests that the unsteadiness is explicable as a partial stall preceding surge. Such a condition was briefly mentioned by Eckardt [11] on the basis of unsteady shroud pressure measurements in a centrifugal compressor during the approach to rotating stall. A condition of partial stall at operating points 2 and 4 is certainly likely because of their proximity to the surge condition. Partial stall at operating point 1, well away from the surge limit, is consistent with the observations of Senoo, et al. [12] who found that their centrifugal compressor could operate stably even when the inducer was stalled. Further, in the discussion to reference [13], it is noted that surge of a centrifugal compressor is brought about by incipient stall in the diffuser; this may be caused by poor aerodynamic conditions leaving the impeller which depend in turn on flow disturbances originating in the inducer. The importance of the inducer flow was mentioned also in Bullock's discussion; he claimed that compressor surging is usually triggered by stalling of the inlet flow, due to separation near the impeller tips on account of an increased flow incidence angle at low flow rate. Bullock stated further that an oscillatory flow phenomenon preceding surge can occur when the total compressor system is stable. He characterized this transition region by erratic pulsations of small magnitude, while distinctly periodic pulsations of larger amplitude were found in reference [13]. The bi-stable condition observed in the present work suggests that the second of these forms of oscillation is more likely.

Explanation of the phenomena would be facilitated by knowledge of the frequency of the instability. The frequency could not be determined from the LDA measurements because the achievable data rate (limited by the concentration of seeding particles and the signal-to-noise ratio) was too low to resolve the time-dependence of the velocity. The frequency could probably be found from records of the unsteady surface pressure on the shroud. Such measurements are to be undertaken as a sequel to the present work.

Conclusions

A strongly defined flow instability was found at the impeller inlet of a centrifugal compressor, particularly near the suction side of the blade passages. The instability, as revealed by detailed velocity

measurements, showed a fluctuation in the magnitude and direction of the flow between two states. The intensity of the instability increased with reduction in the flow rate, pressure ratio and rotational speed. A likely cause for the instability is a condition of partial stall preceding surge. The velocity field measured indiated that a leading edge separation probably occurred, but proof of the existence of separation would require velocity measurements with the laser Doppler anemometer close enough to the blades to demonstrate reverse flow.

Acknowledgments

We are grateful to the Turbocharger department of Brown Boveri for giving permission to publish this work. Dr. P. Spengler assisted greatly in interpreting the experimental results. Extensive help was also received from Dr. P. Iten during the early stages of applying laser anemometry to the centrifugal compressor.

References

1 Späti, H., "Neue BBC-Turbolader VTR "4" für höhere Druckverhältnisse," *Motortechnische Zeitschrift,* Vol. 40, No. 5, May 1979, pp. 223–226.

2 Ribaut, M., "On the Calculation of Three-Dimensional Divergent and Rotational Flow in Turbomachines," ASME *Journal of Fluids Engineering,* Vol. 99, No. 1, Mar. 1977, pp. 187–196.

3 Eckardt, D., "Detailed Flow Investigations within a High-Speed Centrifugal Compressor Impeller," ASME *Journal of Fluids Engineering,* Vol. 98, No. 3, Sept. 1976, pp. 390–402.

4 Schodl, R., "Laser-Two-Focus Velocimetry (L2F) for Use in Aero-Engines," AGARD-LS-90, *Laser Optical Measurement Methods for Aero Engine Research and Development,* Aug.–Sept. 1977, paper 4.

5 Adler, D., and Levy, Y., "A Laser-Doppler Investigation of the Flow inside a Backswept, Closed, Centrifugal Impeller," *Journal of Mechanical Engineering Science,* Vol. 21, No. 1, 1979, pp. 1–6.

6 Durão, D. F. G., Goulas, A., and Whitelaw, J. H., "Measured Velocity Characteristics of the Flow in the Impeller of a Centrifugal Compressor," ASME paper No. 79-HT-32, 1979.

7 Iten, P. D., and Dändliker, R., "A Sampling Wide-Band Demodulator Useful for Laser Doppler Velocimeters," *Proceedings IEEE,* Vol. 60, No. 12, Dec. 1972, pp. 1470–1475.

8 Wisler, D. C. and Mossey, P. W., "Gas Velocity Measurements Within a Compressor Rotor Passage Using The Laser Doppler Velocimeter," ASME JOURNAL OF ENGINEERING FOR POWER, Vol. 95, No. 2, April 1973, pp. 91–96.

9 Clare, H. et al., "Investigation of a V-Gutter Stabilized Flame by Laser Anemometry and Schlieren Photography," AGARD-CP-193, *Applications of Non-Intrusive Instrumentation in Fluid Flow Research,* May 1976, paper 26.

10 Linsi, U., "Versuche an Turbolader-Radialverdichtern," *Brown Boveri Mitteilungen,* Vol. 52, No. 3, Mar. 1965, pp. 161–170.

11 Eckardt, D., "Radialverdichter, Untersuchung der Laufradströmung in Hochbelasteten Radialverdichterstufen," Forschungsvorhaben Nr. 83 und 115, Heft 154, 1974, *Forschungsvereinigung Verbrennungskraftmaschinen,* Frankfurt, Germany.

12 Senoo, Y. et al., "Experimental Study on Flow in a Supersonic Centrifugal Impeller," ASME JOURNAL OF ENGINEERING FOR POWER, Vol. 101, No. 1, Jan. 1979, pp. 32–41.

13 Toyama, K., Runstadler, P. W., and Dean, R. C., "An Experimental Study of Surge in Centrifugal Compressors," ASME *Journal of Fluids Engineering,* Vol. 99, No. 1, Mar. 1977, pp. 115–131.

Laser-Optical Blade Tip Clearance Measurement System

J. P. Barranger
NASA Lewis Research Center,
Cleveland, OH 44135

M. J. Ford
Pratt & Whitney Aircraft Group,
West Palm Beach, Fla.

The need for blade tip clearance instrumentation has been intensified recently by advances in technology of gas turbine engines. A new laser-optical measurement system has been developed to measure single blade tip clearances and average blade tip clearances between a rotor and its gas path seal in rotating component rigs and complete engines. The system is applicable to fan, compressor and turbine blade tipe clearance measurements. The engine mounted probe is particularly suitable for operation in the extreme turbine environment. The measurement system consists of an optical subsystem, an electronic subsystem and a computing and graphic terminal. Bench tests and environmental tests were conducted to confirm operation at temperatures, pressures, and vibration levels typically encountered in an operating gas turbine engine.

Introduction

The need for blade tip clearance instrumentation has been intensified recently by advances in technology of gas turbine engines. Improved engine designs encompass lightweight high-performance concepts such as small thin airfoils for blades. Excess clearance allows a portion of the engine gas to flow over the blade tip without performing useful work. Moreover, insufficient blade tip clearance may cause interference which can jeopardize the engine integrity.

Previously, it had been possible to measure average blade tip clearance over several rotor revolutions, but the system [1] did not have adequate response for transient or single blade tip clearance measurements. The Pratt & Whitney Aircraft Group, Government Products Division, designed and fabricated, under contract to NASA Lewis, a system that possessed adequate time response and that was capable of measuring and displaying single as well as average blade clearances.

This new laser-optical measurement system [2] was designed to measure single blade tip clearances and average blade tip clearances between a rotor and its gas path seal in rotating component rigs and complete engines. The system is applicable to fan, compressor, and turbine blade tip clearance measurements. The engine mounted probe is particularly suitable for operation in the extreme turbine environment.

The measurement system has been bench tested using typical rotor blades up to simulated rotor speeds of 60,000 rpm, blade tip speeds of 610 m/s (2000 ft/s) and blade tip thicknesses as small as 0.79 mm (0.031 in.). These tests showed that the system has an overall clearance measurement range of 0 to 3.05 mm (0.120 in.). Computed two-sigma values based on the best fit calibration curve for the system showed a deviation from best fit of less than 0.025 mm (1 mil), a resolution of less than 0.025 mm (1 mil) and a repeatability of less than 0.05 mm (2 mil).

Environmental tests were also conducted to confirm probe operation at adjacent wall temperatures up to 1300 K (1900° F), gas path operating pressures up to 30 atm, and vibration levels typically encountered in an operating gas turbine engine. Results indicate no degradation in system performance beyond the previously stated bench test data.

The measurement system consists of an optical subsystem, an electronic subsystem and a computing and graphic terminal. The optical subsystem includes an optical probe, fiber optic cables and an environmental enclosure containing the electro-optical components. The electronic subsystem chassis provides the scan, gate, and process functions required for single and average blade clearance measurements. Optical and electronic subsystem control and data presentations are provided by the computing and graphic display terminal. Software programs present data as a plot of clearance versus time or clearance versus blade number.

System Description

The measurement system consists of an optical subsystem, an electronic subsystem and a computing and graphic terminal. Figure 1 illustrates the overall system configuration.

Optical Subsystem. The optical subsystem includes an optical probe, fiber optic cables and environmental enclosure containing the electro-optical components. A schematic of the basic probe optical system is shown in Fig. 2. The light source is imaged on the target blade tip through a lens and a sapphire prism. The reflected light returns through the prism and lens and is focused on the output coherent fiber optic bundle. The radial movement of the blade tip from A to B corresponds to the movement of the light spot from A′ to B′ on the output bundle. The tip clearance is measured relative to the shroud surface by correcting for the fixed zero offset distance between the prism face and the shroud surface. The prism folds the optical path allowing the use of a single probe housing for both the input and output optics. Probe cooling is achieved with dry nitrogen flowing along the inner wall of the probe housing. The prism is spaced away 0.5 mm from the viewing slot at the end of the housing. The nitrogen flow passes across the prism and exits through the slot, thereby keeping the prism face clean. Figure 3 is a photograph of the probe showing the braided stainless steel sheathed optical cables. The probe tip is designed to bayonet fit directly to the shroud. Errors in the zero offset distance induced by thermal growth are minimized by keeping the distance from the bayonet mount to the shroud surface as short

Contributed by the Gas Turbine Division and published in the symposium volume, *Measurement Methods in Rotating Components of Turbomachinery*, ASME, New York, 1980. Manuscript received for publication in the JOURNAL OF ENGINEERING FOR POWER May 22, 1980.

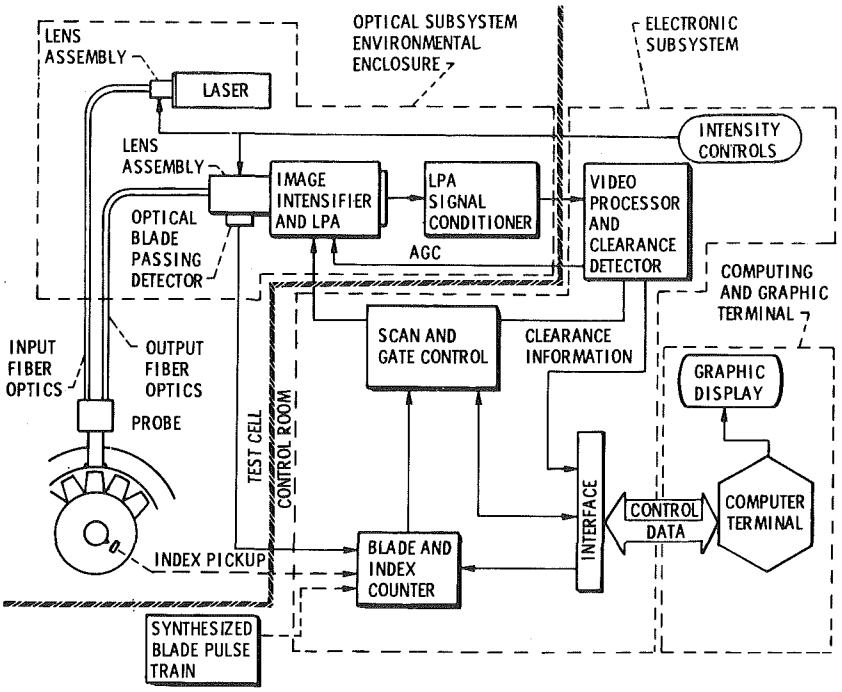

Fig. 1 Overall system configuration

as possible. Note the viewing slot at the tip of the probe.

The environmental enclosure which contains the electro-optical components is connected to the probe by two coherent fiber optic cable bundles 2.74 m in length. The 10 mW helium-neon laser light source (632.8 nm wavelength) is coupled to the input fiber bundle through a lens assembly (Fig. 1). The lens assembly includes a 20 power microscope objective lens to focus the laser beam down to a single fiber of approximately 10 μm in diameter. A graded neutral-density filter wheel located between the laser and the objective lens is used to control the intensity at the fiber. This control is necessary to adjust for the variation in the optical properties of engine blades. Moreover, control is also required to adjust the energy received by the image processing system at different engine speeds and system operating modes.

The output fiber bundle is coupled to the image intensifier through a relay lens assembly and an image intensifier lens. The relay lens assembly serves three purposes: (1) to receive and collimate the laser spot image received from the probe output bundle, (2) to filter out unwanted background radiation by using a laser line band-pass filter, and (3) to collect and detect peripheral radiation from the probe output which is not collected by the relay lens and utilize the energy to produce a blade passing pulse train.

The objective lens of the relay lens assembly views the probe output spot image through a hole in the center of a concave mirror. Approximately 70 percent of the fiber optic bundle output intensity is received by the objective lens while the annular mirror segment collects the peripheral radiation from the bundle which would otherwise be lost. This peripheral radiation is focused onto the tip of a fiber optic light guide and is transmitted to a photomultiplier tube (PMT). As the blades pass by the probe, the photomultiplier tube detects the light pulses and generates a blade passing pulse train.

The collimated and filtered signal radiation from the objective lens is reimaged onto the image intensifier faceplate by the image intensifier lens. The lens aperture is controlled by a motorized iris. The light level at the image intensifier faceplate is thus regulated by both the iris size and by the neutral density filter at the laser output. Moreover, during conditions of sufficient signal radiation, system resolution is enhanced by reducing the size of the iris to a minimum.

The image intensifier is a novel proximity focused microchannel plate type coupled to a linear photodiode array (LPA). The tube is made up of an input window with an S20 photocathode deposited on the inside surface, a microchannel plate, and an output phosphor

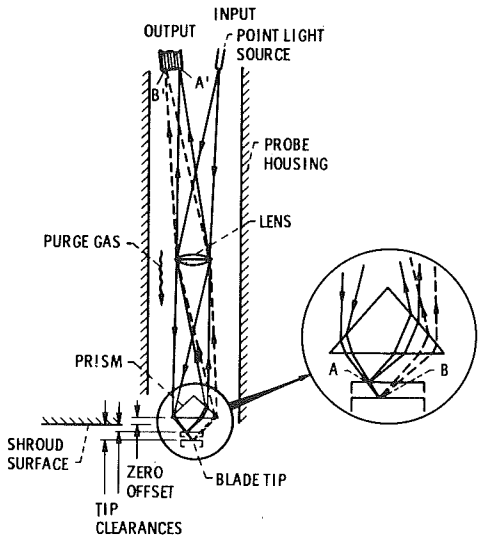

Fig. 2 Basic probe optical system

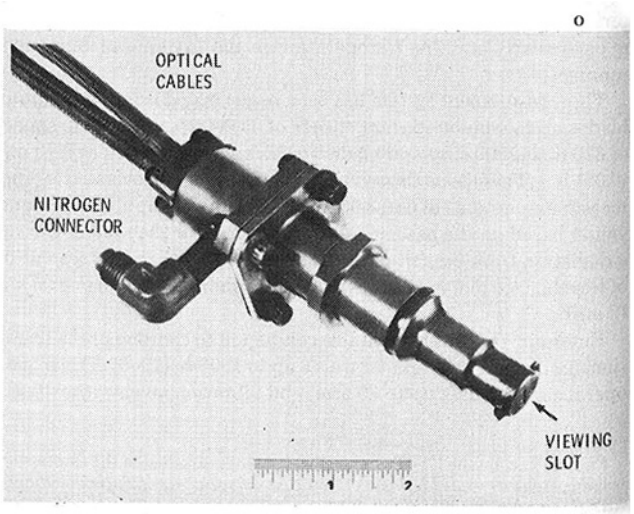

Fig. 3 Probe showing optical cables

screen coupled directly to the LPA by way of a fiber optic faceplate. The array consists of 256 photodiodes each 0.025 mm (1 mil) wide by 0.43 mm (17 mil) long and spaced 0.025 mm (1 mil) center to center. The microchannel plate is an array of 12 μm dia channels fused together into the shape of a thin plate. By applying a voltage across the faces of the plate, electron gain is achieved through secondary emission within each microchannel. The overall light gain is in the range of 1000 to 10,000. The image intensification process is performed internally with no external electronics other than a gateable power supply. The tube is 40 mm in diameter and 30 mm long.

The LPA signal conditioner (Fig. 1) consists of an amplifier and a line driver.

Electronic Subsystem. The electronic subsystem controls the components of the optical subsystem and processes the signal from the LPA signal conditioner. It also interfaces with the computing and graphic terminal by accepting commands and transmitting tip clearance data. The system operating mode is determined by the operator through the keyboard of the terminal. The system software resident in the terminal transforms the operator's request into the appropriate command sequence for transmission to the electronic subsystem. The operator can select any of the following operating modes: (1) *average mode* which is the optical average of all the blades taken each revolution, (2) *single blade mode 1* which is a sequence of selected blades taken one at a time where each blade is averaged over a selected number of revolutions, and (3) *single blade mode 2* which is a sequence of measurements of a single selected blade where each measurements is averaged over a selected number of revolutions. If either of the *single blade* modes is selected the operator also provides *blade number* and number of revolutions information. The *blade number,* in the range 1 to 120, is the sequence of blade numbers for *single blade Mode 1* or the blade number for *single blade Mode 2.* The number of revolutions, in the range 1 to 255, is the number of rotor revolutions that will be optically averaged in the single blade modes. This feature is provided so that the operator may increase the average light level if insufficient radiation is available for proper signal conditioning. In all modes the operator selects a minimum and maximum clearance. When the software has detected a measured clearance at or less than the preselected minimum the *minimum clearance alarm* is activated. When the software has detected a measured clearance at or greater that the preselected maximum the *maximum clearance alarm* is activated. The clearance alarms illuminate front panel alarm indicators on the electronic subsystem.

The electronic subsystem executes the commands from the terminal by sending gate and scan control signals to the image intensifier and the LPA (Fig. 1). In the average mode, the image intensifier is gated on continuously and and LPA optically averages the clearance of all the blades. In the single blade modes, the image intensifier is gated on to view only the requested blade number. The LPA optically averages the clearance for the chosen number of revolutions. In all modes, the video processor and clearance detector (Fig. 1) convert the diode site number with the greatest light level to clearance information. A preselected zero offset feature corrects for the zero offset distance between the probe prism face and the shroud surface (Fig. 2). Thus all clearance data are measured relative to the shroud surface. The video processor also generates an automatic gain control (AGC) voltage to optimize the LPA output. In addition, any detected hardware error in the electronic subsystem generates an error message which is transmitted to the terminal indicating that the data are invalid.

In the blade and index counter, a once-per-rotor-revolution index pulse is used in combination with the blade passing pulse train from the PMT to generate synchronization signals corresponding to the selected blade number. For the infrequent condition where there is insufficient radiation to be detected by the PMT, an externally provided synthesized blade passing pulse train may be substituted.

The general purpose interface bus (IEEE STD 488-1975) is the interface system which connects the electronic subsystem and the computing and graphic terminal. Figure 4 is a photograph of the system hardware with all of the major components labeled. The 30 m (100 ft) interconnecting cable connects the optical and electronic subsystems.

System Displays. The computing and graphic terminal controls the electronics subsystem and provides clearance data presentations. Keyboard entries of test conditions are accepted by programs resident in the terminal core memory. Upon execution, the programs issue control instructions and receive blade tip clearance data in return via the interface. In the *average Mode,* data are presented on the graphic terminal screen in a plot of clearance in mils versus scan # (scan number). This display is illustrated in Fig. 5. The abscissa or scan number axis is similar to a time axis since each scan represents a time equal to approximately the period of one revolution times the number of revolutions. The average of all the scans is indicated as AVG. The maximum and minimum clearances are shown as MAX and MIN, respectively. Figure 6 is the display of the *single blade Mode 1* where data are presented as clearance in mils versus blade number. The *single blade Mode 2* data are presented in a plot of clearance in mils versus scan number. This display is shown in Fig. 7 where again the scan number axis is similar to a time axis. A zoom capability is provided which allows the operator to expand both axes of any plot.

Performance

Bench tests were conducted to determine the measurement system's operational performance characteristics. Both static calibration and dynamic performance were evaluated. Further, the measurement system probe was subjected to environmental conditions typically encountered in an operating gas turbine engine.

Bench Tests. A static calibration was performed with the system probe mounted in a micrometer calibration fixture. Calibration range was from zero to 3.28 mm (129 mil). The distance was measured from probe tip to micrometer face and the increment was one diode site.

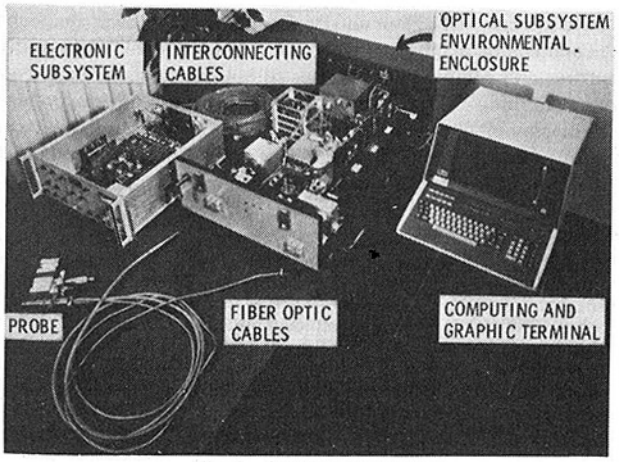

Fig. 4 System components

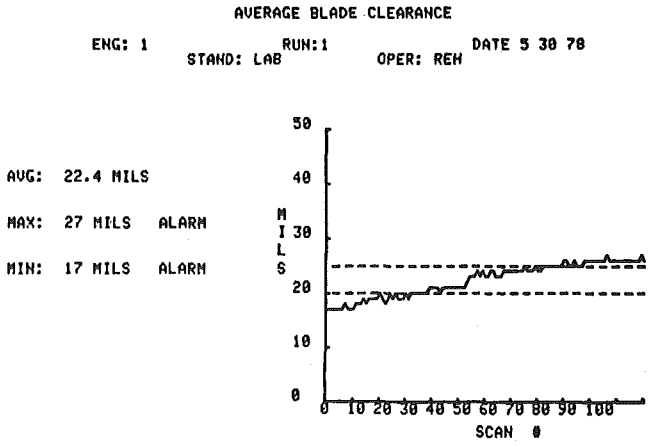

Fig. 5 Graphic terminal display of average blade clearance versus scan number

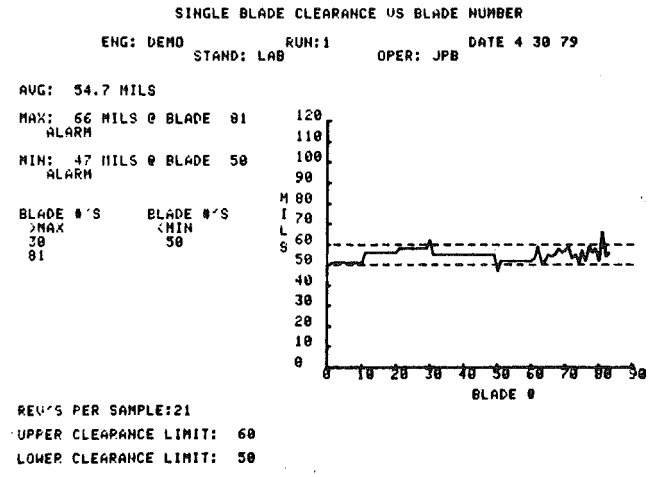

Fig. 6 Graphic terminal display of single blade clearance versus blade number

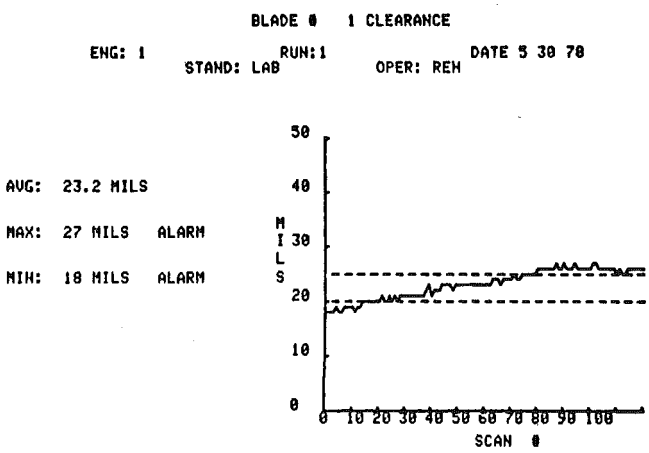

Fig. 7 Graphic terminal display of single blade clearance versus scan number

Each calibration point was set by rotating the micrometer to obtain one diode increment change. The calibration points were plotted as diode site versus micrometer reading. The data were fit to a third order polynomial equation using a least squares deviation method. Two-sigma values show a deviation from best fit of less than 0.025 mm (1 mil).

An upper limit on measurement system resolution was also obtained from the calibration data. Since the system has a nonlinear characteristic, the change in displacement corresponding to one diode site is not uniform. The maximum observed incremental change between diode sites was less than 0.076 mm (3 mil), but 97 percent of the changes were less than 0.05 mm (2 mil). The incremental change for one diode site is twice the resolution since a deviation in displacement equivalent to greater than one half diode site would cause the adjacent site to indicate. Thus the two-sigma value of resolution is less than 0.025 mm (1 mil).

Repeatability data were also recorded for two cycles over the calibration range in increments of 25 diode sites upscale and downscale. Displacements calculated from the diode site using the third order polynomial equation derived previously were compared to measured displacements. The maximum deviation or repeatability was less than 0.06 mm (2 mil).

Dynamic performance of the measurement system was accomplished by using a laboratory simulation of a rotating blade row. An acousto-optic modulator was used to interrupt the laser beam thus producing pulses of light equivalent to a rotating blade row. Rotor speeds up to 60,000 rpm, blade tip speeds up to 610 m/s (2000 ft/s) and blade tip thicknesses down to 0.79 mm (0.031 in.) were simulated. The targets were six blades, two fan, two compressor, and two turbine, all taken out of service with long operating exposure. The clearance was set to 1.27 mm (50.0 mil). The number of revolutions was increased until there was sufficient reflected light for proper signal conditioning. Results of the dynamic tests indicate that no more than 100 revolutions per scan would be required in the worst case and less than 10 in most cases.

Environmental Tests. The environmental evaluation tests subjected the measurement system probe to temperature, pressure, and vibration environments typically encountered in an operating gas turbine engine. The temperature test evaluated the measurement system performance with the probe mounted in a configuration similar to that used in an actual gas turbine installation where adjacent wall temperatures vary from near ambient to 1300 K (1900° F). The test rig basically consisted of a 50 mm dia stainless steel pipe, 150 mm in length, and support hardware. One end of the pipe was inserted into a variable temperature furnace which provided the heat source. At the other end of the pipe, the probe was inserted perpendicular to the pipe axis and through the pipe wall such that the probe tip was flush with the pipe inner wall, thus providing the simulated installation. A hole was provided through the pipe wall opposite the probe to allow for micrometer access. A thermocouple was attached to the pipe inner wall approximately 35 mm from the probe tip center and toward the heat source. The probe was cooled by gaseous nitrogen.

Data were obtained with simulated wall temperatures from approximately 367 to 1300 K. At each temperature a gap of 1.27 mm (50.0 mil) was established by adjusting the micrometer to obtain a zero gap and then adjusting the micrometer to obtain the proper displacement. This procedure minimized any potential errors induced by thermal growth of the test rig.

For the pressure and vibration test, a fixed clearance target adapter was coupled to the probe tip and adjusted to 1.27 mm (50.0 mil). The probe body was then inserted into a pressurization adapter which allowed the probe assembly to be subjected to elevated pressure via the slot opening at the probe tip. In 1 atmosphere increments, the probe was pressurized with gaseous nitrogen from ambient to 30 atm. The measurement system data were taken at each pressure setting. For the vibration test, the probe body was attached to a vibration test shaker by adapter fixtures. These fixtures allowed the probe to be excited along three mutually perpendicular axes, one axis at a time. Along each axis, the probe was subjected to a constant 12.7 mm/s velocity excitation sweep from 50 to 2500 Hz of approximately 10 min duration. Data were obtained during each excitation sweep.

The environmental evaluation tests were designed to test the repeatability of the system under each environmental condition. The repeatability of each test was well within the measurement made during the static calibration, that is, 0.05 mm (2 mil).

Concluding Remarks

A laser-optical measurement system has been described which is designed to measure single blade tip clearances and average blade tip clearances between a rotor and its gas path seal in rotary component rigs and complete engines. The system has a number of innovative features and combine optical, electro-optical, electronic and computer/graphic elements. It is widely applicable for the measurement and display of average and single blade tip clearances in operating rotating machinery over a full range of rotational speeds and a wide variety of blade materials and configurations.

References

1 Drinkuth, W., Alwang, W. G., and House, R., "Laser Proximity Probes for the Measurement of Turbine Blade Tip Running Clearances," *Proceedings of the 20th International Instrumentation Symposium on Advances in Test Measurement, Vol. II, (Instrumentation in the Aerospace Industry)*, Vol. 20, Instrument Society of America, 1974, pp. 133–139.

2 Ford, M. J., et al., "Advanced Optical Blade Tip Clearance Measurement System," FR-10200A, Pratt and Whitney Aircraft Group, West Palm Beach, Fla., 1978. NASA CR-159402, 1978.

A. P. Kurkov
NASA-Lewis Research Center,
Cleveland, OH 44135

Flutter Spectral Measurements Using Stationary Pressure Transducers

Engine-order sampling was used to eliminate the integral harmonics from the flutter spectra corresponding to a case-mounted static pressure transducer. From the optical displacement data it was demonstrated that blade-order sampling of pressure data can yield erroneous results because of the interference caused by blade vibration. Two methods are presented that effectively eliminate this interference and yield the blade-pressure-difference spectra. The phase difference between the differential-pressure and displacement spectra was evaluated.

Introduction

This paper describes a method of analysis that allows one to deduce unsteady forces acting on rotor blades from a pressure measurement made on a casing. To accomplish this, it is necessary to separate the unsteady[1] component of pressure signal from the steady-state component and then transform the unsteady pressure signal from a stationary into a rotating frame of reference. The problem, however, is somewhat more complicated because a blade surface is not only rotating but is also vibrating.

There are two approaches that can be adopted to achieve this objective. Both are based on digital sampling of the data, followed by spectral analysis. One is to concentrate attention on one blade at a time, that is, to sample the data only at the instant a particular blade is under the stationary pressure sensor. The spectral analysis that follows yields the unsteady pressure field associated with a particular blade only. The other approach is to sample pressures from all the blades in succession as they sweep the measurement port in the casing. This approach essentially treats the whole rotor as a system. It is this approach that is adopted here. Its advantage is that the sampling rate is not limited to only once per revolution; consequently, certain vibratory characteristics of the bladed rotor assembly are exhibited that would otherwise be lost.

In addition to the analysis of pressure data, the paper includes the analysis of optical blade-displacements [1, 2]. The method of analysis of displacements is essentially the same as in [2]; however, the method of analysis of pressure data presented here is more general and therefore preferable to that in [2]. The detailed documentation of the test conditions, the flutter boundaries, and the flow conditions in the relative frame of reference is available in [3]. The test point discussed in this report is 125.

In the paper, familiarity with such concepts as the Nyquist frequency and aliasing is assumed. For the reader not familiar with these concepts a number of texts exist [4, 5] where these are discussed. A brief review of the essential features of flutter vibrations is given in Appendix I. A more extensive treatment can be found in [6–8].

[1] The terms unsteady-state and steady-state apply to the rotating frame of reference.

Contributed by the Gas Turbine Division and published in the symposium volume, *Measurement Methods in Rotating Components of Turbomachinery*, ASME, New York, 1980. Manuscript received for publication in the JOURNAL OF ENGINEERING FOR POWER May 22, 1980.

Experimental Measurements

The location of the instrumentation ports for the two types of measurements analyzed in this paper is illustrated in Fig. 1. The blade position in this figure includes incremental changes caused by load and speed that were estimated from the manufacturer's data. Static pressures at other chordwise positions were also available; however, the leading-edge transducer illustrates best the sampling and analysis described in this paper.

The displacement data were recorded on a multichannel direct-record type of tape recorder at 304.8 cm/s (120 in./s). Another FM tape was then generated by replaying the original tape at 7.62 cm/s (30 in./s) and recording the data at 304.8 cm/s (120 in./s). The frequency bandwidths were 2 MHz on the direct-record and 80 kHz on the FM. The direct-record method was used for the original data recording in order to avoid the frequency limitation encountered on the FM recorder. The pressure data, however, were recorded directly on the FM recorder.

Subsequent data processing was performed on a software-based fast Fourier transform (FFT) analyzer equipped with dual magnetic disk drives. The magnetic disks were used for the storage and subse-

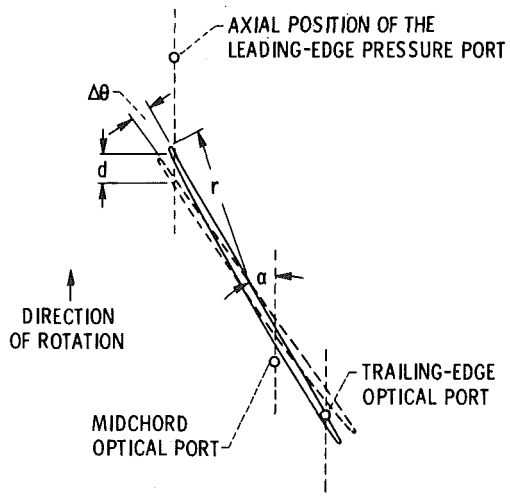

Fig. 1 Location of measurements ports

quent reprocessing of digital data. This capability essentially eliminated the need for the large computer and the central data processing facility that were used in the previous [2] displacement-data analysis. Because of mass storage capability, special sampling techniques could also be used for the pressure data. The effective digitizing rates were 2.09 MHz for the displacement data and 1.31 MHz for the pressure data. These rates were achieved by greatly reducing the speed of the FM tapes on playback.

Analysis of the Displacement Data

As can be seen in Fig. 1, instantaneous blade-tip position measurements were made at two chordwise positions. In addition to these, two reference pulses were recorded, the $1E$ and the $38E$ pulse, which corresponded to the blade passing frequency. These reference signals were generated by two magnetic sensors located opposite the appropriate triggers,which were mounted on the rotor shaft.

In [2] all four channels of data were digitized simultaneously and stored on magnetic tapes. The displacements were obtained by measuring the positions of the trailing-edge pulses relative to the corresponding $38E$ reference pulses. The $1E$ reference pulse provided the orientation in the relative frame of reference. Before the spectral analysis the displacements were referenced to their respective averages in order to eliminate fluctuations resulting from blade-spacing nonuniformities.

In this paper the data were digitized by using the FFT analyzer, which was limited to two channels. Digitized were any two of the three channels comprising the two optical data channels and the $38E$ reference pulse. The $1E$ reference pulse was used to start the digitization and was not itself digitized. Note that either reference pulse could be used to calculate the displacements. The $38E$ reference pulse has been used because of its better signal quality. In other respects the analysis of optical data was the same as in [2].

Figures 2 and 3 present the overall spectra corresponding to the trailing-edge sensor versus the $38E$ signal (relative to which the displacements were computed), the midchord sensor versus the $38E$ signal, and the trailing-edge sensor versus the midchord sensor. A special procedure was followed when these data were digitized in order to assure that the data acquisition was begun with the identical $1E$ reference pulse. This procedure is discussed in Appendix 1 in conjunction with the phasing of pressure and displacement spectra. Because the blades were sampled successively during each revolution, the number of samples per revolution was 38, and the highest detectable frequency was therefore $19E$. The number of data points used in the spectral analysis was 2048, which corresponded to approximately 53.9 revolutions. The flutter frequency obtained independently from strain-gage data was 8.45 E. (All available strain-gage data exhibited the same flutter frequency.)

In Fig. 2, the frequencies corresponding to major peaks are nonintegral by the same amount as the flutter frequency (i.e., 0.45 E). The nodal diameters corresponding to this fraction can be obtained by subtracting the flutter frequency, in engine orders, from each frequency associated with this fraction. The possible range for nodal diameters so obtained is -8 to 10. Beyond this range the nodal diameters correspond to aliased frequencies, which are associated with the fraction 0.55 E. The spectral peaks corresponding to these frequencies are very small.

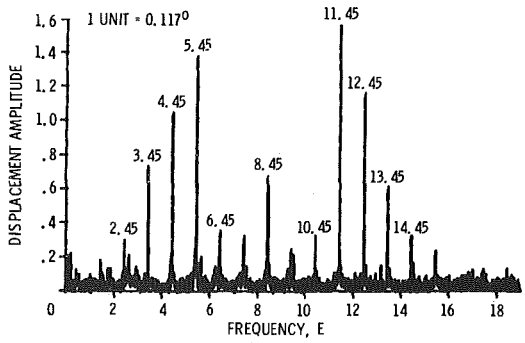

Fig. 2 Displacement-amplitude spectrum, trailing-edge sensor, 1 unit = 1/(16475 *E*)

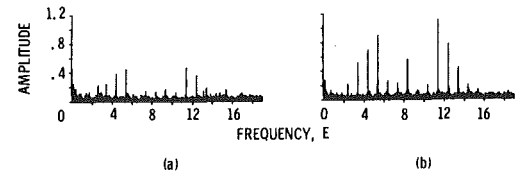

Fig. 3 Displacement spectra corresponding to the midchord (*a*), and the trailing-edge versus midchord sensor (*b*), 1 unit = 1/(16475 *E*)

Table 1 Phase angles, displacement spectra

Figure	Frequency (E)						
	3.45	4.45	5.45	8.45	11.45	12.45	13.45
	Phase angle, deg						
Fig. 2	−65	−61	−57	48	−68	−68	−65
Fig. 3(a)	−56	−54	−49	77	−83	−79	−86
Fig. 3(b)	−66	−64	−59	46	−63	−65	−56

The phase angles corresponding to major peaks (i.e., corresponding to dominant frequency lines associated with major peaks) in Figs. 2 and 3 are presented in Table 1. They were determined by neglecting the slight misalignment of the optical ports relative to the blade chord (Fig. 1). If the trailing-edge sensor were chosen as the base, this correction would amount to adding 11.7 deg to the phase corresponding to the midchord sensor. Because the amplitudes corresponding to this sensor are considerably smaller than those for the trailing-edge sensor, the correction for the phase corresponding to Fig. 3(b), in the last row of Table 1, would be considerably smaller.

Because the phase angles corresponding to a given frequency in Table 1 are close to each other and the spectra in Figs. 2 and 3 are nearly similar, the blade motion can be described as a rotation about a single point. From Figs. 2 and 3, the approximation

$$d = D \times U \sim \frac{r\Delta\theta}{\sin\alpha} \tag{1}$$

and the geometry in Fig. 1, the rotational axis was located at about 44 percent of chord from the leading edge. It is also possible to express the units in Fig. 2 in terms of angular deformation. As noted in this figure one unit corresponds to 0.117 deg.

Nomenclature

A = amplitude
D = displacement in time units or in $1E$ periods, E^{-1}
d = displacement (Fig. 1), $d = D \times U$, cm
E = engine order
j = imaginary unit
N = nodal diameter
n = number of points for spectral analysis
P = unsteady pressure
$\overline{P}$ = steady-state pressure
r = radial coordinate (Fig. 1)
T = sampling period
t = time
U = wheel speed
α = stagger angle (Fig. 1)
ϵ = fraction defined in equation (9)
$\Delta\theta$ = angular deformation (Fig. 1)
Φ = angular coordinate in rotating frame of reference
$\Phi_1 = \Phi$ for blade 1
ϕ = phase angle, equation (2)
ψ = phase angle, equations (7) and (8)
ω = circular frequency

Subscripts

f = flutter
i = corresponds to i^{th} nodal diameter
L = left
P = pressure
R = right
r = rotational

Superscripts

D = displacement
P = pressure

As in [2], the individual blade spectra can be obtained by arranging sampled data in groups so that each group includes successive samples from a particular blade only. Because the sampling for each blade is $1E$, the resulting spectra are folded into the range 0 to $1/2\ E$. Figure 4 presents the flutter amplitudes and phase angles for each blade as derived from the trailing-edge sensor versus $38E$ pulse data corresponding to 64 revolutions. The phase angles were referenced to blade 1 phase angle.

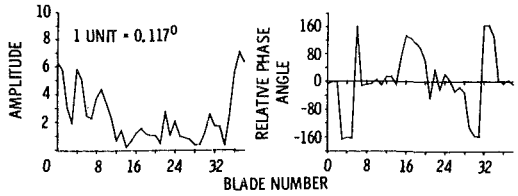

Fig. 4 Displacement amplitude and phase distribution

Analysis of the Pressure Data

Engine-Order Sampling. The main advantage of engine-order sampling is that the steady-state part of the pressure signal can be eliminated so that only the nonintegral, flutter-related spectral peaks remain.

The pressure data discussed in this paper were derived from a single portion of the tape, which was digitized and stored on two magnetic disks. Two channels of data were digitized: the pressure signal from the leading-edge transducer, and the $1E$ reference signal. A total of 66 engine revolutions were stored on disks, and on the average the number of points per channel per revolution was 10 295. This provided sufficient accuracy (i.e., $1/[10\ 295E]$) to illustrate the different sampling methods presented in this paper.

For the spectral analysis presented in this section (Fig. 5) the pressure data were sampled 512 times per revolution, and the total number of revolution was 16. This gave a total of 8192 points, which was the maximum number that could be processed on the FFT analyzer. The nonfluctuating part of the pressure signal was removed by computing the average pressure (over 16 revolutions) for each of the 512 points and then subtracting this average from the corresponding instantaneous pressures.

Although there were only 16 revolutions included in the computation of each average, the removal of the engine-order peaks was fairly effective. The most visible $38E$ peak was reduced in amplitude by about a factor of 34. The aliasing frequency for the data presented in Fig. 5 was 256; however, the contribution to the power spectrum beyond $128E$ (Fig. 5(b)) was very small. This insured against aliasing in the range 0 to $128E$ (Fig. 5(a)).

There are two nonintegral frequency families in Fig. 5 associated with the fractions 0.45 E and 0.55 E. The former is associated with nodal diameters greater than or equal to -8, and the latter with nodal diameters less than -8. This can be seen by expressing the spectral peaks in Fig. 5 as [2]

$$A_i \cos [\omega_r(N_i + \omega_f/\omega_r)t + \phi_i] \tag{2}$$

Because only positive frequencies can be detected by spectral analysis, for $N_i < -\omega_f/\omega_r$, this expression takes the form

$$A_i \cos [\omega_r(-N_i - \omega_f/\omega_r)t - \phi_i] \tag{3}$$

It is seen now that the flutter frequency expressed in engine orders is being subtracted from the positive whole number $-N_i$, yielding the fraction 0.55 E. Note that the phase angle is reflected about the horizontal axis.

It can be shown that if all frequencies corresponding to the significant peaks in Fig. 5 were folded about the frequency multiples of $19E$, as many times as necessary, so that they fall in the range 0 to $19E$, only the frequencies that are also present in Fig. 2 would remain. If pressure transducers were mounted on each blade, the nodal diameters corresponding to these frequencies would be the only ones detected, because in this case the measurement is spatially discrete. It follows therefore that there are no new nodal diameters or modes resulting from the spectral analysis of the pressure data. The apparent nodal diameters seen by the stationary pressure transducers are the result of a complex pressure distribution in the blade channels, the description of which requires a large number of spatial harmonics.

Although spectral results such as those shown in Fig. 5 are illustrative, they are not very convenient for quantitative analysis. To obtain the nodal diameters, it is necessary to fold frequencies in Fig. 5; and to transform the results into a rotating frame of reference, it is necessary to perform superposition [2]. Both require knowledge of

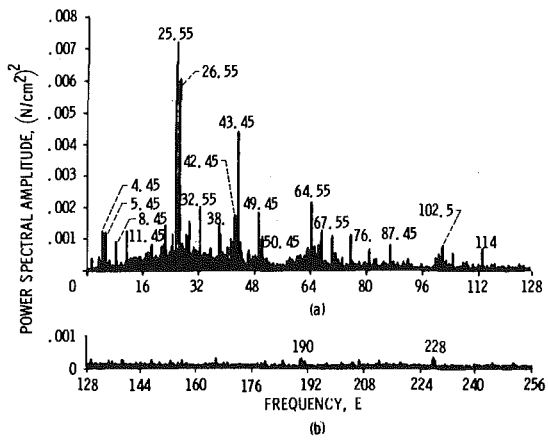

Fig. 5 Power spectrum of the leading-edge pressure transducer signal

the phase angles for all significant peaks in this figure. In view of their large number and wide frequency spread, this is difficult to accomplish. The wide frequency spread also implies a limited accuracy because of the memory limitation of the spectral analyzer.

However, spectral results such as those shown in Fig. 5 can be used for flutter detection. In this case the engine-order sampling could be performed directly by using an angle clock (or angle encoder) [1] as the external sampler. The angle clock is essentially a frequency multiplier that can generate an arbitrary number of pulses per revolution from an input $1E$ pulse. The accuracy of this device, which is now commercially available, is comparable to that achieved presently by using analog tape and peripheral digital storage devices. Removing the nonfluctuating part of the pressure signal essentially involves computing the average, which does not entail any appreciable time delay.

An additional advantage of engine-order sampling is that for the undersampled data the folding occurs about either an integral frequency or an integral frequency plus $1/2\ E$, depending on whether the number of points per revolution is even or odd. Therefore for an even number of points per revolution there would be only two fractions associated with a flutter frequency even for the aliased sampling. For flutter detection a more important consideration than aliasing is that the total number of revolutions included in the sample be large, which is essential for efficient removal of engine-order peaks. As shown later it is also desirable that the number of samples per revolution not be a multiple of the number of rotor blades.

Blade-Passage Sampling. This section presents an alternative method for sampling and analyzing the pressure data. The sampling is performed once per blade passage at the same position relative to the steady-state pressure distribution. Therefore the steady-state distribution had to be determined before the sampling was performed. This was achieved by separating the data recorded on disks into records covering one revolution, as determined from the reference $1E$ pulse data. The points within each revolution were then ordered relative to the start of the revolution, and the corresponding points in each record were averaged over a total number of revolutions. The resulting steady-state distribution consisted of 10,295 points, each representing the average of 66 points. Figure 6 illustrates a typical distribution for a blade passage with the right-hand gradient region enlarged. In this figure the horizontal axis is given in terms of the number of digitized points relative to an arbitrary origin. The basic unit of time is therefore $1/(10\ 295E)$. The marked points in Fig. 6

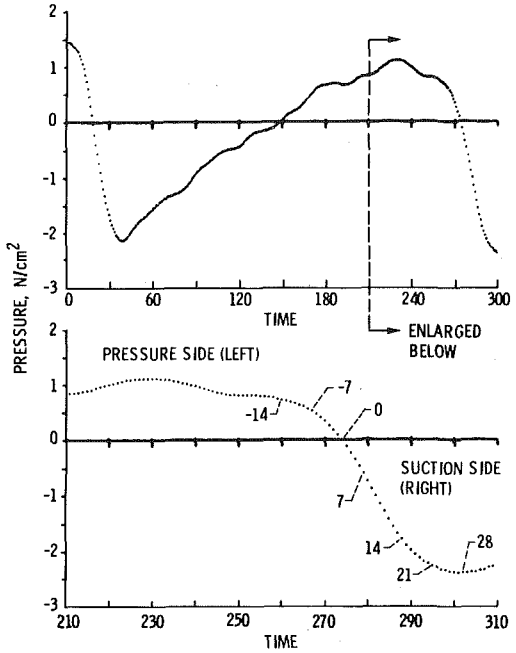

Fig. 6 Steady-state pressure distribution; 1 unit = 1/(10295 E)

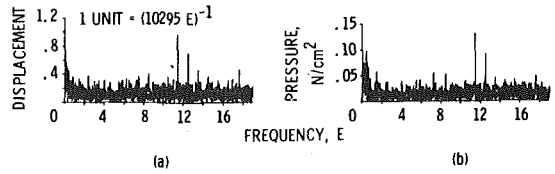

Fig. 7 Apparent displacement and pressure spectra as derived from pressure data by sampling in the steep gradient region

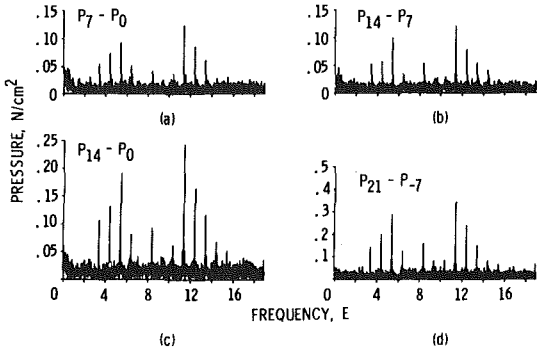

Fig. 8 Pressure-difference spectra, gradient sampling

subdivide the gradient region into equal parts, each of which is seven spaces wide. These points represent the locations relative to the zero crossing, where the pressure was sampled. The zero crossings were used as datum points. They were determined in advance for each blade passage and then stored on a disk.

One important consideration for the sampling in the pressure-gradient region is the blade motion itself. In the units of Fig. 6 the blade displacement was about 5. Motion of this extent introduces a fluctuating pressure in addition to the fluctuations that would be recorded if the blades were not vibrating. It is possible to demonstrate this effect indirectly by showing that the vibratory motion—as derived from the pressure data in the gradient region—does not compare well with the vibratory motion derived from the optical displacement data.

The blade vibration is reflected in the pressure data as a periodic displacement of the gradient portion of the pressure distribution relative to its equilibrium or steady-state distribution. The pressure data can therefore be processed quite similarly to the optical pulse data, that is, by tracking the position of a point corresponding to some constant pressure level in the steep-gradient region of pressure distribution (Fig. 6). The spectral results obtained in such a way are presented in Fig. 7(a). If there were no interference from the pressure fluctuations, these results would be similar to the optical displacement spectrum in Fig. 2. The fact that they are different indicates that there is interference from the pressure fluctuations. Superposition of two signals for an i^{th} nodal diameter can be expressed as

$$A_i{}^D \cos[(\omega_f + \omega_r N_i)t + \psi_i{}^D] + A_i{}^P \left(\frac{d\overline{P}}{dt}\right)^{-1} \cos[(\omega_f + \omega_r N_i)t + \psi_i{}^P] \quad (4)$$

where the superscripts D and P denote, respectively, displacements and pressures and $d\overline{P}/dt$ denotes the steady-state pressure gradient in the steep-gradient region.

The extraction of apparent displacements from pressure data was specifically performed to illustrate the displacement signal contamination due to pressure fluctuations. The sampling was performed at a constant pressure level corresponding to point 7 in Fig. 6. More conventional results in Fig. 7(b), however, were obtained by reversing this process, that is, by sampling pressures at the position relative to the equilibrium zero crossing defined by point 7. Results in these two figures are quite similar. Both represent the summation of two signals: one derived from the pressure fluctuation, and the other from the blade motion, as shown in equation (4). The corresponding expression for Fig. 7(b) would differ only by a multiplicative factor $d\overline{P}/dt$. This expression would illustrate contamination of pressure fluctuations due to blade vibratory motion. The steady-state part of pressure was subtracted from the data for Fig. 7(b). This was also done for all subsequent pressure and pressure-difference spectra.

Table 2 Phase angles, pressure-difference spectra

Figure	Frequency (E)						
	3.45	4.45	5.45	8.45	11.45	12.45	13.45
	Phase angle, deg						
Fig. 8(a)	−144	133	43	−132	−161	98	28
Fig. 8(b)	−144	129	59	−134	−161	101	38
Fig. 8(c)	−144	131	51	−133	−161	99	33
Fig. 8(d)	−149	127	47	−132	−163	96	36
Fig. 10(c)	−142	131	48	−136	−171	90	27
Fig. 11	−133	128	48	−136	−164	95	35

Constant-Gradient Sampling. One solution to this problem is to form a pressure difference in the region where the steady-state pressure gradient is approximately constant. Because the blade displacement is the same on both sides of the blade and the gradient is approximately constant, the contribution to the pressure difference from the blade motion is nearly cancelled.

To illustrate this, pressures were sampled at indicated points in Fig. 6 and then the following differences were formed: $P_7 - P_0$, $P_{14} - P_7$, $P_{14} - P_0$, and $P_{21} - P_{-7}$. The spectra corresponding to these differences are given in Fig. 8, and phase angles are presented in Table 2. The number of sampled data points used for spectral analysis was 2048. Because the pressures in each of these differences were not sampled at the same time, a more exact procedure would be to obtain transforms for each point individually, apply the appropriate correction to the phase angle of one point, and then perform the subtraction in the frequency domain. However, the maximum correction to the phase angle for the results presented in Fig. 8 would be 8 deg. Therefore the results obtained by using the more exact procedure would not differ appreciably from those presented here.

The pressure-difference spectra in Fig. 8 are all qualitatively similar and also similar to the displacement spectrum in Fig. 2. In addition, comparing the amplitudes of corresponding peaks in Fig. 8 indicates that in the approximately constant-gradient region between points 0 and 14 (Fig. 6) the amplitudes are approximately proportional to the number of intervals between the pair of points included in the difference. If this interval is maintained constant, the exact position of the pair of points does not seem to be important. Comparing phase

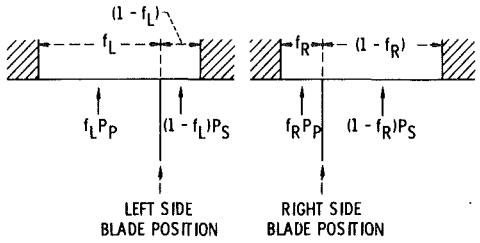

Fig. 9 Smearing effect due to the finite dimensions of the pressure port

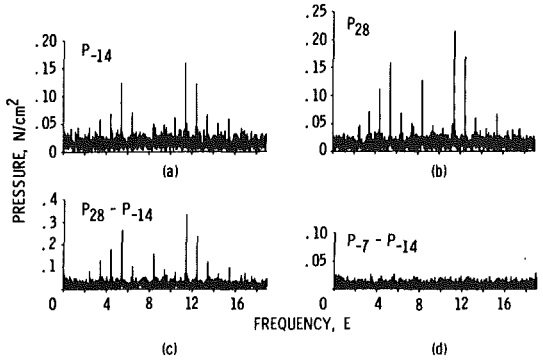

Fig. 10 Spectral results based on sampling outside of the steep-gradient region

angles at a given frequency in Table 2 indicates that they are nearly constant.

These observations can be explained qualitatively on the basis of physical arguments. Because it takes a finite time to traverse the static pressure port and because of the finite blade thickness in the direction of the wheel speed, it is expected that the pressure difference across the blade will be smeared over approximately 10 points. This corresponds to about half the width of the steep-gradient region in Fig. 6. It appears therefore that the smearing of the pressure difference is in part due to dimensional effects.

Considering first the smearing due to static pressure port dimensions only, one can treat the blade as a discontinuity, as shown in Fig. 9. The sketch on the left corresponds to the left-point gradient sampling and that on the right to the right-point gradient sampling (Fig. 6). The instantaneous blade position is defined in terms of the area fraction f, where $f = 0$ corresponds to the position of the blade when it is aligned with the left edge of the port. Subscripts L and R denote left and right positions, and subscripts P and S denote the blade pressure and suction sides. The pressure difference between the right and left pressures is by superposition

$$P_R - P_L = f_R P_P + (1 - f_R)P_S - [f_L P_P + (1 - f_L)P_S]$$

or

$$P_R - P_L = (f_L - f_R)(P_S - P_P) \tag{5}$$

Since all pressure signals possess amplitude and phase, and each fraction f is real, it follows that the pressure difference between the two points in the constant-gradient region has the same phase as the pressure difference between the suction and pressure sides. It can also be seen that the proportionality of the amplitude and the distance between the two points should hold approximately in the central region, where the fraction f is approximately proportional to the blade position.

By using two approximations an explanation could also be offered for the case of finite blade thickness and negligible pressure-port dimensions. The first is the quasi-steady-state assumption, based on the fact that the blade thickness is small compared with the wavelength corresponding to one flutter cycle. The second is the linearity of pressure variation in the tip-clearance region over the distance corresponding to the blade thickness.

Zero-Gradient Sampling. Because interference with pressure fluctuations due to blade motion is proportional to the steady-state pressure gradient, an alternative way of eliminating this interference is to sample in the region where pressure gradients are small, or ideally, zero. For example, Fig. 10(a) presents the spectrum for point −14 (Fig. 6), which is still fairly close to the steep-gradient region of the pressure distribution. This spectrum is qualitatively much closer to the displacement spectrum in Fig. 2 than is the one in Fig. 7(b), which was obtained by sampling the steep-gradient portion of the blade passage.

To obtain the pressure difference across the blade, one also has to select a point in the zero-gradient region on the suction side of the blade. Because of considerable curvature in the steady-state pressure distribution in this region and the blade-to-blade differences, this selection is more difficult. Based on the results obtained so far, one would expect that the spectrum for this point should also be qualitatively similar to the displacement spectrum in Fig. 2. It was found that this condition is reasonably satisfied for point 28 (Fig. 6). The spectrum for this point is presented in Fig. 10(b), the pressure difference spectrum corresponding to points 28 and −14 in Fig. 10(c), and its phase in Table 2. The spectral amplitude and phase for the pressure difference $P_{28} - P_{-14}$ are close to the respective values obtained for $P_{21} - P_{-7}$.

Although it has not been stated explicitly thus far, the underlying assumption for obtaining a valid pressure difference across the blade is that the pressure variation over an interval corresponding to the distance between the two points selected for computation of the difference should be small, except when crossing the blade. One way to check this assumption is to form a pressure difference in the approximately flat region to the left of the zero crossing in Fig. 6 (e.g., $P_{-7} - P_{-14}$). It is not likely that these two points will bracket the blade, and therefore amplitudes should be much smaller than a difference involving the same number of points in the gradient region. This is substantiated by comparing results in Figs. 10(d), 8(a), and 8(b), which correspond, respectively, to $P_{-7} - P_{-14}$, $P_7 - P_0$, and $P_{14} - P_7$ difference.

Smearing Effects Due to Blade Motion. A previous section examined the pressure-difference smearing due to the finite dimensions of the transducer and the blade. However, even in the absence of dimensional effects, some smearing can also occur in the gradient region as a result of blade motion. Because the two sampling positions for the pressure-difference spectra were selected on the basis of the average pressure distribution, and because of blade vibratory motion, it is sometimes possible to have both pressure samples forming a difference on the same side of the blade. This would tend to reduce the magnitude of the pressure difference.

To simulate this effect, two data sets are used that are associated, respectively, with the spectra in Figs. 10(d) and 8(d). The first set, corresponding to Fig. 10(d), is representative of the pressure-difference data when both pressures are on the same side of the blade; and the second, corresponding to Fig. 8(d), is representative of the pressure-difference data when the two pressures forming the difference are on opposite sides of the blade. A third data set was then created by random sampling of the first data set and substitution of the sampled values into corresponding points in the second set. Only points that had not been selected previously were substituted in the second set. In the particular case considered, the third data set consisted of 1024 points from the first set and 1024 points from the second set. Spectral amplitudes for these data are presented in Fig. 11, and phase angles in Table 1. It can be seen that the spectral peaks are approximately proportional to the number of points from the data set corresponding to Fig. 8(d) and that phase angles agree fairly well with other corresponding phase angles in Table 1. Considering the magnitude of peaks in Fig. 11, one can associate this spectrum with the one in Fig. 8(c) that corresponds to the pressure difference $P_{14} - P_0$.

Relative Phase of Pressure Difference

Correlation of differential pressure $P_{14} - P_0$ and displacement spectra is given in detail in Appendix II. The phase difference between the two spectra reduced to the same instant of time and the same

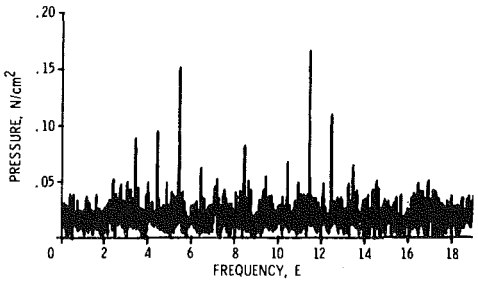

Fig. 11 Pressure spectrum derived from $P_{21} - P_{-7}$ and $P_{-7} - P_{-14}$ data sets by random sampling

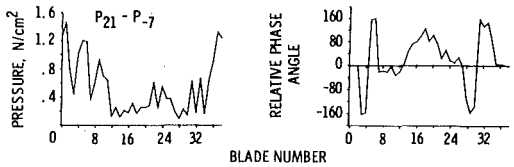

Fig. 12 Differential-pressure amplitude and phase distribution

reference blade is given in Table 3. Because pressure leads displacement, all modes in this table are unstable.

Note that precise determination of the moment coefficient and the work per cycle would require a repeated application of the methods outlined in this paper at the remaining chordwise locations. However, because the unsteady force on the blade during stall flutter is concentrated near the leading edge [9, 10], the conclusion regarding the stability of different modes reached in this paper is not expected to change by this extension.

Discussion of Results

In reviewing the different methods for analyzing pressure data presented in this paper, note that basic to all is engine-order sampling followed by removal of the steady-state part of the pressure signal at each sampled point. If pressure signals are processed mainly for flutter detection, as already mentioned, it is desirable that the number of samples per revolution not be an integral multiple of the number of blades. This assures that pressures at different relative positions in the blade passage are sampled so that the possibility of sampling only in a region where the unsteady pressure signal is small, or perhaps not even detectable, is eliminated. For example, sampling once per blade passage at a point located at 110 intervals relative to the zero crossing (Fig. 6) results in a spectrum with a 11.45 E peak reduced by a factor of 4.6 and a 5.45 E peak reduced by a factor of 2.3 relative to the corresponding peaks in Fig. 10(b).

Blade-order sampling is therefore better suited for postrun data analysis when the precise blade-passage position of the sampled point can be controlled and possible interference due to the steady-state pressure gradient taken into account. Two methods are available to accomplish this: constant-gradient pressure-difference sampling, and zero-gradient sampling. The former method can only provide pressure-difference spectra; the latter also yields the pressure spectra close to the blade surfaces. In general, the applicability of each method will depend on the character of the steady-state distribution. In the particular case considered the constant-gradient method appears to be easier to apply. This method yields correct phase results, and the amplitudes are attenuated approximately as the ratio of the distance between the two points to the distance corresponding to the full extent of the gradient region.

In computing the unsteady work per cycle and interference due to the blade motion is of no consequence since it is either in or out of phase with the displacement and thus does not contribute to the work integrated over a flutter cycle.

The analysis of pressure data has been given thus far in terms of the overall spectra. An analogous procedure would be to use the individual blade spectra, as done in Fig. 4, for the displacements. Figure 12, for example, illustrates such results for the pressure difference P_{21} $- P_{-7}$. Such results were also obtained for all points in Fig. 6 and for all the differential pressures associated with these points. However, the overall spectra, which exhibit system characteristics, were found to be more convenient to use for the analysis. Results such as those in Fig. 12 lead to a discussion of the individual blade characteristics, which appear to be less consistent than the systems as a whole.

Table 3 Differential-pressure phase relative to displacement phase

ΔP	Nodal Diameter						
	−5	−4	−3	0	3	4	5
	Phase angle, deg						
$P_{14} - P_0$	7	11	14	25	53	24	51

Concluding Remarks

An analysis procedure based on engine-order sampling was presented that effectively eliminates the engine harmonics from the overall spectra corresponding to a stationary pressure transducer. It was shown how this procedure can be implemented for on-line flutter detection.

Quantitative spectral analyses of pressure data were performed that were based on blade-order sampling. Optical displacement spectra were used to demonstrate the interference of blade motion with the pressure signal in the steep-gradient portion of the blade passage. Two methods were outlined that yield the blade-pressure-difference spectra and remove the contribution due to blade motion.

Phasing of the blade differential-pressure and displacement spectra at the leading edge indicated that pressure leads displacement for the seven most significant nodal-diameter modes.

References

1 Nieberding, W. C., and Pollack, J. L., "Optical Detection of Blade Flutter," ASME Paper No. 77-GT-66, Mar. 1977.

2 Kurkov, A., and Dicus, J., "Synthesis of Blade Flutter Vibratory Patterns Using Stationary Transducers," ASME Paper No. 78-GT-160, Apr. 1978.

3 Jeffers, J. D., May, A., and Deskin, W. J., "Evaluation of a Technique for Predicting Stall Flutter in Turbine Engines," PWA-FR-9620, Pratt & Whitney Aircraft, West Palm Beach, Fla., Feb. 1978. (NASA CR-135423)

4 Stearns, S. D., *Digital Signal Analysis,* Hayden, Rochelle Park, N.J., 1975.

5 Bendat, J. S., and Piersol, A. G., *Random Data: Analysis and Measurement Procedures,* Wiley-Interscience, New York, N.Y., 1971.

6 Carta, F. O., "Coupled Blade-Disk-Shroud Flutter Instabilities in Turbojet Engine Rotors," ASME JOURNAL OF ENGINEERING FOR POWER, Vol. 89, July 1967, pp. 419–426.

7 Mikolajczak, A. A., et al., "Advances in Fan and Compressor Blade Flutter Analysis and Predictions," *Journal of Aircraft,* Vol. 12, No. 4, Apr. 1975, pp. 325–332.

8 Whitehead, D. S., "Torsional Flutter of Unstalled Cascade Blades at Zero Deflection," Reports and Memoranda No. 3429, Aeronautical Research Council, Great Britain, 1966.

9 Carta, F. O., and St. Hilaire, A. L., "Effect of Interblade Phase Angle and Incidence Angle on Cascade Pitching Stability," ASME Paper No. 79-GT-153, Mar. 1979.

10 Stargardter, H., "Subsonic Transonic Stall Flutter Study," Pratt & Whitney Aircraft, East Hartford, Conn., NASA Contract NAS3-20606.

11 Singleton, R. C., "On Computing the Fast Fourier Transform," *Comm. ACM,* Vol. 10, No. 10, Oct. 1967, pp. 647–654.

APPENDIX I

Flutter Vibrations

Rotor blades in flutter, in general, vibrate with some phase lag between the blades. In a rotating frame of reference one can therefore describe rotor flutter by a wave [2].

$$A \cos (\omega_f t - \Phi N + \phi)$$

where Φ is the angular coordinate, positive in the direction of rotation, and ϕ is the phase angle. If there are 38 blades on the rotor, by varying Φ in the increments of $\Delta\Phi = 2\pi/38$, one can locate all the blades. The interblade phase angle is then $\Delta\Phi N$. Since interblade phase angle can vary only between 0 and 2π, $1 \leq N \leq 38$. N is commonly referred to as the nodal diameter. Each N defines a particular aerodynamic mode

[8]. In a general case of mistuned [8] flutter, several aerodynamic modes are present at the same time so that one must sum contributions from all modes

$$\sum_{i=1}^{38} A_i \cos(\omega_f t - \Phi N_i + \phi_i)$$

It follows from this expression that each wave corresponding to a given N_i rotates relative to the rotor with angular velocity ω_f/N_i. It is in the direction of rotation (forward) for $N_i > 0$, and opposite to the direction of rotation (backward) for $N_i < 0$.

From the point of view of a stationary sensor Φ is not arbitrary, but $\Phi = -\omega_r t$. Thus the signal received by a stationary sensor becomes

$$\sum_{i=1}^{38} A_i \cos[(\omega_f + \omega_r N_i)t + \phi_i]$$

Therefore each aerodynamic mode will be detected as a distinct frequency peak in the spectrum of a stationary sensor.

APPENDIX II

Correlation of Pressure and Displacements

To correlate the measurements recorded on different tapes it was essential to be able to initialize digitization at exactly the same time. This was achieved by using a time code reader that produced a pulse at the instant the continuously read time from the tape matched the preselected time dialed on the time code reader. The data acquisition was begun at the first $1E$ reference pulse following this instant. The coincidence condition was detected under software control, and the $1E$ reference pulse was used as the external trigger. The suggestion for the use of the time coder reader and its implementation in this procedure was made by Jones of NASA Lewis.

Because the time code for the displacement data was not available on the original direct-record tape, it was not possible to correlate directly the pressure and displacement data. (An arbitrary referenced time code, however, was recorded on the FM copy of the displacement data tape, and this enabled repeated replay of this tape at the identical $1E$ reference pulse.) Therefore, to correlate the displacement and pressure data, it was necessary to use the strain-gage data for which the time code was availabe. This was accomplished by using a procedure that is best illustrated by reviewing the resulting expressions for the correlated displacement and pressure signals. For an arbitrary i^{th} nodal diameter these expressions are

$$P, D = \sum_{i=1}^{38} A_i^{P,D} \exp j[\omega_f t - (\Phi - \Phi_1)N_i + \psi_i^{P,D}] \tag{6}$$

where P and D denote pressure and displacement, respectively. Reference time $t = 0$ corresponds to the instant a particular $1E$ reference pulse reaches a predetermined level; and, as indicated, the reference angle corresponds to blade 1 angular positon. The phae angles ψ_i for the displacements and pressures are given, respectively, as

$$\psi_i^D = \phi_i^D + \frac{37}{38} N_i 2\pi - \frac{0.455}{38} 2\pi \frac{\omega_f}{\omega_r} + \phi_1^S - \tan^{-1} \frac{\sum A_i^D \sin\left(\phi_i^D + \frac{37}{38} N_i 2\pi - \frac{0.455}{38} 2\pi \frac{\omega_f}{\omega_r}\right)}{\sum A_i^D \cos\left(\phi_i^D + \frac{37}{38} N_i 2\pi - \frac{0.455}{38} 2\pi \frac{\omega_f}{\omega_r}\right)} \tag{7}$$

$$\psi_i^P = \phi_i^P + \frac{9}{38} N_i 2\pi - \frac{1}{38} 2\pi \frac{\omega_f}{\omega_r} \tag{8}$$

In these expressions ϕ_i's are the i^{th} nodal-diameter phase angles measured relative to the first point in the input data set for spectral analysis. For the displacement data this point corresponded to the first blade that appeared under the sensor following the $1E$ trigger, and for the pressure data it corresponded to the second blade after the $1E$ trigger. (The latter choice was necessary because the first blade under the sensor was slightly past the selected triggering level at the time of $1E$ trigger.) The second terms in these expressions account for the position of blade 1 relative to the reference blades for ϕ_i's, and the third terms account for the time delay between the occurrence of the $1E$ pulse and the instant appropriate reference blades are under the respective sensors. The fourth term in the expression for ψ_i^D, ϕ_1^S, is the phase angle for the blade 1 above-shroud-trailing-edge gage (ASTE gage [3]) relative to the $1E$ trigger, and the last term accounts for the arbitrary time reference for the displacement data. This term represents the phase of blade 1 at the time of $1E$ trigger. It was actually evaluated from the aliased $1/2\ E$ spectrum associated with this blade, and not from the given expression.

The strain-gage phase ϕ_1^S was determined by interpolation between the frequency lines, as in [2]. However, a simpler and more accurate approximation was used for fraction ϵ, which defines the true frequency relative to a neighboring frequency line. This approximation was derived by Braun of NASA Lewis. If ω_f is the true frequency and the two most significant amplitudes are A_1 and A_2 corresponding to frequencies ω_1 and ω_2, and $\omega_1 < \omega_f < \omega_2$, then

$$\epsilon_1 = \frac{(\omega_f - \omega_1)nT}{2\pi} \sim \frac{A_2}{A_1 + A_2} \tag{9}$$

The phase angle corresponding to ω_f is equal to the phase angle at ω_1 minus $\epsilon_1\pi(n-1)/n \sim \epsilon_1\pi$. In practice, the accuracy with which ϵ_1 can be determined is usually limited by the signal-to-noise ratio. An estimate of the accuracy can therefore be made by using this ratio. Another estimate of the accuracy can be obtained by varying parameters in the spectral analysis. When sampling in the approximate range 8 to 32 points per cycle, a spread in the phase angle ϕ_1^S of about 10 deg was encountered. It is therefore estimated that this phase angle is accurate within 5 deg.

Because of the availability of the Singleton FFT-algorithm [11], the spectral analysis of the displacement and pressure data discussed in this section was performed on a large computer. This algorithm does not require that the number of points for spectral analysis be a power of 2. It is possible therefore to select an input data block for the spectral analysis that consists of an integral number of revolutions and has approximately an integral number of cycles. This results in a uniform nonintegrality of flutter peaks and minimizes the fraction ϵ_1 (computed relative to the frequency line corresponding to the dominant peak).

For the displacement data the number of data points was 2470, which corresponds to 65 revolutions and contains 549.1 flutter cycles (associated with $N_i = 0$). For the pressure data the number of data points corresponds to 63 revolutions, and the number of flutter cycles is 523.9. The choice of a different number of revolutions for the pressure data was governed by a slight shift in the flutter frequency expressed in engine orders.

The phase angles corresponding to different peaks in the respective spectra were obtained by using an effective fraction ϵ. For the displacement phase angles the effective fraction was obtained by averaging the ϵ's corresponding to the six most significant peaks; and for the pressure phase angles it was obtained by averaging the ϵ's corresponding to the two most significant peaks. The phase angles were estimated to be accurate within about ± 10 deg.

Temperature and Pressure Measurement Techniques for an Advanced Turbine Test Facility

F. G. Pollack
R. P. Cochran
NASA-Lewis Research Center
Cleveland, Oh

A high pressure (4×10^6 N/m^2), high-temperature (2400 K) turbine test facility is being constructed at the NASA Lewis Research Center for use in turbine cooling research. Several recently developed temperature and pressure measuring techniques will be used in this facility. This paper will briefly describe these measurement techniques, their status, previous applications and some results.

Noncontact surface temperature measurements will be made by optical methods. Radiation pyrometry principles combined with photoelectric scanning will be used for rotating components and infrared photography for stationary components. Contact (direct) temperature and pressure measurements on rotating components will be handled with an 80-channel rotary data package which mounts on and rotates with the turbine shaft at speeds up to 17,500 rpm. The data channels are time-division multiplexed and converted to digital words in the data package. A rotary transformer couples power and digital data to and from the shaft.

Introduction

About ten years ago, a program was initiated at the NASA-Lewis Research Center to improve techniques for measuring temperatures and pressures on gas turbine components associated with turbine cooling research. Means of obtaining experimental measurements of temperatures and pressures under actual or simulated engine environments, particularly on rotating components, was not well developed at that time. Concentrated efforts in this program and from other sources have greatly advanced instrumentation technology for turbomachinery components. This paper will describe the present status of three measurement systems under the NASA-Lewis program. Two are optical systems for measuring metal surface temperatures on stationary vanes and rotating blades in the turbine stage; the third is a rotary data package for transmitting thermocouple and pressure transducer signals from a rotating shaft to a stationary readout. Previous reports on interim or prototype versions of these systems have been made in references [1] and [2].

The specific application for which these instrumentation systems were developed is a NASA-Lewis high-pressure, high-temperature turbine rig reported in reference [3]. This rig will be used to investigate turbine cooling technology for a representative first stage turbine for advanced turbofan engines.

Turbine Rig and Instrumentation

The NASA-Lewis high-pressure high-temperature turbine rig for which these instrumentation systems were developed was designed to provide a turbine test environment of 4×10^6 N/m^2 (40 atm) of pressure and an ultimate gas path temperature of 2400 K. This high gas path temperature approaches stoichiometric conditions for current aircraft hydrocarbon fuels. The turbine rig contains a single stage 0.5 m dia air-cooled turbine with a shaft speed of about 17,000 rpm. These design conditions are representative of an envelope of foreseeable individual maximum levels of operating parameters that might be encountered in the first stage turbine of advanced turbofan engines.

A schematic view of the turbine rig test section (Fig. 1) shows the location of the instrumentation systems. A water-cooled retractable turbine vane camera probe for an IR photography system is mounted at the turbine inlet (Station 4) approximately 4 cm forward of the vane leading edge. A rearward-looking viewing port in the probe is purged with nitrogen to keep the optical surface free of any deposits from the gas path. The probe can be rotated by remote control through an arc of 90 deg to change the field of view. Probe mounting positions at three different circumferential locations are available at Station 4. The probe acutator and the recording camera are attached in tandem to the turbine rig pressure shell along the centerline of the probe and are

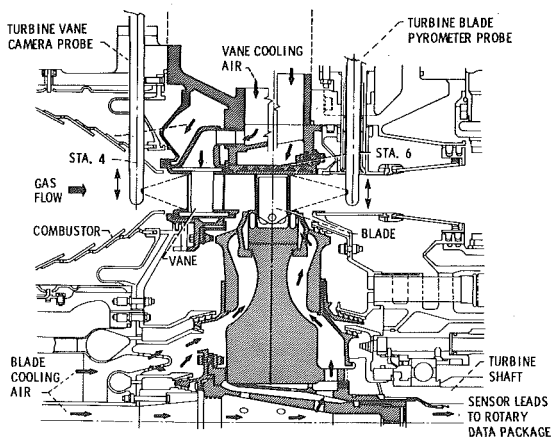

Fig. 1 Turbine test rig section

Contributed by the Gas Turbine Division and published in the symposium volume, *Measurement Methods in Rotating Components of Turbomachinery*, ASME, New York, 1980. Manuscript received for publication in the JOURNAL OF ENGINEERING FOR POWER May 22, 1980.

protected by an environmental enclosure. The camera is directly coupled to the probe and translates and rotates with it.

A water-cooled retractable turbine blade pyrometer probe is mounted at the turbine exit (Station 6) approximately 6 cm downstream of the blade trailing edge. A forward-looking nitrogen-purged viewing port in the probe permits viewing of the rotating blades. The probe contains a fiber optic bundle which extends about 5 m from the viewing port to interface with a sensitive silicon avalanche detector and associated hardware mounted in a protected position removed from the immediate vicinity of the turbine rig. The probe can be rotated by remote control through an arc of 90 deg. Probe mounting positions at three different circumferential locations are available at Station 6.

The rotary data package, not shown in Fig. 1, is centerline-mounted on an extension of the turbine shaft beyond the right edge of the figure. The rotary data package contains pressure transducers and electronics for handling pressure and temperature measurements. Instrumentation leads from temperature and pressure measurement points on the blades and the turbine disk run down the forward face of the disk and through the bore of the disk and the hollow turbine shaft and its extension to the rotary data package. The temperature sensors are sheathed chromel-alumel thermocouples. The pressure sensors are static taps in small diameter stainless steel tubes. Thermocouples along the radial run of the pressure tubing on the turbine disk provide a temperature distribution measurement for making density corrections to sensed pressure to compensate for rotational effects [4, 5].

Optical Surface Temperature Measurements

A surface emits radiation as a function of its absolute temperature. By combining radiation pyrometry and precision imaging, it is possible to obtain research quality temperature measurements over a large area of a heated surface with high spatial resolution. Radiation pyrometry techniques currently in use for determining surface temperatures in gas turbines measure the intensity of near IR radiation (0.9 μm) received from airfoil surfaces in one or several narrow bandwidths. Surface temperatures can then be calculated from the measured received radiation by using suitable calibration techniques.

For stationary vanes, surface radiance distribution can be measured by IR photography. A thermal image of a heated vane is recorded on IR film, the film is developed, and the film density distribution is converted through proper calibration into a surface temperature distribution. Rotating blades can be scanned photoelectrically and the detector output converted again through proper calibration into temperature in near real time. Descriptions of an IR photographic system for vane surface temperature measurements and a photoelectric scanning system for blade surface measurements that were developed for the NASA-Lewis turbine rig are given below.

IR Photography System

IR photography [6] has been used by NASA -Lewis in a number of experimental programs involving turbine cooling and thermal fatigue studies. Experience gained during these experimental programs has resulted in improved borescopes for obtaining quality images and in improved calibration techniques for routinely obtaining accurate relationships between film density and surface temperature. The IR photography system that will be used with the turbine rig was based on these developments.

System Description. The IR photography system for temperature measurements on stationary vanes in the turbine rig is shown in block diagram form on Fig. 2. The system consists of a remote-controlled camera (1) with an optical probe to image the vane radiation through an IR filter onto IR-sensitive film; a film processor (2); a micro-densitometer (3) to measure and record film density information over the entire thermal image; and a computer (4) provided with calibration data to calculate the temperature distribution from the film density record. The final result is a turbine vane temperature record (5) consisting of temperature profiles and two-dimensional contour maps of temperature distribution.

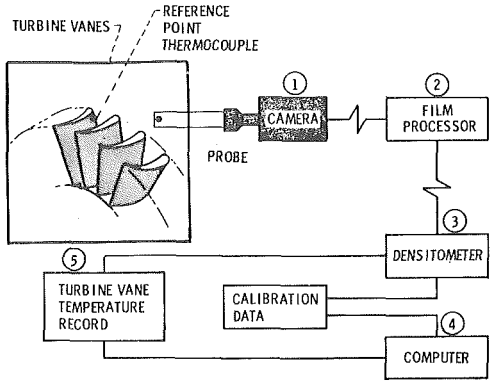

Fig. 2 Infrared photography system for stationary vane

The film calibration technique is detailed in reference [6]. An area of each film is exposed with a calibrated relative energy scale (step tablet on grey scale). This exposure establishes the film (detector) response curve. The film response curve is then correlated with a temperature distribution curve. This latter curve, the distribution of relative radiant energy with temperature, is a plot of Planck's equation integrated over the bandwidth of detection. The detector bandwidth is determined by the filter transmission function and the IR film spectral sensitivity. A thermocouple located on the vane surface in the camera field of view is used as a reference point. At this reference point, one known temperature and one known density are used to correlate the film response and temperature distribution curves. No correction for surface emittance is required with this relative method of temperature calibration.

The advantage of the IR photographic method is that a thermal image of a vane can be recorded in a fraction of a second and the image can be resolved into very small spot sizes with a microdensitometer. A thermal image for a particular camera exposure is limited to an average temperature span of about 200 K. However, this span is more than that required for recording temperature distributions on properly designed cooled vanes. A disadvantage of the method is that temperature data are not available during the time of the test. There is usually a delay of from several hours up to days because of the sequence of procedures required. In most cases this is not a serious drawback, and the detailed information available from a thermal image analysis compensates for the time delay.

Example of Results. An example of a photographic image analysis is shown in Fig. 3. For these tests, a film-cooled turbine vane was heated in a 1530 K gas stream in a thermal stress rig. A conventional photograph of the test vane is included in the figure and is used for dimensional reference and to locate surface features. The thermal image of the heated vane was recorded on 35 mm high speed IR film at a magnification of 0.2. A microdensitometer with a small measuring aperture was used to scan the image in two modes. One mode recorded a density profile scan (10× size) across the image. In this example, it was at the mid span location. The other mode records a contour map (10× size) in equal density increments over the entire thermal image. The density scale on the profile scan was calibrated into a temperature scale using the reference thermocouple and the calibration technique previously described. The contours on the map were converted into temperature by projecting corresponding locations from the mid-span profile curve to the contour map at the mid span location. Generally, all contours can be calibrated from one or two profile scans.

In similar tests, vanes were instrumented with an array of thermocouples. Using one thermocouple as a reference point, the photographically determiend temperatures at all other thermocouple locations agreed to within 1 percent of the temperature (expressed in °C) measured by the thermocouple.

Further Component Improvements. A video densitometry method is being developed to automate and speed-up the film data analysis of thermal images. This method substitutes a commercially available video image processor for the microdensitometer and a computer for the graphs and manual procedures. With the com-

puter-based image processing method, the film frame is indexed over a properly masked light box in a precision film transport mechanism. The light transmitted through the film frame is scanned by a special television camera which was selected by the supplier for its photometric accuracy (shading and linearity). This feature is important since the scanner is the source of the image data that is subsequently processed and analyzed. The output of the scanner is amplified logarithmically. This causes the scanner to operate as a densitometer because, by definition, density is the logarithm of the film transmission factor. The amplified scanner output is then digitized and stored on a magnetic disk.

This information is stored as 480 interlaced lines, each consisting of 620 8-bit picture elements. Each picture element represents one of 256 possible grey values from black (0) to white (255). The image is redisplayed on a television monitor and the grey level of any given point is obtained either from calculated coordinates or from reading the coordinates of a joystick-operated cursor. A calibration scheme to convert grey level to temperature was developed and programmed for the computer.

After further development, this video densitometry method will be added to the current IR photography system to expedite turbine rig film data analysis.

Photoelectric Scanning System

The customized photoelectric scanning system that will be used on the turbine rig is a modified version of a prototype system described in references [7] and [8]. The current system incorporates several improvements including: an electronic shaft angle encoder [9] in place of a magnetic pulse pickup for a more accurate trigger pulse, a reference lamp as part of the fiber optic probe to provide a calibration signal, a pulsed light emitting diode to check frequency response and provision for different wavelegnth (various filters) measurements in anticipation of a need to correct for reflected gas and carbon particle radiation at high gas path pressures. The problem of interfering radiation is discussed in reference [10] along with suggested methods to minimize its effect.

System Description. The customized photoelectric scanning system has optics and high speed electronics that are capable of resolving a spot diameter of 0.1 cm on a blade moving with speeds of the order of 300 to 400 meters per second. Near real time displays of temperature profile are generated for a single blade or for small groups of blades at steady state gas path conditions.

A block diagram of the system is shown in Fig. 4. The protected fiber-optic probe (1) is positioned in the gas path by a remotely controlled actuator and the fiber is focused in the plane of the turbine blades. As the heated blades rotate, the emitted radiation from the spot location (0.1 cm dia instantaneous field of view of the fiber) is transferred optically to a fast response silicon avalanche detector (2), thereby generating a continuous high resolution intensity profile which is monitored continuously on an oscilloscope (3). The amplified detector output is digitized by an analog-to-digital (A/D) converter (4) at ranges up to 2 MHz rate. A blade position sensor (5) supplies a trigger signal when the chosen blade enters the field of view. Starting with this trigger signal, a 200 point sample of the digitized detector output is stored in a high speed memory (6). This process may be repeated a number of times (equivalent to several revolutions of the turbine) to average out random noise. The number of chosen blades (usually 1 to 8) scanned with a 200 point sample is determined by the digitizing frequency and the speed of the turbine. The 200 data points are transferred at a slower rate from the memory to the computer (7) where each point is converted into temperature using pre-recorded calibration information. This calibration information is obtained prior to testing by focusing the optical probe onto an accurately known temperature source and relating the digital output of the A/D converter to the temperature. A blackbody oven is used as the temperature source. Therefore, a correction for the surface emittance of the blade is required with this absolute method of temperature calibration.

The timing and control logic circuit (8) provides interchange of control between the computer, the memory and the A/D converter.

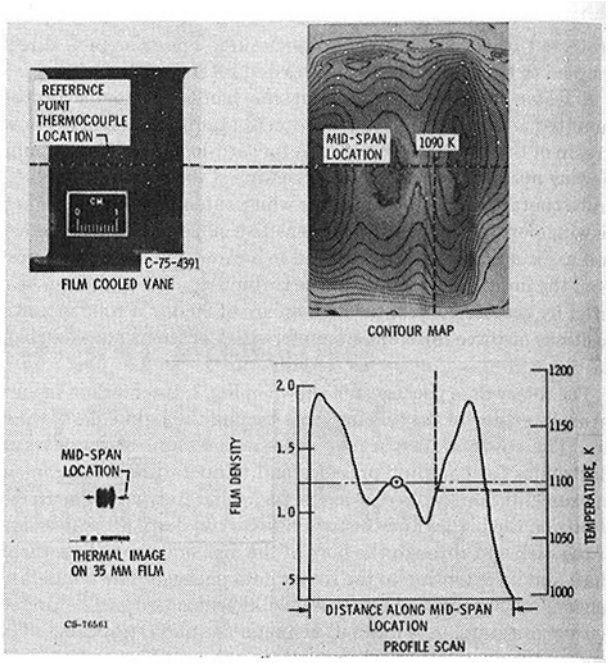

Fig. 3 Turbine vane temperature record

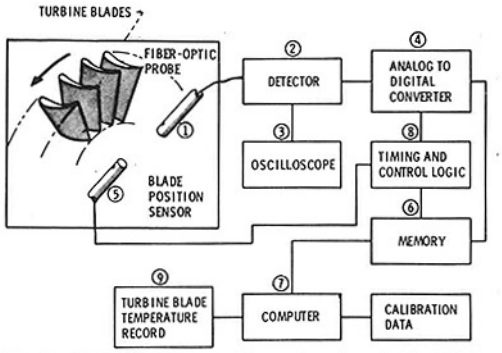

Fig. 4 Photoelectric scanning system for rotating blades

Through the logic circuit, the operator, via the computer, has control over the entire system. Processed data are presented on a CRT display in the form of a temperature profile and a listing of the 200 calibrated points making up the profile. A hard copy of the turbine blade temperature record (9) can be made in about 3 s. In addition to generating a single temperature profile scan record, the system can also obtain a series of scans over a range of radial locations, using the probe actuator, and present them in an isometric view. With additional computer processing the data can alternatively be presented as a two-dimentional contour map of temperature distribution.

Examples of Photoelectric Scanning Results. An example of data obtained with a photoelectric scanning system during a previous test in an engine described in reference [8] is illustrated in Fig. 5. The air-cooled turbine blades shown in the figure were instrumented with surface thermocouples. One blade had a ceramic coating on the surface in the form of a chevron pattern to examine the spatial resolution of the system. Turbine inlet gas temperature was 1640 K while maximum blade temperature was limited to 1200 K by adjusting coolant flow. The tip speed of the blade was 360 meters-per-second. Typical temperature profiles are shown in Fig. 5. In the center is an isometric display of temperature profiles made across the chevron pattern at the scan line locations (1–8) indicated on the blades. The origin of the temperature-position plot is progressively offset with each scan. The isometric view is used to obtain a qualitative record of temperature distribution over the area bounded by the scans as well as to observe surface features like the chevron pattern. The apparent lower temperature of the chevron is due to its lower emittance. In the lower part of Fig. 5 is a quantitative temperature profile at scan location number

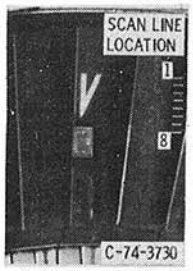

CONVECTION COOLED TURBINE BLADES

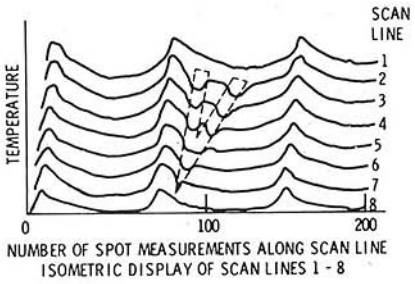

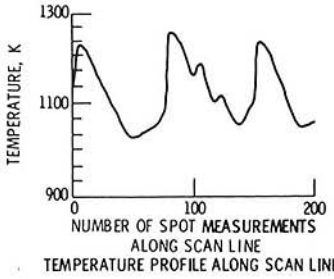

Fig. 5 Turbine blade temperature record

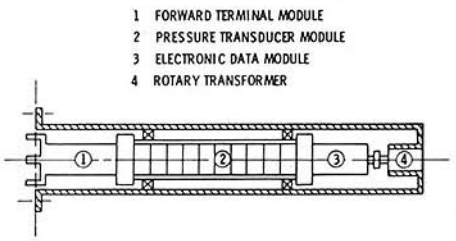

Fig. 6 Rotary data package

three. Comparison of temperatures measured by photoelectric scanning and by thermocouples agreed within 2 percent of the temperature level (expressed in °C).

Rotary Data Package

The purpose of the rotary data package is to house the pressure transducers, to process temperature and pressure signals and to provide a means of transferring these signals from a high-speed shaft to stationary readout equipment. The rotary data package for the turbine rig is designed to operate at a maximum shaft speed of 18,500 rpm. Earlier developmental versions of the current package have been described in references [11] and [12]. These earlier versions, tested at maximum shaft speeds of about 9000 rpm, had separate systems for handling temperature and pressure signals and used slip rings for analog signal transfer and "onshaft" electronic processing and a rotary transformer for digital signal transfer. Extensive engine testing with these units has proven the reliability and accuracy of various system components and has guided the design of the current package.

System Description. The rotary data package for the new turbine rig consists of four main subassemblies or modules as shown in Fig. 6. The package is of modular construction with pneumatic and electrical connectors to facilitate ease of fabrication, assembly and testing. Overall length of the package is approximately 1.0 m and the maximum diam of the stationary outer case is about 0.2 m. At the forward terminal module (1), the data package is coupled mechanically with an extension of the turbine shaft. Pneumatic and pressure tubing and thermocouple leads are routed through this shaft extension.

Differential pressure transducers are mounted on the shaft centerline in the pressure transducer module (2). The electronic data module (3) processes the analog pressure and thermocouple signals and converts them into coded eight-bit digital words. A total of 80 data channels (consisting of 63 thermocouple channels, 14 pressure channels and three calibration channels) can be handled in the electronic data module. However, the current pressure transducer module will accomodate only ten differential pressure transducers.

The rotary transformer (4) couples the coded digital signal train from the rotating electronic data module to stationary instrumentation leads and couples electrical power from a stationary supply to the rotating electronic data and pressure transducer modules.

Pressure Transducers. The differential pressure transducer used in the rotary data package has a four-arm Wheatstone bridge strain gage diffused on a silicon diaphragm. This type of transducer has shown excellent operating characteristics in rotary application testing [13]. The ranges of the transducers used are 0.3, 0.6 and 1.7×10^5 N/m^2 (5, 10, and 25 psig), the physical size of all transducers is the same (about 0.6 cm dia and 1.8 cm length).

Each transducer is enclosed in the center of a capsule (Fig. 7) which provides two sealed chambers corresponding to the transducer pressure inputs. Each chamber contains an 0-ring sealed port that interfaces with the pressure trasnducer module. The capsule also has four hermetically sealed electrical leads for the power and signal connections to the enclosed transducer. Ten such capsules (with differential pressure transducers enclosed) are mounted in tandem along the centerline of the pressure transducer module.

Temperature Signals. The temperature signals in the rotary data package originate from thermocouples in the turbine section of the turbine rig. These signals enter the package through type K (Chromel-Alumel) leads on the centerline of the hollow turbine shaft extension. The type K leads are soldered to strips in the forward terminal module. All internal wiring in the package is done with copper. A monitoring thermistor is mounted on the part holding the soldered strips where the transfer from type K to copper leads occurs. This thermistor is used to obtain a cold junction reference temperature for the thermocouples.

From the forward terminal module, the thermocouple leads are routed along the outer surface of the pressure transducer module to the electronic data module. After processing and conversion to coded digital words in this latter module, the thermocouple signals are transmitted through the rotary transformer to stationary readouts.

Electronic Data Module. The electronic data module (Fig. 8) is an assembly of ten double-sided printed circuit boards with an overall diameter of about 6 cm and an overall length of 15 cm. Commercially available integrated circuits are used whenever possible and those components most sensitive to acceleration forces are mounted near the center of the boards. Interboard connections are made near the periphery of the boards to facilitate testing of the assembled boards. A clear epoxy is used to hold the components securely to the assembly.

A block diagram of the rotary data package including inputs is shown on Fig. 9. The processing of the thermocouple and pressure signals in the electronic data module consists of a sequence of multiplexing, amplifying, converting from analog to digital and transmitting to stationary readouts through the windings of the rotary transformer. The data output was in the form of a digital train of eight-bit words. Electrical power was fed to the package through two of the transformer windings. The power was rectified and regulated in the electronic data module and distributed to the components of this module and to the pressure transducers. The 12 kHz frequency of the input power is used as a timing (clock) signal in the A/D convertor.

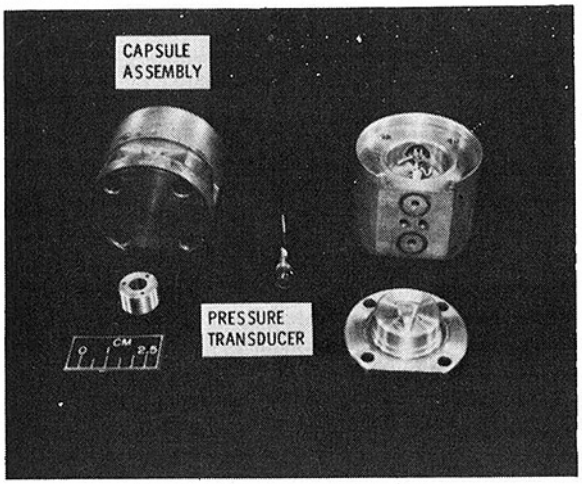

Fig. 7 Pressure transducer capsule

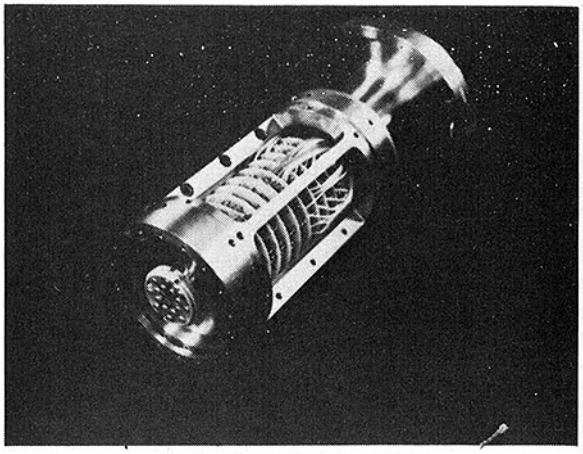

Fig. 8 Electronic data module

A major improvement to the electronic data module in the current data package is the use of complimentary metal-oxide-semi-conductor (CMOS) circuitry. This permits lower power levels and common power supplies to be used. Total power into the transformer is about 4 W. The power regulator is a 15 V I.C. (integrated circuit) which replaces the zener diodes used in the prototype versions.

Prototype Performance. System error on the prototype rotary data package reported in reference [12] was 0.5 percent full scale. Thermocouple readings transmitted digitally via the rotary transformer were compared to simultaneous analog readings from a slip ring assembly. Agreement was within 2° C. Similar characteristics are anticipated with the current package.

Concluding Remarks

Efforts at NASA-Lewis to improve techniques for measuring temperatures and pressures on gas turbine components have resulted in the development of several operating instrumentation systems for use on a high-pressure high-temperature turbine rig. An infrared photography system for obtaining thermal maps of the metal surface temperature on the stationary vanes shows agreement with thermocouple measurements within 1 percent of the temperature reading (expressed in °C). Continuing developmental work on this system will concentrate on replacing the current manual method for film-image analysis with a computerized video densitometer method.

A customized photoelectric scanning system for blade metal surface temperature measurements will resolve a spot diameter of 0.1 cm on a blade moving at about 400 m/s. The data can be displayed in near real time as a spot temperature or as temperature profiles on a single blade or on several adjacent blades. Comparisons of temperatures measured by photoelectric scanning and by thermocouples showed agreement within 2 percent of the temperature level (expressed in °C).

A rotary data package has been developed that will digitize analog temperature and pressure signas on a high-speed (17,000 rpm) shaft and transfer these digitized signals via a rotary transformer to stationary readouts. Agreement between the same thermocouple reading transferred by a prototype of this sytem and by a slip ring was consistently within 2° C.

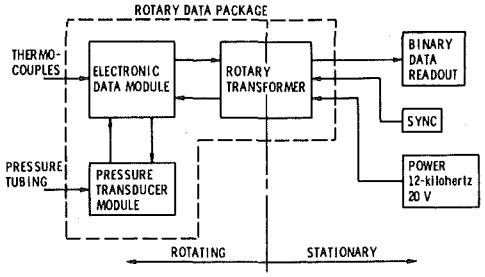

Fig. 9 Rotary data package functional block diagram

References

1 Pollack, F. G., "Advances in Measuring Techniques for Turbine Cooling Test Rigs," NASA TM X-68100, 1972.

2 Pollack, F. G., "Advances in Turbine Blade Temperature Measurements," NASA TM X-71878, 1976.

3 Cochran, R. P. and Norris, J. W., "A High-Pressure, High-Temperature Combustor and Turbine-Cooling Test Facility," NASA TM X-73445, 1976.

4 Liebert, C. H. and Pollack, F. G., "Flow Measurement in Base Cooling on Air Passages of a Rotating Turbine Blade," NASA TN D-7697, 1974.

5 Warshawaky, I., "Instrumentation for Propulsion Systems Development," NASA TM-73840, 1978.

6 Pollack, F. G. and Hickel, R. O., "Surface Temperature Mapping with Infrared Photographic Pyrometry for Turbine Cooling Investigations," NASA TN D-5179, 1969.

7 Buchele, D. R. and Lesco, D. J., "Pyrometer for Measurement of Surface Temperature Distribution on a Rotating Turbine Blade," NSAS TM X-68113, 1972.

8 Uguccini, O. W. and Pollack, F. G., "High-Resolution Surface Temperature Measurements on Rotating Turbine Blades with an Infrared Pyrometer," NASA TN D-8213, 1976.

9 Powell, J. A.: Electronic Shaft Angle Encoder; NASA Tech. Brief B77-10351, 1977.

10 Buchele, D. R., "Pyrometric Surface Temperature Measurement in the Presence of Interfering Radiation," NASA—in process1979.

11 Pollack, F. G., Liebert, C. H., and Peterson, V. S., "Rotating Pressure Measuring System for Turbine Cooling Investigations," NASA TM X-2621, 1972.

12 Lesco, D. J., Sturman, J. C., and Nieberding, W. C., "Rotating Shaft-Mounted Microelectronic Data System," NSAS TN D-5678, 1970.

13 Minkin, H. L., "Performance of Some Miniature Pressure Transducers Subjected to High Rotational Speeds and Centripetal Accelerations," NASA TM X-71791, 1976.

The Design, Development and Operation of Gas Turbine Radio Telemetry Systems

J. G. B. Worthy

Manager,
Electronics and Instrumentation Research Group,
Aero Division,
Rolls-Royce Ltd.,
Derby, England.

Measurements made on the rotating components of aero-gas turbines are among the most difficult of instrumentation problems. Success brings considerable reward, however, by providing a means of verifying design predictions and investigating unforeseen phenomena. This paper describes the Rolls-Royce approach to this problem and the principles used in the design of over 30 radio telemetry systems designed and manufactured within the company. A summary of operating experience reviews the problems encountered and measures taken to overcome them. The paper concludes with an impression of future requirements which are receiving attention.

Introduction

As designs and materials are pushed nearer to their limits, it becomes increasingly necessary for the research, design and development engineer to examine the physical conditions applying to the rotating components of gas turbine aircraft engines. This information is usually obtained by running instrumented development engines on test beds, where service conditions are reproduced as accurately as possible. It is also common practice to evaluate new materials and design techniques on research rigs and finally to demonstrate integrity by flight testing. Information on the rotating components subjected to this testing may be used to verify design predictions and enable more accurate forecasting of component lifetime. This can make big financial savings by allowing longer life to be declared for major components. Rotor measurements can also assist in understanding why a component's behavior is not as predicted. Instrumentation can supply empirical data to support or modify a theoretical model.

The properties of greatest interest are usually temperature and strain (both dynamic and static strain). Sometimes pressure and other measurements are required. Typical subjects for study are vibration modes in shafts, disks and blades, or the strain distribution in disks subjected to a steady load during rotation. Surface temperature distributions are frequently of interest on disks and blades. These requirements may arise on any shaft of a multiple-shaft engine and the problem of making the measurement is particularly acute on the Rolls-Royce RB211 which is a three-shaft configuration.

It is often impossible to mount conventional rubbing slip rings because of restricted space or undesirable because of their inaccuracy and unreliability. An electronic system is required which will transfer measurements made on low, intermediate and high pressure rotors in an operating engine to a stationary point where they can be recorded and analyzed.

Several significant contributions have been made to this problem over the past 20 years. The published work falls into three main categories: the development of in-house systems to solve specific problems, commercial systems for general application, and customer applications of commercial systems. Notable examples are included in the References (1–6). The system of Lesco, et al. [1] is remarkable for its use of digital transmission at a time when integrated circuit technology was in its infancy. O'Brien, et al. [2] have clearly demonstrated the feasibility of transmitting several channels of wide-band pressure information and have successfully applied the technique to the study of rotating compressor blades. The work of Colangelo and Schlereth [3], and Donato and Davis [4] has also added considerably to the knowledge on rotating telemetry. Excellent commercial systems are available as described by Adler [5], and Kemp [6] has described their successful application to gas turbines.

Constraints on the Measuring System

A radio telemetry system specification suffers from conflicting requirements in this environment. It requires high accuracy for engine component life prediction, but must operate over a wide range of temperature and acceleration. It must have a large measurement capacity, but occupy very small volume. It may be required to operate continuously for long periods, inaccessible within an engine, and demonstrate at any time during its operation the accuracy and validity of its output. The system should cater to a wide range of applications and environments using a standard set of modules. These principles dictated the design philosophy of the Rolls-Royce system, and wherever possible advantage has been taken of advances in electronic technology to approach more closely the ideal.

The nature of its business obliged Rolls-Royce to enter the radio telemetry field in this application some 20 years ago. At that time, electronic technology did not permit rotating circuitry and a system was developed based on multi-channel inductive couplings [7].

One pair of couplings supplied power at radio frequency to a strain gauge bridge, another pair transferred the amplitude-modulated bridge output to the ground station. Up to 12 channels were available in this way and the system is still in use in some installations.

As electronic component technology advanced, this technique led to rotating electronic modules for strain gauge polarizing, signal conditioning and radio frequency transmission [8]. The minimum volume was achieved by adopting a policy of minimizing the number of radio frequency transmitter modules, which contained the bulkiest components. The minimum acceptable number of simultaneous

Contributed by the Gas Turbine Division and published in the symposium volume, *Measurement Methods in Rotating Components of Turbomachinery*, ASME, New York, 1980. Manuscript received for publication in the JOURNAL OF ENGINEERING FOR POWER May 22, 1980.

channels was considered to be six, with the requirement for large measurement capacity satisfied by transducer switching on each channel. However this approach was still a compromise in reliability, as one transmitter failure could render several transducers inaccessible.

There was already considerable experience in radio frequency power transfer, so inductive coupling of power was adopted from the very beginning. This avoided the problems of lifetime and reliability associated with batteries operated under these conditions. A further inductive coupling was provided which enabled operator control to be exercised over the rotating electronics. This added complexity was considered justified since confidence in the system was increased by providing a calibration for each transducer during operation and allowing transducer polarization to be removed under operator control.

This latter technique has proved invaluable in distinguishing genuine signals from noise generated by hostile environments or transducer wiring problems. These criteria have remained the basis for the latest radio telemetry systems designed at Rolls-Royce.

Design of Rolls-Royce Telemetry Systems

Figure 1 shows the diversity of applications for the system in the RB211. There are similar applications in most other current engine projects. The three main configurations for high, intermediate and low pressure shafts are shown, with an example of a one-off diagnostic package mounted in the step-aside gearbox.

Figure 2 is a system block diagram, showing the three rotor-to-stator interfaces. The power section comprises an oscillator in the ground station which transfers power at 485KHz across an inductive coupling to power supply modules on the rotor. These modules supply power to the remaining switching, signal conditioning and transmitting modules. In dynamic strain measurement, a control section is included. This section generates a digital code in the ground station containing information on transducer address; whether a calibration signal is to be generated across the transducers and at what frequency; and whether transducer polarizing is to be applied. This code is transferred across a second inductive coupling to transducer switching modules where it is decoded and the system assumes the required function.

The transmission section takes the output signals from the addressed transducers, conditions them and transfers them to the ground station on up to six frequency modulated carriers using a capacitive coupling. FM receivers demodulate these carriers and the resulting information is recorded on analogue magnetic tape. In the case of temperature and static strain measurement, no control section is included and the transducers are time-division multiplexed at a predetermined rate. The transmission section accepts the transducer signals supplied by the multiplexer and transmits them using up to 6 FM carriers. The data are then digitized in the ground station and converted to engineering units by a computer-based data acquisition system.

Most of the logic and switching functions required on the rotor are included in a custom-designed, large-scale integrated circuit, whose block diagram is shown in Fig. 3. This circuit has two main modes of operation. The first is used in dynamic strain circuits, where frequencies between 5Hz and 27KHz are required to be transmitted from a number of strain gauges. Each L.S.I. circuit may have up to 16 gauges connected but has only two analogue output ports. The circuit accepts the digital code which is repeatedly transferred from the stator and checks it for errors. If it detects no errors, the word is loaded into the main store. If an error is detected, the contents of the store remain as they were previously.

The information contained in the store is decoded to give a 1 to 8 transducer selection, a calibration frequency and a polarization control. The I.C. connects the two addressed transducers to its two analogue output ports and polarizes them with constant current if required by the operator. It may also modulate the constant current by an amount determined by precision components, to generate an accurate calibration signal at the required frequency. The I.C. also retransmits the transducer selection address to the ground station using a supplementary FM channel, to assure the operator of the origin of his data. Each I.C. modulates two transmitters, with a present maximum channel capacity of six transmitters and 48 strain gauges.

The second mode of operation of the device is used for static strain, temperature and pressure measuring systems. In the case where data is varying only slowly, the transducers may be accessed sequentially and the custom I.C. can be made to free-run. Its dual switching ca-

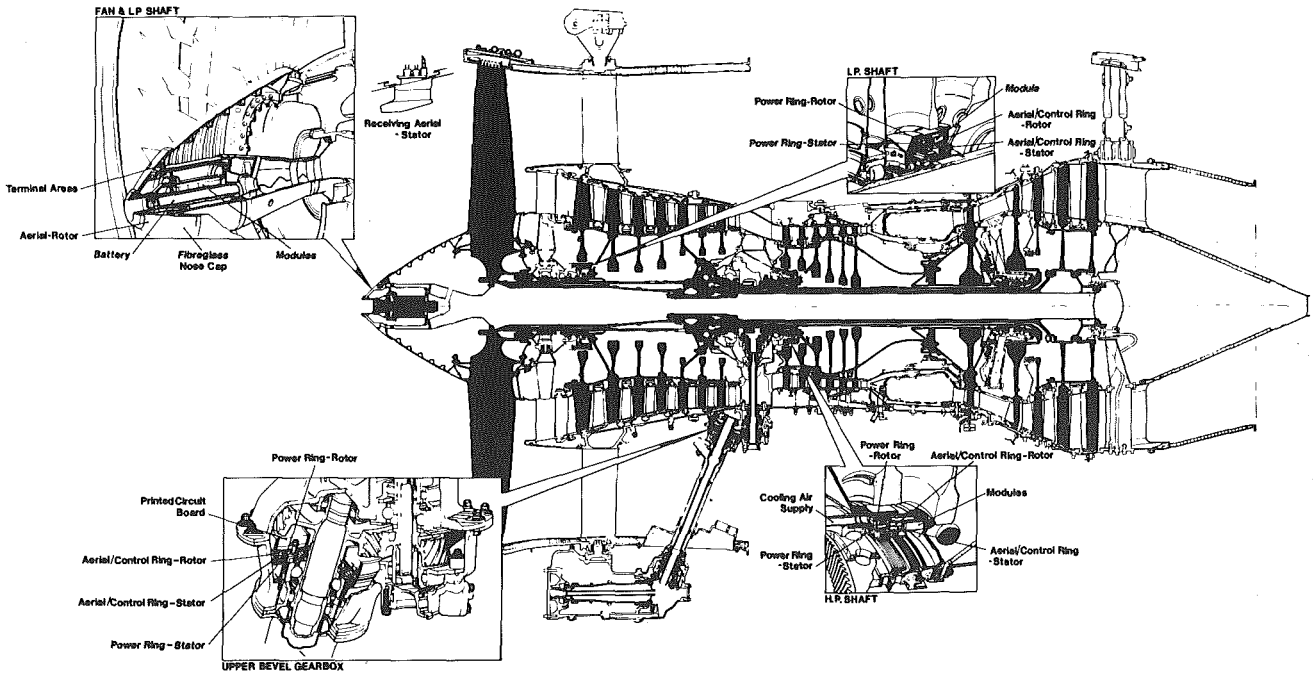

Fig. 1 RB211 radio telemetry systems

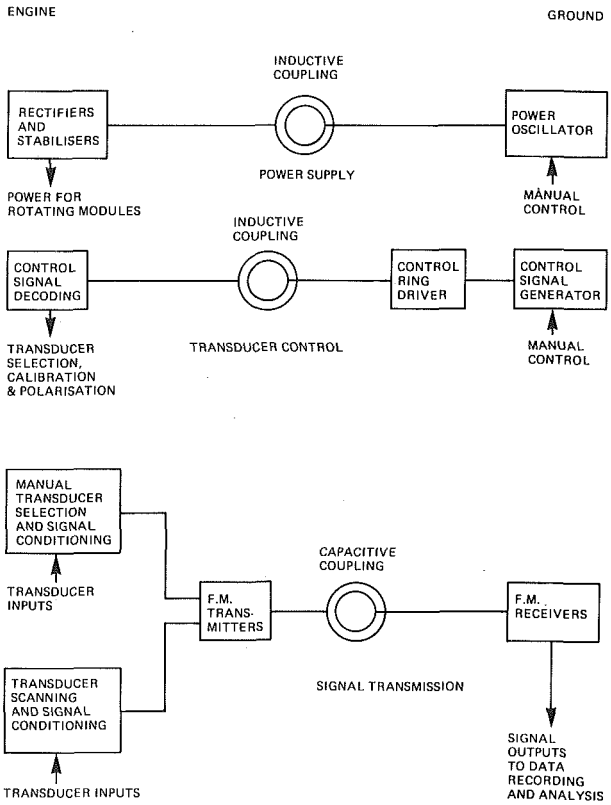

Fig. 2 Block diagram of the telemetry systems

pability is then normally used to switch transducers differentially into a balanced amplifier, reducing its capacity from 2 out of 16 to 1 out of 8. Each I.C. may drive a single transmitter, in which case the capacity is further reduced by the necessity to provide a calibration level in place of one transducer. If thermocouples are the signal source, two further selections are sacrificed; one is dedicated to an external resistive transducer for measuring cold-junction temperature, and another to a precision resistor for calibrating this transducer. This gives the flexibility of allowing cold junctions to be situated on any convenient thermal plane and prevents inaccuracy caused by thermal time delay in compensation devices. Much greater channel capacity per unit volume is achievable at the expense of redundancy by cascading a number of selection I.C's into a single transmitter. Up to 64 selections on one transmitter have been achieved in this way and have run successfully for many hours during engine testing.

The chip layout is shown in Fig. 4. It is specifically designed electrically and mechanically to withstand an environment of 160°C and 30,000 g. The device geometry is determined by a number of process constants which are strongly temperature dependent. In the absence of any information on operation at these temperatures at the time, prolonged testing of standard devices was undertaken under realistic environmental conditions before proceeding with the custom chip. Encouraging results led to the chip design, making use of process characteristics extrapolated to 160°C. All devices functioning at 120°C are acceptable, as this is the present maximum rating for the whole system, but a high proportion of those accepted are within specification at 160°C.

Approximately 35 radio telemetry units based on these principles either exist or are in the course of construction. The majority of systems are configured using a standard range of modules; examples are shown in Fig. 5.

An approved range of standard I.C.'s and discrete components has been drawn up, following extensive environmental testing.

The most common system configuration is that used on H.P. and I.P. shafts where an annulus of modules is contained within a metal ring which also houses the inductive and capacitive couplings. A typical system is shown in Fig. 6. Units of this construction have to survive in environments normally as hot as 350°C, so air cooling is provided to limit the temperature to a minimum of 120°C.

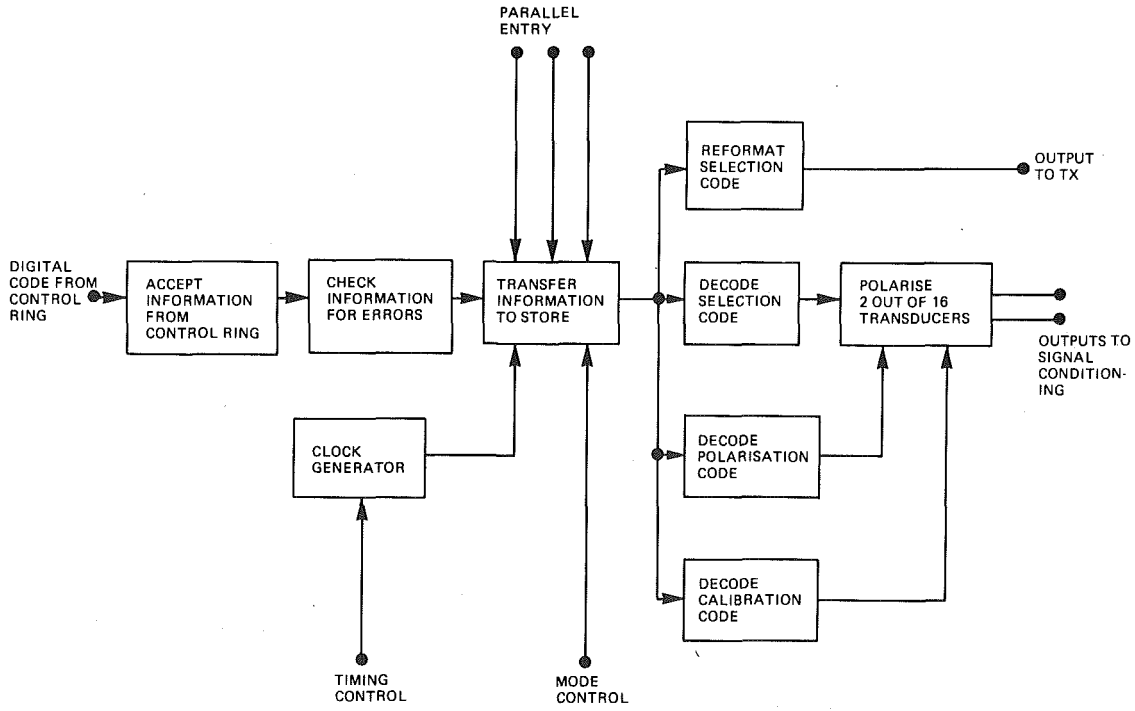

Fig. 3 Block diagram of transducer selection integrated circuit

The top left corner of Fig. 1 shows an L.P. system intended for dynamic strain measurement on the fan and shaft of the RB211 in flight. This system is known as the Battery Energised Radio Telemetry system (B.E.R.T.) This is the only battery-powered system and is rated for approximately 9 hr battery life. Six channels are presently available, with one channel allocated to a temperature multiplexer which monitors the internal temperature distribution in the telemetry system. This environment is controlled by a mixture of ram air and engine anti-icing air to maintain satisfactory conditions for the battery under the extremes of a hot desert airfield and an altitude of 10,000 m. Radio frequency transmission takes place from an antenna in a fiberglass nose cone section to a receiving antenna 1 m away in the engine casing. An existing engine pressure probe is isolated electrically and used as the receiving antenna, to avoid any modification to the engine intake.

A unit referred to as the Radio Frequency Slipring Unit (RUFUS) is a bolt-on replacement package for conventional rubbing slip rings (Fig. 7). This is constructed from the standard modules and opens to provide access to all modules while powered through its inductive coupling. By this means it is easy to service or to change the measurement function without a complete strip. This unit is designed to avoid the problems of short lifetime, noise and inaccuracy associated with slip rings in certain applications.

Performance in Service

Table 1 summarizes test experience with this equipment in the Derby Engine Group of Rolls-Royce. The success rate is the ratio of tests in which the telemetry unit performed adequately, to the total number of tests. The most commonly used system is the dynamic strain, one unit of which has run for over 200 hr. This is considerably longer than the required duration of most development tests. An example of the results obtained after spectral analysis is shown in Fig. 8. This is a form of plotting which presents dynamic strain gauge signals in a manner which is relatively easy to interpret. The thick shaded line across the center reproduces the total signal obtained from

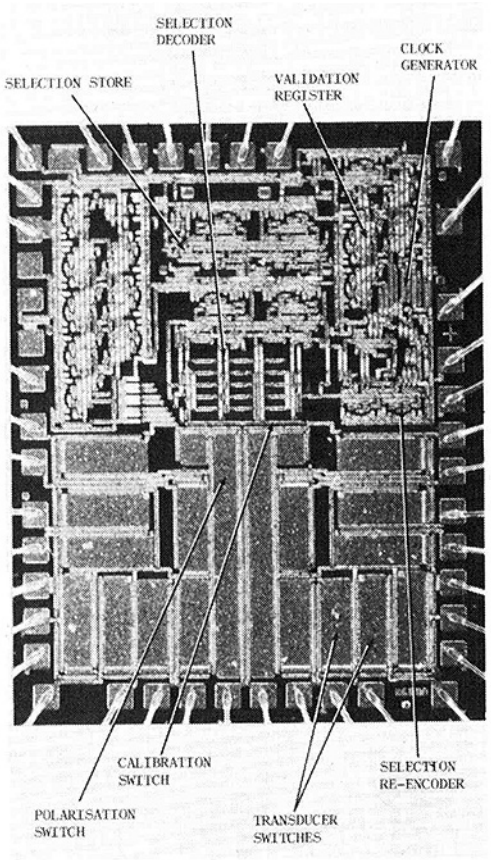

Fig. 4 Transducer selection chip layout

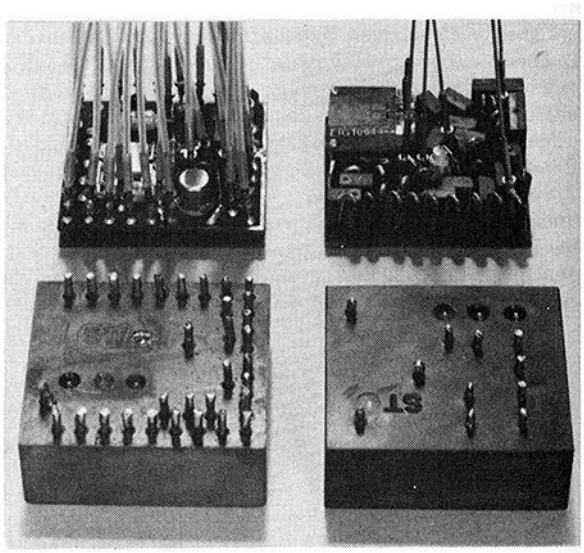

Fig. 5 Standard telemetry module

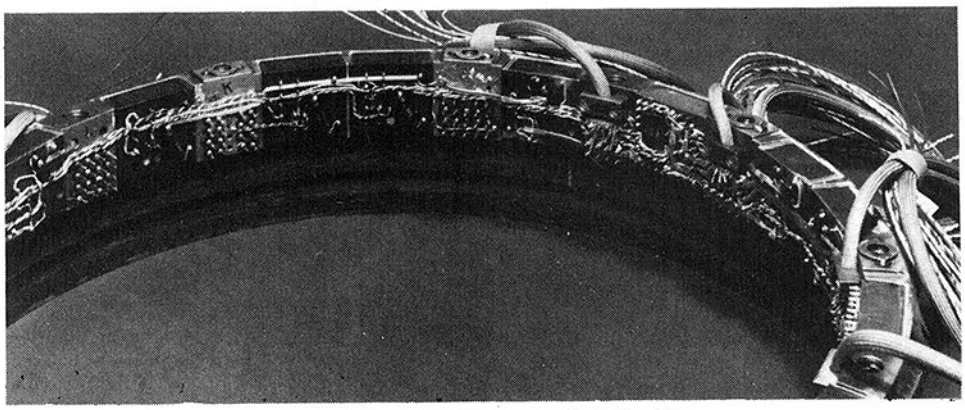

Fig. 6 H.P. and I.P. telemetry unit construction

the strain gauge using a radio telemetry system, during an acceleration followed by a deceleration. Immediately below this is a smoother curve representing H.P. rotor speed with a superimposed scale of percentage of maximum rated speed.

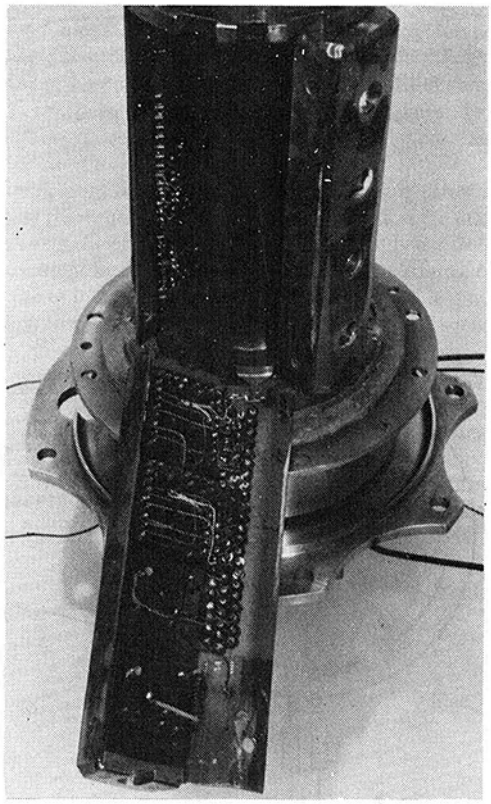

Fig. 7 RUFUS slip ring replacement package

The total strain signal is applied to a real time spectrum analyzer which produces the curves shown in the upper and lower areas of the presentation. The upper display is a plot of frequency (vertically) against time (horizontally). The continuous curves represent forcing vibrations at multiples of engine speed and are intensity-modulated by strain amplitude. Resonances can be detected by local intensification of these curves where they coincide with a component's natural frequency. The lower part of Figure 8 is an alternative plot of the same information, plotted as strain amplitude (vertically) against time (horizontally). The intensification is now proportional to frequency, so that superimposed resonances can be distinguished from each other by the intensity of the plot. Vertical lines have been added to the plot to indicate resonant conditions detectable on both kinds of display. Information presented in this convenient form enables rapid identification of blade and disk vibration modes and determination of whether levels are satisfactorily low. The design of the analysis and display system are beyond the scope of the present paper, which also precludes discussion on the implication of experimental results on engine design.

As an endurance exercise, a slip-ring replacement unit performed correctly through a 70 hr test including 664 cycles from 12,200 to 15,300 rpm. Over 12 hr were spent at the maximum speed.

Table 1 Radio telemetry operating experience in major Derby engine projects up to July 1979

Engine	Type of Unit	No. of Tests	Success Rate (percent)	Total Running Time (hrs)
RB211	HP	28	75	136
	IP	9	78	180
	LP (BERT)	7	83	155
SPEY (Phantom)	HP	20	90	70
ADOUR	HP	5	80	7
RIGS	RUFUS	10	80	145
	HP-TYPE	12	92	482

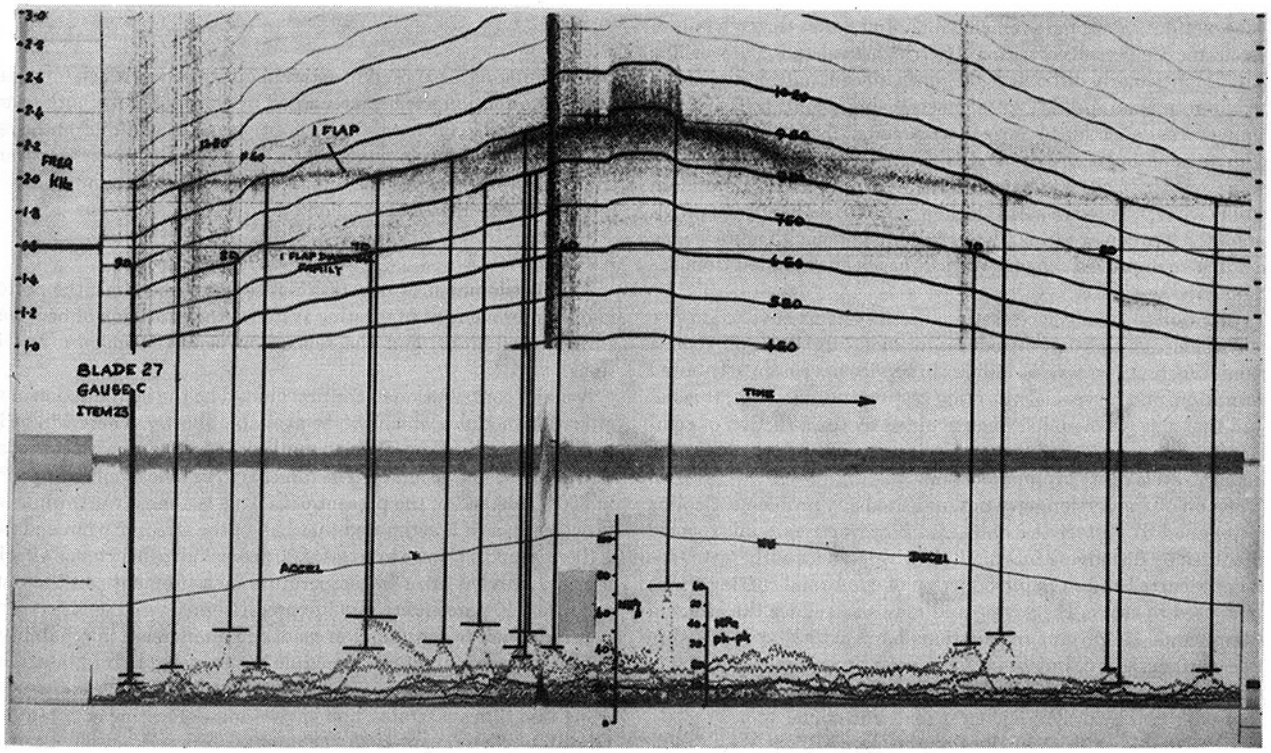

Fig. 8 Presentation of dynamic strain data

The most complex unit so far was configured to measure dynamic strain (8 gauges), static strain (16 bridges and calibrations) and temperature (16 measurements including thermocouples on metal surfaces, resistive transducers on cold junction thermal planes and on bridge completion networks, and calibration sources). Useful results were obtained from this unit during a short test and an example is shown in Fig. 9. However this unit was a major assembly task and required development to reduce the wiring complexity. The highest capacity system so far measured 64 thermocouples an calibrations, and ran successfully in an RB211 test for over 18 hr.

Several problems have arisen during the course of the work which have required system development. Most of these have been due to the hostile environment in which the equipment must work.

Problems due to rotation may degrade the signal quality or cause a total loss of data. The most common problem is the generation of spurious engine rotational frequency signals superimposed on the genuine signals. There are several ways in which this can be generated:

1 Poor antenna design can create enormous variations in received signal strength with rotation, in cases where the antenna circumference is not very small compared with a transmitter wavelength. The signal strength variations range from 1dB over 360 deg in a good design to worse than 40dB in a bad one and may be demodulated to give a spurious output. The solution in such cases is to adopt the antenna configuration shown in Fig. 10.
2 Variable antenna loading can pull the frequency of inadequately buffered transmitters. All transmitters now contain separate oscillator and antenna drive stages.
3 The proximity of stator metal work can cause dielectric variations around transmitter circuits and generate frequency modulation. This has been cured by screening transmitter modules.
4 A combination of poor power-coil and transmitter design can result in power supply ripple at engine rotational frequency and consequent frequency modulation. It is not normally difficult to avoid this problem by adequate design.
5 Lengthy wiring between the rotating electronic system and transducer can cause induced signal generation. Demagnetization of the appropriate engine components can reduce this problem.

More serious rotational problems sometimes arise through failure of electronic components or wiring due to high acceleration. Reversible failure is particularly difficult to diagnose, since it only occurs above a certain rotational speed. Typical mechanisms are integrated circuit bonding wires deflecting to cause short circuits, whisker-construction diodes causing open circuits and wiring shorting to ground when passing over sharp edges. The solutions are to design with aluminium bonding wires, bonded monolithic diodes and to make special provision for the location of wiring. Catastrophic component failure is rare, providing an approved range of devices has been compiled from environmental testing.

In addition to steady acceleration, these systems have to survive an environment which may introduce vibration, lubricating oil, cooling air and sometimes water. No failures in service have been attributed to vibration, and no special vibration testing is carried out. It is believed that this problem has been avoided by the selection of components and manufacturing techniques capable of surviving the necessary levels of steady acceleration.

Tests on oil immersion have not indicated any problems. Cooling air, designed to protect the units, did however create unexpected difficulties by dislodging intermodule wiring on an early test. This has not recurred since the introduction of conformal coating which is now used to secure the wiring and may also reduce the effect of contaminants. Rotor unit installations have not so far resulted in water contamination, but there have been occasional problems in external wiring and junction boxes on test rigs and in flight. These have been cured by providing better seals and connectors.

Special problems exist in the flight system (B.E.R.T.) as radio frequency transmission takes place across open space, and the receiving antenna is exposed to external interference. Much fan strain gauge information has been recorded by this technique both on engines mounted in the normal wing position and in an S-duct at the rear of the aircraft. Development work is proceeding on antenna and transmitter design with the aim of further increasing immunity to interference from commercial and military transmission.

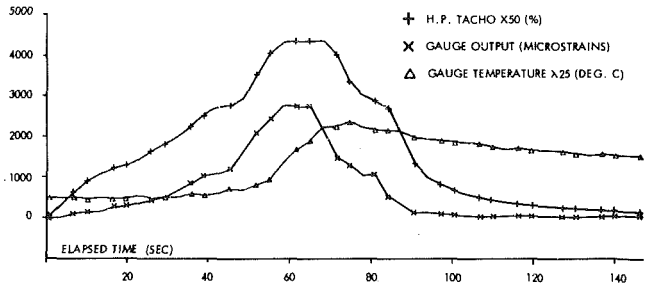

Fig. 9 Temperature and static strain data

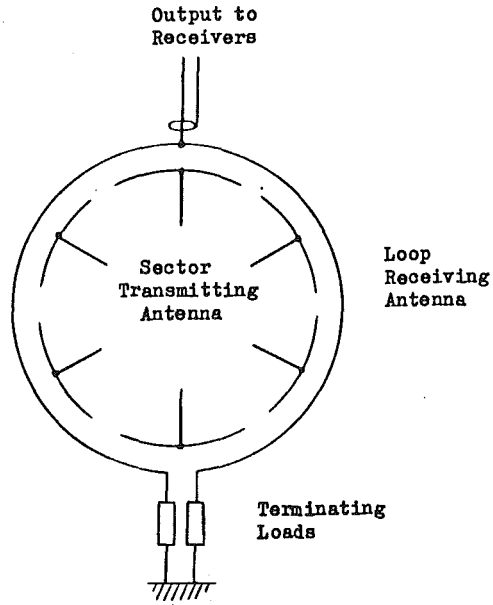

Fig. 10 Preferred antenna configuration

Future Work

The development of new techniques has three aims: the performance improvement of existing systems, the provision of new measuring capabilities, and the relaxation of environmental restrictions.

A major contribution to the first should be the introduction of digitization modules which will be available shortly. These will be introduced into the time-division multiplexed systems with the intention of increasing accuracy. The target is to be able to measure to 3°C in 600°C instead of the present 6°C. This is a most worthwhile improvement, as it is estimated that half of the stress in a hot end disk is thermal and a change in stress of 30 percent gives a factor of 4 in disk life. A 1 percent error in temperature measurement can therefore produce a 10 percent error in life prediction.

A reduction in construction costs and an increase in reliability is expected from a program of module design using hybrid integrated circuit techniques. The present range of modules is to be constructed using thin film substrates, and environmental testing of potentially hazardous components such as chip inductors and tantalum capacitors is proceeding. External intermodule and transducer input wiring

is being experimentally replaced by multi-layer printed wiring but no experience has yet been gained of this technique. A thick film static strain pre-conditioning module is also under development which it is hoped will alleviate the laborious assembly and calibration procedures which afflict the present multiplexed static strain system.

There is a strong case for increasing the operating temperature of both temperature and strain systems. Air cooling presently restricts the ambient temperature to below 120°C but may have a significant effect on the temperatures to be measured. A working temperature of 200°C would reduce the cooling air flow to a satisfactory level. The achievement of operating temperatures only a little higher would enable I.P. systems to operate without cooling air at all and a simple dynamic strain system for flight application is under consideration. Some preparatory work has already been done.

There are new applications for these techniques which will be investigated as resources permit. A new configuration for measuring heat transfer coefficient is to run shortly and a study has been made of a system variant for measuring inter-blade shock patterns. Acoustic emissions are of interest on rotating components and it is intended that a radio transmission system for this application will soon receive attention.

The significant in-house capability in this technology has been invaluable in certificating the RB211 family of engines. The design expertise is always present to support routine engine telemetry testing if required and to respond quickly to any new diagnostic application. It is Rolls-Royce's intention to make significant further progress in this field, which can benefit from most of the rapid advances made in microcircuit technology.

Acknowledgments

The author would like to acknowledge the work of his colleagues in the Electronics and Instrumentation Group of Rolls-Royce, Ltd. who have contributed to the design, development and manufacture of radio telemetry systems. He is also grateful to the Directors of Rolls-Royce Ltd. for permission to publish this paper.

References

1 Lesco, D. J., Sturman, J. C., and Nieberding, W. C., "Rotating Shaft-Mounted Microelectronic Data System," NASA Technical Note, No. D-5678, 1970.

2 O'Brien, W. F., Moses, H. L., and Carter, H. R., "A Multichannel Telemetry System for Flow Research on Turbomachine Rotors," ASME Paper No. 74-GT-112.

3 Colangelo, D., and Schlereth, F., "Special Purpose Telemetry for Jet Engine Environment," *Telemetry Journal,* Vol. 6, No. 2, Feb. 1971.

4 Donato, V., and Davis, S. P., "Radio Telemetry for Strain Measurement in Turbines," *Sound and Vibration,* Vol. 7, No. 4, April 1973, pp 28–34.

5 Adler, A., "Telemetry for Rotating Measurements on Turbomachinery," ASME Paper No. 78-GT-105.

6 Kemp, R. E., "Closed-coupled Telemetry for Measurements on Gas Turbines," *Instrumentation Technology,* Sept. 1978.

7 Drew, D. A., "Developments in Methods of Measuring Stresses in Compressor and Turbine Blades on Test Bed and in Flight," *Proceedings of the Institution of Mechanical Engineers,* Vol. 172, No. 8, 1958.

8 Jones, E. N., "Telemetry of Engine Rotor Test Data," Conference on "Methods of Transmitting Signals from Rotating Plant," Central Electricity England, Research Laboratories, Leatherhead, Surrey, England, June 25, 1970.